

Development of Novel Dyes for Photocatalytic Hydrogen Evolution. Design, Synthesis, Photophysical and Electrochemical Properties along with Time-Resolved Infrared-Spectroelectrochemical Simulation of Photocatalytic Processes.

Martyna Bartusiak B. Sc. (Hons)

A thesis submitted in partial fulfilment for the degree of Ph.D.

Supervisor: Prof. Mary Pryce

School of Chemical Sciences,

Dublin City University

December 2025

Declaration

I hereby certify that this material, which I now submit for assessment on the programme of study leading to the award of Doctor of Philosophy is entirely my own work, and that I have exercised reasonable care to ensure that the work is original and have conformed to the regulations on the use and declaration of Generative AI, and does not to the best of my knowledge breach any law of copyright, and has not been taken from the work of others save and to the extent that such work has been cited and acknowledged within the text of my work. I hereby certify that no Generative AI tools have been used in the creation of the thesis.

Signature: Martyna Bartusiak ID number: 17368533 Date: 08–12–2025

Dedicated to my grandfather Andrzej, who always believed in me and taught me that no dream is beyond reach. I know you are always keeping your fingers crossed for me up there



Pracę tę dedykuję mojemu dziadkowi Andrzejowi, który zawsze we mnie wierzył i nauczył mnie, że żadne marzenie nie jest poza zasięgiem. Wiem, że tam na górze zawsze trzymasz za mnie kciuki



Acknowledgements

Firstly, I would like to express my greatest gratitude and thank you to Professor Mary Pryce. Her passion for research, continuous support and help, allowed me to reach the final stages of my PhD. Thank you, Mary, for always finding time for me despite your busy schedules, for your guidance when it comes to conducting reactions and analysis of the data, and a lot of understanding over the past years. You provided me with countless opportunities and gave me the freedom in the laboratory to pursue my ideas that made me a better scientist but also taught me a lot of important life lessons. You gave me the chance to attend international conferences to present my research, and to carry out studies in different laboratories, and I really appreciate it a lot. Under your supervision, guidance and working in your research group, I have gained a lot of knowledge, experiences and inspiration, which will stay with me for a lifetime, but also, I have met incredible people. I will be forever thankful to you for being my supervisor and for everything you did for me.

I would like to thank my collaborators for all of their help. Thank you to Professor František Hartl and Dr. Martin Pižl for supervising my experiments at RAL, conducting DFT calculations, and for the discussions regarding TRIR-SEC experiments. I am also grateful to Professor Elizabeth Gibson and Dr. Owen Woodford for hosting me at Newcastle University and helping me with TAS and surface studies. Thank you for your guidance, support and willingness to help, I greatly appreciate it.

Thank you to the technicians at DCU in the School of Chemical Sciences. I am very grateful for your help and assistance, you have always ensured that my laboratory work was carried out without any problems, and you have always provided me with words of encouragement throughout the past years.

Thank you to the Mary Pryce Research Group. I will always remember our conference trips, coffee breaks, your help with my presentations and the small chats before starting our reactions! I know that sometimes I was bringing a bit of my stress and panic into your daily lives, but I apologise! I could always count on you to share with you my worries, my stress, and even my tears, and I really appreciate it. Special thanks to Jack, you were always willing to help me and supported me throughout the most difficult times!

I would like to thank my parents and my brother for all their support. Thank you for your sacrifices, opening new opportunities for me, for always believing in me and doing everything in your power to help me succeed especially when we moved to Ireland. You always encouraged and motivated me to do more and do better, and you taught me that with hard work anything could be achieved. Mom, Dad, thank you for everything!

Chciałabym podziękować moim rodzicom i bratu za ich wsparcie. Dziękuję za Wasze poświęcenia, za możliwości, które mi daliście, za wiarę we mnie i robienie wszystkiego, co w Waszej mocy, aby pomóc mi odnieść sukces, szczególnie gdy przeprowadziliśmy się do Irlandii. Zawsze mnie zachęcaliście i motywowaliście do działania i do lepszych wyników, i także nauczyliście mnie, że ciężką pracą można osiągnąć wszystko.

Mamo, Tato, dziękuję Wam za wszystko!

Finally, a huge thank you to my fiancé and my best friend, Jaka. You are the only person who truly knows what was happening behind the scenes of my PhD journey. You were always by my side in the times of so many doubts, stress and panic, and always offered me your support, patience (I must say a lot of patience!) and understanding, even when you were also the one struggling with completing your PhD. You motivated and encouraged me to keep going when all I wanted was to give up and reminded me of my self-worth when I doubted myself too many times. You have really brought light into the darkest moments of my life and shared with me my joy in my happiest times and without you, I can honestly say, that I don't think I would have reached the finish line. Thank you for being my partner, my soulmate, for all of your love, for your support and your belief in me. I will be forever grateful for having you in my life. *Zelo te ljubim ♡!*

"Nothing in life is to be feared, it is only to be understood. Now is the time to understand more, so that we may fear less."

— Maria Skłodowska-Curie

Research Output

Publications

Chapter 2 Bartusiak, M. Z., McGarry, R. J., Varvarezos, L., Brandon, M. P., & Pryce, M. T. (2023). Incorporation of perylene and naphthalene like ligands into ruthenium complexes: Synthesis, photophysical properties and electrochemistry. Coordination Chemistry Reviews, 495, 215365. https://doi.org/10.1016/j.ccr.2023.215365

Poster Presentation

"Application of Porphyrin Aggregation in Dye-Sensitised Solar Cells"- Martyna Bartusiak, Mary T. Pryce, Chemistry Day, 29th April 2022, Dublin City University, Dublin, Ireland.

"Application of Porphyrin Aggregation in Dye-Sensitised Solar Cells"- Martyna Bartusiak, Mary T. Pryce, SFI Marei Seminar, 28th May 2022, University of Galway, Galway, Ireland.

"Time-Resolved Spectroscopic Analysis of Novel Porphyrins and Utilisation of their Aggregation in Dye-Sensitised Solar Cells"- Martyna Bartusiak, Mary T. Pryce, 73rd ICI Chemistry Research Colloquium, 15th June 2022, University College Dublin, Dublin, Ireland.

"A Ruthenium-Naphthalene Diimide Assembly for Hydrogen Generation: Exploiting Charge Separation using Time-Resolved Infrared and Ultrafast Laser Spectroscopy." Martyna Bartusiak, Michael Brandon, Mary T. Pryce. 25th International Symposium on the Photochemistry and Photophysics of Coordination Compounds, 27th July 2023, University of Ulm, Ulm, Germany.

"Photocatalytic Hydrogen Production using a Ruthenium (II)-Naphthalene Diimide [Ru-NDI]$^{2+}$ Photosensitiser Probed by Time-Resolved Infrared Spectroelectrochemistry." Martyna Bartusiak, Martin Pižl, Michael Brandon, Partha Malakar, František Hartl, Mary T. Pryce. 45th International Conference on Coordination Chemistry, 29 – 30th July 2024, Colorado State University Fort Collins, CO, USA.

"TAS and TRIR Spectro-Electrochemical Studies of a Ruthenium-Naphthalene Diimide Ester Complex: Charge Transfer Dynamics and Excited States Populated in Solution and on a NiO Surface" Martyna Bartusiak, Martin Pižl, Florian Cerpentier, Partha Malakar,

Sayantan Bhattacharya, Owen Woodford, František Hartl, Elizabeth A. Gibson, Mary T. Pryce, 26th International Symposium on Photochemistry and Photophysics of Coordination Compounds, 8 – 12th July 2025, Milazzo, Italy.

Awards

Winner of the Visual Communication Competition for Postgraduate Researchers Research on Walls with the picture entitled “Artificial Photosynthesis and its role in the Hydrogen Economy-drawing inspiration from nature, employing dyes and capturing solar energy to generate hydrogen”, 27th September 2023, Dublin City University, Ireland.



Second place award for Postgraduate Flash Talk Presenter at Chemistry Day entitled “Hydrogen Exploration: An enlightening journey through artificial photosynthesis”, 10th May 2024, Dublin City University, Ireland.

Scientific Talks

Talk given to Irish secondary school students entitled “Hydrogen Exploration: An enlightening journey through artificial photosynthesis”, SciFest, 9th May 2024, Dublin City University, Ireland.

Postgraduate Flash Talk at Chemistry Day entitled “Hydrogen Exploration: An enlightening journey through artificial photosynthesis”, 10th May 2024, Dublin City University, Ireland.

Postgraduate Long Talk at Chemistry Day entitled “Photocatalytic Hydrogen Evolution: Closing Chapters of my PhD Journey and Opening Doors to a Sustainable Future”, 16th May 2025, Dublin City University, Ireland.

Table of Contents

Declaration……...i
Acknowledgements……iii
Research Output……...v
Publications……...v
Poster presentation……v
Awards……vi
Scientific Talks……vi
Table of Contents……viii
Table of Figures……xiii
Table of Schemes……xxx
Table of Tables……...xxxii
Table of Equations……xxxiii
Abbreviations……xxxiv
Units of measurement and symbols…… xxxvi
Thesis Abstract……..……xxxvii
CHAPTER 1……1
INTRODUCTION……...1
1.1 Abstract……..……..1
1.2 An Overview of the Energy Crisis: Why is it so important to take an action now?……..... 2
1.3 Addressing the Energy Crisis and Transition from Fossil Fuels to Renewable Sources of Energy……..……..5
1.3.1 Renewable Resources…….....5
1.3.2 Natural Photosynthesis…….....6
1.3.3 Artificial Photosynthesis.....9
1.3.4 The Water-Splitting Process in Photocatalysis.....10
1.4 Hydrogen Fuel as an Essential Component of Future Energy Systems……..……..12
1.4.1 The Hydrogen Prospect by 2050……...13
1.5 Dye-Sensitised Solar Cells……..……...…....13
1.6 Photocatalytic Carbon Dioxide Reduction and the Generation of Valuable Compounds…….....15
1.7 Photocatalytic Systems for Hydrogen Evolution in Solution and Their Components…….....17
1.7.1 Intramolecular and Intermolecular Photocatalytic Assemblies…….....17
1.7.2 Ruthenium-Based Photocatalytic Systems for Hydrogen Evolution.…….....20
1.7.3 Porphyrin-Based Photocatalytic Systems for Hydrogen Evolution…….……27
1.7.4 Naphthalene Diimide Compounds: Could They be Employed in Photocatalytic Hydrogen Evolution? …….....34
1.8 Photophysics and Photochemistry…….....38
1.8.1 Basic Principles of Spectroscopy…….....38
1.8.1.1 The Born Oppenheimer Approximation……...38
1.8.1.2 The Franck-Condon Principle…….....39
1.8.1.3 The Jablonski Diagram: The Foundation of Photophysics and Photochemistry..... 40
1.8.1.4 Molecular Absorption of Light and Electronic Transitions.……..41
1.8.2 Absorption, Emission and Infrared Spectroscopy……42
1.8.3 Time-Correlated Single Photon Counting (TCSPC) ……..……..42
1.8.4 Transient Absorption Spectroscopy (TAS) ……44
1.8.5 Time-Resolved Infrared Spectroscopy (TRIR) ……..45
1.8.6 Electrochemistry and Spectroelectrochemistry……...45

1.9 Parameters for Hydrogen Evolution Quantification……..……46
1.9.1 Turnover number (TON) ……....46
1.9.2 Turnover frequency (TOF) ……47
1.10 Conclusion……..47
1.11 References…….……...48
CHAPTER 2……...62
Incorporation of perylene and naphthalene like ligands into ruthenium complexes: Synthesis, photophysical properties and electrochemistry
2.1 Abstract…….....62
2.2 Introduction……63
2.3 Design and synthesis of molecular structures.……65
2.3.1 Core expansion of NDI/PDIs……..65
2.3.2 Imidization condensation……69
2.3.3 Axial ligation……...81
2.4 Photophysical properties of Ru(II)-NDIs and Ru(II)-PDIs..……..…..…….. 84
2.5 Electrochemistry……..101
2.6 Promising Applications and Conclusion…….……..112
2.7 References……115

CHAPTER 3……121
Ruthenium (II)-Naphthalene Diimide Photosensitiser in Catalytic Hydrogen Production Probed by Time-Resolved Infrared Spectroelectrochemistry
3.1 Abstract……...…….……121
3.2 Introduction……..123
3.3 Results and discussion……..128
3.3.1 Synthesis……...128
3.3.2 UV-vis spectroscopy and emission spectra…….……...……129
3.3.3 Electrochemistry……...131
3.3.3.1 Cyclic Voltammetry……...131
3.3.3.2 UV-vis spectroelectrochemistry…….……...….133
3.3.3.3 IR spectroelectrochemistry……135
3.4 Excited state properties of $RuNDI^{2+}$……136
3.4.1 Parent $RuNDI^{2+}$……136
3.4.2 Electrochemically reduced $RuNDI^{+}$ and RuNDI…….……..139
3.4.3 Nanosecond transient absorption studies in solution……140
3.4.4 Nanosecond transient absorption studies under photocatalytic conditions……141
3.5 Photocatalysis results……...143
3.6 Conclusion……...148
3.7 Experimental……148
3.7.1 Materials and methods……..148
3.7.2 Electrochemical measurements……149
3.7.3 Spectroelectrochemistry.……...149
3.7.4 Nanosecond transient absorption measurements……...149
3.7.5 Time-resolved infrared measurements……..149
3.7.6 Photocatalytic H_2 evolution experiments……..150
3.7.7 DFT calculations……...150
3.8 References……151

CHAPTER 4……157
Time-Resolved Infrared Spectroscopy, Spectroelectrochemical, and Transient Absorption Studies of a Ruthenium-Naphthalene Diimide Ester Complex: Insights into Charge Transfer Dynamics and the Excited States Populated in Solution and on a NiO Surface.
4.1 Abstract……157
4.2 Introduction……159
4.3 Results and discussion……163
4.3.1 Synthesis……163
4.3.2 UV-vis and emission spectroscopy……164
4.3.3 Electrochemistry……165
4.3.4 UV-vis Spectroelectrochemistry (UV-vis-SEC)……167
4.3.5 IR-Spectroelectrochemistry (IR-SEC)……171
4.3.6 Time-Resolved Infrared Spectroscopy (TRIR)……173
4.3.7 Nanosecond transient absorption studies in solution and under photocatalytic conditions (ns-TAS)……175
4.3.8 Picosecond transient absorption (ps-TAS)……179
4.3.9 Time-Resolved Infrared Spectroelectrochemistry (TRIR-SEC)……182
4.3.10 Photocatalytic results……186
4.3.11 Preliminary chronoamperometry measurements and immobilisation studies…187
4.4 Conclusion……189
4.5 Experimental……190
4.5.1 Materials and methods……190
4.5.2 Electrochemical measurements……190
4.5.3 Spectroelectrochemistry……190
4.5.4 Picosecond transient absorption measurements……190
4.5.5 Nanosecond transient absorption measurements……191
4.5.7 Time-resolved infrared measurements……191
4.5.7 Photocatalytic H_2 evolution experiments……191
4.5.8 Chronoamperometry and immobilisation studies on a NiO film……191
4.6 References……192

CHAPTER 5……197
Photophysical Properties and Photocatalytic Performance of Ruthenium (II)-Naphthalene Diimide Photosensitisers/Photocatalysts for H_2 Evolution and CO_2 Reduction: Insights from Time-Resolved Infrared, Ultrafast Transient Absorption, and NiO Surface Studies.
5.1 Abstract……197
5.2 Introduction……199
5.3 Results and discussion……204
5.3.1 Synthesis……204
5.3.2 UV-vis and emission spectroscopy……207
5.3.3 Time-Resolved Infrared Spectroscopy (TRIR)……209
5.3.3.1 TRIR of the Ru-NDI-iodine complex……209
5.3.3.2 TRIR of the Ru-NDI-benzoate complex……209
5.3.3.3 TRIR of the Ru-NDI-bpy complex……210
5.3.3.4 TRIR of the Ru-NDI-ethynyl complex……210
5.3.3.5 TRIR of the Ru-NDI-rhenium complex……211
5.3.3.6 TRIR of the Ru-NDI-ethynyl-rhenium complex……212
5.3.4 Picosecond transient absorption spectroscopy in solution……216
5.3.5 Picosecond transient absorption spectroscopy on NiO……219

5.3.6 Transient absorption spectroscopy (TAS) in solution and under photocatalytic conditions - preliminary studies……221
5.3.7 Photocatalytic results……226
5.3.8 Preliminary chronoamperometry measurements and immobilisation studies…...228
5.4 Conclusion……...230
5.5 Experimental……..…..231
5.5.1 Materials and methods……..231
5.5.2 Picosecond transient absorption measurements……231
5.5.3 Nanosecond transient absorption measurements…….……..231
5.5.4 Time-Resolved Infrared measurements……...….231
5.5.5 Photocatalytic H_2 evolution experiments……..232
5.5.6 Chronoamperometry and immobilisation studies on a NiO film…….……..232
5.6 References……233

CHAPTER 6…….……...….239
Synthesis, Photophysical and Electrochemical Studies of a Porphyrin-Naphthalene Diimide using Picosecond-Nanosecond Transient Absorption Spectroscopy and Assessment for Hydrogen Evolution
6.1 Abstract……239
6.2 Introduction……..241
6.3 Results and discussion……..245
6.3.1 Synthesis……...245
6.3.2 UV-vis and emission spectroscopy…….……...…247
6.3.3 Fluorescence lifetimes using time-correlated single photon counting (TCSPC)...250
6.3.4 Nanosecond transient absorption spectroscopy (ns-TAS)……252
6.3.5 Ultrafast transient absorption spectroscopy (ps-TAS)……..255
6.3.5.1 Ultrafast spectroscopic characterisation of TPP-NDI and Zn-TPP-NDI in solution……..255
6.3.5.2 Ultrafast spectroscopic characterisation of TPP-NDI and Zn-TPP-NDI on the NiO surface……..……..257
6.3.6 Electrochemistry……...261
6.3.7 Rehm-Weller estimation for the thermodynamic driving force for photocatalytic hydrogen evolution……263
6.3.8 Photocatalytic hydrogen evolution……267
6.4 Conclusion……...267
6.5 Experimental……268
6.5.1 Materials and methods……..268
6.5.2 Electrochemical measurements……268
6.5.3 Picosecond transient absorption measurements……268
6.5.4 Nanosecond transient absorption measurements……...…...268
6.5.5 Photocatalytic hydrogen evolution……269
6.5.6 Immobilisation studies on a NiO film……269
6.6 References……....270

CHAPTER 7
Conclusions and future work……..275

Appendix A CHAPTER 3
Ruthenium (II)-Naphthalene Diimide Photosensitiser in Catalytic Hydrogen Production Probed by Time-Resolved Infrared Spectroelectrochemistry - Supplementary Information…….....278

Appendix B CHAPTER 4
Time-Resolved Infrared Spectroscopy, Spectroelectrochemical, and Transient Absorption Studies of a Ruthenium-Naphthalene Diimide Ester Complex: Insights into Charge Transfer Dynamics and the Excited States Populated in Solution and on a NiO Surface - Supplementary Information…….……306

Appendix C CHAPTER 5
Photophysical Properties and Photocatalytic Performance of Ruthenium (II)-Naphthalene Diimide Photosensitisers/Photocatalysts for H_2 Evolution and CO_2 Reduction: Insights from Time-Resolved Infrared, Ultrafast Transient Absorption, and NiO Surface Studies - Supplementary Information…….……..315

Appendix D CHAPTER 6
Synthesis, Photophysical and Electrochemical Studies of a Porphyrin-Naphthalene Diimide using Picosecond-Nanosecond Transient Absorption Spectroscopy and Assessment for Hydrogen Evolution - Supplementary Information…….....…..333

Table of Figures

Chapter 1

Figure 1.1 The demands for fossil fuels in 1900 – 2050. The figure was obtained from the online sources [8]……..….....3

Figure 1.2 The graph represents total energy production and carbon dioxide emissions. Renewable energy supply is projected to increase significantly by 2050. The figure was obtained from the document published online by IEA [10]……..……..3

Figure 1.3 The primary energy inputs in Ireland. Oil and gas contribute significantly, with approximately 7 and 5 million of tonnes of oil equivalent (Mtoe), respectively [14]…….... 4

Figure 1.4 Ireland's total greenhouse gas emissions by industrial sector [14]……4

Figure 1.5 Possible renewable sources of energy. The figure was obtained from the online sources [21]…….……..……..6

Figure 1.6 The declining trend in carbon dioxide emissions upon the incorporation and use of renewable energy in Ireland. The figure was obtained from the document published by SEAI [22]……..6

Figure 1.7 Diagram illustrating the process of natural photosynthesis. The schematic was adapted from literature sources by López Pacheco et al. [28]…….…….....8

Figure 1.8 Schematic diagram representing the process of photocatalysis using titanium dioxide as a semiconductor, adapted from the literature [33]…….…….….10

Figure 1.9 Simplified diagram representing photocatalytic water-splitting process on the semiconductor. The schematic was reproduced based on the literature knowledge and created using PowerPoint® [31, 33, 37].....12

Figure 1.10 Diagram representing photocatalytic water-splitting process on the NiO semiconductor adapted from and examined by Giannoudis et al. [80]…….....14

Figure 1.11 Proton assisted carbon dioxide reactions and their valuable products along with their corresponding electrode potentials vs. standard hydrogen electrode (V) reported at a pH of 7 [101]. …….16

Figure 1.12 Supramolecular photocatalyst for carbon dioxide reduction synthesised and examined by Santoro [87]. ……..16

Figure 1.13 Reductive and oxidative quenching, in which ED is sacrificial electron donor, PS is the photosensitiser and Cat is the catalyst. The figure was adapted from Corredor et al. [109]. …….18

Figure 1.14 Intramolecular system for hydrogen generation. PS = photosensitiser, Cat = catalytic centre, and SD = sacrificial electron donor. The schematic was created using PowerPoint® [102 – 104]……. ……..18
Figure 1.15 Intermolecular system for hydrogen generation. PS = photosensitiser, Cat = catalytic centre, and SD = sacrificial electron donor. The schematic was created using PowerPoint® [104, 115 – 117]..……..19
Figure 1.16 (A) An intramolecular ruthenium photocatalytic assembly proposed by Rau and co-workers [121] incorporating palladium as a catalyst and **(B)** an intramolecular ruthenium photocatalytic assembly proposed by Pffefer et al. [42] incorporating platinum, where L = 4,4'-di-tert-butyl-2,2'-bipyridine. **(C)** an intermolecular ruthenium photocatalytic assembly proposed by Deponti et al. [122]…….……..21
Figure 1.17 An intramolecular RuPt photocatalytic assembly proposed by Cerpentier et al. [110]…….……...23
Figure 1.18 An intramolecular photocatalytic assembly proposed by Das et al. [124], Bindra et al. [125] and Kowacs et al. [123], where **A** = $[Ru(dceb)_2(\mu\text{-bisbpy})PtCl_2][PF_6]_2$, where bisbpy = 2,2':5',3'':6'',2'''-quaterpyridine and **B** = $[Ru(dceb)_2(\mu\text{-2,5 bpp})PtI(solvent)]^{2+}$, where 2,5-bpp = 2,2′,5′,2″-terpyridine and **C** = $[Ru(dceb)_2(\mu\text{-dpp})PdCl_2]$, where dpp = 2,5-di(pyridine-2-yl)pyrazine……..…23
Figure 1.19 An intramolecular photocatalytic assembly proposed by Rau et al. [121] and Karnahl et al. [126]. …….24
Figure 1.20 An intramolecular photocatalytic assembly proposed by Fihri et al. [128] …….25
Figure 1.21 An intermolecular photocatalytic assembly proposed by Camara et al. [129]. …….....25
Figure 1.22 A ruthenium photosensitiser for intermolecular photocatalytic assembly proposed by Rupp et al. [131]. …….....26
Figure 1.23 Schematic diagram of porphyrin framework and chlorophyll molecule [133]. …….27
Figure 1.24 Intramolecular photocatalytic assemblies of zinc porphyrin and cobaloxime proposed by Zhang et al. [134]. ……...28
Figure 1.25 Intermolecular photocatalytic assemblies of NI conjugated porphyrins proposed by Bodedla et al. [135]. ……....29
Figure 1.26 Intramolecular photocatalytic systems of M-1-PtX_2, where M= Zn, Co, Cu and X= Pt and I, proposed by Lang and colleagues [137]……..……...30

Figure 1.27 Intramolecular photocatalytic system proposed by Natali and colleagues [138]. ……...30
Figure 1.28 Intermolecular photocatalytic systems proposed by Giannoudis and colleagues [139]. ……31
Figure 1.29 Intermolecular photocatalytic systems proposed by Zhu and colleagues [140]. ……...32
Figure 1.30 Intermolecular photocatalytic system proposed by Lazarides and colleagues [141]. ……...32
Figure 1.31 Intermolecular photocatalytic system proposed by Sun and colleagues [142]. …….....33
Figure 1.32 NDI-based polymers, PNDI-BT (bithiophene), PNDI-DTBT (4,7-di(thiophen-2-yl)benzo[c][1,2,5]thiadiazole), and PNDI-BP (biphenyl) for the photochemical reduction of CO_2 to CO synthesised by Wang and colleagues [160]……35
Figure 1.33 NDI-based donor-acceptor-donor molecules NDI-2T, NDI-TT, NDI-4T, and NDI-6T proposed by Wang et al. [161]…….……...36
Figure 1.34 NDI-BCOOH unit in the self-assembly photocatalytic system designed by Xu et al. [162]……..……37
Figure 1.35 Structures of NDI-copolymers, NDI-BTF and NDI-BTzF for photocatalytic hydrogen evolution based on Mekhemer's research work [163]…….……37
Figure 1.36 The Franck-Condon principle adapted from the online sources [173]…… 39
Figure 1.37 The Jablonski diagram adopted from Edinburgh Instruments [178]…….....40
Figure 1.38 Time-correlated single photon counting apparatus. The schematic was adapted from the literature [166]…….……43
Figure 1.39 Electronic transition and relaxation pathways in TA spectroscopy, indicating ground-state bleach (GSB), excited state absorption (ESA) and stimulated emission (SE). The figure was adapted from the literature [191]…….....44
Figure 1.40 Schematic of the electrochemical set up. The figure was adapted from the literature [195]…….46

Chapter 2

Figure 2.1 Molecular structure of rylene diimides……...63

Figure 2.2 The general synthetic pathways to alter both NDI and PDI frameworks…….65

Figure 2.3 The energy level diagram for a typical octahedral complex [36], such as $[Ru(bpy)_3]^{2+}$……84

Figure 2.4 The transient absorption spectra of **Ru-NDI-1** at 1, 25, 50, 100 and 250 ps after excitation in CH_3CN. Taken with permission from Chaignon et al. [22]…….....87

Figure 2.5 The energy level diagram of **Ru-PDI-1**. Adapted from Gunderson et al. [12]……..89

Figure 2.6 The energy level diagram for **Ru-PDI-6** following selective excitation [30]……..90

Figure 2.7 Transient absorption profiles following excitation (λ_{ex} = 532 nm) of **Ru-PDI-1** in CH_2Cl_2 at 532 nm. The kinetics trace, measured at 726 nm is shown in the inset. Taken with permission from Gunderson et al. [12]…….....90

Figure 2.8 The schematic energy level diagram for **Ru-NDI-7** and **Ru-NDI-8 [**26]….91

Figure 2.9 The energy level diagram for **Ru-PDI-2 (A)** and **Ru-PDI-3 (B)**, adapted from Dubey et al. [23]…..…….…...94

Figure 2.10 The absorption spectrum of **Ru-PDI-12** in CH_2Cl_2, the uncoordinated PDI (dotted line) and the uncoordinated ruthenium-porphyrin (broken line). Taken with permission from Prodi et al. [33]…….95

Figure 2.11 The energy level diagram for **Ru-PDI-12** showing selective excitation at 530 nm and 585 nm [33]...……..…..…..96

Figure 2.12 The energy level diagram for **Ru-PDI-14** showing selective excitation at 530 and 680 nm [35]……..…….....96

Figure 2.13 The transient absorption spectra of **Ru-PDI-14** in CH_2Cl_2 upon excitation at 680 nm with panel A representing the spectral profiles and panel B displaying kinetic traces at 655 nm and 740 nm respectively. Taken with permission from Amati et al. [35]……..97

Figure 2.14 Time-resolved infrared spectra of Pt(phen-NDI)Cl_2 in CH_2Cl_2 at different time delays following excitation with 395 nm, 150 fs laser pulse along with ground-state FTIR spectrum of Pt(phen-NDI)Cl_2 in CH_2Cl_2 in the spectral range used in the TRIR experiments. Features (B) and (F) correspond to bleach of the ν(CC) and ν(CO) respectively. Features (G) and (D) were attributed to the ν(CO) stretches of the NDI in its triplet state. Feature (C) corresponds to hot triplet NDI, (A) and (E) is due to hot ground state. Taken with permission from Sazanovich et al. [72]……...……..99

Figure 2.15 Transient absorption results obtained for Pt(phen-NDI)Cl_2 in CH_2Cl_2 following excitation with 395 nm, 150 fs laser pulse. Taken with permission from Sazanovich et al. [72]……..…….99
Figure 2.16 Cyclic voltammogram for **Ru-NDI-2** in CH_3CN with 0.1 M $TBAPF_6$ as presented by Skaisgirski et al. [3]……...105
Figure 2.17 Cyclic voltammogram for **Ru-NDI-3** in CH_3CN with 0.1 M $TBAPF_6$ as presented by Skaisgirski et al. [3]……..…….105
Figure 2.18 Cyclic voltammogram of **Ru-PDI-1** in CH_2Cl_2 with 0.1 M $TBAPF_6$ as presented by Gunderson et al. [12]…….106
Figure 2.19 Cyclic voltammogram of **Ru-PDI-6** in CH_3CN with 0.1 M $TBAPF_6$ as presented by Santos et al [30]…….109
Figure 2.20 Differential spectra between the absorption spectrum of the reduced species and the ground state, with permission from Nastasi et al. [29]……..……..110

Chapter 3

Figure 3.1 The structure of **RuNDI^{2+}** complex composing of a ruthenium photosensitiser and NDI electron accepting moiety analysed in this study……127

Figure 3.2 Synthetic scheme for the preparation of **RuNDI^{2+}** and its corresponding reactants NDI-octyl and $[Ru(bpy)_2(phen\text{-}6\text{-}NH_2)]^{2+}$. PF_6^- counter anions are omitted for both the precursor and **RuNDI^{2+}**……....129

Figure 3.3 UV-vis absorption spectrum of 2 x 10^{-4} M **RuNDI^{2+}** in acetonitrile……130

Figure 3.4 (A) Cyclic voltammogram of **RuNDI^{2+}** in DMF/TBAH showing the reduction steps to **RuNDI^{+}** (NDI-based, at R1), **RuNDI** (NDI-based, at R2), **RuNDI^{-}** (bpy-based, at R3), **RuNDI^{2-}** (bpy-based, at R4) and **RuNDI^{3-}** (phen-based, at R5) and also the $Ru^{2+/3+}$ oxidation. **(B)** Overlay of the CVs of **RuNDI^{2+}** (orange) and the individual reference compounds, namely dioctyl-NDI (black) and $[Ru(bpy)_2(phen\text{-}6\text{-}NH_2)]^{2+}$ (purple). Experimental conditions: GC disk working electrode, T = 298 K, v = 100 mV s^{-1}……..…..132

Figure 3.5 The UV-vis absorption spectra of **RuNDI^{2+}** (orange), one-electron-reduced **RuNDI^{+}** (black; formed at R1), and two-electron-reduced **RuNDI** (yellow; formed at R2) in **(A)** ACN/TBAH and **(B)** THF/TBAH. Experimental conditions: Pt minigrid working electrode, OTTLE cell, T = 298 K…….....134

Figure 3.6 IR-SEC spectra of **RuNDI^{2+}** (orange), one-electron reduced **RuNDI^{+}** (black; formed at R1), and double-electron reduced **RuNDI** (yellow; formed at R2). Experimental conditions: Pt minigrid working electrode, OTTLE cell, THF/TBAH, T = 298 K……..136

Figure 3.7 (A) TRIR spectrum of **RuNDI^{2+}** upon excitation at 365 nm recorded in acetonitrile, **(B)** TRIR spectrum of **RuNDI^{2+}** upon excitation at 420 nm, **(C)** TRIR spectrum of **RuNDI^{2+}** upon excitation at 510 nm and **(D, E, F)** decay traces obtained in the TRIR for **RuNDI^{2+}**.....138

Figure 3.8 TRIR spectra recorded upon 510-nm photoexcitation of one-electron-reduced **RuNDI^{+} (A)** and 600-nm photoexcitation of two-electron-reduced **RuNDI (B)** in THF/TBAH, obtained stepwise in situ from **RuNDI^{2+}** using an adapted OTTLE cell…….140

Figure 3.9 Nanosecond transient absorption spectrum of **RuNDI^{2+}** under a nitrogen atmosphere in acetonitrile/TEA/H_2O/$Pt(DMSO)_2I_2$ following excitation at 355 nm at different time delays. Samples were degassed using three freeze-pump-thaw cycles……142

Figure 3.10 The Jablonski energy level diagram for **RuNDI**$^{2+}$ upon excitation at 420 nm using TRIR…….....142
Figure 3.11 UV-vis absorption changes of **RuNDI**$^{2+}$ under spectroelectrochemical and photocatalytic conditions in acetonitrile, triethylamine and water (65:30:5 ratio) upon light irradiation at 470 nm. The figure on the right shows the UV-vis changes after a few minutes of light irradiation followed by aeration of the solution with air to indicate how quickly the reduced species return to parent species in the presence of oxygen…….……..145
Figure 3.12 Time-dependent photocatalytic performance of **RuNDI**$^{2+}$ in acetonitrile, triethylamine and water (65:30:5, v/v) upon light irradiation at 470 nm. TON (black) and TOF (orange) values determined at various time delays…….146
Figure 3.13 Mechanism of photocatalytic hydrogen evolution proposed for the **RuNDI**$^{2+}$ complex…….147

Chapter 4

Figure 4.1 The schematic diagram represents the photosensitiser, **Ru(dceb)-NDI^{2+}** which was assessed for photocatalytic hydrogen evolution. The complex was studied on a nickel oxide surface to study charge injection and charge recombination……...….163

Figure 4.2 Synthetic scheme for the preparation of a **Ru(dceb)-NDI^{2+}** photosensitiser for photocatalytic hydrogen evolution……..……..…….164

Figure 4.3 The electronic absorption and emission spectra of the **Ru(dceb)-NDI^{2+}** complex in acetonitrile……...165

Figure 4.4 A cyclic voltammogram of **Ru(dceb)-NDI^{2+}** in acetonitrile/TBAH. The figure presents the reduction steps to **Ru(dceb)-NDI^{+}** (NDI-based, at R1), **Ru(dceb)-NDI** (NDI-based, at R2), **Ru(dceb)-NDI^{-}** (bpy-based, at R3), **Ru(dceb)-NDI^{2-}** (bpy-based, at R4) and **Ru(dceb)-NDI^{3-}** (phen-based, at R5). Experimental conditions employed glassy working electrode, T = 298 K, and scan rate used v = 100 mV/s. ……..166

Figure 4.5 The UV-vis spectroelectrochemical spectra of (**A**) parent species of **Ru(dceb)-NDI^{2+}** (**B**) the one-electron reduced species **Ru(dceb)-NDI^{+}** following reduction at –0.86 V (**C**) the two-electron reduced **Ru(dceb)-NDI** following reduction at –1.32 V (**D**) the three-electron reduced **Ru(dceb)-NDI^{-}** following reduction at –2.1 V (**E**) an overlay of all the reduced species for the **Ru(dceb)-NDI^{2+}** complex. The spectroelectrochemical analysis was carried in acetonitrile using TBAH as a supporting electrolyte. A Pt minigrid working electrode was used in the OTTLE cell, T = 298 K. The scan rate of 0.002 V/s was applied……...……...170

Figure 4.6 The IR-spectroelectrochemical spectra of **(A)** parent species of **Ru(dceb)-NDI^{2+} (B)** the difference spectrum of one-electron reduced species **Ru(dceb)-NDI^{+} (C)** the difference spectrum of two-electron reduced **Ru(dceb)-NDI (D)** the difference spectrum of three-electron reduced **Ru(dceb)-NDI^{-} (E)** an overlay of all reduced species of the **Ru(dceb)-NDI^{2+}** complex. The spectroelectrochemical analysis was carried in acetonitrile using TBAH as a supporting electrolyte. The experimental set up involved Pt minigrid working electrode, OTTLE cell, T = 298 K. The scan rate of 0.002 V/s was applied.……..172

Figure 4.7 TRIR spectra following excitation of **Ru(dceb)-NDI^{2+}** at 420 nm in **(A)**. TRIR spectra of the **Ru(dceb)-NDI^{2+}** following excitation at 365 nm in **(B)**, schematic of wavelength-dependent behaviour on electron transfer **(C)**, FTIR spectrum of **Ru(dceb)-NDI^{2+}** in **(D)**.……..…....175

Figure 4.8 Nanosecond transient absorption spectrum of the **Ru(dceb)-NDI^{2+}**, which primarily indicates spectral changes from 500 – 550 ns and (inset) represents the decay trace for the triplet lifetime. The ns-TAS measurements were carried out in acetonitrile following excitation at 355 nm. The solution prior to the measurement was freeze-pump-thawed using three cycles……...177
Figure 4.9 Nanosecond transient absorption spectra of the **Ru(dceb)-NDI^{2+}** complex under photocatalytic conditions in a mixture of ACN/TEA and $Pt(DMSO)_2I_2$ following excitation at 355 nm. The graph underneath displays UV-vis-SEC results for the parent species, one- and two-electron reduced species of **Ru(dceb)-NDI^{2+}**……..…...179
Figure 4.10 Transient absorption spectra of **Ru(dceb)-NDI^{2+}**. **(A)** ps-TAS recorded in acetonitrile following excitation at 400 nm. The inset displays kinetic traces at 496, 536, 630 nm. **(B)** ps-TAS recorded on a NiO thin film upon excitation at 400 nm. The inset shows kinetic traces at 474, 530, 605, 690 and 735 nm……...182
Figure 4.11 The TRIR-spectroelectrochemical spectra of **Ru(dceb)-NDI^{2+}** in acetonitrile with 0.1 M TBAH. **(A)** indicates excitation of the one-electron reduced state of **Ru(dceb)-NDI^{+}** at 420 nm, **(B)** excitation of the one-electron reduced **Ru(dceb)-NDI^{+}** at 510 nm and **(C)** presents the FTIR spectrum obtained for **Ru(dceb)-NDI^{+}** and, together with **(D)** the FTIR spectrum of **Ru(dceb)-NDI^{+}**…….....….184
Figure 4.12 The TRIR-spectroelectrochemical spectra of **Ru(dceb)-NDI^{2+}** in acetonitrile with 0.1 M TBAH. **(A)** indicates the two-electron reduced state of the compound **Ru(dceb)-NDI** upon excitation at 600 nm, **(B)** corresponds to the three-electron reduced state **Ru(dceb)-NDI$^{–}$** following excitation at 600 nm and **(C)** presents the FTIR spectrum obtained for **Ru(dceb)-NDI** and **(D)** shows the FTIR spectrum of **Ru(dceb)-NDI$^{–}$** ……..……...……..……..185
Figure 4.13 Time dependent photocatalysis for **Ru(dceb)-NDI^{2+}**. The turnover numbers at various time intervals (brown) and TOF (orange) under photocatalytic conditions in acetonitrile, triethylamine and water (65:30:5 ratio) upon irradiation at 450 nm……187
Figure 4.14 (A) UV-vis absorption spectra of the **Ru(dceb)-NDI^{2+}** complex on a nickel oxide thin film compared to a reference nickel oxide without the dye. **(B)** chopped light chronoamperometry measurements under light irradiation while applying potentials of –0.2 and –0.4 V. The solution was bubbled with argon throughout the experiment, and the scan rate of 10 mV/s was used……188

Chapter 5

Figure 5.1 The structures of the Ru-NDI complexes studied. All complexes include a PF_6^- counterion, which has been excluded from the structural visualisation for clarity…….203

Figure 5.2 Synthetic scheme for the preparation of **Ru-NDI-R** and its corresponding ligands **NDI-R** and the photosensitising moiety **Ru(bpy)$_2$-phen-NH$_2$**, where R = 4-iodoaniline, methyl 4-aminobenzoate and 4-ethynylaniline…….…….205

Figure 5.3 Synthetic scheme for the preparation of **Ru-NDI-rhenium/Ru-NDI-platinum**……206

Figure 5.4 Synthetic scheme for the preparation of **Ru-NDI-ethynyl-rhenium**…..….206

Figure 5.5 (A) Normalised UV-vis absorption spectra of **Ru-NDI-ethynyl**, **Ru-NDI-iodine** and **Ru-NDI-benzoate** recorded in acetonitrile. **(B)** UV-vis absorption spectra of **Ru-NDI-rhenium**, **Ru-NDI-bpy**, **Ru-NDI-platinum** and **Ru-NDI-ethynyl-rhenium** obtained in acetonitrile (0.2 – 0.4 mmol)……208

Figure 5.6 Time-resolved infrared measurements of the **Ru-NDI-iodine** complex recorded in acetonitrile **(A)** following excitation at 365 nm, and **(B)** excitation at 420 nm. The inset data displays kinetic decay traces (in ps), which were obtained using Glotaran analysis……..……213

Figure 5.7 Time-resolved infrared measurements of the **Ru-NDI-benzoate** complex recorded in acetonitrile **(A)** following excitation at 365 nm, and **(B)** excitation at 420 nm. The inset data displays kinetic decay traces (in ps), which were obtained using Glotaran analysis……..……213

Figure 5.8 Time-resolved infrared measurements of the **Ru-NDI-bpy** complex recorded in acetonitrile **(A)** following excitation at 365 nm, and **(B)** excitation at 420 nm. The inset data displays kinetic decay traces (in ps), which were obtained using Glotaran analysis……..214

Figure 5.9 Time-resolved infrared measurements of the **Ru-NDI-ethynyl** complex recorded in acetonitrile **(A)** following excitation at 365 nm, and **(B)** excitation at 420 nm. The inset data displays kinetic decay traces (in ps), which were obtained using Glotaran analysis. ……..……..214

Figure 5.10 Time-resolved infrared measurements of the **Ru-NDI-rhenium** complex recorded in acetonitrile **(A)** following excitation at 365 nm, and **(B)** excitation at 420 nm. The inset data displays kinetic decay traces (in ps), which were obtained using Glotaran analysis……..215

Figure 5.11 Time-resolved infrared measurements of the **Ru-NDI-ethynyl-rhenium** complex recorded in acetonitrile **(A)** following excitation at 365 nm, and **(B)** excitation at 420 nm. The inset data displays kinetic decay traces (in ps), which were obtained using Glotaran analysis……...215
Figure 5.12 Picosecond transient absorption spectra of Ru-NDI complexes were recorded in acetonitrile following excitation at 400 nm, **(A) Ru-NDI-iodine**, **(B) Ru-NDI-benzoate**, **(C) Ru-NDI-bpy**, **(D) Ru-NDI-rhenium**, **(E) Ru-NDI-ethynyl-rhenium, (F) Ru-NDI-platinum**. The inset data displays kinetic decay traces (in ps), which were obtained using Glotaran analysis…….……..…..218
Figure 5.13 Picosecond transient absorption spectra of Ru-NDI complexes were recorded on NiO film following excitation at 400 nm, **(A) Ru-NDI-iodine**, **(B) Ru-NDI-benzoate**, **(C) Ru-NDI-bpy**, **(D) Ru-NDI-rhenium**, **(E) Ru-NDI-ethynyl-rhenium, (F) Ru-NDI-platinum**…….……...…220
Figure 5.14 UV-vis absorption spectra of the Ru-NDI complexes presented in this chapter under photocatalytic conditions prior to the nanosecond transient absorption spectroscopy measurements. The experimental conditions involved a solvent mixture of triethylamine, water, and acetonitrile in the ratio of 30:5:65, respectively with $Pt(DMSO)_2I_2$ as the catalyst (in the non-rhenium complexes). All samples were prepared in a laser cell and deaerated using three cycles of freeze-pump-thaw……....224
Figure 5.15 UV-vis absorption spectra of the Ru-NDI complexes presented in this chapter in acetonitrile prior to the nanosecond transient absorption spectroscopy measurements. All samples were prepared in a laser cell and deaerated using three cycles of freeze-pump-thaw……..……..……..224
Figure 5.16 Nanosecond transient absorption spectra of all the Ru-NDI complexes were recorded under photocatalytic conditions following excitation at 355 nm. The experimental conditions involved a solvent mixture of triethylamine, water, and acetonitrile in the ratio of 30:5:65, with $Pt(DMSO)_2I_2$ acting as a catalyst in the photocatalysis. All samples were prepared in a laser cell and deaerated using three cycles of freeze-pump-thaw. **(A) Ru-NDI-iodine**, **(B) Ru-NDI-benzoate**, **(C) Ru-NDI-bpy**, **(D) Ru-NDI-rhenium**, **(E) Ru-NDI-ethynyl-rhenium**……..…....225
Figure 5.17 UV-vis absorption spectrum of **Ru-NDI-rhenium** complex recorded before and after photocatalysis. Carbon dioxide reduction experiment was carried out using concentration of 0.05 mM for the photocatalysts, and 6 ml mixture of DMF and TEOA (5:1) as well as 0.1 M of BIH was employed……..228

Figure 5.18 UV-vis spectroscopy measurements of Ru-NDI complexes immobilised on the NiO surface……..229
Figure 5.19 Chopped light (light on/light off) chronoamperometry measurements under light irradiation while applying potentials of –0.2 and –0.5 V for the **Ru-NDI-rhenium** complex…….230

Chapter 6

Figure 6.1 Porphyrin-naphthalene diimide assemblies reported in the literature [4, 20 – 23, 34 – 35, 44]……...…244
Figure 6.2 Porphyrin-naphthalene diimide assembly, consisting of a porphyrin electron donor and NDI electron-accepting moiety, the focus of this chapter……..245
Figure 6.3 Synthetic scheme for the preparation of **TPP-NDI** and **Zn-TPP-NDI**…...246
Figure 6.4 (A) Electronic absorption and **(B)** emission spectra of free the base porphyrin **TPP-NDI** and **Zn-TPP-NDI** measured in THF and compared to **TPP-NH_2** following excitation of the Soret band. The inset represents the zoom-in image of the Q-bands region…….249
Figure 6.5 Electronic absorption (brown line) and emission (red line) spectra of **NDI-octyl** measured in THF, following excitation of the NDI band (λ_{exc} = 360 nm)……...249
Figure 6.6 Fluorescence signals obtained following excitation of **TPP-NDI** and **Zn-TPP-NDI**, at either λ_{exc} = 375 or 510 nm. The results were obtained in THF…….……...252
Figure 6.7 Nanosecond transient absorption spectrum of **TPP-NDI (A)** and **Zn-TPP-NDI (B)** in deoxygenated THF upon the excitation at 355 nm at different time delays. Sample was prepared using an absorbance of ~1.0 at the Soret band of porphyrins and the solution was degassed using three freeze-pump-thaw cycles……...254
Figure 6.8 Nanosecond transient absorption spectrum of **TPP-NDI** in deoxygenated ethyl acetate upon the excitation at 355 nm at different time delays. Sample was prepared using an absorbance of ~1.0 at the Soret band of porphyrins and the solution was degassed using three freeze-pump-thaw cycles……...…….254
Figure 6.9 (A) Picosecond transient absorption spectrum of **TPP-NDI** in deoxygenated THF following excitation at 400 nm at different time delays. **(B)** Decay kinetic traces for **TPP-NDI** obtained from Glotaran global analysis……....256
Figure 6.10 (**A)** Picosecond transient absorption spectrum of **Zn-TPP-NDI** in deoxygenated THF following excitation at 400 nm at different time delays. **(B)** Decay kinetic traces for **Zn-TPP-NDI** obtained from Glotaran global analysis……..256

Figure 6.11 UV-vis absorption spectra of **TPP-NDI** and **Zn-TPP-NDI** adsorbed onto NiO surface after 24 hours from a 3 mM THF dye bath……..257
Figure 6.12 (A) Picosecond transient absorption spectrum of **TPP-NDI** on the NiO surface upon the excitation at 400 nm at different time delays. **(B)** Decay kinetic traces for **TPP-NDI** obtained from Glotaran global analysis……...260
Figure 6.13 (A) Picosecond transient absorption spectrum of **Zn-TPP-NDI** on the NiO surface following excitation at 400 nm at different time delays. **(B)** Decay kinetic traces for **Zn-TPP-NDI**……..……260
Figure 6.14 A cyclic voltammogram of **TPP-NDI (A)** and **Zn-TPP-NDI (B)** vs ferrocene was recorded under the following experimental conditions: 1 mM of the compound was dissolved in DMF (dimethylformamide) purged with nitrogen, and 0.1 M tetrabutylammonium hexafluorophosphate serving as the supporting electrolyte. The working electrode used was a glassy carbon electrode, while a platinum wire and an $Ag/AgNO_3$ electrode were employed as the counter and reference electrodes, respectively. The scans were performed at a scan rate of 0.1 V/s……262
Figure 6.15 (A) The superposition of the CVs of the individual moieties, namely **NDI**, **TPP-NH_2** and the dyads **TPP-NDI**, **Zn-TPP-NDI** in order to present a minimal variation in their redox potentials. **(B)** Vertical stacking of CVs offsets for better visualisation and clarity. ……...…….……...…262
Figure 6.16 The equations that summarise the process of photoinduced electron transfer in donor-acceptor assemblies [3, 49]…….....263
Figure 6.17 The equations that summarise the calculations of the Rehm-Weller estimation [3, 49]……...264
Figure 6.18 Spectral overlap of the normalised emission and absorption spectra for both **(A) TPP-NDI** and **(B) Zn-TPP-NDI** in THF…….265
Figure 6.19 The thermodynamic driving force feasibility for electron transfer from the **TPP-NDI** photosensitiser to the NDI acceptor and subsequently to the catalyst……...266
Figure 6.20 The thermodynamic driving force feasibility for electron transfer from the **Zn-TPP-NDI** photosensitiser to the NDI acceptor and subsequently to the catalyst…266

Appendix A

Figure SA3.1 ^{1}H-NMR of NDI-octyl in $CdCl_3$-d_6……..……..….279

Figure SA3.2 ^{1}H-NMR of dioctyl-NDI in $CdCl_3$-d_6……..……..….279

Figure SA3.3 ^{1}H-NMR of $[Ru(bpy)_2Cl_2]$ in DMSO-d_6…….……..……280

Figure SA3.4 ^{1}H-NMR of $[Ru(bpy)_2(phen\text{-}6\text{-}NH_2)]^{2+}$ in DMSO-d_6……..…...281

Figure SA3.5 ^{1}H-NMR of **RuNDI^{2+}** in DMSO-d_6…….……..…….282

Figure SA3.6 ^{13}C-NMR of **RuNDI^{2+}** in DMSO-d_6……..……..……...283

Figure SA3.7 High-resolution ESI-mass spectrum of **RuNDI^{2+}** in acetonitrile, calculated m/z = 485.1259, found in positive mode 485.1248……..…….283

Figure SA3.8 Calculation of molar extinction coefficients……284

Figure SA3.9 Two different structures of **RuNDI^{2+}**…….....285

Figure SA3.10 Frontiers orbitals of **RuNDI$^{2+/+/0}$**……...285

Figure SA3.11 IR spectra of **RuNDI^{2+}** in the ground (black) and triplet state (red). The left spectrum is for *a* structure and the right is for *b* structure from Figure SA3.9……...286

Figure SA3.12 Frontiers orbitals and spin density for ^{3}**RuNDI^{2+}**……..…286

Figure SA3.13 IR spectra of **RuNDI^{x}** (x = 2+, +, 0). The left spectrum is for ***a*** structure, and the right is for ***b*** structure, as shown in Figure SA3.9……..……287

Figure SA3.14 Spin densities in **RuNDI^{+}** showing localisation of the first reduction NDI ligand..…….....287

Figure SA3.15 Spin densities in **RuNDI** showing localisation of the second reduction on bpy; triplet (p0_s3, left), singlet (p0_s1, right)..…….....288

Figure SA3.16 Calculated electronic spectra for **RuNDI$^{2+/+/0}$**. The left spectrum is for ***a*** structure and the right is for ***b*** structure, as shown in Figure SA3.9……...……288

Figure SA3.17 TDDFT-calculated UV-vis absorption spectrum of **RuNDI^{2+}**…….....288

Figure SA3.18 Molecular orbitals involved in electronic transitions of **RuNDI^{2+}** (listed in Table SA3.3)…….....291

Figure SA3.19 TDDFT-calculated UV-vis absorption spectrum of **RuNDI^{+}**……..…292

Figure SA3.20 Molecular spin orbitals involved in electronic transitions of **RuNDI^{+}** (listed in Table SA3.4)..…….....295

Figure SA3.21 TDDFT-calculated UV-vis absorption spectrum of **RuNDI**……....296

Figure SA3.22 Molecular orbitals involved in electronic transitions of **RuNDI** (listed in Table SA3.5)..…….....299

Figure SA3.23 A cyclic voltammogram of **RuNDI^{2+}** in THF/TBAH showing the reductions step to the corresponding monocationic (at R1), neutral (at R2), anionic (at

R3), dianionic (at R4) and trianionic (at R5) species and also $Ru^{2+/3+}$ oxidation. Experimental conditions: glassy carbon working electrode, T = 298 K, v = 100 mV/s...300

Figure SA3.24 A cyclic voltammogram of **RuNDI^{2+}** in acetonitrile/TBAH showing similar pattern as in DMF. Experimental conditions: Pt microdisc working electrode, T = 298 K, v = 100 mV/s.…….....300

Figure SA3.25 The UV-vis absorption spectra of the reference NDI compound (R_1-NDI-R_1 = dioctyl-NDI), parent species [dioctyl-NDI] (orange), one electron-reduced [dioctyl-NDI)]$^{-}$ (yellow), and two-electron-reduced [dioctyl-NDI)]$^{2-}$ (brown) in ACN/TBAH. Experimental conditions: Pt minigrid working electrode, OTTLE cell, T = 298…….301

Figure SA3.26 The UV-vis absorption spectra of $[(Ru(bpy)_2(phen\text{-}6\text{-}NH_2)]^{2+}$ (red), and electron-reduced $[(Ru(bpy)_2(phen\text{-}6\text{-}NH_2)]^{+}$ (brown) in ACN/TBAH. Experimental conditions: Pt minigrid working electrode, OTTLE cell, T = 298 K……...301

Figure SA3.27 TRIR spectra recorded upon 420-nm photoexcitation of parent **RuNDI^{2+}** in THF……302

Figure SA3.28 (A) TRIR spectra recorded upon 510-nm photoexcitation of parent **RuNDI^{2+}** and **(B)** one-electron-reduced **RuNDI^{+}** in ACN/TBAH, obtained in situ from **RuNDI^{2+}** using an adapted OTTLE cell……..……..302

Figure SA3.29 (A) TRIR spectra recorded upon 365-nm photoexcitation of the reference NDI compound (R_1-NDI-R_1 = dioctyl-NDI), parent species [dioctyl-NDI] in THF. **(B)** The FTIR of the NDI compound recorded in THF…..…….…..302

Figure SA3.30 Nanosecond transient absorption spectrum of the ruthenium precursor, $[Ru(bpy)_2(phen\text{-}6\text{-}NH_2)]^{2+}$ under an nitrogen atmosphere in acetonitrile, following excitation at 355 nm at different time delays……..303

Figure SA3.31 Nanosecond transient absorption spectrum of the reference NDI compound (R_1-NDI-R_1 = dioctyl-NDI), under an nitrogen atmosphere in acetonitrile, following excitation at 355 nm at different time delays……..……303

Figure SA3.32 Nanosecond transient absorption spectrum of **Ru-NDI^{2+}** at different time decay constants under an nitrogen atmosphere in acetonitrile/TEA/H_2O/$Pt(DMSO)_2I_2$ following excitation at 355 nm at different time delays. Samples were degassed using three freeze-pump-thaw cycles. **(A)** indicates reduced species of ruthenium, **(B)** and **(C)** indicate formation of the reduced NDI species supported by UV-vis-SEC experiments **(D** and **E)** …….....304

Figure SA3.33 The UV-vis spectrum of **RuNDI^{2+}** in a mixture of acetonitrile, triethylamine and water (65:30:5 ratio) was recorded before (pink) and after (blue) 24 hours of irradiation with a 470 nm light source……..304

Appendix B

Figure SB4.1 ^{1}H-NMR of **Ru(dceb)$_2$Cl$_2$** in DMSO-d$_6$……...……..310
Figure SB4.2 ^{1}H-NMR of the **NDI-phen** ligand in CDCl$_3$-d$_6$……310
Figure SB4.3 ^{1}H-NMR of **Ru(dceb)-NDI^{2+}** in CD$_3$CN-d$_6$……..……..……310
Figure SB4.4 ^{1}H-NMR of **Ru(dceb)-NDI^{2+}** in CD$_3$CN-d$_6$ with assignments……311
Figure SB4.5 ^{13}C-NMR of **Ru(dceb)-NDI^{2+}** in CD$_3$CN-d$_6$……..…….....311
Figure SB4.6 COSY spectrum of **Ru(dceb)-NDI^{2+}**……...…….....311
Figure SB4.7 Aromatic region of the COSY spectrum of **Ru(dceb)-NDI^{2+}**….…….....312
Figure SB4.8 Mass spectrometry results (ESI mode) for **Ru(dceb)-NDI^{2+}**. The measurements were carried out by researchers at the University of Bath……...312
Figure SB4.9 UV-vis absorption spectra of **Ru(dceb)-NDI^{2+}**, before and after photocatalysis (brown and red) and before and after laser studies under photocatalytic conditions (orange and green lines)……313
Figure SB4.10 TRIR spectra recorded upon 510-nm photoexcitation of parent **Ru(dceb-NDI^{2+}** in acetonitrile, using Harrick cell……..…..……313
Figure SB4.11 (A) TRIR spectra recorded upon 510-nm photoexcitation of one-electron-reduced **Ru(dceb)-NDI^{+}** in ACN/TBAH in the range of 1500 – 1650 cm^{-1}, **(B)** TRIR spectra recorded upon 510-nm photoexcitation of one-electron-reduced **Ru(dceb)-NDI^{+}** in ACN/TBAH in the range of 1500 – 1760 cm^{-1}, obtained in situ from **Ru(dceb)-NDI^{2+}** using an adapted OTTLE cell…….……....313
Figure SB4.12 (A) TRIR spectra recorded upon 600-nm photoexcitation of two-electron-reduced **Ru(dceb)-NDI** in ACN/TBAH in the range of 1500 – 1650 cm^{-1}, **(B)** TRIR spectra recorded upon 600-nm photoexcitation of two-electron-reduced **Ru(dceb)-NDI** in ACN/TBAH in the range of 1500 – 1760 cm^{-1}, obtained in situ from **Ru(dceb)-NDI^{2+}** using an adapted OTTLE cell……...…….……314

Appendix C

Figure SC5.1 ^{1}H-NMR of **NDI-iodine** in DMSO-d_6……..……..316
Figure SC5.2 ^{1}H-NMR of **NDI-ethynyl** in DMSO-d_6…….……...316
Figure SC5.3 ^{1}H-NMR of **NDI-benzoate** in DMSO-d_6……317
Figure SC5.4 ^{1}H-NMR of **Ru-NDI-iodine** in DMSO-d_6……..…..……..318
Figure SC5.5 ^{13}C-NMR of **Ru-NDI-iodine** in DMSO-d_6……..……...…318
Figure SC5.6 COSY ^{1}H-NMR of **Ru-NDI-iodine** in DMSO-d_6……...……....319
Figure SC5.7 ESI-mass spectrometry results of **Ru-NDI-iodine** in acetonitrile. ($C_{52}H_{31}F_{12}IN_8O_4P_2Ru$) $[M]^{2+}$ calculated at m/z = 530.0273 and found at 530.0274…...319
Figure SC5.8 ^{1}H-NMR of **Ru-NDI-benzoate** in DMSO-d_6……...……...320
Figure SC5.9 ^{13}C-NMR of **Ru-NDI-benzoate** in DMSO-d_6……...……..320
Figure SC5.10 COSY ^{1}H-NMR of **Ru-NDI-benzoate** in DMSO-d_6……...…….320
Figure SC5.11 ESI-mass spectrometry results of **Ru-NDI-benzoate** in acetonitrile. ($C_{54}H_{34}F_{12}N_8O_6P_2Ru$) $[M]^{2+}$ calculated at m/z = 496.0824 and found at 496.0907……321
Figure SC5.12 ^{1}H-NMR of **Ru-NDI-ethynyl** in DMSO-d_6……....321
Figure SC5.13 ESI-mass spectrometry results of **Ru-NDI-ethynyl** in acetonitrile. ($C_{54}H_{32}F_{12}N_8O_4P_2Ru$) $[M]^{2+}$ calculated at m/z = 479.0797 and found at 479.0832……322
Figure SC5.14 ^{1}H-NMR of **NDI-bpy** in DMSO-d_6……..…….…....323
Figure SC5.15 ^{1}H-NMR of **Ru-NDI-bpy** in DMSO-d_6……..……..……324
Figure SC5.16 ^{13}C-NMR of **Ru-NDI-bpy** in DMSO-d_6……..…….....324
Figure SC5.17 COSY ^{1}H-NMR of **Ru-NDI-bpy** in DMSO-d_6……...…….……325
Figure SC5.18 ESI-mass spectrometry results of **Ru-NDI-bpy** in acetonitrile. ($C_{56}H_{34}N_{10}O_4Ru$) $[M]^{2+}$ calculated at m/z = 506.0906 and found at 506.0942…..…….325
Figure SC5.19 ^{1}H-NMR of **Ru-NDI-rhenium** in DMSO-d_6……..……327
Figure SC5.20 ESI-mass spectrometry results of **Ru-NDI-rhenium** in acetonitrile. ($C_{59}H_{34}ClN_{10}O_7ReRu$) $[M]^{2+}$ calculated at m/z = 659.0445 and found at 659.0464…..327
Figure SC5.21 ^{1}H-NMR of **Ru-NDI-platinum** in DMSO-d_6……..……....328
Figure SC5.22 ESI-mass spectrometry results of **Ru-NDI-platinum** in acetonitrile. ($C_{56}H_{34}I_2N_{10}O_4PtRu$) $[M]^{2+}$ calculated at m/z = 730.4777 and found at 730.4774…….328
Figure SC5.23 ^{1}H-NMR of **Ru-NDI-ethynyl-bpy** in DMSO-d_6…….....330
Figure SC5.24 ESI-mass spectrometry results of **Ru-NDI-ethynyl-bpy** in acetonitrile. ($C_{64}H_{38}F_{12}N_{10}O_4P_2Ru$) $[M]^{2+}$ calculated at m/z = 556.1064 and found at 556.1071…...330
Figure SC5.25 ^{1}H-NMR of **Ru-NDI-ethynyl-rhenium** in DMSO-d_6……...…..331

Figure SC5.26 ESI-mass spectrometry results of **Ru-NDI-ethynyl-rhenium** in acetonitrile. ($C_{67}H_{38}ClF_{12}N_{10}O_7P_2ReRu$) $[M]^{2+}$ calculated at m/z = 709.0605 and found at 709.0615……...……..……331

Figure SC5.27 FTIR spectroscopy results of **Ru-NDI** complexes in acetonitrile. The band (*) at ~1630 cm^{-1} indicates residual solvent…….....332

Appendix D

Figure SD6.1 ^{1}H-NMR of **TPP-NDI** in $DCMd_6$ in the aromatic region……..……..…335

Figure SD6.2 Aliphatic region ^{1}H-NMR in $DCMd_6$ of **TPP-NDI**……..……..….335

Figure SD6.3 Aromatic region ^{1}H-NMR in $DCMd_6$ of **Zn-TPP-NDI**……..……....335

Figure SD6.4 MALDI-TOF MS spectrum of **TPP-NDI** (experimental, black) and simulated isotope pattern (red). The measurements were carried out by researchers at the University of Bath in the UK……..……336

Figure SD6.5 MALDI-TOF MS spectrum of **Zn-TPP-NDI** (experimental, red) and simulated isotope pattern (black). The measurements were carried out by researchers at the University of Bath in the UK……...…..……..……..336

Figure SD6.6 Calculation of molar extinction coefficients for **TPP-NDI** and **Zn-TPP-NDI** attributed to the NDI moiety. The measurements were carried out in THF. The values were obtained at the NDI moiety ($\varepsilon = 3.9 \times 10^4$ $M^{-1}cm^{-1}$, at 356 nm for **Zn-TPP-NDI** and $\varepsilon = 4.7 \times 10^4$ $M^{-1}cm^{-1}$, at 356 nm for **TPP-NDI**)……...……..337

Figure SD6.7 Calculation of molar extinction coefficients for **TPP-NDI** and **Zn-TPP-NDI** attributed to the porphyrin moiety. The measurements were carried out in THF. The values were obtained at 416 and 424 nm for **TPP-NDI** ($\varepsilon = 5.96 \times 10^5$ $M^{-1}cm^{-1}$, at 416 nm) and **Zn-TPP-NDI** ($\varepsilon = 5.74 \times 10^5$ $M^{-1}cm^{-1}$, at 424 nm) respectively…..…..……...338

Table of Schemes

Chapter 2

Scheme 2.1 Simplified synthetic scheme for **Ru-NDI-1** as carried out by Chaignon et al. [22]…….……..66

Scheme 2.2 Simplified synthetic scheme for **Ru-PDI-1**, as carried out by Gunderson et al. [12].……67

Scheme 2.3 Simplified synthetic scheme for **Ru-PDI-2**(**A**) and **Ru-PDI-3(B**), as carried out by Dubey et al. [23]..……..68

Scheme 2.4 Simplified synthetic scheme for **Ru-PDI-4**, as reported by Schulze et al. [7]……69

Scheme 2.5 Simplified synthetic scheme for **Ru-NDI-2** and **Ru-NDI-3**, as reported by Skaisgirski et al. [3], where R = C_6H_{13}……70
Scheme 2.6 Simplified synthetic scheme for **Ru-NDI-4**, as performed by Chaignon et al. [22]……..71
Scheme 2.7 Simplified synthetic scheme for **Ru-NDI-5**, as performed by Frath et al. [15]……..72
Scheme 2.8 Simplified synthetic scheme for **Ru-NDI-6**, as performed by Ji et al. [25].....…..73
Scheme 2.9 Simplified synthetic scheme for **Ru-NDI-7** and **Ru-NDI-8** as performed by Johansson et al. [26]…….……...….73
Scheme 2.10 Simplified synthetic scheme for **Ru-NDI-9** and **Ru-NDI-10** as performed by Johansson et al. [27]……74
Scheme 2.11 Simplified synthetic scheme for **Ru-NDI-11**, (R = H, CH_3) , as reported by Johansson et al. [27] and **Ru-NDI-12**, as reported by Borgstrom et al. [8]…….…….....75
Scheme 2.12 Simplified synthetic scheme for **Ru-NDI-13**, as reported by Baron et al. [28]……..76
Scheme 2.13 Simplified synthetic scheme for **Ru-NDI-14**, as reported by W. Dixon et al. [21]……..76
Scheme 2.14 Simplified synthetic scheme for **Ru-PDI-5**, as reported by Nastasi et al. [29]……..77
Scheme 2.15 Simplified synthetic scheme for **Ru-PDI-6**, as reported by Santos et al. [30]……..78
Scheme 2.16 Simplified synthetic scheme for **Ru-PDI-7**, as reported by Maia et al. [2]……...……78
Scheme 2.17 Simplified synthetic scheme for **Ru-PDI-8**, as reported by Liu et al. [9]……79
Scheme 2.18 Simplified synthetic scheme for **Ru-PDI-9** and **Ru-PDI-10**, as reported by Kodama et al. [31]…….……...…80
Scheme 2.19 Simplified synthetic scheme for **Ru-PDI-11**, as reported by Aksakal et al. [32]……..81
Scheme 2.20 Simplified synthetic scheme for **Ru-PDI-12**, as reported by Prodi et al. [33]……..82
Scheme 2.21 Simplified synthetic scheme for **Ru-PDI-13**, as reported by Rodríguez-Morgade et al. [34]……...83

Scheme 2.22 Simplified synthetic scheme for **Ru-PDI-14**, as reported by Amati et al. [35]……..83

Table of Tables

Chapter 2

Table 2.1 A summarised table of the photophysical properties of a variety of ruthenium polypyridyl complexes, where a = bright $^3MLCT_{phen}$ and b = dark $^3MLCT_{phz}$, bpy = 2,2'-bipyridine, terpy = 2,2′:6′,2″-terpyridine, phen = 1,10-phenanthroline, dppz = dipyrido[3,2-a:2',3'-c]phenazine, mphen = (2-methyl-1,10'-phenanthroline), bqp = 2,6-bis(8'-quinolinyl)pyridine……...85

Table 2.2 A summary of photophysical parameters for Ru-NDI complexes, where a = fluorescence emission lifetimes and b = phosphorescent lifetimes……100

Table 2.3 A summary of photophysical parameters for Ru-PDI complexes, where a = fluorescence and b = phosphorescence……...100

Chapter 3

Table 3.1 Reduction potentials (vs. Fc^+/Fc) of **RuNDI^{2+}**, and reference compounds $[(Ru(bpy)_2(phen\text{-}6\text{-}NH_2]^{2+}$ and R_1-NDI-R_1 (dioctyl-NDI)……132

Table 3.2 The initial turnover numbers for the hydrogen evolution determined for three samples under identical conditions using 470 nm LED and Solar Simulator, followed by the TONs obtained in the subsequent recycling process carried out for each sample…..145

Chapter 4

Table 4.1 Summary of the spectroscopic, electrochemical, and spectroelectrochemical data for the **Ru(dceb)-NDI^{2+}** complex and the reduced species generated. All experiments were conducted in acetonitrile…….…...…167

Chapter 5

Table 5.1 Time-resolved infrared measurements of all Ru-NDI complexes, recorded in acetonitrile following excitation at 365 and 420 nm. The table summarises the kinetic data for the charge separation (τ_{CS}) and charge recombination (τ_{CR}) processes, with the corresponding lifetimes measured in picoseconds…….216

Table 5.2 Picosecond Transient Absorption measurements of all Ru-NDI complexes, recorded in acetonitrile and on a NiO, following excitation at 400 nm. The table summarises the kinetic data for the charge separation (τ_{CS}) and charge recombination (τ_{CR}) processes, with the corresponding lifetimes measured in picoseconds……..221

Table 5.3 Turnover numbers for hydrogen evolution and carbon dioxide reduction by Ru-NDI complexes reported in this work. Hydrogen experiment was carried out using 0.03 mM of photosensitising moieties in 8 ml mixture of ACN: TEA: H_2O (65:30:5) and $Pt(DMSO)_2I_2$ was employed as a catalyst (in non-rhenium complexes). Carbon dioxide reduction experiment was carried out using concentration of 0.05 mM for the photocatalysts, and 6 ml mixture of DMF and TEOA (5:1) as well as 0.1 M of BIH was employed……...227

Chapter 6

Table 6.1 Fluorescent lifetimes were obtained following excitation (375 or 510 nm) of **TPP-NH_2**, **TPP-NDI** and **Zn-TPP-NDI** in a range of solvents. The optical density at the excitation wavelength was ~ 0.2……..……..……..250

Appendix A

Table SA3.1 Energy differences of **RuNDI^{2+}** between structure ***a*** and ***b*** in the ground and triplet excited states……286

Table SA3.2 Energy differences of **RuNDI$^{+/0}$** in all possible reduced states……..…287

Table SA3.3 Major electronic excitations in **RuNDI^{2+}** determined by TDDFT calculations……289

Table SA3.4 Major electronic excitations in **RuNDI^{+}** determined by TDDFT calculations……292

Table SA3.5 Major electronic excitations in **RuNDI** determined by TDDFT calculations……297

Table of Equations

Chapter 1

Equation 1.1 Light reaction scheme in photosynthesis [27]……..7

Equation 1.2 Dark reaction scheme in photosynthesis, where CH_2O represents the general formula of a carbohydrate [27].……..…….……..7

Equation 1.3 Overall reaction of photosynthesis [27]……..…….7

Equation 1.4 Oxidation reaction of water molecule [51]…….11

Equation 1.5 Reduction reaction of water molecule [51]……11

Equation 1.6 Overall reaction of water molecule [51]…….11

Abbreviations

^{1}H-NMR proton nuclear magnetic resonance
^{13}C-NMR carbon nuclear magnetic resonance
ACN acetonitrile
ADC analog-to-digital converter
ATP adenosine triphosphate
Bipytpy 4′-(4-bromophenyl)-4,4‴:4",4‴'-dipyridinyl-2,2':6',2"-terpyridine
BIH 1,3-dimethyl-2-phenyl-2,3-dihydro-1H-benzo[d]imidazole
BL bridging ligand
BOP benzotriazole-1-yloxy-tris (dimethylamino)phosphonium hexafluorophosphate
bpy 2,2'-bipyridine
bqp 2,6-bis(8'-quinolinyl)pyridine
CAT catalyst
CB conduction band
COFs covalent organic frameworks
CV Cyclic Voltammetry
Dceb diethyl[2,2'-bipyridine]-4,4'-dicarboxylate
DCM dichloromethane
DFT density functional theory
DMA N,N-dimethylacetamide
DMF N,N-dimethylformamide
DMSO dimethylsulfoxide
DSSCs Dye-Sensitised Solar Cells
ESA excited state absorption
ET electron transfer
EU European Union
fs femtosecond
FTIR fourier transform infrared
GHEs greenhouse gas emission
GSB ground-state bleach
HER hydrogen evolution reaction
HOMO highest-occupied molecular orbital
IEA the International Energy Agency
IR infrared
IR-SEC infrared-spectroelectrochemistry
ISC intersystem crossing
LC ligand-centered
LECs light-emitting electrochemical cells
LED a light-emitting diode
LUMO lowest-unoccupied molecular orbital
MC metal-centred
MLCT metal-to-ligand charge transfer
MOFs metal organic frameworks
mphen 2-methyl-1,10'-phenanthroline
NADPH nicotinomide adenine dinucleotide phosphate
NDA naphthalenetetracarboxylic acid dianhydride
NDI naphthalene diimide
NECP The National Energy and Climate Plan
NHE normal hydrogen electrode
NiO nickel oxide
NI naphthalimide

ns nanosecond
NTA the National Transport Authority
OER oxygen evolution reaction
OPAs optical parametric amplifiers
OTTLE optically transparent thin-layer electrochemical
PDA perylenetetracarboxylic acid dianhydride
PDI perylene diimide
PDT photodynamic therapy
PEC photoelectrochemical cell
phen 1,10-phenanthroline
ps picosecond
PS photosensitiser
RDIs rylene tetracarboxylic diimides
REDII the second Renewable Energy Directive
ROS reactive oxygen species
SA sacrificial agent
SCE saturated calomel electrode
SE stimulated emission
SEAI the Sustainable Energy Authority of Ireland
SEC spectroelectrochemistry
TAC time-to-amplitude converter
TAS transient absorption spectroscopy
TBAH tetrabutylammonium hexafluorophosphate
tbbpy 4,4'-di-tert-butyl-2,2'-bi-pyridine
TCSPC time-correlated single photon counting
TD-DFT time-dependent density functional theory
TEA triethylamine
TEOA triethanolamine
terpy 2,2′:6′,2″-terpyridine
THF tetrahydrofuran
Tolyltpy 4′-tolyl-2,2′:6′,2′-terpyridine
TOF turnover frequency
TON turnover number
TPA triphenylamine
tpphz tetrapyridophenazine
TRIR time-resolved infrared
TRIR-SEC time-resolved infrared spectroelectrochemistry
UV-vis ultraviolet-visible
UV-vis-SEC ultraviolet-visible spectroelectrochemistry

Units of measurement and symbols

Δ**A** difference in absorption spectrum
Δ**OD** change in optical density
Δ**G°** Gibbs free energy
λ wavelength
λ_{exc} excitation wavelength
λ_{em} emission wavelength
τ lifetime
τ_{fl} fluorescence lifetime
τ_t triplet lifetime
τ_{CS} lifetime of charge separation
τ_{CR} lifetime of charge recombination
ε molar extinction coefficient
µs microsecond
µmol micromole
µmol·g_{cat}^{-1} micromoles per gram of catalyst
cm^{-1} reciprocal wavelength
eV electron volts
fs femtosecond
K Kelvin
KJ kilojoule
L litre
M molar
mg milligram
MJ megajoule
ml millilitre
mm millimolar
mol mole
nm nanometre
ns nanosecond
°C degrees Celsius
ps picosecond
TWh terawatt-hours
vol % percentage volume
W watt
ϕ_{fl} fluorescence quantum yield

Thesis Abstract

Title: Development of Novel Dyes for Photocatalytic Hydrogen Evolution. Design, Synthesis, Photophysical and Electrochemical Properties along with Time-Resolved Infrared-Spectroelectrochemical Simulation of Photocatalytic Processes.

Name: Martyna Bartusiak

The adverse impacts of climate change and global warming on the environment such as, air pollution and deforestation must be mitigated, and renewable sources of energy must be more frequently employed. **Chapter 1** focuses on the scale of greenhouse gas emissions, and it explores solutions for sustainable energy. The primary approach proposed in this thesis involves photocatalytic hydrogen evolution and carbon dioxide valorisation, which can be successfully carried out in laboratory settings using a variety of photosensitisers and photocatalysts. Key components of the photocatalytic processes are described along with photophysical and electrochemical measurements for the analysis of compounds synthesised in this dissertation.

Chapter 2 includes a literature review focussed on the synthesis, photophysical and electrochemical properties of naphthalene diimide (NDI)/perylene diimide (PDI) ruthenium complexes. The review provides a rationale for why Ru-NDIs/PDIs compounds can be utilised for photocatalysis. A ruthenium-naphthalene diimide donor-acceptor system ($RuNDI^{2+}$) was synthesised for hydrogen evolution (**Chapter 3**). The complex was investigated using photophysical and electrochemical techniques, including time-resolved infrared spectroscopy (TRIR) and nanosecond-transient absorption spectroscopy (TAS), spectroelectrochemistry and electrochemistry. Furthermore, photoactive intermediates formed during photocatalysis and their photophysical characteristics were investigated. In **Chapter 4**, the Ru(dceb)-NDI^{2+} (4,4′-di(carboxyethyl)bipyridine ruthenium-naphthalene diimide) photosensitiser was synthesised for hydrogen evolution. Incorporation of the peripheral ester groups was observed to influence the photophysical, electrochemical and spectroelectrochemical properties, as well as hydrogen evolution in comparison to the bipyridine analogue studied in **Chapter 3**. In **Chapter 5**, a range of Ru-NDI complexes were investigated using TRIR and TAS, where the impact of different functional groups on their photophysical properties was studied. In **Chapter 6**, the synthesis, photophysical and electrochemical properties of porphyrin-naphthalene diimide compounds are presented. The Rehm-Weller approach was used to determine the thermodynamic driving force for hydrogen evolution.

CHAPTER 1

INTRODUCTION

1.1 Abstract

Chapter 1 introduces the topic of renewable, sustainable and environment-friendly energy sources and highlights why it is so important to address and find alternative sustainable solutions to overcome or at least slow down the adverse impacts of climate change and global warming on the environment. Negative effects that are present worldwide for example air pollution, significant increase of global temperatures, weather fluctuation and deforestation of the environment, are primarily caused by the burning of fossil fuels and subsequent emission of greenhouse gases into the atmosphere, which are predominantly anthropogenic. Renewable and green sources of energy for example powered by sunlight and wind, which are widely available, are promising solutions to address the negative consequences of climate change. However, in order to incorporate green energy sources more widely into our economy, major changes in industrial processes are necessary to reduce our reliance on fossil fuels. Furthermore, it is governments globally need to invest resources in cleaner and more sustainable energy as well as implement relevant policies regarding the use of fossil fuels.

Potential sustainable solutions include photocatalytic hydrogen evolution and carbon dioxide reduction, and these aspects will be discussed in detail in this dissertation. The photoactive compounds incorporating metals such as ruthenium, rhenium or porphyrin moieties as photosensitisers for the photocatalytic hydrogen evolution are briefly described in this introduction chapter to provide insights into their photophysical and electrochemical properties, their molecular structures and their photocatalytic applications. Additionally, photophysical and electrochemical techniques are described together with the rationale for using the technique. The primary techniques employed in this work include transient absorption studies (TAS), time-resolved infrared studies (TRIR), cyclic voltammetry (CV), electrochemistry, spectroelectrochemistry (SEC) and TRIR combined with SEC (TRIR-SEC) employed for simulating photocatalytic processes.

1.2 An Overview of the Energy Crisis: Why is it so important to take an action now?

In the past few decades our planet has experienced a severe energy crisis including global energy shortage and corresponding high prices that are projected to become even worse. This is primarily caused by a continuous increase in global energy demand and consumption, which is mainly attributed to the development and employment of new technologies involving machinery advancements in industrial processes, as well as continuous expansion of building constructions, agriculture and transportation, and most recently artificial intelligence. Consequently, these sectors of the global economy heavily depend on fossil fuels for example oil, coal and natural gas for driving all of the aforementioned processes. In 2024, global electricity consumption increased by approximately 1100 terawatt-hours (TWh) and gas demand escalated by 115 billion cubic meters [1]. Notably, there is ongoing insufficient use and employment of renewable forms of energy based on wind, solar, and hydro energy into the economy, and further efforts are required to increase their contribution to the energy sources. Currently, only 40% of the total electricity generation comes from the renewable and nuclear sources [1]. This is mainly caused by limited accessibility of sun or wind and there are high costs associated with green technologies including solar panels and wind turbines [2, 3]. For example, the cost of solar panels for a household in Ireland is approximately 7000 – 10,000 euro, which is prohibitive for many [4]. Hence, this highlights the importance of introducing more efficient and more affordable solutions. Greenhouse gas emissions (GHEs), which include carbon dioxide, methane, nitrous oxide increase on an annual basis and hence, they can lead to serious consequences for example damages to nature and species extinction [5 – 7]. In addition, the emission of harmful gases into the atmosphere can have negative impacts on human and animal well-being and health. Figure 1.1 presents that there is a significant increase in the demand for fossil fuels, and currently these values are at a peak. The International Energy Agency (IEA) stated that it might be almost impossible to immediately reduce these numbers and consequently, it will be challenging to achieve the objectives and goals outlined in Paris Agreement, whose main aim is to limit the temperature increase to below 1.5°C to prevent further negative impacts on climate change and reduce gas demand by 75% by 2050 [8, 9]. Even if the goal will be achieved, it will not be possible to mitigate global warming and it will be challenging to completely restore our planet [8, 9]. Governments around the world have committed to take actions and introduce new policies to reduce carbon dioxide emissions and achieve net-zero emissions by 2050, consequently the transition from fossil fuels to renewable

forms of energy and their incorporation into our daily lives must begin now in order to meet this goal [10].

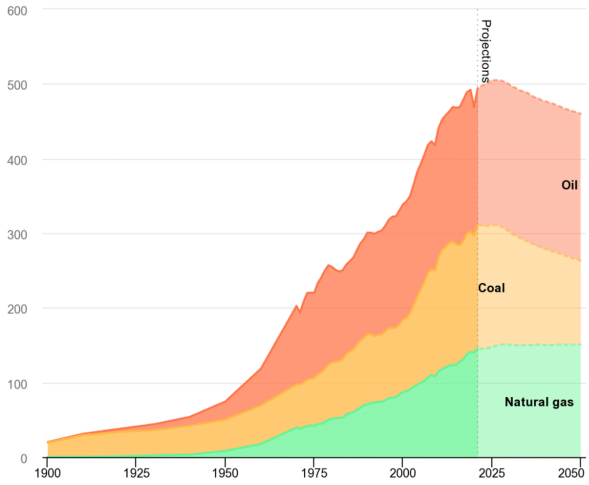


Figure 1.1 The demands for fossil fuels in 1900 – 2050. The figure was obtained from the online sources [8].

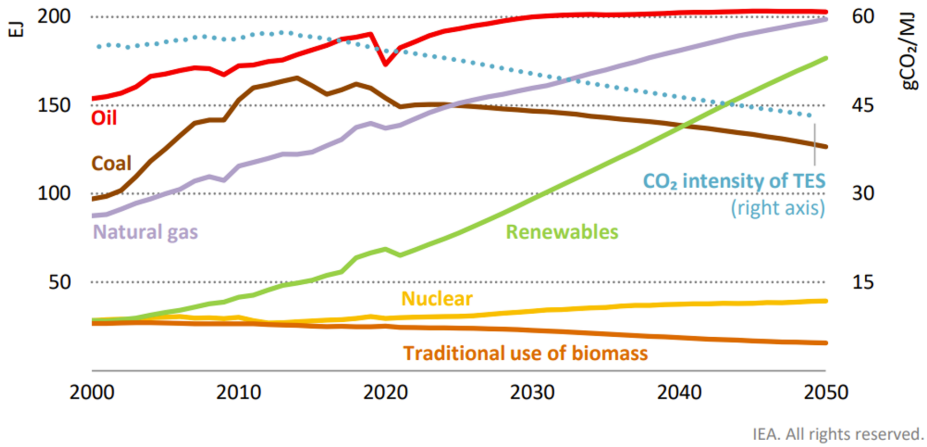


Figure 1.2 The graph represents total energy production and carbon dioxide emissions. Renewable energy supply is projected to increase significantly by 2050. The figure was obtained from the document published online by IEA [10].

In order to highlight how serious the energy crisis has become, it is important to present some of the statistical data and figures. The Sustainable Energy Authority of Ireland (SEAI) stated in 2024 that fossil fuels accounted for 82.7% of the primary energy demand in Ireland [11]. However, on a positive note, in 2023 the highest value of renewable energy was achieved, accounting for 14.1% of Ireland's primary energy [11]. The total energy demand in 2023 was 163.8 TWh and 55.6% of all energy in Ireland accounted for oil products, diesel and petrol and national energy emissions were determined to be 31.4 $MtCO_2eq$ (million tonnes of carbon dioxide equivalent) [11]. Nevertheless, global temperatures continue to rise, and this leads to serious consequences for example weather

changes, extreme heatwaves, floods and storms, which we observe to occur every year with a greater intensity and severity [12 – 14].

The overall amount of carbon dioxide emission coming from fossil fuels in 2023 was determined to be approximately 36.8 billion tonnes [15]. Despite the negative impacts on people's lives and health, the COVID-19 pandemic in 2020 – 2022 showed that by decreasing global economic activities it is possible to slow down the release of greenhouse gases into the atmosphere, and this provided the opportunity for the environment to slightly recover. Many people worked from home, which resulted in a decrease of daily commutes, air travel was significantly reduced, and moreover, many industrial processes were completely stopped. As a result, GHEs decreased temporarily. For example, transport emissions in Ireland decreased to 16% and international aviation went down to 64% during the pandemic [11]. Once, the global economy reopened and lockdown measures were lifted, gas emissions spiked significantly again and unfortunately, these figures are expected to increase in the coming years. However, this showed that by slightly decreasing some of our activities or industrial processes, we can reduce the amount of GHEs.

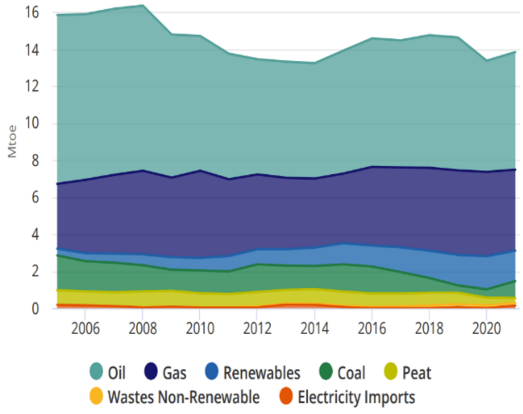


Figure 1.3 The primary energy inputs in Ireland. Oil and gas contribute significantly, with approximately 7 and 5 million of tonnes of oil equivalent (Mtoe), respectively [14].

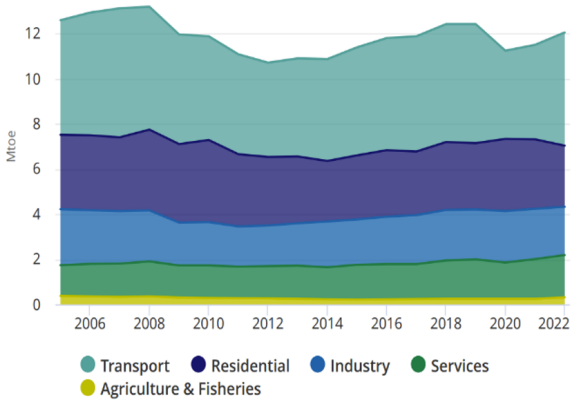


Figure 1.4 Ireland's total greenhouse gas emissions by industrial sector [14].

The global energy consumption, based on projections, is expected to increase by 47% by 2050 and GHEs are projected to rise by 50%, if oil remains the primary source of energy, as observed in Figure 1.3 [14]. The challenges and concerns of the twenty-first century, which include global warming, environmental degradation and excessive energy consumption require the urgent need for innovative and sustainable solutions. Therefore, it is essential that new solutions are developed and implemented for green and renewable energy.

1.3 Addressing the Energy Crisis and Transition from Fossil Fuels to Renewable Sources of Energy

A number of sustainable sources of energy exist, including solar, wind, geothermal, hydropower, and biomass energies [16, 17], which are abundant as depicted in Figure 1.5. Using these sustainable approaches have the potential to reduce GHEs. This dissertation primarily focuses on how the natural process of photosynthesis carried out by plants is mimicked to develop artificial photosynthetic assemblies in a laboratory environment for hydrogen evolution and carbon dioxide reduction reactions. Undoubtedly, hydrogen gas has potential to become a future fuel and replace traditional fossil fuels in combustion.

1.3.1 Renewable Resources

The second Renewable Energy Directive (REDII) represents the European Union's legislation, which is primarily focused on promoting renewable sources of energy. The legislation proposed a target of 32% for overall renewable energy by 2030 and requires all member countries to adhere to these guidelines [18, 19]. The National Energy and Climate Plan (NECP) 2021 – 2030, stated that Ireland's target for renewable energy is 34.1% by 2030, and this value was recently updated to 43% [11, 19, 20]. In 2020, the Renewable Energy target aimed for ~ 10% of energy consumed in road and rail transport to come from renewable sources, and Ireland successfully achieved 10.2%. The next goal is to further increase the incorporation and employment of renewable-based fuels into the Irish economy to 29% by 2030 [11]. This means that the country must develop sustainable methods and focus more on novel scientific research, technological advancements, supported by financial investment. In Figure 1.6, it is clear that the use of wind energy and solar photovoltaic panels along with biomass for electricity generation can reduce carbon dioxide emissions in Ireland. Hence, the country has the potential to become "a greener island" with respect to renewable energy.

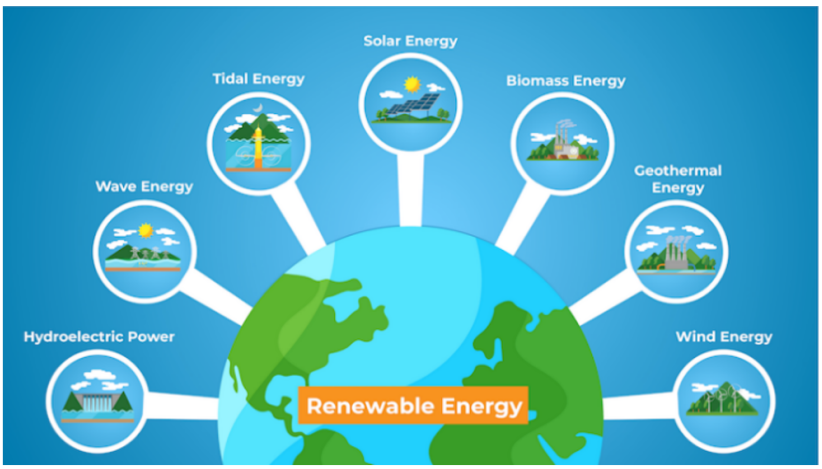


Figure 1.5 Possible renewable sources of energy. The figure was obtained from the online sources [21].

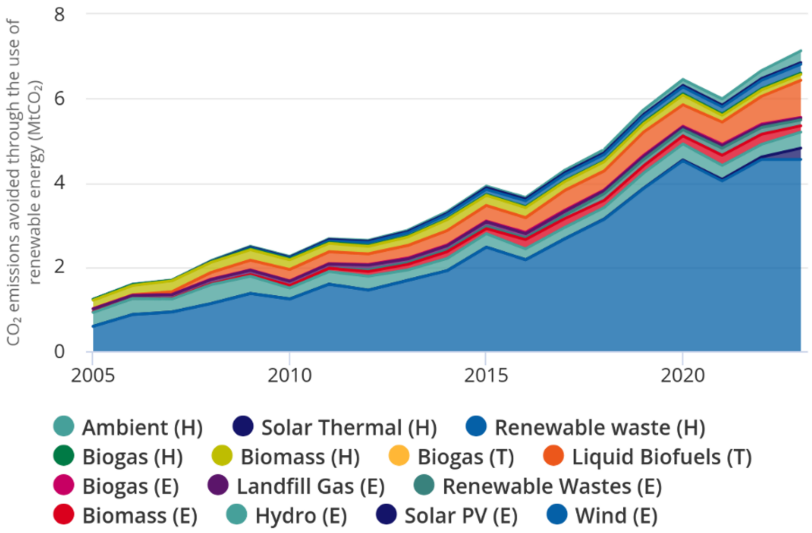


Figure 1.6 The declining trend in carbon dioxide emissions upon the incorporation and use of renewable energy in Ireland. The figure was obtained from the document published by SEAI [22].

1.3.2 Natural Photosynthesis

The process of photosynthesis is one of the most fundamental processes and the primary foundation of the food chain [23, 24]. This natural mechanism inspired the development of photocatalytic assemblies in the laboratory setting, which were used to obtain fundamental knowledge of light-induced reactions. These reactions and their corresponding principles will be briefly summarised in this section. The photosynthesis process requires photosynthetic tetrapyrrole chlorophyll pigments, that absorb in the visible light of the electronic absorption spectrum [25]. Chlorophyll pigments are not only present in plants, but also in algae, and bacteria for example in cyano- and heliobacteria

[26]. These pigments play a significant role as they harvest sunlight and convert solar energy into chemical energy, which is subsequently used to form organic compounds and food for organisms, primarily carbohydrates [26 – 28]. It is also important to highlight, that molecular oxygen gas is released into the atmosphere as a byproduct of the reaction (Figure 1.7), and this has many advantages for the environment because oxygen improves the overall air quality and contributes to the formation of the ozone layer in the atmosphere [27, 28]. The photosynthetic process involves two mechanisms that take place at the same time, and these are defined as light and dark reactions as presented in Figure 1.7. Additionally, both of these take place in plant's organelles called chloroplasts but in different parts and their mechanism is briefly described as follows. Firstly, the light-dependent reaction, which takes place in the thylakoid membrane of the chloroplast, initially starts with the absorption of sunlight by chlorophyll. Photoexcitation leads to electron-hole pairs, with the water molecule is split into oxygen, protons and electrons, as presented in Equation 1.1 [26 – 28]. The next step involves the formation of high-energy molecules for example adenosine triphosphate (ATP) and nicotinomide adenine dinucleotide phosphate (NADPH), and these are further used in the transport of energy, which is necessary for the next process [28]. The dark reaction (Equation 1.2) is also called the Calvin cycle, and it takes place in the stroma of the chloroplast. The protons and electrons formed in the first process are used to convert carbon dioxide to carbohydrates (CH_2O) [27]. Those processes are summarised in the equations below and their standard free energy changes of the reaction, G° are also presented.

$$2H_2O + light \rightarrow O_2 + 4H^+ + 4e^- \ (G^o = +317\ kJ \cdot mol^{-1})$$

Equation 1.1 Light reaction scheme in photosynthesis [27].

$$CO_2 + 4H^+ + 4e^- \rightarrow CH_2O + H_2O \ (G^o = +162\ kJ \cdot mol^{-1})$$

Equation 1.2 Dark reaction scheme in photosynthesis, where CH_2O represents the general formula of a carbohydrate [27].

$$H_2O + light + CO_2 \rightarrow CH_2O + O_2 \ (G^o = +479\ kJ \cdot mol^{-1})$$

Equation 1.3 Overall reaction of photosynthesis [27].

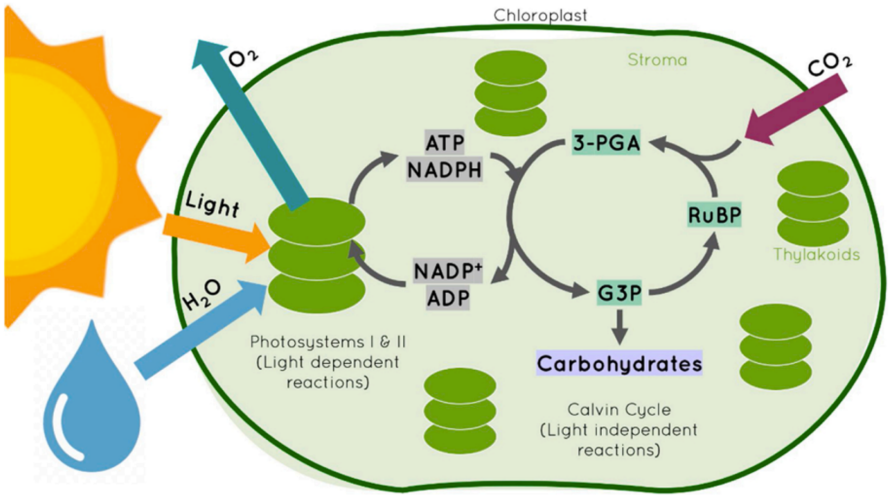


Figure 1.7 Diagram illustrating the process of natural photosynthesis. The schematic was adapted from literature sources by López Pacheco et al. [28].

The most important role of natural photosynthesis is to produce glucose but also this process contributes to the reduction of carbon dioxide levels in the atmosphere. The data indicates that approximately 200 billion tonnes of carbon dioxide can be converted into organic chemical compounds and subsequently around 140 billion tonnes of molecular oxygen can be produced in the atmosphere [27]. These values highlight how important is it to stop deforestation because plants play a crucial role in our environment. Furthermore, the process/mechanism of natural photosynthesis allows us to incorporate its reactions into artificial photosynthesis, which could be carried out in laboratory settings either on the surface of semiconductors or in solution. These concepts are further explained in a greater detail in the next section.

1.3.3 Artificial Photosynthesis

Artificial photosynthesis and its corresponding light-driven chemical reactions are the primary focuses of this dissertation. All of the designed and synthesised compounds in this work including ruthenium, rhenium and porphyrin photosensitising moieties were assessed in photocatalysis reactions, for hydrogen evolution, studied both in solution and on the surface, and for carbon dioxide reduction reactions. The process of artificial photosynthesis follows the principal mechanisms similar to natural photosynthesis carried out by plants, as described in the previous section. However, instead of producing glucose and oxygen, the main objective is to either generate hydrogen or reduce carbon dioxide into its more valuable and less harmful products by employing light-harvesting moieties. Hence, photosynthetic conditions are simulated in laboratory settings. In order to perform artificial photosynthesis in solution, it is important to consider some of the fundamental factors. These include the design of photocatalytic assemblies, with the desired photophysical and electrochemical features, suitable metal catalysts and sacrificial electron donors, experimental conditions including solvent choice, pH and temperature, light sources and many other factors which will be discussed throughout the thesis.

The fundamental idea of artificial photosynthesis in a laboratory setting was proposed by the Italian chemist Giacomo Ciamician in 1912 [29, 30]. In his research paper, he highlighted that six hours of sunshine could produce an amount of heat equivalent to burning 1.35 kg of coal [29, 30]. His work was later expanded by Japanese chemists Kenichi Honda and Akira Fujishima in 1972, who introduced and explained in detail the water-splitting process following irradiation [29, 31]. Their experimental set up involved a photoelectrochemical cell, which consisted of a titanium dioxide (TiO_2) acting as a photoanode semiconductor and a black platinum (Pt) cathode. The cell was placed in water and exposed to UV-light. In this experiment, TiO_2 released an electron upon absorption of a photon, leading to the creation of an electron hole-pair or in other terms a positive charge on Ti. The excited electron moved away from the valance band (VB, the lower energy band) to the conduction band (CB, the higher energy band). Following this, as depicted in Figure 1.8, the electron hole (h^+) on the Ti atom was filled by an electron released from water molecule, oxidising the water to produce oxygen at the photoanode. The released electron was transferred to a proton originating from water. Therefore, by gaining an electron, the proton was reduced to produce hydrogen at the photocathode [29, 31]. In summary, artificial photosynthesis on the surface requires the presence of a photosensitiser, a catalytic centre and an electron-hole pair transfer [29 – 33]. The photon

absorption is influenced by the energy band gap of the semiconductor or the HOMO-LUMO gap of the photosensitiser [32, 33].

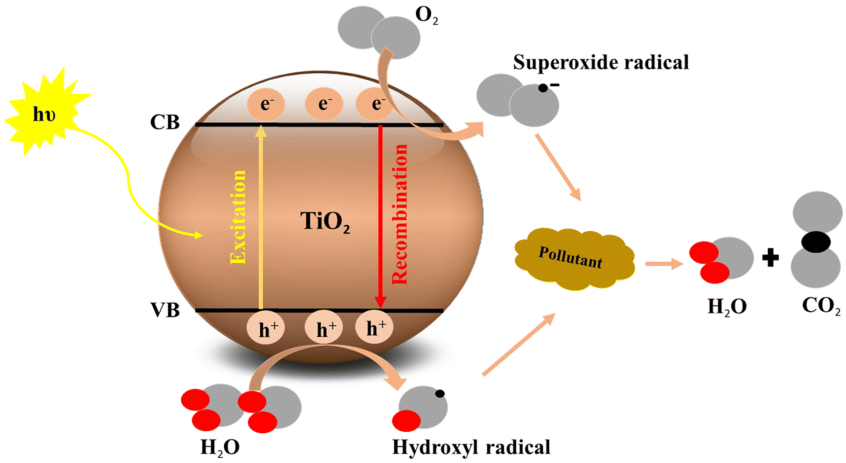


Figure 1.8 Schematic diagram representing the process of photocatalysis using titanium dioxide as a semiconductor, adapted from the literature [33].

Honda's experiment [29, 31] inspired future researchers to develop materials for water splitting. The design of suitable photocatalytic assemblies requires the photosensitisers to absorb in the visible or near-infrared regions [34 – 36]. In the case of semiconductors for example TiO_2, the band gap must be smaller than 3.2 eV, which corresponds to a wavelength less than 387.5 nm, to promote electrons to higher energy levels (from the valence band to the conduction band) [37]. However, the design of photoanode materials with suitable band energy gaps is very challenging and time consuming. This indicates how much more research is necessary to be carried out in the field of artificial photosynthesis.

1.3.4 The Water-Splitting Process in Photocatalysis

The mechanism of photocatalysis can take place in solution and on the surface of a semiconductor. In this section, both mechanisms will be briefly explained. In both cases, the photocatalyst or light-harvester must efficiently absorb the visible light (400 – 700 nm), which is typically supplied by either LED lamps or solar simulator [38]. In studies, which involve semiconductors, this allows to excite and promote an electron from the valence band (VB) to the conduction band (CB) (from lower to higher energy level band), as depicted in Figure 1.8. This process creates an electron-hole pair (h^+) [29 – 33]. The next step involves the transfer of the electrons from the CB to the surface of the catalyst leading to the reduction reaction, which generates hydrogen (HER) as depicted in Equation 1.5, and the electron-holes are transferred from the VB to the surface of the photocatalyst causing an oxidation reaction (OER) to form oxygen as shown in Equation

1.4. The efficient electron transfer can be often enhanced by employing different metal or metal oxides for example Pt, NiO, RuO_2 and TiO_2 [39, 40]. The water-splitting process is an endothermic reaction, which means energy must be supplied for the reaction to take place, and it is necessary to provide a Gibbs free energy of 1.23 eV per electron [41].

Photocatalytic water-splitting process ($H_2O \rightarrow H_2 + ½O_2$) is challenging and requires in addition to the photosensitiser a metal catalyst, for example platinum or palladium, and a sacrificial electron donor such as triethylamine or triethanolamine [42 – 45].

In designing suitable photocatalysts for artificial photosynthesis, it is advantageous to include density functional theory (DFT) calculations, to help identify the excited states populated and determine the HOMO-LUMO gap [46]. Electrochemical studies are often applied for this purpose also, however, these are limited to ground state interactions between the energy levels, instead of excited states [47]. Furthermore, charge recombination must be considered when designing photocatalytic systems, because this is often the bottleneck in photocatalysis [48]. If charge recombination occurs very fast, it prevents electron transfer to the catalyst centre. As a result, photocatalysis does not take place and the charge recombination process could be considered as one of the limiting factors [32, 38 – 52].

$$2H_2O \rightarrow O_2 + 4H^+ + 4e^-$$

Equation 1.4 Oxidation reaction of water molecule [51].

$$2H^+ + 2e^- \rightarrow H_2$$

Equation 1.5 Reduction reaction of water molecule [51].

$$H_2O + 1.23\,eV \rightarrow H_2 + \frac{1}{2}O_2\,(G^o = +237\,kJ \cdot mol^{-1})$$

Equation 1.6 Overall reaction of water molecule [51].

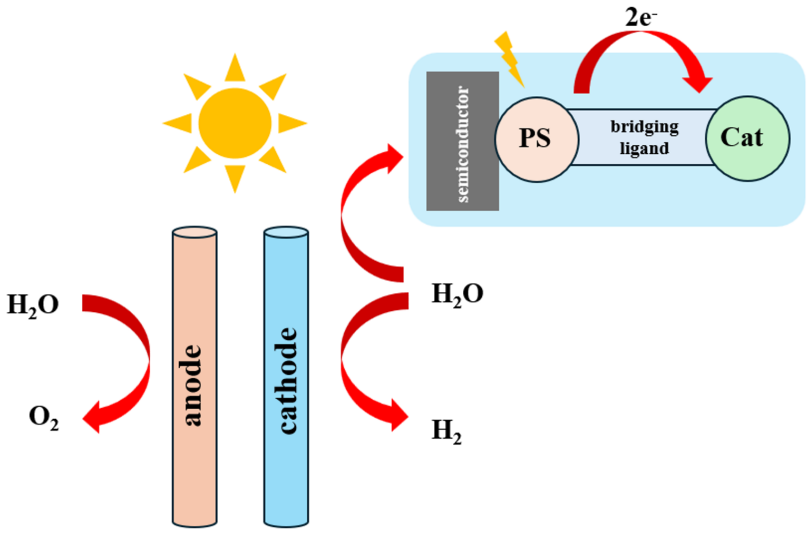


Figure 1.9 Simplified diagram representing photocatalytic water-splitting process on the semiconductor. The schematic was reproduced based on the literature knowledge and created using PowerPoint® [31, 33, 37].

1.4 Hydrogen Fuel as an Essential Component of Future Energy Systems

Obtaining an insight from the literature books, in the 19th century, the French author Jules Verne stated that "water will one day be employed as fuel, that hydrogen and oxygen which constitute it, used singly or together, will furnish an inexhaustible source of heat and light, of an intensity of which coal is not capable" [53, 54]. Hydrogen due to its high-density energy has the potential to replace fossil fuel to some degree [55]. The amount of energy stored by hydrogen is equal to 120 MJ/kg, and this value is almost three times higher in comparison to the energy density of gasoline at 43.4 – 45.8 MJ/kg [56, 57]. Hydrogen gas is gaining popularity for its use in vehicles. An example of that is a collaboration between the National Transport Authority (NTA) of Ireland and Bus Éireann, which involved an investment in three new hydrogen fuelled electric double-decker buses. The buses are currently used on Dublin roads, and the results of this innovative project have been positive, which resulted in a successful reduction of 20,000 litres of diesel and a decrease of 50 tonnes of carbon dioxide emissions [58]. Other examples of sustainable green hydrogen generation methods include the following, microbial biomass conversion, electrolysis and photocatalysis, which produce only water as a byproduct. Therefore, adaptation to this type of energy could achieve zero emissions of greenhouse gases and reduce air pollutants [59]. Hydrogen gas can be used to generate electricity and heat, and, as a result, it could significantly contribute to decarbonisation

of industrial processes [60]. It can become a future energy source, and the hydrogen economy could be expected to be widely expanded.

1.4.1 The Hydrogen Prospect by 2050

The future employment of hydrogen in energy sectors look highly promising. According to the Climate Action and Low Carbon Development Act 2021 Ireland has a to be carbon-neutral economy by 2050. Furthermore, greenhouse gas emissions must be significantly reduced by 51% in 2030 [61, 62]. In addition, the European Union Hydrogen Strategy highlights that hydrogen will contribute to 13 – 14% of EU's energy consumption [62, 63]. Additionally, the National Hydrogen Strategy indicates that the domestic energy demand for hydrogen in Ireland will have to increase to a range of 4.6 – 39 terawatt-hour, while air travel and shipping are expected to be in the range of 19.8 to 74.6 terawatt-hour [62]. The prospects for the integration of hydrogen by 2050 should result in the cost of green hydrogen decreasing to €2.5 – 4.5 c/kilowatt-hour [62]. In conclusion, more advanced methods for transportation, use and storage of hydrogen gas must be developed.

1.5 Dye-Sensitised Solar Cells

Dye-Sensitised Solar Cells (DSSCs) are used to generate electricity upon exposure of organic materials to light in electrochemical cells [64]. One of the first applications of DSSCs involved the extraction of chlorophyll from spinach leaves to form a chlorophyll-sensitised zinc oxide electrode [64, 65]. Following irradiation of the chlorophyll dye, electrons moved into the conduction band of the semiconductor, which consequently led to the generation of electricity [64, 65]. Furthermore, the development of these solar cells continued with the employment of TiO_2 electrodes in order to improve their efficiency. This first application of DSSCs has led to a breakthrough discovery of Grätzel cells by Brian O'Regan and Michael Grätzel [66]. These cells achieved efficiencies of 7% under simulated solar light and 12% in daylight [66]. In the past few years, significant progress has been made in the design and development of efficient DSSCs. However, some limitations and challenges still need to be overcome, and this includes for example long-term stability, electrolyte outflow and dye degradation [67, 68]. Ruthenium complexes [69 – 72] and porphyrin compounds [73 – 76] are often employed in DSSCs.

The fundamental idea of DSSCs can also be employed for hydrogen production, which involves photoelectrochemical water splitting processes and utilises dye-sensitised semiconductors to absorb light [77]. Recently, Baron et al. [78] employed a

pyrrrolopyrrole cyanine photosensitiser, which absorbed light in the near-infrared region of the UV-vis spectrum (~ 700 – 800 nm), and it was sensitised on the TiO_2 surface for photocatalytic hydrogen evolution. The system achieved 400 turnover number (TON) in the presence of ascorbic acid after 6 hours of light irradiation with solar simulator. In another study, Maeda et al. [79] designed a series of ruthenium (II) complexes with differing functional groups at the bipyridine moiety (H, CH_3, CF_3) as photosensitisers and they were immobilised on semiconductor nanosheets ($HCa_2Nb_3O_{10}$). Their Ru-CH_3 system exhibited a significantly higher hydrogen evolution efficiency, which reached 3800 TON after 20 hours of light exposure. Giannoudis et al. [80] examined the photocatalytic performance of a phosphonate-derivatised ruthenium tris-diimine photosensitiser (Figure 1.10), which was sensitised on a nickel oxide (NiO) photocathode, and it was covalently attached to a cobaloxime catalyst. The system achieved approximately 24% Faradaic efficiency for hydrogen production under irradiation at 400 – 800 nm.

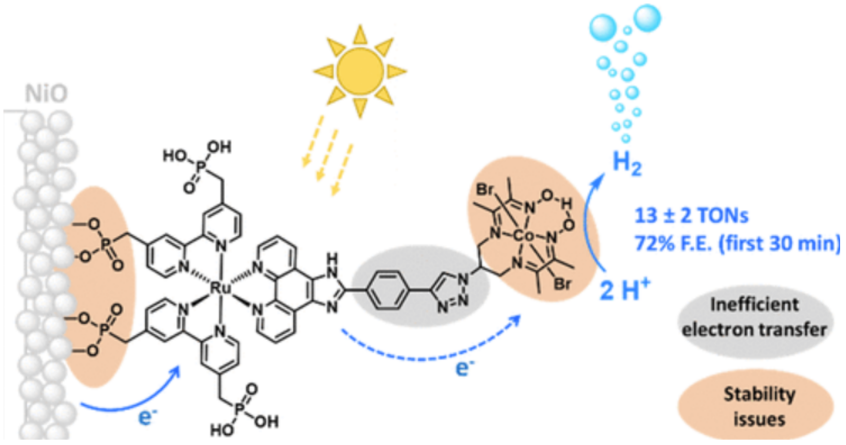


Figure 1.10 Diagram representing photocatalytic water-splitting process on the NiO semiconductor adapted from and examined by Giannoudis et al. [80].

1.6 Photocatalytic Carbon Dioxide Reduction and the Generation of Valuable Compounds

Another example of the photocatalytic process that could be used to combat the release of harmful gases into the atmosphere and subsequently reduce greenhouse gas emissions is the photocatalytic carbon dioxide reduction reaction. This process converts carbon dioxide into more valuable products that are significantly less toxic to the environment. However, the process involves complex electron redox mechanisms and leads to the generation of various products for example methane, carbon monoxide, ethene, ethanol and formic acid [81, 82], as presented in Figure 1.11. One of the challenges when carrying out carbon dioxide reduction, in contrast to the hydrogen evolution reaction, is that carbon dioxide is highly stable and in order to reduce it to anion radical species a power of –1.9 eV vs NHE (normal hydrogen electrode) at pH 7 is necessary [83, 84]. Water can also be a byproduct because carbon dioxide reduction competes with the water-splitting process, as they have comparable reduction potentials. For this reason, a photocatalyst is employed to favour and drive carbon dioxide reduction [85]. Hawecker et al. [86] examined carbon dioxide reduction for a solution of $[ReBr(bpy)(CO)_3]$ (acting as a photosensitiser), $Co(bpy)_3^{2+}$ (acting as a catalyst), and CO_2 in a mixture of triethanolamine and DMF. After 17 hours of light irradiation (1000 W, Xe lamp), this resulted in 0.3 ml of hydrogen produced as well as 11.4 ml of CO evolved. A recent study by Santoro et al. [87] examined a supramolecular photocatalyst containing Ru(II) polypyridine units as photosensitisers and Re(I) moieties as catalytic centres, as presented in Figure 1.12. In addition, a CO_2TEOA adduct was incorporated into the structure to drive CO_2 reduction. The highest turnover number for carbon monoxide formation was reported to be 2695 TON, which was carried out in DMA (N,N-dimethylacetamide)-TEOA mixture with BIH (1,3-dimethyl-2-phenyl-2,3-dihydro-1H-benzo[d]imidazole) acting as the electron reductant, under excitation at 530 nm [87]. The literature presents various systems for carbon dioxide reduction, which incorporate porphyrin systems [88 – 91], ruthenium [92 – 95] and iridium assemblies [96, 97] and rhenium-based catalysts [98 – 100].

$$CO_2 + e^- \rightarrow CO_2^- \qquad (-1.9\,V)$$

$$CO_2 + 2H^+ + 2e^- \rightarrow HCOOH \qquad (-0.61\,V)$$

$$CO_2 + 2H^+ + 2e^- \rightarrow CO + H_2O \qquad (-0.53\,V)$$

$$CO_2 + 4H^+ + 4e^- \rightarrow HCHO + H_2O \qquad (-0.48\,V)$$

$$CO_2 + 6H^+ + 6e^- \rightarrow CH_3OH + H_2O \qquad (-0.38\,V)$$

$$CO_2 + 8H^+ + 8e^- \rightarrow CH_4 + H_2O \qquad (-0.24\,V)$$

$$2CO_2 + 12H^+ + 12e^- \rightarrow C_2H_4 + 4H_2O \qquad (-0.34\,V)$$

Figure 1.11 Proton assisted carbon dioxide reactions and their valuable products along with their corresponding electrode potentials vs. standard hydrogen electrode (V) reported at a pH of 7 [101].

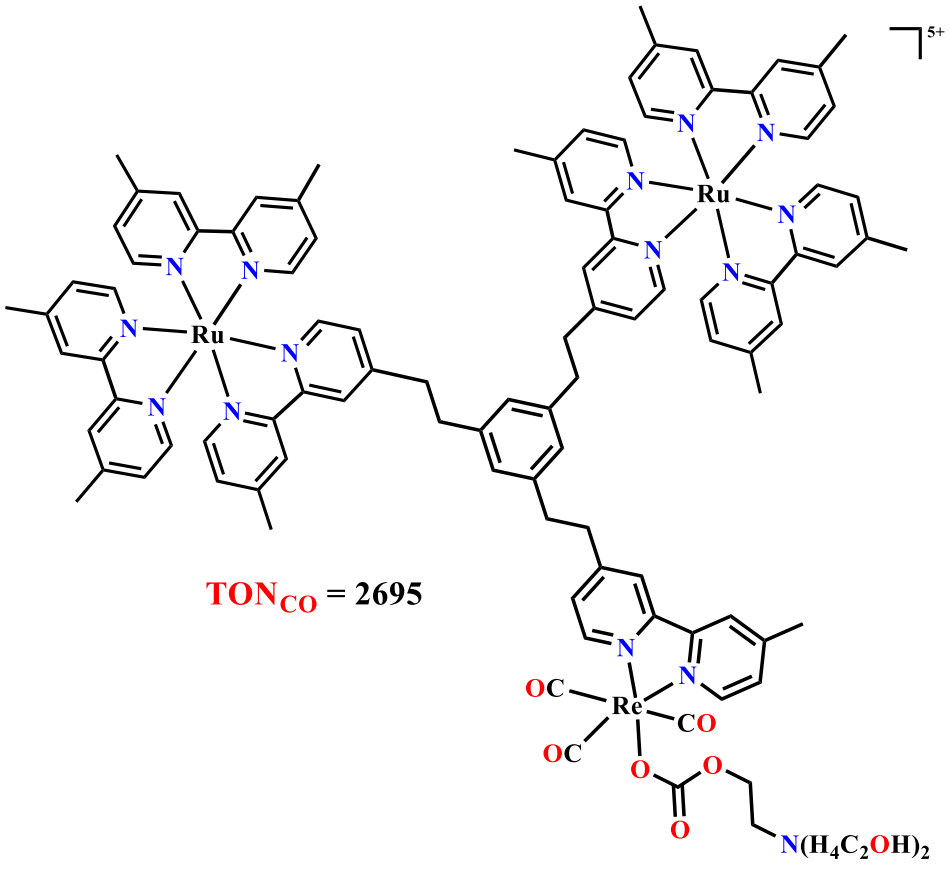


Figure 1.12 Supramolecular photocatalyst for carbon dioxide reduction synthesised and examined by Santoro [87].

1.7 Photocatalytic Systems for Hydrogen Evolution in Solution and Their Components

The primary focus of this dissertation is the design and synthesis of photosensitisers or photocatalysts for hydrogen evolution. These systems include ruthenium and porphyrin-based photosensitisers, which were examined for their hydrogen evolution in solution using both inter- and intramolecular approaches. Additionally, their photophysical, electrochemical and spectroelectrochemical properties were investigated in a great detail.

1.7.1 Intramolecular and Intermolecular Photocatalytic Assemblies

Intramolecular and homogeneous (in solution under photocatalytic conditions) photocatalytic systems employed for photocatalytic hydrogen evolution consist of three primary components, the photosensitiser (PS), bridging ligand (BL) and catalytic centre (Cat), which are connected to one another through a covalent linkage to form a photocatalyst, as presented in Figure 1.14 [102 – 104]. In order to successfully generate hydrogen, it is important to fully understand their mechanism of absorbing light, charge separation and charge recombination processes, as well as the electron transfer pathways occurring within these assemblies. Therefore, detailed electrochemical characterisations and photophysical analyses of these systems must be carried out prior to carrying out photocatalysis. The process of photocatalysis is initiated by dissolving the photocatalyst in a suitable solvent, followed by the addition of sacrificial electron donor, and the exposure of the photosensitiser to the visible light (380 – 700 nm) [105, 106], which subsequently leads to the excitation of an electron from the ground state (GS) or highest occupied molecular orbital (HOMO) to the excited state or lowest unoccupied molecular orbital (LUMO). This process results in the formation of photoexcited charge-separated species (PS*), which possess enough of thermodynamic driving force for proton reduction in water molecules [107, 108]. In summary, electron transfer occurs from the light-harvesting moiety across the bridging ligand and finally to the catalytic centre, where the water-splitting process takes place and this is often called unidirectional electron transfer [103]. Sacrificial electron donors (EDs or SDs) are often employed in the photocatalysis to ensure continuous electron flow to the charge-separated species. Additionally, this employment of ED/SD ensures that these species can return to their initial form, to the ground state and allow the process to take place again, as presented in Figure 1.13 and Figure 1.14. Following light absorption by the photosensitiser and the formation of charge separated species, hydrogen can be produced through fundamental

mechanisms such as reductive and oxidative quenching. Reductive quenching takes place when the electron transfer occurs from the sacrificial electron donor to the photoexcited photosensitiser (the photosensitiser gains the electron and forms PS^{-}) [109]. Consequently, the reduced photosensitiser, PS^{-} species, then transfer electron to the catalytic centre and this leads to the reduction of the water molecule to form hydrogen gas. In oxidative quenching, the electron transfer takes place from the photoexcited photosensitiser to the catalytic centre (the photosensitiser loses the electron and forms PS^{+}), and then these oxidised species return to the initial form, to the ground state upon the addition of the sacrificial electron donor [109]. Intramolecular systems are often studied in the literature, and these include for example ruthenium metal complexes [110, 111], porphyrins [112, 113] and BODIPYS [114].

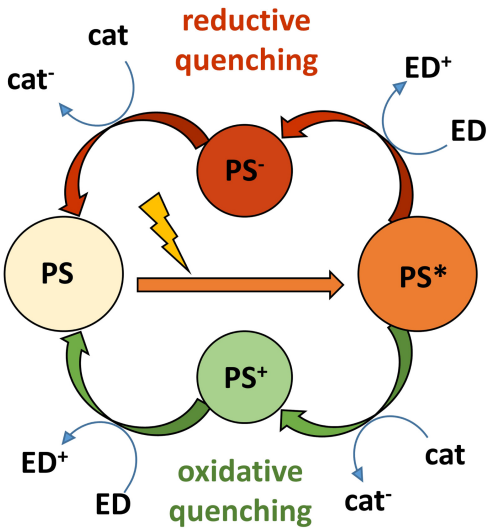


Figure 1.13 Reductive and oxidative quenching, in which ED is sacrificial electron donor, PS is the photosensitiser and Cat is the catalyst. The figure was adapted from Corredor et al. [109].

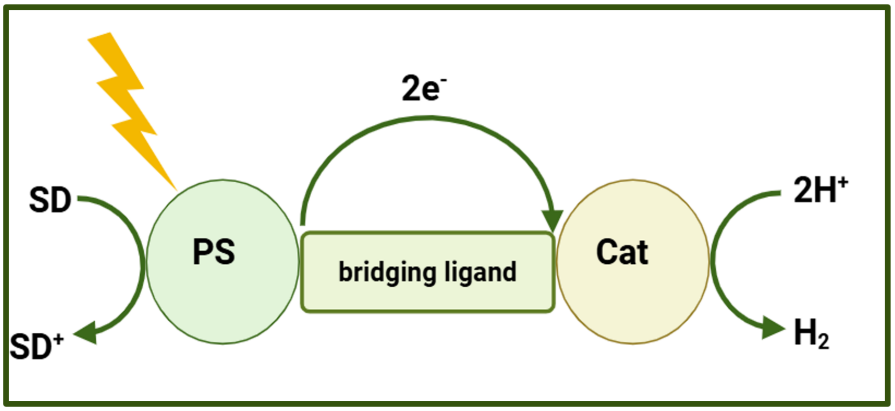


Figure 1.14 Intramolecular system for hydrogen generation. PS = photosensitiser, Cat = catalytic centre, and SD = sacrificial electron donor. The schematic was created using PowerPoint® [102 – 104].

On the other hand, intermolecular photocatalytic assemblies, as illustrated in Figure 1.15, function through a similar mechanism to that of intramolecular systems but in the intermolecular systems, the photosensitiser and catalytic centre are not covalently linked. Their individual components such as the photosensitising moiety and the catalyst are placed in a solution, where they interact with each other through diffusion processes [104, 115 – 117]. In theory, the transfer of electrons from the photosensitiser to the catalytic centre in such assemblies could be more challenging and consequently, it can reduce the efficiency of hydrogen evolution [115], however this is not always the case, as these processes are more complex than that. Therefore, a detailed examination of the photoactive species formed in the photocatalysis is necessary to make better conclusions, on which systems are better suited for this application.

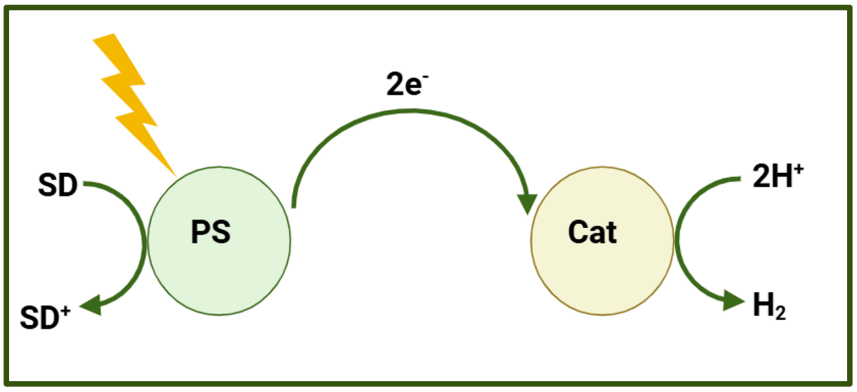


Figure 1.15 Intermolecular system for hydrogen generation. PS = photosensitiser, Cat = catalytic centre, and SD = sacrificial electron donor. The schematic was created using PowerPoint® [104, 115 – 117].

The literature presents many examples of intramolecular and intermolecular systems designed for hydrogen generation through photocatalysis. It is quite challenging to determine the most effective type of systems. Due to diffusion limitations, intermolecular systems could be less efficient, however this is not always true as previously mentioned, and it depends on several factors and photocatalytic conditions. The efficiency and quantity of hydrogen produced, measured in turnover numbers (TONs) often depends on the choice of light-harvester, molecular design, and photocatalytic conditions. In the next section, few examples of inter- and intramolecular systems are briefly summarised in order to provide an overview of the systems suitable for hydrogen evolution. This thesis primarily focusses on ruthenium, rhenium, porphyrin and naphthalene diimide compounds employed for hydrogen generation.

1.7.2 Ruthenium-Based Photocatalytic Systems for Hydrogen Evolution

Since the development of artificial photosynthesis as well as in recent years, ruthenium-based complexes have always gained a lot of interest because of their rich photophysical and electrochemical properties, which make those systems suitable for photocatalytic hydrogen evolution. There are many examples of compounds/complexes in the literature incorporating ruthenium moieties, some of which will be discussed in detail below. One of the first examples of ruthenium in hydrogen evolution was conducted by Lehn and Sauvage in 1977 [118, 119], who made significant discovery, and they became the main contributors to the field of artificial photosynthesis. The authors utilised $[Ru(bpy)_3]^{2+}$ as a light-harvesting moiety, triethanolamine (TEOA) as a sacrificial electron donor, K_2PtCl_4 as a catalyst and $[Rh(bpy)_3]^{3+}$ as a mediator for water reduction. The system was exposed to light absorption with an excitation wavelength exceeding 400 nm, and it characterised with an electron transfer from the excited ruthenium towards rhodium complex and finally to the catalytic centre, K_2PtCl_4. The highest turnover number (TON) of 750 was reported by the authors. One year later, Kalyanasundaram et al. [120] examined $[Ru(bpy)_3]^{2+}$ as an intermolecular system for photocatalytic hydrogen production, similarly to Lehn and Sauvage [118, 119], however they have employed slightly different conditions. The authors investigated the $[Ru(bpy)_3]^{2+}$ complex as a photosensitiser, using methylene viologen as the electron mediator, TEOA as the electron donor and a colloidal PtO_2 catalyst. After 30 minutes of light irradiation, 0.40 ml of H_2 was produced. Later on, Rau and co-workers [121] proposed well-known heterodinuclear, intramolecular Ru-Pd assemblies for the photocatalytic hydrogen generation, in which ruthenium moiety served as a photosensitiser, $PdCl_2$ acted as a catalytic centre and these units were connected through a bridging ligand (tetrapyridophenazine, tpphz) via a conjugated redox π-electron system (Figure 1.16A). The photocatalytic process was carried out in a mixture of acetonitrile and triethylamine (TEA). The highest TON of 56 was achieved upon the light irradiation at 470 nm. The hydrogen evolution for the system without the platinum catalyst in the structure was determined to be 0.56 TON. The authors stated that the quantity of hydrogen evolved was affected by the concentration of TEA. At a TEA concentration of 2.08 mol L^{-1}, hydrogen was obtained with a 56 TON, however at a concentration of 3.6 mol L^{-1} there was no hydrogen produced [121].

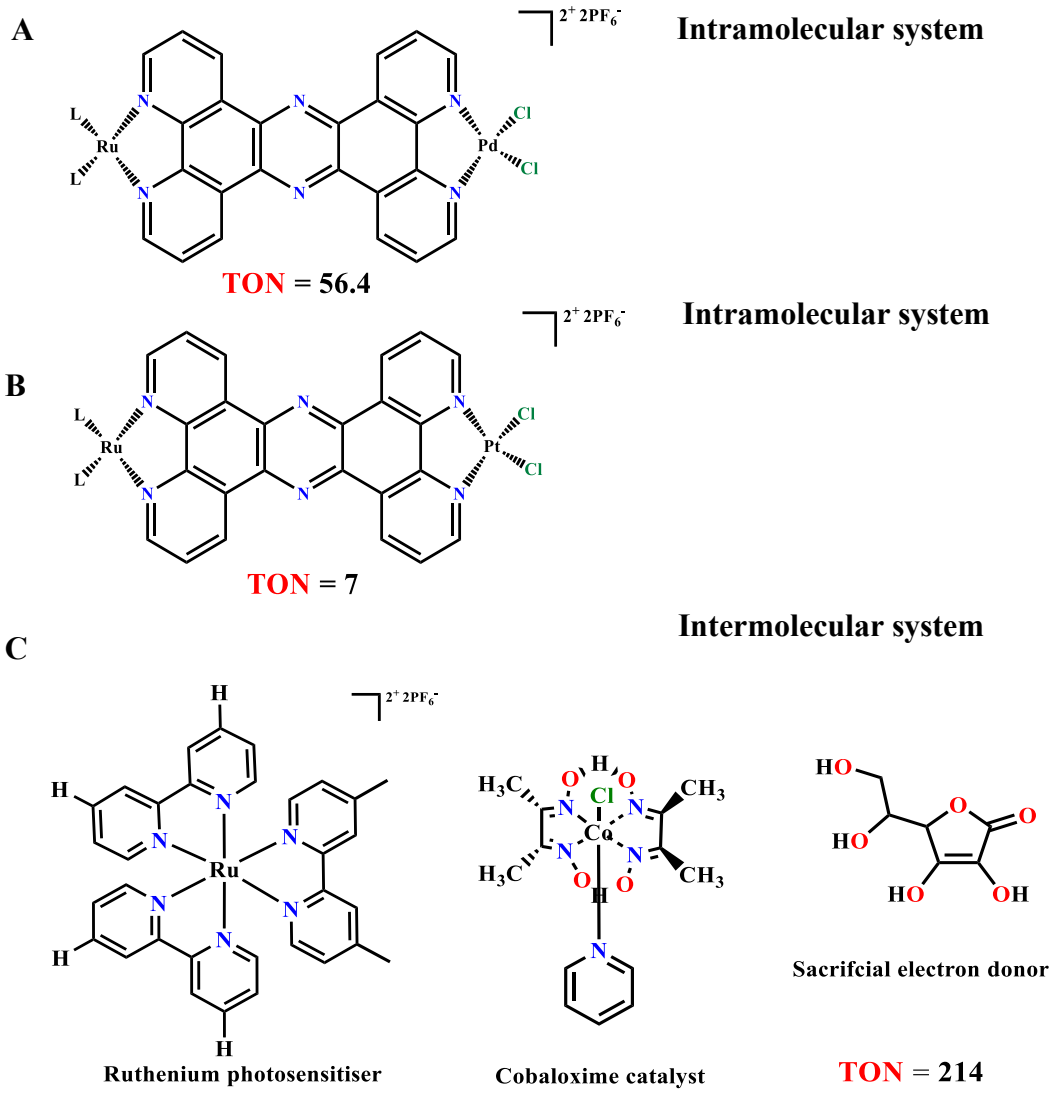


Figure 1.16 (A) An intramolecular ruthenium photocatalytic assembly proposed by Rau and co-workers [121] incorporating palladium as a catalyst and **(B)** an intramolecular ruthenium photocatalytic assembly proposed by Pffefer et al. [42] incorporating platinum, where L = 4,4'-di-tert-butyl-2,2'-bipyridine. **(C)** an intermolecular ruthenium photocatalytic assembly proposed by Deponti et al. [122].

The study from our research group by Cerpentier et al. [110] also focussed on photocatalysts involving ruthenium and platinum in the molecular structure. The authors designed an intramolecular ruthenium system, RuPt as depicted in Figure 1.17, and examined its capabilities for photocatalytic hydrogen evolution in a mixture of acetonitrile, triethylamine and water (60:30:10) using a 470 nm LED. Following light irradiation, after 24 hours, hydrogen was produced with a TON of 81. Under similar conditions (acetonitrile, triethylamine, water at 470 nm light irradiation), Pfeffer et al. [42] reported even lower TONs of 7 for their Ru-Pt dinuclear system, which is also significantly lower than the values reported by Cerpentier at al. [110] (TON = 81) and

Rau et al. [121] for their palladium analogue, Ru-Pd (TON = 56). This shows that the choice of catalyst also has a significant impact on hydrogen evolution efficiency. On the other hand, Deponti et al. [122] examined intermolecular system, which involved ruthenium polypyridine photosensitiser for hydrogen evolution, in the presence of cobaloxime catalyst, and ascorbic acid as the sacrificial electron donor (Figure 1.16C). The highest turnover number of 214 was achieved following light irradiation with a 175 W Xenon arc lamp. This research highlights that intermolecular systems can also generate hydrogen evolution and often they can result in higher TONs in comparison to intramolecular assemblies. Additionally, this indicates that the employment of different catalysts (cobaloxime vs platinum) could potentially have a significant impact on the hydrogen evolution efficiency.

Additionally, the incorporation of ester functional groups by Cerpentier et al. [110] at the bipyridine moiety of the ruthenium systems, was determined to have a positive impact on the rate of hydrogen production. Incorporation of the esters was also examined by Kowacs et al. [123], who designed and synthesised two assemblies $[Ru(bpy)_2(2,5\text{-}bpp)PtIS]^{2+}$ and $[Ru(dceb)_2(2,5\text{-}bpp)PtIS]^{2+}$ where bpy = 2,2′-bipyridine, 2,5-bpp = 2,2′,5′,2″-terpyridine, dceb = 4,4′-di(carboxyethyl)bipyridine, and S = solvent, as presented in Figure 1.18B. The first system (without ester groups) resulted in a TON of 80, and the system with ester groups yielded 650 TON of hydrogen after 18 hours of light irradiation at 470 nm, in a mixture of acetonitrile, water and triethylamine. Das and co-workers [124] also investigated a ruthenium type photocatalyst, $[Ru(dceb)_2(\mu\text{-}bisbpy)PtCl_2][PF_6]_2$, which incorporates ester units in its molecular structure (Figure 1.18A). Under photocatalytic conditions similar to those reported by Kowacs et al. [123] and Cerpentier et al. [110], the authors reported a TON of 286 with 10% water content and 258 TON at 5% water content, when irradiated at 470 nm. Notably, when the platinum catalytic centre was replaced by palladium, the TON value was slightly increased up to 360 TON at 10% water content, and further to 513 TON at 5% water content [124]. In conclusion, these findings suggested that palladium enhances hydrogen evolution efficiency. However, the optimal water content remains unclear, as the TON values do not showcase a consistent trend with respect to water concentration. The aforementioned research studies involving ester groups inspired us to design and examine a ruthenium-based photocatalytic system, which incorporates ester moieties, and this is presented in Chapter 4.

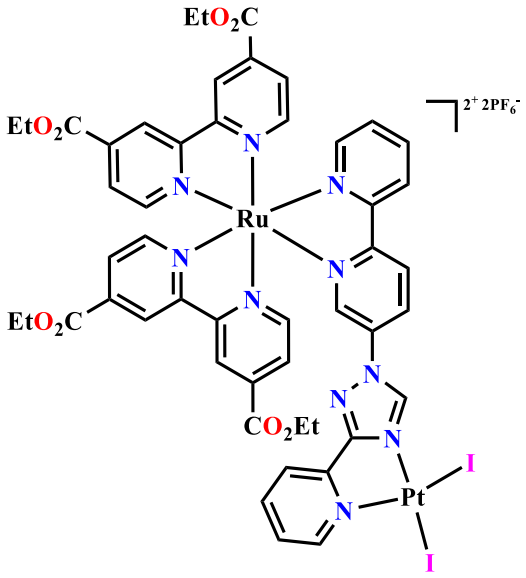


Figure 1.17 An intramolecular RuPt photocatalytic assembly proposed by Cerpentier et al. [110].

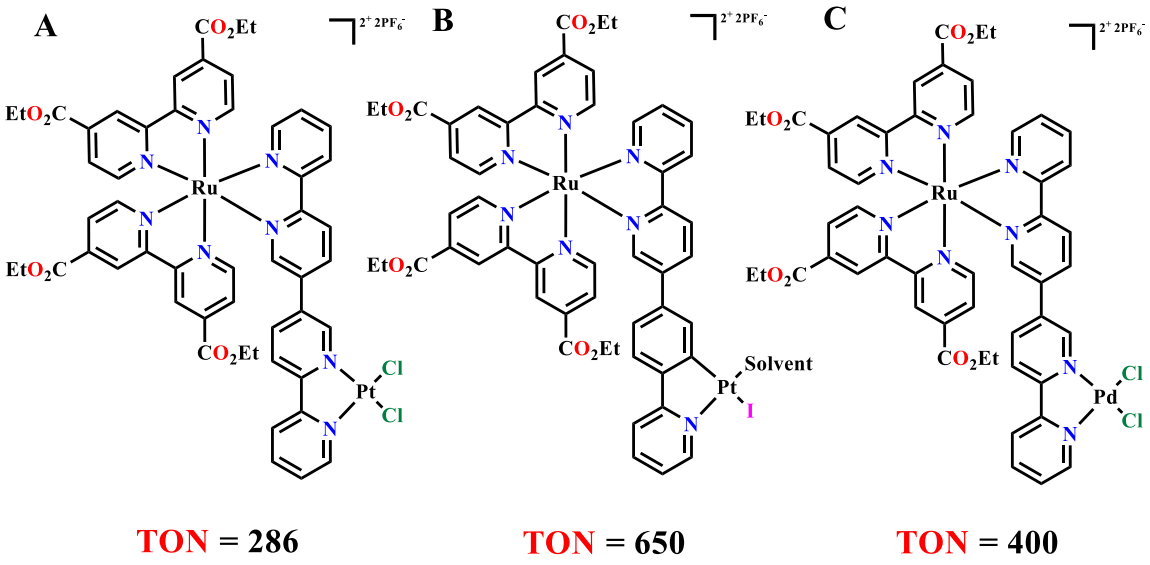


Figure 1.18 An intramolecular photocatalytic assembly proposed by Das et al. [124], Bindra et al. [125] and Kowacs et al. [123], where **A** = $[Ru(dceb)_2(\mu\text{-bisbpy})PtCl_2][PF_6]_2$, where bisbpy = 2,2':5',3'':6'',2'''-quaterpyridine and **B** = $[Ru(dceb)_2(2,5\text{-bpp})PtIS]^{2+}$, where 2,5-bpp = 2,2′,5′,2″-terpyridine and **C** = $[Ru(dceb)_2(\mu\text{-dpp})PdCl_2]^{2+}$, where dpp = 2,5-di(pyridine-2-yl)pyrazine.

Karnahl and co-workers [126] synthesised a heterodinuclear ruthenium assembly similar to the one reported by Rau et al. [121], $[(tbbpy)_2Ru(tpphz)PdCl_2]_2$, (Figure 1.19), where tbbpy = [4,4'-di-tert-butyl-2,2'-bi-pyridine] and tpphz = tetrapyrido[3,2-a:2',3'-c:3'',2''-h:2''',3'''-j]phenazine, which resulted in 209 TON with 10% water content, and this value was increased to 238 TON at 15% water content, following irradiation at 470 nm in the presence of TEA. The authors concluded that hydrogen evolution was influenced by the addition of water, which could enhance the solvent polarity, proton mobility and the stability of the charge-separated species [126]. Incorporating bromine atoms in the bridging ligand resulted in lower hydrogen production efficiency (TON = 94.2) [126]. Tschierlei and co-workers [127] also observed similar water effect in their Ru-Pd photocatalytic assembly, whose structure was the same to the one examined by Rau et al. [121] and Karnahl et al. [126]. The addition of 10 vol % water resulted in higher TONs, with a maximum value of 161 TON. This indicated that water had a positive effect on the hydrogen evolution due to increased solvent polarity and increased efficiency of proton mobility.

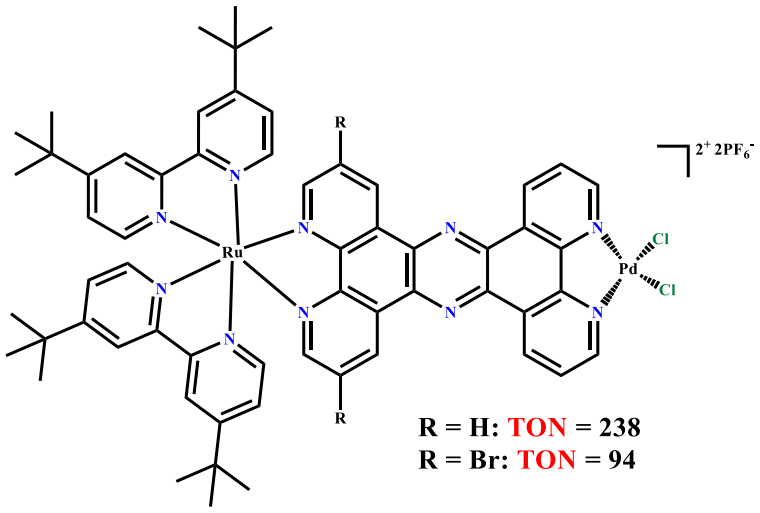


Figure 1.19 An intramolecular photocatalytic assembly proposed by Rau et al. [121] and Karnahl et al. [126].

The aforementioned examples indicate that the overall success of hydrogen evolution is significantly influenced by the choice of peripheral ligands, the light exposure time, water contribution and employment of electron-withdrawing groups. Additionally, other factors for example the use of different catalysts could also contribute to an enhancement of photocatalytic performance. Fihri et al. [128] reported a Ru-Co photocatalytic assembly, where cobalt served as the catalytic center, as presented in Figure 1.20. The system achieved a maximum TON of 103 after 15 hours of light exposure with visible light. It was determined to be competitive, less expensive and as a result more sustainable

compared to the systems incorporating platinum or palladium as catalysts [42, 110, 121, 126, 127].

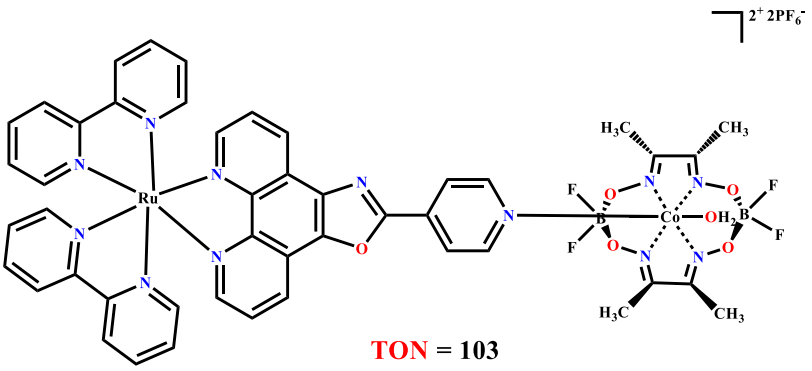


Figure 1.20 An intramolecular photocatalytic assembly proposed by Fihri et al. [128].

A recent publication on ruthenium photocatalytic systems focusses on enhancing the stability and efficiency of hydrogen evolution by incorporating water-soluble $Na_4[Ru((SO_3Ph)_2phen)_3]$ derivative (RuSPhphen, $(SO_3Ph)_2phen$ = disodium (1,10-phenanthroline-4,7-diyl)bis(benzenesulfonate)) instead of typical $[Ru(bpy)_3]^{2+}$ (Figure 1.21) [129]. The system was examined for photocatalytic activity using a cobalt tetraazamacrocyclic complex as the catalyst and ascorbate (HA^-) as the sacrificial electron donor, following light irradiation at 400 – 700 nm. Hydrogen generation with RuShphen achieved TON values of up to 3000 compared to approximately 1630 TON for $[Ru(bpy)_3]^{2+}$ [129].

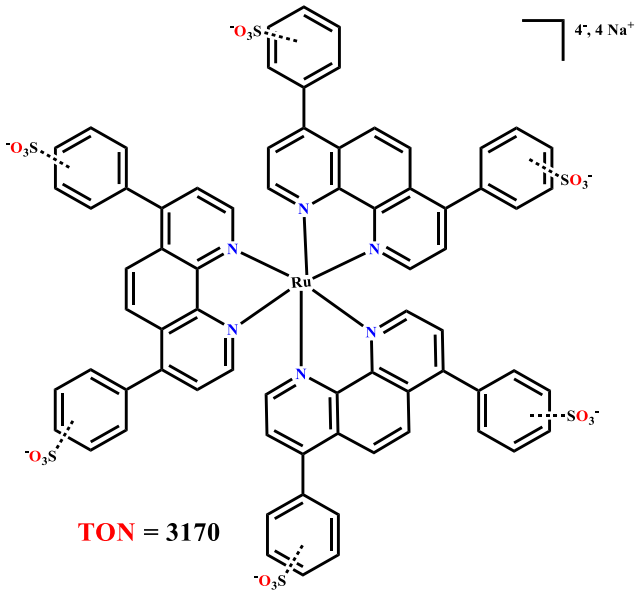


Figure 1.21 An intermolecular photocatalytic assembly proposed by Camara et al. [129].

It is important to mention that intermolecular systems are often capable of outperforming intramolecular systems in hydrogen evolution as observed in studies carried out by Deponti et al. [122]. A more recent example of an intermolecular system developed by Edwards and co-workers [130] involved $[Ru(bpy)_3]^{2+}$ as a photosensitiser, ascorbic acid as an electron donor and a cobalt microperoxidase-11 catalyst, resulting in TONs ranging from 606 to 2390. Rupp et al. [131] synthesised the photosensitiser $[Ru(Tolyltpy)(Bipytpy)](PF_6)_2$, where Bipytpy = 4′-(4-bromophenyl)-4,4‴:4″,4‴′-dipyridinyl-2,2′:6′,2″-terpyridine and Tolyltpy = 4′-tolyl-2,2′:6′,2′-terpyridine (Figure 1.22). The photocatalytic hydrogen evolution experiment was carried out using this photosensitiser, triethanolamine as a sacrificial electron donor, and cobaloxime as a catalyst. The system and the corresponding photocatalytic conditions were impressively stable for 12 days, and a high TON of 764 was achieved upon light irradiation at 450 nm [131].

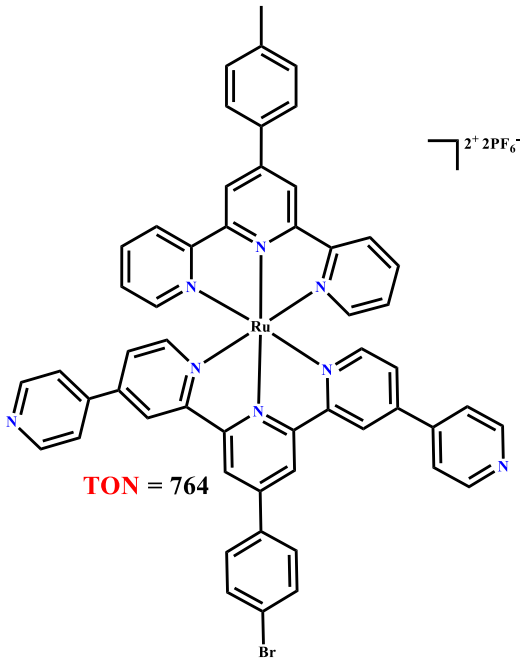


Figure 1.22 A ruthenium photosensitiser for intermolecular photocatalytic assembly proposed by Rupp et al. [131].

1.7.3 Porphyrin-Based Photocatalytic Systems for Hydrogen Evolution

Porphyrin compounds are highly planar, aromatic macrocycles characterised by an 18-π electron conjugated system. The structure of porphyrins resembles that of chlorophyll dye, which is used by plants in natural photosynthesis (Figure 1.23). Porphyrins absorb visible light and are photostable, and as a result they are ideal candidates to mimic photosynthesis and produce hydrogen under photocatalysis conditions [112, 113, 132]. With porphyrins, as with ruthenium complexes, many factors must be considered. The amount of hydrogen generated is highly dependent on the conditions used, the choice of suitable catalyst, modification in bridging ligands, and the effect of incorporating various metals into the porphyrin framework [112]. As no standard experimental conditions exist for photocatalytic hydrogen generation it is difficult to compare systems with one another and determine what exactly is the best for photocatalytic activities. The following examples will highlight how these small variations in the system can influence photocatalytic hydrogen production.

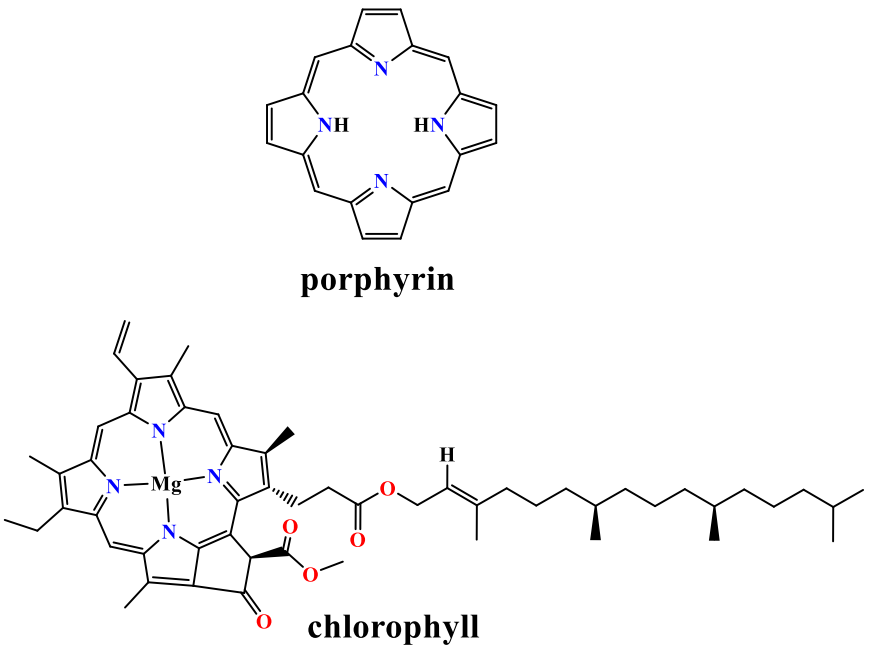


Figure 1.23 Schematic diagram of porphyrin framework and chlorophyll molecule [133].

Zhang et al. [134] designed and examined an intramolecular system that incorporated a zinc porphyrin as a photosensitiser, which was linked to cobalt catalytic center by axial coordination of a pyridyl group at the periphery of the porphyrin (Figure 1.24). The authors used TEA as a sacrificial electron donor, and a mixture of THF and water in a

ratio of 8:2. Following irradiation with an Xe lamp and a cutoff filter ($\lambda > 400$ nm), the system resulted in 46 TON of hydrogen under these photocatalytic conditions. The authors concluded that a short bridge between the porphyrin unit and the cobalt center is required in order to enhance hydrogen evolution (46 TON vs 35 TON, for shorter and longer linkage, respectively). Furthermore, the ligands at the porphyrin framework were substituted with bulky hydrophobic tert-butylbenzene groups. However, the TON values were lower with these groups (TON = 22), which suggested a reduced driving force for the electron transfer [134].

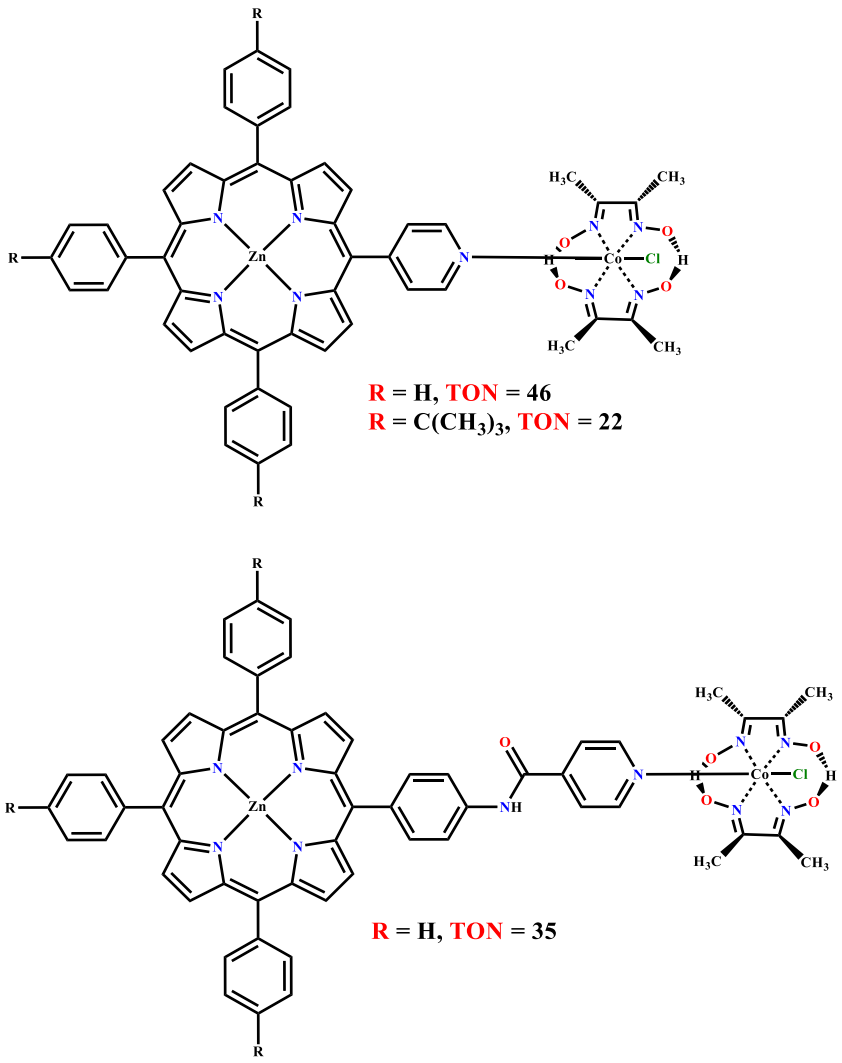


Figure 1.24 Intramolecular photocatalytic assemblies of zinc porphyrin and cobaloxime proposed by Zhang et al. [134].

Another example of the impact of peripheral ligand substitution at the porphyrin framework was examined by Bodedla et al. [135]. The authors synthesised intermolecular porphyrin photocatalytic assemblies, which incorporated naphthalimide moieties (NI) at various positions of the porphyrin ring, as presented in Figure 1.25. Photocatalytic experiments were conducted using the porphyrin system, platinum as a co-catalyst, and TEOA as a sacrificial electron donor. The para-substituted porphyrin generated greater amounts of hydrogen in contrast to the ortho- and meta-substituted ones. The maximum TON was 1265 after one hour of light exposure at 420 nm. The location and position of the NI groups on the phenyl rings of the porphyrin influenced electron transfer between the NI group (acting as an electron donor) and the porphyrin (acting as an electron acceptor), and consequently this affected the excited states populated [135].

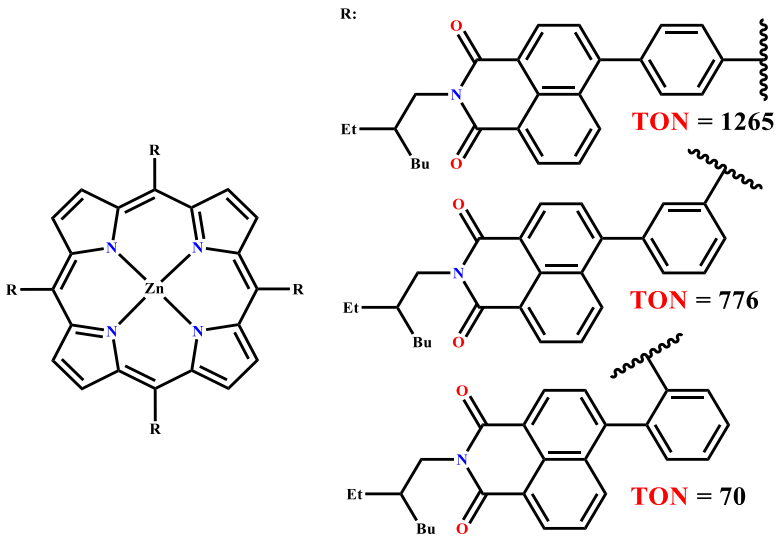


Figure 1.25 Intermolecular photocatalytic assemblies of NI conjugated porphyrins proposed by Bodedla et al. [135].

The metal center of the porphyrin framework also plays a significant role in photocatalytic hydrogen evolution. Many studies focus primarily on zinc porphyrins [43, 134 – 136], however the application of other metals has been also investigated. This is demonstrated by Lang and colleagues [137], who synthesised intramolecular porphyrin assemblies (Figure 1.26) and investigated the impact of zinc, copper, and cobalt on hydrogen evolution efficiency. In their study, the Zn-$PtCl_2$ system, which incorporated a zinc porphyrin and platinum as a catalyst, achieved the highest TON of 16 in an ACN: TEA: H_2O (6:3:1) mixture following irradiation at 470 nm for 24 hours. Under the same photocatalytic conditions, the Co-$PtCl_2$ system showed a maximum TON of <1 and no hydrogen was produced for the Cu-$PtCl_2$ system. Notably, the authors observed that the

$PtCl_2$ catalytic center resulted in higher hydrogen production, compared to the PtI_2 analogue [137].

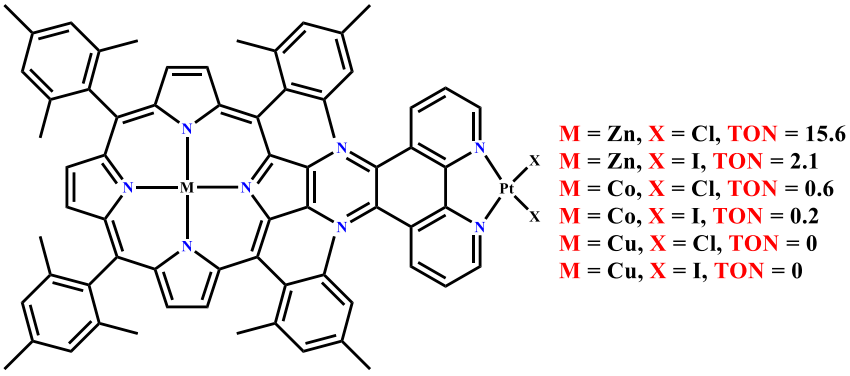


Figure 1.26 Intramolecular photocatalytic systems of M-1-PtX_2, where M= Zn, Co, Cu and X= Pt and I, proposed by Lang and colleagues [137].

Natali et al. [138] proposed aluminium pyridyl porphyrin, which was linked to the cobaloxime catalyst (Figure 1.27), achieving the highest TON of 352. Comparable results were obtained by Giannoudis and colleagues [139]. In their study, both tin and zinc porphyrins were employed for the intermolecular photocatalytic assemblies (Figure 1.28), and the research presented that positively charged ($[ZnTMePyP^{4+}]Cl_4$) and the neutral tin porphyrin derivatives including $Sn(OH)_2TPyP$, $Sn(Cl_2)TPP\text{-}[COOMe]_4$, and $Sn(Cl_2)TPP\text{-}[PO(OEt)_2]_4$ are suitable for hydrogen evolution, reaching maximum TONs of 1135, 303, 128, and 48, respectively [139].

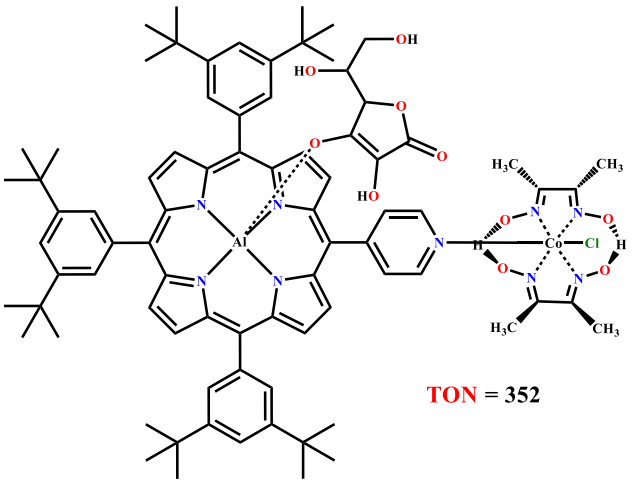


Figure 1.27 Intramolecular photocatalytic system proposed by Natali and colleagues [138].

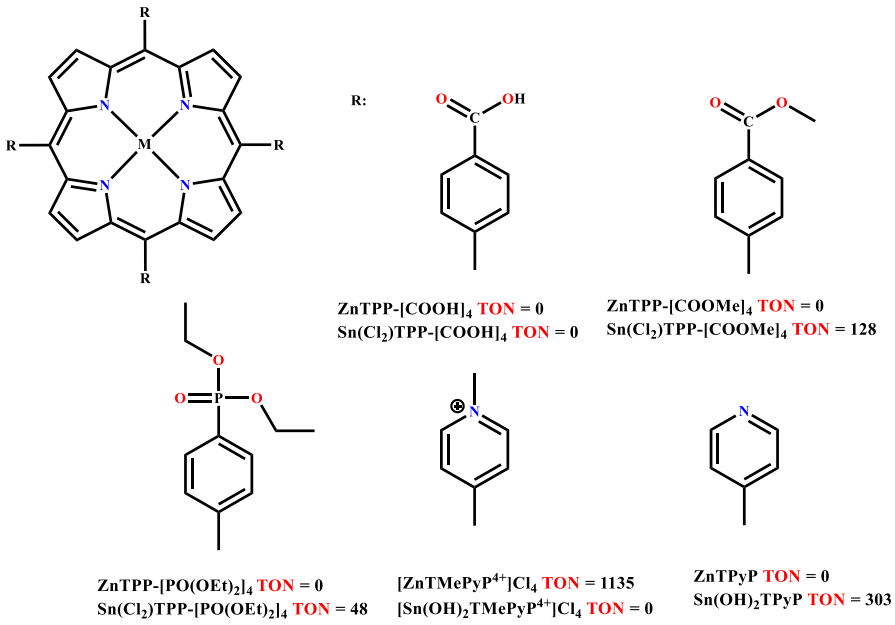


Figure 1.28 Intermolecular photocatalytic systems proposed by Giannoudis and colleagues [139].

The bridge plays an important role in photocatalytic hydrogen evolution in intramolecular systems, as observed in Figure 1.29. Zhu et al. [140] employed a donor-bridge-acceptor conjugated system to promote energy and electron transfer. The synthesised assemblies consisted of porphyrin, which acted as an electron acceptor, triphenylamine (TPA) served as an electron donor and EDTA was used as a sacrificial electron donor. In addition, platinum colloidal solution (H_2PtCl_6) acted as a catalyst. The system, in which the porphyrin and TPA were connected through an ethylene bridge exhibited higher quantity of hydrogen evolved (TON = 6590) whereas when with an ester (TON = 4070) this value decreased. The authors concluded that this difference was accounted for by broader photon absorption and more efficient intramolecular energy transfer [140].

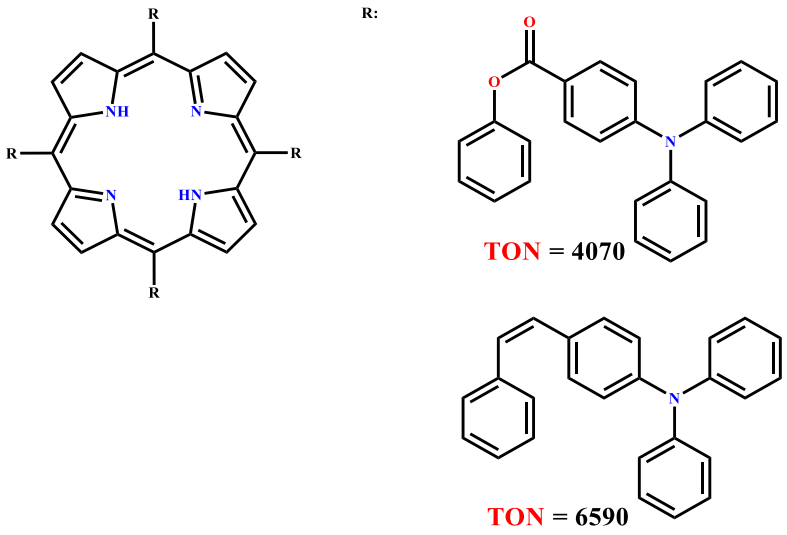


Figure 1.29 Intermolecular photocatalytic systems proposed by Zhu and colleagues [140].

An intermolecular system was proposed by Lazarides and colleagues [141]. The system employed a water-soluble meso-tetrakis(1-methylpyridinium-4-yl)porphyrin chloride $([ZnTMPyP^{4+}]Cl^{-})_4$ (Figure 1.30), a cobaloxime complex as a catalyst, and TEOA as a sacrificial electron donor in a mixture of ACN: H_2O (1:1). The study examined hydrogen evolution at pH values of 7 and 8. The highest TON of 280 was achieved at pH 7 after more than 20 hours of light irradiation ($\lambda > 440$ nm). The experiment was carried out under the same conditions using the non-metalated analogue and resulted in a significantly lower hydrogen evolution rate (TON = 60, after 9 hours of light irradiation). This study demonstrated that pH significantly affects photocatalytic activity and that zinc at the periphery of the porphyrin framework enhances the photocatalytic results.

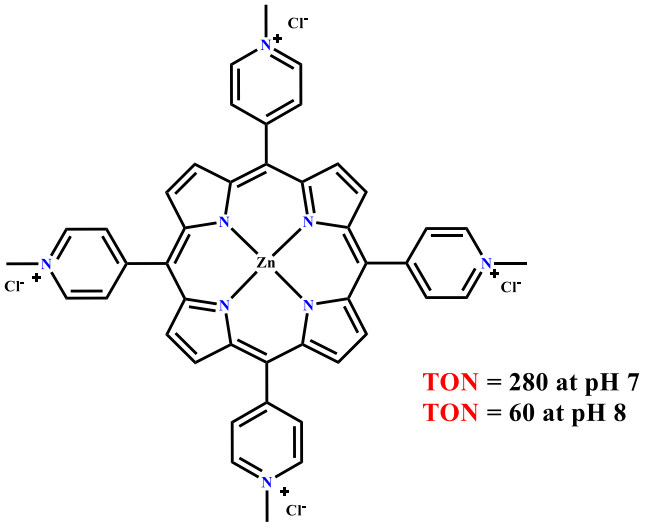


Figure 1.30 Intermolecular photocatalytic system proposed by Lazarides and colleagues [141].

A more recent study carried out by Sun et al. [142] examined photocatalytic activity of porphyrin systems with different functional groups incorporated into porphyrin framework. The authors synthesised three porphyrin complexes, namely PP-NH_2, PP-OH and PP-COOH, where PP = porphyrin moiety (Figure 1.31). Photocatalytic experiments were carried out in THF, using a platinum cocatalyst (H_2PtCl_6) and ascorbic acid as a sacrificial electron donor and the solution was exposed to the light using a Xe lamp. The porphyrin system with the NH_2 group resulted in 1.05 μmol of hydrogen (after 5 hours of light irradiation), while the system functionalised with OH group yielded 4.21 μmol of hydrogen. The highest value of 22.8 μmol of hydrogen was reported for the system with the COOH group. The authors concluded that electron-withdrawing groups such as COOH can drive electron transfer and enhance the stability of the photocatalyst [142].

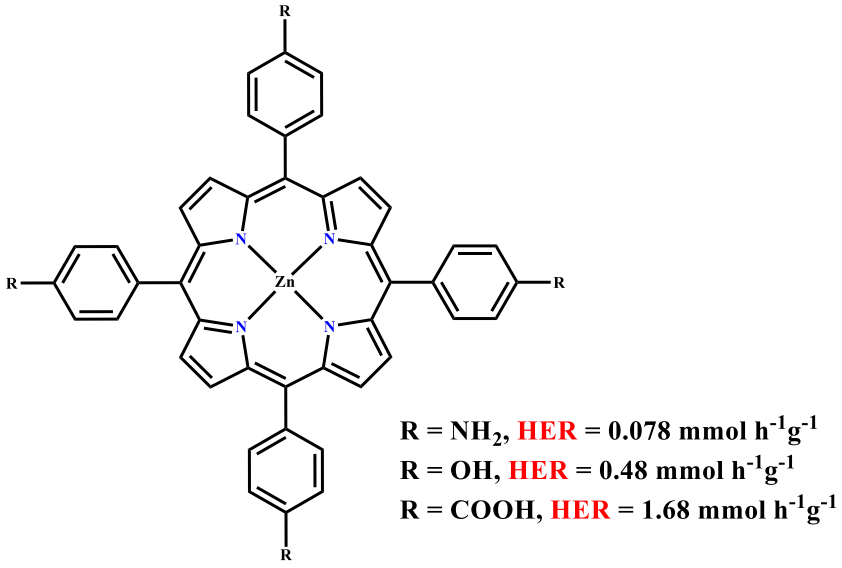


Figure 1.31 Intermolecular photocatalytic system proposed by Sun and colleagues [142].

Based on the aforementioned examples of using porphyrins to mimic photosynthesis for hydrogen evolution, significant amount of progress has been made in this field. Additionally, this research on porphyrins is often advanced by designing porphyrin-based metal and covalent organic framework materials (MOFs/COFs) [143 – 145], as well as by introducing heterogeneous catalysis, which involves working with the surface of semiconductors [146, 147].

1.7.4 Naphthalene Diimide Compounds: Could They be Employed in Photocatalytic Hydrogen Evolution?

Naphthalene diimides (NDIs) compounds belong to the "rylene family" of organic molecules and are employed in a wide range of applications, however their potential in photocatalytic processes is still not very well explored. Nevertheless, their photophysical and electrochemical properties indicate that they could be suitable for the development of photocatalytic systems incorporating NDI moieties. These aspects will be briefly discussed in this section to convince the idea that NDIs are promising candidates and could offer new opportunities in photocatalytic processes. Furthermore, literature review in Chapter 2 presents various ruthenium-NDI complexes, in which their photophysical and electrochemical properties are highlighted in a greater detail.

NDI molecules are distinguished by their π-conjugated benzene rings and the presence of imide bonds in their molecular structures. Consequently, their properties can be easily modified as the imide bonds allow for the attachment of various functional groups as well as the incorporation of metal complexes [148]. For example, NDIs were employed in ruthenium [149 – 151], iridium [152, 153], copper complexes [154, 155] and they were also integrated into porphyrin frameworks [156 – 159]. Therefore, NDIs can act as bridging ligands in order to attach photosensitisers and catalytic centres to form an efficient system for photocatalytic processes. The literature provides only a limited number of examples of such systems, hence it is challenging to highlight their application for photocatalytic hydrogen evolution. As a result, to support the statement and convince the idea that they have a potential in photocatalysis, a few examples of NDI-based conjugated polymers used for carbon dioxide reduction will be discussed along with their electron transfer mechanisms, characteristic features of excited NDI radicals and the types of photocatalytic processes currently involving NDIs.

Wang et al. [160] synthesised NDI-based polymers, namely PNDI-BT (bithiophene), PNDI-DTBT (4,7-di(thiophen-2-yl)benzo[c][1,2,5]thiadiazole), and PNDI-BP (biphenyl), for the photochemical reduction of CO_2 to CO (Figure 1.32). Following light irradiation using solar simulator (in the absence of cocatalyst and organic solvent), the yields of CO formation were 16.3, 31.1 and 90.0 $\mu mol \cdot g_{cat}^{-1}$, respectively. The photocatalytic activity of PNDI-BP was the highest due to its increased electron and exciton lifetimes, reduced charge recombination rate, and lower interfacial charge-transfer resistance. Additionally, the polymer was catalytically stable for more than 330 hours [160]. Another research study on photocatalytic carbon dioxide reduction to form

carbon monoxide was conducted by the same research group [161] and involved the examination of four metal free, NDI-based donor-acceptor-donor molecules, which differed by the number of thiophene units in their structures, NDI-2T, NDI-TT, NDI-4T, and NDI-6T (Figure 1.33). The photocatalytic experiments were carried out in the presence of water, using the solutions of these molecules in chloroform, which were coated on the glass substrate and subsequently placed in a glass reactor and purged with CO_2. Following light irradiation using AM1.5G solar lamp, the yields of CO were 88.4, 111.9, 168.6, and 40.5 μmol g_{cat}^{-1} 24 h^{-1}, respectively (confirmed by the isotope experiment, $^{13}CO_2$). It was observed that increasing the number of thiophene units improved intramolecular charge transfer and elongated the exciton lifetime. Theoretically, this should have provided a greater opportunity for electrons to take part in the CO_2 reduction reaction. Nevertheless, the compound with the highest number of thiophene moieties exhibited the weakest catalytic activity despite its longest exciton lifetime. This was primarily caused by the higher oxidation potential due to electron-donating properties of thiophene units [161].

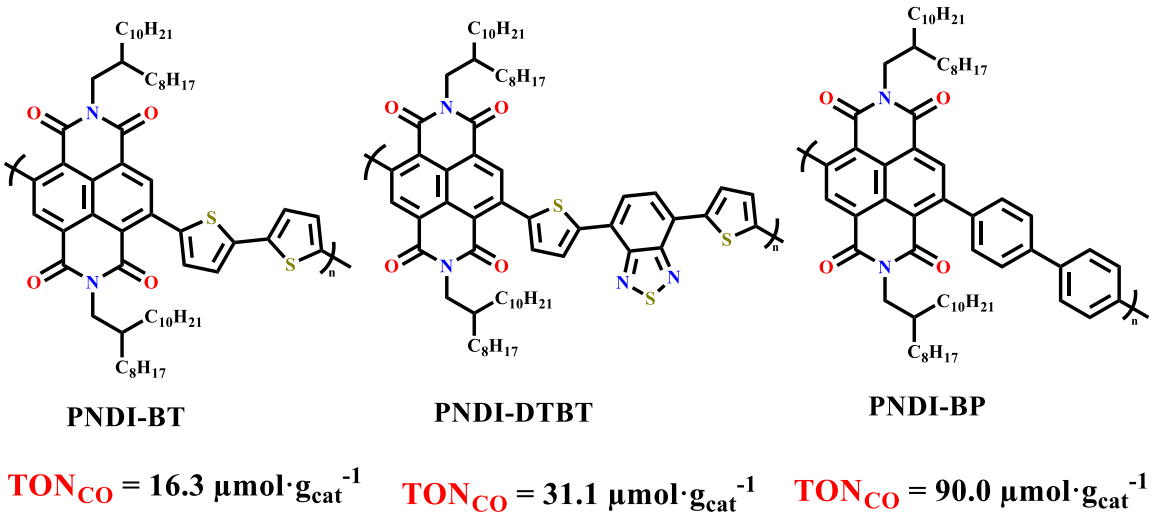


Figure 1.32 NDI-based polymers, PNDI-BT (bithiophene), PNDI-DTBT (4,7-di(thiophen-2-yl)benzo[c][1,2,5]thiadiazole), and PNDI-BP (biphenyl) for the photochemical reduction of CO_2 to CO synthesised by Wang and colleagues [160].

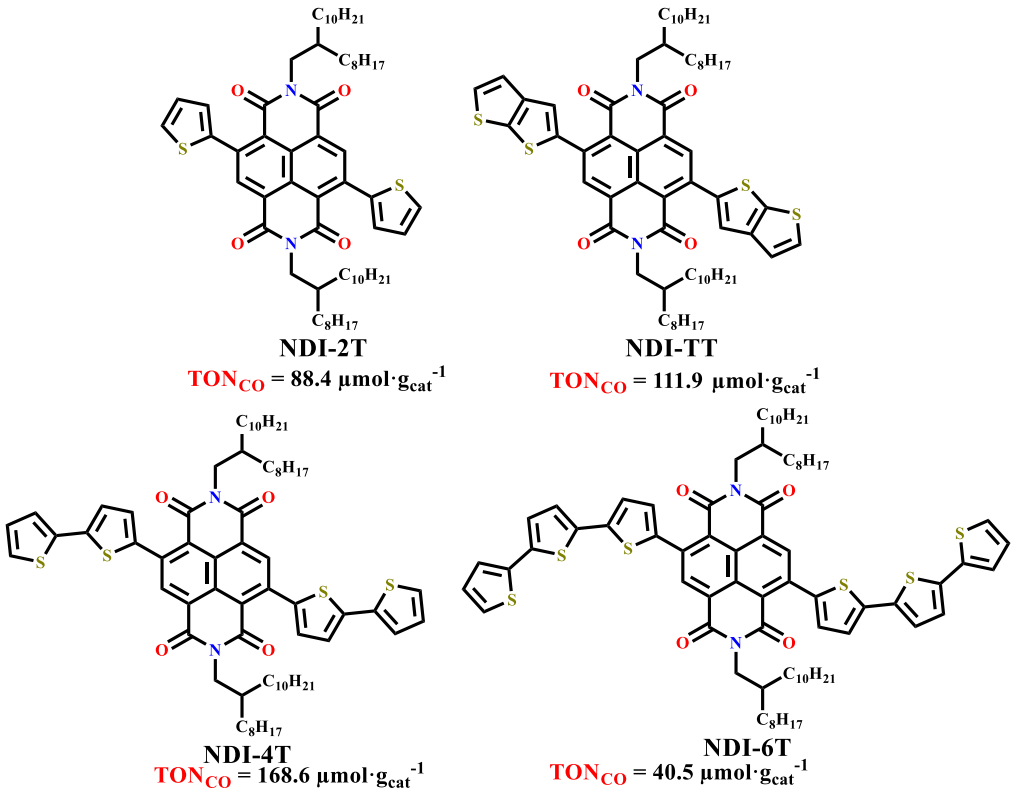
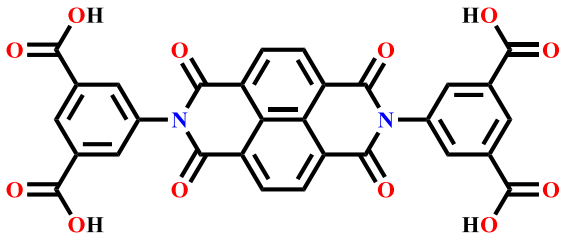


Figure 1.33 NDI-based donor-acceptor-donor molecules NDI-2T, NDI-TT, NDI-4T, and NDI-6T proposed by Wang et al. [161].

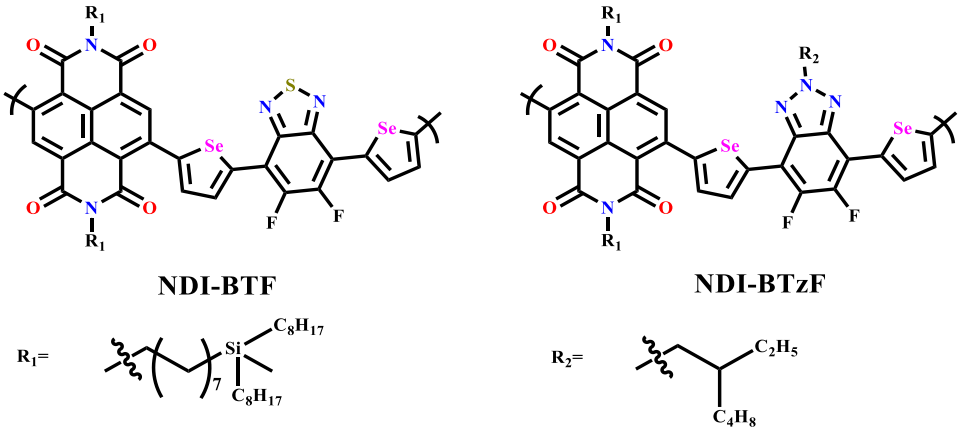
Xu et al. [162] synthesised a dicarboxyphenyl-substituent naphthalenediimide self-assembly supramolecular photocatalyst (SA-NDI-BCOOH) for photocatalytic hydrogen and oxygen evolution (Figure 1.34). The rates of the photocatalytic performance (in the presence of H_2PtCl_6 cocatalyst and ascorbic acid as a sacrificial electron donor upon light irradiation with 300 W Xe lamp, $\lambda \geq 300$ nm) were determined to be 372.8 and 3.8 µmol h^{-1}, respectively. This robust activity of the photocatalyst resulted from the large molecular dipoles of the NDI-BCOOH units caused by the presence of highly electronegative dicarboxyphenyl group, and an enlarged internal electric field that drove directional migration of the photogenerated carriers, in other words, charge separation was highly efficient [162].



TON_{H2} = 372.8 μmol·g_{cat}^{-1}

Figure 1.34 NDI-BCOOH unit in the self-assembly photocatalytic system designed by Xu et al. [162].

Mekhemer et al. [163] designed two naphthalenediimide (NDI)-based organic-conjugated polymer dots (Pdots), namely NDI-BTF and NDI-BTzF for photocatalytic hydrogen evolution (Figure 1.35). The quantities of hydrogen evolved under visible-light irradiation (λ > 420 nm) and in the presence of ascorbic acid were determined to be 1490.7 and 525.0 μmol $g^{-1}h^{-1}$, respectively. These values increased to 3409.6 and 634.6 μmol $g^{-1}h^{-1}$ upon the addition of the surfactant (PS-PEG-COO). The presence of the surfactant improved dispersibility of polymers in aqueous solution, enhanced photostability and increased the performance of hydrogen evolution.



NDI-BTF **NDI-BTzF**

TON_{H2} = 1490.7 μmol·g_{cat}^{-1} TON_{H2} = 525.0 μmol·g_{cat}^{-1}

Figure 1.35 Structures of NDI-copolymers, NDI-BTF and NDI-BTzF for photocatalytic hydrogen evolution based on Mekhemer's research work [163].

Based on the aforementioned examples, NDI could definitely find an application in photocatalytic hydrogen evolution and carbon dioxide reduction reaction. This dissertation primarily focusses on NDI-based ruthenium, rhenium and porphyrin complexes, and their photophysical and electrochemical properties will be described in a greater detail in the following chapters.

1.8 Photophysics and Photochemistry

Photophysical and photochemical analyses of photocatalytic assemblies are necessary to gain fundamental knowledge on how these systems behave upon light absorption. These studies offer insights into photoactive intermediates and photoexcited states formed during photocatalytic processes. Additionally, it is important to investigate the mechanism of formation of these intermediates. These aspects must be properly optimised in order to improve water-splitting or carbon dioxide reduction processes.

Absorption and emission spectra, fluorescence quantum yields, and singlet and triplet lifetimes of excited states measure the ability of a photocatalyst to absorb or emit light but also to determine if electron transfer is efficient and to what extent charge recombination occurs. Additionally, techniques for example transient absorption spectroscopy (TAS), time-correlated single photon counting (TCSPC) and time-resolved infrared spectroscopy (TRIR), provide insights into the dynamics of excited states, distribution and movement of electron density and the formation of charge-separated species. Electrochemistry, when combined with spectroscopy, called spectroelectrochemistry (SEC), allows to monitor the absorption (UV-vis) and infrared stretching vibration properties (IR) of newly formed electron reduced species and study their photophysical properties. Moreover, spectroelectrochemistry combined with TRIR (TRIR-SEC) allows to measure the lifetimes of excited reduced species, which often could suggest what are the limiting factors in photocatalysis. The following sections will provide an overview of commonly used techniques along with their fundamental principles.

1.8.1 Basic Principles of Spectroscopy

1.8.1.1 The Born Oppenheimer Approximation

The Born-Oppenheimer approximation is significant in analysing the spectrum of molecules [164]. It describes the quantum states of molecules, and it distinguishes between the movement of the nuclei and electrons. The molecule possesses rotational energy (observed in microwave region), vibrational energy (infrared region) and electronic energy (UV and visible region). The total energy of a molecule is summarised as follows: $E_{total} = E_{electronic} + E_{vibrational} + E_{rotational}$ [165]. All of these aforementioned energies are related to different molecular motions and hence, they are independent of one another. Additionally, the approximation assumes that the nuclei are stationary during

an electronic transition because nucleus's mass is larger than that of an electron. Consequently, when the molecule absorbs the light, electrons instantaneously move to an excited state electronic state. This transition leads to changes in vibrational and rotational energies, because the electronic wavefunction adapts to the new nuclear coordinates [166]. The same changes in energy are applied when the molecule emits the light, and electrons move from the excited state to the ground state [164 – 166].

1.8.1.2 The Franck-Condon Principle

The principle is related to the Born-Oppenheimer approximation, and it describes and explains the intensity of electronic and vibrational transitions during absorption and emission processes in molecules following irradiation [167, 168]. As electrons are instantaneously promoted to higher energy levels upon exposure to electromagnetic radiation (Figure 1.36), the nucleus remains stationary, as stated by the Born-Oppenheimer approximation. The excited state has different structural properties and larger equilibrium internuclear separation, when compared to the ground state. Hence, changes occur in nuclear configurations once the transition happens. This means, that the excited state is formed with vibrational and rotational excitation [166, 169 – 173].

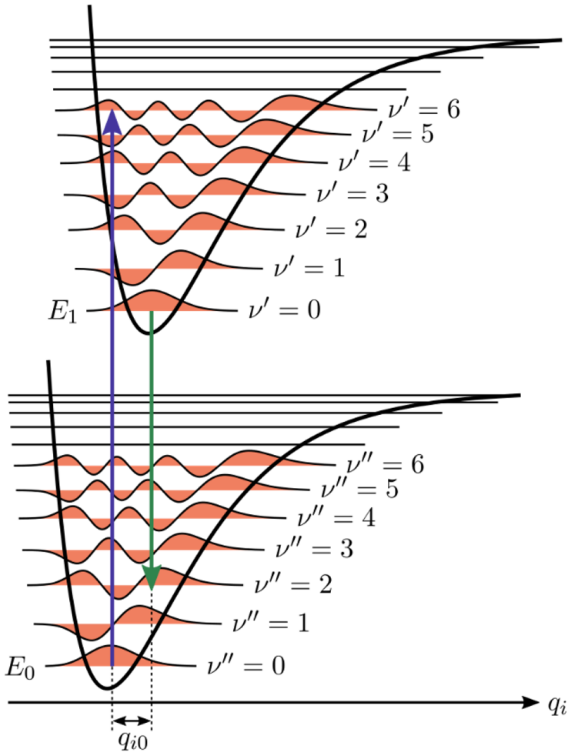


Figure 1.36 The Franck-Condon principle adapted from the online sources [173].

1.8.1.3 The Jablonski Diagram: The Foundation of Photophysics and Photochemistry

The Jablonski Diagram, named after the Polish professor Aleksander Jabłoński, represents the molecular processes that occur between the absorption and emission of light and the excited states populated [174]. The diagram in Figure 1.37 consists of the singlet ground, first and second excited states, represented as S_0, S_1 and S_2, respectively. Once a photosensitiser or a photocatalyst absorbs light, an electron is excited to higher energy level, either to S_1 or higher to S_2. Following this, excited molecules in S_1 can undergo two relaxation pathways, namely radiative decay, known as fluorescence (spin-allowed), where light is emitted, or non-radiative decay where energy is lost as heat. Fluorescence lifetimes of molecules are typically very short 1 x 10^{-5} to 10^{-8} seconds [174 – 176]. Molecules in the excited state can also undergo a spin conversion to the first triplet state, T_1. Emission from T_1 is called phosphorescence (spin-forbidden, it occurs at longer time scale, 1 x 10^{-4} seconds to minutes/hours) and this is evident at higher wavelengths (lower energy) compared to fluorescence [174 – 178]. The conversion of S_1 to T_1 is known as intersystem crossing (ISC). The transition from T_1 to the singlet ground state S_0 is forbidden. Depending on the spin quantum numbers in the excited state, there are two possible transitions, a singlet state where the spins of two electrons are opposed and a triplet state where the spins are parallel [174 – 178].

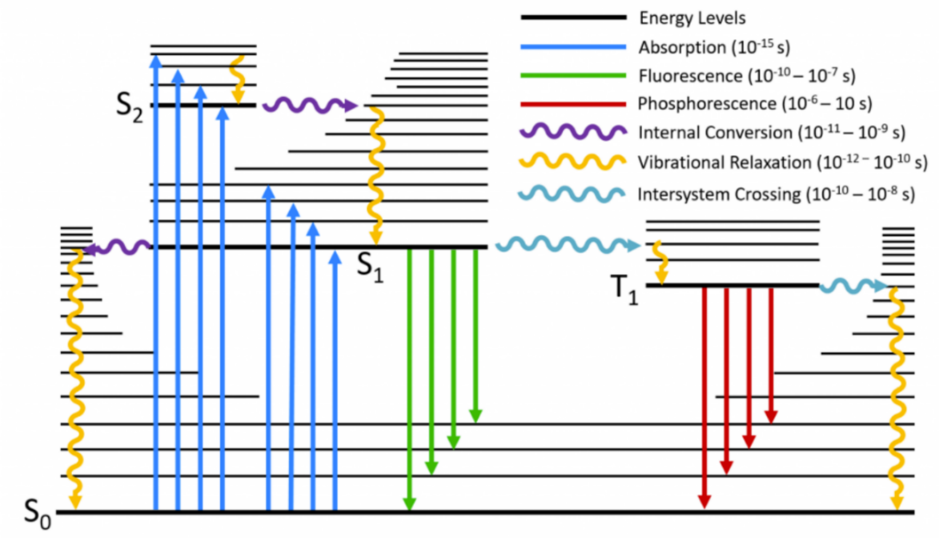


Figure 1.37 The Jablonski diagram adopted from Edinburgh Instruments [178].

1.8.1.4 Molecular Absorption of Light and Electronic Transitions

As described in the previous section, the Jablonski diagram explains different processes occurring within the photocatalytic assemblies, when an electronic transition or excitation takes place upon light irradiation. Following light absorption, an electron is excited from the ground state (S_0 or HOMO of the photosensitising moiety) to an excited state (S_1 or LUMO of the electron accepting bridging ligand). The energy difference between highest occupied molecular orbital (HOMO, π orbital) and lowest unoccupied molecular orbital (LUMO, π^* orbital) is attributed to the HOMO-LUMO gap (band gap energy), and it is a fundamental factor in determining the wavelengths at which the compound can efficiently absorb light [179]. In other words, this allows us to decide what wavelength is a suitable choice to excite the molecules for efficient electron transfer during photocatalysis. Effective electron transfer involves a two-step electron transfer, first an electron is transferred from the light-harvesting unit to the bridging ligands and second, an electron is promoted from the bridging ligand to the catalytic centre in photosynthetic assemblies. It is often desired to increase conjugation in the compounds because it leads to a smaller energy gap between the HOMO and the LUMO levels. Consequently, molecules can absorb light at longer wavelengths (lower energy), pushing it towards the near-infrared spectrum [180, 181]. An example of this is well known chlorophyll molecules present in plants, which characterise with an extended conjugation, hence absorb light at > 500 nm [181]. When a molecule absorbs light of an of a specific wavelength, this results in the formation of various transitions, for example a π-π* ligand-centred (LC) transition, and these are localised on the ligand system, d-d metal-centered (MC) or a dπ-π* metal-to-ligand charge transfer (MLCT) transition in the visible region, which are initiated by the movement of electrons from the metal to the ligand. In general, MLCT transitions exhibit broader and less intense absorption bands than π-π* transitions [182].

1.8.2 Absorption, Emission and Infrared Spectroscopy

UV-vis, emission and IR spectroscopy are techniques employed to study the photophysical properties of compounds. UV-vis spectroscopy measures the ability of a photocatalytic system to absorb light in the UV and visible regions. When combined with electrochemistry called UV-vis spectroelectrochemistry, it allows us to record the UV-vis spectra of the reduced or oxidised species. Emission spectra allow us to determine the singlet lifetimes of the molecules as well as the correct excitation wavelength required to conduct time-correlated single photon counting (TCSPC) studies. IR spectroscopy helps to determine the purity of the synthesised complexes and subsequently confirms the presence of different functional groups present in the structure of photocatalytic assemblies for example carbon-carbon bond (C–C), triple bonds (C≡N, C≡H), carbonyl bonds (C=O) etc. Subsequently, these features are important and are considered to be useful probes in order to carry out further studies like time-resolved infrared (TRIR) and IR combined with electrochemistry to study the properties of the excited states.

1.8.3 Time-Correlated Single Photon Counting (TCSPC)

Time-Correlated Single Photon Counting (TCSPC) was used in this dissertation to measure fluorescence lifetimes (τ) (singlet lifetime) of photocatalytic molecules, which indicate how long molecules remain in an excited state before undergoing radiative-transition from the excited state (S_1) back to the ground state (S_0), indicated by green lines in Figure 1.37. Fluorescence lifetimes are usually reported in the range from a few picoseconds to hundreds of nanoseconds (10^{-10} to 10^{-7} s) and these values can vary in solvents of different polarity and also temperature can affect them [168, 178, 183 – 185]. In Figure 1.38, the TCSPC experimental setup is presented, and it shows the fundamental components like the light source, monochromator, multi-channel analyser and photomultipliers. Additionally, the TCSPC instrument is connected to the computer in order to acquire and process the data.

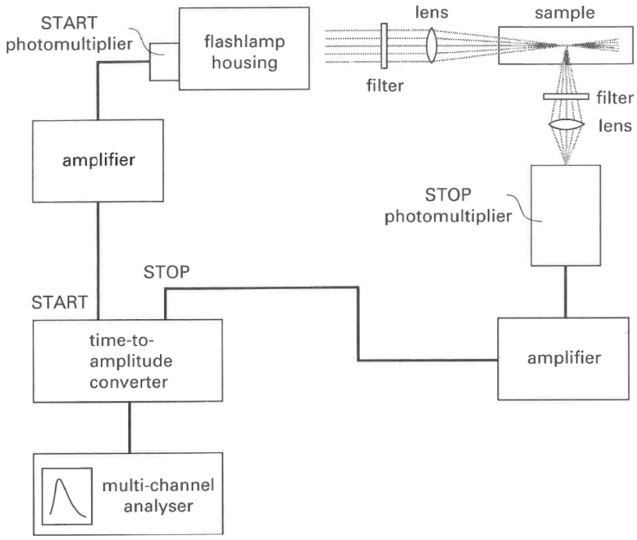


Figure 1.38 Time-correlated single photon counting apparatus. The schematic was adapted from the literature [166].

The analysis of photocatalytic compounds by TCSPC starts by exciting the sample using its appropriate emission wavelength. This is carried out by the excitation light source, which uses rapidly repetitive pulses and low-intensity light. Once the sample emits light, the emitted photons are then transferred to light detectors, which are called photomultipliers. The START photomultiplier contains the excitation light source, and it produces a signal when it detects a pulse of light from the lamp and then triggers the Time-to-Amplitude Converter (TAC) to initiate a voltage ramp. The STOP photomultiplier detects the emission of a photon coming from the sample, and as a result it sends the signal to the TAC to further increase the voltage ramp. The time difference between excitation of the sample and detection of an emission photon is converted into voltage. The voltage is proportional to the time at which each photon arrives [166, 185–189]. The Analog-to-Digital Converter (ADC) converts the voltage into time, and it transfers the data to the digital memory. The histogram is generated by repeating the experiment several times. The histogram presents the number of photons detected as a function of the time interval and represents the fluorescence decay. It provides insight into lifetimes of molecules, however, to achieve an accurate lifetime fit, deconvolution and statistical methods are employed to determine exponential decay values. Consequently, the chi-squared value (χ^2) is employed as a measure of how accurately the data fits to the desired order of exponential decay, ideally χ^2 value has to be below 1.2 and this is automatically calculated in the software [166, 185 – 189].

1.8.4 Transient Absorption Spectroscopy (TAS)

Transient Absorption Spectroscopy (TAS) is a technique that probes the dynamics of excited states of molecules on a short timescale, which measures absorption changes and its corresponding lifetimes [190, 191]. Firstly, the sample is excited by a light source known as “pump pulse”, and the wavelength of the laser source is determined by the absorption wavelength of the molecule. Secondly, changes in absorption with respect to time and wavelength are measured, which is achieved using a second low-energy white pulse, “probe pulse”. As a result, a difference absorption spectrum (ΔA) is then obtained, which indicates the difference between the absorption spectrum of the excited sample and the absorption spectrum of the sample in the ground state (ΔA) [190, 191]. The probe-pulse technique allows to measure lifetimes of excited singlet and triplet states on timescales ranging from nanoseconds (ns) to microseconds (μs) or femtosecond (fs) to picoseconds (ps). The technique helps to understand the nature of electron and energy processes within photocatalytic assemblies. A few key aspects, which are important in the analysis of TAS measurements are briefly described as follows (Figure 1.39). The first is ground-state bleach (GSB), which indicates that molecules are promoted from the ground state to the excited state upon the pump pulse, resulting in a reduction in the number of molecules in the ground state. This is typically observed as a negative signal in the spectrum. The next is excited state absorption (ESA), observed as a positive signal and this corresponds to the formation and population of higher excited states. The third is stimulated emission (SE), during which the excited state, populated by absorption, undergoes emission upon interaction with a probe pulse. This is seen as a negative signal, indicating an increase in light intensity [190, 191].

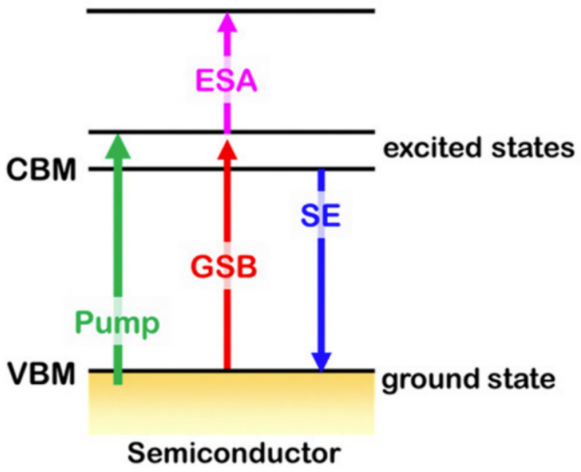


Figure 1.39 Electronic transition and relaxation pathways in TA spectroscopy, indicating ground-state bleach (GSB), excited state absorption (ESA) and stimulated emission (SE). The figure was adapted from the literature [191].

1.8.5 Time-Resolved Infrared Spectroscopy (TRIR)

Time-Resolved Infrared Spectroscopy (TRIR) is a type of transient absorption spectroscopy, which measures changes in absorption (ΔA) of an infrared 'reporter' with respect to time. It follows similar principles to TAS, and it allows to obtain photophysical properties of the excited states of molecules. TRIR spectra are recorded by employing a pulsed or continuous wave infrared probe, which is influenced by the timescale of the excited state processes being examined. A short laser pulse photoexcites the molecule and an infrared probe monitors changes in the absorbance at the selected wavelength [192]. This technique allows for precise monitoring of excited state dynamics and electron density distribution through infrared absorption variations. In order to conduct TRIR studies, the materials of interest must be characterised by the desired functional groups Examples of such groups include nitrile (C≡N) and carbonyl (C=O) stretching modes, which are commonly used to examine charge transfer mechanisms in photocatalytic assemblies [192 – 194].

1.8.6 Electrochemistry and Spectroelectrochemistry

Electrochemistry is a tool, that enables the investigation of electron transfer processes, including oxidation and reduction, that take place within photocatalytic assemblies. The typical and standard electrochemical set up, as presented in Figure 1.40, involves primary components for example the working, counter and reference electrodes and the electrolyte solution. In summary, the supporting electrolyte solution is employed to improve the electrical conductivity and to ensure the electrical circuit completion [195]. The working electrode (such as glassy carbon or platinum) facilitates the reduction and oxidation reactions. Additionally, the voltage of the current is applied to the working electrode, and it is controlled by a potentiostat. Moreover, the reference electrode serves as a reference point against which the potential of other electrodes can be measured, and the counter electrode completes the electrical circuit [195]. Electrochemical studies of photocatalytic assemblies not only determine their redox properties but also, by obtaining their redox potentials, the estimation of the thermodynamic driving forces for processes like water-splitting and carbon dioxide reduction can be conducted [112].

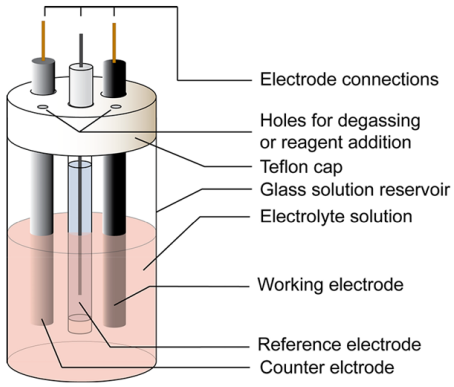


Figure 1.40 Schematic of the electrochemical set up. The figure was adapted from the literature [195].

Electrochemistry combined with UV-vis and IR-spectroscopy (spectroelectrochemistry) allows for the study of the photophysical properties of reduced species. Spectroelectrochemical (SEC) experiments are typically performed using an optically transparent thin-layer electrochemical (OTTLE) cell, a UV/IR spectroscopy instrument, and a potentiostat in order to apply the voltage [196]. This technique allows to observe and monitor absorption changes upon the electrochemical formation of reduced species. Additionally, SEC can be combined with TRIR to measure the lifetimes of these reduced species. Furthermore, it provides a foundation for studying intermediates formed during photocatalytic processes and can help identify limiting factors affecting the overall success of photocatalytic activity.

1.9 Parameters for Hydrogen Evolution Quantification

The quantification of hydrogen evolution and carbon dioxide reduction products are used to evaluate the success of the photocatalytic process, but also to compare the results with those reported in literature. The two important parameters are turnover numbers and turnover frequencies. It is a good practice to use them by researchers, because they enhance clarity, transparency and help to standardise the quantification process in research.

1.9.1 Turnover number (TON)

Turnover number (TON) indicates productivity of the photocatalysis, and it defines the number of moles of product generated per mole of catalyst, as represented in the following equation [197 – 200].

$$TON = \frac{number\ of\ moles\ of\ product\ generated}{number\ of\ moles\ of\ catalyst}$$

Typically, in intramolecular systems, TON is measured with respect to the concentration of the photocatalytic system, and in case of intermolecular systems, TON are calculated based on the concentration of the catalyst which is added to the solution.

1.9.2 Turnover frequency (TOF)

Turnover frequency (TOF) indicates the number of reactant molecules consumed, or product molecules formed per active site per unit time [197 – 200].

$$TOF = \frac{TON}{time\ in\ hours}$$

1.10 Conclusion

This introductory chapter highlighted the need for the utilisation of renewable energy sources, particularly focussing on employment of hydrogen as a fuel. Photocatalytic hydrogen evolution and carbon dioxide reduction, currently being developed in laboratory settings, serve as promising processes, that could be employed widely in the real-life applications to combat the negative consequences of greenhouse gas emissions. Furthermore, this chapter presented a wide range of ruthenium and porphyrin compounds used for photocatalysis and highlighted the fundamental factors and conditions that can affect the photocatalytic process. Photophysical techniques such as TCSPC, TAS, and TRIR serve as excellent approaches to describe their properties, determine the nature of excited states, population of electron upon irradiation, and to obtain and determine their corresponding lifetimes within these molecules. All of these aspects are significant for the development and optimisation of efficient intermolecular and intramolecular photocatalytic assemblies. Additionally, fundamental principles of electrochemical and spectroelectrochemical techniques were described, which can aid photophysical techniques in determining electron transfer pathways and the formation of reduced species, which often take an active part in photocatalysis. Finally, parameters for quantifying hydrogen evolution were briefly described, which could help to standardise calculation methods among researchers in the field of photocatalysis.

1.11 References:

[1]. Growth in global energy demand surged in 2024 to almost twice its recent average - news - IEA. (2025). https://www.iea.org/news/growth-in-global-energy-demand-surged-in-2024-to-almost-twice-its-recent-average

[2]. Huber, S. T., & Steininger, K. W. (2022). Critical sustainability issues in the production of wind and solar electricity generation as well as storage facilities and possible solutions. Journal of Cleaner Production, 339(2022), 130720. https://doi.org/10.1016/j.jclepro.2022.130720

[3]. Osman, A. I., Chen, L., Yang, M., Msigwa, G., Farghali, M., Fawzy, S., Rooney, D. W., & Yap, P.-S. (2022). Cost, environmental impact, and resilience of renewable energy under a changing climate: A Review. Environmental Chemistry Letters, 21(2), 741–764. https://doi.org/10.1007/s10311-022-01532-8

[4]. Solar Panels Ireland cost [and savings]: 2025 guide. PureVolt Solar. (n.d.). https://www.purevolt.ie/domestic-solar/solar-panels-cost-and-returns.php#:~:text=For%20a%20typical%20household%2C%20solar,a%20solar%20storage%20battery%20etc.

[5]. Nunes, L. J. (2023). The Rising Threat of Atmospheric CO_2: A Review on the Causes, Impacts, and Mitigation Strategies. Environments, 10(4), 66. https://doi.org/10.3390/environments10040066

[6]. Filonchyk, M., Peterson, M. P., Zhang, L., Hurynovich, V., & He, Y. (2024). Greenhouse gases emissions and global climate change: Examining the influence of CO_2, CH_4, and N_2O. Science of The Total Environment, 935, 173359. https://doi.org/10.1016/j.scitotenv.2024.173359

[7]. Davis, W. J. (2023). Mass Extinctions and Their Relationship with Atmospheric Carbon Dioxide Concentration: Implications for Earth's Future. Earth's Future, 11(6), e2022EF003336. https://doi.org/10.1029/2022ef003336

[8]. Igini, M. (2023, November 24). COP28 Will be the "Moment of Truth" for Oil and Gas sectors, IEA says. Earth.Org. https://earth.org/cop28-will-be-the-moment-of-truth-for-oil-and-gas-sectors-iea-says/

[9]. The Oil and Gas Industry in Net Zero Transitions. (2024). https://iea.blob.core.windows.net/assets/f065ae5e-94ed-4fcb-8f17-8ceffde8bdd2/TheOilandGasIndustryinNetZeroTransitions.pdf

[10]. Net Zero by 2050 - A Roadmap for the Global Energy Sector. (2021). https://iea.blob.core.windows.net/assets/deebef5d-0c34-4539-9d0c-10b13d840027/NetZeroby2050-ARoadmapfortheGlobalEnergySector_CORR.pdf

[11]. Energy in Ireland 2024 report. (2024, December). https://www.seai.ie/sites/default/files/publications/energy-in-ireland-2024.pdf

[12]. Consequences of climate change. Climate Action. (n.d.). https://climate.ec.europa.eu/climate-change/consequences-climate-change_en

[13]. Ireland's Climate Change Assessment - Synthesis Report, Environmental Protection Agency, Ireland, 2023, https://epa.ie/publications/monitoring--assessment/climate-change/ICCA_Synthesis_Report.pdf

[14]. "Energy Use Overview." Sustainable Energy Authority of Ireland, https://seai.ie/data-and-insights/seai-statistics/key-statistics/energy-use-overview/

[15]. Gcarbonproject. "Fossil CO_2 Emissions at Record High in 2023." Global Carbon Budget, https://globalcarbonbudget.org/fossil-co2-emissions-at-record-high-in-2023/

[16]. Renewable energy: Solar, wind, hydro, geothermal, storage. Factor This™. (2022, March 15). https://renewableenergyworld.com/types-of-renewable-energy/

[17]. "Renewable Energy." WTS Energy, 22 May 2023, https://wtsenergy.com/glossary/renewable-energy/

[18]. Renewable Energy – Recast to 2030 (RED II). The Joint Research Centre: EU Science Hub. (n.d.). https://joint-research-centre.ec.europa.eu/welcome-jec-website/reference-regulatory-framework/renewable-energy-recast-2030-red-ii_en
[19]. Ireland's energy targets. Sustainable Energy Authority of Ireland. (n.d.). https://www.seai.ie/about/irelands-energy-targets#:~:text=As%20per%20the%20National%20Energy,to%20be%20submitted%20in%202024.
[20]. National Energy and Climate Plan (NECP) 2021-2030. gov.ie. (2024). https:// https://www.gov.ie/en/department-of-climate-energy-and-the-environment/publications/national-energy-and-climate-plan-necp-2021-2030/
[21]. Types and sources of renewable energy: Greenesa. Renewable Energy Platform. (2021). https://www.greenesa.com/news/renewable-energy-sources-types
[22]. CO_2 emissions report. Sustainable Energy Authority of Ireland. (n.d.-a). https://www.seai.ie/data-and-insights/seai-statistics/key-publications/co2-emissions-report
[23]. Blankenship, R. E. (1992). Origin and early evolution of photosynthesis. Photosynthesis Research, 33(2), 91–111. https://doi.org/10.1007/bf00039173
[24]. Smith, E. N., van Aalst, M., Tosens, T., Niinemets, Ü., Stich, B., Morosinotto, T., Alboresi, A., Erb, T. J., Gómez-Coronado, P. A., Tolleter, D., Finazzi, G., Curien, G., Heinemann, M., Ebenhöh, O., Hibberd, J. M., Schlüter, U., Sun, T., & Weber, A. P. M. (2023). Improving photosynthetic efficiency toward food security: Strategies, advances, and perspectives. Molecular Plant, 16(10), 1547–1563. https://doi.org/10.1016/j.molp.2023.08.017
[25]. Senge, M., Ryan, A., Letchford, K., MacGowan, S., & Mielke, T. (2014). Chlorophylls, Symmetry, Chirality, and Photosynthesis. Symmetry, 6(3), 781–843. https://doi.org/10.3390/sym6030781
[26]. Xiong, J. (2006). Photosynthesis: what color was its origin? Genome Biology, 7(12), 245. https://doi.org/10.1186/gb-2006-7-12-245
[27]. Johnson, M. P. (2016). Photosynthesis. Essays in Biochemistry, 60(3), 255–273. https://doi.org/10.1042/ebc20160016
[28]. López-Pacheco, I. Y., Rodas-Zuluaga, L. I., Fuentes-Tristan, S., Castillo-Zacarías, C., Sosa-Hernández, J. E., Barceló, D., Iqbal, H. M. N., & Parra-Saldívar, R. (2021). Phycocapture of CO_2 as an option to reduce greenhouse gases in cities: Carbon sinks in urban spaces. Journal of CO_2 Utilization, 53, 101704. https://doi.org/10.1016/j.jcou.2021.101704
[29]. Kathpalia, R., & Kamra Verma, A. (2023). Artificial Photosynthesis as an Alternative Source of Renewable Energy: Potential and Limitations. Physiology. IntechOpen. https://doi.org/10.5772/intechopen.111501
[30]. Ciamician, G. (1912). The Photochemistry of the Future. Science, 36(926), 385–394. https://doi.org/10.1126/science.36.926.385
[31]. Fujishima, A., & Honda, K. (1972). Electrochemical Photolysis of Water at a Semiconductor Electrode. Nature, 238(5358), 37–38. https://doi.org/10.1038/238037a0
[32]. Photochemical Splitting of Water by Artificial Photosynthesis. (n.d.). https://www.pas.va/en/publications/acta/acta24pas/rao.html
[33]. Chakhtouna, H., Benzeid, H., Zari, N., Qaiss, A. el, & Bouhfid, R. (2021). Recent progress on Ag/TiO_2 photocatalysts: photocatalytic and bactericidal behaviors. Environmental Science and Pollution Research, 28(33), 44638–44666. https://doi.org/10.1007/s11356-021-14996-y
[34]. Shi, W., Gao, J., Sun, H., Liu, Z., Guo, F., & Wang, L. (2022). Highly efficient visible/near-infrared light photocatalytic degradation of antibiotic wastewater over 3D yolk-shell $ZnFe_2O_4$ supported 0D carbon dots with up-conversion property. Chinese

Journal of Chemical Engineering, 49, 213–223. https://doi.org/10.1016/j.cjche.2021.11.026
[35]. Han, G., Li, G., Huang, J., Han, C., Turro, C., & Sun, Y. (2022). Two-photon-absorbing ruthenium complexes enable near infrared light-driven photocatalysis. Nature Communications, 13(1), 2288. https://doi.org/10.1038/s41467-022-29981-3
[36]. Sang, Y., Liu, H., & Umar, A. (2015). Cheminform Abstract: Photocatalysis from UV/Vis to Near-Infrared Light: Towards Full Solar-Light Spectrum Activity. ChemInform, 46(16), 559–573. https://doi.org/10.1002/chin.201516352
[37]. Abdelkader, E., Nadjia, L., & Ahmed, B. (2015). Preparation and characterization of novel $CuBi_2O_4/SnO_2$ p–n heterojunction with enhanced photocatalytic performance under UVA light irradiation. Journal of King Saud University - Science, 27(1), 76–91. https://doi.org/10.1016/j.jksus.2014.06.002
[38]. Mohamadpour, F., & Amani, A. M. (2024). Photocatalytic systems: reactions, mechanism, and applications. RSC Advances, 14(29), 20609–20645. https://doi.org/10.1039/d4ra03259d
[39]. Eidsvåg, H., Bentouba, S., Vajeeston, P., Yohi, S., & Velauthapillai, D. (2021). TiO_2 as a Photocatalyst for Water Splitting—An Experimental and Theoretical Review. Molecules, 26(6), 1687. https://doi.org/10.3390/molecules26061687
[40]. Inoue, Y. (2009). Photocatalytic water splitting by RuO_2 - loaded metal oxides and nitrides with d^0 - and d^{10} - related electronic configurations. Energy & Environmental Science, 2(4), 364–386. https://doi.org/10.1039/b816677n
[41]. Song, H., Luo, S., Huang, H., Deng, B., & Ye, J. (2022). Solar-Driven Hydrogen Production: Recent Advances, Challenges, and Future Perspectives. ACS Energy Letters, 7(3), 1043–1065. https://doi.org/10.1021/acsenergylett.1c02591
[42]. Pfeffer, M. G., Schäfer, B., Smolentsev, G., Uhlig, J., Nazarenko, E., Guthmuller, J., Kuhnt, C., Wächtler, M., Dietzek, B., Sundström, V., & Rau, S. (2015). Palladium versus Platinum: The Metal in the Catalytic Center of a Molecular Photocatalyst Determines the Mechanism of the Hydrogen Production with Visible Light. Angewandte Chemie International Edition, 54(17), 5044–5048. https://doi.org/10.1002/anie.201409438
[43]. Chanda, N., Koteshwar, D., Gonuguntla, S., Bojja, S., Pal, U., & Giribabu, L. (2021). Efficient visible-light-driven hydrogen production by Zn–porphyrin based photocatalyst with engineered active donor–acceptor sites. Materials Advances, 2(14), 4762–4771. https://doi.org/10.1039/d1ma00342a
[44]. Mekhemer, I. M., Elsenety, M. M., Elewa, A. M., Huynh, K. D., Samy, M. M., Mohamed, M. G., Dorrah, D. M., Hoang, D. C., Musa, A. F., Kuo, S.-W., & Chou, H.-H. (2024). Push–pull–pull interactions of 2D imide–imine-based covalent organic framework to promote charge separation in photocatalytic hydrogen production. Journal of Materials Chemistry A, 12(18), 10790–10798. https://doi.org/10.1039/d4ta01108b
[45]. Elsayed, M. H., Abdellah, M., Alhakemy, A. Z., Mekhemer, I. M., Aboubakr, A. E., Chen, B.-H., Sabbah, A., Lin, K.-H., Chiu, W.-S., Lin, S.-J., Chu, C.-Y., Lu, C.-H., Yang, S.-D., Mohamed, M. G., Kuo, S.-W., Hung, C.-H., Chen, L.-C., Chen, K.-H., & Chou, H.-H. (2024). Overcoming small-bandgap charge recombination in visible and NIR-light-driven hydrogen evolution by engineering the polymer photocatalyst structure. Nature Communications, 15(1), 707. https://doi.org/10.1038/s41467-024-45085-6
[46]. Hussain, S., Wang, Y., Guo, L., & He, T. (2022). Theoretical insights into the mechanism of photocatalytic reduction of CO_2 over semiconductor catalysts. Journal of Photochemistry and Photobiology C: Photochemistry Reviews, 52, 100538. https://doi.org/10.1016/j.jphotochemrev.2022.100538
[47]. Constable, E. C., Figgemeier, E., Housecroft, C. E., Olsson, J., & Zimmermann, Y. C. (2004). Electrochemical probing of ground state electronic interactions in polynuclear

complexes of a new heteroditopic ligand. Dalton Transactions, (13), 1918–1927. https://doi.org/10.1039/b404602a
[48]. Alhebshi, A., Sharaf Aldeen, E., Mim, R. S., Tahir, B., & Tahir, M. (2021). Recent advances in constructing heterojunctions of binary semiconductor photocatalysts for visible light responsive CO_2 reduction to energy efficient fuels: A review. International Journal of Energy Research, 46(5), 5523–5584. https://doi.org/10.1002/er.7563
[49]. Ma, J., Miao, T. J., & Tang, J. (2022). Charge carrier dynamics and reaction intermediates in heterogeneous photocatalysis by time-resolved spectroscopies. Chemical Society Reviews, 51(14), 5777–5794. https://doi.org/10.1039/d1cs01164b
[50]. Gao, W., Lu, J., Zhang, S., Zhang, X., Wang, Z., Qin, W., Wang, J., Zhou, W., Liu, H., & Sang, Y. (2019). Suppressing Photoinduced Charge Recombination via the Lorentz Force in a Photocatalytic System. Advanced Science, 6(18), 1901244. https://doi.org/10.1002/advs.201901244
[51]. Gupta, U., & Rao, C. N. R. (2017). Hydrogen generation by water splitting using MoS_2 and other transition metal dichalcogenides. Nano Energy, 41, 49–65. https://doi.org/10.1016/j.nanoen.2017.08.021
[52]. Kochuveedu, S. T. (2016). Photocatalytic and Photoelectrochemical Water Splitting on TiO_2 via Photosensitization. Journal of Nanomaterials, 2016, 4073142, 1–12. https://doi.org/10.1155/2016/4073142
[53]. J. Verne, The Mysterious Island, Scribner Armstrong & Co., New York (1876) https://ufdc.ufl.edu/AA00009647/00001/1.
[54]. Jules Verne "The Pioneer of Ideas". HY2GEN. (n.d.). https://www.hy2gen.com/jules-verne
[55]. Ameli, H., Strbac, G., Pudjianto, D., & Ameli, M. T. (2024). A Review of the Role of Hydrogen in the Heat Decarbonization of Future Energy Systems: Insights and Perspectives. Energies, 17(7), 1688. https://doi.org/10.3390/en17071688
[56]. Molloy, P. (2019, October 2). Run on Less with Hydrogen Fuel Cells. RMI. https://rmi.org/run-on-less-with-hydrogen-fuel-cells/
[57]. Mehr, A. S., Phillips, A. D., Brandon, M. P., Pryce, M. T., & Carton, J. G. (2024). Recent challenges and development of technical and technoeconomic aspects for hydrogen storage, insights at different scales; A state of art review. International Journal of Hydrogen Energy, 70, 786–815. https://doi.org/10.1016/j.ijhydene.2024.05.182
[58]. Hydrogen Ireland. (2022, August 8). One Year Of The Hydrogen Bus in Dublin Welcomed. https://hydrogenireland.org/2022/08/08/one-year-of-the-hydrogen-bus-in-dublin-welcomed/
[59]. Le, T. T., Sharma, P., Bora, B. J., Tran, V. D., Truong, T. H., Le, H. C., & Nguyen, P. Q. (2024). Fueling the future: A comprehensive review of hydrogen energy systems and their challenges. International Journal of Hydrogen Energy, 54, 791–816. https://doi.org/10.1016/j.ijhydene.2023.08.044
[60]. Griffiths, S., Sovacool, B. K., Kim, J., Bazilian, M., & Uratani, J. M. (2021). Industrial decarbonization via hydrogen: A critical and systematic review of developments, socio-technical systems and policy options. Energy Research & Social Science, 80, 102208. https://doi.org/10.1016/j.erss.2021.102208
[61]. Climate Action and Low Carbon Development (Amendment) Bill 2021. gov.ie. (2021). https://www.gov.ie/en/department-of-climate-energy-and-the-environment/publications/climate-action-and-low-carbon-development-amendment-bill-2021/
[62]. National hydrogen strategy. National Hydrogen Strategy, 2023. https://assets.gov.ie/static/documents/national-hydrogen-strategy.pdf
[63]. A hydrogen strategy for a climate-neutral Europe, 2020. https://energy.ec.europa.eu/system/files/2020-07/hydrogen_strategy_0.pdf

[64]. Sharma, K., Sharma, V., & Sharma, S. S. (2018). Dye-Sensitized Solar Cells: Fundamentals and Current Status. Nanoscale Research Letters, 13(1), 381. https://doi.org/10.1186/s11671-018-2760-6
[65]. Tributsch, H., & Calvin, M. (1971). Electrochemistry of excited molecules: Photo-electrochemical reactions of chlorophylls. Photochemistry and Photobiology, 14(2), 95–112. https://doi.org/10.1111/j.1751-1097.1971.tb06156.x
[66]. O'Regan, B., & Grätzel, M. (1991). A low-cost, high-efficiency solar cell based on dye-sensitized colloidal TiO_2 films. Nature, 353(6346), 737–740. https://doi.org/10.1038/353737a0
[67]. Ammar, A. M., Mohamed, H. S., Yousef, M. M., Abdel-Hafez, G. M., Hassanien, A. S., & Khalil, A. S. (2019). Dye-Sensitized Solar Cells (DSSCs) Based on Extracted Natural Dyes. Journal of Nanomaterials, 2019, 1–10. https://doi.org/10.1155/2019/1867271
[68]. Sarwar, S., Ko, K.-W., Han, J., Han, C.-H., Jun, Y., & Hong, S. (2017). Improved Long-Term Stability of Dye-Sensitized Solar Cell by Zeolite Additive in Electrolyte. Electrochimica Acta, 245, 526–530. https://doi.org/10.1016/j.electacta.2017.05.191
[69]. Ozawa, H., Sugiura, T., Kuroda, T., Nozawa, K., & Arakawa, H. (2016). Highly efficient dye-sensitized solar cells based on a ruthenium sensitizer bearing a hexylthiophene modified terpyridine ligand. Journal of Materials Chemistry A, 4(5), 1762–1770. https://doi.org/10.1039/c5ta10393b
[70]. Ito, S. (2011). Investigation of Dyes for Dye-Sensitized Solar Cells: Ruthenium-Complex Dyes, Metal-Free Dyes, Metal-Complex Porphyrin Dyes and Natural Dyes. Solar Cells-Dye-Sensitized Devices. Intech. https://doi.org/10.5772/19960
[71]. Ali, M. M., Pervez, W., Ghann, W., & Uddin, J. (2019). Photophysical Studies of Ruthenium-Based Complexes and the Performance of Nanostructured TiO_2 Based Dye Sensitized Solar Cells. Journal of Nanomedicine & Nanotechnology, 10(6). https://doi.org/10.35248/2157-7439.19.10.538
[72]. Fetouh, H. A., Dissouky, A. E., Salem, H. A., Fathy, M., Anis, B., & Hady Kashyout, A. E. (2024). Synthesis, characterization and evaluation of new alternative ruthenium complex for dye sensitized solar cells. Scientific Reports, 14(1), 16718. https://doi.org/10.1038/s41598-024-66808-1
[73]. Birel, Ö., Nadeem, S., & Duman, H. (2017). Porphyrin-Based Dye-Sensitized Solar Cells (DSSCs): A Review. Journal of Fluorescence, 27(3), 1075–1085. https://doi.org/10.1007/s10895-017-2041-2
[74]. Higashino, T., & Imahori, H. (2015). Porphyrins as excellent dyes for dye-sensitized solar cells: Recent developments and insights. Dalton Transactions, 44(2), 448–463. https://doi.org/10.1039/c4dt02756f
[75]. Li, Z., Li, Q., Li, C., & Xie, Y. (2024). Panchromatic porphyrin-based dye-sensitized solar cells: from cosensitization to concerted companion dye approaches. Materials Chemistry Frontiers, 8(3), 652–680. https://doi.org/10.1039/d3qm00770g
[76]. Urbani, M., Grätzel, M., Nazeeruddin, M. K., & Torres, T. (2014). Meso-Substituted Porphyrins for Dye-Sensitized Solar Cells. Chemical Reviews, 114(24), 12330–12396. https://doi.org/10.1021/cr5001964
[77]. Yu, Z., Li, F., & Sun, L. (2015a). Recent advances in dye-sensitized photoelectrochemical cells for solar hydrogen production based on molecular components. Energy & Environmental Science, 8(3), 760–775. https://doi.org/10.1039/c4ee03565h
[78]. Baron, T., Romito, D., Corne, L., Andrin, B., Pellegrin, Y., & Odobel, F. (2024). Dye-Sensitized Photocatalytic Hydrogen Production Promoted by Near-Infrared Pyrrolopyrrole Cyanine Sensitizers. ACS Applied Energy Materials, 7(11), 4690–4697. https://doi.org/10.1021/acsaem.4c00118

[79]. Maeda, K., Sahara, G., Eguchi, M., & Ishitani, O. (2015). Hybrids of a Ruthenium(II) Polypyridyl Complex and a Metal Oxide Nanosheet for Dye-Sensitized Hydrogen Evolution with Visible Light: Effects of the Energy Structure on Photocatalytic Activity. ACS Catalysis, 5(3), 1700–1707. https://doi.org/10.1021/acscatal.5b00040
[80]. Giannoudis, E., Bold, S., Müller, C., Schwab, A., Bruhnke, J., Queyriaux, N., Gablin, C., Leonard, D., Saint-Pierre, C., Gasparutto, D., Aldakov, D., Kupfer, S., Artero, V., Dietzek, B., & Chavarot-Kerlidou, M. (2021). Hydrogen Production at a NiO Photocathode Based on a Ruthenium Dye–Cobalt Diimine Dioxime Catalyst Assembly: Insights from Advanced Spectroscopy and Post-operando Characterization. ACS Applied Materials & Interfaces, 13(42), 49802–49815. https://doi.org/10.1021/acsami.1c12138
[81]. Wang, F., Wang, B., Zhang, T., & Liu, J. (2025). Electrochemical CO_2 reduction to C_{3+} products: A Review. Green Carbon. https://doi.org/10.1016/j.greenca.2025.02.009
[82]. Cao, L., Qi, F., Zhang, N., Pu, Y., Tang, X., & Huang, Q. (2025). Progress and future of CO_2 conversion based on plasma catalysis. DeCarbon, 8, 100109. https://doi.org/10.1016/j.decarb.2025.100109
[83]. Garcia Osorio, D. A., Neri, G., & Cowan, A. J. (2021). Hybrid Photocathodes for Carbon Dioxide Reduction: Interfaces for Charge Separation and Selective Catalysis. ChemPhotoChem, 5(7), 595–610. https://doi.org/10.1002/cptc.202000309
[84]. Kawawaki, T., Akinaga, Y., Yazaki, D., Kameko, H., Hirayama, D., & Negishi, Y. (2023). Promoting Photocatalytic Carbon Dioxide Reduction by Tuning the Properties of Cocatalysts. Chemistry – A European Journal, 29(9), e202203387. https://doi.org/10.1002/chem.202203387
[85]. Belessiotis, G. V., & Kontos, A. G. (2022). Plasmonic silver (Ag)-based photocatalysts for H_2 production and CO_2 conversion: Review, analysis and perspectives. Renewable Energy, 195, 497–515. https://doi.org/10.1016/j.renene.2022.06.044
[86]. Hawecker, J., Lehn, J.-M., & Ziessel, R. (1983). Efficient photochemical reduction of CO_2 to CO by visible light irradiation of systems containing $Re(bipy)(CO)_3X$ or $Ru(bipy)_3^{2+}$–Co^{2+} combinations as homogeneous catalysts. J. Chem. Soc., Chem. Commun., (9), 536–538. https://doi.org/10.1039/c39830000536
[87]. Santoro, A., Cancelliere, A. M., Kamogawa, K., Serroni, S., Puntoriero, F., Tamaki, Y., Campagna, S., & Ishitani, O. (2023). Photocatalyzed CO_2 reduction to CO by supramolecular photocatalysts made of Ru(II) photosensitizers and Re(I) catalytic subunits containing preformed CO_2TEOA adducts. Scientific Reports, 13(1), 11320. https://doi.org/10.1038/s41598-023-38411-3
[88]. Gu, S., Marianov, A. N., Lu, T., & Zhong, J. (2023). A review of the development of porphyrin-based catalysts for electrochemical CO_2 reduction. Chemical Engineering Journal, 470, 144249. https://doi.org/10.1016/j.cej.2023.144249
[89]. Wu, H., Liu, R., Li, D., & Ng, Y. H. (2025). Porphyrin-based metal-organic frameworks for photocatalytic carbon dioxide reduction: Current understanding and challenges. Nano Materials Science. 12, 3–26 https://doi.org/10.1016/j.nanoms.2024.12.003
[90]. Ding, G., Li, C., Chen, L., & Liao, G. (2024). Porphyrin-based metal–organic frameworks for photo(electro)catalytic CO_2 reduction. Energy & Environmental Science, 17(15), 5311–5335. https://doi.org/10.1039/d4ee01748j
[91]. Han, J., Wang, N., Li, X., Lei, H., Wang, Y., Guo, H., Jin, X., Zhang, Q., Peng, X., Zhang, X.-P., Zhang, W., Apfel, U.-P., & Cao, R. (2022). Bioinspired iron porphyrins with appended poly-pyridine/amine units for boosted electrocatalytic CO_2 reduction reaction. eScience, 2(6), 623–631. https://doi.org/10.1016/j.esci.2022.06.003
[92]. Herrero, C., Quaranta, A., El Ghachtouli, S., Vauzeilles, B., Leibl, W., & Aukauloo, A. (2014). Carbon dioxide reduction via light activation of a ruthenium–Ni(cyclam) complex. Physical Chemistry Chemical Physics, 16(24), 12067–12072. https://doi.org/10.1039/c3cp54946a

[93]. Damas, G. B., Ivashchenko, D. A., Rivalta, I., & Araujo, C. M. (2021). Carbon dioxide reduction mechanism on Ru-based electrocatalysts $[Ru(bpy)_2(CO)_2]^{2+}$: insights from first-principles theory. Sustainable Energy & Fuels, 5(23), 6066–6076. https://doi.org/10.1039/d1se01315g
[94]. Boudreaux, C. M., Liyanage, N. P., Shirley, H., Siek, S., Gerlach, D. L., Qu, F., Delcamp, J. H., & Papish, E. T. (2017). Ruthenium(II) complexes of pyridinol and N-heterocyclic carbene derived pincers as robust catalysts for selective carbon dioxide reduction. Chem. Commun., 53(81), 11217–11220. https://doi.org/10.1039/c7cc05706g
[95]. Kamogawa, K., Shimoda, Y., Miyata, K., Onda, K., Yamazaki, Y., Tamaki, Y., & Ishitani, O. (2021). Mechanistic study of photocatalytic CO_2 reduction using a Ru(II)–Re(I) supramolecular photocatalyst. Chemical Science, 12(28), 9682–9693. https://doi.org/10.1039/d1sc02213j
[96]. Kamada, K., Jung, J., Wakabayashi, T., Sekizawa, K., Sato, S., Morikawa, T., Fukuzumi, S., & Saito, S. (2020). Photocatalytic CO_2 Reduction Using a Robust Multifunctional Iridium Complex Toward the Selective Formation of Formic Acid. Journal of the American Chemical Society, 142(23), 10261–10266. https://doi.org/10.1021/jacs.0c03097
[97]. Kuramochi, Y., & Ishitani, O. (2019). An Ir(III) Complex Photosensitizer With Strong Visible Light Absorption for Photocatalytic CO_2 Reduction. Frontiers in Chemistry, 7. https://doi.org/10.3389/fchem.2019.00259
[98]. Shee, U., Khutia, B., Ray, S., Ghosh, S., & Rajak, K. K. (2025). Highly efficient photocatalytic reduction of CO_2 to CO under visible light using rhenium benzo[d]oxazole complexes. Dalton Transactions. 18(54), 7294–7305. https://doi.org/10.1039/d4dt03400g
[99]. Ren, F., Chen, K., Qiu, L., Chen, J., Darensbourg, D. J., & He, L. (2022). Amphiphilic Polycarbonate Micellar Rhenium Catalysts for Efficient Photocatalytic CO_2 Reduction in Aqueous Media. Angewandte Chemie, 134(27), e202200751. https://doi.org/10.1002/ange.202200751
[100]. Li, S.-Y., Meng, S., Zou, X., El-Roz, M., Telegeev, I., Thili, O., Liu, T. X., & Zhu, G. (2019). Rhenium-functionalized covalent organic framework photocatalyst for efficient CO_2 reduction under visible light. Microporous and Mesoporous Materials, 285, 195–201. https://doi.org/10.1016/j.micromeso.2019.05.026
[101]. Lu, S., Lou, F., & Yu, Z. (2022). Recent Progress in Two-Dimensional Materials for Electrocatalytic CO_2 reduction. Catalysts, 12(2), 228. https://doi.org/10.3390/catal12020228
[102]. Nikoloudakis, E., López-Duarte, I., Charalambidis, G., Ladomenou, K., Ince, M., & Coutsolelos, A. G. (2022). Porphyrins and phthalocyanines as biomimetic tools for photocatalytic H_2 production and CO_2 reduction. Chemical Society Reviews, 51(16), 6965–7045. https://doi.org/10.1039/d2cs00183g
[103]. Bagemihl, B., Müller, C., Shillito, G. E., Hartkorn, M., Mengele, A. K., Kupfer, S., Dietzek-Ivanšić, B., & Rau, S. (2024). Steering Photoinduced Electron Transfer in Intramolecular Photocatalysts by Peripheral Ligand Control. ChemistryEurope, 2(6), e202300084. https://doi.org/10.1002/ceur.202300084
[104]. Kowacs, T., Pan, Q., Lang, P., O'Reilly, L., Rau, S., Browne, W. R., Pryce, M. T., Huijser, A., & Vos, J. G. (2015). Supramolecular bimetallic assemblies for photocatalytic hydrogen generation from water. Faraday Discussions, 185, 143–170. https://doi.org/10.1039/c5fd00068h
[105]. Teeuwen, P. C., Melissari, Z., Senge, M. O., & Williams, R. M. (2022). Metal Coordination Effects on the Photophysics of Dipyrrinato Photosensitizers. Molecules, 27(20), 6967. https://doi.org/10.3390/molecules27206967
[106]. Yong, W.-W., Lu, H., Li, H., Wang, S., & Zhang, M.-T. (2018). Photocatalytic Hydrogen Production with Conjugated Polymers as Photosensitizers. ACS Applied Materials & Interfaces, 10(13), 10828–10834. https://doi.org/10.1021/acsami.7b18917

[107]. Bai, Y., Wilbraham, L., Slater, B. J., Zwijnenburg, M. A., Sprick, R. S., & Cooper, A. I. (2019). Accelerated Discovery of Organic Polymer Photocatalysts for Hydrogen Evolution from Water through the Integration of Experiment and Theory. Journal of the American Chemical Society, 141(22), 9063–9071. https://doi.org/10.1021/jacs.9b03591
[108]. Sprick, R. S., Bonillo, B., Clowes, R., Guiglion, P., Brownbill, N. J., Slater, B. J., Blanc, F., Zwijnenburg, M. A., Adams, D. J., & Cooper, A. I. (2015). Visible-Light-Driven Hydrogen Evolution Using Planarized Conjugated Polymer Photocatalysts. Angewandte Chemie, 128(5), 1824–1828. https://doi.org/10.1002/ange.201510542
[109]. Corredor, J., Rivero, M. J., Rangel, C. M., Gloaguen, F., & Ortiz, I. (2019). Comprehensive review and future perspectives on the photocatalytic hydrogen production. Journal of Chemical Technology & Biotechnology, 94(10), 3049–3063. https://doi.org/10.1002/jctb.6123
[110]. Cerpentier, F. J., Karlsson, J., Lalrempuia, R., Brandon, M. P., Sazanovich, I. V., Greetham, G. M., Gibson, E. A., & Pryce, M. T. (2021). Ruthenium Assemblies for CO_2 Reduction and H_2 Generation: Time Resolved Infrared Spectroscopy, Spectroelectrochemistry and a Photocatalysis Study in Solution and on NiO. Frontiers in Chemistry, 9. https://doi.org/10.3389/fchem.2021.795877
[111]. Halpin, Y., Pryce, M. T., Rau, S., Dini, D., & Vos, J. G. (2013). Recent progress in the development of bimetallic photocatalysts for hydrogen generation. Dalton Transactions, 42(46), 16243–16254. https://doi.org/10.1039/c3dt52319e
[112]. O'Neill, J. S., Kearney, L., Brandon, M. P., & Pryce, M. T. (2022a). Design components of porphyrin-based photocatalytic hydrogen evolution systems: A Review. Coordination Chemistry Reviews, 467, 214599. https://doi.org/10.1016/j.ccr.2022.214599
[113]. Manton, J. C., Long, C., Vos, J. G., & Pryce, M. T. (2014). Porphyrin–cobaloxime complexes for hydrogen production, a photo- and electrochemical study, coupled with quantum chemical calculations. Dalton Transactions, 43(9), 3576–3583. https://doi.org/10.1039/c3dt53166j
[114]. Manton, J. C., Long, C., Vos, J. G., & Pryce, M. T. (2014a). A photo- and electrochemical investigation of BODIPY–cobaloxime complexes for hydrogen production, coupled with quantum chemical calculations. Physical Chemistry Chemical Physics, 16(11), 5229–5236. https://doi.org/10.1039/c3cp55347g
[115]. Hansen, S., Klahn, M., Beweries, T., & Rosenthal, U. (2012). An Intermolecular Heterobimetallic System for Photocatalytic Water Reduction. ChemSusChem, 5(4), 656–660. https://doi.org/10.1002/cssc.201100794
[116]. Zhang, J., Ge, Z., Zhong, D., Zuo, J., Robert, M., & Lu, T. (2025). Self-Photosensitizing Cobalt Complexes for Photocatalytic CO_2 Reduction Coupled with CH_3OH Oxidation. Angewandte Chemie, 137(26), e202506060. https://doi.org/10.1002/ange.202506060
[117]. Probst, B., Kolano, C., Hamm, P., & Alberto, R. (2009). An Efficient Homogeneous Intermolecular Rhenium-Based Photocatalytic System for the Production of H_2. Inorganic Chemistry, 48(5), 1836–1843. https://doi.org/10.1021/ic8013255
[118]. Lehn, J. and Sauvage, J.(1977). Chemical storage of light energy: Catalytic generation of hydrogen by visible light or sunlight irradiation of neutral aqueous solutions. Nouveau Journal de Chimie 1: 449–451.
[119]. Kirch, M., Lehn, J., & Sauvage, J. (1979). Hydrogen Generation by Visible Light Irradiation of Aqueous Solutions of Metal Complexes. An approach to the photochemical conversion and storage of solar energy. Helvetica Chimica Acta, 62(4), 1345–1384. https://doi.org/10.1002/hlca.19790620449
[120]. Kalyanasundaram, K., Kiwi, J., & Grätzel, M. (1978). Hydrogen Evolution from Water by Visible Light, a Homogeneous Three Component Test System for Redox

Catalysis. Helvetica Chimica Acta, 61(7), 2720–2730. https://doi.org/10.1002/hlca.19780610740
[121]. Rau, S., Schäfer, B., Gleich, D., Anders, E., Rudolph, M., Friedrich, M., Görls, H., Henry, W., & Vos, J. G. (2006). A Supramolecular Photocatalyst for the Production of Hydrogen and the Selective Hydrogenation of Tolane. Angewandte Chemie International Edition, 45(37), 6215–6218. https://doi.org/10.1002/anie.200600543
[122]. Deponti, E., & Natali, M. (2016). Photocatalytic hydrogen evolution with ruthenium polypyridine sensitizers: unveiling the key factors to improve efficiencies. Dalton Transactions, 45(22), 9136–9147. https://doi.org/10.1039/c6dt01221c
[123]. Kowacs, T., O'Reilly, L., Pan, Q., Huijser, A., Lang, P., Rau, S., Browne, W. R., Pryce, M. T., & Vos, J. G. (2016a). Subtle Changes to Peripheral Ligands Enable High Turnover Numbers for Photocatalytic Hydrogen Generation with Supramolecular Photocatalysts. Inorganic Chemistry, 55(6), 2685–2690. https://doi.org/10.1021/acs.inorgchem.5b01752
[124]. Das, N., Bindra, G. S., Paul, A., Vos, J. G., Schulz, M., & Pryce, M. T. (2017). Enhancing Photocatalytic Hydrogen Generation: The Impact of the Peripheral Ligands in Ru/Pd and Ru/Pt complexes. Chemistry – A European Journal, 23(22), 5330–5337. https://doi.org/10.1002/chem.201605980
[125]. Singh Bindra, G., Schulz, M., Paul, A., Soman, S., Groarke, R., Inglis, J., Pryce, M. T., Browne, W. R., Rau, S., Maclean, B. J., & Vos, J. G. (2011). The effect of peripheral bipyridine ligands on the photocatalytic hydrogen production activity of Ru/Pd catalysts. Dalton Transactions, 40(41), 10812–10814. https://doi.org/10.1039/c1dt11241d
[126]. Karnahl, M., Kuhnt, C., Ma, F., Yartsev, A., Schmitt, M., Dietzek, B., Rau, S., & Popp, J. (2011). Tuning of Photocatalytic Hydrogen Production and Photoinduced Intramolecular Electron Transfer Rates by Regioselective Bridging Ligand Substitution. ChemPhysChem, 12(11), 2101–2109. https://doi.org/10.1002/cphc.201100245
[127]. Tschierlei, S., Karnahl, M., Presselt, M., Dietzek, B., Guthmuller, J., González, L., Schmitt, M., Rau, S., & Popp, J. (2010). Photochemical Fate: The First Step Determines Efficiency of H_2 Formation with a Supramolecular Photocatalyst. Angewandte Chemie International Edition, 49(23), 3981–3984. https://doi.org/10.1002/anie.200906595
[128]. Fihri, A., Artero, V., Razavet, M., Baffert, C., Leibl, W., & Fontecave, M. (2007). Cobaloxime-Based Photocatalytic Devices for Hydrogen Production. Angewandte Chemie, 120(3), 574–577. https://doi.org/10.1002/ange.200702953
[129]. Camara, F., Aguirre-Araque, J. S., Fortage, J., & Collomb, M.-N. (2024). Enhancing the stability of photocatalytic systems for hydrogen evolution in water by using a tris-phenyl-phenanthroline sulfonate ruthenium photosensitizer. Sustainable Energy & Fuels, 8(7), 1457–1472. https://doi.org/10.1039/d3se01556d
[130]. Edwards, E. H., Jelušić, J., Chakraborty, S., & Bren, K. L. (2021). Photochemical hydrogen evolution from cobalt microperoxidase-11. Journal of Inorganic Biochemistry, 217, 111384. https://doi.org/10.1016/j.jinorgbio.2021.111384
[131]. Rupp, M., Auvray, T., Rousset, E., Mercier, G. M., Marvaud, V., Kurth, D. G., & Hanan, G. S. (2019). Photocatalytic Hydrogen Evolution Driven by a Heteroleptic Ruthenium(II) Bis(terpyridine) Complex. Inorganic Chemistry, 58(14), 9127–9134. https://doi.org/10.1021/acs.inorgchem.9b00698
[132]. Spikes, J. D. (1975). Porphyrins and related compounds as photodynamic sensitizers*. Annals of the New York Academy of Sciences, 244(1), 496–508. https://doi.org/10.1111/j.1749-6632.1975.tb41550.x
[133]. Mandal, R., & Dutta, G. (2020). From photosynthesis to biosensing: Chlorophyll proves to be a versatile molecule. Sensors International, 1, 100058. https://doi.org/10.1016/j.sintl.2020.100058
[134]. Zhang, P., Wang, M., Li, X., Cui, H., Dong, J., & Sun, L. (2012). Photochemical hydrogen production with molecular devices comprising a zinc porphyrin and a

cobaloxime catalyst. Science China Chemistry, 55(7), 1274–1282. https://doi.org/10.1007/s11426-012-4514-0
[135]. Bodedla, G. B., Li, L., Che, Y., Jiang, Y., Huang, J., Zhao, J., & Zhu, X. (2018). Enhancing photocatalytic hydrogen evolution by intramolecular energy transfer in naphthalimide conjugated porphyrins. Chemical Communications, 54(82), 11614–11617. https://doi.org/10.1039/c8cc06919k
[136]. Lv, M., Ren, X., Cao, R., Chang, Z., Chang, X., Bai, F., & Li, Y. (2022). Zn (II) Porphyrin Built-in D–A Covalent Organic Framework for Efficient Photocatalytic H_2 Evolution. Polymers, 14(22), 4893. https://doi.org/10.3390/polym14224893
[137]. Lang, P., Habermehl, J., Troyanov, S. I., Rau, S., & Schwalbe, M. (2018). Photocatalytic Generation of Hydrogen using Dinuclear π-Extended Porphyrin–Platinum Compounds. Chemistry – A European Journal, 24(13), 3225–3233. https://doi.org/10.1002/chem.201704999
[138]. Natali, M., Argazzi, R., Chiorboli, C., Iengo, E., & Scandola, F. (2013). Photocatalytic Hydrogen Evolution with a Self-Assembling Reductant–Sensitizer–Catalyst System. Chemistry – A European Journal, 19(28), 9261–9271. https://doi.org/10.1002/chem.201300133
[139]. Giannoudis, E., Benazzi, E., Karlsson, J., Copley, G., Panagiotakis, S., Landrou, G., Angaridis, P., Nikolaou, V., Matthaiaki, C., Charalambidis, G., Gibson, E. A., & Coutsolelos, A. G. (2020). Photosensitizers for H_2 Evolution Based on Charged or Neutral Zn and Sn Porphyrins. Inorganic Chemistry, 59(3), 1611–1621. https://doi.org/10.1021/acs.inorgchem.9b01838
[140]. Zhu, M., Dong, Y., Du, Y., Mou, Z., Liu, J., Yang, P., & Wang, X. (2012). Photocatalytic Hydrogen Evolution Based on Efficient Energy and Electron Transfers in Donor–Bridge–Acceptor Multibranched-Porphyrin-Functionalized Platinum Nanocomposites. Chemistry – A European Journal, 18(14), 4367–4374. https://doi.org/10.1002/chem.201102595
[141]. Lazarides, T., Delor, M., Sazanovich, I. V., McCormick, T. M., Georgakaki, I., Charalambidis, G., Weinstein, J. A., & Coutsolelos, A. G. (2014). Photocatalytic hydrogen production from a noble metal free system based on a water-soluble porphyrin derivative and a cobaloxime catalyst. Chem. Commun., 50(5), 521–523. https://doi.org/10.1039/c3cc45025b
[142]. Sun, M., Fan, X., Guo, S., Nui, X., Tian, L., Wang, A., Wang, R., Chen, W., & Cui, C. (2024a). Substituent Regulating Porphyrin Derivatives for Efficient Photocatalytic Hydrogen Evolution. ChemistrySelect, 9(40), e202402960. https://doi.org/10.1002/slct.202402960
[143]. Wang, S., Li, S., Zheng, C., Feng, H., & Feng, Y.-S. (2023). Bimetallic Porphyrin-Based Metal–Organic Framework as a Superior Photocatalyst for Enhanced Photocatalytic Hydrogen Production. Inorganic Chemistry, 63(1), 554–563. https://doi.org/10.1021/acs.inorgchem.3c03446
[144]. Tang, C., Li, X., Hu, Y., Du, X., Wang, S., Chen, B., & Wang, S. (2024). Porphyrin Based Metal-Organic Framework Materials: Design, Construction, and Application in the Field of Photocatalysis. Molecules, 29(2), 467. https://doi.org/10.3390/molecules29020467
[145]. Prakash, K., Mishra, B., Díaz, D. D., Nagaraja, C. M., & Pachfule, P. (2023). Strategic design of covalent organic frameworks (COFs) for photocatalytic hydrogen generation. Journal of Materials Chemistry A, 11(27), 14489–14538. https://doi.org/10.1039/d3ta02189k
[146]. Nikolaou, V., Agapaki, E., Nikoloudakis, E., Achilleos, K., Ladomenou, K., Charalambidis, G., Triantafyllou, E., & Coutsolelos, A. G. (2023). Highly efficient light driven hydrogen evolution utilizing porphyrin-based nanoparticles. Chemical Communications, 59(75), 11256–11259. https://doi.org/10.1039/d3cc02922k

[147]. Vaz, B., & Pérez-Lorenzo, M. (2023). Unraveling Structure–Performance Relationships in Porphyrin-Sensitized TiO_2 Photocatalysts. Nanomaterials, 13(6), 1097. https://doi.org/10.3390/nano13061097
[148]. Al Kobaisi, M., Bhosale, S. V., Latham, K., Raynor, A. M., & Bhosale, S. V. (2016). Functional Naphthalene Diimides: Synthesis, Properties, and Applications. Chemical Reviews, 116(19), 11685–11796. https://doi.org/10.1021/acs.chemrev.6b00160
[149]. Yang, Y., Zou, X., Sun, Y., Chen, F., Zhao, J., & Gou, S. (2023). Naphthalene Diimide-Functionalized Half-Sandwich Ru(II) Complexes as Mitochondria-Targeted Anticancer and Antimetastatic Agents. Inorganic Chemistry, 62(24), 9649–9660. https://doi.org/10.1021/acs.inorgchem.3c01125
[150]. Ghosh, P., Rashid, A., Mondal, S., Islam, A. S., & Mondal, S. (2024). Naphthalene Diimide and Bis-Heteroleptic Ru(II) Complex-Based Hybrid Molecule with 3-in-1 Functionalities. Chemistry – An Asian Journal, 19(23), e202400724. https://doi.org/10.1002/asia.202400724
[151]. Seven, S., Yigit, E., Bayindir, S., Akman, F., Sevgili, Ö., Dayan, O., & Orak, İ. (2024). The photodiode performances of NDI-appended ruthenium complexes. Nano Express, 5(2), 025002. https://doi.org/10.1088/2632-959x/ad34a4
[152]. Gutiérrez-Peña, C. L., Gutiérrez-Blanco, A., Gusev, D. G., Poyatos, M., & Peris, E. (2024). Lone-Pair-π Bond Strength Unveiled by a Combined Experimental and Computational Study. Angewandte Chemie, 136(32), e202407817. https://doi.org/10.1002/Ange.202407817
[153]. Klein, J. H., Sunderland, T. L., Kaufmann, C., Holzapfel, M., Schmiedel, A., & Lambert, C. (2013). Stepwise versus pseudo-concerted two-electron-transfer in a triarylamine–iridium dipyrrin–naphthalene diimide triad. Physical Chemistry Chemical Physics, 15(38), 16024–16030. https://doi.org/10.1039/c3cp51981c
[154]. Kuang, X., Chen, S., Meng, L., Chen, J., Wu, X., Zhang, G., Zhong, G., Hu, T., Li, Y., & Lu, C.-Z. (2019). Supramolecular aggregation of a redox-active copper-naphthalenediimide network with intrinsic electron conduction. Chemical Communications, 55(11), 1643–1646. https://doi.org/10.1039/c8cc10269d
[155]. Pirota, V., Lunghi, E., Benassi, A., Crespan, E., Freccero, M., & Doria, F. (2021). Selective Binding and Redox-Activity on Parallel G-Quadruplexes by Pegylated Naphthalene Diimide-Copper Complexes. Molecules, 26(16), 5025. https://doi.org/10.3390/molecules26165025
[156]. Mirgane, H. A., More, K. S., Veeranagaiah, N. S., & Bhosale, S. V. (2024). Porphyrin-based covalently bonded nanoarchitectonics of organic donor-acceptor system for artificial photosynthesis: A Review. Dyes and Pigments, 225, 112113. https://doi.org/10.1016/j.dyepig.2024.112113
[157]. Robotham, B., Lastman, K. A., Langford, S. J., & Ghiggino, K. P. (2013). Ultrafast electron transfer in a porphyrin-amino naphthalene diimide dyad. Journal of Photochemistry and Photobiology A: Chemistry, 251, 167–174. https://doi.org/10.1016/j.jphotochem.2012.11.002
[158]. Liu, J., Li, M., Chen, D., Huang, B., He, Q., Ding, S., Xie, W., Wu, F., Chen, L., & Chen, Y. (2020). Introducing Porphyrin Units by Random Copolymerization into NDI-Based Acceptor for All Polymer Solar Cells. Frontiers In Chemistry, 8. https://doi.org/10.3389/fchem.2020.00310
[159]. Wallin, S., Monnereau, C., Blart, E., Gankou, J.-R., Odobel, F., & Hammarström, L. (2010). State Selective Electron Transfer in an Unsymmetric Acceptor−Zn(II)Porphyrin−Acceptor Triad: Toward a Controlled Directionality of Electron Transfer from the Porphyrin S_2 and S_1 States as a Basis for a Molecular Switch. The Journal of Physical Chemistry A, 114(4), 1709–1721. https://doi.org/10.1021/jp907824d

[160]. Wang, S.-H., Khurshid, F., Chen, P.-Z., Lai, Y.-R., Cai, C.-W., Chung, P.-W., Hayashi, M., Jeng, R.-J., Rwei, S.-P., & Wang, L. (2022a). Solution-Processable Naphthalene Diimide-Based Conjugated Polymers as Organocatalysts for Photocatalytic CO_2 Reaction with Extremely Stable Catalytic Activity for Over 330 Hours. Chemistry of Materials, 34(11), 4955–4963. https://doi.org/10.1021/acs.chemmater.2c00168
[161]. Wang, S.-H., Chen, P.-Z., Chen, Y.-Y., Khurshid, F., Cai, C.-W., Lai, Y.-Y., Chung, P.-W., Jeng, R.-J., Rwei, S.-P., & Wang, L. (2022a). Naphthalene Diimide-Based Donor–Acceptor–Donor Small Molecules as Metal-Free Organocatalysts for Photocatalytic CO_2 Reaction. ACS Applied Materials & Interfaces, 14(38), 43109–43115. https://doi.org/10.1021/acsami.2c08531
[162]. Xu, S., Chen, S., Li, Y., Gao, Q., Luo, X., Li, M., Ren, L., Wang, P., Liu, L., Wang, J., Chen, X., Chen, Q., & Zhu, Y. (2024). Dual Function of Naphthalenediimide Supramolecular Photocatalyst with Giant Internal Electric Field for Efficient Hydrogen and Oxygen Evolution. Small, 20(32), 2400344. https://doi.org/10.1002/smll.202400344
[163]. Mekhemer, I. M., Wu, Y., Elewa, A. M., Chen, W., Chueh, C., & Chou, H. (2024). Naphthalenediimide-Based Polymer Dots with Dual Acceptors as a New Class of Photocatalysts for Photocatalytic Hydrogen Generation under Visible Light Irradiation. Solar RRL, 8(6), 2300994. https://doi.org/10.1002/solr.202300994
[164]. Combes, J. M., Duclos, P., & Seiler, R. (1981b). The Born-Oppenheimer Approximation. Rigorous Atomic and Molecular Physics, 185–213. https://doi.org/10.1007/978-1-4613-3350-0_5
[165]. McNab, I. R. (2017). Rotational spectroscopy, Theory. Encyclopedia of Spectroscopy and Spectrometry, 978–987. https://doi.org/10.1016/b978-0-12-803224-4.00273-9
[166]. Gilbert, A., & Baggott, J. (1991). Essentials of Molecular Photochemistry. Blackwell Scientific Publications, London, pp. 33, 70 – 80, 114 – 117.
[167]. Gupta, V. P. (2016). Interaction of Radiation and Matter and Electronic Spectra. Principles and Applications of Quantum Chemistry, 291–337. https://doi.org/10.1016/b978-0-12-803478-1.00009-1
[168]. Zhang, J. X. J., & Hoshino, K. (2019). Optical transducers: Optical molecular sensing and spectroscopy. Molecular Sensors and Nanodevices, 231–309. https://doi.org/10.1016/b978-0-12-814862-4.00005-3
[169]. Condon, E. U. (1928). Nuclear Motions Associated with Electron Transitions in Diatomic Molecules. Physical Review, 32(6), 858–872. https://doi.org/10.1103/physrev.32.858
[170]. Franck, J., & Dymond, E. G. (1926). Elementary processes of photochemical reactions. Transactions of the Faraday Society, 21(February), 536–542. https://doi.org/10.1039/tf9262100536
[171]. Condon, E. (1926). A Theory of Intensity Distribution in Band Systems. Physical Review, 28(6), 1182–1201. https://doi.org/10.1103/physrev.28.1182
[172]. Löfgren, R., Öberg, S., & Larsson, J. A. (2022). The diamond NV-center transition energies in the vicinity of an intrinsic stacking fault. AIP Advances, 12(3), 035009. https://doi.org/10.1063/5.0080096
[173]. Franck–Condon Principle (2025) Wikipedia. Available at: https://en.wikipedia.org/wiki/Franck%E2%80%93Condon_principle
[174]. Jablonski, A. (1933). Efficiency of Anti-Stokes Fluorescence in Dyes. Nature, 131(3319), 839–840. https://doi.org/10.1038/131839b0
[175]. Berezin, M. Y., & Achilefu, S. (2010). Fluorescence Lifetime Measurements and Biological Imaging. Chemical Reviews, 110(5), 2641–2684. https://doi.org/10.1021/cr900343z

[176]. Tang, Y., & Tang, B.-Z. (2022). Handbook of Aggregation-Induced Emission, Volume 1 Tutorial Lectures and Mechanism Studies. John Wiley & Sons, Incorporated. https://doi.org/10.1002/9781119643098
[177]. Pope, T., Eng, J., Monkman, A., & Penfold, T. J. (2024). Spin-Vibronic Intersystem Crossing and Molecular Packing Effects in Heavy Atom Free Organic Phosphor. Journal of Chemical Theory and Computation, 20(3), 1337–1346. https://doi.org/10.1021/acs.jctc.3c01220
[178]. What is a Jablonski Diagram (Perrin-Jablonski Diagram)? - Edinburgh Instruments. (2021). https://www.edinst.com/resource/what-is-a-jablonski-diagram-perrin-jablonski-diagram/
[179]. Chauke, N. M., Mohlala, R. L., Ngqoloda, S., & Raphulu, M. C. (2024). Harnessing visible light: enhancing TiO_2 photocatalysis with photosensitizers for sustainable and efficient environmental solutions. Frontiers in Chemical Engineering, 6. https://doi.org/10.3389/fceng.2024.1356021
[180]. Narsaria, A. K., Poater, J., Fonseca Guerra, C., Ehlers, A. W., Lammertsma, K., & Bickelhaupt, F. M. (2018). Rational design of near-infrared absorbing organic dyes: Controlling the HOMO–LUMO gap using quantitative molecular orbital theory. Journal of Computational Chemistry, 39(32), 2690–2696. https://doi.org/10.1002/jcc.25731
[181]. Clayden, J. (2001). Organic Chemistry. Oxford University Press, pp.149
[182]. Ishii, K., & Kato, M. (2023). Theoretical Background of Photophysical Properties. The Materials Research Society Series, 23–35.
https://doi.org/10.1007/978-981-99-0260-6_3
[183]. Jena, S., & Parker, L. L. (2022). Fluorescence Lifetime Imaging Probes for Cell-Based Measurements of Enzyme Activity. Methods in Molecular Biology, 133–162. https://doi.org/10.1007/978-1-0716-1811-0_9
[184]. Deepa, H. R., Thipperudrappa, J., & Suresh Kumar, H. M. (2020). Effect of temperature on fluorescence quenching and emission characteristics of laser dyes. Journal of Physics: Conference Series, 1473(1), 012046.
https://doi.org/10.1088/1742-6596/1473/1/012046
[185]. Moger, J., Gribbon, P., Sewing, A., & Winlove, C. P. (2006). The Application of Fluorescence Lifetime Readouts in High-Throughput Screening. SLAS Discovery, 11(7), 765–772. https://doi.org/10.1177/1087057106291541
[186]. Kafle, B. P. (2020). Molecular luminescence spectroscopy. Chemical Analysis and Material Characterization by Spectrophotometry, 269–296.
https://doi.org/10.1016/b978-0-12-814866-2.00009-9
[187]. What is the Best Setup of Time Correlated Single Photon Counting (TCSPC)? Check simtrum solution here! https://www.simtrum.com/WebShop/SolutionInfo.aspx?id=1672
[188]. TCSPC. (n.d.). https://www2.chemistry.msu.edu/faculty/blanchardlab/Tcspc.html
[189]. Smith, D. A., McKenzie, G., Jones, A. C., & Smith, T. A. (2017). Analysis of time-correlated single photon counting data: A comparative evaluation of deterministic and probabilistic approaches. Methods and Applications in Fluorescence, 5(4), 042001. https://doi.org/10.1088/2050-6120/aa8055
[190]. Berera, R., van Grondelle, R., & Kennis, J. T. (2009). Ultrafast transient absorption spectroscopy: principles and application to photosynthetic systems. Photosynthesis Research, 101(2–3), 105–118. https://doi.org/10.1007/s11120-009-9454-y
[191]. Zhang, J., Zhu, B., Zhang, L., & Yu, J. (2023). Femtosecond transient absorption spectroscopy investigation into the electron transfer mechanism in photocatalysis. Chemical Communications, 59(6), 688–699. https://doi.org/10.1039/d2cc06300j
[192]. Munson, K. T., Kennehan, E. R., & Asbury, J. B. (2019). Structural origins of the electronic properties of materials via time-resolved infrared spectroscopy. Journal of Materials Chemistry C, 7(20), 5889–5909. https://doi.org/10.1039/c9tc01348b

[193]. Koike, K., Grills, D. C., Tamaki, Y., Fujita, E., Okubo, K., Yamazaki, Y., Saigo, M., Mukuta, T., Onda, K., & Ishitani, O. (2018). Investigation of excited state, reductive quenching, and intramolecular electron transfer of Ru(II)–Re(I) supramolecular photocatalysts for CO_2 reduction using time-resolved IR measurements. Chemical Science, 9(11), 2961–2974. https://doi.org/10.1039/c7sc05338j
[194]. Sumner, E., Pižl, M., McQuaid, K. T., & Hartl, F. (2024). Nitrile Substituents at the Conjugated Dipyridophenazine Moiety as Infrared Redox Markers in Electrochemically Reduced Heteroleptic Ru(II) Polypyridyl Complexes. Inorganic Chemistry, 63(5), 2460–2469. https://doi.org/10.1021/acs.inorgchem.3c03484
[195]. Elgrishi, N., Rountree, K. J., McCarthy, B. D., Rountree, E. S., Eisenhart, T. T., & Dempsey, J. L. (2017). A Practical Beginner's Guide to Cyclic Voltammetry. Journal of Chemical Education, 95(2), 197–206. https://doi.org/10.1021/acs.jchemed.7b00361
[196]. Room temperature OTTLE cell: Spectroelectrochemistry reading. Spectroelectrochemistry. (2019, April 26). https://research.reading.ac.uk/spectroelectrochemistry/optically-transparent-thin-layer-electrochemical-cells/room-temperature-ottle-cell/
[197]. Kozuch, S., & Martin, J. M. (2012). "Turning Over" Definitions in Catalytic Cycles. ACS Catalysis, 2(12), 2787–2794. https://doi.org/10.1021/cs3005264
[198]. Serpone, N., Salinaro, A., Emeline, A., & Ryabchuk, V. (2000). Turnovers and photocatalysis. A mathematical description. Journal of Photochemistry and Photobiology A: Chemistry, 130(2–3), 83–94. https://doi.org/10.1016/s1010-6030(99)00217-8
[199]. Balzani, V. C., Paola Juris, Alberto. (2024). Photochemistry and Photophysics: Concepts, Research, Applications. Wiley-VCH, pp. 408.
[200]. Meena, B., Chandrasekharan Meenu, P., & G. Smirniotis, P. (2025). Unravelling the Role of Hydrogen Evolution Reaction Co-Catalysts in Photocatalytic Water Splitting: Mechanistic Insights and Material Strategies. Photocatalysis: Research and Potential, 2(1), 10005–10005. https://doi.org/10.70322/prp.2025.10005

CHAPTER 2

Incorporation of perylene and naphthalene like ligands into ruthenium complexes: Synthesis, photophysical properties and electrochemistry

Martyna Z. Bartusiak, Ross J. McGarry, Lazaros Varvarezos, Michael P. Brandon, Mary T. Pryce

Published Work Coordination Chemistry Reviews Volume 495, 15 November 2023, 215365

MB & RG contributed equally to this work

2.1 Abstract

Functionalisation of ruthenium complexes with rylene diimides, a class of organic molecules based on a naphthalene scaffold connected through a peri-substitution pattern and capped by electron withdrawing imide functional groups, has grown in interest in recent years. These complexes exhibit favourable chemical, photophysical and electrochemical properties that can be combined with straightforward synthetic methodologies. These highly conjugated molecular architectures have garnered interest in various research fields, as they can be coordinated to a wide range of metal moieties. Consequently, such assemblies can promote absorption of visible light and improve the efficacy of their respective compounds for use in various applications. This Review focusses on the current state of research and developments in the field of ruthenium naphthalene diimides (Ru-NDIs) and ruthenium perylene diimides (Ru-PDIs). It provides an overview of the photophysical and electrochemical properties, potential applications, and synthetic approaches for the core expansion of ruthenium naphthalene and perylene diimides.

Contribution:

The following aspects were completed by MB: Introduction, description of synthetic procedures and photophysical properties of ruthenium complexes incorporating naphthalene diimides, promising applications of NDIs and PDIs and conclusion section. Partial contribution to electrochemical discussion on naphthalene diimides. In addition, MB was responsible for drawing and representing all synthetic schemes and figures regarding all compounds mentioned in this review.

2.2 Introduction

Pioneering work by Vollmann and colleagues [1] in the 1930s paved the way for designing and synthesising unsubstituted rylene-based molecular architectures. Since then, rylene tetracarboxylic diimides (**RDIs**) have become an active research field. RDIs constitute a family of organic molecules that are characterised by the presence of two six-membered dicarboxylic electron-withdrawing imide functional groups fused to naphthalene units (see Fig. 2.1). More recently, RDI units have been covalently attached to metal centres such as ruthenium moieties, which have been employed to enhance the properties and applications of these assemblies [2, 3].

In recent years, incorporation of 1,4,5,8-naphthalenediimide (**NDI**) and 3,4,9,10-perylenediimide (**PDI**) building blocks into ruthenium (II) complexes has received considerable interest because of their facile functionalisation and tuneable photophysical properties. Symmetrical and asymmetrical NDIs and PDIs compounds can be synthesised through simple reactions using commercially available 1,4,5,8-naphthalenetetracarboxylic acid dianhydride (**NDA**) or 3,4,9,10-perylenetetracarboxylic acid dianhydride (**PDA**) through imidization with a primary amine [4]. Additionally, alternative approaches to modify NDIs and PDIs are via halogenation substitution reactions or axial ligation. The resulting products are photochemically stable conjugated compounds, with rigid planar structures and the nitrogen atoms can be replaced with a wide range of alkyl or aryl groups, resulting in the development of novel organic materials with tuneable optical, electronic and physical properties [5, 6].

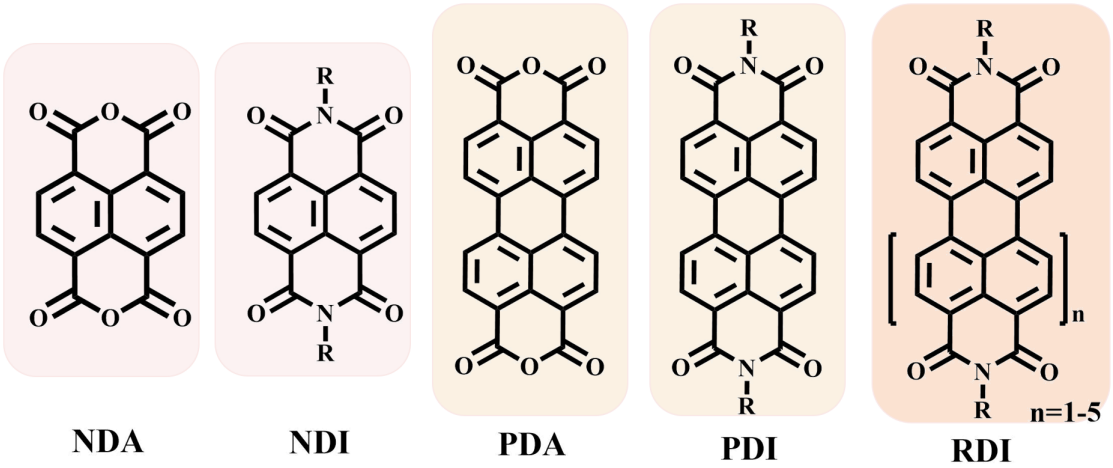


Figure 2.1 Molecular structure of rylene diimides.

Complexation of the NDI/PDI aromatic core with ruthenium (II) moieties enhances the optical and photophysical properties of the metal complexes in various ways: by providing a red-shift of the metal-to-ligand charge-transfer (MLCT) absorption band [7 – 9], broadening the absorbance in the visible region [10, 11] and generating long-lived excited states [12]. Importantly, a key goal from a synthetic standpoint is the design of molecular assemblies for effective light-induced charge separation. The formation of these states is a result of an electron transfer (ET) process that can be monitored by time resolved studies ranging from the nanosecond to the femtosecond timescales [13, 14]. Studying the electrochemical behaviour offers insights into electron donor and acceptor energy levels and the energetic barriers to electron transfer processes [9, 15], thus allowing for targeted design of various Ru-NDI/PDI complexes.

In recent years there is growing interest in the applications of NDI/PDIs complexes [16 – 20]. The aforementioned properties, render these molecular systems ideal candidates for use in a diverse range of fields, such as artificial light harvesting systems [9], DNA intercalation [21] and photodynamic therapy [2] (PDT). This review provides an overview of the development of the numerous synthetic strategies used by various research groups which can be employed to tune the applications potential of these rylene ruthenium compounds. Furthermore, the spectral and photophysical properties of the metal complexes are described alongside, their corresponding electrochemical behaviour. Finally, an overview of promising potential applications is outlined for this family of materials.

2.3 Design and synthesis of molecular structures.

Although, there are several pathways to modify NDI/PDIs, incorporation of ruthenium moieties into the NDI/PDI unit is broadly classified into three approaches: core expansion, imidization and axial coordination (Fig. 2.2). In core expansion, the system is directly attached to the naphthalene moieties. Imidization is employed to introduce various substituents at the imide position, whereas axial coordination involves metal coordination to the NDI/PDI units. The following section has been organised according to these three approaches.

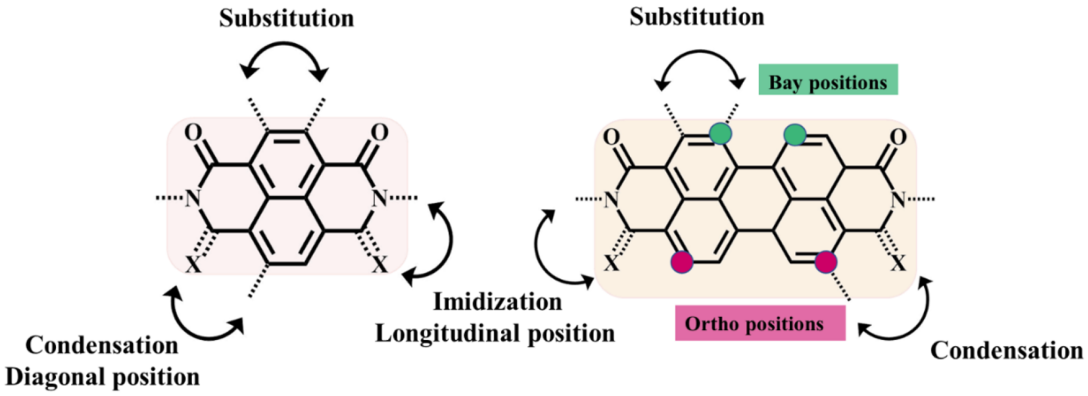
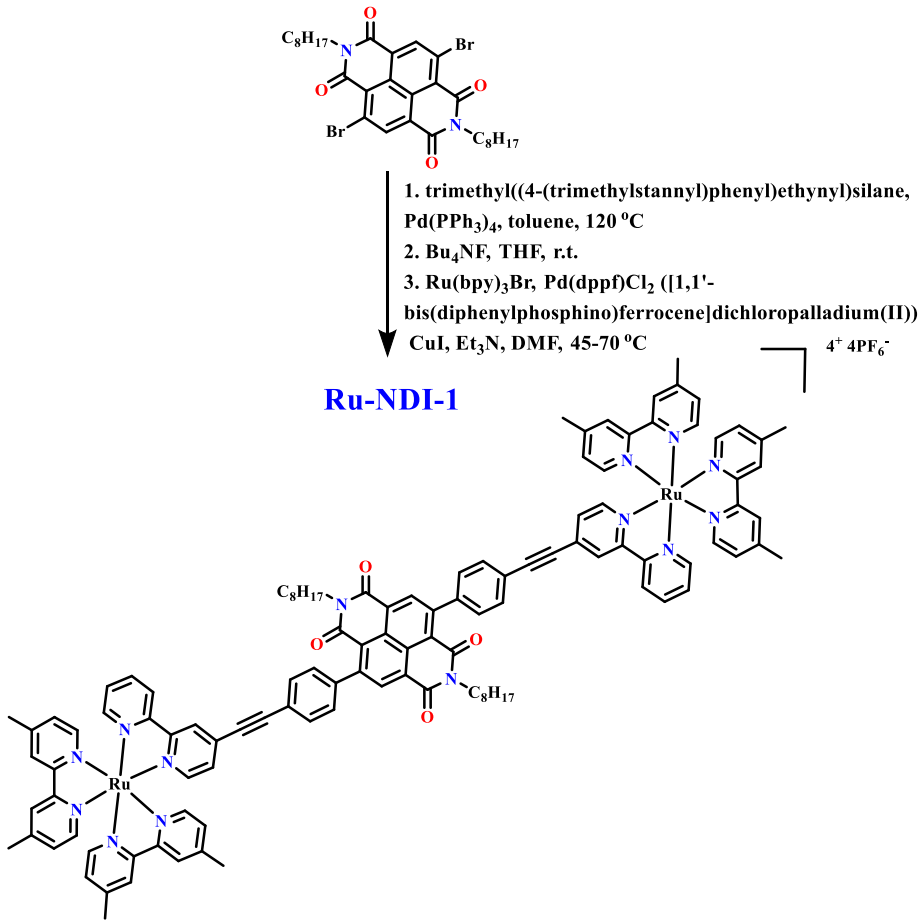


Figure 2.2 The general synthetic pathways to alter both NDI and PDI frameworks.

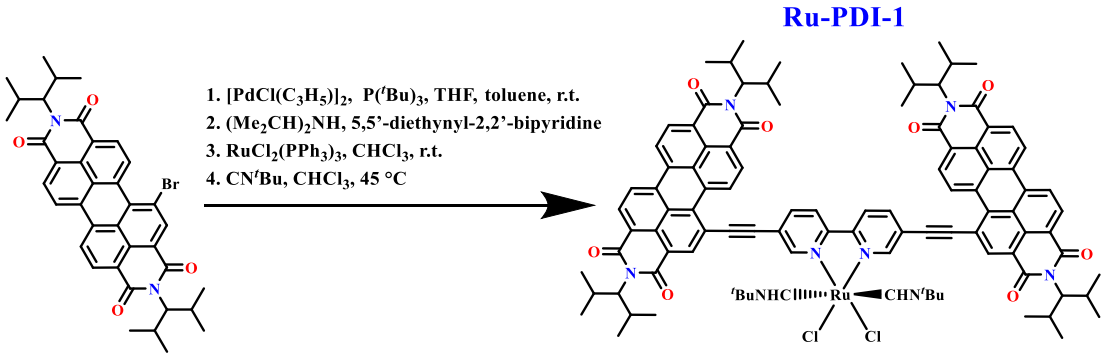
2.3.1 Core expansion of NDI/PDIs

Core expansion typically involves insertion of additional groups onto the naphthalene subunits of the NDI/PDIs molecules. This is usually initiated from the corresponding halogenated naphthalene dianhydride, which opens the core to various cross coupling or substitution reactions. This methodology was utilised by Chaignon et al. [22] to prepare a number of Ru-NDI complexes. The compound **Ru-NDI-1** was prepared by subjecting dibromo-NDI to a series of cross coupling reactions, resulting in the covalent attachment of the $[Ru(bpy)_3]^{2+}$ moiety through an ethynyl bridge (Scheme 2.1).

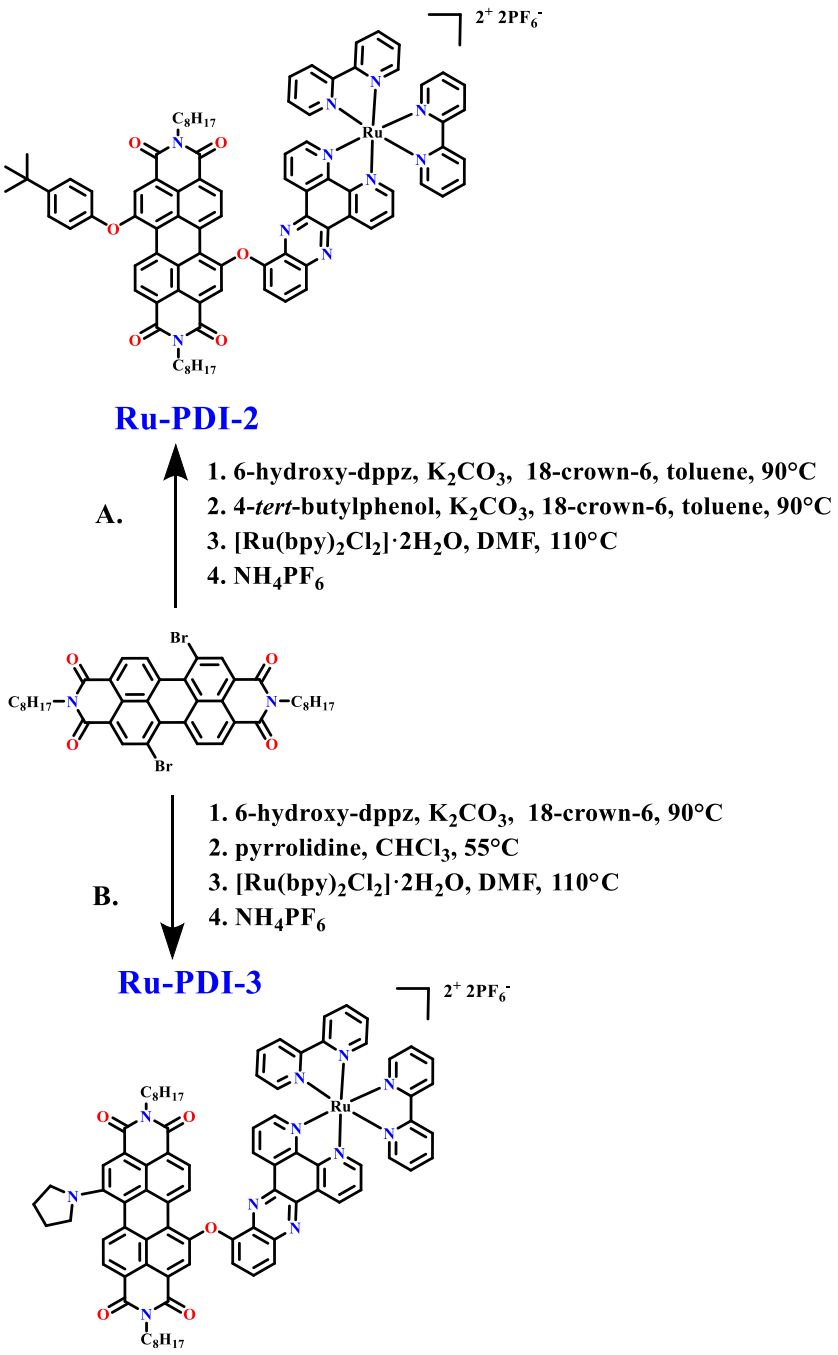


Scheme 2.1 Simplified synthetic scheme for **Ru-NDI-1** as carried out by Chaignon et al. [22].

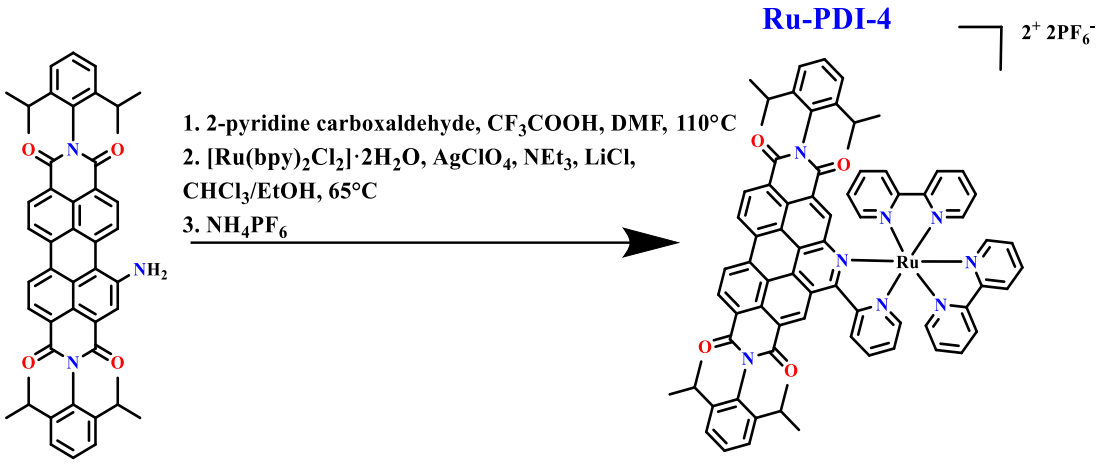
A similar approach, using an analogous ethynyl linkage, can also be applied to PDIs, as demonstrated by Gunderson et al. [12]. In their work, they synthesised a symmetrical ruthenium-perylene complex via Sonogashira coupling at the bay position of PDI, referred to as **Ru-PDI-1** (Scheme 2.2). Dubey et al. [23] showed that the bromination of NDI/PDIs is not exclusively used for cross coupling (Scheme 2.3). Instead, they used simple ether linkages to couple a dipyridophenazine (dppz) ruthenium complex to a perylene moiety, **Ru-PDI-2** (Scheme 2.3A). Furthermore, using the same ether linkages, solubility was enhanced by the addition of 2,4-di-*tert*-butylphenol. An alternative approach to increase the solubility was possible by incorporating pyrrolidine, and reacting with bromine, as in **Ru-PDI-3** (Scheme 2.3B). A different strategy for core expansion was applied by Schulze et al. [7]. Instead of halogenation, they attached an amino group to a PDI core and further reacted this with 2-pyridinecarboxaldehyde to form an extended pseudo-bipyridine analogue. Ruthenium bipyridine was then coordinated to form the final product, **Ru-PDI-4** (Scheme 2.4).



Scheme 2.2 Simplified synthetic scheme for **Ru-PDI-1**, as carried out by Gunderson et al. [12].



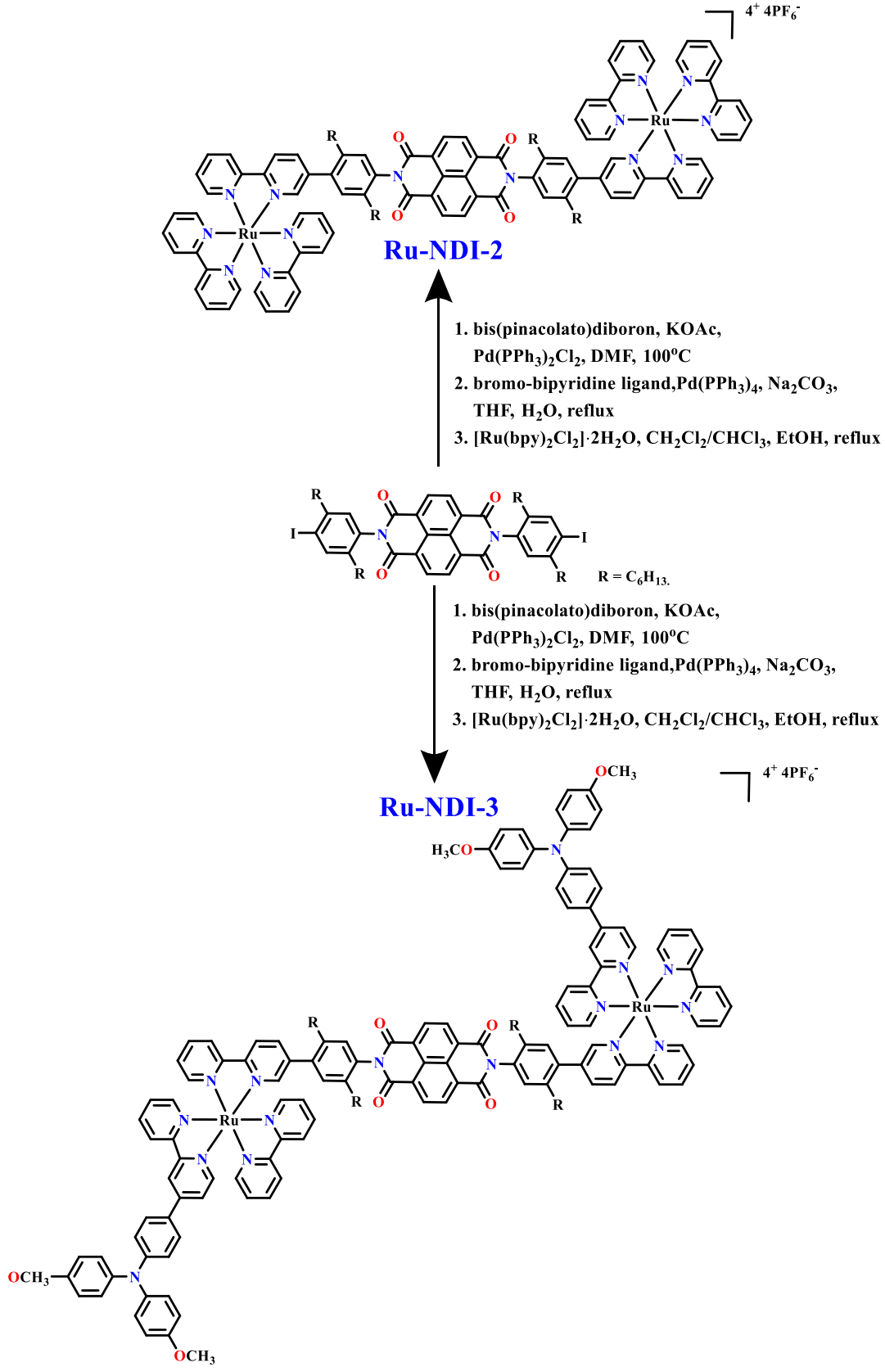
Scheme 2.3 Simplified synthetic scheme for **Ru-PDI-2**(**A**) and **Ru-PDI-3(B**), as carried out by Dubey et al. [23].



Scheme 2.4 Simplified synthetic scheme for **Ru-PDI-4**, as reported by Schulze et al. [7].

2.3.2 Imidization condensation

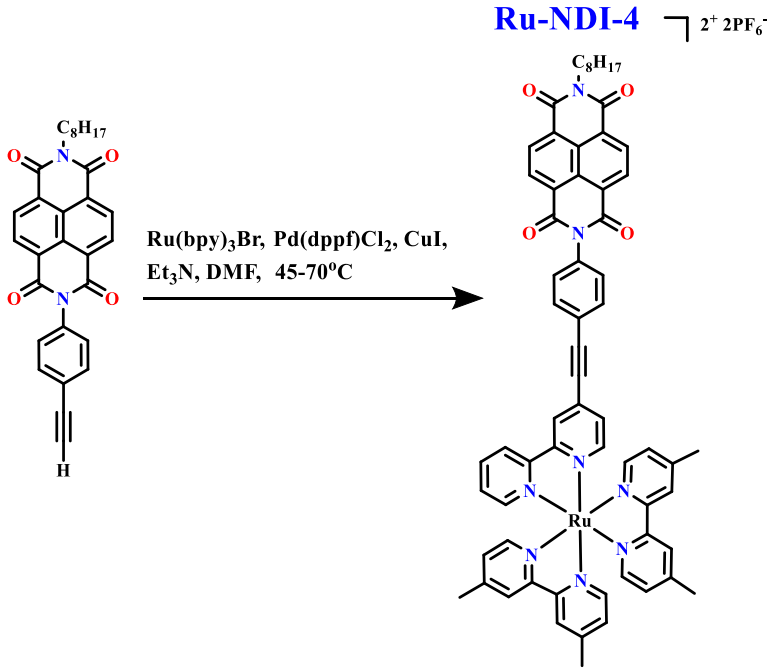
Imidization typically involves the reaction of the dianhydride form of NDI/PDI with primary amines. Skaisgirski et al. [3], used this method to synthesise a series of bis-(ruthenium)-NDI complexes. In order to connect the NDI and ruthenium moieties and form the triad **Ru-NDI-2**, benzene rings were employed in the axial position (Scheme 2.5). The structure was further modified by attaching a substituted triphenylamine unit, to the 5 positions on the bipyridine in both of the ruthenium centres, to form a structurally analogous pentad, **Ru-NDI-3**.



Scheme 2.5 Simplified synthetic scheme for **Ru-NDI-2** and **Ru-NDI-3**, as reported by Skaisgirski et al. [3], where R = C_6H_{13}.

Formation of mono-ruthenium-NDI/PDI complexes can be carried out in a similar vein to that described above, with one major hurdle, the undesirable formation of di-

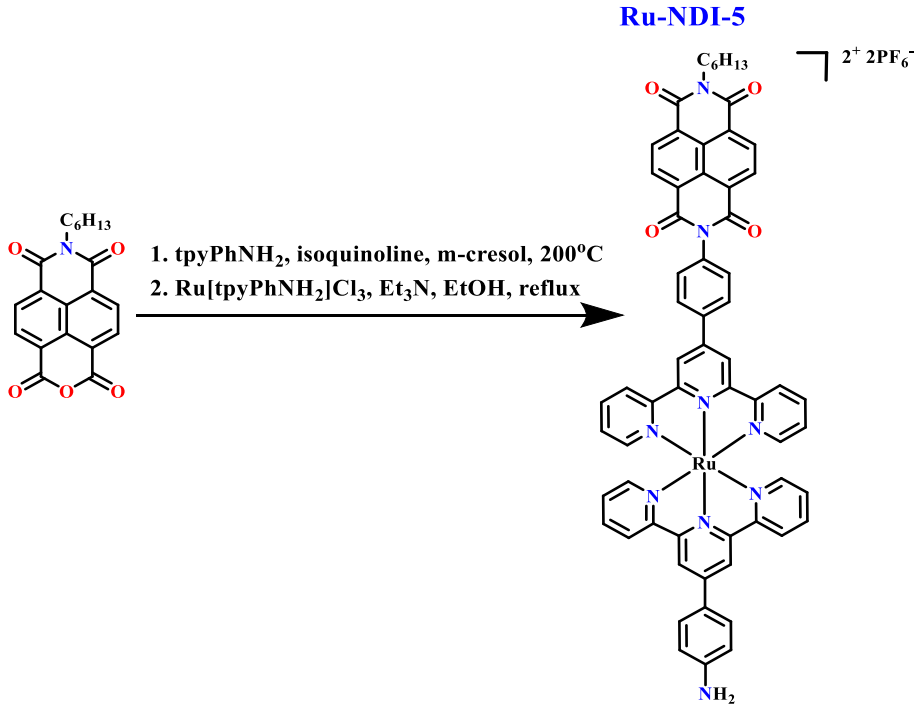
substituted by-products. In such cases, it is common to first react NDA/PDA with a primary amine to block reactions occurring at one of the anhydride positions. This reaction is best illustrated by the reaction of PDA with octylamine [24]. In this case, the octylamine is a bystander in all subsequent reactions, thus preventing the formation of di-substituted by-products. However, the drawback of this, is that the formation of the mono-imide deactivates the second anhydride group, thereby making subsequent reactions more difficult, and potentially reducing yields. On the upside, the addition of octylamine (or similar groups) generally improves the solubility in common organic solvents.



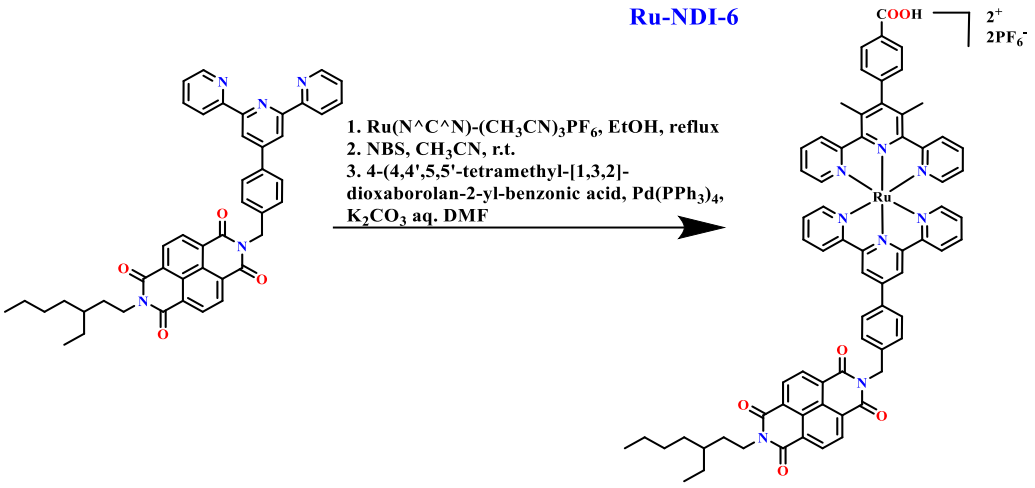
Scheme 2.6 Simplified synthetic scheme for **Ru-NDI-4**, as performed by Chaignon et al. [22].

This approach, using octylamine based NDA precursors, was adopted by Chaignon et al. [22] to synthesise the mono-ruthenium compound, **Ru-NDI-4**, through an imidization condensation. It was possible to synthesise the ruthenium-NDI complex by the introduction of an ethynyl-benzene linker, using Sonogashira-coupling (Scheme 2.6). Frath et al. [15] synthesised the asymmetrical **Ru-NDI-5** complex employing a donor-acceptor strategies (Scheme 2.7). The use of hexylamine, instead of octylamine, was used to both prevent formation of di-substituted by-products and enhance solubility. A structurally comparable complex **Ru-NDI-6** was synthesised by Ji et al. [25], however, with the addition of a carboxylic acid group on the ruthenium for surface functionalisation (Scheme 2.8). Another example of this type of systems was reported by Johansson and co-workers [26]. The latter group have also developed a similar series of photosensitiser-

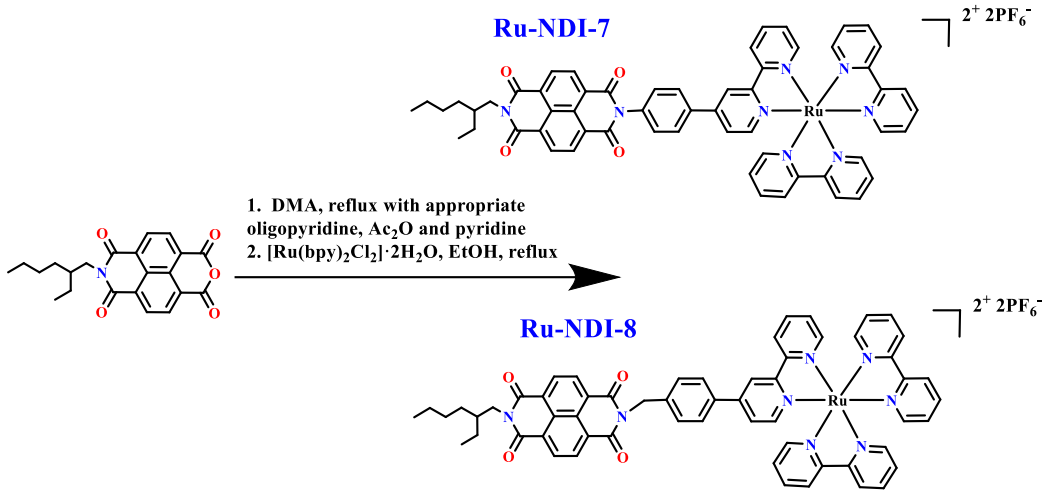
electron acceptor complexes [26], **Ru-NDI-7** and **Ru-NDI-8**, with differing linkers in the axial position, in order to investigate charge-transfer processes (Scheme 2.9). In a subsequent study, Johansson, and co-workers [27] prepared a set of asymmetrically substituted ruthenium (II)-NDI derivatives, with the addition of various donor units such bpyAla, bpyTyr and dpaTyr (bis 2,6-(dipicolylaminomethyl)tyrosine ethyl ester) to the ruthenium chromophore, **Ru-NDI-9/10** (Scheme 2.10) and **Ru-NDI-11** (Scheme 2.11). This work was then extended by Borgstrom et al. [8], who coordinated manganese into the molecular framework in order to further enhance the properties of these compounds, **Ru-NDI-12** (Scheme 2.11). Baron et al. [28] used click chemistry to add a triazole bridge between the ruthenium and the NDI units, leading to the synthesis of **Ru-NDI-13** (Scheme 2.12). An alternative linker was employed by W. Dixon et al. [21], to bridge a ruthenium bipyridine complex to NDI, where amide bonds were used to give **Ru-NDI-14**. This Ru-complex was synthesised by reacting 2,2′-bipyridine-5-carboxylic acid using BOP (benzotriazole-1-yloxy-tris (dimethylamino)phosphonium hexafluorophosphate) as a coupling agent with N-3-aminopropyl-N′-3-dimethylaminopropyl-NDI (Scheme 2.13). In order to prevent formation of bis-products, 1,3-diaminopropane was employed.



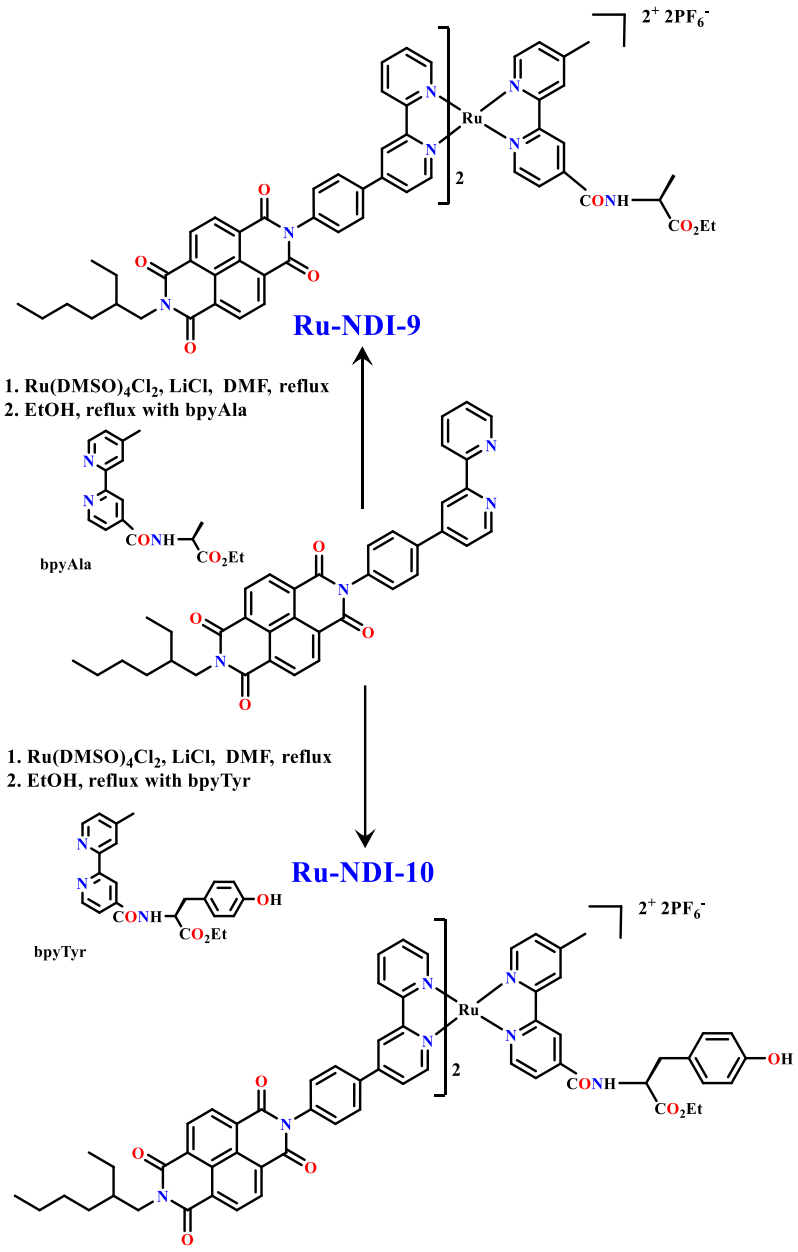
Scheme 2.7 Simplified synthetic scheme for **Ru-NDI-5**, as performed by Frath et al. [15].



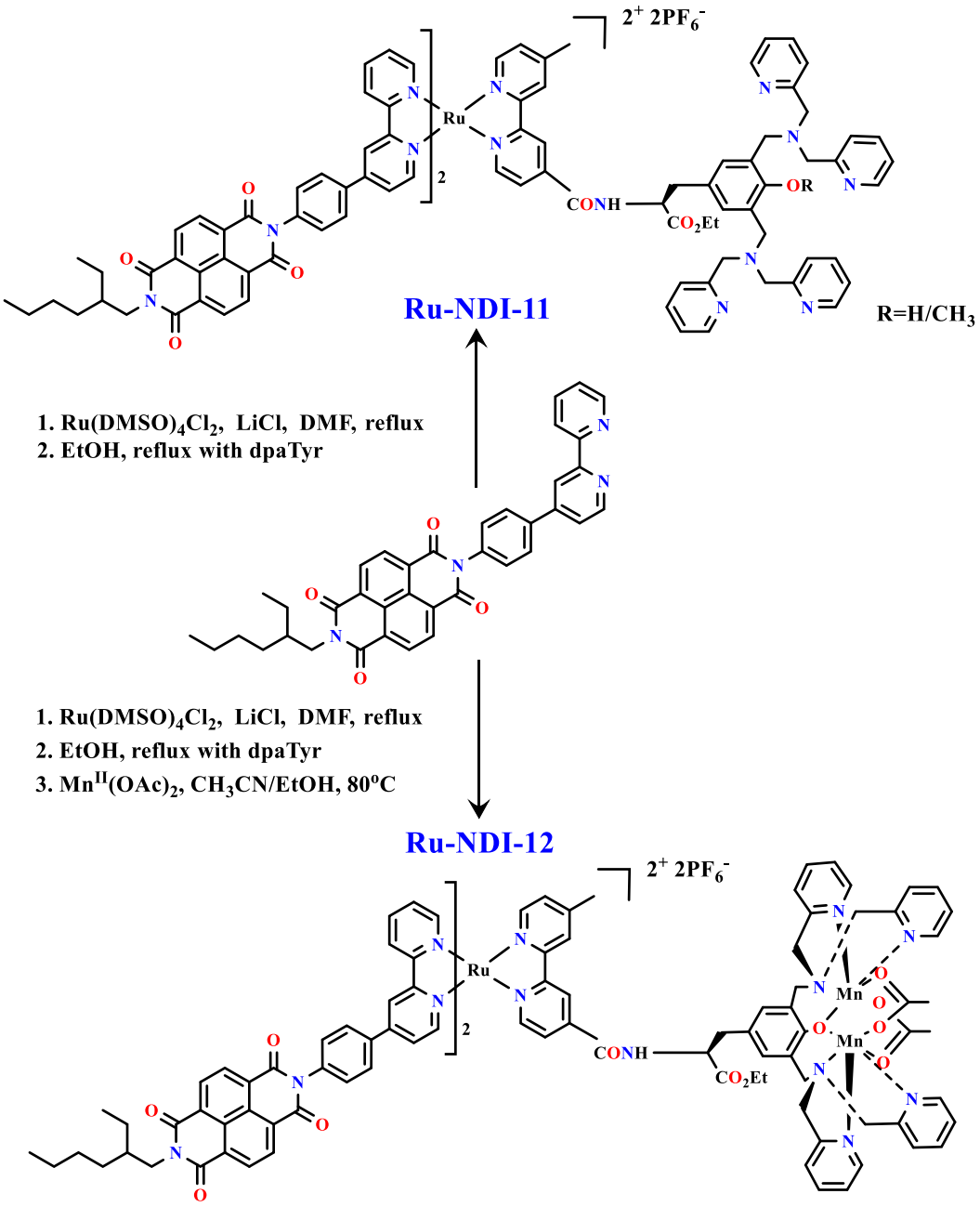
Scheme 2.8 Simplified synthetic scheme for **Ru-NDI-6**, as performed by Ji et al. [25].



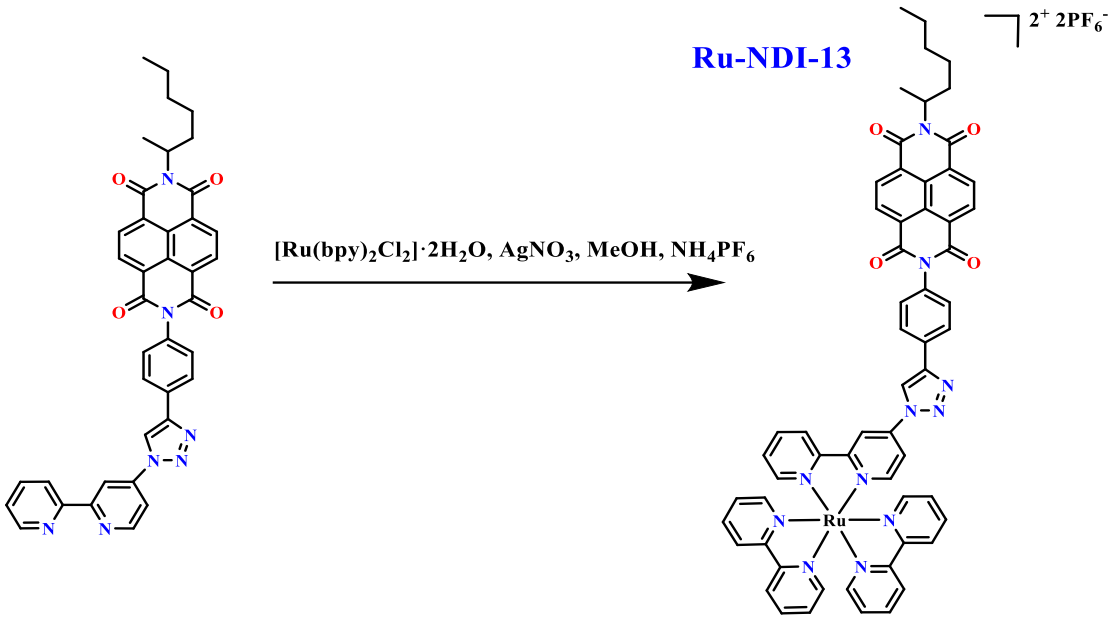
Scheme 2.9 Simplified synthetic scheme for **Ru-NDI-7** and **Ru-NDI-8** as performed by Johansson et al. [26].



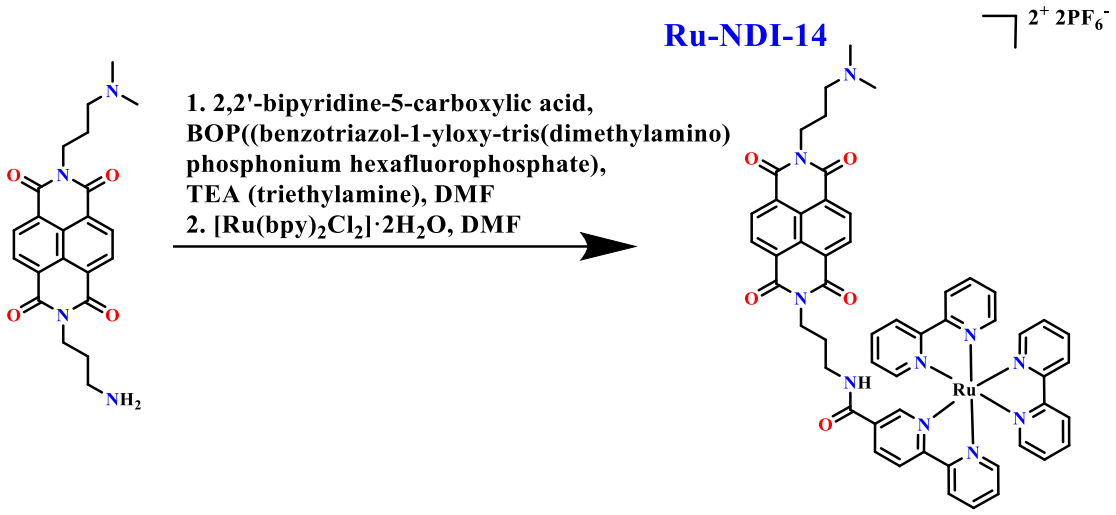
Scheme 2.10 Simplified synthetic scheme for **Ru-NDI-9** and **Ru-NDI-10** as performed by Johansson et al. [27].



Scheme 2.11 Simplified synthetic scheme for **Ru-NDI-11**, (R = H, CH_3) , as reported by Johansson et al. [27] and **Ru-NDI-12**, as reported by Borgstrom et al. [8].

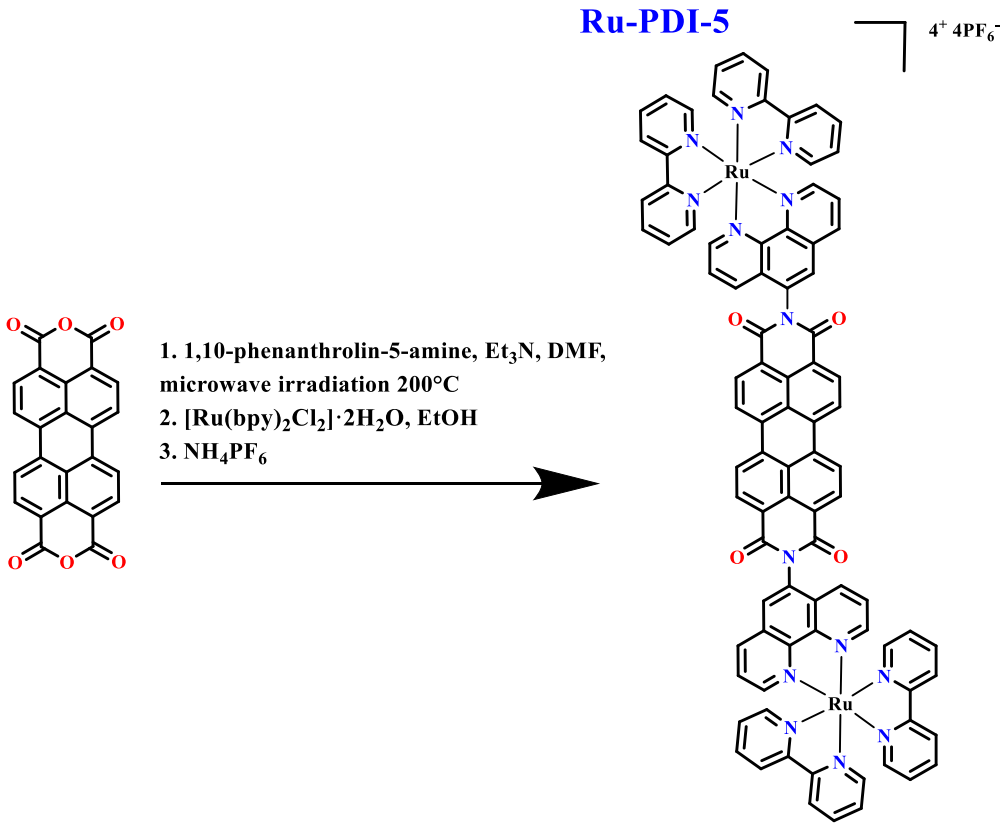


Scheme 2.12 Simplified synthetic scheme for **Ru-NDI-13**, as reported by Baron et al. [28].

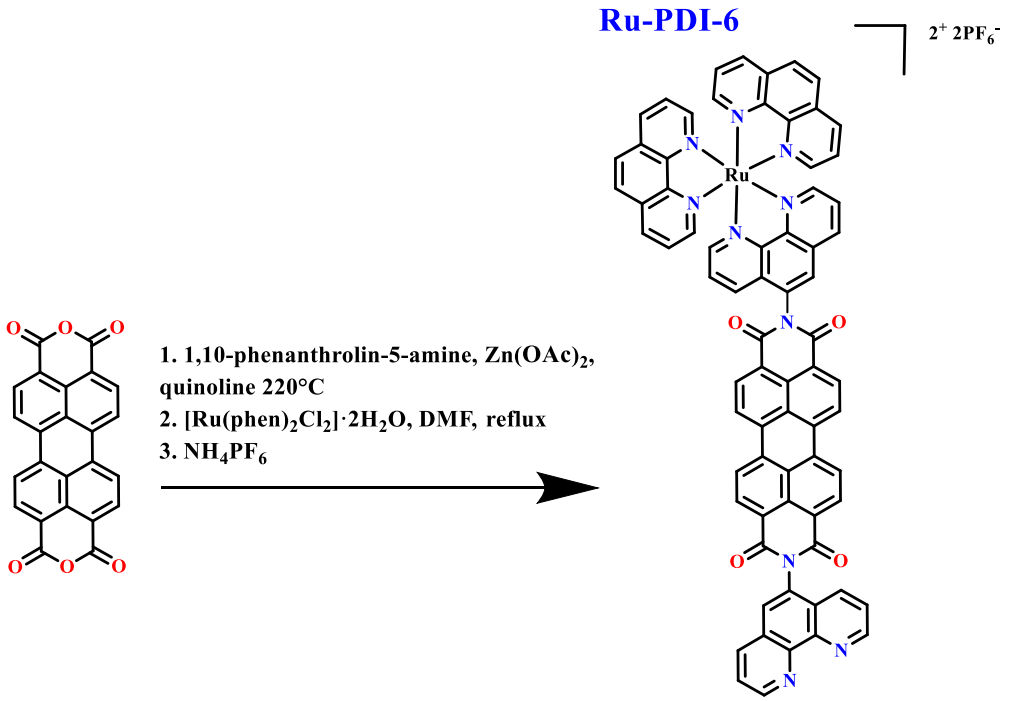


Scheme 2.13 Simplified synthetic scheme for **Ru-NDI-14**, as reported by W. Dixon et al. [21].

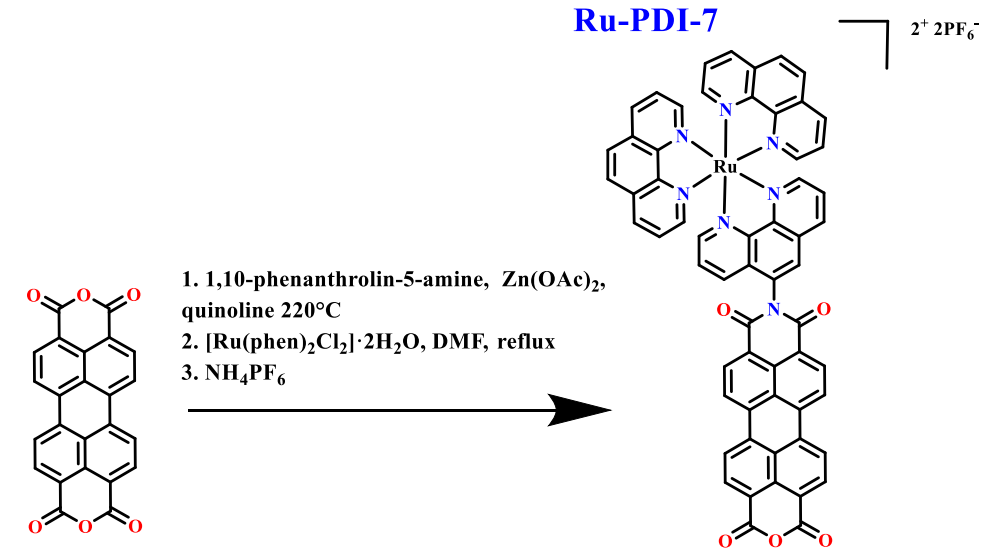
As with NDIs, PDIs can be modified through imidization condensation reactions, using similar analogous synthetic strategies. Nastasi et al. [29], used microwave irradiation and formed a bis-phenanthroline perylene complex. The resulting compound was subsequently reacted with two equivalents of ruthenium bipyridine to yield the final product, **Ru-PDI-5** (Scheme 2.14). A similar product, **Ru-PDI-6**, was presented by Santos et al. [30]. In their work, a bis-phenanthroline ligand was formed, to which a single ruthenium phenanthroline moiety was attached (Scheme 2.15). An extension of this work was then performed by Maia et al. [2] in which they formed the mono-imide ruthenium-perylene complex, with reduced yields (Scheme 2.16). Liu et al. [9] made a structurally related compound, **Ru-PDI-8**, however the perylene core was modified by the addition of 4-methylphenol. Furthermore, the use of thiocyanate instead of a bipyridine unit, was employed to enhance their function as a solar cell material (Scheme 2.17).



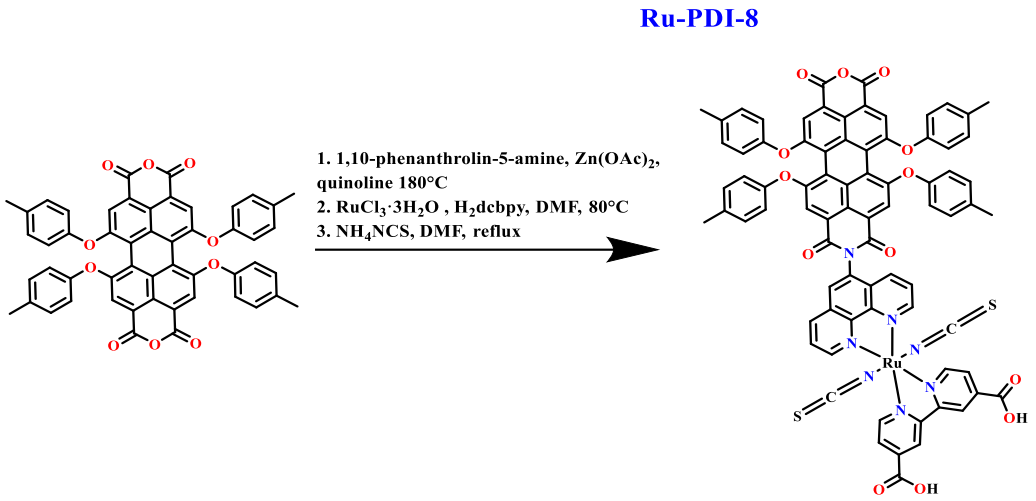
Scheme 2.14 Simplified synthetic scheme for **Ru-PDI-5**, as reported by Nastasi et al. [29].



Scheme 2.15 Simplified synthetic scheme for **Ru-PDI-6**, as reported by Santos et al. [30].

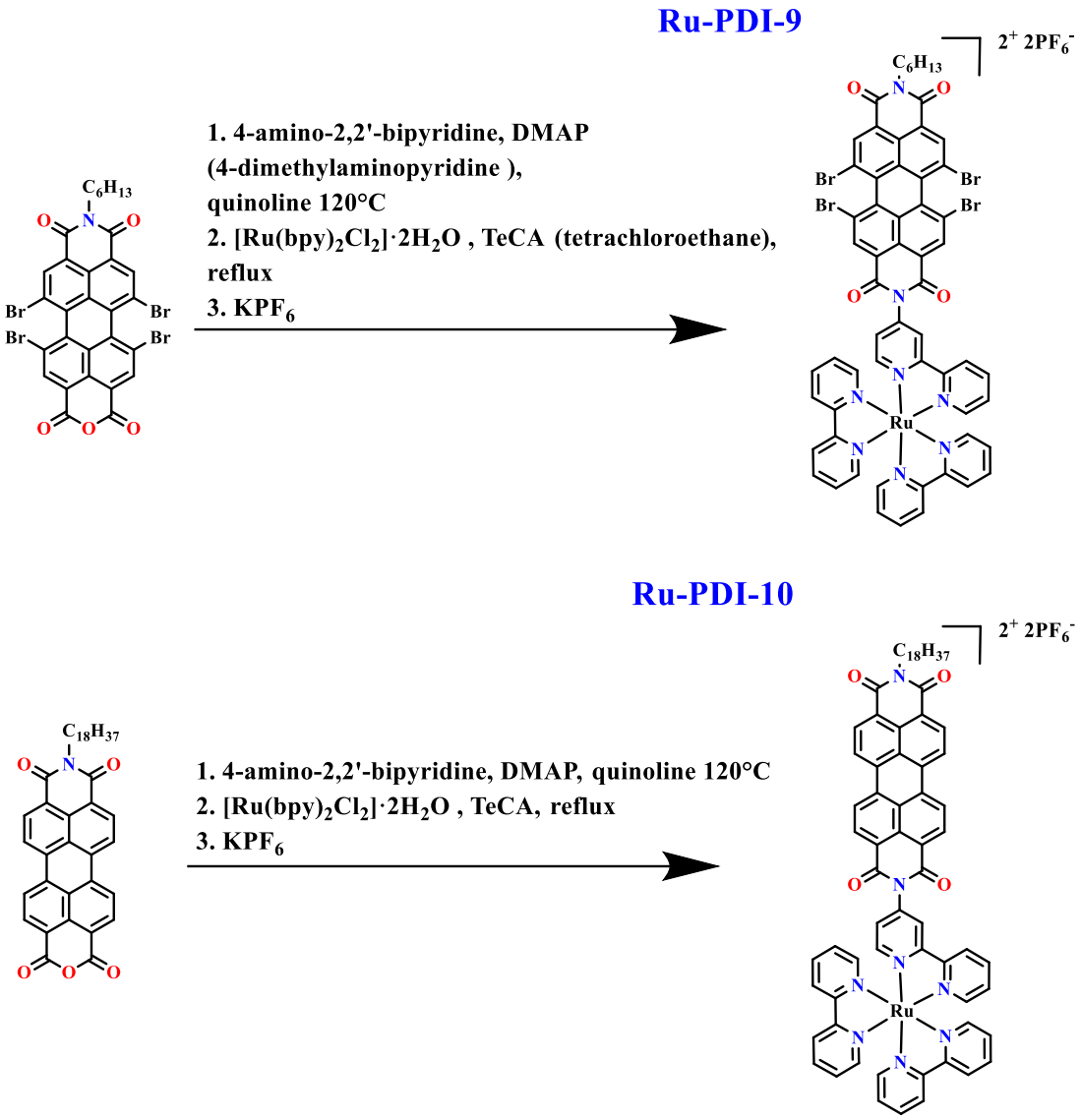


Scheme 2.16 Simplified synthetic scheme for **Ru-PDI-7**, as reported by Maia et al.[2].

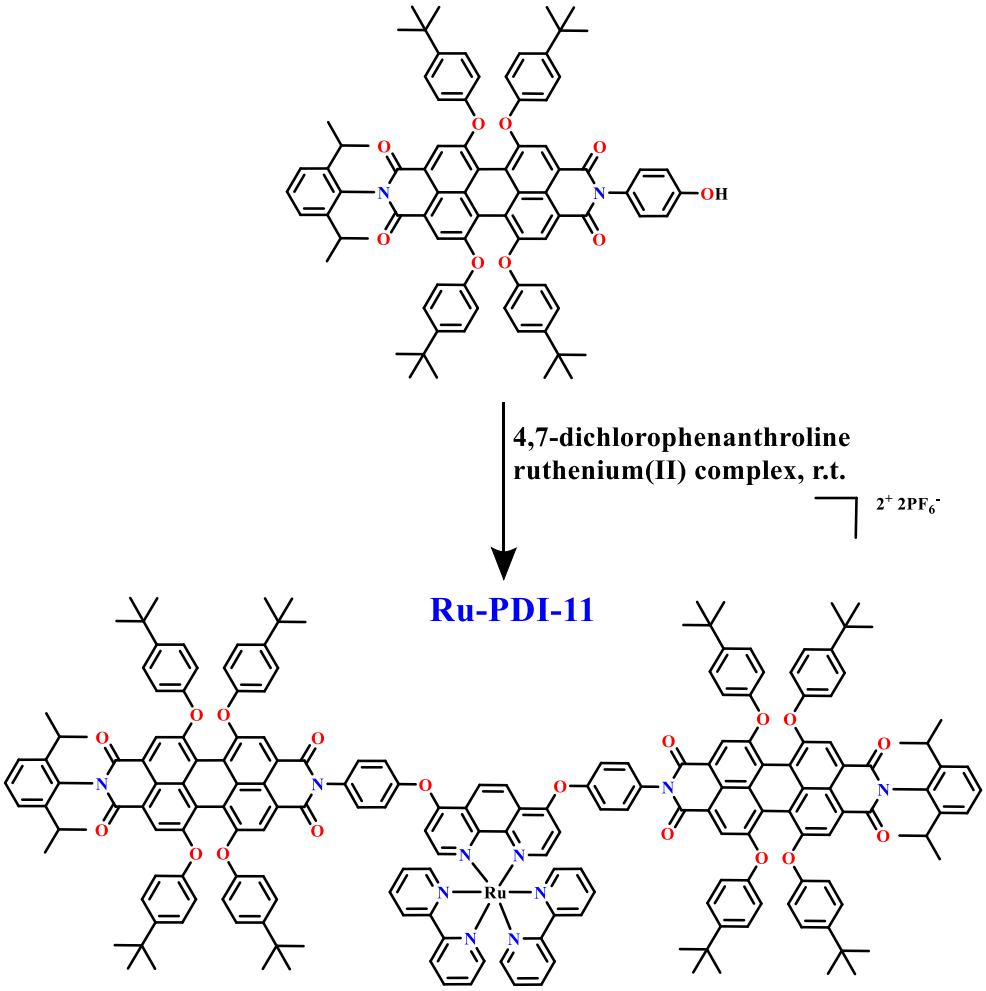


Scheme 2.17 Simplified synthetic scheme for **Ru-PDI-8**, as reported by Liu et al. [9].

Kodama et al. [31] designed a pair of asymmetrical ruthenium-perylene compounds (Scheme 2.18). The first compound, **Ru-PDI-9**, involved the functionalisation of tetra-bromo-perylene with amino-bipyridine. The use of hexylamine in the second imide position was used to prevent formation of bis-products and also to increase solubility. For the second compound **Ru-PDI-10**, the solubility was further enhanced by the use of octadecylamine, instead of hexylamine. In this case, however, they used a non-halogenated perylene. Aksakal et al. [32] employed a related strategy to enhance the solubility of their ruthenium-bis (PDI) assembly. This was achieved through the substitution of the bay positions of the perylene moiety, with 4-*tert*-butylphenol, which had the additional benefit of reducing the tendency of perylene to form aggregates. The resulting PDI scaffold was then attached to a phenanthroline unit using an ester linkage to form the final ruthenium-PDI compound, **Ru-PDI-11** (Scheme 2.19).



Scheme 2.18 Simplified synthetic scheme for **Ru-PDI-9** and **Ru-PDI-10**, as reported by Kodama et al. [31].

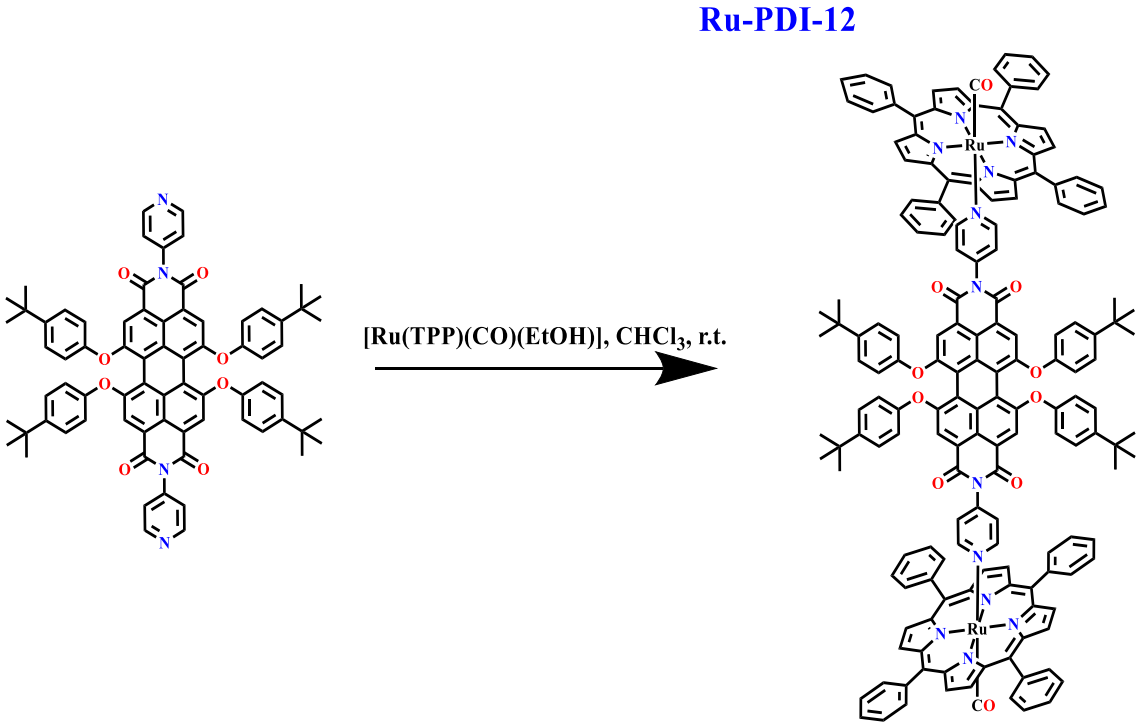


Scheme 2.19 Simplified synthetic scheme for **Ru-PDI-11**, as reported by Aksakal et al. [32].

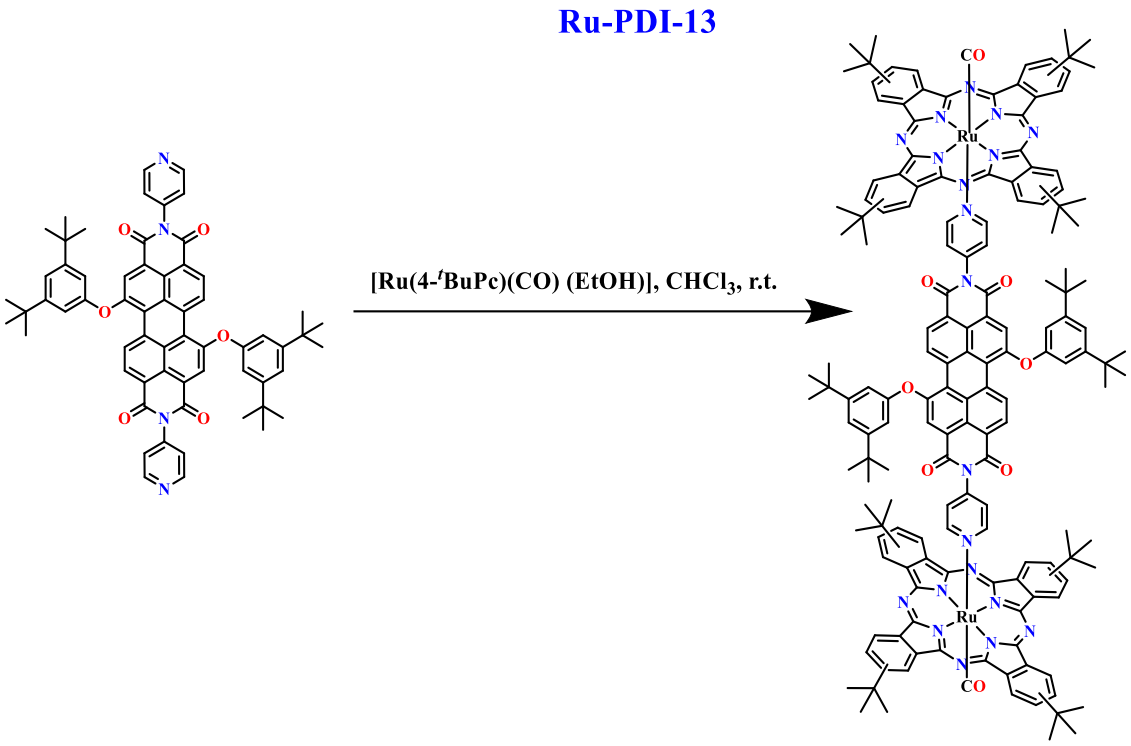
2.3.3 Axial ligation

Axial ligation, coordinating a complex along the imide position, is also an effective synthetic strategy that can produce interesting supramolecular assemblies with unique photophysical properties, such as long-lived triplet states and wavelength dependant lifetimes. Using this approach, Prodi et al. [33] synthesised a porphyrin-perylene complex, **Ru-PDI-12** (Scheme 2.20), by using amino-pyridine as a bridge between the perylene and ruthenium-porphyrin, Ru(CO)TPP, forming a coordination assembly. Rodríguez-Morgade et al. [34], demonstrated that this method can be applied to more than porphyrins. Utilising a phthalocyanine, Ru(CO)Pc, they synthesised a bis(ruthenium)-perylene supramolecular assembly, **Ru-PDI-13** in a similar manner. The presence of *tert*-butyl substituents, on both the phthalocyanine and the PDI units,

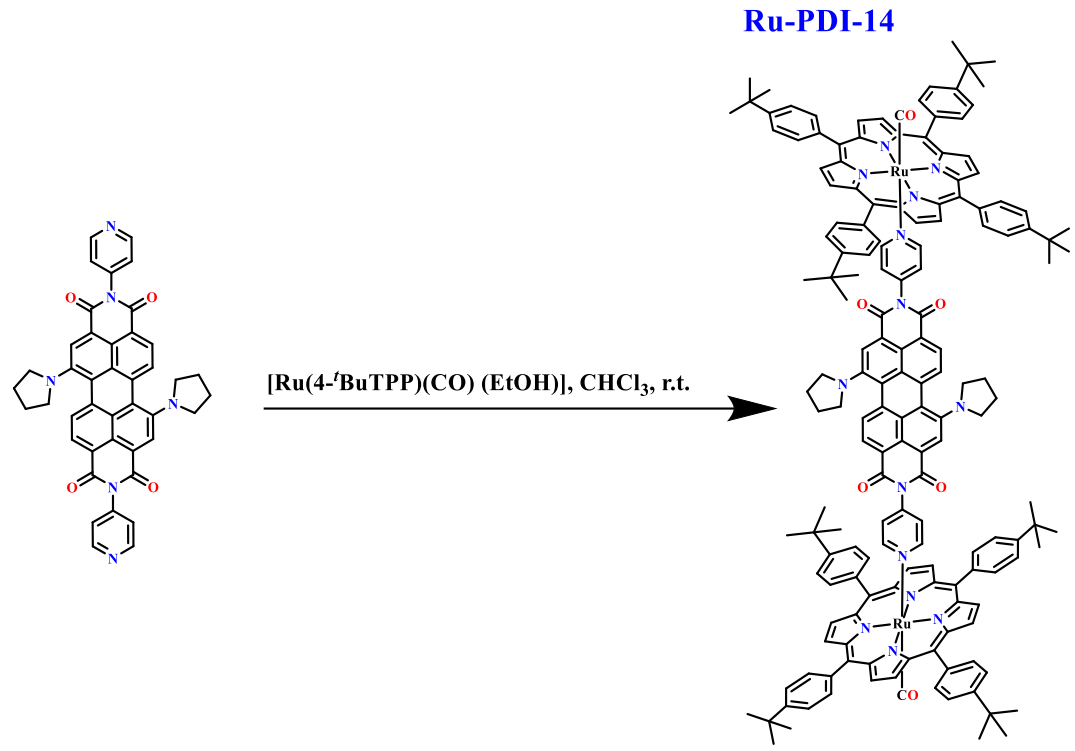
enhanced solubility in common organic solvents and reduced aggregation (Scheme 21). The same methodology was applied by Amati et al. [35], employing Ru(CO)^{t}BuTPP to help minimise aggregation, forming a ruthenium-porphyrin assembly, **Ru-PDI-14**. They also used pyrrolidine groups in the bay position (Scheme 2.22), which had the added benefit of increasing the HOMO-LUMO band gap of the system, which modified its photophysical properties.



Scheme 2.20 Simplified synthetic scheme for **Ru-PDI-12**, as reported by Prodi et al. [33].



Scheme 2.21 Simplified synthetic scheme for **Ru-PDI-13**, as reported by Rodríguez-Morgade et al. [34].



Scheme 2.22 Simplified synthetic scheme for **Ru-PDI-14**, as reported by Amati et al. [35].

2.4 Photophysical properties of Ru(II)-NDIs and Ru(II)-PDIs.

As this review focusses on ruthenium moieties covalently attached to either NDI/PDI, the photophysical properties of $[Ru(bpy)_3]^{2+}$ complex will briefly be discussed. $[Ru(bpy)_3]Cl_2$ features pseudo-O_h symmetry, with the low oxidation state of ruthenium stabilised by the π-acceptor ligand 2,2'-bipyridine (bpy), which results in a $(t_{2g})^6$ low-spin configuration [36] (Fig. 2.3). The UV-vis absorption spectrum is characterised by a MLCT absorption feature, at 452 nm, (extinction coefficient of 13,000 $M^{-1}cm^{-1}$) [37], which gives rise to the distinct orange colour. Additional absorption bands observed at 350 nm, are attributed to weak d-d metal-centred transitions. In addition, the feature observed at 285 nm, corresponds to ligand centered $\pi \rightarrow \pi^*$ transitions [36]. The complex is luminescent and features a broad emission band with a Gaussian profile, centred at 615 nm, which is assigned to ^{3}MLCT based emission [37]. In nitrogen purged water, the triplet quantum yield is 0.042 [36] for $[Ru(bpy)_3]Cl_2$. This triplet emission quantum yield increases to 0.059 in acetonitrile [37]. Upon light absorption, the S_1 state is populated, (assigned to singlet charge transfer state from the ruthenium centre to bipyridine ligand [36, 38]) and within 200 fs, the complex undergoes ultrafast conversion to a long-lived triplet excited state [36], with a lifetime of *ca*. 890 ns in acetonitrile and 720 ns in ethanol [37]. This T_1 excited state returns to the ground state either by emission or non-radiative relaxation processes.

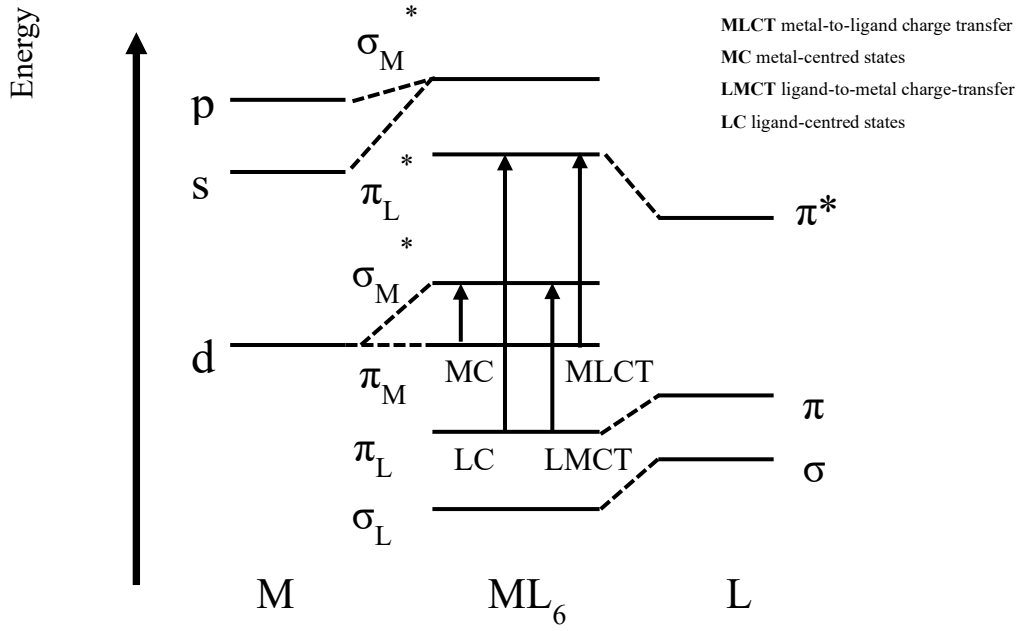


Figure 2.3 The energy level diagram for a typical octahedral complex [36], such as $[Ru(bpy)_3]^{2+}$.

Ruthenium polypyridine compounds are extensively studied owing to chemical stability and long-lived excited states, facilitating a broad range of applications. Modification of the prototypical $[Ru(bpy)_3]^{2+}$ complex allows for tailoring of the properties for the desired application [39 – 46]. Replacing a bipyridine ligand with other organic ligands modifies the photophysical properties of the ruthenium complex and typically leads to lowering of the MLCT band gap or introducing intra-ligand/ligand-metal transitions. Some representative cases are summarised below in Table 2.1.

Table 2.1 A summarised table of the photophysical properties of a variety of ruthenium polypyridyl complexes, where **a** = bright $^3MLCT_{phen}$ and **b** = dark $^3MLCT_{phz}$, **bpy** = 2,2'-bipyridine, **terpy** = 2,2′:6′,2″-terpyridine, **phen** = 1,10-phenanthroline, dppz = dipyrido[3,2-a:2',3'-c]phenazine, **mphen** = (2-methyl-1,10'-phenanthroline), **bqp** = 2,6-bis(8'-quinolinyl)pyridine.

Compound Name	^{1}MLCT	^{3}MLCT	MC	Solvent
$[Ru(bpy)_3Cl_2]$	< 200 fs	1.1 μs	–	MeCN[37]
$[Ru(terpy)_3Cl_2]$	<200 fs	250 ps	–	MeCN[47]
	<200 fs	970 ns[a]	–	MeCN[48]
$[Ru(phen)_2(dppz)Cl_2]$	<200 fs	5 ps[a] / 250 ps[b]	–	H_2O[49]
$[Ru(mphen)_3]^{2+}$	<200 fs	4 ps	422 ps	MeCN[50]
$[Ru(bqp)_2]^{2+}$	< 200 fs	3.0 μs	–	MeOH-EtOH (1:4)[51]

The photophysics of ruthenium assemblies such as those described in this review is frequently studied using transient absorption spectroscopy. Pump-probe transient absorption spectroscopy is an extension of the flash photolysis that enables the monitoring of transient species which are generated following excitation of the parent

complex [52, 53]. A “pump” pulse is used to excite the complex resulting in the population of electronic excited state(s). This is followed by a time-delayed “probe” pulse, which is used to interrogate the evolution of these excited state(s). More specifically, the temporal evolution of the light-induced excitation is monitored by measuring the variation in the intensity of the probe pulse. In the case of nanosecond transient absorption, a Xe arc lamp typically serves as the probe pulse and facilitates monitoring of excited states on the ns-ms timescale.

With the progress in laser technology [54 – 56], ultrashort laser pulses in the visible to UV spectral region have become routinely available serving as both the pump and probe pulses in the transient absorption spectroscopy. Alternatively, CaF_2, Al_2O_3, or YAG crystals can be used to generate a broadband white-light continuum serving as the probe pulse, thus offering the advantage to probe the sample at a broad range of wavelengths. The difference absorption (ΔA) spectrum is measured by recording the transmitted intensity of the probe beam with and without the pump, for different pump-probe delays. The temporal resolution of the system is defined by the cross-correlation function between the pump and the probe beams in the sample.

Both NDIs and PDIs exhibit good thermal and photochemical stability. NDIs are typically colourless compounds with strong absorption bands at approximately 380, 360, and 340 nm arising from $\pi \rightarrow \pi^*$ transitions. In comparison to PDIs, NDIs only absorb UV irradiation below 400 nm due to decreased conjugation. In contrast to NDIs, PDIs are deep red in colour, with strong absorptions between 450 to 530 nm and signature transitions at ~ 490 and ~ 525 nm, corresponding to $\pi \rightarrow \pi^*$ transitions. PDI is emissive with λ_{max} at 530 nm (CH_2Cl_2) and a high fluorescence quantum yield ($\Phi_{fl} = 0.99$). The lifetimes of these dyes are typically in the order of a few nanoseconds [57, 58]. Both molecules exhibit aromatic π-stacking and van der Waals interactions [5, 59, 60].

Both NDI and PDI are electron deficient compounds [5, 11, 61 – 64], due to the presence of the diimide withdrawing groups. Consequently, when coupled with electron-rich compounds such as ruthenium complexes, they form “donor-acceptor” systems [65]. The formation of such assemblies leads to photophysical properties differing from that of both parents. Several characteristic examples of both Ru(II)-NDI and Ru(II)-PDI are presented below. By judicious choice of ligand around the Ru (II) coordination sphere, the photophysical behaviour of the complex can be modulated. In the following section the absorption and emission spectra (where applicable) are described, together with the

quantum yields and time-resolved spectroscopic measurements, ranging from the femtosecond to the microsecond timescale, which provides a broad overview of the various excited states that can be populated.

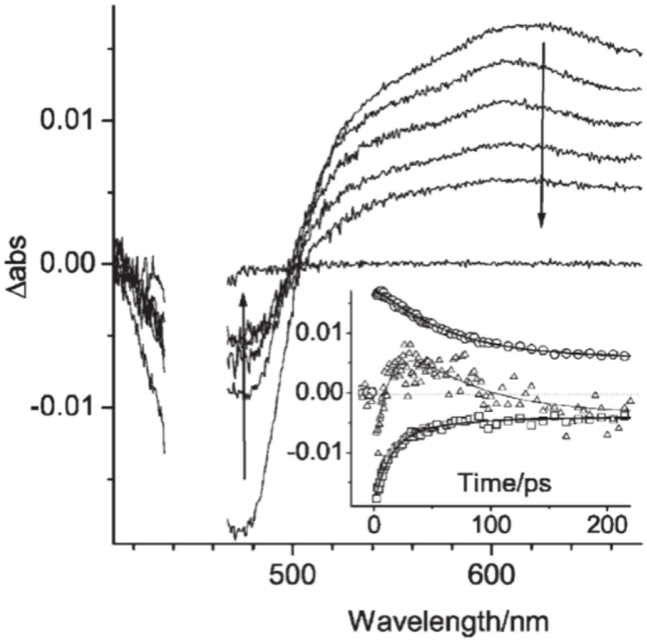


Figure 2.4 The transient absorption spectra of **Ru-NDI-1** at 1, 25, 50, 100 and 250 ps after excitation in CH_3CN. Taken with permission from Chaignon et al. [22].

Chaignon et al. [22] reported that the UV-vis absorption spectra of the ruthenium complexes, **Ru-NDI-1** and **Ru-NDI-4** exhibited two distinct components, arising from the ruthenium (II) metal centre and the NDI unit. The MLCT band of the Ru-complex was observed at 450 nm, whereas the NDI absorption was centred around 400 nm. In the emission spectrum, a broad band was observed at 666 nm in acetonitrile. The UV-vis spectral features of **Ru-NDI-2** (the Ru centre connected to the NDI core via the imide position) were reported to be broadly similar to that of the **Ru-NDI-1** (Table 2.2). These structural differences however, had an impact on the lifetimes for these complexes. **Ru-NDI-1** exhibited charge separation with a lifetime of 52 ps, followed by fast charge recombination, $\tau = 14$ ps (Fig. 2.4 shows the transient absorption spectra for **Ru-NDI-1**). A ^{3}MLCT emission lifetime of 30 ps was also measured. By linking the Ru centre to the NDI core via the imide position as in **Ru-NDI-2**, a significant increase in the charge recombination lifetime, from 14 ps to 20 ns was observed. Transient absorption studies ($\lambda_{exc} = 532$ nm) were performed on **Ru-NDI-2**, in deaerated CH_3CN and revealed that the intramolecular electron transfer from photoexcited $[Ru(bpy)_3]^{2+}$ photosensitisers to the NDI unit occurred within 300 ps, followed by thermal charge recombination (electron transfer from NDI^- to $[Ru(bpy)_3]^{3+}$) exhibiting a lifetime of *ca*. 20 ns. Thus, it was

observed that the charge separation lifetimes were of the same order, whereas the charge recombination lifetimes were significantly different. In the former case, there was enhanced communication between the Ru centre and the NDI core, whereas the communication was less so in the latter case.

A comparison between the **Ru-PDI-1**and **Ru-PDI-6** suggests that the position of the Ru metal center has a less pronounced influence on the photophysical properties on PDI based ruthenium complexes, as opposed to the aforementioned NDI-based compounds. Gunderson et al. [12] studied the photophysical properties of the perylene ruthenium complex, **Ru-PDI-1**. The compound exhibited strong absorptions at 543 and 505 nm, corresponding to the first and second vibronic transitions of the PDI moiety. The peak at 450 nm corresponded to MLCT transitions of the ruthenium complex, while the band at 380 nm belonged to contributions arising from the ethynyl bipyridine. Fluorescence spectra for both the bipyridine-perylene ligand and the ruthenium coordinated analogue were recorded. The ligand displayed an emission with λ_{max} = 569 nm (Φ_{fl} = 0.62), and a lifetime of 4.55 ns. However, following coordination of the ruthenium centre, the fluorescence was completely quenched. Ultrafast transient absorption spectroscopy measurements (see Fig. 2.7) were performed at 532 nm (100 fs pulse duration), where the PDI moiety was selectively excited. This led to population of a charge separated state within 150 fs. Similar to **Ru-NDI-1**, the compound underwent fast charge recombination (τ = 63 ps). An alternative pathway involved the formation of a triplet PDI excited state, (^{3}PDI*−Ru(II)), which subsequently decayed to the ground state (τ = 39 μs). Both processes are summarised in the energy level diagram shown in Fig. 2.5.

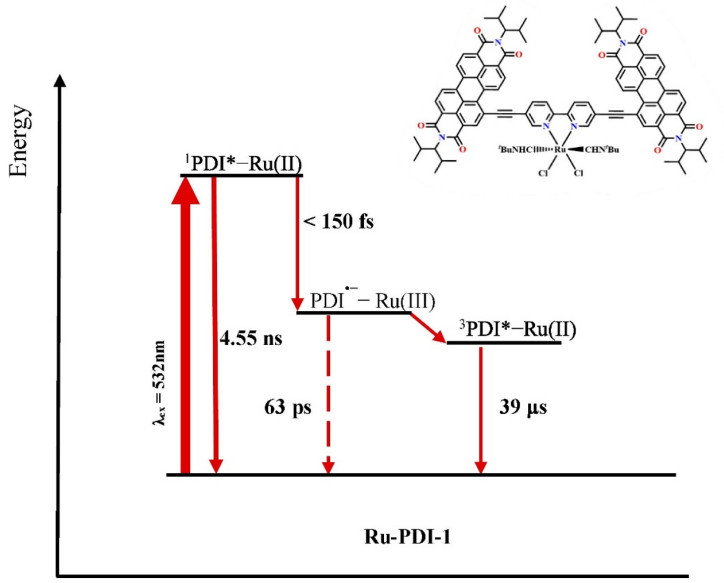


Figure 2.5 The energy level diagram of **Ru-PDI-1**. Adapted from Gunderson et al. [12].

Santos et al. [30] studied **Ru-PDI-6**, which had a broad absorption spectrum in the visible region, with absorption features at 450, 500 and 530 nm corresponding to perylene $\pi \rightarrow \pi^*$ transitions and ruthenium MLCT transitions at 420 and 500 nm. As observed in the absorption spectrum, each component could be selectively excited. Excitation at 525 nm led to population of the S_1 excited state of the PDI moiety and formation of a charge separated state, Ru(III)-PDI$^{\bullet-}$ within 2.9 ps. This excited state in turn relaxed to the triplet excited state of PDI (τ = 28 ps). Using flash photolysis, the lifetime of this triplet state was measured as 1.8 µs. On the other hand, upon irradiation at 450 nm, the [Ru(II)(phen)$_3$]$^{2+}$ moiety was mainly excited, resulting in the population of the Ru ^{1}MLCT state and subsequently, population of the Ru ^{3}MLCT state following fast intersystem crossing. An electron transfer process subsequently occurred within 8.3 ps, generating the charge separated Ru(III)-PDI$^{\bullet-}$ state. As in the case of 525 nm excitation, the triplet state of PDI was then formed which in turn decayed to the ground state (see Fig. 2.6).

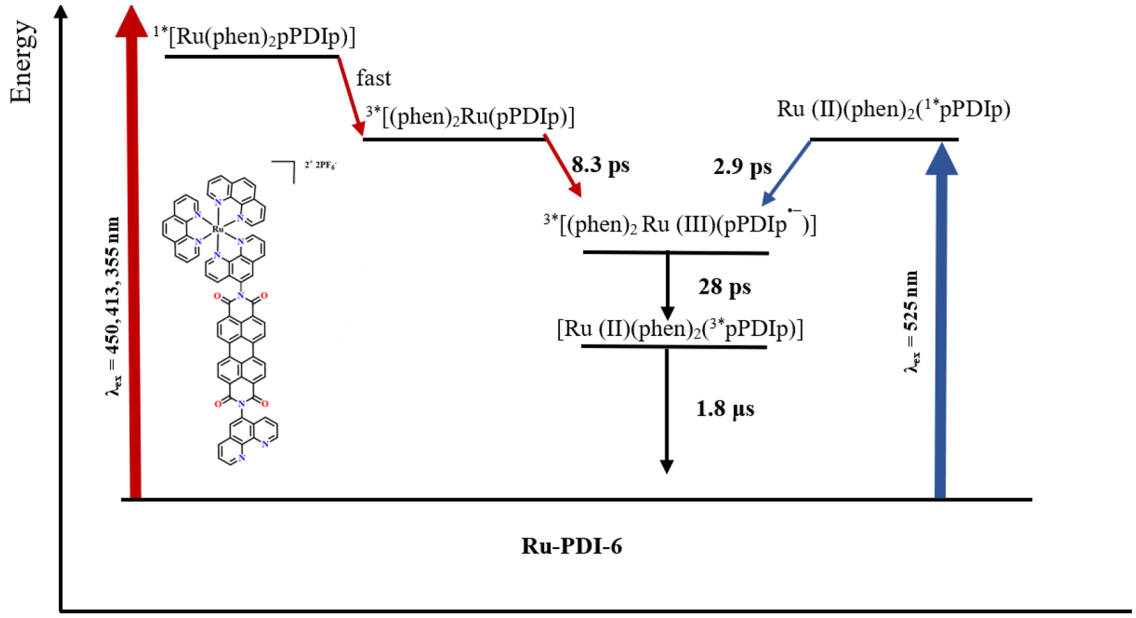


Figure 2.6 The energy level diagram for **Ru-PDI-6** following selective excitation [30].

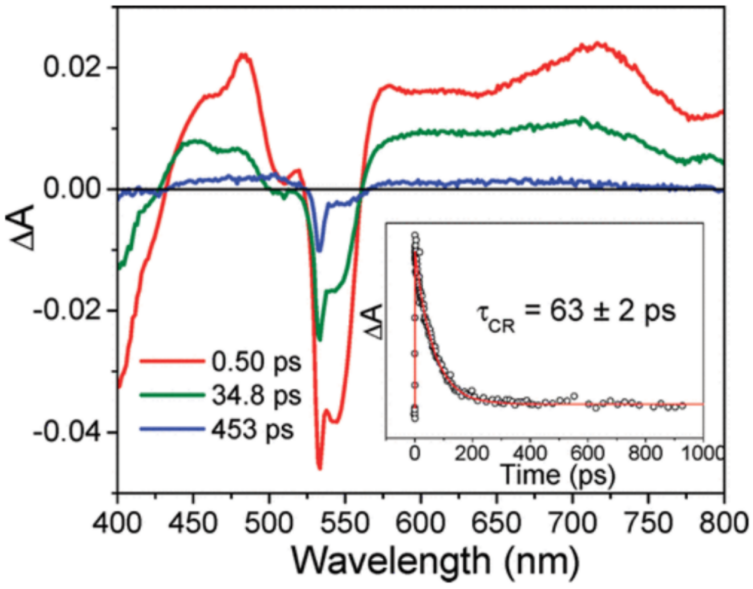


Figure 2.7 Transient absorption profiles following excitation (λ_{ex} = 532 nm) of **Ru-PDI-1** in CH_2Cl_2 at 532 nm. The kinetics trace, measured at 726 nm is shown in the inset. Taken with permission from Gunderson et al. [12].

Another interesting system was presented by Johansson et al. [26], who studied the effect of the distance between the Ru centre and the imide position on charge recombination. In this respect, **Ru-NDI-7** and **Ru-NDI-8** were studied. The UV-vis spectrum for the **Ru-NDI-7** and **Ru-NDI-8** complexes was similar to that described previously, with the MLCT band at 465 nm ($\varepsilon = 2.4 \times 10^4$ $M^{-1}cm^{-1}$) corresponding to the ruthenium chromophore. Furthermore, the absorption bands at 378, 358, 340 nm were attributed to the $\pi \rightarrow \pi^*$ transitions of the naphthalene diimide moiety. Ultrafast transient absorption spectroscopy ($\lambda_{ex.} = 400$ nm, 150 fs pulse duration) in addition to nanosecond flash photolysis time-resolved measurements, revealed that despite the extra methylene link in **Ru-NDI-8**, no effect on the rate of formation of the Ru(III)-$NDI^{\bullet-}$ anion was observed, and they attributed this finding to steric influences. The corresponding lifetimes are displayed in the diagram below (Fig. 2.8).

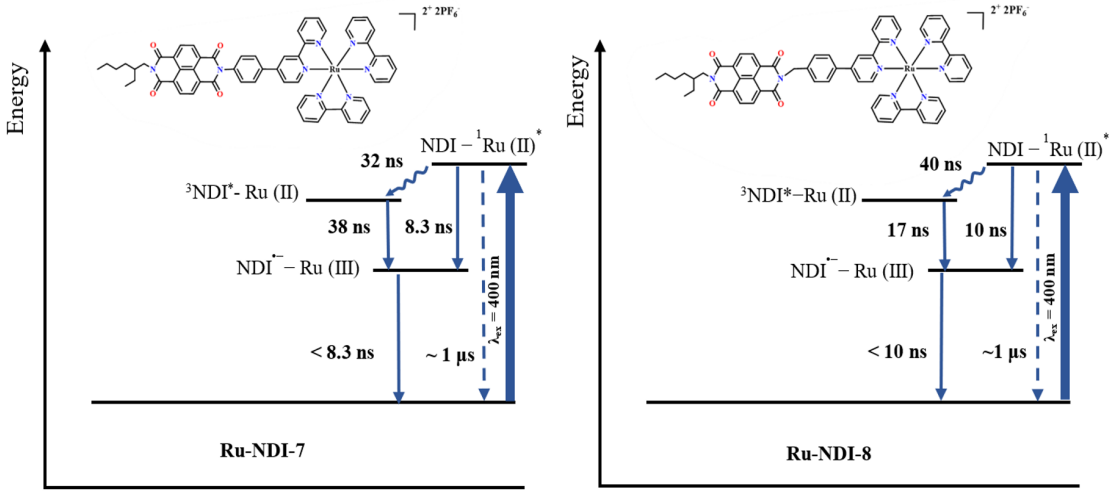


Figure 2.8 The schematic energy level diagram for **Ru-NDI-7** and **Ru-NDI-8 [**26].

In a more recent study, Ji and co-workers [25], replaced the bipyridine ligands attached to the Ru centre with terpyridine analogues. They observed ligand-centred $\pi \rightarrow \pi^*$ transitions for **Ru-NDI-6**, in the UV region, and a broad intense absorption in the visible region extending to 510 nm. The emission spectrum, had a maximum centered at 764 nm, suggesting population of a ^{3}MLCT state. The absorption and emission measurements indicated weak electronic coupling between the ruthenium chromophore and the NDI unit. Time-resolved studies demonstrated population of excited states, with broad absorption bands centred at 618 nm and below 400 nm, both attributed to ^{3}MLCT excited states. Following initial formation of the ^{3}MLCT, the NDI radical anion subsequently formed within 90 ps, with bands at 472, 623, and 677 nm. The NDI radical anion

underwent charge recombination and decayed back to the ground state, over 282 ps, regenerating the parent compound. It should be noted that the replacement of the bipyridine ligand with terpyridine led to a faster charge recombination lifetime (*ca*. 10 ns vs 241 ps) (see **Ru-NDI-8** vs **Ru-NDI-6**).

Another interesting example was presented by Johansson et al. [27]. In their work, the UV-vis absorption spectra of **Ru-NDI-11** had a MLCT band at 465 nm ($\varepsilon = 2.4 \times 10^4\ M^{-1}cm^{-1}$) corresponding to the ruthenium chromophore. Furthermore, the absorption bands at 378, 358, 340 nm were attributed to the $\pi \rightarrow \pi^*$ transitions of the naphthalene diimide moiety. Intramolecular charge separation in the **Ru-NDI-11** was probed by laser flash photolysis. Upon selective excitation of the Ru moiety (at 455 nm), a long-lived charge-separated state was formed. A biexponential decay (0.3 μs, 10 μs) was assigned to the charge recombination of $NDI^{\bullet-}$-Ru(III) back to the ground state. The authors suggested that the two different components could be attributed to two different isomers.

As an extension to the aforementioned work, Borgstrom et al. [8] modified the compound presented by Johansson et al. [27], with the addition of manganese, which acted as an electron donor, in order to replicate the natural photosynthetic process. The UV-vis absorption spectrum of the **Ru-NDI-12** exhibited the typical characteristics of the $[Ru(bpy)_3]^{2+}$ MLCT band, but with a red-shift of 10 nm, to 462 nm.

Furthermore, strong $\pi \rightarrow \pi^*$ transitions from the NDI moieties were apparent at 378, 358, and 340 nm. Intense $\pi \rightarrow \pi^*$ transitions in the UV region at 296 and 235 nm were also observed, arising from the bipyridine ligands coordinated to the ruthenium centre. At room temperature, the compound exhibited an emission spectrum with a maximum at 640 nm, which was redshifted in comparison to $[Ru(bpy)_3]^{2+}$, but with a similar spectral profile. However, the emission intensity was suppressed by up to 95% with respect to $[Ru(bpy)_3]^{2+}$. The authors performed transient absorption measurements ($\lambda_{ex.} = 455$ nm) and probed the photophysics of the complexes. Initially a *Ru(II) based excited state formed, which subsequently decayed, leading to generation of the reduced $NDI^{\bullet-}$. The authors reported lifetimes of 10 ns and 30 ns for **Ru-NDI-11** (at 298 K) and 9 and 25 ns for **Ru-NDI-12**. Importantly, no evidence for a long-lived Ru(III) state was observed. This suggested that a fast ($\tau < 30$ ns at 298 K) secondary electron-transfer step followed the initial photo-oxidation of the Ru unit, leading to repopulation of the Ru (II) centre. In the case of **Ru-NDI-11**, the secondary electron-transfer process was assigned to recombination and regeneration of the ground state. On the other hand, the long-lived

$NDI^{\bullet-}$ state observed in **Ru-NDI-11**, allowed the authors to suggest that the regeneration of Ru(II) was due to electron transfer from the Mn^{2+} unit to the Ru moiety. The lifetime of the long-lived charge separated states of **Ru-NDI-12** was extracted by means of a triexponential fit and reported as 15 μs, 200 μs and 2.3 ms (at 298 K). The authors ascribed the presence of multiple kinetic components to the existence of different isomers.

A thorough investigation by Dubey et al. [23] was performed on **Ru-PDI-2** and **Ru-PDI-3** (see Table 2.3). For both complexes, the lifetimes of the charge separated state/recombination process were of the same order of magnitude to those described previously, ranging from *ca*. 3 ps to *ca*. 80 ps (summarised below in Fig. 2.9). Following excitation of **Ru-PDI-2** or **Ru-PDI-3** at 420 nm, two photochemical pathways are possible as depicted in Fig. 2.9. The authors showed that in the case of **Ru-PDI-3**, the PDI core acted as an electron donor as opposed to an acceptor, and this is attributed to the presence of the pyrrolidine substituent in the bay position.

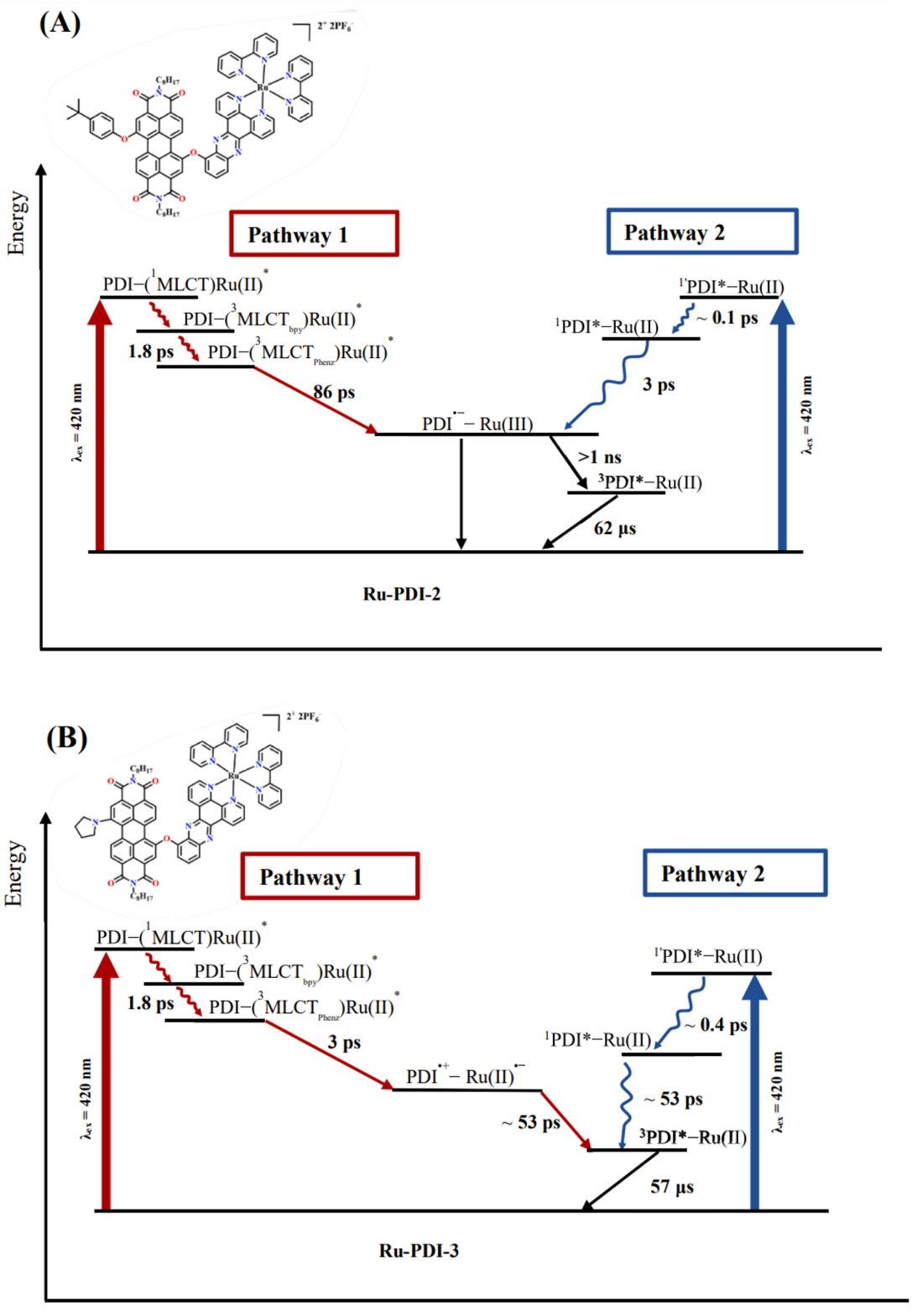


Figure 2.9 The energy level diagram for **Ru-PDI-2 (A)** and **Ru-PDI-3 (B)**, adapted from Dubey et al. [23].

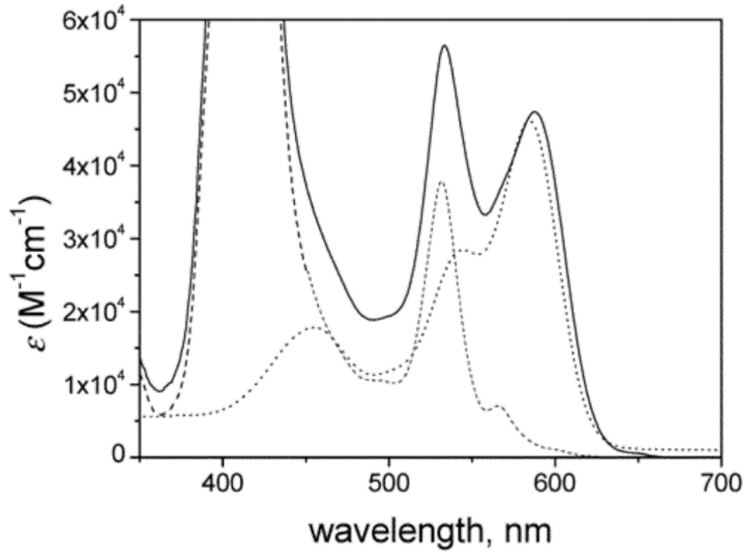


Figure 2.10 The absorption spectrum of **Ru-PDI-12** in CH_2Cl_2, the uncoordinated PDI (dotted line) and the uncoordinated ruthenium-porphyrin (broken line). Taken with permission from Prodi et al. [33].

The absorption spectrum of the ruthenium-perylene assembly, **Ru-PDI-12**, reported by Prodi et al. [33] was best described as a sum of the two individual units (see Fig. 2.10), the ruthenium-porphyrin and the perylene bis(imide) core, reflecting the supramolecular nature of the system, with strong absorption peaks observed at 410, 520 and 585 nm. Due to the heavy atom effect, the ruthenium introduced strong spin-orbit coupling that facilitated crossing to the triplet surface, resulting in quenching of the fluorescence (λ_{max} = 620 nm, Φ_{fl} = 0.001) with respect to the uncoordinated PDI core (λ_{max} = 620 nm, Φ_{fl} = 0.95).

This facilitated selective excitation of each component in the molecular assembly. Upon irradiation at 585 nm, the PDI moiety was selectively excited, which led to formation of a $Ru(S_0) \rightarrow PDI^{-}/Ru^{+}$ charge transfer state (τ = 5.6 ps). This species subsequently underwent charge recombination with a lifetime of 270 ps. Excitation at 530 nm led to the population of the S_1 state of the porphyrin unit. This was followed by fast relaxation to the T_1 state within a picosecond. This triplet state then decayed, by means of an energy transfer process within 720 ps, forming the triplet PDI state, $[PDI(S_0)/{}^*Ru(T_1) \rightarrow {}^*PDI(T_1)/Ru(S_0)]$ (see Fig. 2.11) which relaxed to the ground state within 9.8 μs.

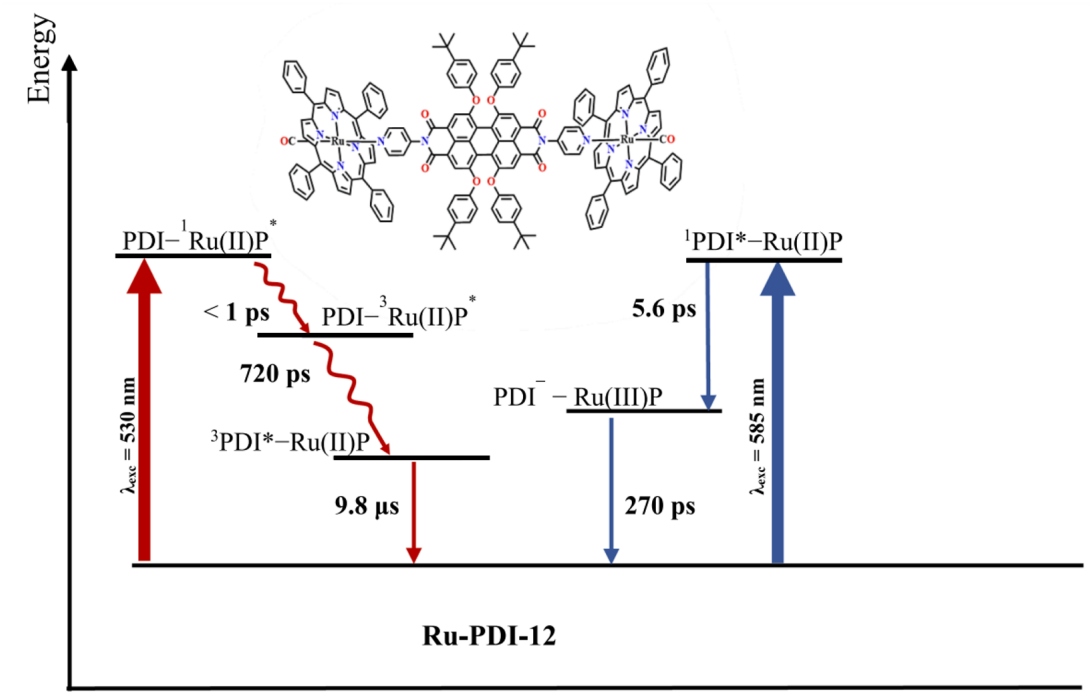


Figure 2.11 The energy level diagram for **Ru-PDI-12** showing selective excitation at 530 nm and 585 nm [33].

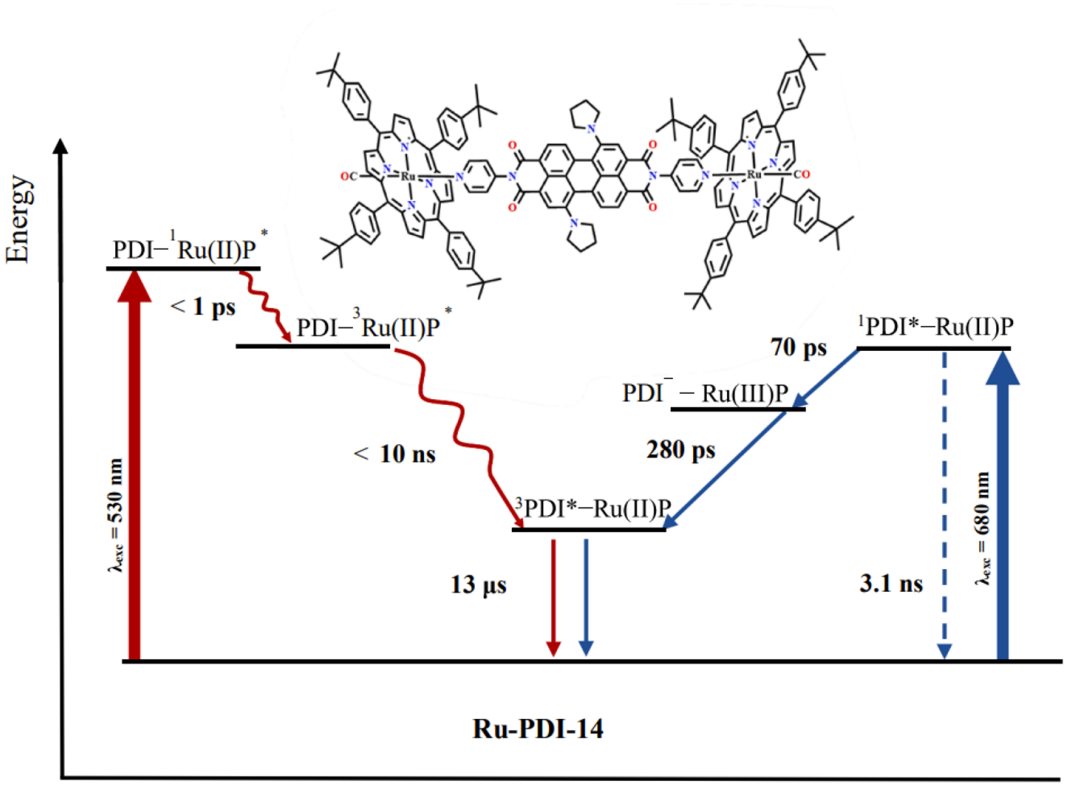


Figure 2.12 The energy level diagram for **Ru-PDI-14** showing selective excitation at 530 and 680 nm [35].

A closely related complex, **Ru-PDI-14**, was studied by Amati et al. [35]. Again, the absorption spectrum of this molecule corresponded to the sum of the individual spectra of the two moieties, (summarised in Table 2.3) thus allowing for selective excitation. Upon irradiation at 680 nm (Fig. 2.12), the singly excited [^{1}PDI*−Ru(II)P] (P = porphyrin macrocycle) was populated, with a fluorescence lifetime of 3.1 ns. Furthermore, a charge separated [PDI^{-}-Ru(III)P] state also formed, within 70 ps. They also measured the charge recombination process, with a lifetime of 280 ps in $CHCl_3$. However, it was possible to selectively populate the singlet PDI−^{1}Ru(II)P * state, by using the appropriate excitation (530 nm). Fast intersystem crossing ($\tau < 1$ ps) took place, leading to population of the PDI−^{3}Ru(II)P * triplet state. Relaxation of the porphyrin triplet state led to the formation of the triplet PDI state. The PDI triplet state decayed to the ground state, with a lifetime of 13 μs (Fig. 2.13).

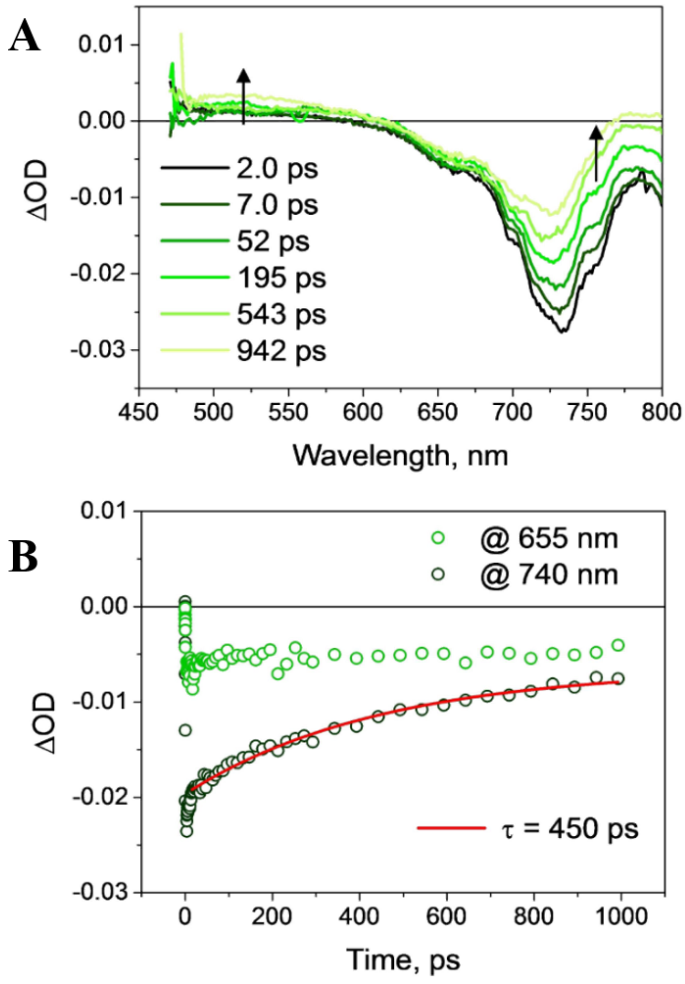


Figure 2.13 The transient absorption spectra of **Ru-PDI-14** in CH_2Cl_2 upon excitation at 680 nm with panel A representing the spectral profiles and panel B displaying kinetic traces at 655 nm and 740 nm respectively. Taken with permission from Amati et al. [35].

As seen above, several studies in the literature have utilised TA spectroscopy to monitor the dynamics in Ru-NDI/PDI systems, but to the best of our knowledge no time-resolved infrared spectroscopy [66] (TRIR) studies have been reported on the Ru-NDI/PDI systems to date. Optical parametric amplifiers [67] (OPAs) have been developed allowing for the generation of ultrashort MIR pulses. Hence, following the same principle as in UTAS, in the TRIR technique, a UV-vis laser pulse is used to populate an excited electronic state of the sample under investigation, followed by a time-delayed MIR laser pulse, used to track the induced dynamics. In that case, the characteristic vibrational frequencies (termed "reporter" modes), such as those associated with the carbonyl (CO) group of the NDI/PDI in the complexes, can be monitored. This allows to probe with high specificity the light-induced vibrational dynamics of molecule(s) under investigation. TRIR spectroscopy has been applied to ruthenium complexes [46, 50, 68] and NDI systems [69 – 71] and it is somewhat surprising that Ru-NDI/PDI complexes have not been studied using TRIR given the excellent IR signatures that the NDI/PDI units contain. Sazanovich et al. [72] applied a combination of ps-TAS, ns-TAS and ps-TRIR measurements to investigate the time- resolved dynamics of a Pt-NDI based system (see Fig. 2.14). The ps-TAS technique (Fig. 2.15) and nanosecond flash photolysis showed the presence of four species. Upon excitation, a singlet ^{1}NDI (0.9 ps) and a singlet ^{1}MLCT (<200 fs) were both populated independently. Following internal conversion, a short-lived ^{3}MLCT (3 ps) and a long-lived ^{3}NDI (520 μs) state were observed. In addition to these lifetimes, the complementary usage of ps TRIR spectroscopy also allowed for the direct observation of short-lived hot species (19 ps), not observed in the ps-TAS spectra, and was assigned to vibrational relaxation of ^{1}NDI and ^{3}NDI states, respectively.

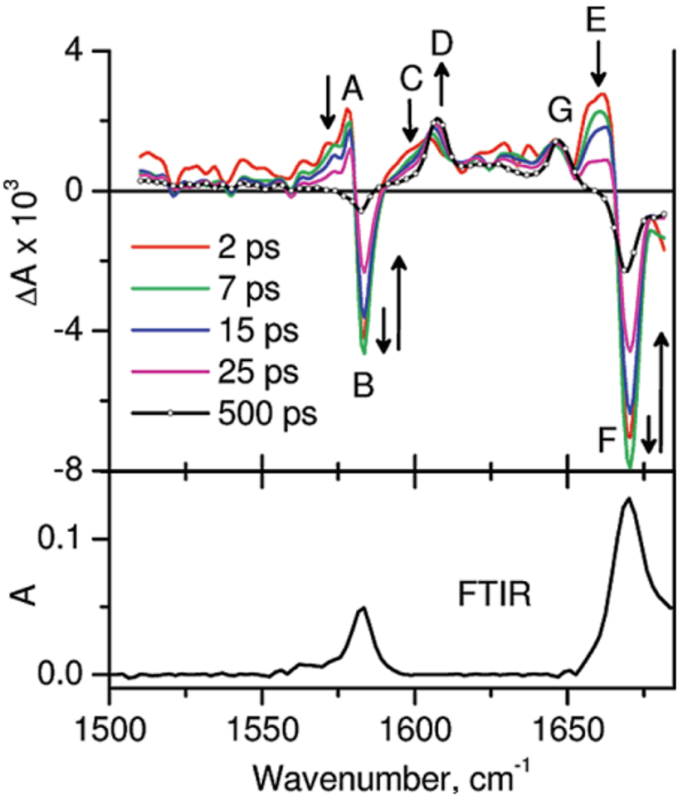


Figure 2.14 Time-resolved infrared spectra of Pt(phen-NDI)Cl_2 in CH_2Cl_2 at different time delays following excitation with 395 nm, 150 fs laser pulse along with ground-state FTIR spectrum of Pt(phen-NDI)Cl_2 in CH_2Cl_2 in the spectral range used in the TRIR experiments. Features (B) and (F) correspond to bleach of the ν(CC) and ν(CO) respectively. Features (G) and (D) were attributed to the ν(CO) stretches of the NDI in its triplet state. Feature (C) corresponds to hot triplet NDI, (A) and (E) is due to hot ground state. Taken with permission from Sazanovich et al. [72].

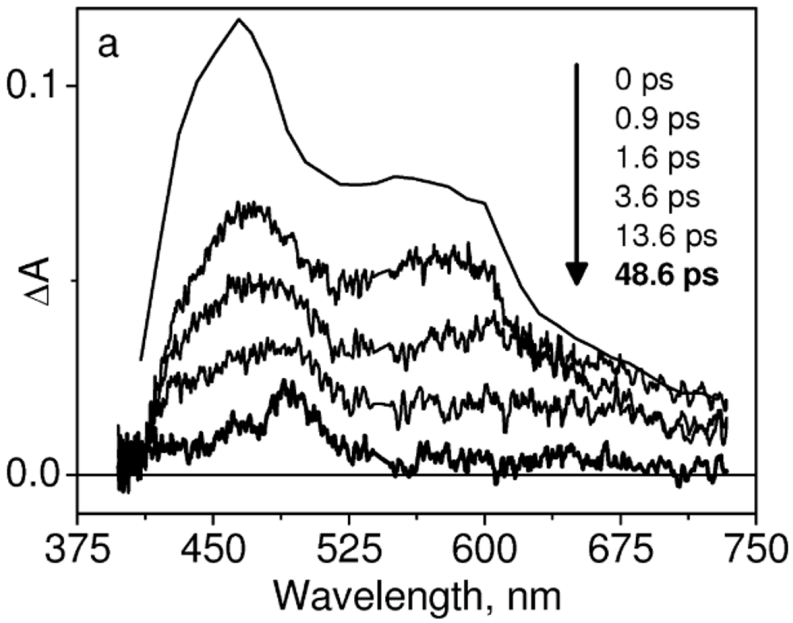


Figure 2.15 Transient absorption results obtained for Pt(phen-NDI)Cl_2 in CH_2Cl_2 following excitation with 395 nm, 150 fs laser pulse. Taken with permission from Sazanovich et al. [72].

Table 2.2 A summary of photophysical parameters for Ru-NDI complexes, where a = fluorescence emission lifetimes and b = phosphorescent lifetimes.

Compound Name	Solvent	Absorbance *NDI π → π*, (nm)*	Absorbance *Ru MLCT (nm)*	Emission (nm)	Lifetimes	Triplet Quantum Yields
Ru-NDI-1	DMF	285, 368, 375	450	605	30 ps[b]	—
Ru-NDI-2	CH_3CN	295, 350, 380	460	—	—	—
Ru-NDI-3	CH_3CN	295, 350, 380	480	—	—	—
Ru-NDI-4	DMF	285, 325, 375	480	605	63 ns[b]	—
Ru-NDI-5	—	—	—	—	—	—
Ru-NDI-6	DMF	275, 350,365	515	764	> 3 ns[b]	—
Ru-NDI-7	CH_3CN	378, 358, 339, 288, 236	456	594	~1 μs[b]	
Ru-NDI-8	CH_3CN	379, 359, 340, 289, 237	456	593	~1 μs[b]	
Ru-NDI-9	—	—	—	—	—	—
Ru-NDI-10	—	—	—	—	—	—
Ru-NDI-11	CH_3CN	378, 358, 340	465	—	27 ns[b], 7 ns[a]	
Ru-NDI-12	CH_3CN	378, 358, 340	462	640	40 ns[b], 7 ns[a]	
Ru-NDI-13	CH_3CN	380, 360, 340, 290	460	635	750 ns	0.14
Ru-NDI-14	2.5 mM Na_2HPO_4, 7.5 mM NaH_2PO_4, 0.1 M NaCl, pH 6.5	382, 360	452	624	0.62 ns, 1.99 ns[a], 12.6 ns[b]	0.053

Table 2.3 A summary of photophysical parameters for Ru-PDI complexes, where a = fluorescence and b = phosphorescence.

Compound Name	Solvent	Absorbance PDI $S_1 - S_0$	Absorbance Ru MLCT	Emission (nm)	Lifetimes	Quantum Yields
Ru-PDI-1	DCM	543, 505	400, 450	—	4.55 ns[b], 39 μs[a]	—
Ru-PDI-2	CH_3CN	650	~450	~750	57 μs[b]	0.0033[b]
Ru-PDI-3	CH_3CN	580	~ 450	~750	62 μs[b]	0.02[b]
Ru-PDI-4	DCM	550	520	484/780	4.2 μs[b]	0.11[b]
Ru-PDI-5	DMF	530, 490	450	—	> 3 ns[b]	—
Ru-PDI-6	CH_3CN	530, 490	450	600, 530	1.8 μs[b]	0.0629[b]
Ru-PDI-7	DMSO	533, 493, 462	overlapped	~ 550	5.06 ns[a], 156 ns[b]	—
Ru-PDI-8	DMF	580, 540, 447	450	—	—	—
Ru-PDI-9	DMF	530, 500, 450	~450	569	—	—
Ru-PDI-10	DMF	530, 500, 450	~450	567	—	—
Ru-PDI-11	DMSO	580	450	615	1.04 ns[a], 5.65 ns[b]	—
Ru-PDI-12	CH_2Cl_2	410, 520, 585	overlapped	620	9.8 μs[a]	0.001[a]
Ru-PDI-13	$CHCl_3$	652, 560, 296	overlapped	587^{Ru} 660^{PDI}	115 ns[a]	$0.0001_{(660\ nm)}$ [a]
Ru-PDI-14	CH_2Cl_2	720, 650, 570, 530, 490		680	13 μs[a]	

2.5 Electrochemistry

Electrochemical characterisation of Ru-NDI/Ru-PDIs, usually by either cyclic voltammetry or differential pulse voltammetry, has often been conducted to complement photophysical studies. The measured redox potentials can be used to estimate the thermodynamic driving force for charge transfer from a donor to an acceptor moiety using the so- called Rehm-Weller approach, reviewed by us elsewhere [73]. Most of the studies reviewed in this section have used glassy carbon working electrodes and tetrabutylammonium hexafluorophosphate ($TBAPF_6$) as the background electrolyte, therefore we specified the working electrode, or the electrolyte, only in cases where these have not been used.

Frath et al. [15] employed cyclic voltammetry to analyse the electrochemical properties of **Ru-NDI-5** in acetonitrile. The positive potential region revealed two waves. The first, an irreversible feature at E_{pa} = 1.08 V/SCE was attributed to the oxidation of the aniline group on the terpyridine ligand at the opposite side of the coordination sphere from the NDI. The second, a quasi-reversible wave at $E_{1/2}$ = 1.32 V/SCE was ascribed to the $Ru^{3+/2+}$ redox transition of the metal center. The negative region displayed four partially reversible reduction waves. The least negative; those at $E_{1/2}$ = −0.52 V/SCE and $E_{1/2}$ = −0.95 V/SCE, were assigned to the reduction of the NDI fragment, while the other two at $E_{1/2}$ = −1.30 V/SCE and $E_{1/2}$ = −1.49 V/SCE, corresponded to the reduction of the terpyridine ligands. There was no discernible impact of the electron-withdrawing NDI moiety on the oxidation of the **Ru-NDI-5** complex as compared to the reference compound $Ru(tpy)_2PhNH_2$, nor were the NDI reduction waves significantly affected by the **Ru-NDI-5** complex. Such an observation (i.e., that the voltammetric profile of the dyad was essentially a superposition of those of the individual components with little perturbation of the characteristic redox potentials) was regarded as desirable for a donor-acceptor dyad, since it suggested only minimal conjugation occurred between the donor and acceptor components in the ground-state, which may serve to inhibit backward electron transfer following photoexcitation.

Johansson et al. [26] probed the electrochemical properties of their Ru-NDIs complexes in acetonitrile using cyclic voltammetry and differential pulse voltammetry. The negative region for **Ru-NDI-7** displayed five reversible reduction peaks, two of them (−0.975 and −1.370 V/Fc^+/Fc) were assigned to the NDI moiety and the other three (−1.730, −1.910 and −2.155 V/Fc^+/Fc) were assigned to the bipyridine ligands. A single reversible wave

in the positive region with $E_{1/2}$ = 0.870 V/Fc^{+}/Fc was attributed to the $Ru^{3+/2+}$ redox couple. Similar reduction and oxidation potentials were reported for **Ru-NDI-8**. The authors considered two possible quenching mechanisms for the $[Ru(bpy)_3]^{2+}$ excited state - either by energy transfer to yield the NDI triplet, or through electron transfer to give the NDI radical. The thermodynamic driving force for the former was estimated to be 0.05 – 0.09 eV, calculated from the differences of E_{00} for the Ru ^{3}MLCT and ^{3}NDI states. The energy for the ruthenium triplet, $E_{00}(^3MLCT)$, was derived from the emission maximum at 77 K. Considering this value of E_{00}, and the measured $Ru^{3+/2+}$ and $NDI^{0/-}$ redox potentials, the Rehm-Weller approach was used to estimate a driving force of 0.24 – 0.31 eV for photo-induced electron transfer to form NDI^{-}. This larger driving force suggested the likelihood of quenching by electron, rather than by energy transfer.

In a parallel study [27], the same workers detailed the electrochemical characterisation in acetonitrile of **Ru-NDI-11** complex with donor species attached to the bipyridine ligand on the opposite side of the metal center to the NDI bridge. For **Ru-NDI-11**, where R = H/CH_3 additional irreversible anodic peaks were observed in the positive range at potentials below the oxidation of the metal centre. These however were proposed to be related to oxidations on the donor unit. The reductive electrochemistry was not outlined, however the authors noted that for these complexes, adsorption occurred onto the glassy carbon surface on the cathodic sweep at potentials similar to the first NDI Borgstrom et al. [8] constructed an energy level diagram for **Ru-NDI-12**. This was based on electrochemical data for **Ru-NDI-11** without the manganese moiety reported by Johansson and co-workers, which suggested $E_{1/2}$ = +0.88 V/Fc^{+}/Fc for the $Ru^{3+/2+}$ transition and $E_{1/2}$ = −0.97 V for the first reduction on the NDI fragment. Furthermore, the complex without the NDI moiety exhibited reversible processes at +0.10 V/Fc_{+}/Fc ($Mn_2^{II,III/II,II}$), +0.63 V($Mn_2^{II,III/II,II}$) and −1.6 V (($[Ru(bpy)_3]^{2+/+}$). The energy level diagram revealed a significantly greater driving force for quenching by $Mn^{II,II}{}_2$ -*Ru(II)-NDI → $Mn^{II,II}{}_2$-*Ru(III)-$NDI^{\bullet-}$ compared to $Mn^{II,II}{}_2$ -*Ru(II)-NDI → $Mn^{II,II}{}_2$ -*Ru(II)-*NDI. Also thermodynamically favoured was the subsequent transition of $Mn_2^{II,II}$-*Ru(III)-$NDI^{\bullet-}$ to $Mn_2^{II,III}$ -*Ru(II)-$NDI^{\bullet-}$ from which non-radiative decay to the initial ground state occurred.

Chaignon et al. [22] reported redox waves in DMF at 1.21 and 1.28 V/SCE, for **Ru-NDI-1** and **Ru-NDI-4**, respectively, which were attributed to the ruthenium moiety. Voltammetric features at −0.48 and −0.56 V were assigned to the first reduction of the NDI moiety in either (2.04 eV) and the ^{3}NDI state (2.03 eV) were very similar, an excited

state case. Again, the possibility of ^{3}MLCT quenching by either triplet energy equilibrium with delayed Ru emission would be expected for triplet transfer, or by electron transfer to yield Ru(III)-NDI$^{\bullet-}$ was considered. energy transfer. By contrast, a Rehm-Weller type estimation based on Given that the spectroscopically derived E_{00} values for the ^{3}MLCT state the measured redox potentials, predicted Gibbs free energy changes, ΔG^0, of −0.35 and −0.20 eV for the electron transfer route in the cases of **Ru-NDI-1** and **Ru-NDI-4**, respectively. Although moderate, these driving forces exceeded that for the triplet-to-triplet transition and suggested quenching by electron transfer to the NDI entity, which also accorded with the measured lifetimes of the complexes.

Baron et al. [28] studied the electrochemical properties of **Ru-NDI-13** by cyclic voltammetry with a background electrolyte of tetrabutylammonium perchlorate (TBAP) in acetonitrile. A reversible oxidation potential at +1.36 V/SCE was assigned to the ruthenium moiety and three quasi reversible waves in the negative region observed at − 1.20 V to − 1.68 V corresponded to the one electron reduction of each of the bipyridines in the coordination sphere. Two further reversible reduction waves at −0.53 V and −0.88 V were ascribed to the single and double reduction of the NDI unit. Reductive adsorption onto the glassy carbon working electrode was also reported in this study.

Ji et al. [25] studied the redox properties of **Ru-NDI-6** measured at a platinum working electrode in a TBAP/DMF electrolyte solution. The CV displayed a single reversible oxidation event at +0.68 V/NHE assigned to $Ru^{3+/2+}$ couple. This relatively low oxidation potential was attributed to the strong σ donating ability of the carbon anion which destabilised the HOMO through its delocalization onto the N^C^N ligand. Cathodic peaks with characteristic half-wave potentials of −0.33 and −0.84 V were assigned to the first two reductions of the NDI moiety. Both the oxidation potentials and reduction potentials of terpyridyl moieties of the **Ru-NDI-6** complex were almost unchanged relative to the NDI-free ruthenium analogue suggesting negligible ground state interactions between the ruthenium chromophore and the NDI acceptor. Spectroelectrochemical data for **Ru-NDI-6** showed a broad absorption in the visible region with a distinct peak at 475 nm, and a weak and broad absorption peak at 605 nm. These spectral features were in good agreement with the reported NDI$^{\bullet-}$ absorption in the literature and confirmed that the first reduction of the complex was NDI centred.

From photophysical data, the authors calculated that the electron transfer rate from the ruthenium chromophore to the NDI unit was approximately two orders of magnitude

higher when **Ru-NDI-6** was anchored on an NiO photocathode compared to a solution phase measurement in acetonitrile. This could be rationalised through the electrochemical data. A Rehm-Weller analysis of the solution case was conducted where the difference the between estimated ruthenium excited state oxidation potential ($E_{1/2}(Ru^{3+/2+})$-$E_{00}(^3MLCT)$) and the first NDI reduction potential ($E_{1/2}(NDI^{0/-})$ yielded a driving force of 0.7 eV. In the case of the photocathode, the injection of a hole into the valence band of NiO yielded the reduced sensitiser upon photoexcitation. In this instance the driving force for electron transfer was given by the difference between the first reduction potential of the chromophore (terpyridyl centred, $E_{1/2} = -1.33$ V) and $E_{1/2}$ ($NDI^{0/-}$) = −0.33 V. The resulting value of $-\Delta G^0 = 1.0$ eV exceeded that for electron transfer from Ru ^{3}MLCT to NDI, thereby accounting for the enhanced rate in the NiO immobilised case.

Skaisgirski et al. [3] performed voltametric characterisation of the triad **Ru-NDI-2** and the pentad **Ru-NDI-3**, at a platinum electrode in acetonitrile. The resulting CVs were essentially a superposition of those of the individual components. The classic NDI profile of two, reversible, one-electron redox transitions were evident in the negative region with $E_{1/2}$ values (vs. Fc^+/Fc) of −0.83 V and −1.33 V for the triad (Fig. 2.16), and −0.89 V and −1.34 V for the pentad (Fig. 2.17). Characteristic reductions of the bipyridine cyclometalated ligands appeared at more negative potentials. Quasi-reversible waves corresponding to the metal centred $Ru^{3+/2+}$ reaction were noted at 1.0 V. For **Ru-NDI-3**, an additional feature ($E_{1/2}$ = 0.38 V) was attributed to the reversible oxidation of the peripheral triarylamine moieties.

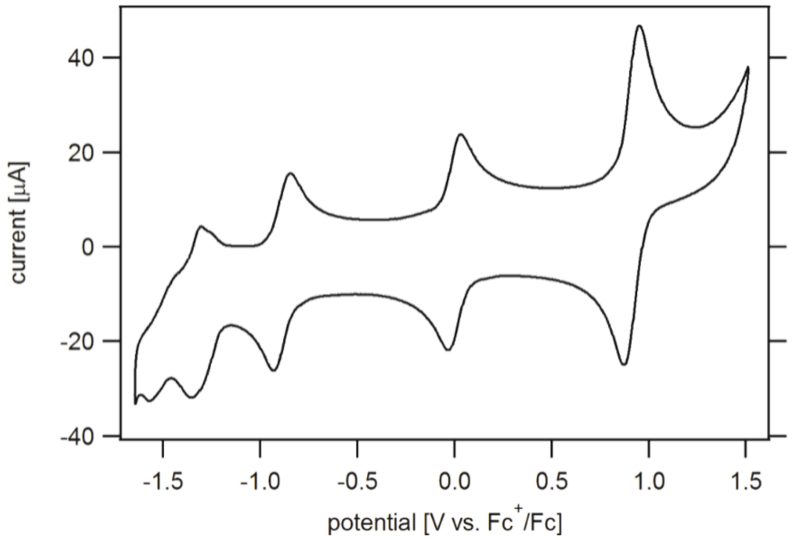


Figure 2.16 Cyclic voltammogram for **Ru-NDI-2** in CH_3CN with 0.1 M $TBAPF_6$ as presented by Skaisgirski et al. [3].

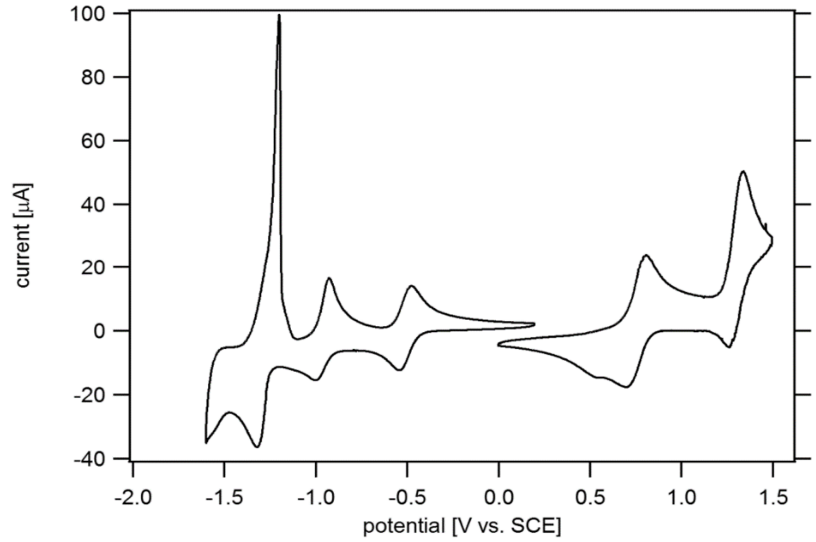


Figure 2.17 Cyclic voltammogram for **Ru-NDI-3** in CH_3CN with 0.1 M $TBAPF_6$ as presented by Skaisgirski et al. [3].

Prior to reviewing the electrochemistry of Ru-PDI species it is worth noting that Lee et al. [74] conducted voltammetric studies on several PDI species at a platinum working electrode in a mixed dichloromethane/acetonitrile solvent. At negative potentials, each of the PDI compounds exhibited two reversible one-electron reductions corresponding to the formation of the radical anion, followed by the dianion at a lower potential.

Furthermore, a single reversible one-electron process was registered for each molecule at quite positive potentials (≥1.6 V vs SCE) and was attributed to the radical cation. UV-vis spectroelectrochemistry yielding characteristic absorbance spectra for the PDI radical

anion and dianion were also reported. This work serves as a useful reference for the interpretation of the voltametric responses of more complex PDI-containing compounds.

Gunderson et al. [12] performed electrochemical experiments on **Ru-PDI-1** in DCM. A first reversible reduction was seen at −0.52 V/SCE followed by a second reversible reduction −0.76 V/SCE. These reductions were attributed to the perylene moiety-radical anion and dianion formation. A reversible redox feature at 0.68 V/SCE was attributed to $Ru^{3+/2+}$ couple, since, with reference to aforementioned report of Lee et al. [74], the formation of the PDI radical cation was not expected until significantly higher potentials. To further study the system, spectroelectrochemical studies were performed. The first electrochemical reduction, −0.52 V, resulted in the formation of two sharp peaks at 710 nm, and bleaching of the bands at 400 nm, 505 nm and 547 nm belonging to PDI. These spectral features corresponded to the formation of the perylene radical anion. Similarly, oxidation at 0.68 V led to the formation of an absorption band at 430 nm, in agreement with the assignment of the first oxidation product to Ru(III) bipyridine. The energy of the singlet excited state on the PDI subunit was determined by averaging the lowest energy absorption and the highest energy fluorescence maximum to provide an E_{00} value for a thermodynamic feasibility analysis. Considering this E_{00} value and the measured redox potentials for the $Ru^{3+/2+}$ and $PDI^{0/-}$ transitions, a value for the free energy of charge separation, ΔG_{cs}, of −1.03 eV was calculated. This confirmed a significant driving force for quenching of the Ru(II)-^{1}*PDI state through electron transfer to yield Ru(III)-$PDI^{\bullet-}$ (Fig. 2.18).

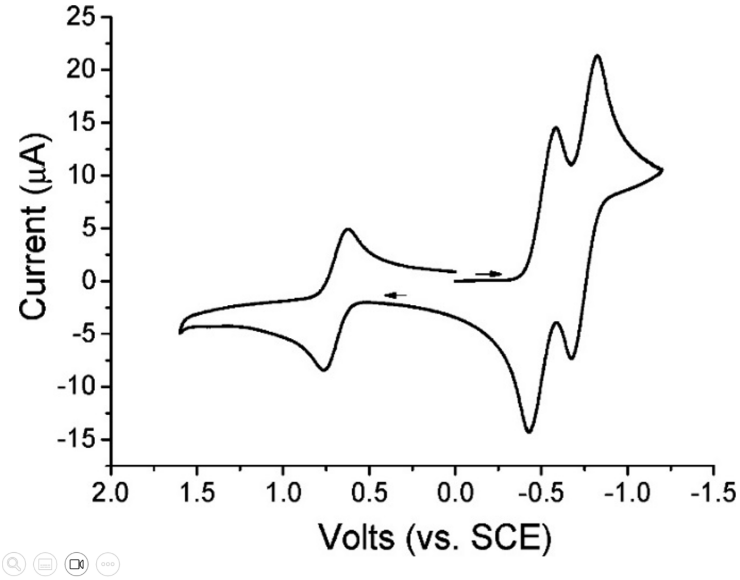


Figure 2.18 Cyclic voltammogram of **Ru-PDI-1** in CH_2Cl_2 with 0.1 M $TBAPF_6$ as presented by Gunderson et al. [12].

Dubey et al. [23] used differential pulse voltammetry to study the redox properties of their **Ru-PDI-2** and **Ru-PDI-3** systems in benzonitrile at a platinum working electrode. **Ru-PDI-3** displayed two one-electron oxidations at +0.90 V/Ag/AgCl and +1.38 V/Ag/AgCl. These were attributed to oxidations of the pyrrolidinyl-functionalised PDI with an overlapping contribution of the Ru^{2+} oxidation signal at +1.38 V. Three one-electron reductions were observed at −0.67 V, −0.87 V and −0.99 V, with the least negative ascribed to the first PDI centred reduction. **Ru-PDI-2** also displayed two one-electron oxidations, albeit at higher potentials of +1.42 V (overlap of phenoxy-functionalised PDI, and Ru^{2+} oxidations) and +1.70 V (PDI centred). The negative range exhibited one-electron reductions at −0.55 V, −0.80 V and −0.97 V. The cathodic shift in the measured potentials for the pyrrolidinyl-PDI containing species relative to that with the phenoxy side group was consistent with pyrrolidinyl-PDI being a reasonable electron donor, and phenoxy-PDI being a good electron acceptor.

The energies of charge separation were calculated from the difference between the first oxidation potential of the donor, and the first reduction potential of the acceptor. For **Ru-PDI-3**, electron transfer from the PDI subunit to yield $PDI^{\bullet+}$-$Ru(II)^{\bullet+}$ offered the lowest energy requirement of 1.77 eV, while for **Ru-PDI-2**, electron transfer in the opposite direction to give $PDI^{\bullet-}$-Ru(III), constituted the lowest energy pathway (1.97 eV). When comparing the energies of these charge-separated states to those of the excited states, it was observed that for **Ru-PDI-3**, the only viable route is from the ruthenium triplet excited state. However, for **Ru-PDI-2**, both the ruthenium triplet and the perylene singlet states lied above the 1.97 eV required to affect the $PDI^{\bullet-}$-Ru(III) charge-separated state, and therefore thermodynamic driving forces existed regardless of which part of the dyad was photoexcited.

Schulze et al. [7] performed electrochemical studies on **Ru-PDI-4** complex in DCM. The experiments revealed an anodic shift of the characteristic PDI reductive waves of the complex with respect to the free ligand, from −1.06 V and −1.34 V vs Fc^{+}/Fc, to −0.85 V and −1.23 V for the ruthenium complex. Bipyridine reductions were observed at − 1.86 V and −2.15 V. A reversible wave corresponding to $Ru^{3+/2+}$ redox switching process was centred at +1.02 V, which represented a positive shift relative to $[Ru(bpy)_3]^{2+}$ (+0.88 V). The authors justifiably commented that these observed redox shifts were a consequence of the electron-withdrawing nature of the electron-poor PDI unit. Since in this case, the electrochemical response of **Ru-PDI-4** complex was not a simple superposition of the individual characteristics of its components, it was evident that coordination of the Ru

centre in close proximity to the PDI core facilitated ground state electronic interaction between these two bound moieties. As previously observed, this was not desirable if excited state quenching through donor-acceptor electron transfer was targeted, however in this study the aim was to deliver PDI singlet to PDI triplet intersystem crossing followed by phosphorescence from the latter state.

Liu et al. [9] conducted voltammetry in DMF in order to deduce the suitability of **Ru-PDI-8** for use as an anode photosensitizer in a dye- sensitized solar cell (DSC). The oxidation potential ($Ru^{3+/2+}$ transition) could be correlated with the HOMO level and was measured as +0.87 V (vs NHE). Following photoexcitation in a DSC, the resultant hole in the HOMO level must be filled by electron transfer from an iodide ion. The redox potential of the I_3^- /I^- couple was ~0.4 V/NHE - since this was lower in potential (and therefore higher in energy) compared to the measured HOMO level, a driving force existed for the required reaction. A HOMO-LUMO gap ($E_{0\text{-}0}$) of 1.63 eV was estimated from the onset wavelength of absorption of the dye on TiO_2. Subtraction of $E_{0\text{-}0}$ from the potential of the HOMO, suggested a LUMO potential of the order of −0.7 V/NHE. Since this potential lies below the conduction band edge of TiO_2 (−0.5 V), transfer of a photo-excited electron from **Ru-PDI-8** the conduction band of a TiO_2 anode was also feasible. This analysis confirmed the thermodynamic compatibility of this dye with TiO_2 for DSC application.

Santos et al. [30] measured the electrochemical potentials of **Ru-PDI-6**, in acetonitrile using a platinum disk working electrode. At negative potentials, voltammetric waves assigned to the anionic radical PDI/$PDI^{\bullet-}$, and the dianion PDI^- /PDI^{2-} were found at $E_{1/2}$ = −0.27 V (Ag/AgCl) and $E_{1/2}$ = −0.55 V, respectively. Further reductions at $E_{1/2}$ = −1.20 V and $E_{1/2}$ = −1.45 were ascribed to the ruthenium bound phenanthroline ligands. Otherwise, a redox couple at +1.50/+1.43 V ($E_{1/2}$ = +1.47) was assigned to the $Ru^{3+/2+}$ redox process (see Fig. 2.19). The authors also performed UV-vis spectroelectrochemical studies. Oxidation of the complex at +1.57 V led to the formation of Ru(III) with the generation of absorption bands at 440, 280 and 250 nm. The reduction of Ru(III) was not reversible. Reductive electrolysis revealed the formation of an absorption band at 704 nm, assigned to the formation of the anionic complex PDI^-. At −0.76 V, the dianionic complex PDI^{2-} was formed, with the formation of a band at λ_{max} = 565 nm. The oxidation of the anionic radicals was not reversible.

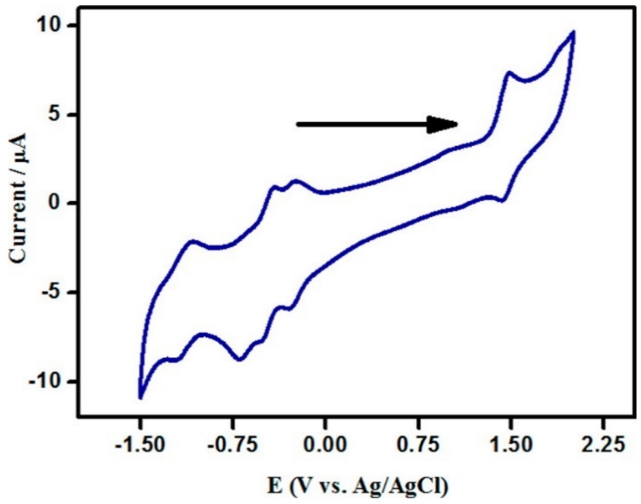


Figure 2.19 Cyclic voltammogram of **Ru-PDI-6** in CH_3CN with 0.1 M $TBAPF_6$ as presented by Santos et al [30].

A Rehm-Weller analysis based on the measured electrochemical and spectroscopic data was used to confirm the feasibility of reaching the PDI triplet excited state via the intermediate charge-separated state Ru(III)-$PDI^{\bullet-}$. The difference between the $E_{1/2}(Ru^{3+/2+})$ and $E_{1/2}(PDI/ PDI^{\bullet-})$ suggested a required charge separation energy of 1.75 eV. This was more than covered by the ^{3}MLCT E_{00} value of 2.1 eV, indicating the existence of a driving force of 0.35 eV. At wavelengths ≥ 525 nm light absorption occurred via the PDI moiety of the dyad. This wavelength corresponded to an E_{00} value of 2.36 eV, indicating that Ru(III)-$PDI^{\bullet-}$ could also be achieved through quenching of the PDI singlet excited state with $\Delta G_{cs} = -0.61$ eV.

Nastasi et al. [29] reported the redox potentials of **Ru-PDI-5** complex, measured in acetonitrile. The system displayed two reversible one-electron reductions at –0.37 and –0.61 V /SCE respectively and were assigned to the PDI core. Other reduction processes were observed at potentials greater than –1.0 V for the complex, however the processes were strongly irreversible and ill behaved, and so were not further studied. A reversible one electron oxidation was measured at +1.31 V and was assigned to the $Ru^{3+/2+}$ transition. In conjunction to the electrochemical results, spectroelectrochemical measurements were performed by reduction of the complex at –0.37 V, then plotting the differential spectrum (see Figure 2.20). There was a bleaching of the PDI bands between 420 – 550 nm and a formation of new absorption bands between 570 – 700 nm, was related to the formation of a PDI radical anion. To assist in the interpretation of photophysical results, the thermodynamic feasibility of the formation of a Ru(III)-$PDI^{\bullet-}$ charge separated state was interrogated using the Rehm-Weller approach. The difference between the metal centred oxidation potential and the first PDI reduction potential

indicated an energy requirement of 1.69 eV. From the relevant emission spectrum, the energy of the singlet π - π* state of the PDI was estimated at 2.32 eV, and so the formation of the charge-separated state was favoured by 0.63 eV. The authors constructed an energy level diagram to show that the charge-separated entity could then form the ^{3}π - π* PDI state (ΔG_{cs} = −0.49 eV), which ultimately decayed to the ground state in a radiationless process on a ns timescale.

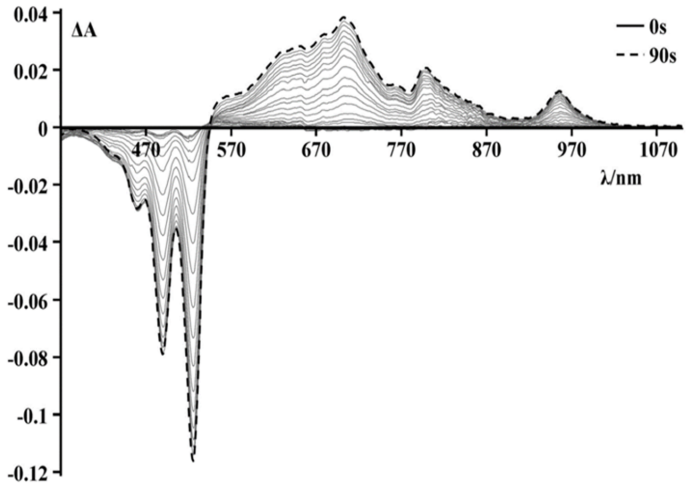


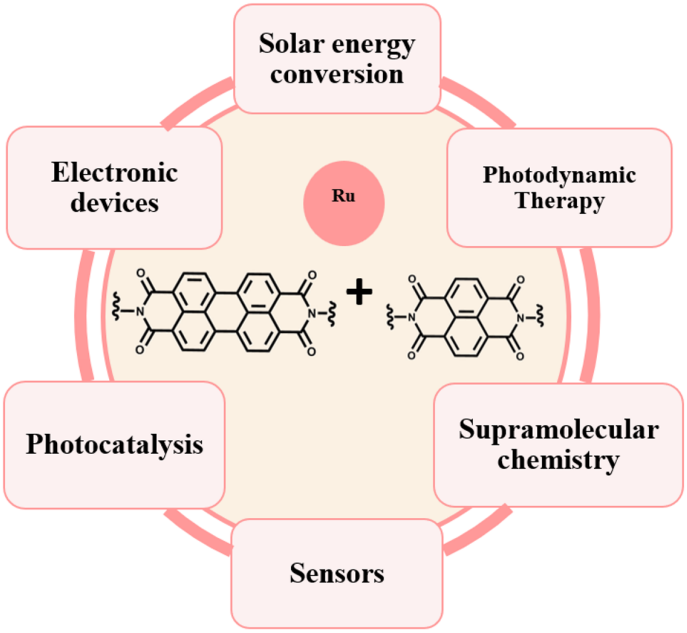
Figure 2.20 Differential spectra between the absorption spectrum of the reduced species and the ground state, with permission from Nastasi et al. [29].

Rodríguez-Morgade et al. [34] performed electrochemical studies on the **Ru-PDI-13** assembly and its individual components. A silver wire was employed as the reference electrode; however, it was unclear if the reported potentials related directly to this or if they have been corrected to another scale. In *ortho*-dichlorobenzene, Ru(CO)Pc showed two reversible oxidations, at +0.66 V and at +1.42 V. For the discrete PDI entity, the first reversible one-electron reduction was observed at around −0.6 V. For the combined system, the oxidation peak shifted to +0.74 V, while a more moderate shift of 0.04 V was noted for the first reduction feature. The formation of the donor-acceptor hybrid Ru(CO)Pc$^{\bullet+}$-PDI$^{\bullet-}$-Ru(CO)Pc was targeted. The difference between the PDI first reduction potential and the phthalocyanine first oxidation potential suggested an energetic requirement of 1.23 eV to generate the radical ion pair. On the other hand, the measured fluorescence maxima were used to estimate the singlet excited- state energy of Ru(CO)Pc and PDI as 1.87 and 2.11 eV, respectively. Accordingly, spontaneous charge separation was energetically favourable upon photoexcitation of either the Ru(CO)Pc center (ΔG_{cs} = −0.64 eV), or the PDI entity (ΔG_{cs} = −0.88 eV).

In summary, electrochemical characterisation of Ru(II)-NDI or Ru (II)-PDI species generally revealed two reversible, one-electron reduction processes attributable to the formation of the diimide radical anion, and at somewhat lower potential the dianion. For the various molecules reviewed here, the gap between the first and second reduction potentials was somewhat smaller in the case of PDIs (generally ~ 0.25 – 0.30 V) compared to the NDIs (~ 0.40 – 0.50 V). This is consistent with the findings of Lee et al. [74] that the inter-reduction potential gap for diimides decreases with increasing size of the aromatic core. This behaviour was proposed to arise on the basis that the excess electronic charge introduced by the first reduction is localised onto one of the imide groups. The addition of a second electron will therefore be subject to Coulombic repulsion. As the extent of the aromatic structure increases on going from NDIs to PDIs, the resonance energy will increase, thereby enhancing charge delocalization. This is turn is expected to lower the energy barrier to dianion formation.

The characteristic reduction process of the Ru cyclometallation ligands encountered in our survey tend to arise at more negative potentials compared to the two diimine reductive transitions. The metal centred $Ru^{3+/2+}$ redox reaction is usually manifested as a reversible (or quasi-reversible) redox wave in the positive region, with the exact potential exhibiting significant sensitivity to the ligand environment. The reversible formation of the $NDI^{\bullet+}$ radical cation may be encountered at potentials more positive than the Ru oxidation if voltammetry measurements are extended sufficiently far in the anodic direction.

2.6 Promising Applications and Conclusion



As highlighted in this review, Ru(II)-NDIs and Ru(II)-PDIs are extensively utilised as electron acceptors/donors and as supramolecular structural components for assemblies. Modifications of the NDI/PDI core and coordination to ruthenium (II) moieties, leads to the formation of highly coloured compounds, with conducting properties and with tuneable photophysical and/or electrochemical behaviour. This type of system has found application in a variety of fields, including but not limited to solar energy, medicinal chemistry and electronic devices.

In the field of solar energy, Ru(II)-NDIs/PDIs can be employed to emulate the natural photosynthesis process of converting light energy into chemical energy [9, 75, 76]. Donor-chromophore-acceptor systems are advantageous for enhancing efficient light-driven electron transfer, in which long-lived charge separated states are generated. This was observed in the findings reported by Johannson et al. [26, 27], Chaignon et al. [22], Borgstrom et al. [8] and Skaisgirski et al. [3]. For example, **Ru-NDI-12** was characterised with the very long-lived charge separation and a second chain of electron transfer processes, hence this complex might be a viable imitation of charge separation in Photosystem II involving the $CaMn_4$ cluster [8]. Similarly, Liu et al. [9] assessed their **Ru-PDI-8** for use in dye sensitised solar cells, with an overall conversion efficiency of 1.7%.

Furthermore, Ru(II)-NDIs/Ru(II)-PDIs can be potentially used in medicinal applications. Dixon et al. [21] demonstrated the applicability of their complex as a DNA binding target, where studied the influence of DNA intercalation on the properties of **Ru-NDI-14** and

found that there was no significant effect on the electron transfer process. In addition, Mari et al. [77] studied cellular uptake of **Ru-PDI-4** in HeLa cells. Organelle distribution was then determined, and it was found that the compound was localized in the mitochondria. The suitability of rylene-ruthenium materials in PDT was also demonstrated by Aksakal et al. [32]. In their work, they investigated the performance of **Ru-PDI-11** for photocyctoxicity, where they obtained a singlet oxygen quantum yield of 30% in DMSO following irradiation at 632 nm, via the indirect method, using methylene blue as a reference. To build on this result, in vitro photodynamic measurements were performed. Using the human chronic myeloid leukaemia cell line (K562), a 50% reduction in cell viability was observed after 5 h. Furthermore, the complex itself showed little to no dark toxicity. In a more recent investigation carried out by Yang et al. [78], a half-sandwich Ru(II) complex functionalised with a NDI moiety was examined, revealing noteworthy spectroscopic properties. The complex exhibited broad red emission bands, and the authors stated that this could be advantageous for bioimaging applications. The apoptosis of breast carcinoma cells was caused by this compound through reactive oxygen species (ROS)-mediated mitochondria-related mechanisms. A substantial 50% reduction in cell viability was observed after 48 h, and the concentration required to inhibit growth (IC_{50}) was determined to be 6.78 ± 1.16 [μM] [78].

Finally in the field of electronic devices, Frath et al. [15] reported a structurally robust model with favourable electron transport from the donor to the acceptor, which promoted strong rectification activity. The novel graftable dyad, **Ru-NDI-5**, could be utilised to develop large-area molecular junctions, which could contribute to implementations in memory and rectifiers [15].

This review highlights further opportunities for the development of synthetic strategies, novel applications, and future prospects for the introduction of different metals such as iridium [77, 79], copper [80, 84], iron [80], rhenium [81], zinc [82], manganese [83] in addition to the incorporation of perylene and naphthalene diimide ligands to the ruthenium metal centre. For example, Costa et al. [79] synthesised a dyad consisting of a PDI ligand coordinated to the iridium. The complex presented high quantum yields, and efficient deep-red electroluminescence which could be utilised in light-emitting electrochemical cells (LECs) [79]. Further research carried out by Mari et al. [77] investigated the potential of the iridium-PDI complex as a photosensitiser in PDT. The complex exhibited long emission lifetime of 33 μs, good singlet oxygen quantum yield of 85 – 87% and excellent phototoxicity on cancer cell lines. Koenig et al. [81] assessed

a PDI-rhenium bipyridine compound for its photocatalytic CO_2 reduction performance, with a turnover number (TON) of 234 reported. Other interesting results were presented by Pirota et al. [84] which highlight new possibilities for the binding and damaging parallel RNA G-quadruplexes using NDI complexes. The authors designed copper-NDI complexes for the selective cleavage of RNA structures triggered by ROS, and those compounds exhibited remarkable binding constants at physiological pH, of 16 – 18 log units [84]. Consequently, the development of copper-NDIs complexes could be a desirable strategy for medicinal purposes. A more recent study conducted by Liu et al. [85] showed that metal-organic-frameworks (MOFs) consisting of coordination of NDI moiety to nickel ion could be utilised as a cathode material for aqueous zinc-ion batteries because of their excellent stability in aqueous solutions over a wide pH range, together with a specific capacity of 90.7 mAh g^{-1} at current density of 50 mA g^{-1}.

The aforementioned examples of various NDI/PDIs complexes employing different metals highlights how the incorporation of NDI/PDI scaffolds into new compounds/materials opens up a wide range of promising future applications and is not exclusive to ruthenium systems.

To conclude, this review examined a range of Ru(II)-NDI and Ru(II)-PDI compounds. The most common synthetic pathways were summarised to highlight the various ways these interesting materials can be exploited to develop novel complexes. The corresponding photophysical properties were described, including both the fundamental behaviour and the applicability of the photosensitisers. In addition, emphasis was placed on the electrochemical measurements that can supplement photophysical techniques in probing charge-separation and electron transfer pathways in Ru(II)-NDI or Ru(II)-PDI complexes. The combination of spectroscopically derived HOMO-LUMO energy gaps, and electrochemically determined redox potentials, offer fundamental insights into the energy level profiles of these molecules. Finally, potential applications in several fields with societal and economic impact were highlighted.

2.7 References

[1]. H. Vollmann, H. Becker, M. Corell, H. Streeck, Beitrage zur Kenntnis des Pyrens und seiner Derivate, Justus Liebigs Ann. Chem. 531 (1) (1937) 1–159, https://doi.org/10.1002/jlac.19375310102

[2]. P.J.S. Maia, I. Aguiar, M. Santos Velloso, D. Zhang, E.R. Santos, J.R. Oliveira, J. C. Junqueira, M. Selke, R.M. Carlos, Singlet oxygen production by a polypyridine ruthenium (II) complex with a perylene monoimide derivative: A strategy for photodynamic inactivation of Candida albicans, J. Photochem. Photobiol. Chem. 353 (2018) 536–545, https://doi.org/10.1016/j.jphotochem.2017.12.020

[3]. M. Skaisgirski, X. Guo, O.S. Wenger, Electron Accumulation on Naphthalene Diimide Photosensitized by $[Ru(2,2'\text{-Bipyridine})_3]^{2+}$, Inorg. Chem. 56 (5) (2017) 2432–2439, https://doi.org/10.1021/acs.inorgchem.6b02446

[4]. S.V. Bhosale, M.A. Kobaisi, R.W. Jadhav, P.P. Morajkar, L.A. Jones, S. George, Naphthalene diimides: perspectives and promise, Chem. Soc. Rev. 50 (17) (2021) 9845–9998, https://doi.org/10.1039/d0cs00239a

[5]. V. Pirota, M. Nadai, F. Doria, S.N. Richter, Naphthalene Diimides as Multimodal G-Quadruplex-Selective Ligands, Molecules 24 (3) (2019) 426, https://doi.org/10.3390/molecules24030426

[6]. S.-L. Suraru, F. Würthner, Strategies for the Synthesis of Functional Naphthalene Diimides, Angew. Chem. Int. Ed. 53 (29) (2014) 7428–7448, https://doi.org/10.1002/anie.201309746

[7]. M. Schulze, A. Steffen, F. Würthner, Near-IR Phosphorescent Ruthenium(II) and Iridium(III) Perylene Bisimide Metal Complexes, Angew. Chem. Int. Ed. 127 (5) (2015) 1590–1593, https://doi.org/10.1002/ange.201410437

[8]. M. Borgstrom, N. Shaikh, O. Johansson, M.F. Anderlund, S. Styring, B. Åkermark, A. Magnuson, L. Hammarstrom, Light Induced Manganese Oxidation and Long-Lived Charge Separation in a $Mn_2^{II,II}$– $Ru^{II}(bpy)_3$− Acceptor Triad, J. Am. Chem. Soc. 127 (49) (2005) 17504–17515, https://doi.org/10.1021/ja055243b

[9]. B. Liu, W. Zhu, W. Wu, K.M. Ri, H. Tian, Hybridized ruthenium(II) complexes with high molar extinction coefficient unit: Effect of energy band and adsorption on photovoltatic performances, J. Photochem. Photobiol. Chem. 194 (2–3) (2008) 268–274, https://doi.org/10.1016/j.jphotochem.2007.08.023

[10]. G. Koyyada, P. Kumar CH, P. Salvatori, G. Marotta, M.G. Lobello, O. Bizzarri, F. De Angelis, C. Malapaka, New terpyridine-based ruthenium complexes for dye sensitized solar cells applications, Inorg. Chim. Acta 442 (2016) 158–166. https://doi.org/10.1016/j.ica.2015.11.031

[11]. H. El-Batal, K. Guo, X. Li, C. Wesdemiotis, C.N. Moorefield, G.R. Newkome, Perylene-Based Bis-, Tetrakis-, and Hexakis(terpyridine) Ligands and Their Ruthenium(II)-Bis(terpyridine) Complexes: Synthesis and Photophysical Properties, Eur. J. Org. Chem. 18 (2013) 3640–3644, https://doi.org/10.1002/ejoc.201300329

[12]. V.L. Gunderson, E. Krieg, M.T. Vagnini, M.A. Iron, B. Rybtchinski, M. R. Wasielewski, Photoinduced Singlet Charge Transfer in a Ruthenium(II) Perylene-3,4:9,10-bis(dicarboximide) Complex, J. Phys. Chem. B 115 (23) (2011) 7533–7540, https://doi.org/10.1021/jp2016374

[13]. F.N. Castellano, Transition metal complexes meet the rylenes, Dalton Trans. 41 (28) (2012) 8493–8501, https://doi.org/10.1039/c2dt30765k

[14]. A.H. Zewail, Femtochemistry: Atomic-Scale Dynamics of the Chemical Bond, Chem. A Eur. J. 104 (24) (2000) 5660–5694, https://doi.org/10.1021/jp001460h

[15]. D. Frath, V.Q. Nguyen, F. Lafolet, P. Martin, J.-C. Lacroix, Electrografted monolayer based on a naphthalene diimide–ruthenium terpyridine complex dyad:

efficient creation of large-area molecular junctions with high current densities, Chem. Commun. 53 (80) (2017) 10997–11000, https://doi.org/10.1039/C7CC04972B
[16]. J. Wu, M. Peng, M. Mu, J. Li, M. Yin, Perylene diimide supramolecular aggregates: Constructions and sensing applications, Supramol. Mater. 2 (2023), 100031, https://doi.org/10.1016/j.supmat.2023.100031
[17]. P.I. Scheurle, A. Biewald, A. Mahringer, A. Hartschuh, D.D. Medina, T. Bein, A Novel Electrically Conductive Perylene Diimide-Based MOF-74 Series Featuring Luminescence and Redox Activity, Small Struct. 3 (5) (2022) 2100195, https://doi.org/10.1002/sstr.202100195
[18]. Y. Hou, Z. Zhang, L. Ma, R. Shi, S. Ling, X. Li, G. He, M. Zhang, Perylene Diimide-Based Multicomponent Metallacages as Photosensitizers for Visible Light-Driven Photocatalytic Oxidation Reaction, CCS Chem. 4 (8) (2021) 2604–2611, https://doi.org/10.31635/ccschem.021.202101382
[19]. V. Rai, L. Gerhard, N. Balzer, M. Valasek, C. Holzer, L. Yang, M. Wegener, C. Rockstuhl, M. Mayor, W. Wulfhekel, Activating Electroluminescence of Charged Naphthalene Diimide Complexes Directly Adsorbed on a Metal Substrate, Phys. Rev. Lett. 130 (3) (2023), 036201, https://doi.org/10.1103/PhysRevLett.130.036201
[20]. J.-J. Liu, J.-J. Fu, T. Liu, X. Shen, F.-X. Cheng, The modulation effect of an electronrich guest on the luminescence of naphthalene diimide-based metal–organic frameworks, Inorg. Chem. Front. 9 (15) (2022) 3898–3906, https://doi.org/10.1039/D2QI00768A
[21]. D.W. Dixon, N.B. Thornton, V. Steullet, T. Netzel, Effect of DNA Scaffolding on Intramolecular Electron Transfer Quenching of a Photoexcited Ruthenium(II) Polypyridine Naphthalene Diimide, Inorg. Chem. 38 (24) (1999) 5526–5534, https://doi.org/10.1021/ic971446s
[22]. F. Chaignon, M. Falkenstrom, S. Karlsson, E. Blart, F. Odobel, L. Hammarstrom, Very large acceleration of the photoinduced electron transfer in a Ru $(bpy)_3$–naphthalene bisimide dyad bridged on the naphthyl core, Chem. Commun. (2006) 64–66 https://doi.org/10.1039/B615085C
[23]. R.K. Dubey, M. Niemi, K. Kaunisto, K. Stranius, A. Efimov, N.V. Tkachenko, H. Lemmetyinen, Excited-State Interaction of Red and Green Perylene Diimides with Luminescent Ru(II) Polypyridine Complex, Inorg. Chem. 52 (17) (2013) 9761–9773, https://doi.org/10.1021/ic400474b
[24]. Y. Nagao, T. Misono, Synthesis and Reactions of Perylenecarboxylic Acid Derivatives. VIII. Synthesis of N-Alkyl-3,4:9,10-Perylenetetracarboxylic Monoanhydride Monoimide, BCSJ 54 (4) (1981) 1191–1194, https://doi.org/10.1246/bcsj.54.1191
[25]. Z. Ji, Y. Wu, Photoinduced Electron Transfer Dynamics of Cyclometalated Ruthenium(II)–Naphthalenediimide Dyad at NiO Photocathode, J. Phys. Chem. C 117 (36) (2013) 18315–18324, https://doi.org/10.1021/jp405659m
[26]. O. Johansson, M. Borgstrom, R. Lomoth, M. Palmblad, J. Bergquist, L. Hammarstrom, L. Sun, B. Åkermark, Electron Donor− Acceptor Dyads Based on Ruthenium(II) Bipyridine and Terpyridine Complexes Bound to Naphthalenediimide, Inorg. Chem. 42 (9) (2003) 2908–2918, https://doi.org/10.1021/ic020420k
[27]. O. Johansson, H. Wolpher, M. Borgstrom, L. Hammarstrom, J. Bergquist, L. Sun, B. Åkermark, Intramolecular charge separation in a hydrogen bonded tyrosine–ruthenium(II)–naphthalene diimide triad, Chem. Commun. (2004) 194–195, https://doi.org/10.1039/B308101J
[28]. A. Baron, C. Herrero, A. Quaranta, M.-F. Charlot, W. Leibl, B. Vauzeilles, A. Aukauloo, Efficient electron transfer through a triazole link in ruthenium(II) polypyridine type complexes, Chem. Commun. 47 (39) (2011) 11011–11013, https://doi.org/10.1039/c1cc13683f

[29]. F. Nastasi, G.L. Ganga, S. Campagna, Z. Syrgiannis, F. Rigodanza, S. Vitale, A. Licciardello, M. Prato, Multichromophoric hybrid species made of perylene bisimide derivatives and Ru(II) and Os(II) polypyridine subunits, PCCP 19 (21) (2017) 14055–14065, https://doi.org/10.1039/c7cp01597f
[30]. E.R. dos Santos, J. Pina, T. Venancio, C. Serpa, J.M.G. Martinho, R.M. Carlos, Photoinduced Energy and Electron-Transfer Reactions by Polypyridine Ruthenium (II) Complexes Containing a Derivatized Perylene Diimide, J. Phys. Chem. C 120 (40) (2016) 22831–22843, https://doi.org/10.1021/acs.jpcc.6b06693
[31]. K. Kodama, A. Kobayashi, T. Hirose, Synthesis and spectral properties of ruthenium (II) complexes based on 2,2′-bipyridines modified by a perylene chromophore, Tetrahedron Lett. 54 (40) (2013) 5514–5517, https://doi.org/10.1016/j.tetlet.2013.07.150
[32]. N.E. Aksakal, H.H. Kazan, E.T. Eçik, F. Yuksel, A novel photosensitizer based on a ruthenium(II) phenanthroline bis(perylenediimide) dyad: synthesis, generation of singlet oxygen and in vitro photodynamic therapy, New J. Chem. 42 (21) (2018) 17538–17545, https://doi.org/10.1039/c8nj02944j
[33]. A. Prodi, C. Chiorboli, F. Scandola, E. Iengo, E. Alessio, R. Dobrawa, F. Würthner, Wavelength-Dependent Electron and Energy Transfer Pathways in a Side-to-Face Ruthenium Porphyrin/Perylene Bisimide Assembly, J. Am. Chem. Soc. 127 (5) (2005) 1454–1462, https://doi.org/10.1021/ja045379u
[34]. M.S. Rodríguez-Morgade, T. Torres, C. Atienza-Castellanos, D.M. Guldi, Supramolecular Bis(rutheniumphthalocyanine)− Perylenediimide Ensembles: Simple Complexation as a Powerful Tool toward Long-Lived Radical Ion Pair States, J. Am. Chem. Soc. 128 (47) (2006) 15145–15154, https://doi.org/10.1021/ja0622195
[35]. A. Amati, M. Natali, M.T. Indelli, E. Iengo, F. Würthner, Photoinduced Energy- and Electron-Transfer Processes in a Side-to-Face Ru^{II}-Porphyrin/Perylene-bisimide Array, ChemPhysChem 20 (17) (2019) 2195–2203, https://doi.org/10.1002/cphc.201900611
[36]. Photochemistry and Photophysics, https://www.wiley.com/en-us/Photochemistry+and+Photophysics%3A+Concepts%2C+Research%2C+Applications-p-9783527671045 (accessed 10 January 2023).
[37]. M. Montalti, A. Credi, L. Prodi, Handbook of Photochemistry (3rd ed.), CRC Press/ Taylor&Francis., 2006, https://doi.org/10.1201/9781420015195
[38]. A.C. Bhasikuttan, M. Suzuki, S. Nakashima, T. Okada, Ultrafast Fluorescence Detection in Tris(2,2‘-bipyridine)ruthenium(II) Complex in Solution: Relaxation Dynamics Involving Higher Excited States, J. Am. Chem. Soc. 124 (28) (2002) 8398–8405, https://doi.org/10.1021/ja026135h
[39]. N.A. Lee, K.T. Ngo, G.E. Gilligan, M. Lamberto, J. Rochford, Non-innocent ligand flavone and curcumin inspired ruthenium photosensitizers for solar energy conversion, PCCP 23 (31) (2021) 16516–16524, https://doi.org/10.1039/D1CP01853A
[40]. K.T. Ngo, N.A. Lee, S.D. Pinnace, J. Rochford, Engineering of Ruthenium(II) Photosensitizers with Non-Innocent Oxyquinolate and Carboxyamidoquinolate Ligands for Dye-Sensitized Solar Cells, Chem. – Eur. J. 23 (31) (2017) 7497–7507, https://doi.org/10.1002/chem.201605991
[41]. J.L. Boyer, J. Rochford, M.-K. Tsai, J.T. Muckerman, E. Fujita, Ruthenium complexes with non-innocent ligands: Electron distribution and implications for catalysis, Coord. Chem. Rev. 254 (3–4) (2010) 309–330, https://doi.org/10.1016/j.ccr.2009.09.006
[42]. C. Bhaumik, D. Saha, S. Das, S. Baitalik, Synthesis, Structural Characterization, Photophysical, Electrochemical, and Anion-Sensing Studies of Luminescent Homoand Heteroleptic Ruthenium(II) and Osmium(II) Complexes Based on Terpyridylimidazole Ligand, Inorg. Chem. 50 (24) (2011) 12586–12600, https://doi.org/10.1021/ic201610w
[43]. J. Karges, S. Kuang, F. Maschietto, O. Blacque, I. Ciofini, H. Chao, G. Gasser,

Rationally designed ruthenium complexes for 1- and 2-photon photodynamic therapy, Nat. Commun. 11 (2020) 3262, https://doi.org/10.1038/s41467-020-16993-0
[44]. Z.-B. Zheng, Q.-Y. Huang, Y.-F. Han, J. Zuo, Y.-N. Ma, Ruthenium(II) complexbased chemosensors for highly sensitive and selective sequential recognition of copper ion and cyanide, Sens. Actuators B Chem. 253 (2017) 203–212, https://doi.org/10.1016/j.snb.2017.06.145
[45]. M. Kaufmann, C. Müller, A.A. Cullen, M.P. Brandon, B. Dietzek, M.T. Pryce, Photophysics of Ruthenium(II) Complexes with Thiazole π-Extended Dipyridophenazine Ligands, Inorg. Chem. 60 (2) (2021) 760–773, https://doi.org/10.1021/acs.inorgchem.0c02765
[46]. F.J.R. Cerpentier, J. Karlsson, R. Lalrempuia, M.P. Brandon, I.V. Sazanovich, G. M. Greetham, E.A. Gibson, M.T. Pryce, Ruthenium Assemblies for CO2 Reduction and H2 Generation: Time Resolved Infrared Spectroscopy, Spectroelectrochemistry and a Photocatalysis Study in Solution and on NiO, Front. Chem. 9 (2021), https://doi.org/10.3389/fchem.2021.795877
[47]. P. Pal, S. Mukherjee, D. Maity, S. Baitalik, Synthesis, Photophysics, and Switchable Luminescence Properties of a New Class of Ruthenium(II)–Terpyridine Complexes Containing Photoisomerizable Styrylbenzene Units, ACS Omega 3 (10) (2018) 14526–14537, https://doi.org/10.1021/acsomega.8b01927
[48]. M.K. Brennaman, J.H. Alstrum-Acevedo, C.N. Fleming, P. Jang, T.J. Meyer, J. M. Papanikolas, Turning the $[Ru(bpy)_2dppz]^{2+}$ Light-Switch On and Off with Temperature, J. Am. Chem. Soc. 124 (50) (2002) 15094–15098, https://doi.org/10.1021/ja0279139
[49]. A.A. Cullen, C. Long, M.T. Pryce, Explaining the role of water in the "light-switch" probe for DNA intercalation: Modelling water loss from $[Ru(phen)_2(dppz)]^{2+}\cdot 2H_2O$ using DFT and TD-DFT methods, J. Photochem. Photobiol. Chem. 410 (2021), 113169, https://doi.org/10.1016/j.jphotochem.2021.113169
[50]. Q. Sun, B. Dereka, E. Vauthey, L.M.L. Daku, A. Hauser, Ultrafast transient IR spectroscopy and DFT calculations of ruthenium(II) polypyridyl complexes, Chem. Sci. 8 (1) (2016) 223–230, https://doi.org/10.1039/c6sc01220e
[51]. M. Abrahamsson, M. Jager, T. Osterman, L. Eriksson, P. Persson, H.C. Becker, O. Johansson, L. Hammarstrom, A 3.0 μs Room Temperature Excited State Lifetime of a Bistridentate Ru^{II}– Polypyridine Complex for Rod-like Molecular Arrays, J. Am. Chem. Soc. 128 (39) (2006) 12616–12617, https://doi.org/10.1021/ja064262y
[52]. W.T. Pollard, R.A. Mathies, Analysis of Femtosecond Dynamic Absorption Spectra of Nonstationary States, Annu. Rev. Phys. Chem. 43 (1992) 497–523, https://doi.org/10.1146/annurev.pc.43.100192.002433
[53]. M.-H. Ha-Thi, G. Burdzinski, T. Pino, P. Changenet, Transient Absorption Spectroscopy in Inorganic Systems, Springer Handb. Inorg. Photochem. (2022) 107–130, https://doi.org/10.1007/978-3-030-63713-2_5
[54]. S. Backus, C.G. Durfee III, M.M. Murnane, H.C. Kapteyn, High power ultrafast lasers, Rev. Sci. Instrum. 69 (3) (1998) 1207–1223, https://doi.org/10.1063/1.1148795
[55]. D. Strickland, G. Mourou, Compression of amplified chirped optical pulses, Opt. Commun. 56 (3) (1985) 219–221, https://doi.org/10.1016/0030-4018(85)90120-8
[56]. U. Keller, G.W. 'tHooft, W.H. Knox, J.E. Cunningham, Femtosecond pulses from a continuously self-starting passively mode-locked Ti:sapphire laser, Opt. Lett. 16 (13) (1991) 1022. https://doi.org/10.1364/OL.16.001022
[57]. W.E. Ford, P.V. Kamat, Photochemistry of 3,4,9,10-perylenetetracarboxylic dianhydride dyes. 3. Singlet and triplet excited-state properties of the bis(2,5-ditert-butylphenyl)imide derivative, J. Phys. Chem. 91 (25) (1987) 6373–6380, https://doi.org/10.1021/j100309a012

[58]. W.R. Ware, P.T. Cunningham, Fluorescence Lifetime and Fluorescence Enhancement of Perylene Vapor, J. Chem. Phys. 44 (11) (1966) 4364–4365, https://doi.org/10.1063/1.1726640
[59]. M. Zubiria-Ulacia, J.M. Matxain, D. Casanova, The role of CT excitations in PDI aggregates, PCCP 22 (28) (2020) 15908–15918, https://doi.org/10.1039/d0cp02344b
[60]. X. Fang, H. Ke, L. Li, M.-J. Lin, Structural insights into the aggregation-induced emission mechanism of naphthalene diimide solids, Dyes Pigm. 145 (2017) 469–475, https://doi.org/10.1016/j.dyepig.2017.06.044
[61]. I.A. Howard, F. Laquai, P.E. Keivanidis, R.H. Friend, N.C. Greenham, Perylene Tetracarboxydiimide as an Electron Acceptor in Organic Solar Cells: A Study of Charge Generation and Recombination, J. Phys. Chem. C 113 (50) (2009) 21225–21232, https://doi.org/10.1021/jp907633g
[62]. J. Hu, X. Liu, K. Wang, M. Wu, H. Huang, D. Wu, J. Xia, A perylene diimide electron acceptor with a triphenylamine core: promoting photovoltaic performance via hot spin-coating, J. Mater. Chem. C 8 (6) (2020) 2135–2141, https://doi.org/10.1039/c9tc05713g
[63]. Y. Zagranyarski, L. Chen, Y. Zhao, H. Wonneberger, C. Li, K. Müllen, Facile Transformation of Perylene Tetracarboxylic Acid Dianhydride into Strong DonorAcceptor Chromophores, Org. Lett. 14 (21) (2012) 5444–5447, https://doi.org/10.1021/ol302519q
[64]. C. Falkenberg, C. Uhrich, B. Maennig, M.K. Riede, K. Leo, 1,4,5,8-Naphthalenetetracarboxylic dianhydride as transparent electron transport material in organic p-i-n solar cells, Proc. SPIE 6999 (2008) 69990S, https://doi.org/10.1117/12.782340
[65]. G.D. Pantos, Naphthalenediimide and its Congeners: From Molecules to Materials, RSC Publ. (2017), https://doi.org/10.1039/9781782621386
[66]. D.C. Grills, M.W. George, Handbook of Vibrational Spectroscopy, 2006.
[67]. M. Towrie, A.W. Parker, W. Shaikh, P. Matousek, Tunable picosecond optical parametric generator-amplifier system for time resolved Raman spectroscopy, Meas. Sci. Technol. 9 (5) (1998) 816, https://doi.org/10.1088/0957-0233/9/5/012
[68]. K.M. Omberg, J.R. Schoonover, J.A. Treadway, R.M. Leasure, R.B. Dyer, T. J. Meyer, Mid-Infrared Spectrum of $[Ru(bpy)_3]^{2+}$*, J. Am. Chem. Soc. 119 (30) (1997) 7013–7018, https://doi.org/10.1021/ja970511u
[69]. N. Pearce, K.E.A. Reynolds, S. Kayal, X.Z. Sun, E.S. Davies, F. Malagreca, C. J. Schürmann, S. Ito, A. Yamano, S.P. Argent, M.W. George, N.R. Champness, Selective photoinduced charge separation in perylenediimide-pillar[5]arene rotaxanes, Nat. Commun. 13 (2022) 415, https://doi.org/10.1038/s41467-022-28022-3
[70]. A.J. Taylor, E.S. Davies, J.A. Weinstein, I.V. Sazanovich, O.V. Bouganov, S. A. Tikhomirov, M. Towrie, J. McMaster, C.D. Garner, Ultrafast Intramolecular Charge Separation in a Donor-Acceptor Assembly Comprising Bis(η^5-cyclopentadienyl)molybdenum Coordinated to an Ene-1,2-dithiolatenaphthalenetetracarboxylicdiimide Ligand, Inorg. Chem. 51 (24) (2012) 13181–13194, https://doi.org/10.1021/ic301436t
[71]. G.A. Farrow, M. Quick, S.A. Kovalenko, G. Wu, A. Sadler, D. Chekulaev, A.A. P. Chauvet, J.A. Weinstein, N.P. Ernsting, On the intersystem crossing rate in a Platinum(II) donor–bridge–acceptor triad, PCCP 23 (38) (2021) 21652–21663, https://doi.org/10.1039/d1cp03471e
[72]. I.V. Sazanovich, M.A.H. Alamiry, J. Best, R.D. Bennett, O.V. Bouganov, E.S. Davies, V.P. Grivin, A.J.H.M. Meijer, V.F. Plyusnin, K.L. Ronayne, A.H. Shelton, S. A. Tikhomirov, M. Towrie, J.A. Weinstein, Excited State Dynamics of a Pt^{II} Diimine Complex bearing a Naphthalene-Diimide Electron Acceptor, Inorg. Chem. 47 (22) (2008) 10432–10445, https://doi.org/10.1021/ic801022h

[73]. J.S. O'Neill, L. Kearney, M.P. Brandon, M.T. Pryce, Design components of porphyrin-based photocatalytic hydrogen evolution systems: A review, Coord. Chem. Rev. 467 (2022), 214599, https://doi.org/10.1016/j.ccr.2022.214599
[74]. S.K. Lee, Y. Zu, A. Herrmann, Y. Geerts, K. Müllen, A.J. Bard, Electrochemistry, Spectroscopy and Electrogenerated Chemiluminescence of Perylene, Terrylene, and Quaterrylene Diimides in Aprotic Solution, J. Am. Chem. Soc. 121 (14) (1999) 3513–3520, https://doi.org/10.1021/ja984188m
[75]. A. Isakova, S. Karuthedath, T. Arnold, J.R. Howse, P.D. Topham, D.T.W. Toolan, F. Laquai, L. Lüer, Efficient long-range electron transfer processes in polyfluorene–perylene diimide blends, Nanoscale 10 (23) (2018) 10934–10944, https://doi.org/10.1039/c8nr01064a
[76]. G. Hu, H.S. Kang, A.K. Mandal, A. Roy, C. Kirmaier, D.F. Bocian, D. Holten, J. S. Lindsey, Synthesis of arrays containing porphyrin, chlorin, and perylene-imide constituents for panchromatic light-harvesting and charge separation, RSC Adv. 8 (42) (2018) 23854–23874, https://doi.org/10.1039/c8ra04052d
[77]. C. Mari, H. Huang, R. Rubbiani, M. Schulze, F. Würthner, H. Chao, G. Gasser, Evaluation of Perylene Bisimide-Based Ru^{II} and Ir^{III} Complexes as Photosensitizers for Photodynamic Therapy, Eur. J. Inorg. Chem. 12 (2017) 1745–1752, https://doi.org/10.1002/ejic.201600516
[78]. Y. Yang, X. Zou, Y. Sun, F. Chen, J. Zhao, S. Gou, Naphthalene Diimide Functionalized Half-Sandwich Ru(II) Complexes as Mitochondria-Targeted Anticancer and Antimetastatic Agents, Inorg. Chem. 62 (24) (2023) 9649–9660, https://doi.org/10.1021/acs.inorgchem.3c01125
[79]. R.D. Costa, F.J. Cespedes-Guirao, E. Ortí, H.J. Bolink, J. Gierschner, F. Fernandez-Lazaro, A. Sastre-Santos, Efficient deep-red light-emitting electrochemical cells based on a perylenediimide-iridium-complex dyad, Chem. Commun. 26 (2009) 3886–3888, https://doi.org/10.1039/b905367k
[80]. K. Qvortrup, A.D. Bond, A. Nielsen, C.J. McKenzie, K. Kilså, M.B. Nielsen, Perylenediimide—metal ion dyads for photo-induced electron transfer, Chem. Commun. 17 (2008) 1986–1988, https://doi.org/10.1039/b719243f
[81]. J.D. Koenig, W.E. Piers, G.C. Welch, Promoting photocatalytic CO_2 reduction through facile electronic modification of N-annulated perylene diimide rhenium bipyridine dyads, Chem. Sci. 13 (4) (2022) 1049–1059, https://doi.org/10.1039/d1sc05465a
[82]. X. Lu, W. Zhu, Y. Xie, X. Li, Y. Gao, F. Li, H. Tian, Near-IR Core-Substituted Naphthalenediimide Fluorescent Chemosensors for Zinc Ions: Ligand Effects on PET and ICT Channels, Chem. Eur. J. 16 (28) (2010) 8355–8364, https://doi.org/10.1002/chem.201000461
[83]. G.-B. Li, J.-H. Shi, R.-K. Pan, S.-G. Liu, Synthesis, crystal structure, and fluorescence property of cobalt(II) and manganese(II) complexes based on N, N′-bis (4-pyridylmethyl)naphthalene diimide, Inorg. Nano-Met. Chem. 47 (7) (2017) 1017–1022, https://doi.org/10.1080/24701556.2016.1278555
[84]. V. Pirota, E. Lunghi, A. Benassi, E. Crespan, M. Freccero, F. Dora, Selective Binding and Redox-Activity on Parallel G-Quadruplexes by Pegylated Naphthalene Diimide-Copper Complexes, Molecules 26 (16) (2021) 5025, https://doi.org/10.3390/molecules26165025
[85]. Y. Liu, Z. Li, Y. Han, Z. Ji, H. Li, Y. Liu, Y. Wei, C. Chen, X. He, M. Wu, Highly Stable Metal–Organic Framework with Redox-Active Naphthalene Diimide Core as Cathode Material for Aqueous Zinc-Ion Batteries, ChemSusChem 16 (7) (2023), https://doi.org/10.1002/cssc.202202305

CHAPTER 3

Ruthenium (II)-Naphthalene Diimide Photosensitiser in Catalytic Hydrogen Production Probed by Time-Resolved Infrared Spectroelectrochemistry

Martyna Bartusiak[1], Martin Pižl[2,4], Partha Malakar[3], Sayantan Bhattacharya[3], František Hartl[4], Mary T. Pryce[1]

[1]School of Chemical Sciences, Dublin City University, Ireland

[2]Department of Inorganic Chemistry, University of Chemistry and Technology Prague, Technická 5, 16628 Prague, Czech Republic

[3]Rutherford Appleton Laboratory, Harwell Campus, Didcot OX11 0QX, UK

[4]Department of Chemistry, University of Reading, Whiteknights, Reading RG6 6DX, UK

3.1 Abstract

To understand and highlight fundamental processes like charge accumulation and charge separation in artificial photosynthetic assemblies for hydrogen evolution, the novel ruthenium-naphthalene diimide donor-acceptor dyad **RuNDI^{2+}**, [Ru(bpy)$_2$(phen-6-NDI-octyl)]$^{2+}$ (bpy = 2,2'-bipyridine, phen = 1,10-phenanthroline), was synthesised. The complex was studied with a range of techniques, including time-resolved infrared spectroscopy (TRIR), nanosecond transient absorption spectroscopy (ns-TAS) and spectroelectrochemistry. This study focussed on evaluating the potential of a **RuNDI^{2+}** photosensitiser for hydrogen evolution and simulating the photocatalytic environment by combining ns-transient absorption spectroscopy (ns-TAS) as well as ps-ns time-resolved infrared (TRIR) laser spectroscopy with spectroelectrochemistry (TRIR-SEC). This approach is one of the first examples of the successful application of ps-TRIR-SEC in probing intermediates formed during charge-transfer photocatalysis. Prior to the TRIR-SEC studies, the photodynamic process in **RuNDI^{2+}** was probed using conventional ps-TRIR spectroscopy by monitoring the absorption of carbonyl groups on the NDI unit. Following excitation at 420 nm, the IR ν(C=O) bands at 1723, 1711, 1690 and 1674 cm^{-1} depleted within the pulse, with new bands forming at 1645 and 1612 cm^{-1}. The latter set has been assigned to the charge-separated species, **[Ru^{III}-NDI^{-}]$^{2+}$** formed rapidly following optical excitation. The lifetimes for both the charge separation and charge recombination processes were determined to be τ_{CS} = 51 ps and τ_{CR} = 266 ps, respectively. When **RuNDI^{2+}** was singly reduced within an optically transparent thin-layer electrochemical OTTLE cell, new ν(C=O) bands of **RuNDI^{+}** were observed at 1641, 1606 and 1515 cm^{-1}. The concomitant NDI-localised reduction of this led to generation of **RuNDI**, with NDI ν(C=O) bands further red-shifted to 1596 and 1530 cm^{-1}.

Photoexcitation of the solution containing **RuNDI** at 600 nm gave transient species with bands at 1625, 1576 and 1506 cm^{-1}, which decayed on the picosecond time scale to the ground state. These experimental results were evaluated with the aid of DFT and TD-DFT calculations. Photocatalysis was carried out using the $[Pt(DMSO)_2I_2]$ catalyst, and reached TON of 64 within 6 h. Additionally, recycling of the photocatalytic solution for hydrogen production was assessed, with continued generation of hydrogen observed over three cycles.

Contribution:

In this chapter, I was responsible for writing all sections and analysing the obtained results. I characterised the complex using a range of techniques and probed the photophysics using nanosecond transient absorption and emission spectroscopy, and in addition I performed electrochemical and spectroelectrochemical measurements. TRIR measurements were conducted at the Rutherford Appleton Laboratory in the UK, in collaboration with Prof. Hartl. I carried out photocatalytic experiments and processed all data using the Glotaran software.

3.2 Introduction

Climate change and increasing global energy consumption are primarily caused by the overdependence on fossil fuels, and these are significant threats to our planet as the burning of fossil fuels generates around 75% of the total greenhouse gas emissions and notably contributes to approximately 90% of total CO_2 emissions [1]. The excessive use of fossil fuels causes negative effects on natural habitats, human and animal well-being, environmental diversity, deforestation, and air pollution. In 2023, the International Energy Agency (IEA) reported that there were approximately 37.4 billion tonnes of carbon emitted [2]. A thorough analysis of current data indicates that the world is expected to surpass the global temperature increase limit of 1.5°C, which was proposed to reduce and minimise the adverse impact on climate change [3, 4]. When temperatures and greenhouse gas emissions continue to rise or remain at current levels, it will be challenging to adhere to the Paris Agreement temperature target [4, 5]. The transition away from fossil fuels towards renewable forms of energy must be ramped up to reach net-zero emissions by 2050 [3 – 5]. Consequently, immediate action is needed, and hence, the development of novel materials, is urgently required. Light-harvesting compounds that can harvest light energy from the sun's spectrum have the potential to be at the forefront of current approaches to limit the use of fossil fuels as we work towards "Artificial Photosynthesis" and a "Hydrogen Economy".

To design efficient artificial photosynthetic assemblies for hydrogen evolution, it is essential to understand the capture, storage, and conversion of solar energy. Charge separation plays a significant role in photocatalytic assemblies for hydrogen production [6]. If the process of charge separation is not efficient, it can adversely affect the amount of hydrogen evolved. Charge accumulation is also important because it involves the accumulation of separated electrons in specific sites within the photocatalytic systems [6 – 8]. In designing materials for high hydrogen production, the following key factors should be considered, and these are selection of a photosensitising unit that absorbs light in the visible region, prevention of charge recombination, and supply of the continuous flow of electrons by sacrificial electron donors under homogenous conditions to drive the desired reduction of water molecules.

In artificial photosynthetic processes, two general approaches are frequently employed: intramolecular and intermolecular. Under homogeneous conditions, a photosensitiser, a catalytic centre and a sacrificial electron donor are required to cooperate. In an

intramolecular assembly, a molecular bridge connects the individual moieties by covalent bonds, whereas in an intermolecular approach, the separate components interact by diffusion that may limit the efficiency of the electron transfer step and decrease the quantity of hydrogen evolved [9]. The pioneering example of a ruthenium complex designed for hydrogen generation was published in 1977 by Lehn and Sauvage [10, 11]. They employed $[Ru(bpy)_3]^{2+}$ as a photosensitiser, triethylethanolamine (TEOA) as a sacrificial electron donor, $K_2[PtCl_4]$ as the catalyst and $[Rh(bpy)_3]^{3+}$ as an electron mediator for water reduction. The mixture was irradiated at $\lambda_{exc} > 400$ nm and generated a turnover number (TON) of 750 for hydrogen evolution.

O'Reilly et al. [12] reported a bimetallic intramolecular $RuPt_{dpph}$ complex based on 4,7-diphenyl-1,10-phenanthroline (dpph) peripheral ligands and a 2,2':5',2''-terpyridine (tpy) bridging ligand which under visible excitation (at 470 nm) yielded a TON = 54 for hydrogen evolution. A similar value (TON = 56) was reported by Rau et al. [13] for an intramolecular system where a ruthenium unit employed 4,4'-di-tert-butyl-2,2'-bipyridine as a peripheral ligand and it was linked by a tetrapyridophenazine bridge to the catalytic centre ($PdCl_2$). The amount of hydrogen evolved was affected by the concentration of TEA as the sacrificial electron donor and the irradiation times. Furthermore, the authors suggested that the photocatalytic activity of the system could further be improved by adjusting the HOMO-LUMO energy gap to alter orbital energies, which requires modifying the design of the bridging ligands or incorporating peripheral groups on the bipyridine [13].

In contrast, an intermolecular assembly designed by Natali and co-workers [14] used $[Ru(bpy)_3]^{2+}$ as a photosensitiser, ascorbic acid as a sacrificial electron donor and a cobalt (II) porphyrin catalyst ($Co(II)NMeTPyP^{4+}$, where $NMeTPyP^{4+}$ = meso-tetrakis(1-methylpyridinium-4-yl)-porphyrin), which resulted in impressive TONs for hydrogen, ranging from 269 to 725 (using 175 W Xenon arc lamp, cut-off at 400 nm). Cerpentier et al. [15] designed an intramolecular ruthenium system and examined its ability to produce hydrogen in a mixture of acetonitrile, triethylamine, and water (60:30:10) using a 470 nm LED. After 24 hours, the authors reported low TON = 81 for hydrogen evolution. However, Karnahl and co-workers [16] developed a heterodinuclear ruthenium complex $[(tbbpy)_2Ru\text{-}(tpphz)PdCl_2](PF_6)_2$, where tbbpy = 4,4'-di-tert-butyl-2,2'-bipyridine and tpphz = tetrapyridophenazine that performed better at TON = 238, which, while not substantial, is still greater than the previously aforementioned examples [12, 13, 15]. The TON values varied with the water content, with a maximum TON reported for solutions

composed of 15% of water, triethylamine, and acetonitrile (TON = 238 at 15% of water and TON = 153 at 2% of water). The positive impact of increased water content on photocatalysis was attributed to the presence of more stable charge-separated states being formed, consequently, the second charge transfer process was more efficient. At the same time, the authors substituted the hydrogen atoms in the bridging ligand with bromine $[(tbbpy)_2Ru(Br_2tpphz)PdCl_2](PF_6)_2$ in order to examine the impact of structural modification and the influence of electron-withdrawing groups on the photocatalytic activities. However, this led to a decrease in TON (94.2 at 7.1% of water) which was attributed to a slower electron transfer from the photosensitiser to the catalytic centre [16].

While both intra- and intermolecular approaches generate molecular hydrogen, the efficiency is dependent on multiple factors, including experimental parameters, photostability, light sources, instrumental set-up, and concentrations of not only the light-harvesting units and the catalysts but also the sacrificial electron donor. Moreover, in the literature, most studies focus only on the amount of hydrogen generated and there is a lack of detailed description of intermediates formed during the photocatalytic process.

Recently, Hagmeyer et al. [17] reported redox titrations using a ruthenium tris-diimine complex, which incorporated an alloxazine-based diamine ligand, together with DFT calculations. Their aim was to simulate photocatalytic conditions and identify the reduced intermediates generated during the process. This study confirmed that a long-lived excited state ^{3}MLCT, was localised on the alloxazine ligand and was assigned to a singly reduced species, which are photoactive intermediates for photocatalytic performance. The singly reduced form of the complex exhibited an absorption band extended towards near-IR at 610 nm, which was attributed to the D_9 doublet excited state (ILCT within the alloxazine ligand) [17].

The excited-state lifetimes of a photosensitiser are crucial factors in photocatalytic processes as electron transfer must occur from the ruthenium photosensitising unit to the NDI acceptor, followed by the electron transfer to the catalytic centre [18]. Incorporation of the NDI moiety into the ruthenium complex has the potential to extend the excited state lifetime by elongating the π-conjugation of the system and introducing a π-accepting ligand. The increased π-conjugation has the potential to stabilise the LUMO orbital and lead to an increase in the ^{3}MLCT-^{3}MC energy gap, which furthermore, results in the improved excited state lifetime and light absorption [19, 20]. Additionally, the presence

of π-accepting ligand could contribute to the increase in the energy gap between ^{3}MLCT and MC state because of their high ligand field strength [19, 20].

To address those important aspects of designing an efficient system for hydrogen generation, our focus was to introduce highly conjugated and electron-accepting moieties, namely 1,4,5,8-naphthalene-diimides (NDIs). NDIs contribute to an enhanced absorption of visible light [21], facilitate electron transfer [22] and consequently enhance photocatalytic processes for example photocatalytic degradation of cationic dyes, carbon dioxide reduction reactions and water-splitting processes [23 – 27]. Wang et al. [27] synthesised a number of metal-free NDI-based donor-acceptor-donor systems, which demonstrated good catalytic activity in reducing CO_2 to CO in the presence of water (168.6 μmol g_{cat}^{-1} 24 h^{-1}). The NDI moiety acted as an electron acceptor, which exhibited longer exciton lifetimes, low charge recombination rate and improved mobility of formed charge carriers. Further research conducted by the same group [28] reported organic NDI-based conjugated polymers with excellent stability over 330 h, during photocatalytic CO_2 reduction. They used a PNDI-BT (naphthalenediimide-based polymer with bithiophene moiety) without additional co-catalysts, which in the presence of molecular sieves, with H_2O/triethylamine yielded 214.8 μmol·g_{cat}^{-1} of CO and 61.4 μmol·g_{cat}^{-1} of CH_4 over 18 h following irradiation using a AM1.5G solar lamp at 1 sun intensity.

A novel ruthenium(II)-naphthalene diimide complex $[Ru(bpy)_2(phen\text{-}6\text{-}NDI\text{-}octyl)]^{2+}$ (**RuNDI^{2+}**, Figure 3.1) was synthesised as the photosensitiser for hydrogen evolution. The intermediates formed during photocatalysis and the processes governing charge accumulation on the NDI units within the ruthenium-NDI dyad were studied using TRIR-SEC and ns-TAS. TRIR-SEC opens new possibilities for studying the intermediates formed in photocatalysis and allows us to gain insights into the various factors which could limit the photosensitiser's overall effectiveness. During the course of these studies Carlos et al. [29] reported a reversible equilibrium for the population of ^{3}CS and ^{3}CSS in a Ru(phen)−naphthalene diimide (RupNDIp) dyad. The authors reported UV-vis spectroelectrochemical measurements and observed that the RupNDIp system exhibits distinct absorption bands attributed to $pNDIp^{\bullet-}$ (radical anion) and $pNDIp^{2-}$ (dianion). Furthermore, using excitation at 350 nm, ^{1}pNDIp was populated, which returned to the ground state via internal conversion. Another decay pathway of ^{1}pNDIp occurred via transfer of energy to the ^{1}MLCT of the ruthenium moiety, followed by intersystem crossing to the ^{3}MLCT. Following irradiation at 450 nm, the ^{3}MLCT was quenched due

to the equilibrium with the ^{3}CSS, $^3[Ru^{3+}(phen^{\bullet-})_2(pNDIp)]$ and $^3[Ru^{3+}(phen)_2(pNDIp^{\bullet-})]$ [29].

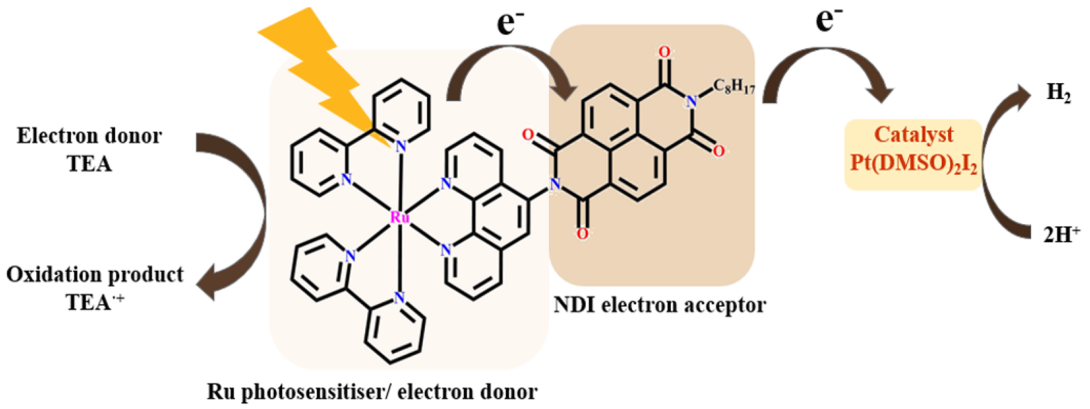


Figure 3.1 The structure of **RuNDI**$^{2+}$ complex composing of a ruthenium photosensitiser and NDI electron accepting moiety analysed in this study.

3.3 Results and discussion

3.3.1 Synthesis

The **RuNDI^{2+}** dyad was synthesised in three steps (see Figure 3.2 and Synthesis Section in Appendix A). Briefly, the precursor (NDI-octyl) was prepared by condensation of the commercially available 1,4,5,8-naphthalenetetracarboxylic dianhydride (NDA) with octylamine, following a procedure reported in the literature [30] (Figure 3.2, Step 1). The octylamine chain was used to prevent the formation of the di-substituted by-product and enhance the solubility of the final complex in organic solvents, as discussed in the literature review [31] and included in Chapter 2. The precursor of the light-harvesting moiety in the dyad, $[Ru(bpy)_2(phen\text{-}6\text{-}NH_2)]^{2+}$, was synthesised via a reaction between $[Ru(bpy)_2Cl_2]$ and 1,10-phenathrolin-6-amine. Ultimate **RuNDI^{2+}** was then obtained from the condensation of NDI-octyl with $[Ru(bpy)_2(phen\text{-}6\text{-}NH_2)]^{2+}$. All compounds synthesised in this study were characterised by ^{1}H-NMR and mass spectrometry. The formation of the final product was confirmed by the disappearance of the broad singlet at 6.9 ppm in the proton ^{1}H-NMR, which corresponded to the amine (NH_2) functional group. This indicated the complete consumption of $[Ru(bpy)_2\text{-}phen\text{-}6\text{-}NH_2]^{2+}$ in the reaction. Additionally, the aromatic protons on the NDI unit appeared as a multiplet in the range of 8 – 9 ppm and are deshielded because of the presence of electron-withdrawing imide groups. Furthermore, the singlet at 7.10 ppm in $[Ru(bpy)_2\text{-}(phen\text{-}6\text{-}NH_2)]^{2+}$ shifted downfield to approximately 8.7 ppm upon the attachment of the NDI moiety, corresponding to a phenanthroline proton near the nitrogen atom of NDI framework. The mass spectrum obtained for **RuNDI^{2+}** together with the isotope pattern confirmed successful synthesis of **RuNDI^{2+}**. The FTIR spectra of **RuNDI^{2+}** show four carbonyl stretching vibrations ($\nu_{C=O}$) at 1672, 1690, 1710 and 1725 cm^{-1}. Through thorough purification, the **RuNDI^{2+}** complex was non-emissive. DFT calculations determined two possible structures differing in the orientation of the alkyl chain on the NDI moiety. It has been concluded that structure B is more favourable by 0.66 kcal/mol (Figure SA3.9 and Table SA3.1 in Appendix A).

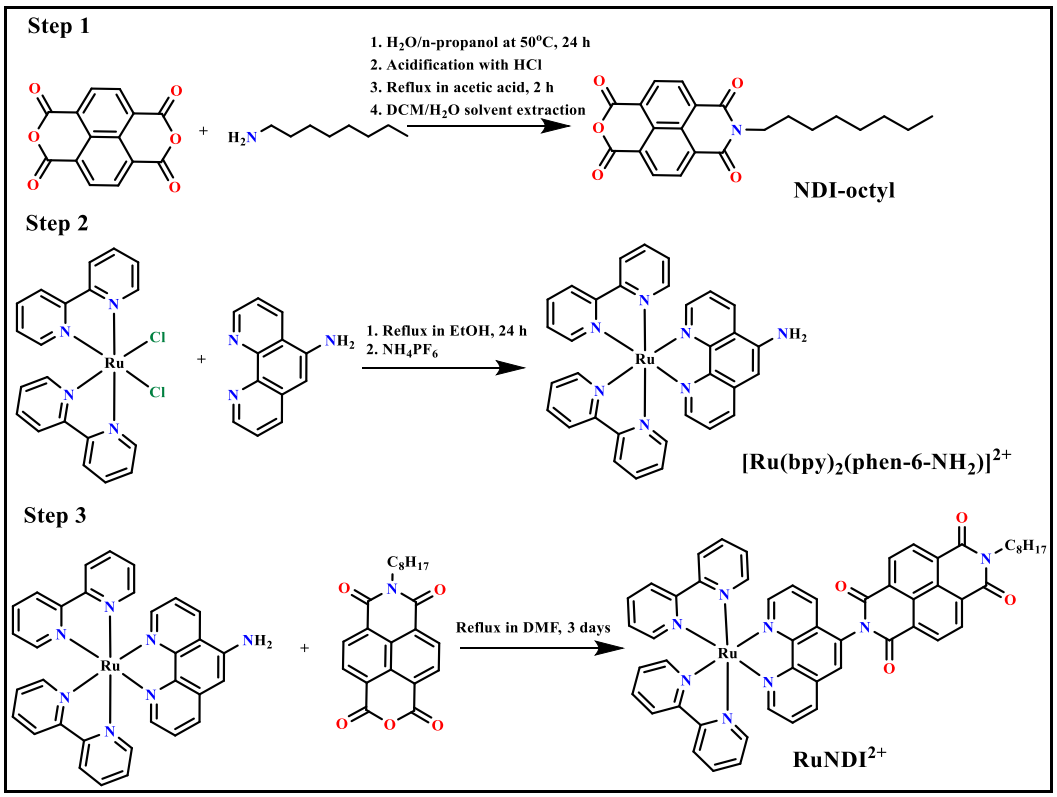


Figure 3.2 Synthetic scheme for the preparation of **RuNDI**$^{2+}$ and its corresponding reactants NDI-octyl and [Ru(bpy)$_2$(phen-6-NH$_2$)]$^{2+}$. PF_6^- counter anions are omitted for both the precursor and **RuNDI**$^{2+}$.

3.3.2 UV-vis spectroscopy and emission spectra

The UV-vis absorption spectrum for **RuNDI**$^{2+}$ is depicted in Figure 3.3, and the absorption bands observed at 235 and 296 nm are attributed to ligand-centred (LC) π-π* transitions occurring on both the bridging (phenanthroline moiety) and peripheral ligands (bipyridine units) [32]. This is consistent with the literature, where LC transitions typically occur at UV wavelengths below 300 nm [33]. The complex exhibits the characteristic features in the visible region associated with a metal-to-ligand charge transfer (MLCT) band at 450 nm, indicating transitions from the ruthenium metal centre to the bipyridine/phenanthroline ligand (d_π(Ru)→π*(phen) and d_π(Ru)→π*(bpy)) [33 – 35]. Moreover, strong π-π* transitions from the π-conjugated NDI framework are evident at 385, 360, and 345 nm [31, 36 – 40]. The electronic absorption spectrum of **RuNDI**$^{2+}$ was also supported by TD-DFT calculations. The calculated results are summarised in Figures SA3.17 and SA3.18 and Table SA3.3 (Appendix A). Mixed d_π(Ru)→π*(phen) and d_π(Ru)→π*(bpy) transitions, are calculated at 483 and 476 nm (HOMO→LUMO+1/LUMO+2) and 443 nm (HOMO–1→LUMO+1), forming a tail of the experimental absorption band at 450 nm that mainly belongs to other

d_π(Ru)→π*(phen) and d_π(Ru)→π*(bpy) MLCT excitations originating in HOMO–2 and calculated at 426 and 422 nm. The same applies for then other resolved MLCT absorption band at 430 nm, which is dominated by the d_π(Ru)→π*(phen) and d_π(Ru)→π*(bpy) transitions. The vibronically structured absorption band between 340 – 380 nm has been assigned to ligand-centred (IL) transitions π(NDI)→π*(NDI), which is consistent with the HOMO–3→LUMO excitation calculated at 379 nm. The UV absorption at 275 nm is dominated by mixed π(phen)/π(bpy)→π*(phen)/π*(bpy) intraligand transitions.

The standard reference used for comparison, $[Ru(bpy)_3]^{2+}$, exhibits broad phosphorescence at 615 nm with the lifetime of 890 ns [41]. However, no phosphorescence was detected for **RuNDI^{2+}**, regardless of the excitation wavelength employed (340 – 380, 420 and 450 nm). Borgstrom et al. [38] reported an analogous ruthenium-naphthalene diimide complex, a $Mn_2^{II,II}$ - Ru^{II}-NDI triad and similarly to our study the emission was significantly quenched by 95% due to the presence of the attached NDI. Other work such as by Dixon et al. [40] reported emissive ruthenium NDI system, with lifetimes of 70 ns and 415 ns in water, with the longer component assigned to a $[Ru(bpy)_3]^{2+}$ impurity. Baron et al. [42] reported a singlet state emission lifetime of 750 ns for a Ru-NDI system in acetonitrile. However, Johansson et al. [37] reported significantly shorter lifetimes in the range of 0.2 – 7.9 ns for their series of ruthenium-NDI complexes $[Ru^{II}(bpy)_2(bpy\text{-}X\text{-}NDI)$, where X = $-CH_2-$, tolylene, or phenylene.

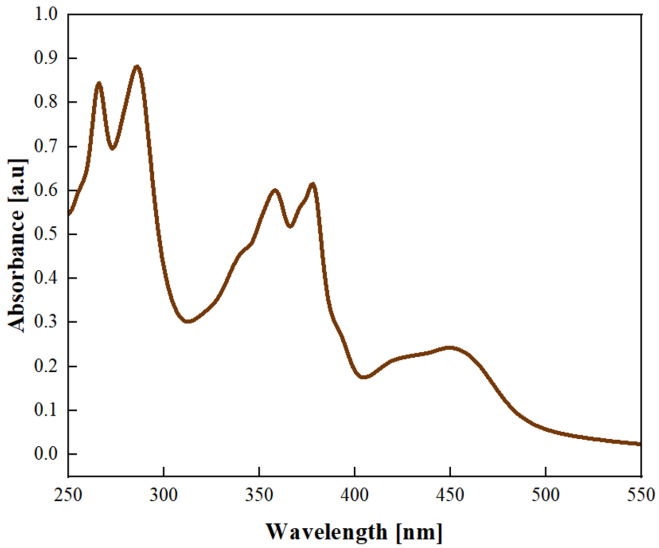


Figure 3.3 UV-vis absorption spectrum of 2 x 10^{-4} M **RuNDI^{2+}** in acetonitrile.

3.3.3 Electrochemistry

3.3.3.1 Cyclic Voltammetry

Conventional cyclic voltammetry (CV) of **RuNDI**$^{2+}$ was conducted in anhydrous DMF (Figure 3.4A), THF (Figure SA3.23, Appendix A) and acetonitrile (Figure SA3.24, Appendix A). The CV scans in DMF and acetonitrile are comparably well defined, whilst those in THF are affected by low analyte solubility and reveal adsorption features. The redox behaviour of **RuNDI**$^{2+}$ (Figure 3.4A) was studied together with the reference compounds $[(Ru(bpy)_2(phen\text{-}6\text{-}NH_2)]^{2+}$ and R_1-NDI-R_1 ($R_1 = C_8H_{17}$) compounds (Figure 3.4B) and the CV data are summarised in Table 3.1.

The cyclic voltammogram **RuNDI**$^{2+}$ displayed five reversible reduction wave and one quasi-reversible oxidation wave. The reduction waves at E° = –0.94 V (R1) and –1.41 V (R2) are consistent with the sequential double reduction of the NDI moiety attached to phen, in line with the reduction potentials of reference dioctyl-NDI (R_1-NDI-R_1), the NDI-localised LUMO of **RuNDI**$^{2+}$ (Figure SA3.18, Appendix A), the spin density on NDI in singly reduced **RuNDI**$^{+}$ (Figures SA3.10 and SA3.14, Appendix A) and the NDI^{2-} -based HOMO in two-electron-reduced **RuNDI** (Figure SA3.22, Appendix A). The remaining three reduction waves at E° = –1.80 V (R3), –1.97 V (R4) and –2.26 V correspond to the sequential one-electron reductions of the 2,2'-bipyridine ligands and the 1,10-phenanthroline ligand bearing donor NDI^{2-}, respectively. This assignment is also consistent with the CV of $[Ru(bpy)_2(phen\text{-}6\text{-}NH_2)]^{2+}$, where similarly the one-electron reduction of electron-rich phen-6-NH_2 is the most negative in the series. The reversible oxidation wave at E° = 0.89 V has been attributed to the $Ru^{2+/3+}$ redox couple.

This is supported by the literature [37], as a similar ruthenium-NDI complex, $[Ru^{II}(bpy)_2(bpy\text{-}NDI)]$ in which reduction of the NDI fragment was observed has potentials at $E_{1/2}$ = –0.97 and –1.37 V [37]. Additionally, the voltametric profile of **RuNDI**$^{2+}$ closely resembles that reported in the literature for $[Ru(phen)_3]^{2+}$ and $[Ru(bpy)_3]^{2+}$ complexes, presenting three reversible reductions of the bipyridine/phenanthroline complexes at approximately –1.7, –1.9 and –2.0 V while the oxidation potential was determined to be at 0.8 V [43]. Similar findings were reported by Frath et al. [44], for a ruthenium-NDI compound incorporating (4-aminophenyl)-2,2':6' ,2''-terpyridine. They reported reduction potentials at $E_{1/2}$ = –1.30 V/SCE and $E_{1/2}$ = –1.49 V/SCE, which were attributed to the reduction of terpyridine ligands. The reduction potential reported by the authors at $E_{1/2}$ = –0.52 V/SCE and $E_{1/2}$ = –0.95 V/SCE are

attributed to reduction of the NDI moiety. A single reversible wave in the positive region with $E_{1/2}$ = 0.79 V/SCE was attributed to the $Ru^{3+/2+}$ redox couple [44].

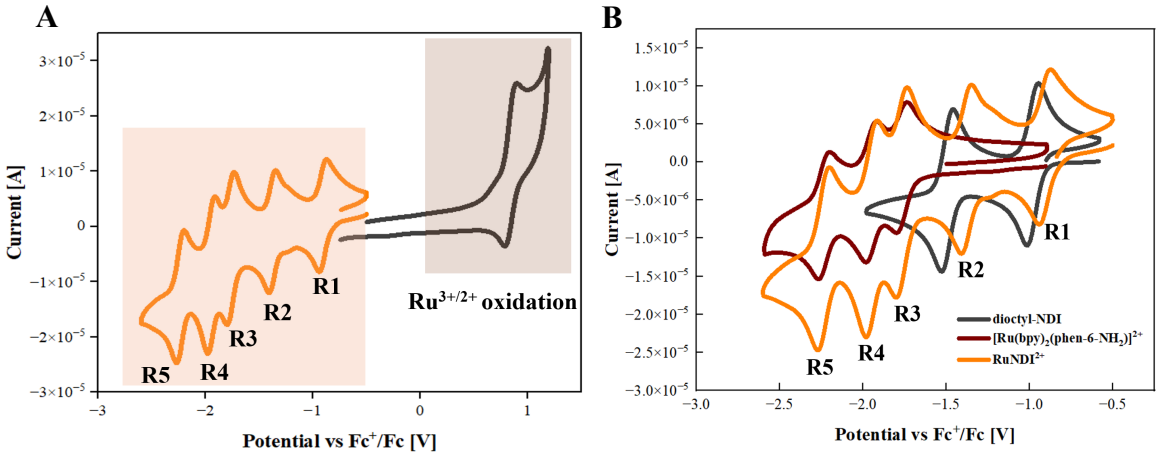


Figure 3.4 (A) Cyclic voltammogram of **RuNDI**$^{2+}$ in DMF/TBAH showing the reduction steps to **RuNDI**$^{+}$ (NDI-based, at R1), **RuNDI** (NDI-based, at R2), **RuNDI**$^{-}$ (bpy-based, at R3), **RuNDI**$^{2-}$ (bpy-based, at R4) and **RuNDI**$^{3-}$ (phen-based, at R5) and also the $Ru^{2+/3+}$ oxidation. **(B)** Overlay of the CVs of **RuNDI**$^{2+}$ (orange) and the individual reference compounds, namely dioctyl-NDI (black) and $[Ru(bpy)_2(phen\text{-}6\text{-}NH_2)]^{2+}$ (purple). Experimental conditions: GC disk working electrode, T = 298 K, v = 100 mV s^{-1}.

Table 3.1 Reduction potentials (vs. Fc^{+}/Fc) of **RuNDI**$^{2+}$, and reference compounds $[(Ru(bpy)_2(phen\text{-}6\text{-}NH_2)]^{2+}$ and R_1-NDI-R_1 (dioctyl-NDI).

Compound	E° (V) R1	E° (V) R2	E° (V) R3	E° (V) R4	E° (V) R5
RuNDI^{2+} [a]	–0.94	–1.41	–1.80	–1.97	–2.26
RuNDI^{2+} [b]	–0.94	–1.39	–1.78	–1.96	–2.23
RuNDI^{2+} [c]	–0.98	–1.45	–1.63	–1.83	–1.99
$[(Ru(bpy)_2(phen\text{-}6\text{-}NH_2)]^{2+}$ [a]	–	–	–1.80	–1.97	–2.26
R_1-NDI-R_1 [a]	–1.01	–1.52	–	–	–

[a] in DMF/TBAH. [b] in ACN/TBAH. [c] in THF/TBAH.

3.3.3.2 UV-vis spectroelectrochemistry

A UV-vis spectroelectrochemical study was conducted with **RuNDI**$^{2+}$ in acetonitrile to probe the initial reductions, which are based on the NDI-octyl moiety (R1 and R2, Figure 3.5A). The remaining reductions, steps R3 – R5, suffered from irreversible passivation of the Pt minigrid working electrode in the optically transparent thin-layer electrochemical (OTTLE) cell used to carry out the UV-vis SEC experiment. NDIs can undergo chemically or electrochemically reversible one- and two-electron reductions to form radical anions and dianions, which are stable in the absence of oxygen. They exhibit characteristic intense absorption in the visible and near-infrared region, making them efficient light harvesters [39, 45 – 48].

The one-electron reduction is accompanied by new absorption bands at 473, 589, 604, and 773 nm are assigned to **RuNDI**$^{+}$ (Figure 3.5A). These features are in line with the absorption bands of reduced species of the reference dioctyl-NDI compound (R_1-NDI-R_1, Figure SA3.25 in Appendix A). Further reduction resulted in the depletion of radical anion **RuNDI**$^{+}$ and led to the formation of the two-electron reduced **RuNDI** species, with new bands at 395, 417, 505 and 606 nm. During the reduction, the colour of the solution changed from orange to red for the monoanion to green for the two-electron-reduced species. The TD-DFT calculations were performed for one- and two-electron-reduced species (Figure SA3.16b, Appendix A). The analysis of calculated spectra of **RuNDI**$^{+}$ can be found in Figures SA3.19 and SA3.20 and Table SA3.4, while results for **RuNDI** are highlighted in Figures SA3.21 and SA3.22 and Table SA3.5, Appendix A.

Sazanovich et al. [48] reported UV-vis spectroelectrochemistry studies on a platinum-NDI compound (Pt(phen-NDI)Cl_2). The authors identified the NDI-monoanion with bands at 474, 588, 606, 693 and 770 nm and the NDI-dianion at 420, 519, 559 and 607 nm, attributed to the reduced NDI species. These bands observed following reduction of the Pt-NDI complex, are at similar wavelengths to that following reduction of **RuNDI**$^{2+}$.

Gosztola et al. [46] conducted a comprehensive study on aromatic diimide N,N′-bis(2,5-di-tert-butylphenyl)-naphthalene-1,8:4,5-tetracarboxydiimide, which focused on the properties and potential applications of the NDI radical anions formed. The authors highlighted that the radical anions, generated upon irradiation, were strong reductants, and could be utilised in photochemical electron transfer reactions. The neutral N,N′-bis(2,5-di-tert-butylphenyl)-naphthalene-1,8:4,5-tetracarboxydiimide exhibited absorption bands at 361 and 381 nm. Upon formation of the mono-anion, new bands were

observed at 474, 605, 698, and 777 nm. Upon further reduction, the dianion was formed with bands at 400, 423, 520, 563, 612 nm. They reported that the molar absorption coefficients of the radical anions are equal or greater to those of parent neutral species [46].

The spectroelectrochemical experiments were also carried out in tetrahydrofuran (THF). The **RuNDI^{2+}** was dissolved in THF and purged with nitrogen (Figure 3.5B). There were no notable shifts in the wavelength of absorption maxima of the reduced species in THF or acetonitrile used.

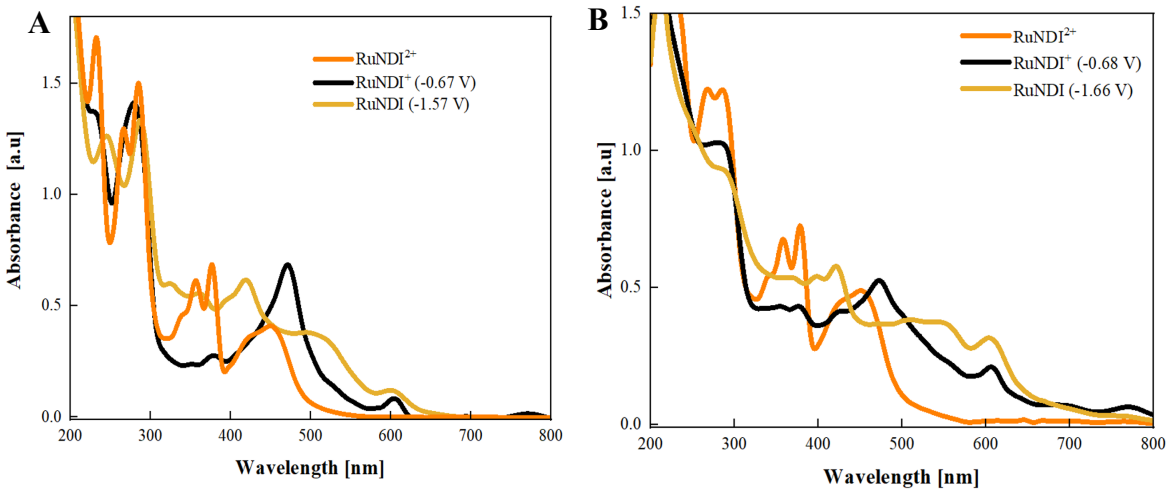


Figure 3.5 The UV-vis absorption spectra of **RuNDI^{2+}** (orange), one-electron-reduced **RuNDI^{+}** (black; formed at R1), and two-electron-reduced **RuNDI** (yellow; formed at R2) in **(A)** ACN/TBAH and **(B)** THF/TBAH. Experimental conditions: Pt minigrid working electrode, OTTLE cell, T = 298 K.

3.3.3.3 IR spectroelectrochemistry

The presence of carbonyl (C=O) stretching vibrations in the NDI unit serves as an excellent IR probe for studying electrochemically triggered or photoinduced electron transfer processes within the complex. The IR spectrum of parent **RuNDI^{2+}** exhibits four NDI-based carbonyl-stretching vibrations at 1672, 1690, 1710 and 1725 cm^{-1} and a combined ν(C=C/C=N) NDI-skeletal mode at 1583 cm^{-1} (see Figure 3.6). Upon the one-electron reductions R1 and R2 localised on NDI, as revealed by the CV study, these IR bands shift significantly to smaller wavenumbers (Figure 3.6). The one-electron-reduced species (**RuNDI^{+}**) displays two resolved ν(C=O) bands at 1603(s) and 1640(vs) cm^{-1} and the ν(C=C/C=N) band at 1515 cm^{-1}. These assignments are corroborated by DFT calculations, which indicated a red shift of the absorption bands and increase in absorption compared to **RuNDI^{2+}** (Figure SA3.13, Appendix A). The two-electron-reduced **RuNDI** formed at R2, displays IR ν(C=O) bands further red-shifted to 1523(m), 1543(sh) and 1600(s) cm^{-1}, in line with DFT calculations (Figure SA3.13, Appendix A). Further support comes from the literature, as Sazanovich et al. [48] reported for (Pt(phen-NDI)Cl_2) complex, bands at 1514, 1592, 1631, and 1660 cm^{-1} for the NDI monoanion [Pt(phen-NDI)Cl_2]$^{-}$, and for the dianion [Pt(phen-NDI)Cl_2]$^{2-}$ at 1519, 1599, 1629 and 1639 cm^{-1}. The authors assigned the band at 1583 cm^{-1}, which is also present in **RuNDI^{2+}**, to the ν(C=C) stretching vibration of the aromatic rings of the NDI based on the density functional theory calculations.

Another study conducted by the same research group [49] focused on a molybdenum ene-1,2-dithiolate-naphthalenetetracarboxylicdiimide complex. The FTIR spectrum of the compound revealed the corresponding skeletal and carbonyl stretching modes of neutral NDI at 1582, 1669, 1678, 1708, and 1717 cm^{-1} and singly reduced NDI moiety at 1514, 1592, 1629 cm^{-1}. These observations defined the LUMO localised on the NDI moiety, much like the LUMO of **RuNDI^{2+}**. The second reduction at R2 is undoubtedly also localised on NDI, forming a spin-doublet **RuNDI**.

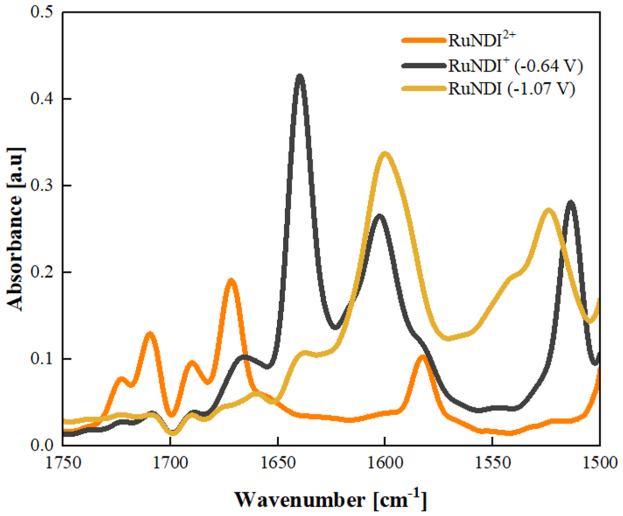


Figure 3.6 IR-SEC spectra of **RuNDI^{2+}** (orange), one-electron reduced **RuNDI^{+}** (black; formed at R1), and double-electron reduced **RuNDI** (yellow; formed at R2). Experimental conditions: Pt minigrid working electrode, OTTLE cell, THF/TBAH, T = 298 K.

3.4 Excited state properties of RuNDI^{2+}

3.4.1 Parent RuNDI^{2+}

TRIR measurements were used to study the excited-state dynamics of **RuNDI^{2+}** in solution. The C=O and aromatic ring stretching vibrations localised on the NDI moiety allow us to gain insights into the change in electron density following optical excitation and monitor the direction of charge transfer following excitation [49, 50]. To the best of our knowledge, there have been no TRIR studies reported for ruthenium(II) α-diimine complexes incorporating NDI moieties to date.

TRIR studies were conducted (see Figure 3.7 (A-C)) following excitation of **RuNDI^{2+}** at 365, 420 and 510 nm in acetonitrile. At excitation of 365 nm, the parent carbonyl stretching vibrations at 1725, 1714, 1690 and 1673 cm^{-1} deplete within the laser pulse, with the "grow in" of new carbonyl bands at lower stretching vibrations at 1612 and 1607 cm^{-1}. Similarly, at the excitation of 420 and 510 nm, the parent carbonyl stretching vibrations at 1723, 1711, 1690 and 1674 cm^{-1} deplete within the laser pulse, with the "grow in" of new carbonyl bands at lower stretching vibrations at 1612 and 1645 cm^{-1}. The latter set is assigned to the charge-separated species, [**Ru^{III}-NDI^{-}**]. The new transient bands exhibit characteristic and distinct stretching vibrations of one electron reduced species of the NDI, as observed in Figure 3.6. Notably, following excitation at 365 nm, the charge-separated state forms more rapidly in comparison to other excitations

wavelengths employed. Based on TDDFT analysis (Figure SA3.18, Table SA3.3 Appendix A), the excitation at 365 nm leads mainly to π(NDI)→π*(NDI) (HOMO–3→LUMO) transitions. The corresponding lifetimes for the charge separation and charge recombination processes were determined to be τ_{CS} = 17 ps and τ_{CR} = 142 ps (excitation at 365 nm). Following excitation at 420 and 510 nm, it can be observed that the transient bands exhibit the same intensity and form relatively slower than with high energy excitation. The lifetimes for the charge separation and charge recombination processes were determined to be τ_{CS} = 51 ps and τ_{CR} = 266 ps (excitation at 420 nm), respectively. The shift of the organic carbonyl to lower wavenumber indicates that charge transfer occurs from the ruthenium centre towards the phenanthroline ligand and to the remote NDI unit. TD-DFT calculations indicate that the HOMO→LUMO transition in **RuNDI**$^{2+}$ has zero oscillator strength (Table SA3.3). This indicates that there is likely zero spatial overlap between the HOMO and LUMO surfaces, attributed to zero transition dipole moment. Consequently, the charge-separated state cannot be populated directly upon photoinduced excitation. The population of the CS state takes place indirectly by first irradiating a higher energy MLCT state, followed by transition from Ru(II)→phen/bpy, which is populated directly by 420 nm excitation.

The standard reference compound, dioctyl-NDI was also analysed using TRIR with excitation at 365 nm (Figure SA3.29, Appendix A). The parent carbonyl stretching vibrations at 1670 and 1710 cm^{-1}, deplete within the laser pulse, accompanied by the formation of new carbonyl bands at lower frequencies at 1608 and 1647 cm^{-1}. These new bands persist beyond the experimental window, and their lifetime was determined using ns-TAS measurements (Figure SA3.31, Appendix A).

Scattergood et al. [51] reported TRIR studies of Pt(II) trans-acetylide system, NAP≡Pt(PBu$_3$)$_2$-Cl, where NAP = 4-ethynyl-N-octyl-1,8-naphthalimide. Excitation of the system at 400 nm, led to the formation of transient bands at 1500, 1560 and 1613 cm^{-1}, which were attributed to the reduced NAP. The authors assigned the excited state to a charge-transfer state, which was populated by the electron transfer from the metal-acetylide to the NAP electron acceptor. In addition, three transient bands at 1590, 1640 and 1950 cm^{-1} corresponded to the ^{3}NAP state. Due to the lack of TRIR data on Ru-NDI complexes in the literature, the closest analogue for comparison was a cyclopentadienyl molybdenum metal centre as the donor instead of ruthenium. Comparable observations were reported in the TRIR spectra reported by Taylor et al. [49] for the cyclopentadienyl molybdenum-NDI system. The authors carried out TRIR experiments following

excitation at 400 nm and reported transient bands at 1629, 1590, 1514 cm^{-1}, while ground state bleaches were evident at 1711 and 1673 cm^{-1}. Their conclusion agrees with the transient bands attributed to the NDI^{-} anion, indicating the Ru^{III}-NDI^{-} CS excited state, albeit with a substantially shorter lifetime of 1.88 ps. The second component with a lifetime of 22 ps was assigned to cooling of the vibrationally hot states and charge-separated states.

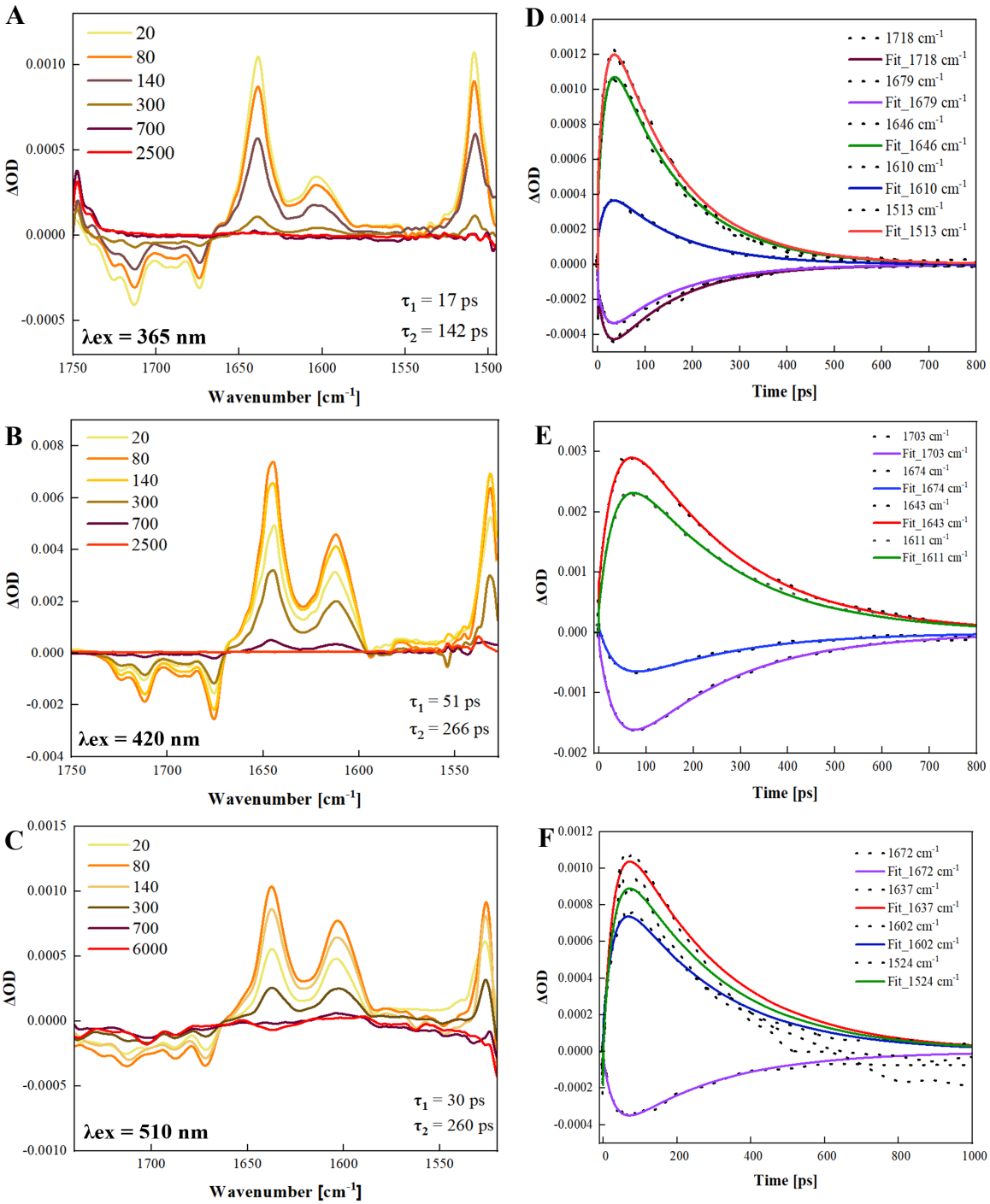


Figure 3.7(A) TRIR spectrum of **$RuNDI^{2+}$** upon excitation at 365 nm recorded in acetonitrile, **(B)** TRIR spectrum of **$RuNDI^{2+}$** upon excitation at 420 nm, **(C)** TRIR spectrum of **$RuNDI^{2+}$** upon excitation at 510 nm and **(D, E, F)** decay traces obtained in the TRIR for **$RuNDI^{2+}$**.

3.4.2 Electrochemically reduced RuNDI$^+$ and RuNDI

TRIR-SEC were performed to further characterise the **RuNDI**$^+$ and **RuNDI** species and assign their electronic transitions at 510 and 600 nm (cf. their UV-vis absorption spectra in Figure 3.5). The sample was initially reduced to **RuNDI**$^+$ in the OTTLE cell and subsequently excited at 510 nm. The **RuNDI**$^+$ species generated presents three distinct ground state bleach stretching vibrations bands at 1513, 1601 and 1639 cm^{-1} (Figure 3.8A). When this solution is irradiated with the 510-nm laser pulse, these three bands deplete within the laser pulse, with new transient vibrations observed at ~ 1502, ~ 1566, and ~ 1627 cm^{-1}, which decay over ~ 30 ps. Based on TDDFT analysis (Table SA3.4, Appendix A), the excitation at 510 nm leads mainly to π(NDI)→π*(NDI) (α–HOSO→α–LUSO+11, β–HOSO→β–LUSO+3) transitions, with a small contribution of the π(NDI)→π*(phen) (β–HOSO→β–LUSO+4) transition. In the case of the two electron-reduced species, **RuNDI**, the pump pulse was changed to 600 nm (Figure 3.8B). The two ground-state ν(C=O)-stretching vibrations at 1522 and 1597 cm^{-1} were bleached and new transient bands grew at 1506, 1576 and 1625 cm^{-1}. Similarly to excited **RuNDI**$^+$, the transient species of **RuNDI** decayed within 20 ps. Based on the similarity of these stretching vibrations to those of the ground-state precursor and TDDFT calculations, the excited states observed are localised on the NDI unit (HOMO→LUMO+9, Table SA3.5, Figure SA3.22, Appendix A).

Comparable results were obtained for singly reduced **RuNDI**$^+$ in acetonitrile (Figure SA3.28, Appendix A). Unfortunately, the 2e-reduced species could only be analysed using TRIR in THF and not in acetonitrile. Moreover, the complex passivated the spectroelectrochemical cell, resulting in weak signals.

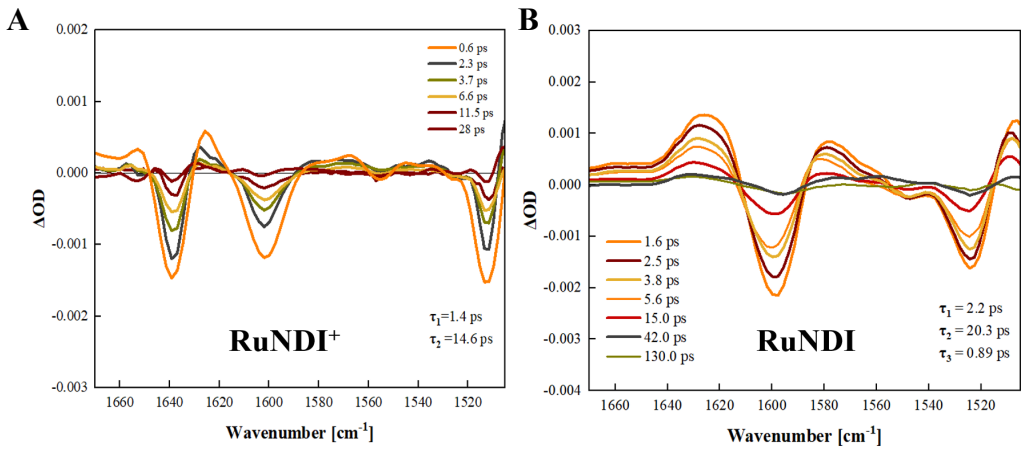


Figure 3.8 TRIR spectra recorded upon 510-nm photoexcitation of one-electron-reduced **RuNDI^{+} (A)** and 600-nm photoexcitation of two-electron-reduced **RuNDI (B)** in THF/TBAH, obtained stepwise in situ from **RuNDI^{2+}** using an adapted OTTLE cell.

3.4.3 Nanosecond transient absorption studies in solution

Nanosecond transient absorption studies were carried out to probe further the excited state properties of the **RuNDI^{2+}** complex. The study was carried out in acetonitrile following excitation at 355 nm, however no lifetimes were reported, indicating the absence of the triplet lifetime. This observation is different to the other NDI-based compounds reported in the literature, where excitation at 355 nm, has led to population of a ^{3}NDI state, and this will be discussed in the next section. The ruthenium precursor, as well as the reference dioctyl-NDI, were also examined using ns-TAS measurement following excitation at 355 nm. These results are presented in Figure SA3.30 and Figure SA3.31. The ns-TAS spectrum of the $[(Ru(bpy)_2(phen\text{-}6\text{-}NH_2)]^{2+}$ complex shows a ground-state bleach at 450 nm, together with an excited-state absorption observed at ~ 520 nm. The lifetime of the ^{3}MLCT state was determined to be 938 ns. The dioctyl-NDI compound exhibits bleaching of the ground state in the range of 360 – 380 nm, and distinct excited-state features at 475 and 600 nm, which are assigned to ^{3}NDI transient species ($\tau_t > 30$ µs) [52, 53].

For example, Chen and co-workers [52] reported the nanosecond TA spectrum (following excitation at 355 nm) for the NDI compound ($\tau_t = 70$ µs), with bleaching of the ground state in the region 350 – 380 nm range, and a broad excited state absorption in the 380 – 500 nm range. The analogous series of anthracene (An)−naphthalenediimide (NDI) electron donor−acceptor dyads namely 2-An-Ph-NDI, 9-An-Ph-NDI and 9-An-NDI (differing by the linkage of the anthracene moiety), had a lifetime of 321, 85 and 68 µs, respectively. Green et al. [50] reported the TAS spectrum following the light excitation at

355 nm for the N,N'-bis(2,2,6,6-tetramethyl-Ar-oxidopiperidin-4-yl)-l,4,5,8-naphthalenediimide compound, where they observed the generation of new transient bands at 460 and 485 nm. They reported that the ^{3}NDI transient species exhibited a significant sensitivity to oxygen, demonstrating a lifetime of 1 μs, which substantially increased to 25 μs when the solution was purged with nitrogen. The authors based their observations on the triplet state with similar characteristics to that of N-phenyl-1,8-naphthalen-imide which was reported in the literature [50, 53]. Johansson and co-workers [37] studied a similar ruthenium-NDI compound, to the **RuNDI^{2+}** discussed here. They reported a lifetime of 17 ns for the Ru^{III}-$NDI^{\bullet-}$ species following excitation at 460 nm. In their studies, they reported two routes for population of the Ru^{III}-$NDI^{\bullet-}$ species. They proposed that 80% of the charge separation occurred via electron transfer via population of ^{3}MLCT Ru(II)-to-bpy/phen with 20% via population of a ^{3} IL NDI. On the other hand, Carlos et al. [29] reported the ^{3}MLCT phosphorescence band (from $^3[Ru(phen^{\bullet-})_2(pNDIp)]^{2+}$ to $[Ru(phen)_2(pNDIp)]^{2+}$) at 610 nm for their RupNDIp complex with the emission lifetime of 540 ns, following excitation at 450 nm.

3.4.4 Nanosecond transient absorption studies under photocatalytic conditions

Nanosecond transient absorption studies were carried out under photocatalytic conditions (Figure 3.9 and Figure SA3.32 Appendix A) in a mixture of acetonitrile, triethylamine, and water (65:30:5 ratio), with $[Pt(DMSO)_2I_2]$ as the catalyst (see Photocatalysis results for more details). Under photocatalytic conditions, new transient bands were observed and tentatively assigned to the reduced NDI species (see Figure 3.9). Following excitation at 355 nm, a bleach was observed at 475 and 610 nm which correspond to the one electron reduced absorption feature for **RuNDI$^+$**, previously described in the UV-SEC results. Concomitant with the bleach, an excited state absorption feature was observed in the range of 500 – 520 nm and is attributed to the one electron reduced species of **$[Ru(bpy)_2(phen\text{-}6\text{-}NDI\text{-}octyl)]^+$** [54]. The presence of these species was further confirmed by UV-SEC experimental measurements (Figure SA3.26, in Appendix A). For example, Gotico et al. [55] reported ns-TAS studies for the trisbipyridine Ru-Re dyad linked through a triazole moiety in acetonitrile, in the presence of sodium ascorbate, following excitation at 460 nm. The authors attributed the transient band at 510 nm to the photoreduced ruthenium moiety.

In addition, for **RuNDI^{2+}**, when the transient band at ~ 515 nm decays to the ground state, new transient bands form at 395 and 415 nm, tentatively assigned to formation of the two-electron reduced species (**RuNDI**).

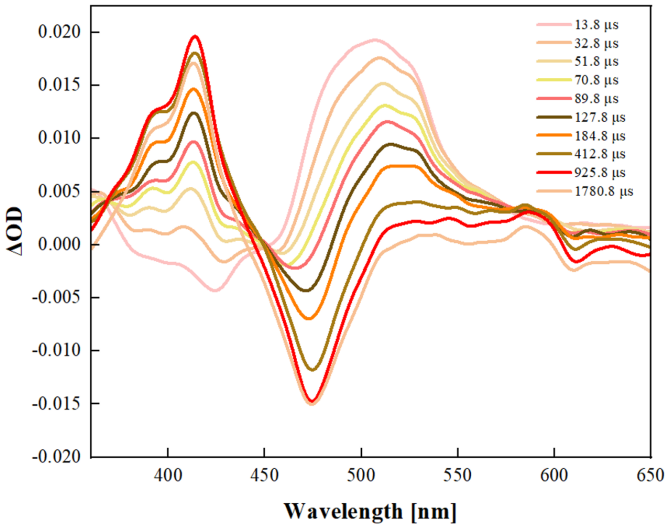


Figure 3.9 Nanosecond transient absorption spectrum of **RuNDI^{2+}** under a nitrogen atmosphere in acetonitrile/TEA/H_2O/Pt(DMSO)$_2I_2$ following excitation at 355 nm at different time delays. Samples were degassed using three freeze-pump-thaw cycles.

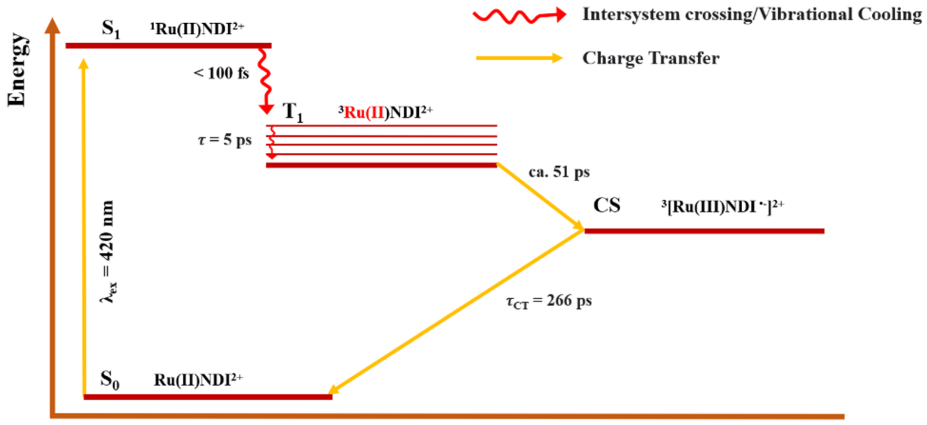


Figure 3.10 The Jablonski energy level diagram for **RuNDI^{2+}** upon excitation at 420 nm using TRIR.

In summary, the Jablonski energy diagram in Figure 3.10 was proposed to summarise the excited states populated in the **RuNDI^{2+}** dyad. Upon excitation at 420 nm, ^{1}Ru(II)NDI is populated, which undergoes rapid intersystem crossing (ISC) to the ^{3}MLCT state within the femtosecond timeframe (τ < 100 fs) which is facilitated by the heavy metal effect of ruthenium [56]. After formation of the ^{3}MLCT, a charge separated state [**Ru^{III}-NDI^{-}**] forms within 50 ps, resulting in the formation of the NDI$^{\bullet-}$ radical anion, with the charge recombination lifetime of ~ 260 ps.

3.5 Photocatalysis results

Photocatalytic hydrogen evolution was carried out in a mixture of acetonitrile, triethylamine, and water (65:30:5 ratio), and $[Pt(DMSO)_2I_2]$ as the catalyst. Typically, $[Pt(DMSO)_2I_2]$ is used in intramolecular assemblies where it is coordinated to ruthenium complexes [12, 57, 58]. However, in this case, the **RuNDI**$^{2+}$ photosensitiser is examined for hydrogen evolution using intermolecular approach, with a platinum catalyst added to the solution.

The irradiation source was either a 470 nm LED or a Solar Simulator (400 nm – 1100 nm spectral range). The highest turnover number (TON) for hydrogen evolution was 64, which was obtained after 6 h. Control experiments were also conducted, and no hydrogen was detected when the solution contained only the platinum catalyst, only the photosensitiser moiety or when it was kept in the dark. The initial solution before photocatalysis was yellow, which gradually changed to green after a period of 5 minutes following irradiation (470 nm). The spectral changes obtained from the UV-vis analysis (Figure 3.11) and change in colour is tentatively assigned to photochemical reduction of the NDI moiety by triethylamine (TEA) in a deoxygenated solution upon irradiation [39]. The spectral changes are similar to those observed in the spectroelectrochemical studies discussed previously. Under photocatalysis the complex and its parent species are photochemically reduced by TEA, leading to the formation of the reduced NDI species (**RuNDI**$^{+}$ and **RuNDI**), which are stable in the absence of oxygen. However, upon exposure to oxygen, the solution reverted back to its original yellow colour, suggesting that the oxygen acts as an electron acceptor, converting the reduced NDI species back to the neutral **RuNDI**$^{2+}$ [59]. Moreover, the photochemical reduction of the **RuNDI**$^{2+}$ was monitored using UV-vis absorption under photocatalytic conditions (Figure 3.11). Upon light irradiation at 470 nm, the formation of two-electron reduced species **RuNDI** occurred within a few minutes, exhibiting absorption bands at 389, 416, 453, 544, and 594 nm. These reduced **RuNDI** species were stable under anaerobic conditions for the duration of the experiment. After 85 minutes, the solution was aerated and the UV-vis a spectrum was recorded. Once aerated, the system returned to its neutral state (**RuNDI**$^{2+}$). The sample was then degassed again, and within 5 minutes, the solution once more formed the reduced species. Based on the observations, the formation of singly reduced species, **RuNDI**$^{+}$ occurs within a few seconds of light exposure, while the formation of the doubly electron reduced species **RuNDI** takes more time. It is likely that **RuNDI**$^{+}$ (from **RuNDI**$^{2+}$) and **RuNDI** (from **RuNDI**$^{+}$) are formed by the same

mechanism, via reduction of Ru(III) with TEA in the respective optically populated Ru(III)-NDI MLCT excited states. This provides an explanation for the delayed formation of **RuNDI** (minutes) compared to **RuNDI**$^{+}$ (seconds), as **RuNDI**$^{+}$ must first accumulate.

The mechanism of hydrogen generation for the **RuNDI**$^{2+}$ complex (Figure 3.13) is initiated by the reduction of Ru(III) by triethylamine, either in the ^{3}MLCT excited state Ru(III)-phen^{-}-NDI or in the concomitant ^{3}CS state Ru(III)-phen-NDI^{-}. This leads in both cases to the formation of one electron reduced species, **RuNDI**$^{+}$. Subsequently, **RuNDI**$^{+}$ absorbs visible light and may reach the ^{3}MLCT excited state Ru(III)-phen^{-}-NDI^{-}. Furthermore, Ru(III) is reduced by TEA to form Ru(II)-phen^{-}-NDI^{-} that converts to more stable Ru(II)-phen-NDI^{2-} = **RuNDI**. Finally, to rationalise the hydrogen generation, Pt(II) is reduced to Pt(0), which reacts with $2H^{+}$ to form molecular hydrogen.

However, determining which intermediate is the most active in photocatalytic performance and under photochemical conditions is challenging, as many other kinetic processes could take place [17]. This opens new possibilities by applying TRIR, TRIR-SEC, ns-TA and UV-SEC to simulate photocatalytic conditions in order to identify the presence of different intermediates in photocatalytic hydrogen evolution and the examination of their photophysical properties.

Analogous studies were conducted by Santos et al. [59] using a ruthenium perylene diimide compound (pPDI). The authors reported the colour changes of the complex during reductive and oxidative processes. Light irradiation at 420 nm produced a green solution, suggesting the presence of one-electron reduced species pPDI$^{\bullet-}$. Upon further exposure to light, the solution changed to a violet colour, assigned to the formation of the two-electron reduced species pPDIp^{2-}. In the absence of oxygen, the absorption spectrum of the reduced species exhibited no changes, thereby demonstrating good photostability. However, upon exposure to oxygen, the initial absorbance spectrum of the compound was recovered [59].

Inspired by the work of Santos [59], where they demonstrated the reversibility of the reduced species upon exposure to and absence of oxygen, we examined the feasibility of a recycling process for hydrogen evolution. The experimental procedure involved preparing a solution of **RuNDI**$^{2+}$ in a Schlenk tube under nitrogen (mixture of acetonitrile, triethylamine, and water 65:30:5 ratio). The sample was irradiated at 470 nm or using Solar Simulator for 3 hours and head space analysis using Gas Chromatography

quantified the amount of hydrogen generated. Following the initial measurement, the sample was exposed to oxygen and aerated with air. Subsequently, the same solution was freeze-pump-thawed again and exposed to light at 470 nm or using Solar Simulator for a further 3 hours. The measurement was recorded again. The study was conducted and repeated for three samples as shown in Table 3.2. Notably, each cycle resulted in the hydrogen evolution, albeit with a decrease in TONs.

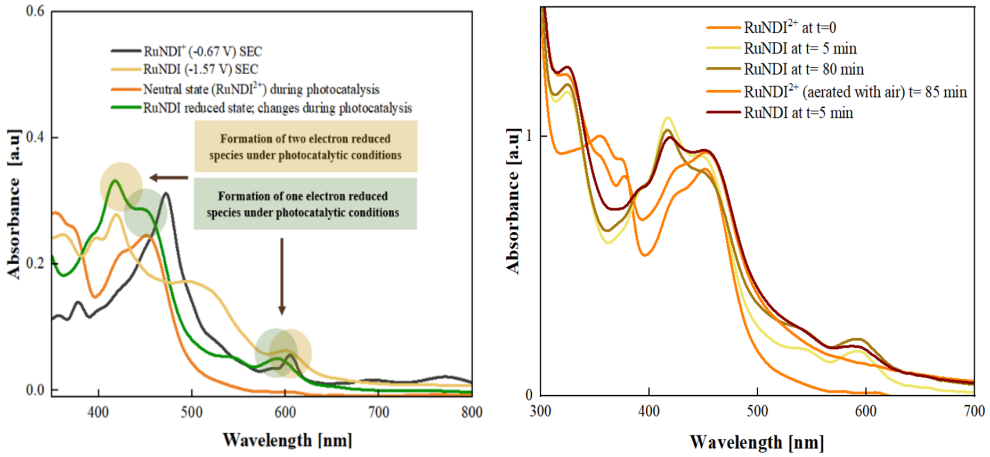


Figure 3.11 UV-vis absorption changes of **RuNDI^{2+}** under spectroelectrochemical and photocatalytic conditions in acetonitrile, triethylamine and water (65:30:5 ratio) upon light irradiation at 470 nm. The figure on the right shows the UV-vis changes after a few minutes of light irradiation followed by aeration of the solution with air to indicate how quickly the reduced species return to parent species in the presence of oxygen.

Table 3.2 The initial turnover numbers for the hydrogen evolution determined for three samples under identical conditions using 470 nm LED and Solar Simulator, followed by the TONs obtained in the subsequent recycling process carried out for each sample.

	Sample 1 [a]	**Sample 2** [b]	**Sample 3** [c]
Initial TON	53	59	48
Recycling I	52	34	36
Recycling II	14	14	22
Recycling III	12	–	17

[a] Sample irradiated for **2 h** using Solar Simulator. [b] Sample irradiated for **3 h** using Solar Simulator. [c] Sample irradiated for **2 h** using 470-nm LED.

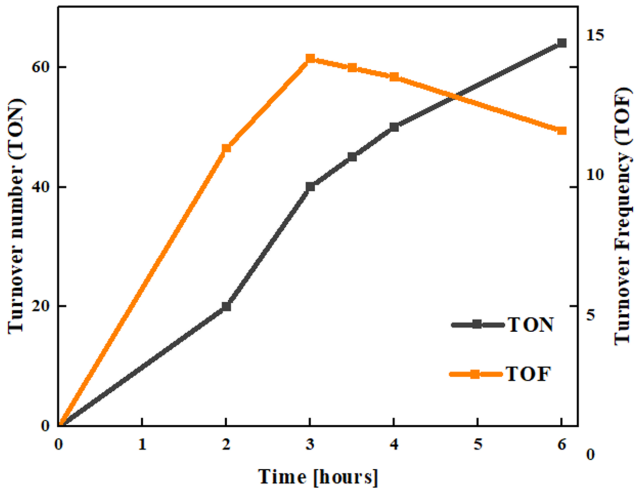


Figure 3.12 Time-dependent photocatalytic performance of **RuNDI**$^{2+}$ in acetonitrile, triethylamine and water (65:30:5, v/v) upon light irradiation at 470 nm. TON (black) and TOF (orange) values determined at various time delays.

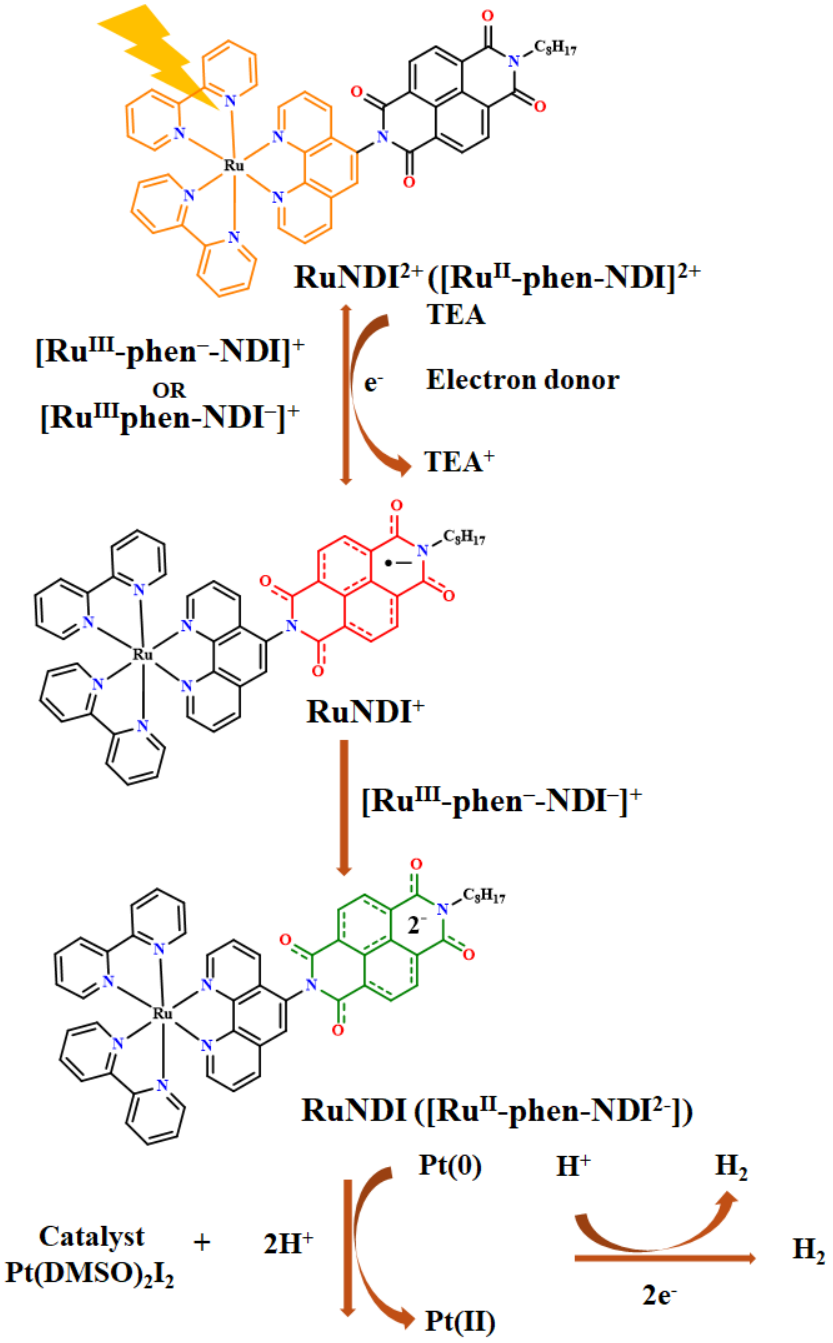


Figure 3.13 Mechanism of photocatalytic hydrogen evolution proposed for the **RuNDI^{2+}** complex.

3.6 Conclusion

A novel ruthenium (II)-naphthalene diimide (**RuNDI^{2+}**) photosensitiser was successfully synthesised and examined for photocatalytic hydrogen evolution. The ground state UV-vis absorption spectra were composed of contributions from both components, the NDI and $[Ru(bpy)_2\text{-phen-6-}NH_2]^{2+}$. The CV of **RuNDI^{2+}** displayed two reversible reductions, that were assigned to the one and two-electron-reduced NDI species. A further three reductions were attributed to the bipyridine and phenanthroline ligands. UV-vis/IR and TRIR-spectroelectrochemistry were employed to identify the intermediates formed during the photocatalytic process, together with nanosecond transient absorption spectroscopy. The mechanism of hydrogen generation for the **RuNDI^{2+}** complex was initiated by the reduction of Ru(III) by triethylamine, followed by the formation of one electron reduced species, **RuNDI^{+}**. Further irradiation of **RuNDI^{+}** in the presence of triethylamine, led to the formation of **RuNDI**. This enabled the population of two electrons, which were subsequently employed to reduce the protons in the water molecule, resulting in hydrogen evolution. Additionally, the **RuNDI^{2+}** complex was tested for its recyclability, which demonstrated the feasibility of reusing the same sample for hydrogen evolution. Further work will focus on designing an intramolecular system incorporating ruthenium and NDI, where all of the components are covalently bonded together. Consequently, this system will be compared with the intermolecular assembly studied in this research to study the intermediates formed and its characteristics using TRIR-SEC or ns-TAS.

3.7 Experimental

3.7.1 Materials and methods

All chemicals and anhydrous solvents used in this chapter were supplied by Aldrich Chemicals Co. and Fluorochem Ltd. FTIR measurements were carried out on Perkin-Elmer 2000 FTIR spectrophotometer in acetonitrile/THF. All ^{1}H-NMR spectra were recorded on Bruker 600 MHz spectrometer using deuterated dimethyl sulfoxide and chloroform. UV-vis and Emission Spectroscopy spectra were recorded on a Duetta Absorbance and Fluorescence Spectrometer, Horiba Scientific. Mass Spectrometry was obtained from the University of Bath, UK.

3.7.2 Electrochemical measurements

All experiments were conducted with 1 mM or 0.5 mM solutions of the ruthenium complex in spectroscopic grade DMF, THF or acetonitrile containing dry 10^{-1} M tetrabutylammonium hexafluorophosphate (TBAH) as supporting electrolyte. All solutions were purged for 20 minutes with nitrogen before conducting the measurements. A glassy carbon disk (polished with a diamond paste and cleaned in ultrasonic bath) and platinum wire were used as working and counter electrodes, respectively, together with an $Ag/AgNO_3$ reference electrode. Ferrocene was added as standard at the end of each measurement and all obtained potentials were corrected versus ferrocene. Experimental conditions: GC disk working electrode, T = 298 K, v = 100 mV s^{-1}.

3.7.3 Spectroelectrochemistry

Spectroelectrochemical measurements were carried out using an OTTLE cell [60], supplied by Spectroelectrochemistry Reading. The cell consisted of a platinum mesh working electrode, platinum mesh counter electrode and silver wire pseudo reference electrode. The solutions were prepared with concentration of 1.5 mM (for UV-vis-SEC) or 10 mM (for IR-SEC) complexes in anhydrous acetonitrile or tetrahydrofuran containing 3×10^{-1} M TBAH. IR spectroelectrochemistry was conducted using the Perkin-Elmer 2000 FTIR spectrophotometer. UV-vis spectroelectrochemical measurements were conducted using Agilent 8453 UV-vis spectrophotometer equipped with Agilent ChemStation software.

3.7.4 Nanosecond transient absorption measurements

Ns-TAS were recorded using the LP980 transient absorption spectrometer, Edinburgh Instruments, using excitation at 355 nm. All samples were deaerated over three cycles of freeze-pump-thaw before measurements. The optical density of the samples was in the range ~ 0.3 at 355 nm.

3.7.5 Time-resolved infrared measurements

TRIR spectra were recorded using the ULTRA instrument at the Central Laser Facility in the Rutherford Appleton Laboratory in the United Kingdom [61]. The measurements were carried out using 420, 510, and 600 nm excitation with 1 μJ power in a 0.1 mm pathlength Harrick cell using acetonitrile, and tetrahydrofuran. All data was analysed using Glotaran analysis [62].

3.7.6 Photocatalytic H_2 evolution experiments

Photocatalytic hydrogen evolution was carried in a 19 ml glass Schlenk tube stopped with an air-tight rubber spectrum. The sample (0.02 mmol) and the catalyst (0.02 mmol) were dissolved in a 65:30:5 mixture of acetonitrile, triethylamine and water. The freeze-pump-thaw procedure was used to ensure inert condition in the solution. The solution under a nitrogen atmosphere was then exposed to light irradiation at 470 nm using LEDs with 20 mW output power or G2V Optics Solar Simulator, Sunbrick [63]. Gas Chromatography was used to quantify the amount of hydrogen, after specific time intervals (30 min, 1h, 2h etc.) 1 ml of photocatalytic solution was injected into the instrument.

3.7.7 DFT calculations

DFT calculations were performed in Gaussian 16, Revision C01 (G16) [64], together with the three-parameterized Becke, Lee, Yang, and Park (B3LYP) functional [65, 66]. For the Ru atom, a quasi-relativistic effective-core pseudopotential and corresponding optimised basis set [67] was used, and for non-metal atoms, the 6-311G(d) basis set [68]. Solvent effects (THF) were described by the conductor-like polarisable continuum model (CPCM) [69]. In all cases, semi-empirical dispersion contributions were taken into account by the inclusion of Grimme's D3BJ model [70]. Open shell systems were calculated using the unrestricted Kohn-Sham approach (UKS), and time-dependent DFT (TD-DFT) was used to calculate electronic transitions and analyse them in terms of contributing one-electron excitations [71].

3.8 References

[1]. United Nations. (n.d.-b). Causes and effects of climate change. United Nations. https://www.un.org/en/climatechange/science/causes-effects-climate-change#:~:text=Fossil%20fuels%20%E2%80%93%20coal%2C%20oil%20and,of%20all%20carbon%20dioxide%20emissions

[2]. CO2 emissions in 2023 – analysis - IEA. (2024). https://www.iea.org/reports/co2-emissions-in-2023

[3]. Masson-Delmotte, V., P. Zhai, H.-O. Pörtner, D. Roberts, J. Skea, P.R. Shukla, A. Pirani, W. Moufouma-Okia, C. Péan, R. Pidcock, S. Connors, J.B.R. Matthews, Y. Chen, X. Zhou, M.I. Gomis, E. Lonnoy, T. Maycock, M. Tignor, and T. Waterfield IPCC, 2018: Global Warming of 1.5°C. An IPCC Special Report on the impacts of global warming of 1.5°C above pre-industrial levels and related global greenhouse gas emission pathways, in the context of strengthening the global response to the threat of climate change, sustainable development, and efforts to eradicate poverty. Cambridge University Press, https://www.ipcc.ch/site/assets/uploads/sites/2/2022/06/SR15_Full_Report_HR.pdf

[4]. Ireland's Climate Change Assessment - Synthesis Report. (2023). https://www.epa.ie/publications/monitoring--assessment/climate-change/ICCA_Synthesis_Report.pdf

[5]. The Paris Agreement. (2016). https://unfccc.int/sites/default/files/resource/parisagreement_publication.pdf

[6]. Zhang, X., Cheng, L., Tian, Y., Zhang, Y., & Wang, S. (2025). Improving the charge separation efficiencies of ternary metal sulfides for photocatalytic hydrogen production. Chemical Communications, 61(61), 11330–11352. https://doi.org/10.1039/d5cc03093e

[7]. Machín, A., Cotto, M., Ducongé, J., & Márquez, F. (2023). Artificial Photosynthesis: Current Advancements and Future Prospects. Biomimetics, 8(3), 298. https://doi.org/10.3390/biomimetics8030298

[8]. Maeda, K. (2011). Photocatalytic water splitting using semiconductor particles: History and recent developments. Journal of Photochemistry and Photobiology C: Photochemistry Reviews, 12(4), 237–268. https://doi.org/10.1016/j.jphotochemrev.2011.07.001

[9]. Halpin, Y., Pryce, M. T., Rau, S., Dini, D., & Vos, J. G. (2013b). Recent progress in the development of bimetallic photocatalysts for hydrogen generation. Dalton Transactions, 42(46), 16243–16254. https://doi.org/10.1039/c3dt52319e

[10]. Lehn, J. and Sauvage, J. (1977). Chemical storage of light energy: Catalytic generation of hydrogen by visible light or sunlight irradiation of neutral aqueous solutions. Nouveau Journal de Chimie 1: 449–451

[11]. Kirch, M., Lehn, J., & Sauvage, J. (1979). Hydrogen Generation by Visible Light Irradiation of Aqueous Solutions of Metal Complexes. An approach to the photochemical conversion and storage of solar energy. Helvetica Chimica Acta, 62(4), 1345–1384. https://doi.org/10.1002/hlca.19790620449

[12]. O'Reilly, L., Pan, Q., Das, N., Wenderich, K., Korterik, J. P., Vos, J. G., Pryce, M. T., & Huijser, A. (2018). Hydrogen-Generating Ru/Pt Bimetallic Photocatalysts Based on Phenyl-Phenanthroline Peripheral Ligands. ChemPhysChem, 19(22), 3084–3091. https://doi.org/10.1002/cphc.201800658

[13]. Rau, S., Schäfer, B., Gleich, D., Anders, E., Rudolph, M., Friedrich, M., Görls, H., Henry, W., & Vos, J. G. (2006). A Supramolecular Photocatalyst for the Production of Hydrogen and the Selective Hydrogenation of Tolane. Angewandte Chemie International Edition, 45(37), 6215–6218. https://doi.org/10.1002/anie.200600543

[14]. Natali, M., Luisa, A., Iengo, E., & Scandola, F. (2014). Efficient photocatalytic hydrogen generation from water by a cationic cobalt(II) porphyrin. Chemical Communications, 50(15), 1842–1844. https://doi.org/10.1039/c3cc48882a

[15]. Cerpentier, F. J., Karlsson, J., Lalrempuia, R., Brandon, M. P., Sazanovich, I. V., Greetham, G. M., Gibson, E. A., & Pryce, M. T. (2021). Ruthenium Assemblies for CO_2 Reduction and H_2 Generation: Time Resolved Infrared Spectroscopy, Spectroelectrochemistry and a Photocatalysis Study in Solution and on NiO. Frontiers in Chemistry, 9. https://doi.org/10.3389/fchem.2021.795877
[16]. Karnahl, M., Kuhnt, C., Ma, F., Yartsev, A., Schmitt, M., Dietzek, B., Rau, S., & Popp, J. (2011). Tuning of Photocatalytic Hydrogen Production and Photoinduced Intramolecular Electron Transfer Rates by Regioselective Bridging Ligand Substitution. ChemPhysChem, 12(11), 2101–2109. https://doi.org/10.1002/cphc.201100245
[17]. Hagmeyer, N., Schwab, A., Mroweh, N., McManus, C., Varghese, M., Mouesca, J., Gambarelli, S., Kupfer, S., Chavarot-Kerlidou, M., & Dietzek-Ivanšić, B. (2024). Spectroscopic Investigation of a Ruthenium Tris-Diimine Complex Featuring a Bioinspired Alloxazine Ligand. ChemPhotoChem, 8(12), e202400175. https://doi.org/10.1002/cptc.202400175
[18]. Tyson, D. S., Luman, C. R., Zhou, X., & Castellano, F. N. (2001). New Ru(II) Chromophores with Extended Excited-State Lifetimes. Inorganic Chemistry, 40(16), 4063–4071. https://doi.org/10.1021/ic010287g
[19]. Kim, D., Dang, V. Q., & Teets, T. S. (2024). Improved transition metal photosensitizers to drive advances in photocatalysis. Chemical Science, 15(1), 77–94. https://doi.org/10.1039/d3sc04580c
[20]. Singh, P., Rana, P. J., & Kar, P. (2017). Effect of electron withdrawing substituent and extended π- conjugation on photophysical properties of Ruthenium polyterpyridine D-P-A complexes and interfacial studies with semiconducting TiO_2 nanoparticle: Experimental and computational evidences. Journal of Photochemistry and Photobiology A: Chemistry, 346, 416–430. https://doi.org/10.1016/j.jphotochem.2017.06.027
[21]. Liao, Q., Kang, Q., Yang, Y., Zheng, Z., Qin, J., Xu, B., & Hou, J. (2022). Highly Stable Organic Solar Cells Based on an Ultraviolet-Resistant Cathode Interfacial Layer. CCS Chemistry, 4(3), 938–948. https://doi.org/10.31635/ccschem.021.202100852
[22]. Choi, J., Kim, K.-H., Yu, H., Lee, C., Kang, H., Song, I., Kim, Y., Oh, J. H., & Kim, B. J. (2015). Importance of Electron Transport Ability in Naphthalene Diimide-Based Polymer Acceptors for High-Performance, Additive-Free, All-Polymer Solar Cells. Chemistry of Materials, 27(15), 5230–5237. https://doi.org/10.1021/acs.chemmater.5b01274
[23]. Caby, S., Bouchet, L. M., Argüello, J. E., Rossi, R. A., & Bardagi, J. I. (2021). Excitation of Radical Anions of Naphthalene Diimides in Consecutive- and Electro-Photocatalysis. ChemCatChem, 13(13), 3001–3009. https://doi.org/10.1002/cctc.202100359
[24]. Sun, M. Y., Bai, F. Y., Guan, Q. L., Xing, Y. H., & Xu, F. (2022). Construction of naphthalene diimide-based cadmium complexes and their application in iodine adsorption, photochromism, and photocatalysis. CrystEngComm, 24(47), 8309–8320. https://doi.org/10.1039/d2ce01192a
[25]. Liu, J.-J., Xia, S.-B., Liu, T., He, C.-X., Suo, H., & Liu, J. (2021). Electron-deficient naphthalene diimide directed metal halides with visible light driven photocatalytic properties. Journal of Solid-State Chemistry, 295, 121900. https://doi.org/10.1016/j.jssc.2020.121900
[26]. Xu, X., Meng, L., Zhang, J., Yang, S., Sun, C., Li, H., Li, J., & Zhu, Y. (2023). Full-Spectrum Responsive Naphthalimide/Perylene Diimide with a Giant Internal Electric Field for Photocatalytic Overall Water Splitting. Angewandte Chemie, 136(5), e202308597. https://doi.org/10.1002/ange.202308597
[27]. Wang, S.-H., Chen, P.-Z., Chen, Y.-Y., Khurshid, F., Cai, C.-W., Lai, Y.-Y., Chung, P.-W., Jeng, R.-J., Rwei, S.-P., & Wang, L. (2022). Naphthalene Diimide-Based Donor–Acceptor–Donor Small Molecules as Metal-Free Organocatalysts for Photocatalytic CO_2

Reaction. ACS Applied Materials & Interfaces, 14(38), 43109–43115. https://doi.org/10.1021/acsami.2c08531
[28]. Wang, S.-H., Khurshid, F., Chen, P.-Z., Lai, Y.-R., Cai, C.-W., Chung, P.-W., Hayashi, M., Jeng, R.-J., Rwei, S.-P., & Wang, L. (2022). Solution-Processable Naphthalene Diimide-Based Conjugated Polymers as Organocatalysts for Photocatalytic CO_2 Reaction with Extremely Stable Catalytic Activity for Over 330 Hours. Chemistry of Materials, 34(11), 4955–4963. https://doi.org/10.1021/acs.chemmater.2c00168
[29]. Pereira, L. M., de Oliveira, D. F., Tiburcio, M. A., Ribeiro, G. H., Moraes, C. A., Neto, F. O., Camargo, A. J., De Boni, L., Nascimento, O. R., Homem, M. G., & Carlos, R. M. (2025). Exploring the Reversible Equilibrium State between ^{3}CS and ^{3}CSS in a Ru(phen)–Naphthalene Diimide Dyad. Inorganic Chemistry, 64(17), 8544–8553. https://doi.org/10.1021/acs.inorgchem.4c05443
[30]. Ghule, N. V., La, D. D., Bhosale, R. S., Al Kobaisi, M., Raynor, A. M., Bhosale, S. V., & Bhosale, S. V. (2016). Effect of Amide Hydrogen Bonding Interaction on Supramolecular Self-Assembly of Naphthalene Diimide Amphiphiles with Aggregation Induced Emission. ChemistryOpen, 5(2), 157–163. https://doi.org/10.1002/open.201500201
[31]. Bartusiak, M. Z., McGarry, R. J., Varvarezos, L., Brandon, M. P., & Pryce, M. T. (2023a). Incorporation of perylene and naphthalene like ligands into ruthenium complexes: Synthesis, photophysical properties and electrochemistry. Coordination Chemistry Reviews, 495, 215365. https://doi.org/10.1016/j.ccr.2023.215365
[32]. Queyriaux, N., Giannoudis, E., Lefebvre, J., Artero, V., & Chavarot-Kerlidou, M. (2019). Synthesis of Ruthenium Tris-Diimine Photosensitizers Substituted by Four Methylphosphonate Anchoring Groups for Dye-Sensitized Photoelectrochemical Cell Applications. European Journal of Inorganic Chemistry, 2019(15), 2154–2161. https://doi.org/10.1002/ejic.201900151
[33]. Volman, D.H., Hammond, G.S. and Neckers, D.C. (2009) Photochemistry and Luminescence of Cyclometallated Complexes, in Advances in Photochemistry. Volume 17. Wiley, pp. 20–25.
[34]. Ghosh, A., Mandoli, A., Kumar, D. K., Yadav, N. S., Ghosh, T., Jha, B., Thomas, J. A., & Das, A. (2009a). DNA binding and cleavage properties of a newly synthesised Ru(II)-polypyridyl complex. Dalton Transactions, (42), 9312–9321. https://doi.org/10.1039/b906756f
[35]. Johansson, O., Wolpher, H., Borgström, M., Hammarström, L., Bergquist, J., Sun, L., & Åkermark, B. (2004). Intramolecular charge separation in a hydrogen bonded tyrosine–ruthenium(II)–naphthalene diimide triad. Chem. Commun., (2), 194–195. https://doi.org/10.1039/b308101j
[36]. Kumari, N., Naqvi, S., & Kumar, R. (2017a). Naphthalene diimide self-assembled ribbons with high electrical conductivity and mobility without doping. Journal of Materials Science, 53(6), 4046–4055. https://doi.org/10.1007/s10853-017-1829-4
[37]. Johansson, O., Borgström, M., Lomoth, R., Palmblad, M., Bergquist, J., Hammarström, L., Sun, L., & Åkermark, B. (2003). Electron Donor−Acceptor Dyads Based on Ruthenium(II) Bipyridine and Terpyridine Complexes Bound to Naphthalenediimide. Inorganic Chemistry, 42(9), 2908–2918. https://doi.org/10.1021/ic020420k
[38]. Borgström, M., Shaikh, N., Johansson, O., Anderlund, M. F., Styring, S., Åkermark, B., Magnuson, A., & Hammarström, L. (2005). Light Induced Manganese Oxidation and Long-Lived Charge Separation in a $Mn_2^{II,II}$–$Ru^{II}(bpy)_3$−Acceptor Triad. Journal of the American Chemical Society, 127(49), 17504–17515. https://doi.org/10.1021/ja055243b
[39]. Skaisgirski, M., Guo, X., & Wenger, O. S. (2017a). Electron Accumulation on Naphthalene Diimide Photosensitized by $[Ru(2,2'\text{-bipyridine})_3]^{2+}$. Inorganic Chemistry, 56(5), 2432–2439. https://doi.org/10.1021/acs.inorgchem.6b02446

[40]. Dixon, D. W., Thornton, N. B., Steullet, V., & Netzel, T. (1999). Effect of DNA Scaffolding on Intramolecular Electron Transfer Quenching of a Photoexcited Ruthenium(II) Polypyridine Naphthalene Diimide. Inorganic Chemistry, 38(24), 5526–5534. https://doi.org/10.1021/ic971446s
[41]. Montalti, M., Michl, J., & Balzani, V. (2006). Handbook of Photochemistry. Photophysical Properties of Transition Metal Complexes, Taylor & Francis, pp. 377-421.
[42]. Baron, A., Herrero, C., Quaranta, A., Charlot, M.-F., Leibl, W., Vauzeilles, B., & Aukauloo, A. (2011). Efficient electron transfer through a triazole link in ruthenium(II) polypyridine type complexes. Chemical Communications, 47(39), 11011–11013. https://doi.org/10.1039/c1cc13683f
[43]. Van der Westhuizen, D., von Eschwege, K. G., & Conradie, J. (2019). Electrochemistry and spectroscopy of substituted $[Ru(phen)_3]^{2+}$ and $[Ru(bpy)_3]^{2+}$ complexes. Electrochimica Acta, 320, 134540. https://doi.org/10.1016/j.electacta.2019.07.051
[44]. Frath, D., Nguyen, V. Q., Lafolet, F., Martin, P., & Lacroix, J.-C. (2017). Electrografted monolayer based on a naphthalene diimide–ruthenium terpyridine complex dyad: efficient creation of large-area molecular junctions with high current densities. Chemical Communications, 53(80), 10997–11000. https://doi.org/10.1039/c7cc04972b
[45]. Tran, T.-T., Pino, T., & Ha-Thi, M.-H. (2019). Watching Intermolecular Light-Induced Charge Accumulation on Naphthalene Diimide by Tris(bipyridyl)ruthenium(II) Photosensitizer. The Journal of Physical Chemistry C, 123(47), 28651–28658. https://doi.org/10.1021/acs.jpcc.9b09556
[46]. Gosztola, D., Niemczyk, M. P., Svec, W., Lukas, A. S., & Wasielewski, M. R. (2000a). Excited Doublet States of Electrochemically Generated Aromatic Imide and Diimide Radical Anions. The Journal of Physical Chemistry A, 104(28), 6545–6551. https://doi.org/10.1021/jp000706f
[47]. Balzer, N., Lukášek, J., Valášek, M., Rai, V., Sun, Q., Gerhard, L., Wulfhekel, W., & Mayor, M. (2021). Synthesis and Surface Behaviour of NDI Chromophores Mounted on a Tripodal Scaffold: Towards Self-Decoupled Chromophores for Single-Molecule Electroluminescence. Chemistry – A European Journal, 27(47), 12144–12155. https://doi.org/10.1002/chem.202101264
[48]. Sazanovich, I. V., Alamiry, M. A., Best, J., Bennett, R. D., Bouganov, O. V., Davies, E. S., Grivin, V. P., Meijer, A. J., Plyusnin, V. F., Ronayne, K. L., Shelton, A. H., Tikhomirov, S. A., Towrie, M., & Weinstein, J. A. (2008). Excited State Dynamics of a Pt^{II} Diimine Complex Bearing a Naphthalene-Diimide Electron Acceptor. Inorganic Chemistry, 47(22), 10432–10445. https://doi.org/10.1021/ic801022h
[49]. Taylor, A. J., Davies, E. S., Weinstein, J. A., Sazanovich, I. V., Bouganov, O. V., Tikhomirov, S. A., Towrie, M., McMaster, J., & Garner, C. D. (2012). Ultrafast Intramolecular Charge Separation in a Donor–Acceptor Assembly Comprising Bis(η^5-cyclopentadienyl)molybdenum Coordinated to an Ene-1,2-dithiolate-naphthalenetetracarboxylicdiimide Ligand. Inorganic Chemistry, 51(24), 13181–13194. https://doi.org/10.1021/ic301436t
[50]. Green, S., & Fox, M. A. (1995). Intramolecular Photoinduced Electron Transfer from Nitroxyl Radicals. The Journal of Physical Chemistry, 99(40), 14752–14757. https://doi.org/10.1021/j100040a026
[51]. Scattergood, P. A., Delor, M., Sazanovich, I. V., Bouganov, O. V., Tikhomirov, S. A., Stasheuski, A. S., Parker, A. W., Greetham, G. M., Towrie, M., Davies, E. S., Meijer, A. J., & Weinstein, J. A. (2014). Electron transfer dynamics and excited state branching in a charge-transfer platinum(II) donor–bridge-acceptor assembly. Dalton Trans., 43(47), 17677–17693. https://doi.org/10.1039/c4dt01682c

[52]. Chen, X., Sukhanov, A. A., Taddei, M., Dick, B., Zhao, J., Voronkova, V. K., & Di Donato, M. (2022). Charge Separation/Recombination, Intersystem Crossing, and Unusually Slow Intramolecular Triplet–Triplet Energy Transfer in Naphthalenediimide–Anthracene Compact Energy Donor–Acceptor Dyads. The Journal of Physical Chemistry Letters, 13(37), 8740–8748. https://doi.org/10.1021/acs.jpclett.2c02118
[53]. Demeter, A., Biczok., Berces, T., Wintgens, V., Valat, P., & Kossanyi, J. (1993). Cheminform Abstract: Laser Photolysis Studies of Transient Processes in the Photoreduction of Naphthalimides by Aliphatic Amines. Cheminform, 24(31). https://doi.org/10.1002/chin.199331086
[54]. Ishitani, O., Ishii, K., Yanagida, S., Pac, C., Ohno, T., & Yoshimura, A. (1989). A New Mechanistic Channel for Photochemical Electron Transfer of Tris(2,2′-bipyridine)ruthenium(II) with Triethylamine. Possible Participation of a Nonemitting Excited State. Chemistry Letters, 18(2), 217–220. https://doi.org/10.1246/cl.1989.217
[55]. Gotico, P., Tran, T., Baron, A., Vauzeilles, B., Lefumeux, C., Ha-Thi, M., Pino, T., Halime, Z., Quaranta, A., Leibl, W., & Aukauloo, A. (2021). Tracking Charge Accumulation in a Functional Triazole-Linked Ruthenium-Rhenium Dyad Towards Photocatalytic Carbon Dioxide Reduction. ChemPhotoChem, 5(7), 654–664. https://doi.org/10.1002/cptc.202100010
[56]. Tilley, A. J., Kim, M. J., Chen, M., & Ghiggino, K. P. (2013). Photo-induced energy transfer in ruthenium-centred polymers prepared by a raft approach. Polymer, 54(12), 2865–2872. https://doi.org/10.1016/j.polymer.2013.03.064
[57]. Bagemihl, B., Müller, C., Shillito, G. E., Hartkorn, M., Mengele, A. K., Kupfer, S., Dietzek- Ivanšić, B., & Rau, S. (2024). Steering Photoinduced Electron Transfer in Intramolecular Photocatalysts by Peripheral Ligand Control. ChemistryEurope, 2(6), e202300084. https://doi.org/10.1002/ceur.202300084
[58]. Maloul, S., van den Borg, M., Müller, C., Zedler, L., Mengele, A. K., Gaissmaier, D., Jacob, T., Rau, S., Dietzek-Ivanšić, B., & Streb, C. (2021). Multifunctional Polyoxometalate Platforms for Supramolecular Light-Driven Hydrogen Evolution. Chemistry – A European Journal, 27(68), 16846–16852. https://doi.org/10.1002/chem.202103817
[59]. Santos, E. R., Pina, J., Venâncio, T., Serpa, C., Martinho, J. M., & Carlos, R. M. (2016). Photoinduced Energy and Electron-Transfer Reactions by Polypyridine Ruthenium(II) Complexes Containing a Derivatized Perylene Diimide. The Journal of Physical Chemistry C, 120(40), 22831–22843. https://doi.org/10.1021/acs.jpcc.6b06693
[60]. Room temperature OTTLE cell: Spectroelectrochemistry reading. Spectroelectrochemistry. (2019, April 26). https://research.reading.ac.uk/spectroelectrochemistry/optically-transparent-thin-layer-electrochemical-cells/room-temperature-ottle-cell/
[61]. Greetham, G. M., Burgos, P., Cao, Q., Clark, I. P., Codd, P. S., Farrow, R. C., George, M. W., Kogimtzis, M., Matousek, P., Parker, A. W., Pollard, M. R., Robinson, D. A., Xin, Z.-J., & Towrie, M. (2010). Ultra: A Unique Instrument for Time-Resolved Spectroscopy. Applied Spectroscopy, 64(12), 1311–1319. https://doi.org/10.1366/000370210793561673
[62]. Snellenburg, J. J., Laptenok, S. P., Seger, R., Mullen, K. M., & Stokkum, I. H. (2012). Glotaran: A Java-Based Graphical User Interface for the R Package TIMP. Journal of Statistical Software, 49(3), 1–22. https://doi.org/10.18637/jss.v049.i03
[63]. LED solar simulator manufacturer: Sunbrick Solar Simulator. G2V Optics Inc. (2025, June 17). https://g2voptics.com/
[64]. Gaussian 16 Rev. C.01; Wallingford, CT, 2016.
[65]. Becke, A. D. (1993). Density-functional thermochemistry. III. The role of exact exchange. The Journal of Chemical Physics, 98(7), 5648–5652. https://doi.org/10.1063/1.464913

[66]. Lee, C., Yang, W., & Parr, R. G. (1988). Development of the Colle-Salvetti Correlation-Energy Formula into a Functional of the Electron Density. Physical Review B, 37(2), 785–789. https://doi.org/10.1103/physrevb.37.785
[67]. Andrae, D., Häussermann, U., Dolg, M., Stoll, H., & Preuss, H. (1990). Energy-adjustedab initio pseudopotentials for the second and third row transition elements. Theoretica Chimica Acta, 77(2), 123–141. https://doi.org/10.1007/bf01114537
[68]. Krishnan, R., Binkley, J. S., Seeger, R., & Pople, J. A. (1980). Self-consistent molecular orbital methods. XX. A basis set for correlated wave functions. The Journal of Chemical Physics, 72(1), 650–654. https://doi.org/10.1063/1.438955
[69]. Cossi, M., Rega, N., Scalmani, G., & Barone, V. (2003). Energies, Structures, and Electronic Properties of Molecules in Solution with the C-PCM Solvation Model. Journal of Computational Chemistry, 24(6), 669–681. https://doi.org/10.1002/jcc.10189
[70]. Grimme, S., Ehrlich, S., & Goerigk, L. (2011). Effect of the damping function in dispersion corrected density functional theory. Journal of Computational Chemistry, 32(7), 1456–1465. https://doi.org/10.1002/jcc.21759
[71]. Vlček, A., & Záliš, S. (2007). Modeling of charge-transfer transitions and excited states in d^6 transition metal complexes by DFT techniques. Coordination Chemistry Reviews, 251(3–4), 258–287. https://doi.org/10.1016/j.ccr.2006.05.021

Chapter 4

Time-Resolved Infrared Spectroscopy, Spectroelectrochemical, and Transient Absorption Studies of a Ruthenium-Naphthalene Diimide Ester Complex: Insights into Charge Transfer Dynamics and the Excited States Populated in Solution and on a NiO Surface.

Martyna Bartusiak[1], Martin Pižl[2,4], Florian Cerpentier[1], Partha Malakar[3], Sayantan Bhattacharya[3], Owen Woodford[5], František Hartl[4], Elizabeth A. Gibson[5], Mary T. Pryce[1]

[1]School of Chemical Sciences, Dublin City University, Ireland

[2]Department of Inorganic Chemistry, University of Chemistry and Technology Prague, Technická 5, 16628 Prague, Czech Republic

[3]Rutherford Appleton Laboratory, Harwell Campus, Didcot OX11 0QX, UK

[4]Department of Chemistry, University of Reading, Whiteknights, Reading RG6 6DX, UK

[5]Energy Materials Laboratory, Department of Chemistry, School of Natural and Environmental Science, Newcastle University, Newcastle upon Tyne, United Kingdom

4.1 Abstract

In this study, a novel ruthenium-naphthalene diimide complex, **Ru(dceb)-NDI^{2+}**, was proposed as a photosensitiser for photocatalytic hydrogen evolution, where dceb = 4,4′-di(carboxyethyl)bipyridine. Time-Resolved Infrared spectroscopy (TRIR) serves as an excellent technique for probing excited states populated following excitation. Incorporation of the peripheral ester groups was observed to significantly impact on the photophysical, electrochemical and spectroelectrochemical properties, as well as hydrogen evolution efficiency. In TRIR, excitation at 420 nm led to depletion of the carbonyl bands for the ester group at 1729 cm^{-1}, together with the formation of a band at 1706 cm^{-1}. This new band is assigned to population of a ruthenium ^{3}MLCT$_{EtOOC–bpy}$ with the lifetime persisting beyond the experimental set-up. When the excitation energy was increased to 365 nm, the TRIR spectra are significantly different. Excitation at 365 nm, results in depletion of the ester carbonyl vibration at 1729 cm^{-1} with new transient bands at 1677 and 1650 cm^{-1} which are assigned to the NDI excited state. As these new bands for the NDI excited state shift to lower frequency compared to the parent bands it indicates an increase in electron density on the NDI moiety following excitation. Simultaneously, a transient band at 1718 cm^{-1} attributed to the organic carbonyl groups of the ester-functionalised bipyridine ligands also formed. Similarly to TRIR studies carried out at 420 nm excitation, the transient band at 1718 cm^{-1} is attributed to population of a ruthenium ^{3}MLCT$_{EtOOC–bpy}$ state. TRIR-spectroelectrochemical studies (TRIR-SEC) were also carried out using an optically transparent thin-layer electrochemical cell (OTTLE cell) to explore the spectral profile and the kinetics of the reduced species of the

complex. Picosecond transient absorption spectroscopy (ps-TAS) was carried out both in solution and on a nickel oxide surface, to probe forward and backward electron transfer kinetics. On nickel oxide film (NiO), new transient bands formed at 474, 530, 605, 690, and 735 nm. The spectral profile of these absorption bands suggests an efficient electron transfer which gives rise to an NDI charge-separated state, $Ru(dceb)^{III}$-$NDI^{–}$. Nanosecond transient absorption spectroscopy (ns-TAS) studies were carried out to determine the lifetimes of the triplet, $^{3}MLCT_{EtOOC–bpy}$ of ruthenium (II) (τ = 439 ns). When this experiment is carried out under photocatalytic conditions, this lifetime is significantly increased, indicating that the photocatalytic assemblies behave differently under photocatalytic conditions. Additionally, given the wavelength-dependent nature of the photophysics from TRIR studies, photocatalysis was carried out following irradiation at both 365 and 450 nm using $[Pt(DMSO)_2I_2]$ as a catalyst and triethylamine (TEA) as a sacrificial electron donor. The highest turnover number (TON) obtained was 100, following irradiation at 450 nm, after 7 hours of light. Following irradiation at 365 nm, a TON of 50 was obtained. Preliminary studies, including chronoamperometry and immobilisation studies on a NiO film, were also carried out using a photoelectrochemical (PEC) cell.

Contribution:

In this chapter, I was responsible for writing all sections and analysing the obtained results. I characterised the complex using a range of techniques and probed the photophysics using nanosecond transient absorption and emission spectroscopy, and in addition I performed spectroelectrochemical measurements. Picosecond transient absorption studies were carried out at the Newcastle University and TRIR measurements were conducted at the Rutherford Appleton Laboratory in the UK, in collaboration with Prof. Hartl and Prof. Gibson. I carried out photocatalytic experiments, surface studies on a NiO and processed all data using the Glotaran software.

4.2 Introduction

There is no doubt, that addressing and overcoming current and global energy challenges requires the development of innovative methods and solutions to combat climate change and prevent further environmental damage from occurring. In order to do that, all economies around the world must propose new policies regarding the emission of greenhouse gases and implement major changes within the society to minimise the severe consequences of global warming in the coming years. Since 2010, there has been reported a 50% increase in the Earth's average temperature when compared the data to the period from 1970 to 2010 [1]. Furthermore, based on forecasts and values obtained from literature sources, the current rate of global warming could increase by 0.27°C every ten years [1, 2]. Photocatalytic hydrogen evolution and the utilisation of sustainable fuels produced from renewable sources of energy are a promising solution to supress the increase in greenhouse gas emissions and consequently reduce the impact of climate change on the environment. However, they have to be more frequently employed to achieve this goal. Currently, hydrogen production carried out using photocatalysis is only studied in a laboratory setting but it serves as a foundation for fundamental knowledge, which could pave the way for large-scale production in the future. Notably, hydrogen gas has the potential as a "future fuel" due to its high energy content per unit of weight, for example 1 kg of hydrogen has the same energy content as 3.3 kg of gasoline [3, 4]. Currently, the utilisation of hydrogen as a fuel remains relatively low with only 2% of the overall energy consumption in Europe attributed to hydrogen in 2022 [5, 6]. Unfortunately, 96% of this hydrogen was produced from natural gas, which resulted in a significant amount of carbon dioxide emissions [5, 6]. In the coming years, the European Union (EU) is determined to take action, and introduce more effective measures and prioritise renewable hydrogen production methods. The REPowerEU Strategy of 2022 focusses on the transition towards green and renewable sources of energy and it aims to produce 10 million tonnes of hydrogen and import the same quantity by 2030 [5]. Furthermore, hydrogen is projected to contribute 10% of the EU's energy consumption by 2050 [5 – 7]. This highlights the need to expand further the field of photocatalytic hydrogen evolution, develop sustainable and efficient systems, and thoroughly investigate photophysical and electrochemical properties of photocatalytic assemblies. Hence, the introduction of new methods for addressing environmental challenges could be facilitated. The more fundamental knowledge that is acquired in laboratory settings, the greater the likelihood of establishing a well-developed hydrogen economy in the

future, which will include diverse methods for harvesting sunlight, producing, storing, transporting and utilising hydrogen gas as a sustainable fuel. A wide variety of ruthenium complexes have been employed for photocatalytic hydrogen evolution [8 – 11]. However, this chapter will primarily focus on these ruthenium complexes featuring different substituents on the peripheral ligands localised on bipyridine [12 – 17]. These studies examined the performance of trisbipyridyl ruthenium ($[Ru(bpy)_3]^{2+}$) for photocatalytic hydrogen generation, where the substituents on the peripheral ligands were varied. For example, studies from our research group [12] have focussed on ruthenium-platinum/palladium intramolecular assemblies including $[Ru(bpy)_2(2,5\text{-bpp})PtIS]^{2+}$, where bpy = 2,2' bipyridine, 2,5-bpp = 2,2′,5′,2″-terpyridine, S = solvent. The ruthenium centre acts as the light-harvesting moiety, together with a terpyridine bridging ligand, and a platinum or palladium as the catalytic centre. When ester groups were attached to bipyridine to form $[Ru(dceb)_2(2,5\text{-bpp})PtIS]^{2+}$, where dceb = 4,4′-di(carboxyethyl)bipyridine, a 8-fold (TON of 650) increase in turnover numbers (TONs) was observed for hydrogen evolution, compared to the bipyridine analogue $[Ru(bpy)_2(2,5\text{-bpp})PtIS]^{2+}$ (TON of 80). In the case of the palladium assembly $[Ru(bpy)_2(2,5\text{-bpp})PdClS]^{2+}$, a TON of 120 was obtained which increased to 400 for $[Ru(dceb)_2(2,5\text{-bpp})PdClS]^{2+}$. This work was subsequently extended [13], to investigate the photophysical properties of $[Ru(dceb)_2(2,5\text{-bpp})PtIS]^{2+}$complex to identify the excited states populated, to gain an insight into why hydrogen evolution significantly increases following incorporation of the ester groups at the peripheral bipyridine ligands. Transient absorption studies, indicates that when ester groups are added to the bipyridine moiety the ^{3}MLCT (metal-to-ligand charge transfer) energy level is lowered, resulting in population of the ^{3}MLCT within 535 fs. As a result, the electron initially moves from the ruthenium photosensitiser towards the peripheral bipyridine ligand, as opposed to the catalytic centre. This creates an 'electron reservoir' on the peripheral ligands, which is proposed as the explanation for the enhanced photocatalytic efficiency reported by Pan et al. [13]. Cerpentier et al. [14] extended this research by replacing the terpyridine bridging ligand with 3,5-di(pyridine-2-yl)-1,2,4-triazolate (bpt). In their study, the highest TON of 81 was achieved for the ($[Ru(dceb)_2(bpt)PtI(H_2O)](PF_6)_2$) complex. The study confirmed that the presence of esters reduced the LUMO energies of the peripheral bipyridine ligand, resulting in localisation of the ^{3}MLCT excited state on these peripheral ligands following excitation. Unfortunately, the authors did not provide TON values for the analogous complex without the esters for comparison.

Another research study conducted by Müller et al. [15] investigated intramolecular ruthenium photocatalytic assemblies, which consisted of a tetrapyrido-phenazine (tpphz) bridging ligand and either a 4,4'-di-tert-butyl-2,2'-bipyridine (tbbpy) or 4,4'-di-trifluoromethyl-2,2'-bipyridine (F = fbpy) peripheral ligands incorporated into Ru(II)-Pt(II)-complexes (Ru-tpphz-PtI_2 and ^{F}Ru-tpphz-PtI_2, respectively). The electron-withdrawing CF_3 groups were found to stabilise the LUMOs of the fbpy ligands, which resulted in lower electron density on the ruthenium center. The authors confirmed this using UV-vis absorption spectroscopy, where the MLCT band of ^{F}Ru-tpphz-PtI_2 was red-shifted by 0.06 eV, and the ligand-centered (LC) transition was blue-shifted by 0.17 eV, in contrast to Ru-tpphz-PtI_2. Additionally, UV-vis-SEC experiments revealed that the singly reduced form of ^{F}Ru-tpphz-PtI_2 exhibited stronger absorbance in the 300 - 400 nm range, compared to the singly reduced Ru-tpphz-PtI_2 [15].

More recently, Bagemihl et al. [16] studied $[(prbim)_2Ru(tpphz)PtI_2]^{2+}$, a similar complex to that reported by Müller et al. [15], however, in their study, the authors incorporated a different peripheral ligand, an N,N'-propylene-protected 1H,1'H-2,2'-biimidazole (prbim) to further investigate the influence of peripheral ligands on unidirectional electron transfer (from the ruthenium to the tpphz bridging ligand), instead of non-directional electron transfer (from the ruthenium to the peripheral ligand), which had been observed in studies involving ester substituents [12 – 14]. The authors concluded, that the prbim ligand acts as a spectator ligand, as it facilitates unidirectional electron transfer upon excitation (at 400 and 470 nm) to the tpphz bridge, but it also destabilises the $MLCT_{prbim}$, which prevents the desired electron transfer from the ruthenium to the platinum catalyst. Based on the aforementioned studies, it can be concluded that successful photocatalysis depends not only on the choice of a suitable photosensitising moiety, bridging ligands or catalysts, but also the experimental conditions. Furthermore, slight variations in the groups substituted to the peripheral ligands, can result in significant differences in the ability of the photocatalytic system to produce hydrogen. This emphasises the importance of modifying the photocatalytic assemblies [12 – 16].

Ester groups not only enhance the efficiency of hydrogen evolution but have also been used for chemisorption onto nickel oxide (NiO) in surface studies. For example, Põldme et al. [17] investigated two photocatalytic assemblies, namely $[Ru(decb)_2(bpt)PdCl(H_2O)](PF_6)_2$ and $[Ru(decb)_2(2,5\text{-}bpp)PtI(CH_3CN)](PF_6)_2$ where decb = 4,4'-diethylcarboxy-2,2'-bipyridine, bpp = 2,2':5', 2''-terpyridine, bpt = 3,5-bis(2-pyridyl)-1,2,4-triazole).

Transient Absorption Spectroscopy (TAS), supported by density functional theory (DFT) calculations, indicates that the presence of the ester ligands lowers the energy of the ^{3}MLCT, with the unpaired spin localised on a peripheral ligand [12 – 14]. The authors have also employed TRIR studies to study the excited state both in solution and on nickel oxide surface. When the $[Ru(decb)_2(2,5\text{-}bpp)PtI(CH_3CN)](PF_6)_2$, complex was studied in solution, electron transfer took place in the direction of the peripheral ligands, whereas in $[Ru(decb)_2(bpt)PdCl(H_2O)](PF_6)_2$ electron transfer took place towards the bridging bpt ligand [17]. Hydrogen experiments were carried out on a NiO surface and the highest TON of 147 was obtained for $[Ru(decb)_2(2,5\text{-}bpp)PtI(CH_3CN)](PF_6)_2$ and a TON of 41 was recorded for $[Ru(decb)_2(bpt)PdCl(H_2O)](PF_6)_2$. In addition, TRIR and TAS studies indicated efficient photoinduced electron transfer from the NiO surface to the adsorbed photocatalysts [17].

In this study, the **Ru(dceb)-NDI^{2+}** complex was proposed as a photosensitiser for photocatalytic hydrogen evolution. The ester substituents were incorporated based on previous studies by the group, as it led to an enhancement in hydrogen generation, and furthermore can be used as a "reporter" of the excited states populated in TRIR studies. Additionally, picosecond (ps) and nanosecond (ns) TAS measurements were performed. Electrochemical and spectroelectrochemical experiments were performed to help in identifying the intermediates formed during photocatalysis. TRIR studies indicate wavelength-dependent photophysics which is not commonly reported in the literature, with the excited state(s) populated varying with the excitation wavelength used. The complex was also studied using Time-Resolved Infrared Spectroscopy (TRIR) combined with spectroelectrochemistry (TRIR-SEC) in order to gain deeper insights into the kinetics of the photoactive intermediates. The naphthalene diimide (NDI) moiety due to the carbonyl stretching vibrations (C=O) are excellent reporters for these studies and can track electron transfer pathways as was discussed in Chapter 3. Furthermore, TAS measurements were carried out following chemisorption of the **Ru(dceb)-NDI^{2+}** complex on nickel oxide to study charge injection.

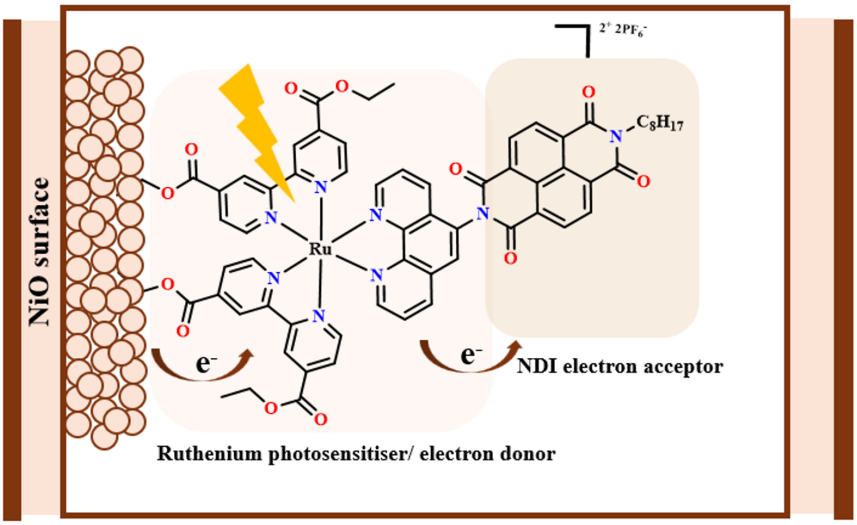


Figure 4.1 The schematic diagram represents the photosensitiser, **Ru(dceb)-NDI^{2+}** which was assessed for photocatalytic hydrogen evolution. The complex was studied on a nickel oxide surface to study charge injection and charge recombination.

4.3 Results and discussion

4.3.1 Synthesis

The **Ru(dceb)-NDI^{2+}** complex was synthesised in a similar manner to that of **RuNDI^{2+}**, as described in Chapter 3 (see Figure 4.2 and Synthesis Section in Appendix B). First, the precursor (NDI-octyl) was synthesised, by condensation of 1,4,5,8-naphthalenetetracarboxylic dianhydride (NDA), commercially available from ®Fluorochem Ltd., with octylamine, as commonly reported in the literature [18] and as described in Chapter 3. Subsequently, NDI-octyl was reacted with 5-amino-1,10-phenathroline by refluxing in acetic acid overnight to form NDI-phen (Step 1, Figure 4.2). The ruthenium complex was prepared by first synthesising $Ru(dceb)_2Cl_2$ following a literature method [14], and subsequent reaction with NDI-phen, in ethanol at reflux temperature. The final **Ru(dceb)-NDI^{2+}** complex was characterised by NMR (^{1}H, ^{13}C, COSY, See Figure SB4.1 – SB4.7 in Appendix B) and mass spectrometry (Figure SB4.8 in Appendix B). The FTIR spectrum of **Ru(dceb)-NDI^{2+}** displays carbonyl stretching vibrations at 1584, 1669, 1687, 1709 and 1729 cm^{-1}. For this complex, the NDI-based carbonyl stretching vibrations overlap with those of the ester functional groups.

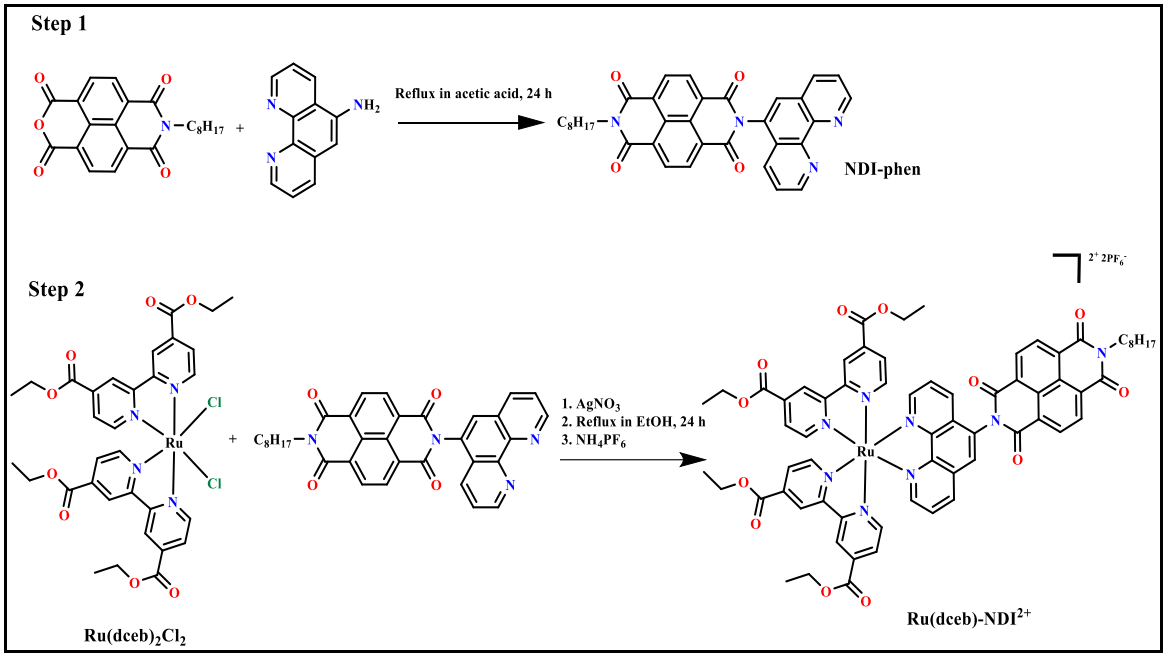


Figure 4.2 Synthetic scheme for the preparation of a **Ru(dceb)-NDI^{2+}** photosensitiser for photocatalytic hydrogen evolution.

4.3.2 UV-vis and emission spectroscopy

The UV-vis absorption and emission spectra for the **Ru(dceb)-NDI^{2+}** complex are presented in Figure 4.3 with the absorption bands summarised in Table 4.1. The spectra closely resemble previously reported findings for similar ruthenium-NDI complexes [19 – 23]. The **Ru(dceb)-NDI^{2+}** complex is characterised by an intense, broad absorption band at approximately λ_{max} = 450 – 460 nm, attributed to metal-to-ligand charge transfer (MLCT) from ruthenium to the ligand [24, 25]. The bands at 360 and 380 nm correspond to π - π* transitions within the electron-accepting NDI moiety [26, 27]. Additionally, the bands at 262 and 308 nm are associated with ligand-centered (LC) π-π* transitions, on the phenanthroline and bipyridine units [28, 29].

Upon excitation at 360 or 450 nm, the **Ru(dceb)-NDI^{2+}** complex exhibits a broad emission centered at λ_{max} = 650 nm. This emission profile resembles the standard ruthenium reference compound, $[Ru(bpy)_3]^{2+}$ [30, 31]. Generally, incorporation of naphthalene diimide moieties results in quenching of the emission due to electron transfer from the electron donor (ruthenium unit) towards the electron acceptor NDI, as reported in the literature and discussed for **RuNDI^{2+}** in Chapter 3 [30, 32 – 33]. However, in the case of **Ru(dceb)-NDI^{2+}**, the emission is not quenched. This suggests that the ester

functional groups reduce the efficiency of the electron transfer to the NDI, because of their electron-withdrawing nature. The fluorescence lifetime of the **Ru(dceb)-NDI^{2+}** was measured at 650 nm following excitation at 355 nm in acetonitrile under deoxygenated conditions. A monoexponential signal was observed with a lifetime of 439 ns assigned to population of the ^{3}MLCT state of the Ru(II) center [14, 28, 34 – 35].

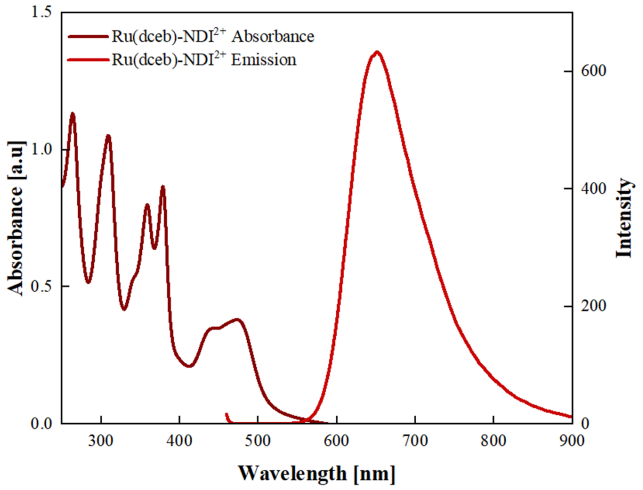


Figure 4.3 The electronic absorption and emission spectra of the **Ru(dceb)-NDI^{2+}** complex in acetonitrile.

4.3.3 Electrochemistry

Electrochemical measurements were carried out for the **Ru(dceb)-NDI^{2+}** complex to determine its redox behaviour, which will be used further in spectroelectrochemical studies. Cyclic voltammetry was carried out in acetonitrile using 0.5 mm of the **Ru(dceb)-NDI^{2+}** and 0.1 M tetrabutylammonium hexafluorophosphate (TBAH) was used as the supporting electrolyte. The solution was purged with nitrogen prior to measurements. Additionally, all potentials were recorded against a ferrocene/ferrocenium (vs Fc^{+}/Fc) redox couple. The reduction potentials obtained during the experiments are summarised in Table 4.1. The **Ru(dceb)-NDI^{2+}** complex showcases electrochemical behaviour to that of similar type ruthenium-NDI complexes reported in the literature [19 – 23]. The negative region displayed five reversible to quasi-reversible waves (Figure 4.4). The first and second anodic peaks at E° = –0.90 and –1.36 V (vs Fc^{+}/Fc) are consistent with reductions based on the NDI moiety [19 – 23]. Furthermore, the three reduction potentials at –1.54, –2.0, –2.25 V are attributed to reductions of the phenanthroline and bipyridine ligands [14, 36 – 38]. For example, electrochemical studies by Villani at al. [36] showed that for the standard reference $[Ru(bpy)_3]^{2+}$, the three reduction potentials were determined at $E_{½}$ = –1.75, –1.94 and –2.18 V (vs Fc^{+}/Fc). Barbante et al. [37] examined

the electrochemical properties of tris(2,2'-bipyridine)ruthenium(II) with dimethyl 2,2'-bipyridine-4,4' dicarboxylate substituent on the peripheral ligands of the bipyridine moiety. For the tris(2,2'-bipyridine)ruthenium(II) complex, the authors observed similar reduction potentials to the ones reported by Villani et al. [36], and these were reported to be –1.75, –1.94 and –2.18 V, in addition the oxidation potential was determined at $E_{½}$ = 0.89 V. Upon the functionalisation of the bipyridine moiety in tris(2,2'-bipyridine)ruthenium(II) with electron withdrawing ester moieties, there was a positive shift by approximately 0.20 V observed in reduction and oxidation potentials in contrast to the unsubstituted analogue. The reduction potentials for the ester substituted analogue were $E_{½}$ = –1.39, –1.85 and –2.05 V. The oxidation potential was shifted to more positive values and was measured at 0.98 V, compared to the previously reported value of 0.89 V [37]. Another study from our research group involving electrochemical studies of ruthenium complexes, which incorporated ester moieties was carried out by Cerpentier et al. [14]. The authors assigned the reduction potentials at $E_{½}$ = –1.41 and –1.54 V to reduction at the ester functionalised bipyridine ligands in the $[Ru(dceb)_2(bpt)Re(CO)_3Cl](PF_6)$ complex, and these values closely align with the ones observed for the **Ru(dceb)-NDI^{2+}** complex. Additionally, they reported two oxidation potentials at $E_{½}$ = 0.68 and 0.81 V [14]. Notably for the **Ru(dceb)-NDI^{2+}** complex, no oxidation was observed in the positive region, which typically occurs at 0.15 – 1.62 V for Ru^{II}-Ru^{III} oxidations [38], and this may be due to the electron-withdrawing ester groups.

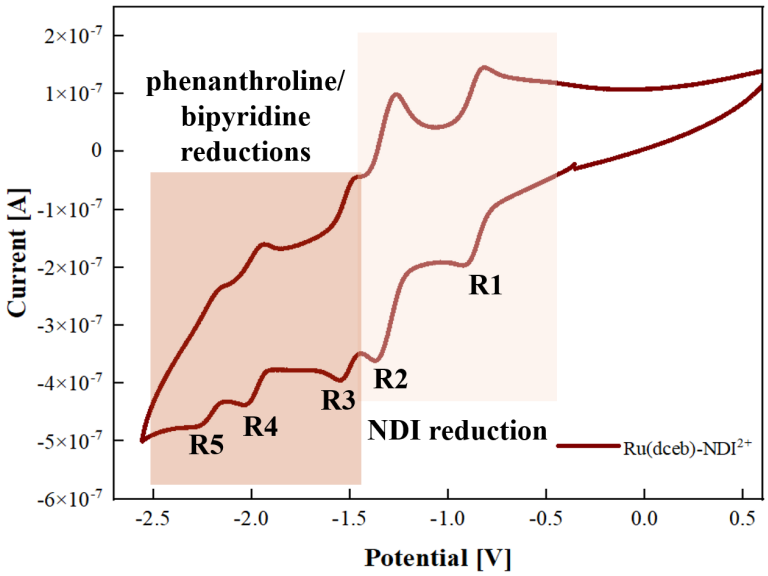


Figure 4.4 A cyclic voltammogram of **Ru(dceb)-NDI^{2+}** in acetonitrile/TBAH. The figure presents the reduction steps to **Ru(dceb)-NDI^{+}** (NDI-based, at R1), **Ru(dceb)-NDI** (NDI-based, at R2), **Ru(dceb)-NDI^{-}** (bpy-based, at R3), **Ru(dceb)-NDI^{2-}** (bpy-based, at R4) and **Ru(dceb)-NDI^{3-}** (phen-based, at R5). Experimental conditions employed glassy working electrode, T = 298 K, and scan rate used v = 100 mV/s.

Table 4.1 Summary of the spectroscopic, electrochemical, and spectroelectrochemical data for the **Ru(dceb)-NDI^{2+}** complex and the reduced species generated. All experiments were conducted in acetonitrile.

UV-vis absorption	**λ_{max} (nm)**
Ru(dceb)-NDI^{2+}	262, 308, 360, 380, 450
Electrochemistry	**E° (V)**
Ru(dceb)-NDI^{2+}	–0.90, –1.36, –1.54, –2.00, –2.25
UV-vis Spectroelectrochemistry	**λ_{max} (nm)**
Ru(dceb)-NDI^{+} one-electron reduced	308, 358, 374, 400, 474, 584, 605, 690, 768
Ru(dceb)-NDI two-electron reduced	310, 395, 416, 471, 603
Ru(dceb)-NDI^{-} three-electron reduced	366, 396, 417, 511, 548, 597
IR-Spectroelectrochemistry	**ν_{CO} (cm^{-1})**
Ru(dceb)-NDI^{+}	1515, 1599, 1637, 1730
Ru(dceb)-NDI	1519, 1599, 1635, 1693, 1727
Ru(dceb)-NDI^{-}	1523, 1599, 1680

4.3.4 UV-vis Spectroelectrochemistry (UV-vis-SEC)

Electrochemistry, combined with UV-vis spectroscopy, was employed to monitor the spectral changes in the UV-vis absorption spectra of the electrochemically reduced species when solutions containing **Ru(dceb)-NDI^{2+}** was reduced. A spectroelectrochemical optically transparent thin layer electrode (OTTLE) cell was used, and all reduced species were obtained in a stepwise manner by varying the potential. Firstly, the **Ru(dceb)-NDI^{2+}** complex was dissolved in acetonitrile/TBAH and purged with nitrogen. Subsequently, the solution was placed in the OTTLE cell, and the potential was applied. Simultaneously, the UV-vis absorption spectra were recorded following the electrochemical reduction of the parent complex at the specific applied potentials.

It is well known from the literature that the reduced species of NDI have characteristic absorption bands and undergo distinct colour changes upon chemical (for example by addition of triethylamine) or electrochemical reduction (applying the electrochemical potential) [23, 39 – 41]. Notably, following reduction, the absorption bands for NDI

extend into the near-infrared region (~ 600 – 800 nm) [39, 40]. In Chapter 3, the role of these intermediates in hydrogen evolution was discussed. Andric et al. [39] reported UV-vis-SEC studies for naphthalene diimide compounds with alkyl substituents at the imide position, which differed in the chain length. Using an OTTLE cell in DMF, the authors examined the reduced species and reported that the one-electron reduced NDI, substituted with the alkyl group $-CH_2(CH_2)_3CH_3$ exhibited absorption bands at 272, 337, 376, 400, 474, 608, 679, and 755 nm. Upon further reduction, the two-electron reduced species displayed absorption bands at 376, 396, 420, 508, 550, and 597 nm. In another study, Karoń et el. [40] investigated NDIB-NH_2 (N-butyl naphthalenediimide) using Bu_4NPF_6/ACN for spectroelectrochemical analysis. The first electron reduction resulted in the formation of a strong absorption band at 480 nm, accompanied by weaker bands at 530, 610, 680 and 760 nm. Further electrochemical reduction led to changes in the UV-vis spectrum above 390 nm, with broader and less structured bands and an intense absorption feature at 590 nm was reported. These spectral changes indicated conversion of the neutral parent complex to the one- and two electron reduced forms of NDIB-NH_2 [40].

Displayed in Figure 4.5 (A – D) are the UV-vis spectra of each reduced species in Figure 4.5E. Following an applied potential of –0.86 V, in an acetonitrile solution of **Ru(dceb)-NDI^{2+}** the one electron reduced species, **Ru(dceb)-NDI^{+}** forms. The UV-vis spectrum for this complex, exhibited weaker absorption bands corresponding to the NDI parent species at approximately 380 nm and new absorption bands at 474 and 605 nm, with additional, weaker and broader bands at 690 and 768 nm (Figure 4.5B). Further reduction at –1.32 V led to a decrease in the intensity of these absorption bands at 474 and 605 nm, and the formation of new bands at 395 and 416 nm (Figure 4.5C). These changes in UV-vis absorption spectra indicate the formation of the two-electron reduced species, **Ru(dceb)-NDI**. Applying a higher potential of –2.1 V led to a third reduction with the formation of **Ru(dceb)-NDI^{-}**. This latter species is characterised by the appearance of a new and relatively broad absorption band at 366 nm and a decrease in absorbance of the bands at 474 and 605 nm. Additionally, the bands in the region 470 – 620 nm appeared significantly broader, and a strong absorption band was evident at 544 nm (Figure 4.5D). The disappearance of the band at ~ 310 nm in the three electron reduced species suggests significant changes are most likely occurring at the ester-functionalised bipyridine ligands, instead of on the NDI moiety and this is further supported by literature findings [14].

The first and second electron reduced species are assigned to reductions at the NDI moiety, however the assignment of the third reduction for **Ru(dceb)-NDI^{2+}** is less straightforward. For example, Cerpentier et al. [14] reported that for the [Ru(dceb)$_2$(bpt)Re(CO)$_3$Cl](PF$_6$) complex the reduced species exhibited absorption bands at 276, 352, 444 and 548 nm and similarly to **Ru(dceb)-NDI^{2+}**, the band at ~ 310 nm disappeared upon electrochemical reduction. The authors concluded that the band at 444 nm was attributed to a ligand-to-metal charge transfer (LMCT), while the band at 548 nm was attributed to a ligand centered π-π* transition. They assigned the second reduction on the second peripheral ligand [14].

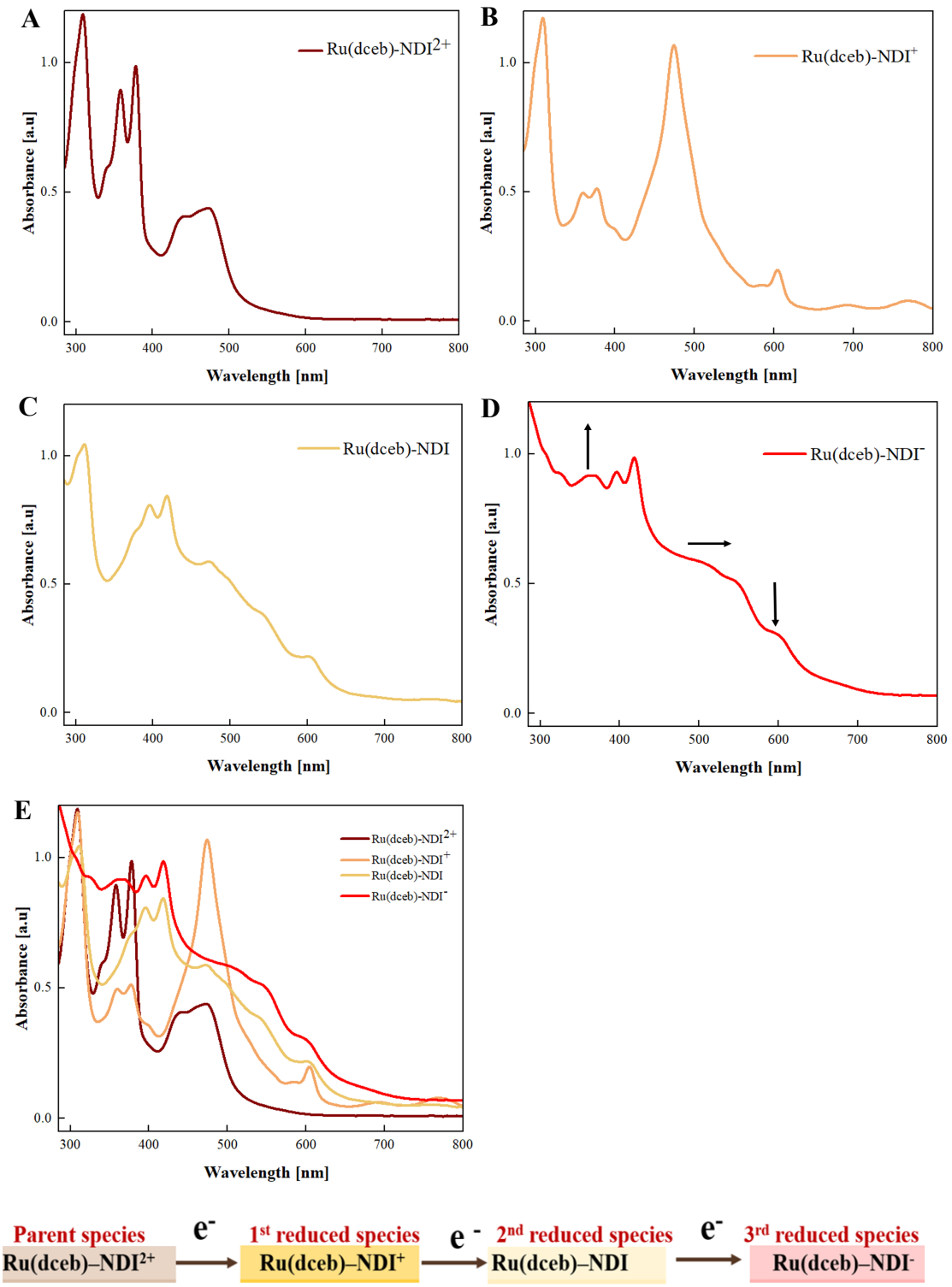


Figure 4.5 The UV-vis spectroelectrochemical spectra of (**A**) parent species of **Ru(dceb)-NDI^{2+}** (**B**) the one-electron reduced species **Ru(dceb)-NDI^{+}** following reduction at –0.86 V (**C**) the two-electron reduced **Ru(dceb)-NDI** following reduction at –1.32 V (**D**) the three-electron reduced **Ru(dceb)-NDI^{-}** following reduction at –2.1 V (**E**) an overlay of all the reduced species for the **Ru(dceb)-NDI^{2+}** complex. The spectroelectrochemical analysis was carried in acetonitrile using TBAH as a supporting electrolyte. A Pt minigrid working electrode was used in the OTTLE cell, T = 298 K. The scan rate of 0.002 V/s was applied.

4.3.5 IR-Spectroelectrochemistry (IR-SEC)

Spectroelectrochemical measurements for the **Ru(dceb)-NDI^{2+}** complex and the reduced species were also carried out by combining electrochemistry with IR spectroscopy (IR-SEC). The carbonyl stretching vibrations (C=O) localised on both the NDI unit and the ester groups on the peripheral ligands enable monitoring of these stretching vibrations, and the localisation of the electron in the reduced species, when the potential is applied. The wavenumber for the reduced species formed will provide an insight into the location of the reduction, which subsequently aids TRIR-SEC studies, which are discussed in the following sections. The IR-SEC experiment, similarly to UV-vis SEC was carried out in acetonitrile with TBAH acting as the supporting electrolyte in an OTTLE cell. The individual reductions were monitored and recorded using FTIR in a stepwise manner. The IR difference spectra of each reduced species were obtained by subtracting the spectrum of the previously formed reduced species and are presented in Figure 4.6 (A – D). The neutral parent species, **Ru(dceb)-NDI^{2+}**, before applying the potential, displays carbonyl stretching vibrations at 1584, 1669, 1687, 1709 and 1729 cm^{-1} (Figure 4.6A). The C=O vibrations, localised both on the NDI unit and on the ester groups, overlap in the range 1670 – 1730 cm^{-1}, with the band at 1584 cm^{-1} assigned to the aromatic rings of the NDI moiety, based on the literature reports [42]. Following the first-electron reduction, the IR stretching vibrations corresponding to the parent species decrease and appear as negative bands in Figure 4.6B. New stretching vibrations were observed and are shifted to lower wavenumbers at 1515, 1599, and 1637 cm^{-1} (Figure 4.6B) and are assigned to **Ru(dceb)-NDI^{+}**. Further reduction leads to the bleaching of the stretching vibrations corresponding to the one–electron reduced species and new bands grew-in at 1519, 1599 and 1693 cm^{-1}, indicating the formation of the two-electron reduced species **Ru(dceb)-NDI** (Figure 4.6C). When the solution was further reduced, leading to the three-electron reduced species, **Ru(dceb)-NDI^{-}** absorption bands form at 1523, 1599, and 1680 cm^{-1} together with a bleach at 1729 cm^{-1}, corresponding to the ester vibrational mode (Figure 4.6D). The key findings from this study indicate that the first and second reductions occur on the NDI moiety [42]. The band at approximately 1730 cm^{-1} remains unchanged during the first and second reductions and is assigned to the C=O stretching mode of the ester groups. Notably, this band is shifted to lower wavenumber during the third reduction, which indicates an increase in electron density on the ester.

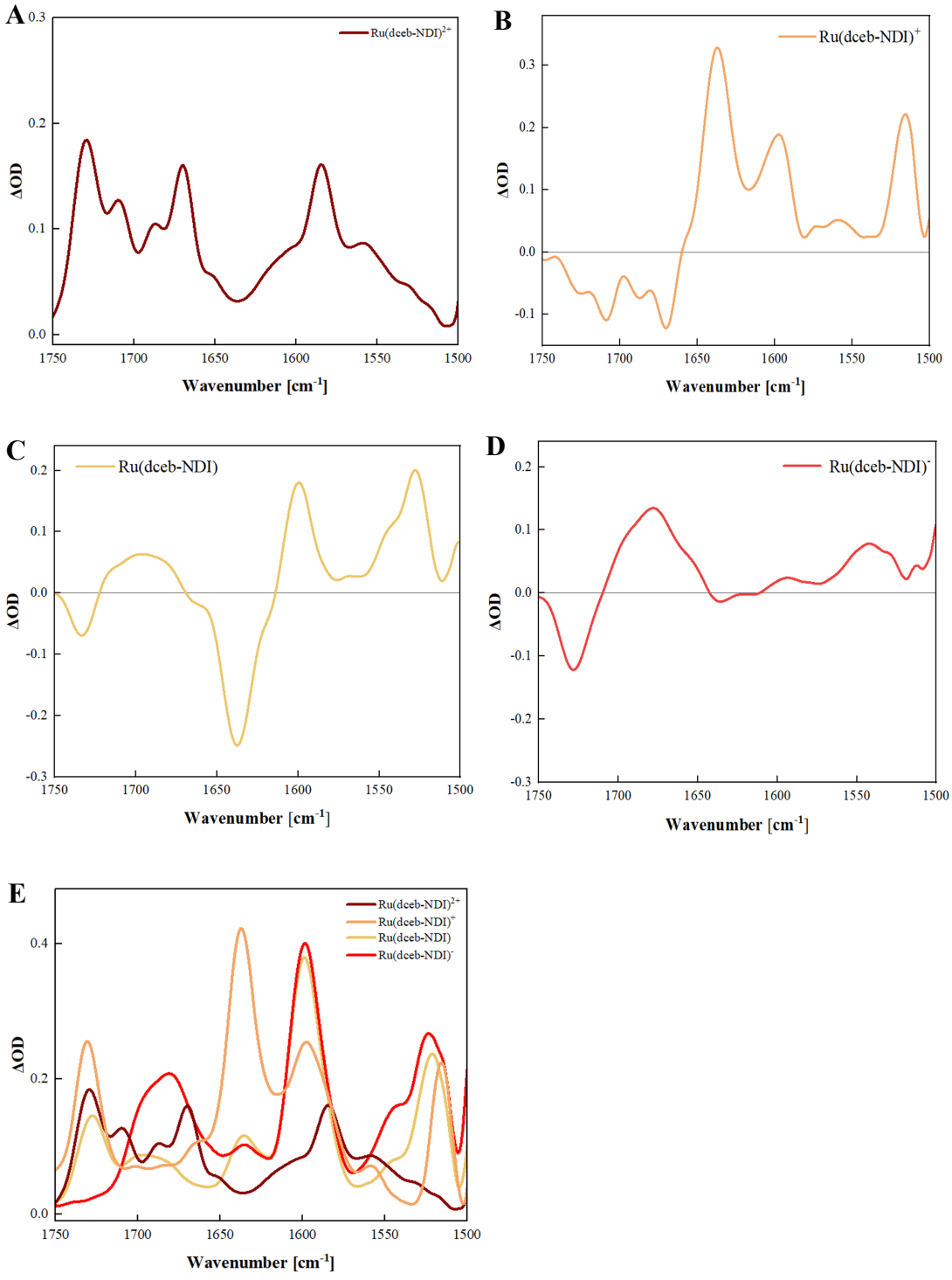


Figure 4.6 The IR-spectroelectrochemical spectra of **(A)** parent species of **Ru(dceb)-NDI^{2+} (B)** the difference spectrum of one-electron reduced species **Ru(dceb)-NDI^{+} (C)** the difference spectrum of two-electron reduced **Ru(dceb)-NDI (D)** the difference spectrum of three-electron reduced **Ru(dceb)-NDI^{-} (E)** an overlay of all reduced species of the **Ru(dceb)-NDI^{2+}** complex. The spectroelectrochemical analysis was carried in acetonitrile using TBAH as a supporting electrolyte. The experimental set up involved Pt minigrid working electrode, OTTLE cell, T = 298 K. The scan rate of 0.002 V/s was applied.

4.3.6 Time-Resolved Infrared Spectroscopy (TRIR)

TRIR studies were carried out to probe the excited state properties, and kinetics of the charge separation and charge recombination processes. The ester functional groups localised on the peripheral ligands, together with the carbonyl groups of the NDI unit act as excellent probes for TRIR studies, which facilitates tracking of electron transfer processes following photoexcitation on the ultrafast time scales. The resulting spectra with their corresponding kinetic traces following excitation of **Ru(dceb)-NDI^{2+}** are presented in Figure 4.7 (A – B). All kinetic traces were analysed using Glotaran [43].

TRIR spectroscopy was carried out in acetonitrile using two excitation wavelengths, 420 nm (Figure 4.7A) and 365 nm (Figure 4.7B). As observed previously, the FTIR spectrum for **Ru(dceb)-NDI^{2+}** displays carbonyl stretching vibrations at 1584, 1669, 1687, 1709 and 1729 cm^{-1}. The carbonyl stretching vibrations of the NDI moiety overlap with those of the ester groups. Following excitation at 420 nm, the ester band at 1729 cm^{-1} depletes, together with the formation of a new transient band at 1706 cm^{-1}. This new band at approximately 20 cm^{-1} lower in frequency indicates population of a $^{3}MLCT_{EtOOC-bpy}$ [14, 17]. On the time base that the experiments were conducted, no evidence for recovery of the signal was observed. At this excitation wavelength (420 nm) no transient signals were observed that suggest electron transfer towards the NDI.

The TRIR spectra following excitation of **Ru(dceb)-NDI^{2+}** at 420 nm, is consistent with literature findings, where Cerpentier et al. [14] investigated the ester containing $[Ru(dceb)_2(bpt)Re(CO)_3Cl](PF_6)$ complex. In these, the authors observed a shift to lower energy (with a C=O stretching vibration at 1730 cm^{-1}) upon photoexcitation at 510 nm, similar to our results, indicating electron transfer from the ruthenium towards the peripheral ligands. Likewise, similar TRIR spectra were reported by Põldme et al. [17], who observed a bleach at 1730 cm^{-1}, corresponding to carbonyl ester groups following excitation at 470 nm.

In contrast, upon excitation at 365 nm (Figure 4.7B), the **Ru(dceb)-NDI^{2+}** complex behaves differently, and two distinct excited states are populated. Following excitation at this higher energy wavelength, the parent carbonyl stretching vibration depletes at 1729 cm^{-1}, and new bands concomitantly form at 1718, 1677 and 1650 cm^{-1}.

The organic carbonyl groups of the ester-functionalised bipyridine ligands deplete at 1729 cm^{-1} with formation of a transient band at 1718 cm^{-1}. This new band is assigned to the

ruthenium $^3MLCT_{EtOOC–bpy}$ state [14, 17], which persists onto the nanosecond time scale. This behaviour is consistent with studies carried out following excitation at 420 nm. The two additional transient bands at 1677 and 1650 cm^{-1} are assigned to formation of a charge-separated state. The lifetime for the charge recombination process was determined to be τ_{CR} = 306 ps, using Glotaran analysis. The carbonyl stretching vibration on the NDI unit, assigned to the charge-separated (^3CS) excited state $Ru(dceb)^{III}$-$NDI^{–}$ state shift to lower energy compared to the parent bands in the ground state. The bands at 1677 and 1650 cm^{-1} decay to the ground-state within 9500 ps.

Auty et al. [44] reported TRIR studies for a NDI-Pt-PTZ complex (PTZ = phenothiazine) following excitation at 520 nm. Ground-state bleaches for the ν(CO) of the NDI moiety, were observed at 1663 and 1700 cm^{-1}, while aromatic vibrations for the NDI unit were evident at 1565 cm^{-1}. The C=O stretching vibrations were shifted to lower frequency, together with an enhancement in the vibrational modes for the excited state. The transient bands at 1519, 1592 and 1626 cm^{-1} following excitation of the NDI-Pt-PTZ complex were assigned to formation of a charge-separated state.

The TRIR data clearly demonstrate the wavelength dependent photophysics following excitation of the **Ru(dceb)-NDI^{2+}** complex at both 420 and 365 nm. In designing complexes for various applications, it is important to understand the excited states populated, for the application.

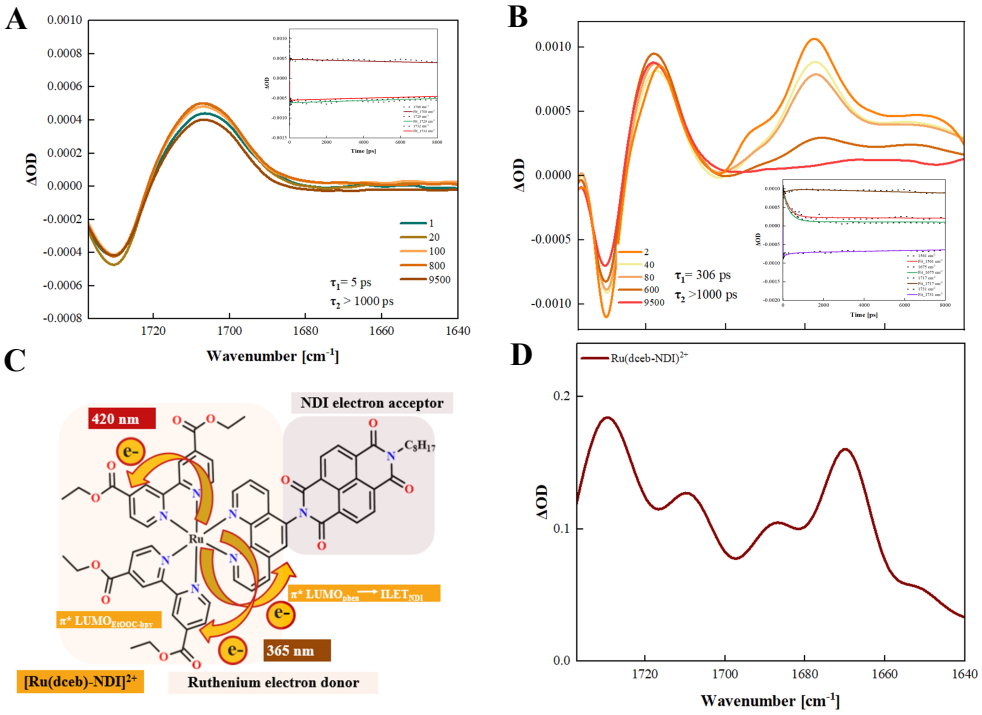


Figure 4.7 TRIR spectra following excitation of **Ru(dceb)-NDI^{2+}** at 420 nm in **(A)**. TRIR spectra of the **Ru(dceb)-NDI^{2+}** following excitation at 365 nm in **(B)**, schematic of wavelength-dependent behaviour on electron transfer **(C)**, FTIR spectrum of **Ru(dceb)-NDI^{2+}** in **(D)**.

4.3.7 Nanosecond transient absorption studies in solution and under photocatalytic conditions (ns-TAS)

Nanosecond transient absorption spectroscopy measurements were performed in acetonitrile, as well as under photocatalytic conditions to further investigate the photophysical properties of the photoactive intermediates formed during photocatalysis. These experiments were carried out following excitation at 355 nm.

Upon excitation at 355 nm, the transient absorption map displayed in Figure 4.8 was obtained. The bleach observed at 450 nm corresponds to the MLCT in the parent ruthenium complex. The bleaches at 360 and 380 nm correspond to ground-state absorption of the naphthalene diimide unit (π-π* transitions). New transient bands are evident at 330, 350 and 380 nm, which are assigned to a Ru ^{3}MLCT $_{EtOOC–bpy}$. The lifetime of the excited state was determined to be 439 ns. O'Reilly [45] reported in her PhD dissertation, ns-TAS studies for a [Ru(dceb)$_2$(bpt)](PF$_6$) complex and observed new absorption bands at approximately 350 and 380 nm, which were assigned to charge transfer towards the ester moieties. Pan et al. [13] carried out ps-TAS measurements in acetonitrile for a [Ru(dceb)$_2$(2,5-bpp)PtIS]$^{2+}$ complex, following excitation at 460 nm.

The spectral changes they reported to population of a $^{3}MLCT_{EtOOC–bpy}$ (ester functionalised peripheral ligand) excited state. The nanosecond-TAS studies reported here for the **Ru(dceb)-NDI^{2+}** complex are similar to those reported by O'Reilly [45] and Pan et al. [13].

Typically, metal complexes and organic compounds incorporating NDI ligand exhibit long-lived excited states and are characterised by distinct absorption bands in the spectral profile of ns-TAS, and examples of such systems are described as follows. For example, Wu et al. [46] studied an NDI triad using nanosecond transient absorption spectroscopy. Following excitation at 530 nm in toluene, the authors observed excited state absorption features between 400 – 500 nm and 650 – 750 nm, with a lifetime of 276 μs, which they assigned to the ^{3}NDI excited state. Another study by Doria et al. [47] focused on examination of the triplet excited states of the bromo- and alkylamino-substituted NDI compounds. The authors reported that upon excitation at 355 nm, new transient bands were observed in the region 380 – 700 nm, with a dominant band at 430 nm. The triplet lifetimes for their library of NDI compounds were in the range 8 – 30 μs. In contrast, the TAS spectrum of **Ru(dceb)-NDI^{2+}** is primarily dominated by the excited state of ruthenium moiety, specifically the photoinduced population of ester-functionalised ligand (Ru $^{3}MLCT_{EtOOC–bpy}$) and there is no evidence for the formation of a long-lived triplet excited state of NDI as in studies conducted by Wu and Doria et al. [46, 47].

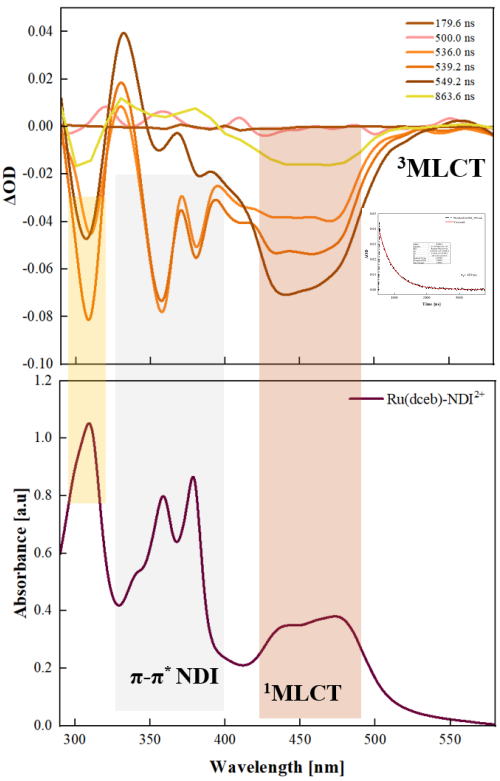


Figure 4.8 Nanosecond transient absorption spectrum of the **Ru(dceb)-NDI^{2+}**, which primarily indicates spectral changes from 500 – 550 ns and (inset) represents the decay trace for the triplet lifetime. The ns-TAS measurements were carried out in acetonitrile following excitation at 355 nm. The solution prior to the measurement was freeze-pump-thawed using three cycles.

Nanosecond transient absorption studies were also carried out under photocatalytic conditions in the presence of triethylamine (Figure 4.9), similarly to studies carried out in Chapter 3. The laser sample was prepared in such a way to match the conditions those used in photocatalysis (see Photocatalytic results section). The complex was dissolved in acetonitrile, with triethylamine as the sacrificial electron donor and $Pt(DMSO)_2I_2$ was used as the catalyst. The mixture was placed in a laser cell and freeze-pumped-thawed three times. Prior to excitation, the UV-vis absorption was recorded, and new absorption bands were evident at 475 and 608 nm, which are similar in position to the bands of the one-electron reduced species, indicating chemical reduction by triethylamine (in the absence of oxygen), (see Figure SB4.9 in Appendix B). Upon excitation at 355 nm, ground-state bleaches occurred at 475 and 608 nm, which is attributed to one-electron reduced species, **Ru(dceb)-NDI^{+}** as observed in UV-vis-SEC experiments. A transient band was observed between 500 – 550 nm and this could correspond to population of the ^{3}MLCT of Ru(II) centre or the one-electron reduced species of the $[Ru(bpy)_3]^{2+}$ complex [48 – 51]. For example, Rivarola et al. [50] examined the photophysical properties of $[Ru(bpy)_3]^{2+}$ in the presence of various amines including triethylamine using ns-TAS

measurements. Following excitation at 532 nm, the complex exhibited a distinct transient band at ~ 510 nm, which was attributed to the one-electron reduction ($[Ru(bpy)_3]^+$) of the $[Ru(bpy)_3]^{2+}$ complex. Similar ns-TAS studies of the $[Ru(bpy)_3]^{2+}$ complex in triethylamine were carried out by Ishitani et al. [51], in which the authors concluded that $[Ru(bpy)_3]^+$ is formed following light irradiation in the presence of triethylamine [50, 51]. In our studies of **Ru(dceb)-NDI^{2+}**, it is difficult to determine the nature of the transient band observed at 500 – 550 nm under photocatalytic conditions. However, this band is most likely attributed to one-electron ruthenium reduced species, $Ru(dceb)_2phen^+$. Nevertheless, its absorption features cannot be determined following chemical reduction with triethylamine, as the NDI moiety is also reduced under these conditions. As a result, there could be overlapping signals from both the chemically reduced NDI and the ruthenium moiety.

Additionally, the excited state absorption features at 395 and 416 nm suggests formation of the two-electron reduced species, **Ru(dceb)-NDI** and with the spectral changes similar to those observed in UV-vis-SEC measurements, following electrochemical reduction of **Ru(dceb)-NDI^{2+}**, (Figure 4.9). Kim et al. [52] studied the photophysical properties for the anion radical of N,N-dioctylnaphthalene diimide ($NDI^{\cdot -}$), using TAS (they used 3-nitrobenzaldhyde as a chemical redundant instead of triethylamine as used in our studies). Following excitation at 605 nm, the authors reported that a ground-state bleach at 473 nm was due to the one-electron reduced species on the NDI moiety, which closely aligns with our studies, where bleaches at 475 and 608 nm, were attributed to one-electron reduced species, **Ru(dceb)-NDI$^+$**.

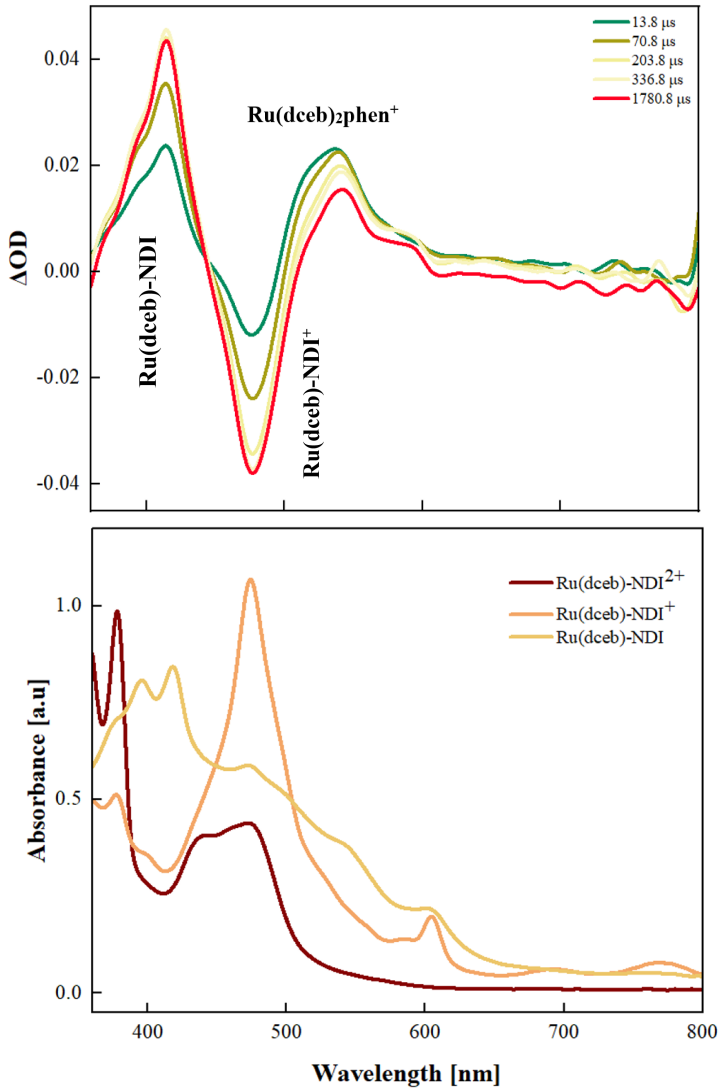


Figure 4.9 Nanosecond transient absorption spectra of the **Ru(dceb)-NDI^{2+}** complex under photocatalytic conditions in a mixture of ACN/TEA and Pt(DMSO)$_2$I$_2$ following excitation at 355 nm. The graph underneath displays UV-vis-SEC results for the parent species, one- and two-electron reduced species of **Ru(dceb)-NDI^{2+}**.

4.3.8 Picosecond transient absorption (ps-TAS)

Picosecond transient absorption spectroscopy was performed to further examine the kinetics and dynamics of the electron transfer on the ultrafast timescale. These experiments were conducted in solution using acetonitrile, and also when the **Ru(dceb)-NDI^{2+}** complex was chemisorbed onto nickel oxide (Figure 4.10). The primary goal of these measurements was to compare the photophysical processes in solution versus on a semiconductor surface. In acetonitrile solution, upon excitation at 400 nm, a ground-state bleach was observed at ~ 470 nm (within the instrumental response), which corresponds

to the MLCT in the ruthenium complex (Figure 4.10A) [17, 53]. This bleach persists beyond the 7 ns experimental window ($\tau > 7000$ ps). Moreover, photoexcitation at 400 nm leads to the population of the ^{3}MLCT $_{EtOOC–bpy}$ excited state of ruthenium within the laser pulse, indicated by a positive absorption in the range of 500 – 750 nm. Additionally, a weak signal at 605 nm was observed, which could indicate the charge-separate state of the NDI, Ru(dceb)^{III}-NDI$^{–}$. The changes observed in the UV-vis spectra are supported by literature findings. Similar results were obtained by Põldme et al. [17] for [Ru(decb)$_2$(2,5-bpp)PtI(CH_3CN)](PF_6)$_2$. Following excitation at 470 nm, a ground state bleach was observed at approximately 500 nm together with an absorption band at ~ 380 nm. These features along with a broad transient band exceeding 500 nm were attributed to the ^{3}MLCT excited state species and persisted beyond the 3 ns experimental window [17].

The behaviour differed when the **Ru(dceb)-NDI^{2+}** complex was sensitised on a nickel oxide films (Figure 4.10B). Following excitation at 400 nm a ground-state bleach was observed at ~ 450 nm. Within the laser pulse (Figure 4.10B) transient bands appeared, which were attributed to the ^{3}MLCT $_{EtOOC–bpy}$ excited state of the ruthenium complex, as observed in studies carried out in solution. Additionally, new transient features were evident at 474, 530, 605, 690 and 735 nm. The spectral profile of these absorption bands suggests the formation of the charge-separated-state Ru(dceb)^{III}-NDI$^{–}$, specifically the one-electron reduced species of the NDI. The formation of these one-electron reduced species is more evident on a NiO film than in solution.

There are only a few studies reported in the literature where naphthalene-diimide-type complexes are coated on surfaces and studied using ps-TAS. One example is work carried out by Ji et al. [54], who investigated the photoinduced electron transfer kinetics of a Ru(II)-NDI dyad sensitised on a NiO photocathode using femtosecond transient absorption spectroscopy. The dyad incorporated a terpyridine ligand coordinated to the ruthenium center and the carboxylic acid group was attached to the ligand to facilitate anchoring on the NiO surface. The complex was immobilised on a NiO film via the carboxylic acid functional group, and this enabled hole injection within ~180 fs. Subsequently, this led to an electron transfer to the NDI to form the interfacial charge-separated state [NiO(h$^+$)-Ru(II)-NDI$^{–}$]. The ultrafast formation of this charge-separated state was attributed to rapid hole injection, which effectively led to the population of the electron on the NDI unit. The authors reported transient bands at 474, 614, and 681 nm, which are similar to our results, and were assigned to the one electron-reduced NDI

species. The study concluded that the electron transfer is significantly faster (rate constant of 9.1 x 10^{11} s^{-1}) on the surface than in solution (rate constant of 1.1 x 10^{10} s^{-1}).

Another TAS study focussing on NDI on nickel oxide was conducted by Ye et al. [55]. The authors observed that in solution, NDI exhibits singlet excited-state absorption at around 550 nm. However, on a NiO film, the excited NDI state shifted from 550 nm to approximately 480 nm within a few picoseconds, which was attributed to the population of the electron on NDI species. The rate constant for hole injection from the excited NDI species to NiO surface was determined to be 8.4 × 10^{11} s^{-1}, τ = 1.2 ps, and this value closely aligns with the results obtained by Ji et al. [54]. Bentounsi et al. [56] examined the DPP-NDI system, which consisted of the naphthalene diimide moiety and diketopyrrolopyrrole (DPP) dye. Transient absorption spectroscopy studies indicated that excitation of the DPP dye facilitates efficient electron transfer from the NiO valence band to the NDI, which leads to formation of a long-lived charge-separated state (170 μs). This process results in a hole at NiO (positive charge), and the subsequent generation of the NDI reduced species [56].

Summarising ps-TAS studies, following excitation of **Ru(dceb)-NDI^{2+}** at 400 nm in solution, only a ground-state bleach is observed (with only a small feature at 605 nm that could be attributed to Ru(dceb)^{III}-NDI$^{–}$, though it has low absorption). Upon photoexcitation at 400 nm on a NiO surface, efficient photoinduced electron transfer occurs from the NiO semiconductor to the NDI. The electron from the valence band of the semiconductor was injected into NDI, resulting in a hole/positive charge on a NiO. This leads to the population of the ^{3}MLCT $_{EtOOC–bpy}$ excited state of ruthenium within the laser pulse, which is distinguished by a positive absorption starting at 500 nm and exceeding 750 nm within the experimental window. This spectral feature was also observed in the solution studies. Furthermore, over 235 ps, signature bands for one-electron reduced species of the NDI grow in at 474, 530, 605, 690 and 735 nm, leading to the formation of a charge-separated state Ru(dceb)^{III}-NDI$^{–}$. This charge-separated state recombines on the nanosecond timescale, but this is not complete within the experimental window (7 ns). When comparing the solution and surface studies, the formation of charge-separated state Ru(dceb)^{III}-NDI$^{–}$ is more evident on a NiO. These spectral changes are consistent with those reported in the literature by Ji et al. [54]

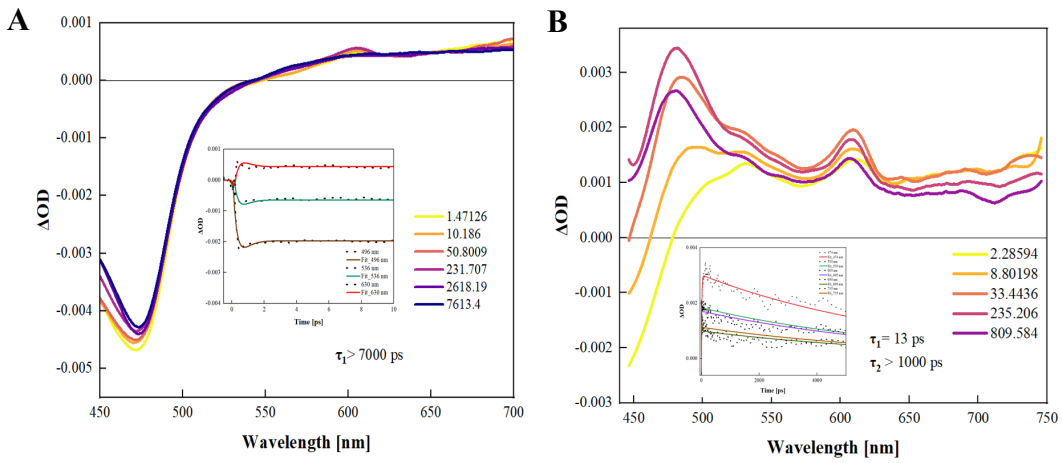


Figure 4.10 Transient absorption spectra of **Ru(dceb)-NDI^{2+}**. **(A)** ps-TAS recorded in acetonitrile following excitation at 400 nm. The inset displays kinetic traces at 496, 536, 630 nm. **(B)** ps-TAS recorded on a NiO thin film upon excitation at 400 nm. The inset shows kinetic traces at 474, 530, 605, 690 and 735 nm.

4.3.9 Time-Resolved Infrared Spectroelectrochemistry (TRIR-SEC)

As was observed in Chapter 3, TRIR-SEC technique provides a mechanism to probe the potential photoactive intermediates formed during photocatalysis. This study enables to model the photocatalytic conditions in the OTTLE cell and facilitates the investigation of electron transfer kinetics and pathways. Consequently, this allows us to gain an insight into the properties of these intermediates. Based on our previous studies, it is evident that the **Ru(dceb)-NDI^{2+}** complex behaves differently in solution, under photocatalytic conditions and when chemisorbed on the NiO surface. The experimental set up involves stepwise electrochemical reduction of the **Ru(dceb)-NDI^{2+}** complex with the formation of the reduced species confirmed by TRIR using excitation wavelengths corresponding to their absorption bands.

The **Ru(dceb)-NDI^{2+}** complex was reduced in the OTTLE cell at ~ –0.9 V to form the one-electron reduced species, **Ru(dceb)-NDI^{+}**, and subsequently excited at 420 nm (Figure 4.11A). This resulted in the depletion of the bands assigned to the ground state bleach of the ester moiety and the reduced NDI species with the bands at 1729 (ground-state bleach of the ester), 1637, 1596 and 1527 cm^{-1} (reduced NDI). Concomitantly, new bands form at 1702, 1668 cm^{-1}. The new transient band at ~ 1700 cm^{-1} is assigned to a ν(C=O) stretching vibration on the ester groups. When the same solution is excited at 510 nm, ground-state bleaches related to the reduced NDI are observed at 1637, 1601 and 1520 cm^{-1} with new and weak vibrational features at ~ 1624, ~ 1587, and ~ 1512 cm^{-1},

which decay over ~ 1000 ps (Figure 4.11B). Additionally, the depletion of the ester band is observed at 1729 cm^{-1} (ground state bleach of the ester moiety) with a formation of new relatively weak transient species at approximately 1718 – 1660 cm^{-1} (Figure SB4.11 in Appendix B).

When the **Ru(dceb)-NDI^{2+}** complex was further reduced in the OTTLE cell at ~ –1.2 V to form the two-electron reduced species, **Ru(dceb)-NDI**, the excitation wavelength was changed to 600 nm, corresponding to the absorption band of **Ru(dceb)-NDI** observed in the UV-vis-SEC measurements. When the sample was excited, bleaches were evident at ~ 1520 and ~ 1600 cm^{-1}, with new transient bands at 1628, 1578 and 1511 cm^{-1}, which similarly to one-electron reduced species, decay over ~ 1000 ps. Moreover, the depletion of the ester band is observed at 1729 cm^{-1} and a new transient band in the range of 1711 – 1660 cm^{-1} is evident. This new transient band appears to be significantly weaker when compared with experiments carried out for one-electron reduced species (Figure SB4.12 in Appendix B).

Further reduction resulted in the formation of the three-electron reduced species, **Ru(dceb)-NDI^{-}**, and subsequent excitation at 600 nm, led bleaches at ~1520 and ~1600 cm^{-1}, and new bands at 1576 and 1511 cm^{-1} (Figure 4.12B). These new transient bands had a relatively short lifetime when compared to the other species formed during the first and second reductions of the **Ru(dceb)-NDI^{2+}** complex.

The nature of the transient bands of the reduced species of the **Ru(dceb)-NDI^{2+}** complex is difficult to determine, as their absorption features are relatively weak. However, future studies, including density functional theory (DFT) calculations will be carried out to better understand these characteristic features and their origin.

Notably, NDI-based complexes along with photocatalytic systems for hydrogen evolution are not commonly studied in the literature using TRIR-SEC, however this presents new possibilities to examine electron transfer and its kinetics, in order to probe further the photoactive intermediates formed during the photocatalysis.

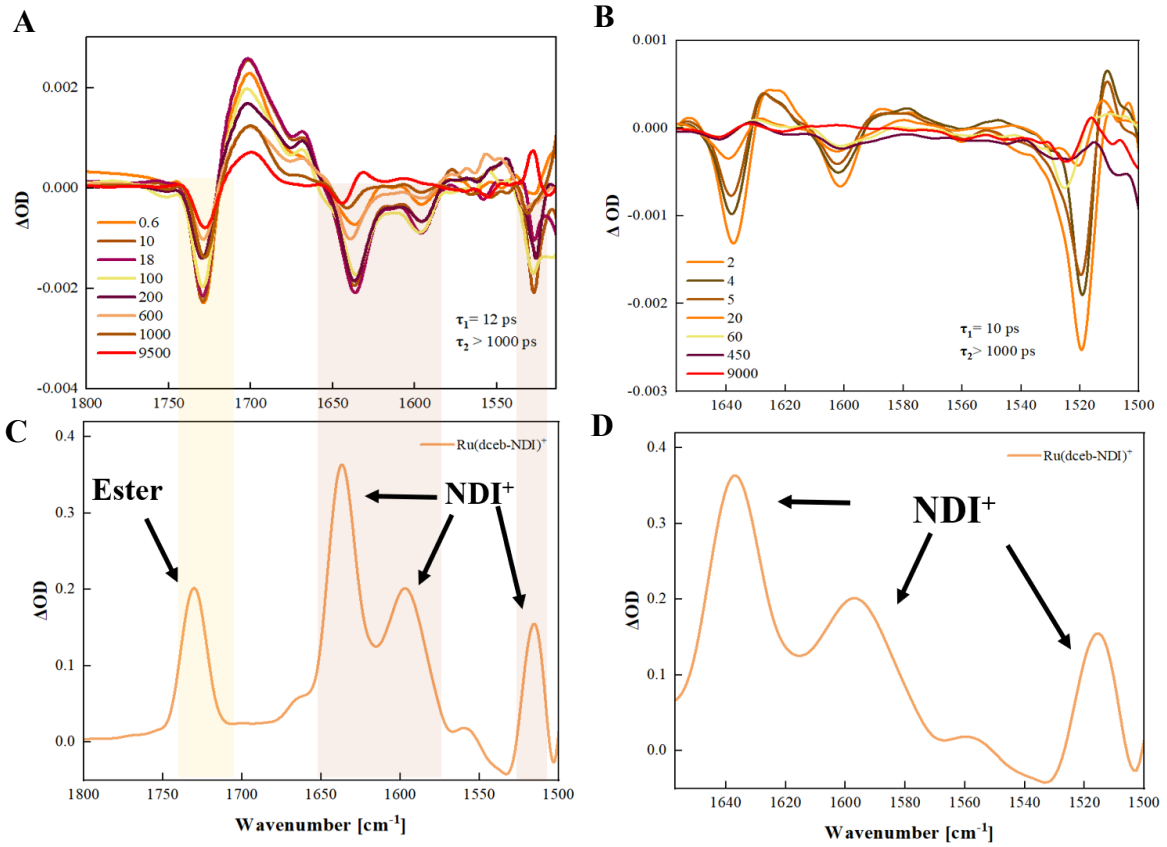


Figure 4.11 The TRIR-spectroelectrochemical spectra of **Ru(dceb)-NDI^{2+}** in acetonitrile with 0.1 M TBAH. **(A)** indicates excitation of the one-electron reduced state of **Ru(dceb)-NDI^{+}** at 420 nm, **(B)** excitation of the one-electron reduced **Ru(dceb)-NDI^{+}** at 510 nm and **(C)** presents the FTIR spectrum obtained for **Ru(dceb)-NDI^{+}** and, together with **(D)** the FTIR spectrum of **Ru(dceb)-NDI^{+}**.

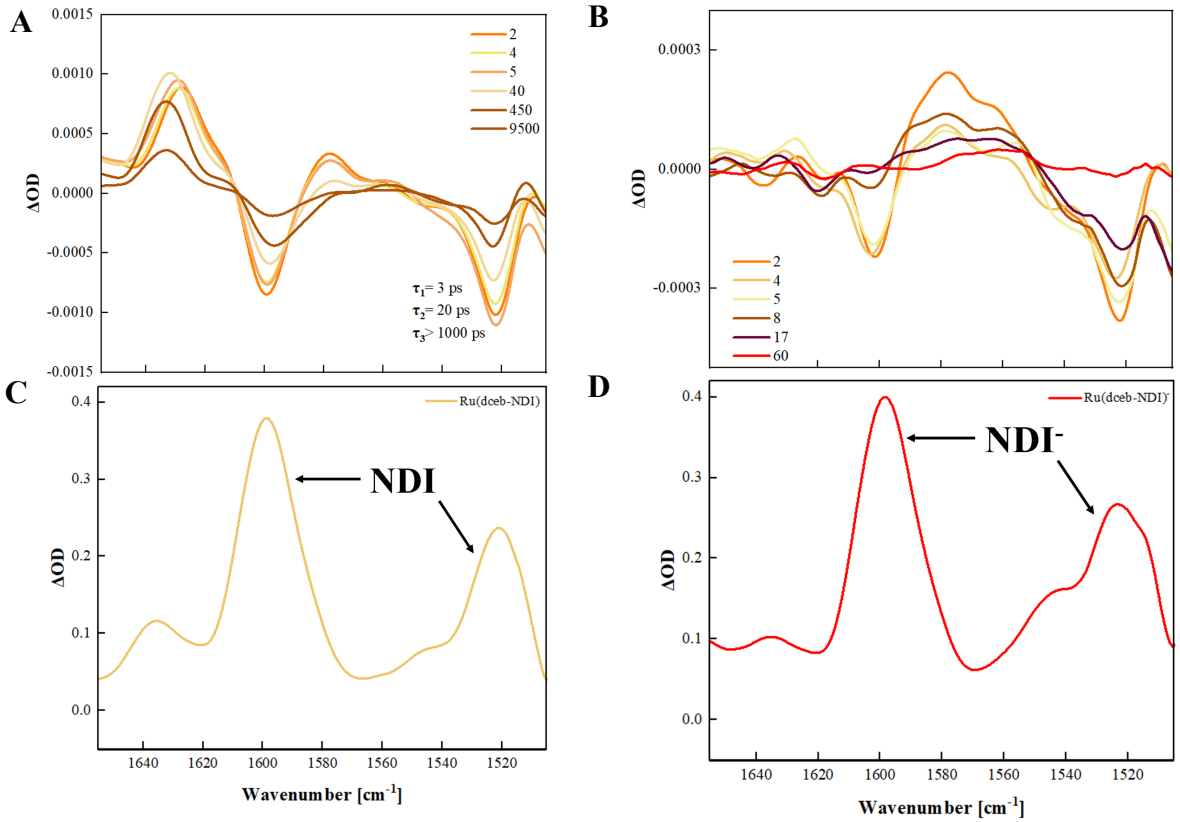


Figure 4.12 The TRIR-spectroelectrochemical spectra of **Ru(dceb)-NDI^{2+}** in acetonitrile with 0.1 M TBAH. **(A)** indicates the two-electron reduced state of the compound **Ru(dceb)-NDI** upon excitation at 600 nm, **(B)** corresponds to the three-electron reduced state **Ru(dceb)-NDI^{-}** following excitation at 600 nm and **(C)** presents the FTIR spectrum obtained for **Ru(dceb)-NDI** and **(D)** shows the FTIR spectrum of **Ru(dceb)-NDI^{-}**.

4.3.10 Photocatalytic results

Solutions containing the photosensitising unit **Ru(dceb)-NDI^{2+}** in acetonitrile, which contained triethylamine acting as a sacrificial electron donor, and deionised water serving as a proton source in a 65:30:5 ratio together with $Pt(DMSO)_2I_2$ as a catalyst were assessed for hydrogen generation. The samples were irradiated in a photoredox box equipped with LEDs at 365 or at 450 nm. The highest hydrogen evolution production was observed after 7 hours, when irradiated at 450 nm, achieving a TON of 100 (Figure 4.13). Following irradiation at 365 nm, a TON of 50 was obtained. Control experiments (containing only the photosensitising unit, **Ru(dceb)-NDI^{2+}** or the platinum catalyst, $Pt(DMSO)_2I_2$) confirmed that no hydrogen production occurred in the absence of light, catalyst or the photosensitising unit. The UV-vis absorption spectra were recorded before and after photocatalysis (see Figure SB4.9 in Appendix B). Based on the UV spectra it can be concluded, that in the absence of oxygen the one-electron reduced species forms almost instantly following reduction by triethylamine. The reduced species remains stable throughout the experiment when the Schlenk tube is closed. However, when obtaining the UV spectra of the solution before and after photocatalysis, the Schlenk tube was exposed to oxygen, and there is no evidence for the presence of one-electron reduced species in solution. It is important to highlight that these species are highly sensitive to oxygen. A TON for hydrogen of 100 surpasses that of the **RuNDI^{2+}** complex discussed in Chapter 3, which lacks the ester groups. These results indicate that the ester groups not only influence the photophysical and spectroelectrochemical properties but also enhances hydrogen evolution. Similar observations were obtained by Bindra et al. [57]. The authors reported that no hydrogen evolution was observed for their RuPd complex, however upon incorporation of ester groups in their EtOOC-RuPd complex, a TON of 400 was achieved. This increase in the photocatalytic performance, indicates that modification of the peripheral ligands affects the photophysical properties and leads to the higher TONs for hydrogen evolution. Pan et al. [13] suggested that incorporation of the ester groups results in stabilisation of the ^{3}MLCT, as the peripheral ligands act as electron reservoirs and consequently this influences the pathway of the second electron transfer during photocatalysis [13]. The enhanced photocatalytic activity upon incorporation of the ester groups remains a subject for further studies, and density functional theory (DFT) calculations would be required for this purpose.

Photocatalytic hydrogen evolution using **Ru(dceb)-NDI^{2+}** was also investigated under similar conditions but instead of adding $Pt(DMSO)_2I_2$, the complex was immobilised on

TiO_2 together with platinum nanoparticles, following the method reported in the literature [58]. TiO_2 platinum nanoparticles were added to a triethylamine sacrificial electron donor solution, containing the **Ru(dceb)-NDI^{2+}** complex. The solution was degassed using three freeze-pump-thaw cycles and subsequently sonicated for 20 minutes, followed by irradiation with a 450 nm LED. Unfortunately, hydrogen evolution was lower compared to the typical photocatalytic conditions without TiO_2, achieving a turnover number of 39 after 6 hours of irradiation.

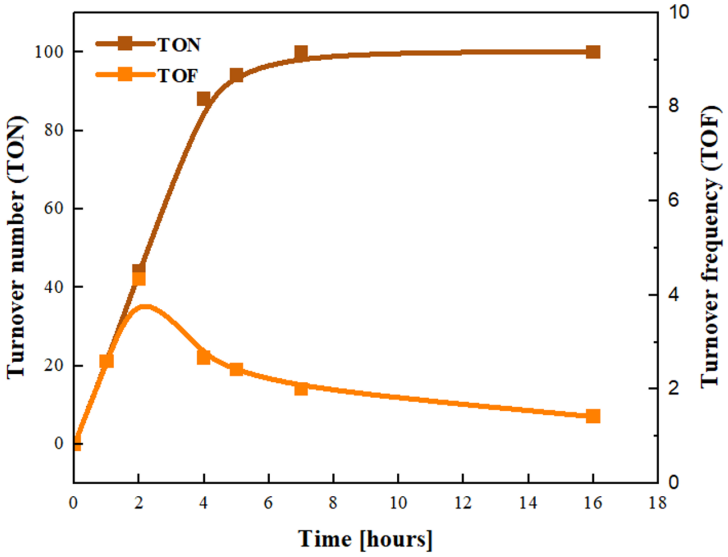


Figure 4.13 Time dependent photocatalysis for **Ru(dceb)-NDI^{2+}**. The turnover numbers at various time intervals (brown) and TOF (orange) under photocatalytic conditions in acetonitrile, triethylamine and water (65:30:5 ratio) upon irradiation at 450 nm.

4.3.11 Preliminary chronoamperometry measurements and immobilisation studies

As the **Ru(dceb)-NDI^{2+}** complex generates hydrogen, the complex was immobilised on nickel oxide thin films. The study was conducted using methods reported in the literature [14, 59], employing a photoelectrochemical (PEC) test device equipped with a three-electrode glass cell, where the complex was immobilised on a thin mesoporous NiO film, approximately 1.5 micron thick. The counter electrode was a platinum wire, and the reference electrode was Ag/AgCl (with 0.1 M KCl acting as the supporting electrolyte). The **Ru(dceb)-NDI^{2+}** complex was dissolved in acetonitrile (dye bath at a concentration 3 mM), and the NiO films, composed of fluoride-doped tin oxide glass, were immersed in this solution and allowed to adsorb overnight. Afterwards, the NiO films sensitised with the **Ru(dceb)-NDI^{2+}**, were dried at 450°C, and cooled to room temperature. The PEC device was filled with an electrolyte solution and purged with argon. All electrodes

together with the NiO film were connected to a potentiostat, and a 300 W Xe arc lamp was used as the irradiation source [14, 59].

Linear sweep voltammetry (chronoamperometry) was used to apply a potential to the PEC device, and the current was measured while the cell was exposed to the light. The current response was recorded both with the light on and off, which allows the current response to be analysed and the optimal potential for the photoelectrocatalytic hydrogen evolution experiment to be determined (Figure 4.14B). The optimised photocurrent value obtained was at –0.2 V, which appeared to be the most stable throughout the experiment. This indicates that upon irradiation, changes take place on the electrode and efficient charge separation within the system takes place, which results in the negative current response [17].

The photoelectrocatalytic hydrogen evolution experiment remains a subject for further studies however, the chronoamperometry and immobilisation studies demonstrate promising potential for the **Ru(dceb)-NDI^{2+}** for this application.

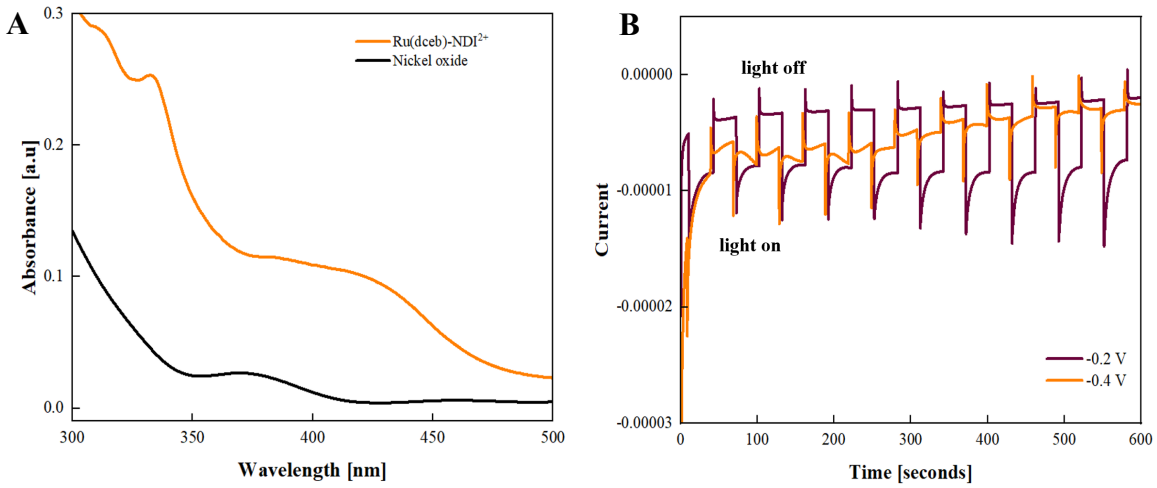


Figure 4.14 (A) UV-vis absorption spectra of the **Ru(dceb)-NDI^{2+}** complex on a nickel oxide thin film compared to a reference nickel oxide without the dye. **(B)** chopped light chronoamperometry measurements under light irradiation while applying potentials of –0.2 and –0.4 V. The solution was bubbled with argon throughout the experiment, and the scan rate of 10 mV/s was used.

4.4 Conclusion

The **Ru(dceb)-NDI^{2+}** complex was successfully synthesised for photocatalytic hydrogen production. The complex was studied using electrochemical and spectroelectrochemical techniques. In the cyclic voltammetry studies, the first and second anodic peaks at E° = –0.90 and –1.36 V (vs Fc^{+}/Fc) were attributed to the two reductions of the NDI moiety and the further three reductions at –1.54, –2.0, –2.25 V were assigned to the phenanthroline and bipyridine ligands. UV-vis-SEC and IR-SEC were used to probe the properties of these reduced species. Additionally, ns and ps-TAS measurements provided insights into the behaviour of the complex at early times in solution, as well as under photocatalytic conditions and on NiO films. Using ns-TAS measurements under photocatalytic conditions, formation of the one-electron reduced species, **Ru(dceb)-NDI^{+}** is supported by UV-vis-SEC experiments. The bands at 395 and 416 nm in the UV-vis spectra confirmed the formation of the two-electron reduced species, **Ru(dceb)-NDI**. The **Ru(dceb)-NDI^{2+}** complex was efficiently adsorbed on a NiO surface and studied using picosecond TAS. Results indicated that the charge-separated state $Ru(dceb)^{III}$–NDI^{-} state formed over hundreds of picoseconds, with recombination occurring on the nanosecond timescale.

TRIR studies highlight wavelength dependent photophysics. Photocatalytic hydrogen production resulted in TONs of ~ 100 for hydrogen production which is higher than that of the bipyridine analogue. Therefore, the incorporation of ester groups opens new possibilities for tuning the properties of the complex, while employment of NDI units due to their C=O stretching vibrations enable monitoring of electron transfer pathways and electron density using TRIR.

4.5 Experimental

4.5.1 Materials and methods

All materials and methods employed in this chapter were similar to the ones reported in the previous chapters. All chemicals and solvents necessary for the synthesis and for the analysis were supplied by Aldrich Chemicals Co. and Fluorochem Ltd. FTIR spectra was obtained using a Shimadzu IRAffinity-1 FTIR spectrophotometer. NMR spectra of all synthesised complexes and ligands were obtained from Bruker 600 MHz spectrometer in deuterated dimethyl sulfoxide, acetonitrile and chloroform. UV-vis and Emission Spectroscopy spectra were recorded on a Duetta Absorbance and Fluorescence Spectrometer. Mass spectrometry results were obtained by researchers at the University of Bath.

4.5.2 Electrochemical measurements

All electrochemical experiments were conducted with 0.5 mM solutions of the **Ru(dceb)-NDI^{2+}** complex in acetonitrile with 0.1 M tetrabutylammonium hexafluorophosphate as supporting electrolyte. A glassy carbon electrode, platinum wire and $Ag/AgNO_3$ electrode were used as working, counter and reference electrode. All obtained potentials were corrected versus ferrocene. T = 298 K, and scan rate used v = 100 mV/s.

4.5.3 Spectroelectrochemistry

Spectroelectrochemical measurements (IR/UV-vis-SEC) were carried out using an OTTLE cell obtained from Spectroelectrochemistry Reading which consisted of a platinum mesh working electrode, platinum mesh counter electrode and silver wire pseudo reference electrode [60]. The solutions were prepared at concentration of 1.5 mM (for UV-vis-SEC) or 10 mM (for IR-SEC) in an anhydrous acetonitrile with 0.1 M tetrabutylammonium hexafluorophosphate as supporting electrolyte. T = 298 K, and scan rate used v = 0.002 V/s.

4.5.4 Picosecond transient absorption measurements

Ps-TAS were recorded using a Helios spectrometer from Ultrafast Systems, with a Solstice Ace laser at the Newcastle University in the United Kingdom. The absorption of the samples was in the range 0.3 – 0.9 at 400 nm.

4.5.5 Nanosecond transient absorption measurements

Nanosecond TAS were recorded using the LP980 transient absorption spectrometer, Edinburgh Instruments, using excitation at 355 nm. All samples were deaerated over three cycles of freeze-pump-thaw before measurements. The optical density of the samples was ~ 0.3 at the excitation wavelength of 355 nm. The same method was employed for the ns-TAS measurements under photocatalytic conditions (for this, the sample (0.03 mmol) and the catalyst (0.03 mmol) were dissolved in a 65:30:5 mixture of acetonitrile, triethylamine and deionised water) and then the solution was excited at 355 nm.

4.5.6 Time-Resolved Infrared measurements

TRIR spectra were recorded using the ULTRA instrument at the Central Laser Facility in the Rutherford Appleton Laboratory in the United Kingdom [61]. All TRIR spectra were collected using 365, 420, 510, and 600 nm excitation with 1 μJ power in a 0.1 mm pathlength Harrick cell, all compounds were dissolved in acetonitrile.

4.5.7 Photocatalytic H_2 evolution experiments

Photocatalytic hydrogen evolution was carried in a 19 ml glass Schlenk tube stopped with an air-tight rubber spectrum. The sample (0.03 mmol) and the catalyst (0.03 mmol) were dissolved in a 65:30:5 mixture of acetonitrile, triethylamine and deionised water. The freeze-pump-thaw procedure was used to ensure inert condition in the solution. The solution under a nitrogen atmosphere was then exposed to light irradiation at 450 nm using a photoredox box supplied by HepatoChem [62]. Gas Chromatography was used to quantify the amount of hydrogen produced.

4.5.8 Chronoamperometry and immobilisation studies on a NiO film

Photoelectrochemical measurements were carried out at the Newcastle University in the United Kingdom. The NiO sol gel was prepared by mixing anhydrous $NiCl_2$ (1 g) and tri-block co-polymer F108 [poly (ethylene glycol)-block-poly (propylene glycol)-block-poly (ethylene glycol)] (1 g) in ethanol (6 ml) and ultrapure water (5 ml). The solution was aged for two weeks [14, 59]. The NiO films were prepared using conductive fluorine doped tin oxide glass and placed in dye baths overnight. Finally, the films were dried at 450°C and cooled down to room temperature.

4.6 References

[1]. Hansen, J. E., Kharecha, P., Sato, M., Tselioudis, G., Kelly, J., Bauer, S. E., Ruedy, R., Jeong, E., Jin, Q., Rignot, E., Velicogna, I., Schoeberl, M. R., von Schuckmann, K., Amponsem, J., Cao, J., Keskinen, A., Li, J., & Pokela, A. (2025). Global Warming Has Accelerated: Are the United Nations and the Public Well-Informed? Environment: Science and Policy for Sustainable Development, 67(1), 6–44. https://doi.org/10.1080/00139157.2025.2434494

[2]. Hansen, J. E., Sato, M., Simons, L., Nazarenko, L. S., Sangha, I., Kharecha, P., Zachos, J. C., von Schuckmann, K., Loeb, N. G., Osman, M. B., Jin, Q., Tselioudis, G., Jeong, E., Lacis, A., Ruedy, R., Russell, G., Cao, J., & Li, J. (2023). Global warming in the pipeline. Oxford Open Climate Change, 3(1), kgad008. https://doi.org/10.1093/oxfclm/kgad008

[3]. U.S. Energy Information Administration - EIA - independent statistics and analysis. Hydrogen explained - U.S. Energy Information Administration (EIA). (2023). https://www.eia.gov/energyexplained/hydrogen/#:~:text=However%2C%20hydrogen%20is%20useful%20as,greater%20use%20in%20the%20future.

[4]. AEM vs. PEM electrolysers: Hydrogen production in the Enapter Handbook. Enapter Handbook. (n.d.). https://handbook.enapter.com/knowledge_base/aem_technology.html

[5]. The New European Commission and how it sees the role of renewable hydrogen. European Chair for Sustainable Development and Climate Transition. (2025, March 4). https://www.sciencespo.fr/psia/chair-sustainable-development/2025/03/04/the-new-european-commission-and-how-it-sees-the-role-of-renewable-hydrogen/#:~:text=Further%20concrete%20objectives%20are%20set,of%20the%20EU’s%20energy%20demand.

[6]. Hydrogen. Energy. (2022). https://energy.ec.europa.eu/topics/eus-energy-system/hydrogen_en

[7]. REPowerEU. European Commission. (n.d.). https://commission.europa.eu/strategy-and-policy/priorities-2019-2024/european-green-deal/repowereu-affordable-secure-and-sustainable-energy-europe_en

[8]. Deponti, E., & Natali, M. (2016). Photocatalytic hydrogen evolution with ruthenium polypyridine sensitizers: unveiling the key factors to improve efficiencies. Dalton Transactions, 45(22), 9136–9147. https://doi.org/10.1039/c6dt01221c

[9]. Watanabe, M. (2017). Dye-sensitized photocatalyst for effective water splitting catalyst. Science and Technology of Advanced Materials, 18(1), 705–723. https://doi.org/10.1080/14686996.2017.1375376

[10]. Fukuzumi, S., Kobayashi, T., & Suenobu, T. (2010). Photocatalytic Production of Hydrogen by Disproportionation of One-Electron-Reduced Rhodium and Iridium–Ruthenium Complexes in Water. Angewandte Chemie, 123(3), 754–757. https://doi.org/10.1002/ange.201004876

[11]. Camara, F., Aguirre-Araque, J. S., Fortage, J., & Collomb, M.-N. (2024). Enhancing the stability of photocatalytic systems for hydrogen evolution in water by using a tris-phenyl-phenanthroline sulfonate ruthenium photosensitizer. Sustainable Energy & Fuels, 8(7), 1457–1472. https://doi.org/10.1039/d3se01556d

[12]. Kowacs, T., O’Reilly, L., Pan, Q., Huijser, A., Lang, P., Rau, S., Browne, W. R., Pryce, M. T., & Vos, J. G. (2016). Subtle Changes to Peripheral Ligands Enable High Turnover Numbers for Photocatalytic Hydrogen Generation with Supramolecular Photocatalysts. Inorganic Chemistry, 55(6), 2685–2690. https://doi.org/10.1021/acs.inorgchem.5b01752

[13]. Pan, Q., Freitag, L., Kowacs, T., Falgenhauer, J. C., Korterik, J. P., Schlettwein, D., Browne, W. R., Pryce, M. T., Rau, S., González, L., Vos, J. G., & Huijser, A. (2016). Peripheral ligands as electron storage reservoirs and their role in enhancement of

photocatalytic hydrogen generation. Chemical Communications, 52(60), 9371–9374. https://doi.org/10.1039/c6cc05222c
[14]. Cerpentier, F. J., Karlsson, J., Lalrempuia, R., Brandon, M. P., Sazanovich, I. V., Greetham, G. M., Gibson, E. A., & Pryce, M. T. (2021). Ruthenium Assemblies for CO_2 Reduction and H_2 Generation: Time Resolved Infrared Spectroscopy, Spectroelectrochemistry and a Photocatalysis Study in Solution and on NiO. Frontiers in Chemistry, 9. https://doi.org/10.3389/fchem.2021.795877
[15]. Müller, C., Friedländer, I., Bagemihl, B., Rau, S., & Dietzek-Ivanšić, B. (2021). The electron that breaks the catalyst's back – excited state dynamics in intermediates of molecular photocatalysts. Physical Chemistry Chemical Physics, 23(48), 27397–27403. https://doi.org/10.1039/d1cp04498b
[16]. Bagemihl, B., Müller, C., Shillito, G. E., Hartkorn, M., Mengele, A. K., Kupfer, S., Dietzek- Ivanšić, B., & Rau, S. (2023). Steering Photoinduced Electron Transfer in Intramolecular Photocatalysts by Peripheral Ligand Control. ChemistryEurope, 2(6), e202300084. https://doi.org/10.1002/ceur.202300084
[17]. Põldme, N., O'Reilly, L., Fletcher, I., Portoles, J., Sazanovich, I. V., Towrie, M., Long, C., Vos, J. G., Pryce, M. T., & Gibson, E. A. (2019). Photoelectrocatalytic H_2 evolution from integrated photocatalysts adsorbed on NiO. Chemical Science, 10(1), 99–112. https://doi.org/10.1039/c8sc02575d
[18]. Ghule, N. V., La, D. D., Bhosale, R. S., Al Kobaisi, M., Raynor, A. M., Bhosale, S. V., & Bhosale, S. V. (2016). Effect of Amide Hydrogen Bonding Interaction on Supramolecular Self-Assembly of Naphthalene Diimide Amphiphiles with Aggregation Induced Emission. ChemistryOpen, 5(2), 157–163. https://doi.org/10.1002/open.201500201
[19]. Bartusiak, M. Z., McGarry, R. J., Varvarezos, L., Brandon, M. P., & Pryce, M. T. (2023). Incorporation of perylene and naphthalene like ligands into ruthenium complexes: Synthesis, photophysical properties and electrochemistry. Coordination Chemistry Reviews, 495, 215365. https://doi.org/10.1016/j.ccr.2023.215365
[20]. Yang, Y., Zou, X., Sun, Y., Chen, F., Zhao, J., & Gou, S. (2023). Naphthalene Diimide-Functionalized Half-Sandwich Ru(II) Complexes as Mitochondria-Targeted Anticancer and Antimetastatic Agents. Inorganic Chemistry, 62(24), 9649–9660. https://doi.org/10.1021/acs.inorgchem.3c01125
[21]. Rashid, A., Mondal, S., Musha Islam, A. S., Mondal, S., & Ghosh, P. (2024). Naphthalene Diimide and Bis-Heteroleptic Ru(II) Complex-Based Hybrid Molecule with 3-in-1 Functionalities. Chemistry – An Asian Journal, 19(23), e202400724. https://doi.org/10.1002/asia.202400724
[22]. Johansson, O., Wolpher, H., Borgström, M., Hammarström, L., Bergquist, J., Sun, L., & Åkermark, B. (2004). Intramolecular charge separation in a hydrogen bonded tyrosine–ruthenium(II)–naphthalene diimide triad. Chem. Commun., (2), 194–195. https://doi.org/10.1039/b308101j
[23]. Skaisgirski, M., Guo, X., & Wenger, O. S. (2017). Electron Accumulation on Naphthalene Diimide Photosensitized by $[Ru(2,2'\text{-bipyridine})_3]^{2+}$. Inorganic Chemistry, 56(5), 2432–2439. https://doi.org/10.1021/acs.inorgchem.6b02446
[24]. Durham, B., Caspar, J. V., Nagle, J. K., & Meyer, T. J. (1982). Photochemistry of tris(2,2'-bipyridine)ruthenium(2+) ion. Journal of the American Chemical Society, 104(18), 4803–4810. https://doi.org/10.1021/ja00382a012
[25]. Lakowicz, J. R. (2013). Principles of Fluorescence Spectroscopy. Third Edition, Springer, pp. 683-688. https://link.springer.com/book/10.1007/978-0-387-46312-4
[26]. Erten, S., Posokhov, Y., Alp, S., & Icli, S. (2005). The study of the solubility of naphthalene diimides with various bulky flanking substituents in different solvents by UV-vis spectroscopy. Dyes and Pigments, 64(2), 171–178. https://doi.org/10.1016/j.dyepig.2004.04.011

[27]. Quinn, S., Davies, E. S., Pfeiffer, C. R., Lewis, W., McMaster, J., & Champness, N. R. (2017). Core-Substituted Naphthalene Diimides: Influence of Substituent Conformation on Strong Visible Absorption. ChemPlusChem, 82(3), 489–492. https://doi.org/10.1002/cplu.201700059
[28]. Balzani, V., Campagna, S., & Accorsi, G. (2007). Photochemistry and Photophysics of Coordination Compounds: Ruthenium. Springer, pp. 123–138.
[29]. Hug, S. J., & Boxer, S. G. (1996). Dipolar character of ligand-centered transitions in transition metal tris-bipyridyl complexes. Inorganica Chimica Acta, 242(1–2), 323–327. https://doi.org/10.1016/0020-1693(96)04882-7
[30]. Kojima, T. (2024). Redox-Based Catalytic Chemistry of Transition Metal Complexes. pp. 10–30. https://doi.org/10.1039/9781837676484
[31]. Mareeswaran, P. M., Rajkumar, E., Sathish, V., & Rajagopal, S. (2013). Electron transfer reactions of ruthenium(II)–bipyridine complexes carrying tyrosine moiety with quinones. Luminescence, 29(7), 754–761. https://doi.org/10.1002/bio.2617
[32]. Johansson, O., Borgström, M., Lomoth, R., Palmblad, M., Bergquist, J., Hammarström, L., Sun, L., & Åkermark, B. (2003). Electron Donor−Acceptor Dyads Based on Ruthenium(II) Bipyridine and Terpyridine Complexes Bound to Naphthalenediimide. Inorganic Chemistry, 42(9), 2908–2918. https://doi.org/10.1021/ic020420k
[33]. Borgström, M., Shaikh, N., Johansson, O., Anderlund, M. F., Styring, S., Åkermark, B., Magnuson, A., & Hammarström, L. (2005). Light Induced Manganese Oxidation and Long-Lived Charge Separation in a $Mn_2^{II,II}$–$Ru^{II}(bpy)_3$−Acceptor Triad. Journal of the American Chemical Society, 127(49), 17504–17515. https://doi.org/10.1021/ja055243b
[34]. Kajiwara, T., Hashimoto, K., Kawai, T., & Sakata, T. (1982). Dynamics of luminescence from $Ru(bpy)_3Cl_2$ adsorbed on semiconductor surfaces. The Journal of Physical Chemistry, 86(23), 4516–4522. https://doi.org/10.1021/j100220a013
[35]. Kalyanasundaram, K. (1982). Photophysics, photochemistry and solar energy conversion with tris(bipyridyl)ruthenium(II) and its analogues. Coordination Chemistry Reviews, 46, 159–244. https://doi.org/10.1016/0010-8545(82)85003-0
[36]. Villani, E., Sakanoue, K., Einaga, Y., Inagi, S., & Fiorani, A. (2022). Photophysics and electrochemistry of ruthenium complexes for electrogenerated chemiluminescence. Journal of Electroanalytical Chemistry, 921, 116677. https://doi.org/10.1016/j.jelechem.2022.116677
[37]. Barbante, G. J., Hogan, C. F., Wilson, D. J., Lewcenko, N. A., Pfeffer, F. M., Barnett, N. W., & Francis, P. S. (2011b). Simultaneous control of spectroscopic and electrochemical properties in functionalised electrochemiluminescent tris(2,2′-bipyridine)ruthenium(II) complexes. The Analyst, 136(7), 1329–1338. https://doi.org/10.1039/c0an00952k
[38]. Eskelinen, E., Luukkanen, S., Haukka, M., Ahlgrén, M., & Pakkanen, T. A. (2000a). Redox and photochemical behaviour of ruthenium(II) complexes with H_2dcbpy ligand (H_2dcbpy = 2,2′-bipyridine-4,4′-dicarboxylic acid). Journal of the Chemical Society, Dalton Transactions, (16), 2745–2752. https://doi.org/10.1039/b0047511
[39]. Andric, G., Boas, J. F., Bond, A. M., Fallon, G. D., Ghiggino, K. P., Hogan, C. F., Hutchison, J. A., Lee, M. A.-P., Langford, S. J., Pilbrow, J. R., Troup, G. J., & Woodward, C. P. (2004). Spectroscopy of Naphthalene Diimides and Their Anion Radicals. Australian Journal of Chemistry, 57(10), 1011–1019. https://doi.org/10.1071/ch04130
[40]. Karoń, K., Rode, J. E., Kaczorek, D., Kawęcki, R., Pluczyk-Małek, S., Łapkowski, M., Ostrowski, S., Lyczko, K., & Dobrowolski, J. Cz. (2023). UV–vis and ECD spectroelectrochemistry of atropisomeric naphthalenediimide derivative. Spectrochimica Acta Part A: Molecular and Biomolecular Spectroscopy, 288, 122089. https://doi.org/10.1016/j.saa.2022.122089

[41]. Bhosale, S. V., Jani, C. H., & Langford, S. J. (2008). Cheminform Abstract: Chemistry of Naphthalene Diimides. ChemInform, 39(21). https://doi.org/10.1002/chin.200821252
[42]. Sazanovich, I. V., Alamiry, M. A., Best, J., Bennett, R. D., Bouganov, O. V., Davies, E. S., Grivin, V. P., Meijer, A. J., Plyusnin, V. F., Ronayne, K. L., Shelton, A. H., Tikhomirov, S. A., Towrie, M., & Weinstein, J. A. (2008). Excited State Dynamics of a Pt^{II} Diimine Complex Bearing a Naphthalene-Diimide Electron Acceptor. Inorganic Chemistry, 47(22), 10432–10445. https://doi.org/10.1021/ic801022h
[43]. Snellenburg, J. J., Laptenok, S. P., Seger, R., Mullen, K. M., & Stokkum, I. H. (2012). Glotaran: A Java-Based Graphical User Interface for the R Package TIMP. Journal of Statistical Software, 49(3), 1–22. https://doi.org/10.18637/jss.v049.i03
[44]. Auty, A. J., Scattergood, P. A., Keane, T., Cheng, T., Wu, G., Carson, H., Shipp, J., Sadler, A., Roseveare, T., Sazanovich, I. V., Meijer, A. J., Chekulaev, D., Elliot, P. I., Towrie, M., & Weinstein, J. A. (2023b). A stronger acceptor decreases the rates of charge transfer: ultrafast dynamics and on/off switching of charge separation in organometallic donor–bridge–acceptor systems. Chemical Science, 14(41), 11417–11428. https://doi.org/10.1039/d2sc06409j
[45]. O'Reilly, L. (2019). Synthesis, Characterisation, Time-Resolved and Photocatalytic Studies of Inorganic Assemblies for Hydrogen Generation (thesis). Dublin City University. School of Chemical Sciences, Dublin.
[46]. Wu, S., Zhong, F., Zhao, J., Guo, S., Yang, W., & Fyles, T. (2015). Broadband Visible Light-Harvesting Naphthalenediimide (NDI) Triad: Study of the Intra-/Intermolecular Energy/Electron Transfer and the Triplet Excited State. The Journal of Physical Chemistry A, 119(20), 4787–4799. https://doi.org/10.1021/acs.jpca.5b01448
[47]. Doria, Filippo, Manet, I., Grande, V., Monti, S., & Freccero, M. (2013). Water-Soluble Naphthalene Diimides as Singlet Oxygen Sensitizers. The Journal of Organic Chemistry, 78(16), 8065–8073. https://doi.org/10.1021/jo401347z
[48]. Müller, P., & Brettel, K. (2012). $[Ru(bpy)_3]^{2+}$ as a reference in transient absorption spectroscopy: differential absorption coefficients for formation of the long-lived ^{3}MLCT excited state. Photochemical & Photobiological Sciences, 11(4), 632–636. https://doi.org/10.1039/c2pp05333k
[49]. Khnayzer, R. S., Thoi, V. S., Nippe, M., King, A. E., Jurss, J. W., El Roz, K. A., Long, J. R., Chang, C. J., & Castellano, F. N. (2014). Towards a comprehensive understanding of visible-light photogeneration of hydrogen from water using cobalt(II) polypyridyl catalysts. Energy Environ. Sci., 7(4), 1477–1488. https://doi.org/10.1039/c3ee43982h
[50]. Rivarola, C. R., Bertolotti, S. G., & Previtali, C. M. (2006). Photoreduction of $Ru(bpy)_3^{2+}$ by Amines in Aqueous Solution. Kinetics Characterization of a Long-Lived Nonemitting Excited State. Photochemistry and Photobiology, 82(1), 213–218. https://doi.org/10.1562/2005-05-31-ra-558
[51]. Ishitani, O., Ishii, K., Yanagida, S., Pac, C., Ohno, T., & Yoshimura, A. (1989). A New Mechanistic Channel for Photochemical Electron Transfer of Tris(2,2′-bipyridine)ruthenium(II) with Triethylamine. Possible Participation of a Nonemitting Excited State. Chemistry Letters, 18(2), 217–220. https://doi.org/10.1246/cl.1989.217
[52]. Kim, S., Zeman, C. J., Gobeze, H. B., Duvva, N., & Schanze, K. S. (2025). Photoinduced electron transfer from the naphthalene diimide anion radical doublet excited state. Chemical Communications, 61(29), 5511–5514. https://doi.org/10.1039/d5cc00190k
[53]. O'Reilly, L., Pan, Q., Das, N., Wenderich, K., Korterik, J. P., Vos, J. G., Pryce, M. T., & Huijser, A. (2018a). Hydrogen-Generating Ru/Pt Bimetallic Photocatalysts Based on Phenyl-Phenanthroline Peripheral Ligands. ChemPhysChem, 19(22), 3084–3091. https://doi.org/10.1002/cphc.201800658

[54]. Ji, Z., & Wu, Y. (2013). Photoinduced Electron Transfer Dynamics of Cyclometalated Ruthenium (II)–Naphthalenediimide Dyad at NiO Photocathode. The Journal of Physical Chemistry C, 117(36), 18315–18324. https://doi.org/10.1021/jp405659m
[55]. Ye, C., Cheng, H., Wrede, S., Diring, S., Tian, H., Odobel, F., & Hammarström, L. (2023). Charge Recombination Deceleration by Lateral Transfer of Electrons in Dye-Sensitized NiO Photocathode. Journal of the American Chemical Society, 145(20), 11067–11073. https://doi.org/10.1021/jacs.3c00269
[56]. Bentounsi, Y., Seintis, K., Diring, S., Vauthey, E., & Odobel, F. (2021). Click Chemistry on NiO Photocathode to Postfunctionalize a Diketopyrrolopyrrole Sensitizer by Naphthalene Diimide Electron Acceptor. ACS Applied Energy Materials, 4(3), 2629–2636. https://doi.org/10.1021/acsaem.0c03200
[57]. Singh Bindra, G., Schulz, M., Paul, A., Soman, S., Groarke, R., Inglis, J., Pryce, M. T., Browne, W. R., Rau, S., Maclean, B. J., & Vos, J. G. (2011a). The effect of peripheral bipyridine ligands on the photocatalytic hydrogen production activity of Ru/Pd catalysts. Dalton Transactions, 40(41), 10812–10814. https://doi.org/10.1039/c1dt11241d
[58]. Sabatini, R. P., McCormick, T. M., Lazarides, T., Wilson, K. C., Eisenberg, R., & McCamant, D. W. (2011). Intersystem Crossing in Halogenated Bodipy Chromophores Used for Solar Hydrogen Production. The Journal of Physical Chemistry Letters, 2(3), 223–227. https://doi.org/10.1021/jz101697y
[59]. Cullen, A. A., Heintz, K., O'Reilly, L., Long, C., Heise, A., Murphy, R., Karlsson, J., Gibson, E., Greetham, G. M., Towrie, M., & Pryce, M. T. (2020). A Time-Resolved Spectroscopic Investigation of a Novel BODIPY Copolymer and its Potential Use as a Photosensitiser for Hydrogen Evolution. Frontiers in Chemistry, 8. https://doi.org/10.3389/fchem.2020.584060
[60]. Room temperature OTTLE cell: Spectroelectrochemistry reading. Spectroelectrochemistry. (2019, April 26). https://research.reading.ac.uk/spectroelectrochemistry/optically-transparent-thin-layer-electrochemical-cells/room-temperature-ottle-cell/
[61]. Greetham, G. M., Burgos, P., Cao, Q., Clark, I. P., Codd, P. S., Farrow, R. C., George, M. W., Kogimtzis, M., Matousek, P., Parker, A. W., Pollard, M. R., Robinson, D. A., Xin, Z.-J., & Towrie, M. (2010). Ultra: A Unique Instrument for Time-Resolved Spectroscopy. Applied Spectroscopy, 64(12), 1311–1319. https://doi.org/10.1366/000370210793561673
[62]. Leading photoreactor manufacturer. HepatoChem. (n.d.). https://hepatochem.com/?gad_source=1&gad_campaignid=20187654459&gbraid=0AAAADzmD52Oj7WXlMHqgHs-1JqmN4zwQ&gclid=CjwKCAjwwNbEBhBpEiwAFYLtGLIjECwDdq_DvmHpviyvX-MUeUCfqosZyl1G7RIz34yGDDax9w7TExoCZ98QAvD_BwE

Chapter 5

Photophysical Properties and Photocatalytic Performance of Ruthenium (II)-Naphthalene Diimide Photosensitisers/Photocatalysts for H_2 Evolution and CO_2 Reduction: Insights from Time-Resolved Infrared, Ultrafast Transient Absorption, and NiO Surface Studies.

Martyna Bartusiak[1], Martin Pižl[2,4], Partha Malakar[3], Sayantan Bhattacharya[3], František Hartl[4], Owen Woodford[5], Elizabeth A. Gibson[5], Mary T. Pryce[1]

[1]School of Chemical Sciences, Dublin City University, Ireland

[2]Department of Inorganic Chemistry, University of Chemistry and Technology Prague, Technická 5, 16628 Prague, Czech Republic

[3]Rutherford Appleton Laboratory, Harwell Campus, Didcot OX11 0QX, UK

[4]Department of Chemistry, University of Reading, Whiteknights, Reading RG6 6DX, UK

[5]Energy Materials Laboratory, Department of Chemistry, School of Natural and Environmental Science, Newcastle University, Newcastle upon Tyne, United Kingdom

5.1 Abstract

A series of ruthenium (II)-naphthalene diimide (Ru-NDIs) assemblies were successfully synthesised and systematically examined using a wide range of photophysical techniques. These photocatalytic systems were employed for hydrogen evolution and carbon dioxide reduction. Various functional groups were incorporated into the complexes for example ester groups (in **Ru-NDI-benzoate**) and iodine atoms (in **Ru-NDI-iodine**) to explore the influence of electron-withdrawing effects on their photophysical properties. In addition, a triple bond (**Ru-NDI-ethynyl**) was used to investigate changes in the excited-state behaviour and track electron density upon photoexcitation. In addition, rhenium and platinum catalysts (**Ru-NDI-rhenium**, **Ru-NDI-ethynyl-rhenium**, **Ru-NDI-platinum**) were introduced to evaluate the potential of these Ru-NDIs assemblies in photocatalytic hydrogen evolution and carbon dioxide reduction reactions. Time-resolved infrared spectroscopy (TRIR) was utilised to probe the excited state dynamics of these complexes and monitor changes in electron density upon photo-induced excitation. An enhancement in absorption in the ν(C=O) stretching vibrations was observed for the transient species and also enhancement was evident for the triple bond feature but to a lesser extent. Moreover, new transient bands were observed at lower wavenumbers, which indicated electron transfer from the ruthenium center towards the NDI unit, and this resulted in the formation of the charge-separated state upon light irradiation at 365 and 420 nm.

Furthermore, nanosecond and picosecond transient absorption studies (ns/ps-TAS) were conducted on these Ru-NDI complexes following excitation at 355 and 400 nm to gain further insights into the behaviour of the photoactive species in solution under photocatalytic conditions and to examine hole injection on nickel oxide surfaces. Finally, the Ru-NDI complexes synthesised in this work were assessed for photocatalytic applications such as hydrogen evolution and carbon dioxide reduction. The highest turnover number (TON) for hydrogen evolution was observed for the **Ru-NDI-benzoate** complex, which reached 24 TON after 4 hours of light irradiation. Additionally, **Ru-NDI-rhenium** and **Ru-NDI-ethynyl-rhenium** exhibited photocatalytic activity for carbon dioxide reduction with TON values of 122 and 113, respectively. This chapter highlights key findings from the TRIR and ps/ns-TAS investigations, which offer a unique perspective on these types of assemblies, as this area of research is not actively explored in the current literature.

Contribution:

In this chapter, I was responsible for writing all sections and analysing the obtained results. I have synthesised all complexes and carried out experimental studies, including absorption and emission spectroscopy. I performed nanosecond transient absorption studies in solution and under photocatalytic conditions. Picosecond transient absorption studies were carried out at the Newcastle University and TRIR measurements were conducted at the Rutherford Appleton Laboratory in the UK. In addition, I carried out photocatalytic experiments, surface studies on a NiO and processed all data using the Glotaran software.

5.2 Introduction

Renewable and green energy can be successfully produced in the process of photocatalysis, which could be applied to generate hydrogen by harnessing sunlight [1, 2]. However, the design, development, and synthesis of light-harvesting materials for photocatalytic applications for example hydrogen evolution and carbon dioxide reduction reactions are definitely challenging. These materials must be designed in a such manner that they can be synthesised relatively easy and in high yields but also efficiently harvest sunlight, facilitate necessary redox reactions and subsequently, produce clean hydrogen gas or convert carbon dioxide into more valuable products such as carbon monoxide and formic acid without release of greenhouse gases as byproducts of these processes [3 – 5]. The design and synthetic pathways of such photosensitisers or photocatalysts require significant efforts and various structural modifications to ensure that the resulting photoactive assemblies achieve and exhibit the desired photophysical properties for efficient photocatalytic processes. Consequently, it is necessary to gain deeper insights into these materials in order to understand their behaviour under irradiation. Furthermore, these investigations help to determine the photophysical properties of the photoactive species being formed, monitor how quickly and efficiently electron transfer occurs, and provide insights into the formation of charge-separated states, as well as their dynamics and the kinetics of charge recombination, charge separation and carrier relaxation processes [6 – 8]. In order to design and synthesise suitable photocatalytic assemblies, several characteristics of these systems must be considered. For example, these complexes must efficiently absorb light in the UV-visible region, have high molar extinction coefficients, good photostability and effectively transfer electrons to the catalytic sites within the assembly [9 – 11]. Unfortunately, it is not a straightforward process to design these systems and predict the properties of these materials and that is why, researchers often depend on trial and error because relatively small modifications and incorporation of various ligands or metals to the molecular structures can significantly impact their photophysical properties, as it was discussed in Chapter 4 and observed in the literature [12 – 14]. Therefore, it is important to conduct detailed studies of these light-harvesting systems and highlight how different substituents are capable of influencing the photophysical properties and photocatalytic performance, which is the primary focus of this chapter. This research chapter can serve as a guide for other researchers in designing and optimising more efficient photocatalytic assemblies in the future. One of the most effective and efficient photophysical techniques for probing the

dynamics and kinetics of these photocatalytic systems are time-resolved infrared spectroscopy (TRIR) and UV-vis transient absorption spectroscopy (TAS) [15, 16]. TRIR provides valuable insights into the molecular and structural characteristics of light-harvesting materials and allows a deeper understanding of the excited states populated [16]. Distinct shifts in vibrational frequencies help us to determine the movement of electron density within the system, which provides a better understanding of where the electron is localised and how the excited state differs from the ground state upon photoexcitation [16]. Incorporation of functional groups such as carbonyl bonds (C=O) [17 – 19], nitrile groups (CN) [20, 21] and triple bonds (C≡C) [22] are considered to be suitable for TRIR spectroscopy and serve as reporters for the excited states. TRIR has been widely employed in the analysis of various photocatalytic assemblies to investigate the reaction mechanisms and the formation of charge-separated states. For example, Cullen et al. [22] conducted TRIR studies on their BODIPY copolymer (photosensitiser), incorporating diethynylbenzene, to examine its capabilities for photocatalytic hydrogen evolution. Upon excitation of the BODIPY copolymer at 525 nm, the authors observed a signal at 2023 cm^{-1}, which corresponded to the triple bond in the excited state, and another signal at 2339 cm^{-1} corresponding to the triple bond in the ground state. This significant shift to lower energy by ~ 300 cm^{-1} in the excited state was attributed to charge transfer from the triple bond to the BODIPY in the excited state. Furthermore, the signal in the excited state was characterised by an enhancement in absorbance. Another study utilising TRIR was conducted by Nurttila et al. [23] on a supramolecular zinc porphyrin-based metal-organic cage, $Fe_4(Zn\text{-}L)_6$, which was employed for hydrogen production. Upon excitation at 585 nm, the TRIR difference spectra exhibited bleaching of the parent compound at 2043 and 1989 cm^{-1}, along with the formation of new transient bands at 2022 and 1958 cm^{-1}. These new bands were assigned to the one-electron reduced species, which confirmed that photoinduced electron transfer took place. In this system a lifetime of 0.5 ps was determined for charge separation while charge recombination occurred with a time constant of 37 ps [23]. Transient absorption spectroscopy (TAS) is also an excellent technique for probing the properties of excited states. For example, Sabatini et al. [24] synthesised a series of chalcogenorhodamine dyes incorporating oxygen, sulfur and selenium atoms in the xanthylium core and used them for solar hydrogen evolution with TiO_2 as the catalyst. Ultrafast TAS showed that electron transfer occurred rapidly on thin films of TiO_2 in acetonitrile, while slower electron transfer was observed under hydrogen production conditions (using colloidal TiO_2 particles, acetonitrile and ascorbic acid). This difference was attributed to aggregation of the dye, as the presence of acetonitrile and

water reduces dye aggregation and consequently results in slower electron transfer dynamics. The TAS data revealed that upon excitation, the dyes undergo fast intersystem crossing to form the triplet state, which is important for driving electron transfer and facilitating hydrogen evolution. For the dye with selenium, intersystem crossing occurred within 27 ps and the triplet state persisted throughout the experiment on the nanosecond timescale [24]. Another interesting study was carried out by Giannoudis et al. [25] with zinc and tin porphyrins, which were used as photosensitisers for hydrogen evolution, with cobaloxime complexes acting as a catalyst. The authors performed TAS measurements to investigate the charge transfer dynamics both in solution and under photocatalytic conditions in the presence of the cobaloxime-based catalyst (CoNMeim), and triethanolamine serving as a sacrificial electron donor. The triplet state lifetimes were determined to be sufficiently long, in the range of 70 – 200 μs [25]. Photocatalytic assemblies are also often characterised using TRIR, when they are immobilised on surfaces for example TiO_2 or NiO. In a study by Abdellah et al. [26], the molecular catalyst $[Re^{I}Br(bpy)(CO)_3]$ was immobilised onto the TiO_2 semiconductor. TRIR analysis revealed that the photocatalytic reduction of CO_2 to CO is initiated by ultrafast electron injection from the excited catalyst into the TiO_2 conduction band. Subsequently, this was followed by a rapid two-electron oxidation of triethanolamine, which was coordinated to the rhenium center. The electrons injected onto the semiconductor were stored in the conduction band on the millisecond to second timescale [26]. Põldme et al. [27] studied a ruthenium-based photocatalyst for hydrogen evolution, immobilised onto a NiO surface, and used TRIR spectroscopy to probe its excited state dynamics. Following excitation at 470 nm in solution, the ν(C=O) bond (at 1730 cm^{-1}) depleted within the laser pulse (200 fs), which resulted in the formation of a new band at lower wavenumber ν(1714 cm^{-1}) attributed to the ^{3}MLCT excited state species. The TRIR studies on a NiO surface indicated that the parent bleach and the absorption band at 1689 cm^{-1} recovered within 200 ps. This rapid decay corresponded to the formation of the ^{3}MLCT excited state species, and this spectral feature was consistent with the solution studies [27]. The aforementioned examples highlight the importance of utilising TRIR and TAS to characterise the photophysical properties of photosensitisers in photocatalytic processes and these techniques will be primarily employed in this chapter to examine Ru-NDI assemblies synthesised in this work.

In this chapter, a series of ruthenium (II)-NDI complexes were synthesised and analysed using standard techniques such as UV-vis and emission spectroscopy, as well as more

advanced photophysical techniques such as TRIR and ps/ns-TAS. These complexes include **Ru-NDI-benzoate**, **Ru-NDI-iodine**, **Ru-NDI-ethynyl**, **Ru-NDI-bpy**, **Ru-NDI-ethynyl-rhenium**, **Ru-NDI-rhenium** and **Ru-NDI-platinum**, and these are presented in Figure 5.1. Furthermore, TAS measurements on the picosecond and nanosecond timescales were carried out in solution, under photocatalytic conditions, and on a NiO surface. Finally, photocatalysis was performed to assess these compounds for hydrogen production. Additionally, Ru-NDI complexes containing rhenium catalyst were tested for carbon dioxide reduction reactions. This work primarily focuses only on the photophysical properties, which could provide insights for further optimisation in the future.

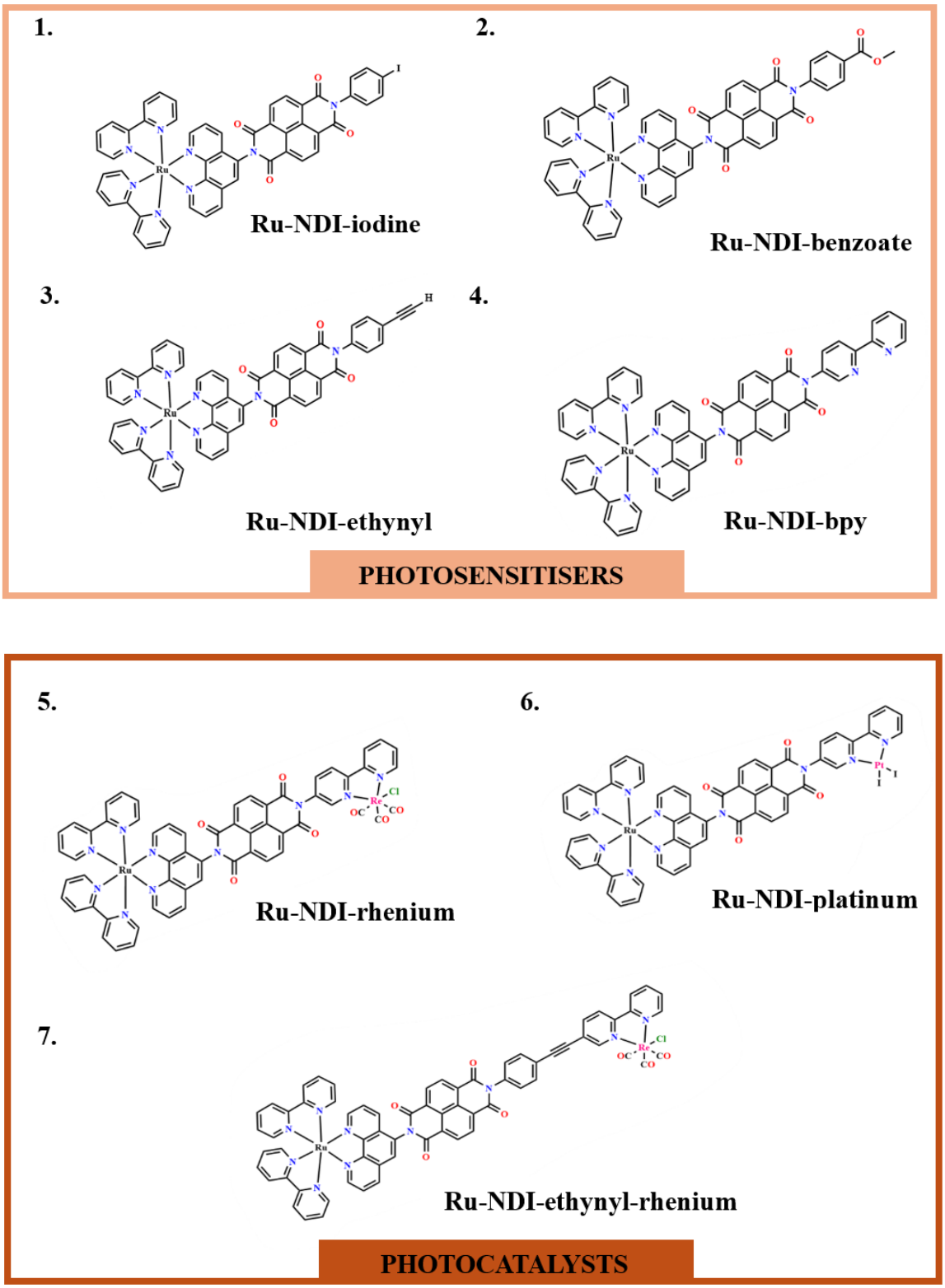


Figure 5.1 The structures of the **Ru-NDI** complexes studied. All complexes include a PF_6^- counterion, which has been excluded from the structural visualisation for clarity.

5.3 Results and discussion

5.3.1 Synthesis

All ruthenium-NDI complexes reported and discussed in this chapter were synthesised using similar experimental procedures to that described in Chapter 3 and Chapter 4. All experimental and synthetic methods are provided in greater detail in Appendix C. In summary, all NDI-based precursors were synthesised following a condensation (imidization) reaction between 1,4,5,8-naphthalenetetracarboxylic dianhydride (NDA) and various amines (R-NH_2), where R = 5-amino-2,2'-bipyridine, 4-iodoaniline, methyl 4-aminobenzoate, or 4-ethynylaniline. This reaction was followed by overnight reflux in dimethylformamide (DMF) (Figure 5.2, Step 1) [28]. Subsequently, these NDI-R ligands, were used without further purification, and were then coordinated to the ruthenium photosensitising moiety (the solution was brought to reflux temperature in DMF for three days, Figure 5.2, Step 3). Thin-layer-chromatography (TLC) was used throughout the synthesis to ensure full consumption of the starting materials. The resulting ruthenium photosensitisers namely **Ru-NDI-iodine**, **Ru-NDI-benzoate**, **Ru-NDI-ethynyl**, and **Ru-NDI-bpy** were purified using column chromatography with a mobile phase consisting of acetonitrile, water and saturated KNO_3 aqueous solution (ratio 10:1:0.1). **Ru-NDI-ethynyl** was very challenging to synthesise due to the low yield and thus was only studied using TRIR. For photocatalytic complexes containing rhenium, the condensation reaction was carried out first, followed by coordination of the rhenium centre to the bipyridine moiety using $Re(CO)_5Cl$ [29]. Complexation of the rhenium centre was monitored using FTIR spectroscopy, and the final purification of the **Ru-NDI-rhenium** and **Ru-NDI-ethynyl-rhenium** complexes was carried out by washing with diethyl ether. In the case of the platinum complexes, $Pt(DMSO)_2I_2$ was employed for the coordination. However, the resulting **Ru-NDI-platinum** complex exhibited poor solubility in organic solvents, hence its analysis was limited, and this complex was only studied using TAS measurements and photocatalysis. The **Ru-NDI-ethynyl-rhenium** complex was synthesised by employing well-known Sonogashira coupling reaction of **Ru-NDI-iodine** with 5-ethynyl-2,2'-bipyridine and using triethylamine, copper (II) iodide, and tetrakis(triphenylphosphine) palladium (0), followed by refluxing in DMF overnight (Figure 5.4) [30]. The final product was confirmed by the disappearance of the signal at ~ 4 ppm, which corresponded to the triple bond, C≡C-H in 5-ethynyl-2,2'-bipyridine. The successful synthesis of all complexes was confirmed by NMR spectroscopy and mass spectrometry (Figure SC5.1 – SC5.26 in Appendix C). The FTIR spectra of the Ru-NDI

complexes (Figure SC5.27 in Appendix C) exhibit carbonyl stretching vibrations characteristic of the NDI moiety in the range of 1500 – 1750 cm^{-1}. Additionally, the carbonyl stretching vibrations associated with the rhenium metal centre appear between 2000 – 2100 cm^{-1}, whereas the alkyne (triple bond) stretching vibration were difficult to detect using IR spectroscopy, however these were confirmed using ^{1}H-NMR.

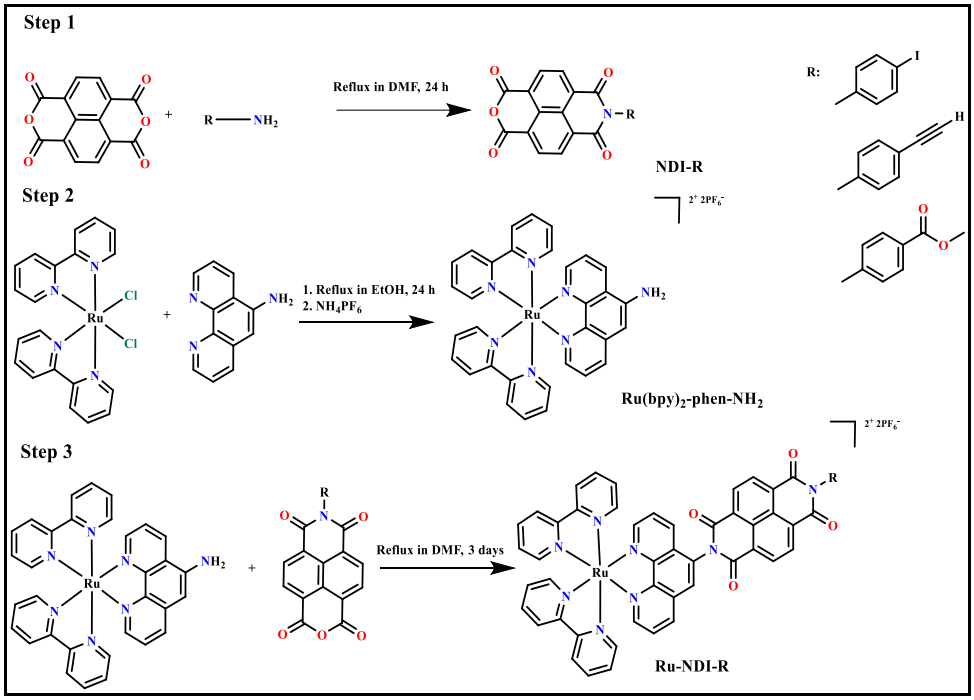


Figure 5.2 Synthetic scheme for the preparation of **Ru-NDI-R** and its corresponding ligands **NDI-R** and the photosensitising moiety **Ru(bpy)$_2$-phen-NH$_2$**, where R = 4-iodoaniline, methyl 4-aminobenzoate and 4-ethynylaniline.

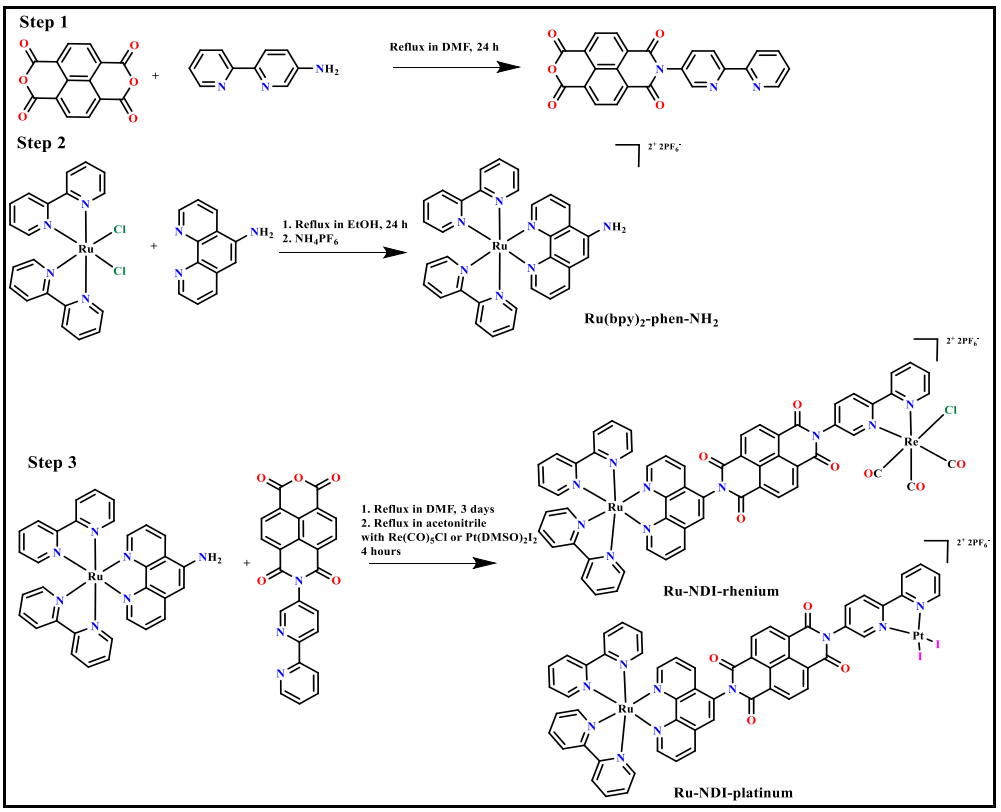


Figure 5.3 Synthetic scheme for the preparation of **Ru-NDI-rhenium/Ru-NDI-platinum**.

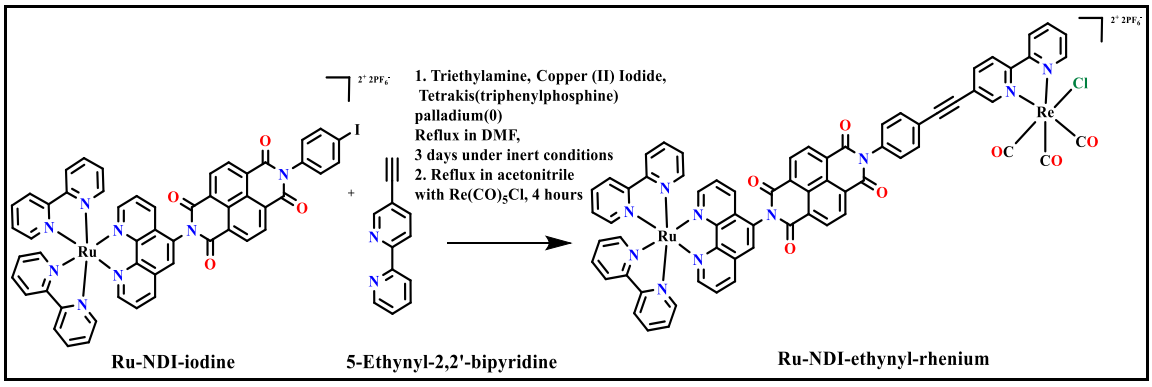


Figure 5.4 Synthetic scheme for the preparation of **Ru-NDI-ethynyl-rhenium**.

5.3.2 UV-vis and emission spectroscopy

UV-vis and emission spectroscopy measurements were carried out in acetonitrile, as presented in Figure 5.5. Emission spectra were recorded following excitation at both 450 (excitation of the ruthenium moiety) and 360 nm (excitation of the NDI unit). However, no emission was detected for any of these complexes. This indicates that the emission from the ruthenium ^{3}MLCT (metal-to-ligand charge transfer) state is quenched upon coordination with the NDI moiety, as observed for other complex in this dissertation (Chapter 3) and discussed in the literature [31 – 33]. It is important to highlight that this finding is also very helpful during synthesis and purification, as emission in this case suggests incomplete reaction or traces of uncoordinated ruthenium precursor, in this case **Ru(bpy)$_2$-phen-NH$_2$**. Rashid et al. [33] synthesised the Ru-NDI[PF_6]$_4$ complex, which incorporated 1,10-phenathroline and triazole-pyridine ligands linked to the NDI and reported a similar observation, in that the compounds were also non-emissive following coordination with NDI. The NDI moiety acts as an electron acceptor, whereas the Ru(II) center is an electron donor. Therefore, the electron transfer occurs from the ruthenium center towards the NDI, which subsequently leads to the formation of the charge separated state [33, 34]. This process involves quenching of ^{3}MLCT state due to electron transfer to NDI moiety, hence the Ru-NDI[PF_6]$_4$ complex was not emissive [33]. A recent study by Pereira et al. [35], investigated the [Ru(phen)$_2$(pNDIp)]$^{2+}$ complex, which is emissive with a band at 610 nm, attributed to ^{3}MLCT phosphorescence, and a lifetime of 540 ns in dimethyl sulfoxide. The absorption spectra of all the Ru-NDI complexes reported in this chapter exhibit similar spectral profiles with no significant shifts in the absorption bands observed upon coordination with different metals or with various functional groups. The absorption band at 450 nm is attributed to the MLCT from the ruthenium centre [33, 36 – 38], whereas the bands at approximately 350 – 380 nm correspond to π-π* transition in the NDI moiety [39 – 41]. It is important to highlight that the increased conjugation (due to the extended molecular structure employing a bipyridine moiety, triple bonds and electron-withdrawing groups) in the **Ru-NDI-bpy**, **Ru-NDI-rhenium**, **Ru-NDI-platinum** and **Ru-NDI-ethynyl-rhenium** does not result in a shift of the absorption bands towards the near-infrared region. The absence of any red-shifts of the absorption bands could be due to the orthogonality of the N-aryl substituents at the NDI rings, hence steric restriction limits any π conjugation off the NDI moiety with the N-substituents. In order to achieve this, it would be necessary to further increase the

conjugation and modify the HOMO-LUMO gap, for example by incorporating polymers in the molecular structures [42 – 44].

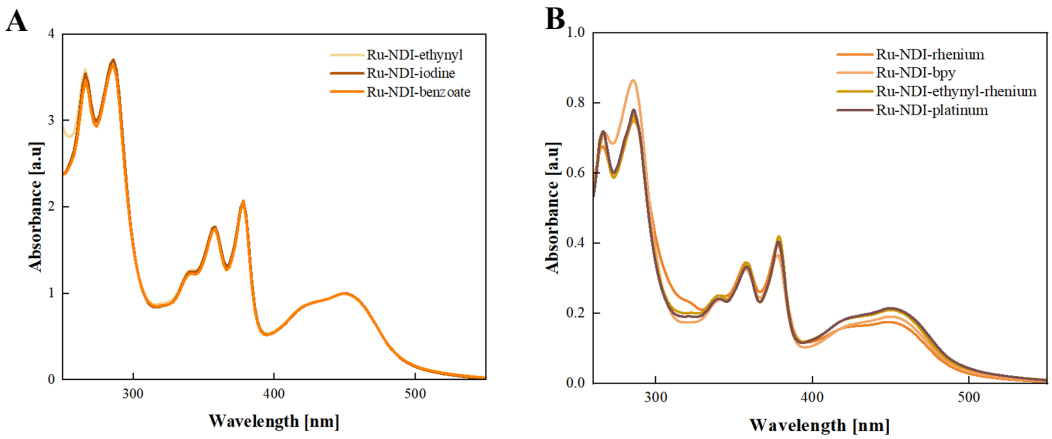


Figure 5.5 (A) Normalised UV-vis absorption spectra of **Ru-NDI-ethynyl**, **Ru-NDI-iodine** and **Ru-NDI-benzoate** recorded in acetonitrile. **(B)** UV-vis absorption spectra of **Ru-NDI-rhenium**, **Ru-NDI-bpy**, **Ru-NDI-platinum** and **Ru-NDI-ethynyl-rhenium** obtained in acetonitrile (0.2 – 0.4 mmol).

5.3.3 Time-Resolved Infrared Spectroscopy (TRIR)

TRIR spectroscopy measurements for **Ru-NDI-iodine**, **Ru-NDI-benzoate**, **Ru-NDI-ethynyl**, **Ru-NDI-bpy**, **Ru-NDI-rhenium**, and **Ru-NDI-ethynyl-rhenium** were performed following excitation at both 365 and 420 nm in acetonitrile. The study was carried out to investigate the electron transfer kinetics and determine where the electron density is primarily localised upon photoexcitation.

5.3.3.1 TRIR of the Ru-NDI-iodine complex

For **Ru-NDI-iodine** (Figure 5.6 (A – B)), following excitation at 365 nm, ground-state bleaches were evident at 1723, and 1688 cm^{-1} and were attributed to the parent carbonyl ν(C=O) stretching vibrations localised on the NDI framework [45 – 47]. In addition, the band at 1585 cm^{-1} was assigned to the aromatic rings of the NDI unit ν(C=C) [48]. In addition, new transient bands formed at lower wavenumbers, at 1649 and 1610 cm^{-1} within 40 ps. The shift of organic carbonyl bands ν(C=O) of the excited species to lower frequency indicates charge transfer from the ruthenium unit towards the NDI moiety, and a subsequent formation of the charge-separated state **[Ru^{III}-NDI^{-}-iodine]**. The charge-separation and charge-recombination lifetimes were determined to be 21 and 311 ps, respectively. Upon excitation at 420 nm, the **Ru-NDI-iodine** complex, exhibited similar stretching vibrational features as well as comparable charge-separation and charge-recombination kinetics (τ_{CS} = 28 and τ_{CR} = 202 ps) to those observed upon excitation at higher energy of 365 nm.

5.3.3.2 TRIR of the Ru-NDI-benzoate complex

For the **Ru-NDI-benzoate** complex (Figure 5.7 (A – B)), following excitation at 365 nm, ground-state bleaches were observed at 1723, 1711 and 1645 cm^{-1}. The new transient bands at 1692 and 1664 cm^{-1}, which similarly to **Ru-NDI-iodine**, C=O bands shifted to lower wavenumbers, and were assigned to formation of the charge separated state **[Ru^{III}-NDI^{-}-benzoate]**, with an increased electron density on the NDI. However, in **Ru-NDI-benzoate**, these new transient bands appear to be at a higher wavenumber (1692 and 1664 cm^{-1}) in comparison to **Ru-NDI-iodine** (at 1649 and 1610 cm^{-1}). The charge-separation and charge-recombination lifetimes were determined to be τ_{CS} = 26 and τ_{CR} = 231 ps, respectively. Similar spectral features with new transient bands appearing at 1645 and 1609 cm^{-1} and kinetics were observed when the excitation wavelength was changed to 420 nm (τ_{CS} = 25 and τ_{CR} = 257 ps).

5.3.3.3 TRIR of the Ru-NDI-bpy complex

Following excitation of the **Ru-NDI-bpy** complex (Figure 5.8 (A – B)) at 365 nm, ground-state bleaches were observed at 1721, 1685 and 1580 cm^{-1}, together with new transient bands at 1649 and 1605 cm^{-1}. Similarly to the previous Ru-NDI complexes, the transient bands in **Ru-NDI-bpy** were shifted to lower wavenumber by ~ 70 cm^{-1} in comparison to the parent bleaches and are assigned to the formation of a charge-separated state, **[Ru^{III}-NDI^{-}-bpy]**. The charge-separation and charge-recombination were determined to be τ_{CS} = 18 and τ_{CR} = 239 ps, respectively. Similar spectral features and kinetics for **Ru-NDI-bpy** were observed following excitation at 420 nm (τ_{CS} = 20 and τ_{CR} = 207 ps). Pearce et al. [46] reported a similar observation in their study of $NDIS_0$-PTZ, a system which incorporated a naphthalene diimide (NDI) and a phenothiazine moiety (PTZ). They reported that upon excitation at 355 nm, the new transient bands were observed at lower wavenumbers to those of the parent. A rapid initial process, lasting approximately 1 ps, resulted in an enhancement of these transient features with minimal changes to the parent bands. This behaviour was attributed to the formation of a charge-transfer state, which subsequently decayed back to the ground state within 250 ps [46].

5.3.3.4 TRIR of the Ru-NDI-ethynyl complex

The **Ru-NDI-ethynyl** complex was primarily designed and synthesised for TRIR analysis with the aim of investigating whether an enhancement in the absorption of ν(C≡C) of the excited-state could be detected following photoexcitation, and to help map the nature of the excited states populated. Stitch at al. [21] reported the results from a TRIR study, following excitation of a Ru(II)polypyridyl complex, $[Ru(phen)_2(11,12\text{-dCN-dppz})]^{2+}$, which incorporated nitrile ν(C≡N) functional groups. The authors observed a significant enhancement in the ν(C≡N) stretching vibration in the excited state, which was attributed to changes in electron density within the aromatic system. Similarly, Liu et al. [49] focused on the behaviour of ν(C≡N) stretching vibrations and concluded that photoexcitation leads to an enhancement in the stretching vibration. This effect was attributed to the electron-withdrawing nature of the nitrile group, which leads to an increased electron density in the phenyl ring, and the charge transfer, which subsequently results in elongation of the C≡N bond [49]. In contrast, in the case of the **Ru-NDI-ethynyl** complex (Figure 5.9 (A – B)), a minor increase in absorption for the triple bond was observed following excitation at 365 nm. This suggests that upon excitation at 365 nm, which is mainly NDI based transitions, the electron distribution shifts slightly towards

the triple bond. The bleaches at 1739, 1697 and 1584 cm^{-1} correspond to the ν(C=O) stretching vibrations in the parent complex. In addition, new ν(C=O) transient bands were evident at 1656, 1611 and 1517 cm^{-1}, indicating the formation of the charge-separated state, **[Ru^{III}-NDI^{-}-ethynyl]**. The bleach attributed to the triple bond was difficult to determine, however the excited state absorption feature was recorded at 2030 cm^{-1}. This could suggest that there is some degree of enhancement present in the excited state, which highlights the possibility of charge transfer from the NDI moiety towards the triple bond. The charge-separation and charge-recombination were determined to be τ_{CS} = 11 and τ_{CR} = 238 ps, respectively. Upon excitation at 420 nm, the **Ru-NDI-ethynyl** complex exhibited similar vibrational features as well as comparable charge-separation and charge-recombination kinetics (τ_{CS} = 24 and τ_{CR} = 286 ps), however the signals corresponding to the triple bond in the ground- and excited-state were particularly weak, hence the analysis of these signals following excitation at 420 nm was not possible.

5.3.3.5 TRIR of the Ru-NDI-rhenium complex

Following excitation at 365 nm, the **Ru-NDI-rhenium** complex (Figure 5.10A), similarly to other aforementioned complexes, exhibited ground-state bleaches at 1718, 1685 and 1584 cm^{-1} (NDI based ν(C=O) stretching vibrations), in addition to depletion of metal carbonyl bands (rhenium centre) at 2014, 1921 and 1905 cm^{-1}. New transient bands were evident at 2001, 1890, 1649 and 1609 cm^{-1}. The first set of new transient bands at 2001 and 1890 cm^{-1} is attributed to changes in the electron density of the metal carbonyl groups. These new transient bands slightly shifted slightly to lower wavenumbers in comparison to the parent bands. This shift indicates an increase in electron density on the rhenium centre, highlighting the possibility of electron transfer from the ruthenium center via the NDI moiety towards the rhenium metal centre. Additionally, new ν(C=O) transient bands were evident at 1649 and 1609 cm^{-1}, indicating the formation of the charge-separated state, **[Ru^{III}-NDI^{-}-rhenium]**. The charge-separation and charge-recombination were determined to be τ_{CS} = 16 and τ_{CR} = 164 ps, respectively. Following excitation at 420 nm, the **Ru-NDI-rhenium** complex (Figure 5.10B), similarly to the excitation at 365 nm, exhibited ground-state bleaches at 1718, 1685 and 1584 cm^{-1} assigned to the NDI moiety and weak depletion of metal carbonyl bands (rhenium centre) was evident at 2025, 1921 and 1906 cm^{-1}. The charge-separation and charge-recombination were determined to be τ_{CS} = 11 and τ_{CR} = 93 ps, respectively.

5.3.3.6 TRIR of the Ru-NDI-ethynyl-rhenium complex

For the **Ru-NDI-ethynyl-rhenium** complex excitation at 365 nm, led to bleaching of the parent NDI bands at ν(C=O) 1729, 1686 and 1576 cm^{-1}, and at 2003, 1911 and 1900 cm^{-1} for the metal rhenium stretching vibrations. The stretching vibration corresponding to the triple bond were weak with a signal at 2039 cm^{-1}. New transient bands were evident at 2027, 1983, 1860, 1640 and 1600 cm^{-1}. These new bands are assigned to formation of a CS excited state. The charge-separation and charge-recombination were determined to be τ_{CS} = 5 and τ_{CR} = 775 ps, respectively. Charge recombination for this complex is notably longer in comparison to the other complexes studied in this chapter. No signals were observed in the triple bond region at this excitation wavelength. When comparing different excitation wavelengths, it can be observed, that there is a greater enhancement in the absorption of the transient band at ~ 1860 cm^{-1} using 420 nm excitation. This could possibly indicate that there is a greater electron density localised on the rhenium centre when the **Ru-NDI-ethynyl-rhenium** is excited at lower energy. Martinez et al. [50] investigated the electronic and excited-state properties of a reduced NDI complex incorporating $Re(bpy)(CO)_3Cl$. The authors conducted femtosecond mid-IR spectroscopy measurements and reported that the carbonyl ligands of the rhenium center are present in the range of 1850 – 2100 cm^{-1}. Following excitation at 605 nm, the ground-state absorptions at 1892, 1910 and 2018 cm^{-1}, underwent bleaching with new transient bands at 1861 and 1994 cm^{-1} (lifetime of approximately 11.6 ps) [50]. In a subsequent study, the same research group [51] examined photoinduced electron transfer from the reduced NDI moiety towards the rhenium center in a Phbpy-Re-PyPhPDI^{1-} assembly. Femtosecond time-resolved IR again exhibited ν(C=O) stretching vibrations localised on the rhenium moiety, within the same spectral range of 1850 – 2100 cm^{-1}. Upon excitation, the ground-state absorptions at 2046 cm^{-1} and 1928 cm^{-1} were bleached and new transient bands were formed at 2020 cm^{-1} and 1885 cm^{-1}. These aforementioned results focus primarily on the carbonyl stretching vibrations localised at the rhenium center and are similar to the spectral results obtained for our Ru-NDI complexes incorporating rhenium (**Ru-NDI-rhenium** and **Ru-NDI-ethynyl-rhenium**).

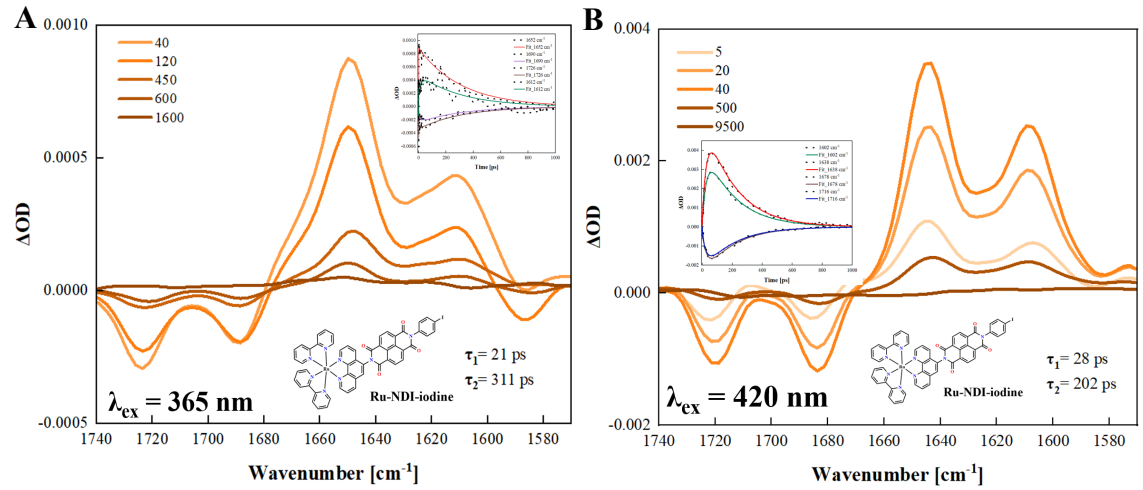


Figure 5.6 Time-resolved infrared measurements of the **Ru-NDI-iodine** complex recorded in acetonitrile **(A)** following excitation at 365 nm, and **(B)** excitation at 420 nm. The inset data displays kinetic decay traces (in ps), which were obtained using Glotaran analysis.

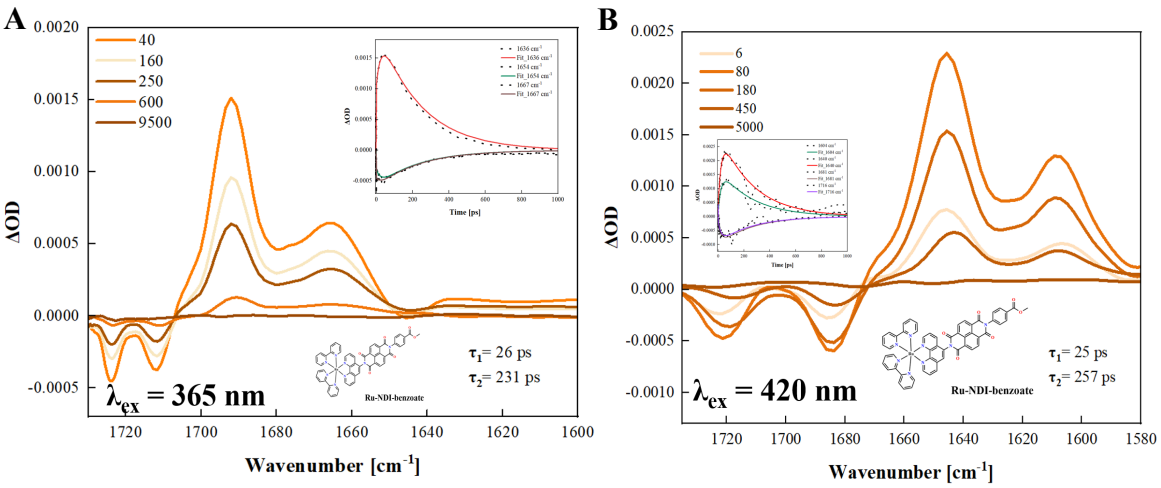


Figure 5.7 Time-resolved infrared measurements of the **Ru-NDI-benzoate** complex recorded in acetonitrile **(A)** following excitation at 365 nm, and **(B)** excitation at 420 nm. The inset data displays kinetic decay traces (in ps), which were obtained using Glotaran analysis.

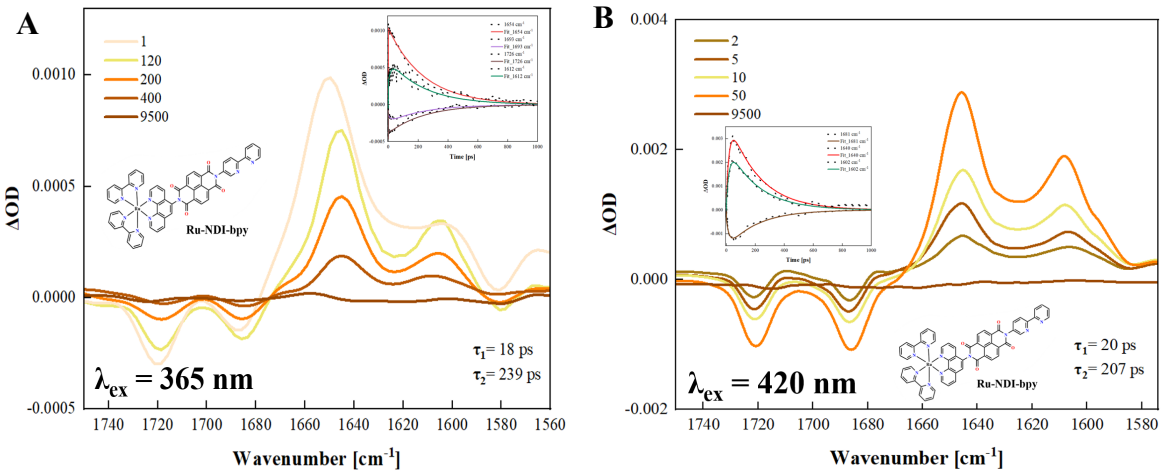


Figure 5.8 Time-resolved infrared measurements of the **Ru-NDI-bpy** complex recorded in acetonitrile **(A)** following excitation at 365 nm, and **(B)** excitation at 420 nm. The inset data displays kinetic decay traces (in ps), which were obtained using Glotaran analysis.

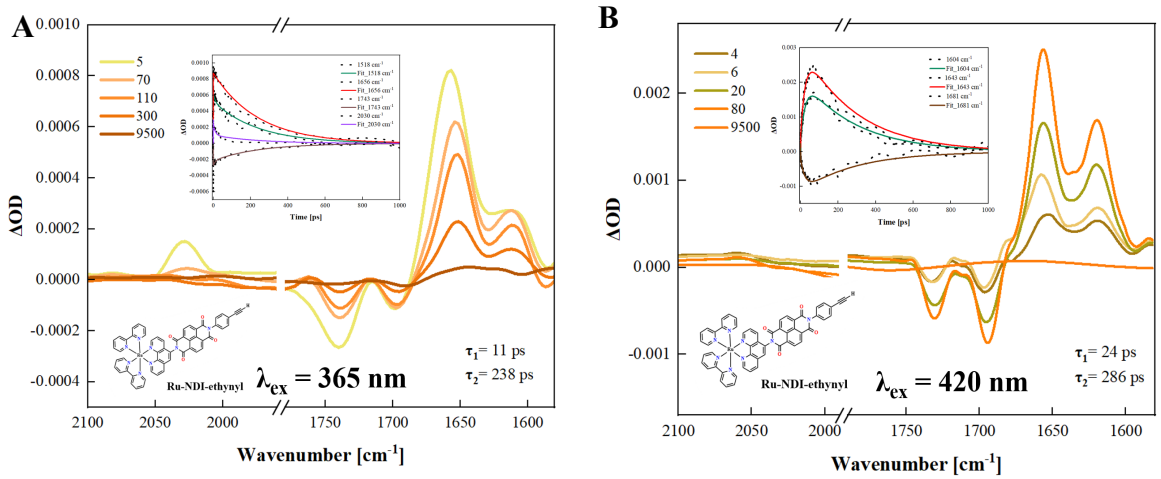


Figure 5.9 Time-resolved infrared measurements of the **Ru-NDI-ethynyl** complex recorded in acetonitrile **(A)** following excitation at 365 nm, and **(B)** excitation at 420 nm. The inset data displays kinetic decay traces (in ps), which were obtained using Glotaran analysis.

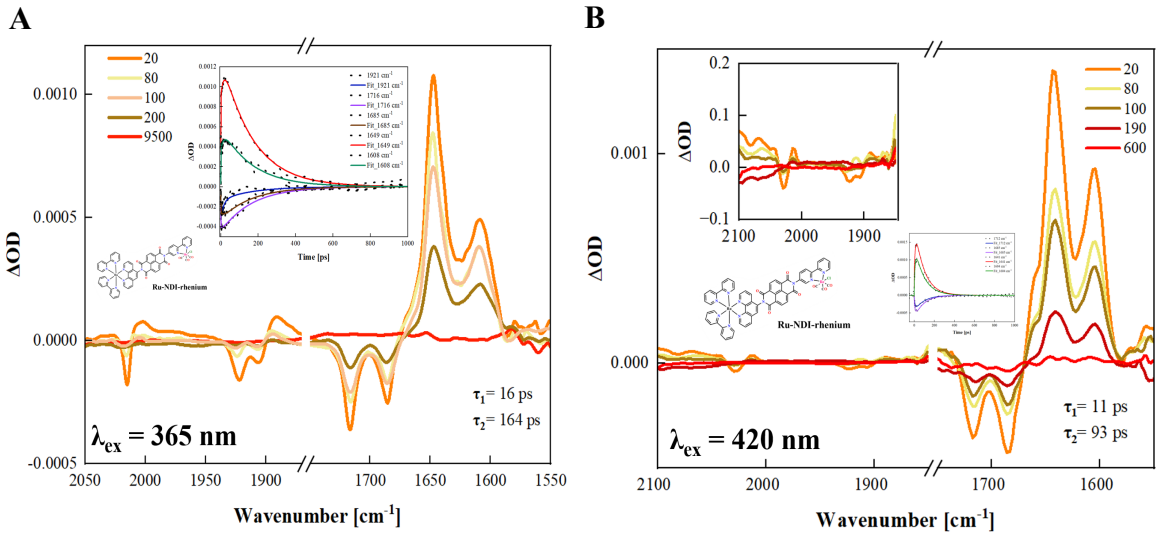


Figure 5.10 Time-resolved infrared measurements of the **Ru-NDI-rhenium** complex recorded in acetonitrile **(A)** following excitation at 365 nm, and **(B)** excitation at 420 nm. The inset data displays kinetic decay traces (in ps), which were obtained using Glotaran analysis.

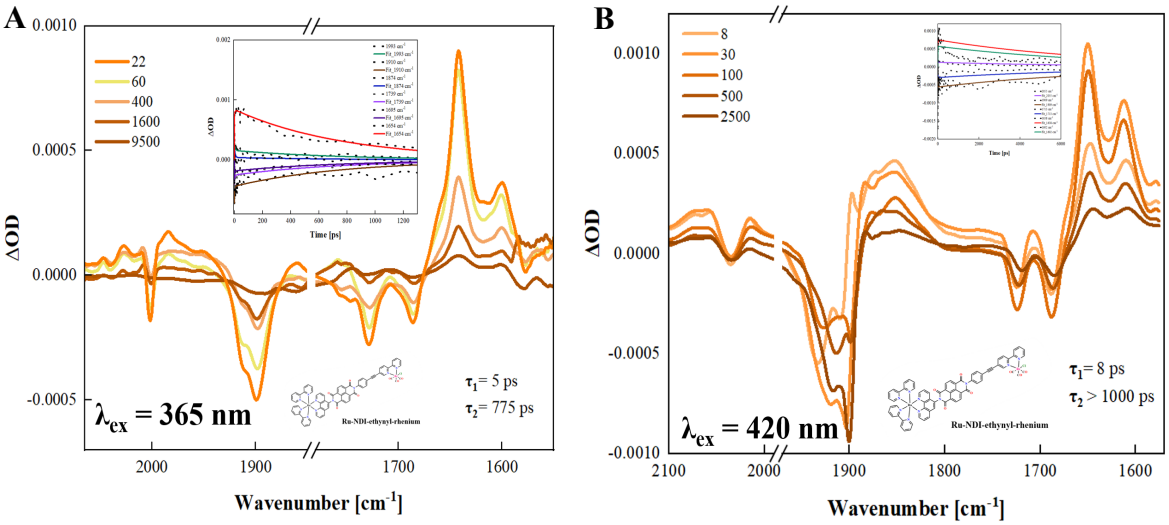


Figure 5.11 Time-resolved infrared measurements of the **Ru-NDI-ethynyl-rhenium** complex recorded in acetonitrile **(A)** following excitation at 365 nm, and **(B)** excitation at 420 nm. The inset data displays kinetic decay traces (in ps), which were obtained using Glotaran analysis.

Table 5.1 Time-resolved infrared measurements of all Ru-NDI complexes, recorded in acetonitrile following excitation at 365 and 420 nm. The table summarises the kinetic data for the charge separation (τ_{CS}) and charge recombination (τ_{CR}) processes, with the corresponding lifetimes measured in picoseconds.

Compound	Excitation at 365 nm		Excitation at 420 nm	
	Charge separation (τ_{CS})	Charge recombination (τ_{CR})	Charge separation (τ_{CS})	Charge recombination (τ_{CR})
Ru-NDI-iodine	21	311	28	202
Ru-NDI-benzoate	26	231	25	257
Ru-NDI-bpy	18	239	20	207
Ru-NDI-ethynyl	11	238	24	286
Ru-NDI-rhenium	16	164	11	93
Ru-NDI-ethynyl-rhenium	5	775	8	>1000

5.3.4 Picosecond transient absorption spectroscopy in solution

Picosecond Transient Absorption Spectroscopy was carried out for all the Ru-NDI complexes, in acetonitrile solution following excitation at 400 nm (Figure 5.12 (A – F)). These studies were carried out to probe the photophysical properties of these complexes in solution at the ultrafast timescale. All lifetimes and kinetic traces were calculated and determined using Glotaran analysis. In all Ru-NDI complexes following excitation, a ground-state bleach was observed at approximately 450 nm, which corresponds to the MLCT in the ruthenium complex. Initially following excitation, a new broad absorption occurs in the range of 500 – 750 nm and is assigned to population of the $^{3}MLCT_{bpy}$ excited state of ruthenium (the first spectrum in the figures below). Over the subsequent picosecond time scale (up to 400 ps) new transient bands features grow in at 474, 530, 604 and 700 nm. These features are tentatively assigned to formation of the charge-separate state of the NDI, Ru^{III}-NDI^{-} [52 – 55]. The charge separation lifetimes for all the Ru-NDI compounds studied ranged from 1 – 27 ps. The new transient bands decayed back to the ground state within 1000 ps for all complexes, with charge recombination

lifetimes in the range 15 – 480 ps. For most of the complexes, the band at 474 nm is the dominant spectral feature in all spectra. However, in the case of **Ru-NDI-ethynyl-rhenium** and **Ru-NDI-platinum,** this feature is less intense and appears equivalent in intensity to the absorption band at 605 nm. The reason for this behaviour remains unclear at this stage. Pereira et al. [35] carried out ps-TAS measurements on a Ru-NDI type complex similar to the ones presented in this work, however in their system, the authors employed a phenanthroline moiety as opposed to a bipyridine ligand and the NDI unit. Upon excitation at 450 nm, the authors reported similar transient spectra with bands at 497, 550 and 610 nm, which are attributed to the formation of one-electron reduced species, $RupNDIp^{\bullet-}$. A charge separation lifetime of 14 ps and charge recombination of 110 ps was reported by the authors [35].

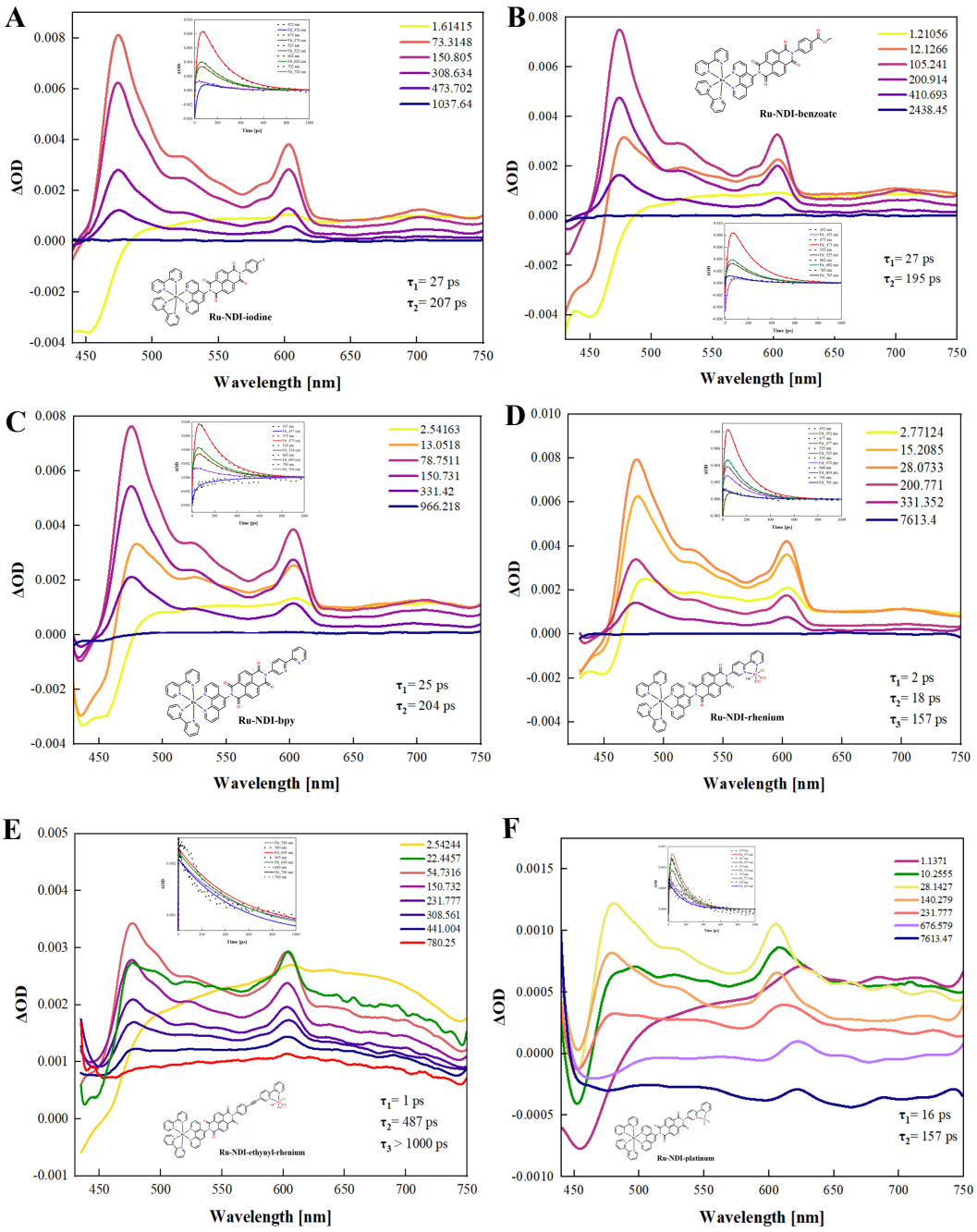


Figure 5.12 Picosecond transient absorption spectra of Ru-NDI complexes were recorded in acetonitrile following excitation at 400 nm, **(A) Ru-NDI-iodine**, **(B) Ru-NDI-benzoate**, **(C) Ru-NDI-bpy**, **(D) Ru-NDI-rhenium**, **(E) Ru-NDI-ethynyl-rhenium, (F) Ru-NDI-platinum**. The inset data displays kinetic decay traces (in ps), which were obtained using Glotaran analysis.

5.3.5 Picosecond transient absorption spectroscopy on NiO

TAS measurements were also carried out on NiO films following 400 nm laser excitation and the spectral changes shown in Figures 5.13 (A – F) for the Ru-NDI complexes when immobilised on NiO. These studies were carried out to probe the photophysical properties of these complexes on a NiO surface, as understanding these processes is essential for their potential use in dye-sensitised solar cells or dye-sensitised photoelectrochemical cells. Similar to the TAS studies in acetonitrile, most of the complexes exhibit a ground-state bleach at around 450 nm, which corresponds to the MLCT transition of ruthenium. Within ~ 1 – 10 picoseconds, new transient bands appear at approximately 474, 530, 605 and 700 nm, assigned to the formation of the charge-separate state of the NDI, Ru^{III}-NDI^{-}, as observed in the solution studies.

The lifetimes obtained from the Glotaran analysis for **NiO|Ru-NDI-iodine**, (Figure 5.13A) were $\tau_1 = 1$ ps, $\tau_2 = 76$ ps, in addition to a longer-lived component with $\tau_3 > 1000$ ps. **NiO|Ru-NDI-bpy** exhibited similar spectral profile (Figure 5.13C) with time constants of $\tau_1 = 1$ ps, $\tau_2 = 38$ ps, $\tau_2 > 1000$ ps. The shorter lifetime components are attributed to hole injection (electron transfer from the NiO to the Ru-NDI system), and a lifetime of > 1000 ps indicates slow charge-recombination [56, 57].

For all Ru-NDI complexes, in solution, the band at 474 nm was the dominant feature in the spectra of all complexes. However, on the surface, this band is less intense for all complexes and is similar in intensity to the band at approximately 605 nm. In the case of **NiO|Ru-NDI-ethynyl-rhenium** the bands attributed to the charge separated species are very weak. The lifetimes of the longer-lived component exceed the instrumental limit of 7000 ps, which indicates that the charge-separated states, Ru^{III}-NDI^{-}, are longer-lived than in solution. This suggests that the electron transfer from the NiO semiconductor to the Ru-NDI complexes leads to the formation of charge-separated species. The ultrafast formation of these charge-separated species is attributed to efficient hole injection, which subsequently results in the population of the electron on the NDI moiety [56, 57]. Ultrafast hole injection from the excited NDI onto NiO is necessary for photocatalytic and solar cell applications [58]. Additionally, the lifetime component of $\tau > 1000$ ps indicates that the behaviour of the excited states is different from the one observed in solution [27]. Consequently, this observation highlights the potential of these complexes as promising photosensitisers/photocatalysts in energy-based applications.

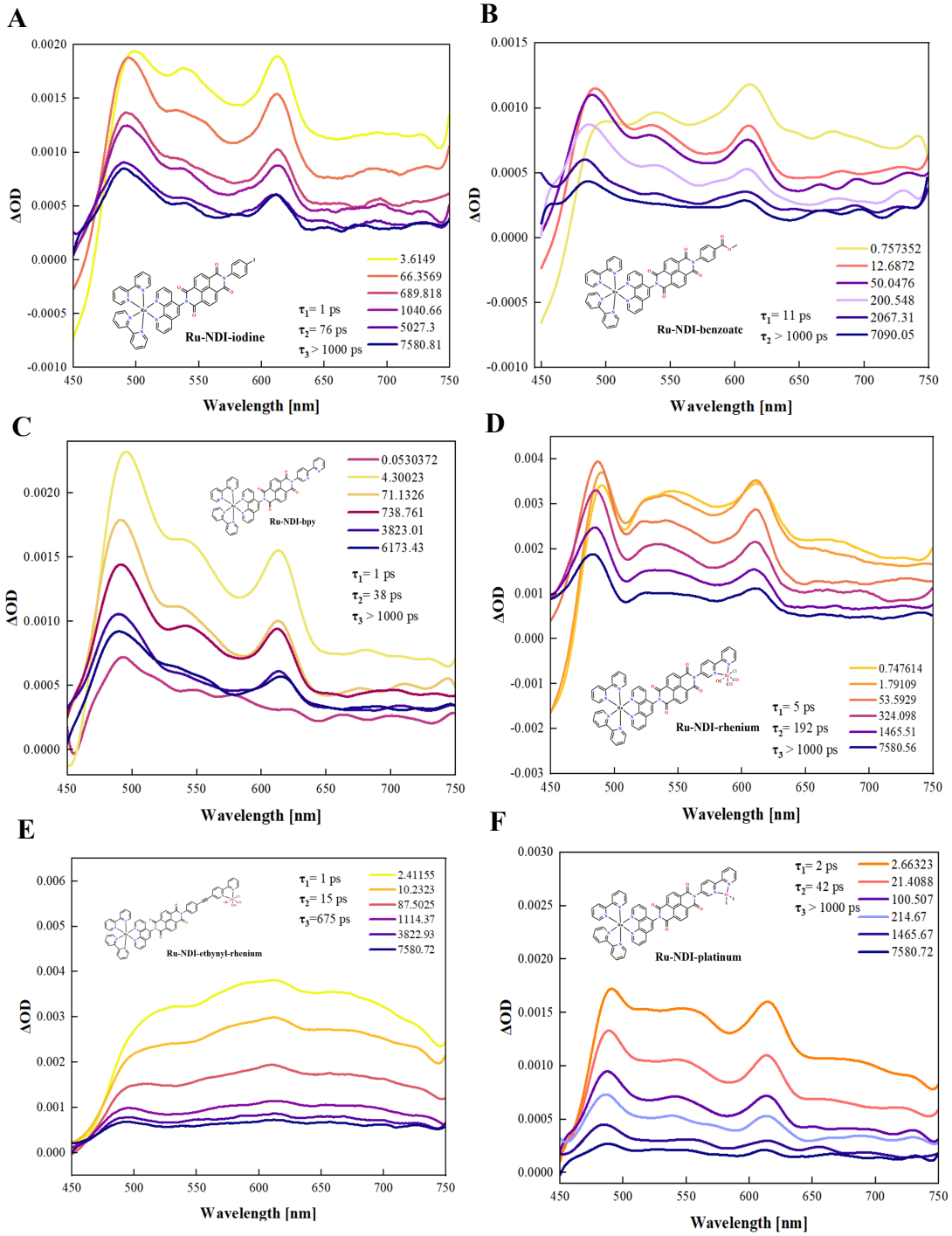


Figure 5.13 Picosecond transient absorption spectra of Ru-NDI complexes were recorded on NiO film following excitation at 400 nm, **(A) Ru-NDI-iodine**, **(B) Ru-NDI-benzoate**, **(C) Ru-NDI-bpy**, **(D) Ru-NDI-rhenium**, **(E) Ru-NDI-ethynyl-rhenium**, **(F) Ru-NDI-platinum**.

Table 5.2 Picosecond Transient Absorption measurements of all Ru-NDI complexes, recorded in acetonitrile and on a NiO, following excitation at 400 nm. The table summarises the kinetic data for the charge separation (τ_{CS}) and charge recombination (τ_{CR}) processes, with the corresponding lifetimes measured in picoseconds.

Compound	In solution		On a NiO surface	
	Charge separation (τ_{CS})	Charge recombination (τ_{CR})	Charge separation (τ_{CS})	Charge recombination (τ_{CR})
Ru-NDI-iodine	27	207	1	> 1000
Ru-NDI-benzoate	27	195	11	> 1000
Ru-NDI-bpy	25	204	1	> 1000
Ru-NDI-platinum	16	157	2	> 1000
Ru-NDI-rhenium	2	157	2	> 1000
Ru-NDI-ethynyl-rhenium	1	487 (a longer component of >1000 ps was also observed)	1	675

5.3.6 Transient absorption spectroscopy (TAS) in solution and under photocatalytic conditions - preliminary studies

Transient Absorption Spectroscopy was also conducted on the nanosecond timescales to investigate the excited-state properties of all ruthenium-NDI complexes synthesised in this work and to determine the nature and presence of the long-lived excited states, which are necessary for photocatalytic hydrogen evolution [59]. Nanosecond TAS, following excitation at 355 nm, was performed both in acetonitrile solution, as well as under photocatalytic conditions to probe the behaviour of the systems during photocatalysis.

In the nanosecond TAS experiments carried out in acetonitrile solution, following excitation at 355 nm, no long-lived triplet excited states were observed. This is consistent with the $RuNDI^{2+}$ complex discussed in Chapter 3. Additionally, these results are further supported by literature findings [60]. Another study involving NDI-complexes, also reported no evidence for the triplet excited state [61]. The authors synthesised rhodamine-bromonaphtalenediimide (RB-NDI) dyad and they focused on the modulation of triplet state behaviour. Nanosecond TAS measurements revealed the absence of triplet states the

RB-NDI dyad in solution (dichloromethane and methanol), which indicated that quenching occurs because of electron transfer from the spirolactam rhodamine to the NDI unit, and this conclusion agrees with the results obtained by Johansson et al. [60]. However, the study highlighted that under acidic conditions using trifluoroacetic acid (TFA), it was possible to populate the triplet state, but under basic environments for example by using triethylamine (TEA), the triplet state is switched off. Upon the addition of TFA, a transient signal resembling that of the excited NDI was observed and was assigned to the triplet state in RB-NDI+TFA which is delocalised over the NDI and rhodamine moieties, with a lifetime of 9.89 μs [61].

Inspired by the work of Cui and co-workers [61], and to further validate the concepts investigated in Chapter 3 and Chapter 4, we decided to conduct ns-TAS studies under photocatalytic conditions. The purpose of these studies was to demonstrate how different the behaviour of the photocatalytic assemblies can be in solution versus under photocatalysis conditions. In solution, as previously stated no long-lived triplet excited states were observed. The ns-TAS studies under photocatalytic conditions (TEA: H_2O: ACN and $Pt(DMSO)_2I_2$ added as a catalyst, see Photocatalytic results section for more details) were carried out for **Ru-NDI-iodine**, **Ru-NDI-benzoate**, **Ru-NDI-rhenium**, **Ru-NDI-bpy** and **Ru-NDI-ethynyl-rhenium** following excitation at 355 nm and this is presented in Figure 5.16 (A – E). Ground-state bleaching of the parent bands was typically observed in the range 480 – 490 nm. For **Ru-NDI-iodine**, transient bands appeared at 395 and 415 and 510 nm. In the **Ru-NDI-benzoate complex**, these bands were similar to those in **Ru-NDI-iodine**, however an additional band at 440 nm was also observed. In the case of the **Ru-NDI-bpy** complex, the transient bands are observed at 395, 415 and 515 nm, together with a broad shoulder at 440 nm. For **Ru-NDI-rhenium** a transient band was observed at 485 nm, with no additional bands observed, as was the case for the other complexes. For the **Ru-NDI-ethynyl-rhenium** complex, transient bands are observed at 395, 415 and 470 nm, together with a broad band centered between 600 – 700 nm. The transient absorption spectra under photocatalytic conditions for **Ru-NDI-rhenium** and **Ru-NDI-ethynyl-rhenium** appear slightly different in contrast to other complexes, as they do not show a ground-state bleach at approximately 480 nm. This suggests the absence of one-electron reduced species. The lifetimes were not determined, as they exceed the instrumental limit (ms time scale). In order to analyse the TAS data, the UV-vis absorption spectrum of all complexes was recorded prior to laser measurement, which helped in interpreting the TAS data results.

Before the laser measurements, all complexes exhibited the characteristic absorption properties of the electron reduced species of NDI (Figure 5.14). As observed in the previous chapters of this dissertation and in the studies reported in literature, NDI can undergo electrochemical or chemical reduction to form both one- and two- electron reduced species [52 – 55]. Under photocatalytic conditions and in the absence of oxygen, these species are successfully generated. However, it is challenging to isolate each individual electron reduced species through chemical reduction, but this can be done more efficiently using electrochemical reduction, as observed in the previous chapters of this dissertation. For the purpose of these studies, only chemical reduction with triethylamine was employed, which resulted in a mixture of both one- and two-electron reduced species under photocatalytic conditions, as also observed in the TAS measurements. The ground-state bleaching at approximately 480 nm is associated with the one electron reduced species of the NDI, whereas the transient bands between 390 and 415 nm are attributed to the two-electron reduced species of the NDI. An additional transient band at 500 nm is assigned to the deprotonated ruthenium moiety [62]. Since the electron reduced species of Ru-NDI complexes were discussed in previous chapters, this chapter focused on tuning the triplet excited state of the ruthenium-NDI complexes and their long-lived excited states which are necessary for photocatalytic applications. Hence, no spectroelectrochemical analysis was performed. The purpose in this research chapter was only to probe the photophysical properties of the photocatalytic assemblies under photocatalysis conditions.

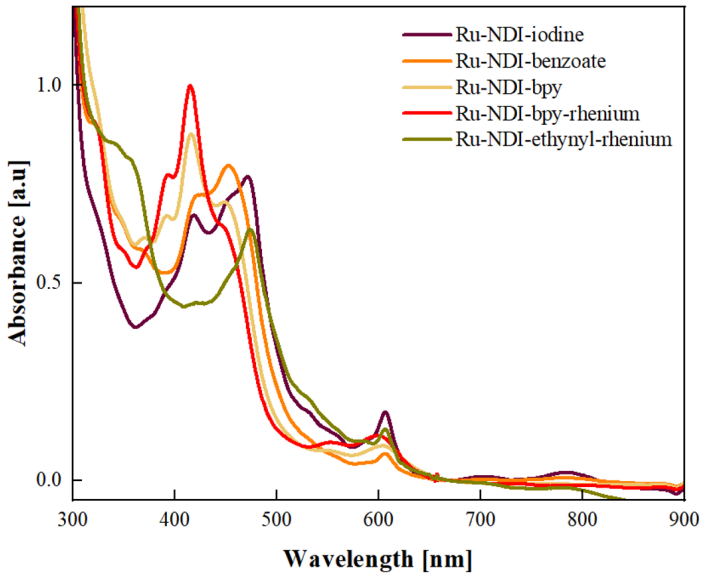


Figure 5.14 UV-vis absorption spectra of the Ru-NDI complexes presented in this chapter under photocatalytic conditions prior to the nanosecond transient absorption spectroscopy measurements. The experimental conditions involved a solvent mixture of triethylamine, water, and acetonitrile in the ratio of 30:5:65, respectively with $Pt(DMSO)_2I_2$ as the catalyst (in the non-rhenium complexes). All samples were prepared in a laser cell and deaerated using three cycles of freeze-pump-thaw.

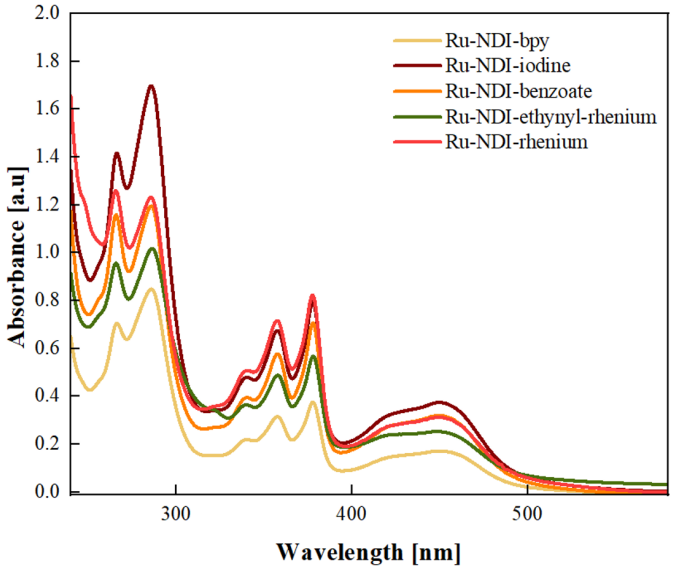


Figure 5.15 UV-vis absorption spectra of the Ru-NDI complexes presented in this chapter in acetonitrile prior to the nanosecond transient absorption spectroscopy measurements. All samples were prepared in a laser cell and deaerated using three cycles of freeze-pump-thaw.

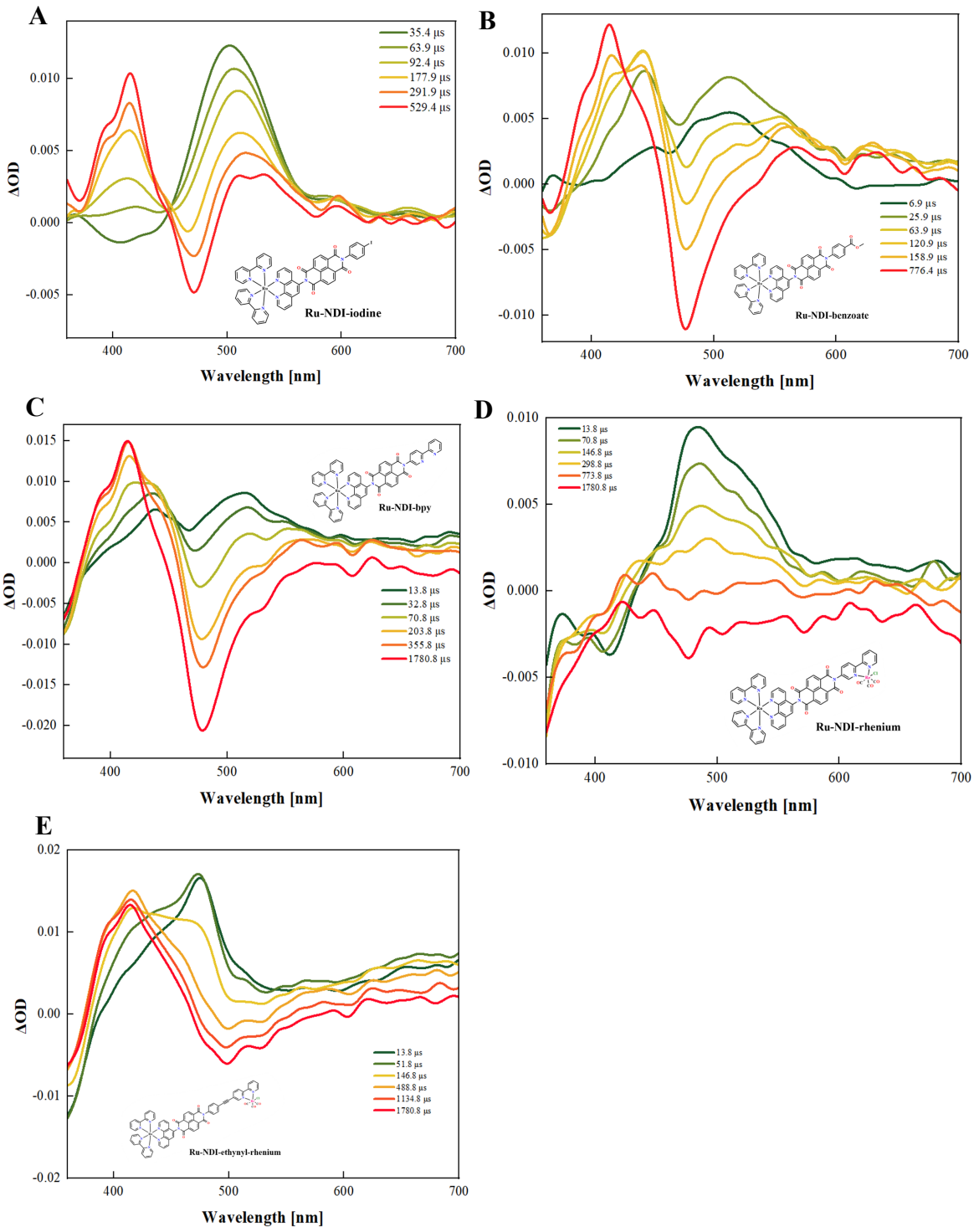


Figure 5.16 Nanosecond transient absorption spectra of all the Ru-NDI complexes were recorded under photocatalytic conditions following excitation at 355 nm. The experimental conditions involved a solvent mixture of triethylamine, water, and acetonitrile in the ratio of 30:5:65, with $Pt(DMSO)_2I_2$ acting as a catalyst in the photocatalysis. All samples were prepared in a laser cell and deaerated using three cycles of freeze-pump-thaw. **(A) Ru-NDI-iodine**, **(B) Ru-NDI-benzoate**, **(C) Ru-NDI-bpy**, **(D) Ru-NDI-rhenium**, **(E) Ru-NDI-ethynyl-rhenium**.

5.3.7 Photocatalytic results

The use of Ru-NDI type complexes is relatively uncommon in the literature, however, these systems function as efficient electron donor-acceptor assemblies [54, 60], exhibiting unique photophysical properties, and based on the results presented in this work, they have a potential for applications in photocatalytic hydrogen evolution and carbon dioxide reduction. Although these complexes do not exhibit long-lived triplet excited states in solution, their behaviour under photocatalytic conditions changes and indicates population of a triplet state, with lifetimes extending into the microsecond to millisecond range. This is necessary for successful hydrogen production. In this study, all Ru-NDI complexes were examined for their photocatalytic capabilities. Hydrogen evolution experiments were carried out in acetonitrile using triethylamine (TEA) as a sacrificial electron donor, water as a proton source (volume of 0.4 ml) and $Pt(DMSO)_2I_2$ as the catalyst, under light irradiation with an LED at 450 – 470 nm for 4 hours. This catalyst was added to the solution of complexes that did not incorporate a catalyst in the structure. The ratio of these reagents was selected to be 65:30:5 (ACN: TEA: H_2O). Intermolecular photocatalytic assemblies namely **Ru-NDI-iodine**, **Ru-NDI-benzoate**, **Ru-NDI-ethynyl**, **Ru-NDI-bpy** required the addition of the platinum catalyst to the mixture. In contrast, intramolecular photocatalytic systems **Ru-NDI-rhenium**, **Ru-NDI-ethynyl-rhenium** and **Ru-NDI-platinum** contained rhenium or platinum catalysts covalently attached to the photosensitiser, hence there was no need for additional catalyst in the solution. Carbon dioxide reduction experiments were conducted following a method reported in the literature in a 5:1 DMF to triethanolamine (TEOA) mixture, using TEOA as a sacrificial electron donor and 1,3-dimethyl-2-phenyl-2,3-dihydro-1H-benzo[d]-imidazole (BIH) as a reductant [63]. The concentration of the photocatalysts was 0.05 mM, and these were dissolved in 6 ml mixture of DMF and TEAO (5:1) and 0.1 M of BIH was employed. The solutions were purged with carbon dioxide for 5 minutes and irradiated at 450 nm under constant stirring. The highest turnover number (TON) for hydrogen evolution was observed for **Ru-NDI-benzoate**, which reached 24 TON after 4 hours of light irradiation. **Ru-NDI-iodine** achieved a TON of 17, while **Ru-NDI-bpy** showed a comparable value of 16 TON. Carbon dioxide reduction experiments were conducted for **Ru-NDI-rhenium** and **Ru-NDI-ethynyl-rhenium** with BIH and without the BIH reductant. The experiment without BIH exhibited poor photocatalytic performance, and no significant values were observed for CO formation. However, these compounds exhibited good photocatalytic activities in the presence of BIH, and the

turnover numbers were determined to be 122 TON for **Ru-NDI-rhenium** and 113 TON for **Ru-NDI-ethynyl-rhenium**. The UV-vis absorption spectra of the **Ru-NDI-rhenium** complex (Figure 5.17) measured before and after the photocatalysis suggested the formation of electron reduced species of NDI moiety.

Table 5.3 Turnover numbers for hydrogen evolution and carbon dioxide reduction by Ru-NDI complexes reported in this work. Hydrogen experiment was carried out using 0.03 mM of photosensitising moieties in 8 ml mixture of ACN: TEA: H_2O (65:30:5) and $Pt(DMSO)_2I_2$ was employed as a catalyst (in non-rhenium complexes). Carbon dioxide reduction experiment was carried out using concentration of 0.05 mM for the photocatalysts, and 6 ml mixture of DMF and TEOA (5:1) as well as 0.1 M of BIH was employed.

Compound	**Turnover number (TON_{H2}) Hydrogen evolution**	**Turnover number (TON_{CO}) Carbon dioxide reduction**
PHOTOSENSITISERS		
Ru-NDI-iodine	17	N/A
Ru-NDI-benzoate	24	N/A
Ru-NDI-bpy	16	N/A
Ru-NDI-ethynyl	2	N/A
PHOTOCATALYSTS		
Ru-NDI-rhenium without BIH with BIH	0.2 11	2 122
Ru-NDI-ethynyl-rhenium without BIH with BIH	2 38	0.08 113
Ru-NDI-platinum	0.2	N/A

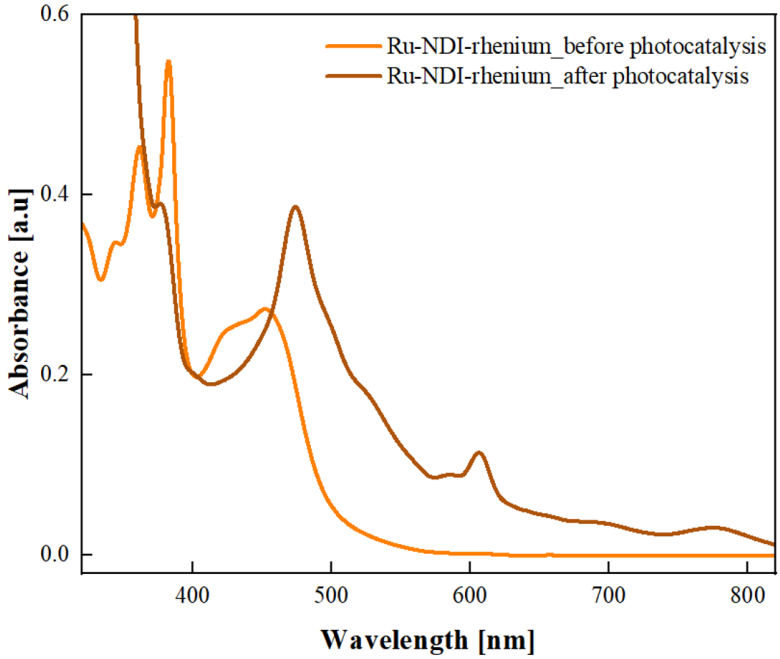


Figure 5.17 UV-vis absorption spectrum of **Ru-NDI-rhenium** complex recorded before and after photocatalysis. Carbon dioxide reduction experiment was carried out using concentration of 0.05 mM for the photocatalysts, and 6 ml mixture of DMF and TEOA (5:1) as well as 0.1 M of BIH was employed.

5.3.8 Preliminary chronoamperometry measurements and immobilisation studies

In order to evaluate the photochemical behaviour, chronoamperometry measurements were performed using a photoelectrochemical set up to determine the photocurrent response of the complexes under light irradiation on a NiO surface. These investigations were carried out at Newcastle University in the United Kingdom. The experimental procedure was similar to that described in previous chapters and reported in the literature [64]. Prior to conducting the photocatalytic reactions, immobilisation studies were carried out as presented in Figure 5.18. All the Ru-NDI complexes were successfully adsorbed onto the NiO surface, and their MLCT as well as LC transitions were slightly red-shifted in the UV-vis spectrum. For the photocatalytic hydrogen generation reaction, a three-electrode glass cell was employed, with the Ru-NDI complexes immobilised on the NiO surface, acting as the working electrode. A platinum wire served as the counter electrode, and an Ag/AgCl electrode in a 0.1M KCl electrolyte aqueous solution was used as the reference electrode. For the carbon dioxide reduction reaction (photocatalysis carried out on a NiO film), similar conditions were applied, however, a 50 mmol of $NaHCO_3$ electrolyte aqueous solution was used instead, and the device was purged with carbon dioxide gas [64]. The photoelectrochemical device was subjected to a constant voltage, while being exposed to light irradiation employing a white LED. This allowed us to

observe and examine the changes in the photocurrent in response to light on/off cycles. Among the Ru-NDI complexes discussed in this work, **Ru-NDI-rhenium** (Figure 5.19) exhibited the most promising photocurrent response, with an applied potential of –0.2 V. Under continuous irradiation, the current remains stable throughout the experiment. The highest photocurrent was obtained when the sample was irradiated. Typically, in chronoamperometry measurements, a rectangular shaped response of the current is observed, which is assigned to charge-discharge of a double layer capacitor. Hence, the charge/discharge current is said to be proportional to the rate of the applied potential [65, 66]. In the case of **Ru-NDI-rhenium**, the current drop at the beginning of each "sit opening" does not resemble the "ideal rectangular" shape, which could be attributed to mass transfer limitations [66, 67]. The increase in the current is not linear and possibly this observation could be due to the diffusion of the K^+ cation through the NiO pores to stabilise the reduced photocatalyst.

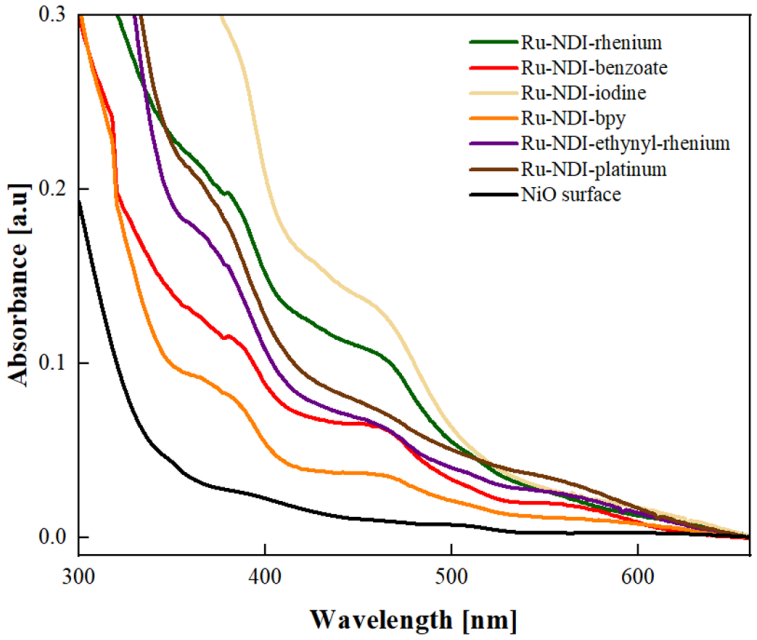


Figure 5.18 UV-vis spectroscopy measurements of Ru-NDI complexes immobilised on the NiO surface.

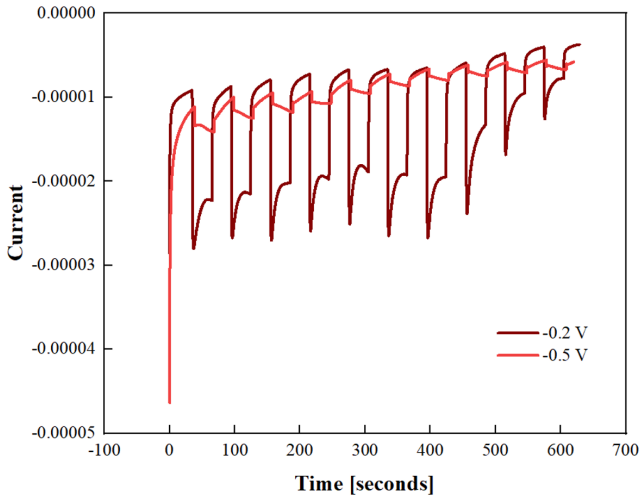


Figure 5.19 Chopped light (light on/light off) chronoamperometry measurements under light irradiation while applying potentials of –0.2 and –0.5 V for the **Ru-NDI-rhenium** complex.

5.4 Conclusion

All Ru-NDI complexes developed and synthesised in this study were thoroughly investigated using a wide range of photophysical techniques. Structural modifications, incorporation of different substituents and increased conjugation did not result in any significant shifts in the absorption bands. The UV-vis spectra remained unchanged and did not extend into the near-infrared region. In solution using ns-TAS, no signals that persisted on the nanosecond timescales were observed. However, the photophysical behaviour changed under photocatalytic conditions. Transient absorption bands attributed to the reduced NDI species, where the ground-state bleaching at around 500 nm corresponded to the one-electron reduced species and the transient band at 390 – 415 nm indicated the two-electron reduced species of the NDI. This study indicates that under photocatalytic conditions, the triplet excited state can be populated. TRIR studies revealed that there is a significant enhancement in band associated with the ν(C=O) stretching vibrations, and a smaller enhancement for the triple bonds. New transient bands were observed at lower wavenumbers, following excitation at 365 and 420 nm, which were assigned to a charge-separated state. Picosecond TAS measurements on nickel oxide thin films revealed that the transient species are formed faster on the semiconductor compared to the ones observed in solution. The decay of the charge-separated species and the charge-recombination processes were significantly slower on the surface, and this is necessary for the dye-sensitised solar cells-based applications. Moreover, on the NiO surface, this suggested that the electron transfer occurred faster and more efficiently than in solution, which facilitated the generation of charge-separated NDI reduced species.

Although, the Ru-NDI complexes exhibited poor photocatalytic activity for hydrogen evolution, they remain promising candidates for future examinations. Moreover, the electrochemical potential obtained from chronoamperometry measurements suggests that they could be suitable for further investigation in photocatalytic carbon dioxide reduction, when immobilised on a NiO surface.

5.5 Experimental

5.5.1 Materials and methods

All materials were purchased from Aldrich Chemicals Co. and Fluorochem Ltd. The FTIR was obtained using Perkin-Elmer 2000 FTIR spectrophotometer. NMR was conducted using Bruker 600 MHz spectrometer. UV-vis and Emission Spectroscopy spectra were recorded on a Duetta Absorbance and Fluorescence Spectrometer. Mass Spectrometry was conducted by researchers at the University of Bath.

5.5.2 Picosecond transient absorption measurements

Picosecond TAS were recorded at the Newcastle University in the United Kingdom. The optical density of the samples was in the range 0.3 - 0.9 at 400 nm laser excitation. All data was processed using Glotaran [68].

5.5.3 Nanosecond transient absorption measurements

Nanosecond TAS were recorded using the LP980 transient absorption spectrometer, Edinburgh Instruments, using excitation at 355 nm. All samples were deaerated using three cycles of freeze-pump-thaw. The optical density of the samples was ~ 0.3 – 0.6 at 355 nm laser excitation. The same method was employed for the ns-TAS measurements under photocatalytic conditions (for this, the sample (0.03 mmol) and the catalyst (0.03 mmol) were dissolved in a 65:30:5 mixture of acetonitrile, triethylamine and deionised water) and then the solution was excited at 355 nm.

5.5.4 Time-Resolved Infrared measurements

TRIR spectra were recorded using the ULTRA instrument at the Central Laser Facility in the Rutherford Appleton Laboratory in the United Kingdom [69]. All TRIR spectra were collected using 365 and 420 nm excitation with 1 μJ power in a 0.1 mm pathlength Harrick cell. All data was processed using Glotaran [68].

5.5.5 Photocatalytic H_2 evolution experiments

Photocatalytic hydrogen evolution was carried in a 19 ml glass Schlenk tube stopped with an air-tight rubber spectrum. The sample (0.03 mmol) and the catalyst (0.03 mmol) were dissolved in a 65:30:5 mixture of acetonitrile, triethylamine and deionised water. The freeze-pump-thaw procedure was used to ensure inert condition in the solution. The solution under a nitrogen atmosphere was then exposed to light irradiation at 450 or 470 nm using a photoredox box supplied by HepatoChem [70]. Gas Chromatography was used to quantify the amount of hydrogen produced.

5.5.6 Chronoamperometry and immobilisation studies on a NiO film

Photoelectrochemical measurements were carried out at the Newcastle University in the United Kingdom, following the same method reported in the previous chapters and documented in the literature [64].

5.6 References

[1]. Zhou, J., Tian, Y., Gu, H., & Jiang, B. (2025). Photocatalytic hydrogen evolution: Recent advances in materials, modifications, and photothermal synergy. International Journal of Hydrogen Energy, 115, 113–130. https://doi.org/10.1016/j.ijhydene.2025.03.088

[2]. Oh, V. B.-Y., Ng, S.-F., & Ong, W.-J. (2022). Is photocatalytic hydrogen production sustainable? – Assessing the potential environmental enhancement of photocatalytic technology against steam methane reforming and electrocatalysis. Journal of Cleaner Production, 379, 134673. https://doi.org/10.1016/j.jclepro.2022.134673

[3]. Yang, X., & Wang, D. (2018). Photocatalysis: From Fundamental Principles to Materials and Applications. ACS Applied Energy Materials, 1(12), 6657–6693. https://doi.org/10.1021/acsaem.8b01345

[4]. Gao, H., Zhang, J., Zhang, F., Jing, J., & Li, W.-Y. (2024). Enhanced formic acid production for CO_2 photocatalytic reduction over Pd/H-TiO_2 catalyst. Frontiers of Chemical Science and Engineering, 18(11), 134. https://doi.org/10.1007/s11705-024-2485-2

[5]. B., A., A., J., Rao, A. S., Nagarkar, S. S., Dutta, A., Duttagupta, S. P., Prabhu, S. S., & Pinto, R. (2024). Challenges in photocatalytic hydrogen evolution: Importance of photocatalysts and photocatalytic reactors. International Journal of Hydrogen Energy, 81, 1442–1466. https://doi.org/10.1016/j.ijhydene.2024.07.262

[6]. Li, N., Ma, Y., & Sun, W. (2024). Exploring the Dynamics of Charge Transfer in Photocatalysis: Applications of Femtosecond Transient Absorption Spectroscopy. Molecules, 29(17), 3995. https://doi.org/10.3390/molecules29173995

[7]. Choi, J., Jung, W., Gonzalez-Carrero, S., Durrant, J. R., Cha, H., & Park, T. (2024). Understanding charge carrier dynamics in organic photocatalysts for hydrogen evolution. Energy & Environmental Science, 17(21), 7999–8018. https://doi.org/10.1039/d4ee01808g

[8]. Gao, W., Lu, J., Zhang, S., Zhang, X., Wang, Z., Qin, W., Wang, J., Zhou, W., Liu, H., & Sang, Y. (2019). Suppressing Photoinduced Charge recombination via the Lorentz Force in a Photocatalytic System. Advanced Science, 6(18), 1901244. https://doi.org/10.1002/advs.201901244

[9]. Wang, P., Guo, S., Wang, H.-J., Chen, K.-K., Zhang, N., Zhang, Z.-M., & Lu, T.-B. (2019b). A broadband and strong visible-light-absorbing photosensitizer boosts hydrogen evolution. Nature Communications, 10(1), 3155. https://doi.org/10.1038/s41467-019-11099-8

[10]. Wang, Y., Huang, Y., Chen, S., Gao, J., Zhang, Y., Duan, Y., & Deng, P. (2023). Construction of Robust Iridium(III) Complex-Based Photosensitizer for Boosting Hydrogen Evolution. Inorganic Chemistry, 62(19), 7212–7219. https://doi.org/10.1021/acs.inorgchem.2c04471

[11]. Yu, Y., Yang, Z., Xia, Y., Lv, Y., Zhang, W., Lin, C., & Shao, C. (2023). Rational design and performance prediction of organic photosensitizer based on TATA+ dye for hydrogen production by photocatalytic decomposition of water. Frontiers in Chemistry, 11. https://doi.org/10.3389/fchem.2023.1210501

[12]. Kowacs, T., O'Reilly, L., Pan, Q., Huijser, A., Lang, P., Rau, S., Browne, W. R., Pryce, M. T., & Vos, J. G. (2016). Subtle Changes to Peripheral Ligands Enable High Turnover Numbers for Photocatalytic Hydrogen Generation with Supramolecular Photocatalysts. Inorganic Chemistry, 55(6), 2685–2690. https://doi.org/10.1021/acs.inorgchem.5b01752

[13]. Sun, M., Fan, X., Guo, S., Nui, X., Tian, L., Wang, A., Wang, R., Chen, W., & Cui, C. (2024). Substituent Regulating Porphyrin Derivatives for Efficient Photocatalytic

Hydrogen Evolution. Chemistry Select, 9(40), e202402960. https://doi.org/10.1002/slct.202402960
[14]. Ru, C., Chen, P., Wu, X., Chen, C., Zhang, J., Zhao, H., Wu, J., & Pan, X. (2022). Enhanced Built-in Electric Field Promotes Photocatalytic Hydrogen Performance of Polymers Derived from the Introduction of B←N Coordination Bond. Advanced Science, 9(35), 2204055. https://doi.org/10.1002/advs.202204055
[15]. Ma, J., Miao, T. J., & Tang, J. (2022). Charge carrier dynamics and reaction intermediates in heterogeneous photocatalysis by time-resolved spectroscopies. Chemical Society Reviews, 51(14), 5777–5794. https://doi.org/10.1039/d1cs01164b
[16]. Munson, K. T., Kennehan, E. R., & Asbury, J. B. (2019). Structural origins of the electronic properties of materials via time-resolved infrared spectroscopy. Journal of Materials Chemistry C, 7(20), 5889–5909. https://doi.org/10.1039/c9tc01348b
[17]. Turner, J. J., George, M. W., Poliakoff, M., & Perutz, R. N. (2022). Photochemistry of transition metal carbonyls. Chemical Society Reviews, 51(13), 5300–5329. https://doi.org/10.1039/d1cs00826a
[18]. Alberding, B. G., Brown-Xu, S. E., Chisholm, M. H., Epstein, A. J., Gustafson, T. L., Lewis, S. A., & Min, Y. (2013). Photoinduced charge transfer involving a MoMo quadruply bonded complex to a perylene diimide. Dalton Transactions, 42(15), 5275–5280. https://doi.org/10.1039/c3dt32750g
[19]. Mezzetti, A., Schnee, J., Lapini, A., & Di Donato, M. (2022). Time-resolved infrared absorption spectroscopy applied to photoinduced reactions: how and why. Photochemical & Photobiological Sciences, 21(4), 557–584.
https://doi.org/10.1007/s43630-022-00180-9
[20]. Sumner, E., Pižl, M., McQuaid, K. T., & Hartl, F. (2024). Nitrile Substituents at the Conjugated Dipyridophenazine Moiety as Infrared Redox Markers in Electrochemically Reduced Heteroleptic Ru(II) Polypyridyl Complexes. Inorganic Chemistry, 63(5), 2460–2469. https://doi.org/10.1021/acs.inorgchem.3c03484
[21]. Stitch, M., Avagliano, D., Graczyk, D., Clark, I. P., González, L., Towrie, M., & Quinn, S. J. (2023). Good Vibrations Report on the DNA Quadruplex Binding of an Excited State Amplified Ruthenium Polypyridyl IR Probe. Journal of the American Chemical Society, 145(39), 21344–21360. https://doi.org/10.1021/jacs.3c06099
[22]. Cullen, A. A., Heintz, K., O'Reilly, L., Long, C., Heise, A., Murphy, R., Karlsson, J., Gibson, E., Greetham, G. M., Towrie, M., & Pryce, M. T. (2020). A Time-Resolved Spectroscopic Investigation of a Novel BODIPY Copolymer and its Potential Use as a Photosensitiser for Hydrogen Evolution. Frontiers in Chemistry, 8. https://doi.org/10.3389/fchem.2020.584060
[23]. Nurttila, S. S., Becker, R., Hessels, J., Woutersen, S., & Reek, J. N. (2018). Photocatalytic Hydrogen Evolution by a Synthetic [FeFe] Hydrogenase Mimic Encapsulated in a Porphyrin Cage. Chemistry – A European Journal, 24(61), 16395–16406. https://doi.org/10.1002/chem.201803351
[24]. Sabatini, R. P., Eckenhoff, W. T., Orchard, A., Liwosz, K. R., Detty, M. R., Watson, D. F., McCamant, D. W., & Eisenberg, R. (2014). From Seconds to Femtoseconds: Solar Hydrogen Production and Transient Absorption of Chalcogenorhodamine Dyes. Journal of the American Chemical Society, 136(21), 7740–7750. https://doi.org/10.1021/ja503053s
[25]. Giannoudis, E., Benazzi, E., Karlsson, J., Copley, G., Panagiotakis, S., Landrou, G., Angaridis, P., Nikolaou, V., Matthaiaki, C., Charalambidis, G., Gibson, E. A., & Coutsolelos, A. G. (2020). Photosensitizers for H_2 Evolution Based on Charged or Neutral Zn and Sn Porphyrins. Inorganic Chemistry, 59(3), 1611–1621. https://doi.org/10.1021/acs.inorgchem.9b01838
[26]. Abdellah, M., El-Zohry, A. M., Antila, L. J., Windle, C. D., Reisner, E., & Hammarström, L. (2017). Time-Resolved IR Spectroscopy Reveals a Mechanism with

TiO_2 as a Reversible Electron Acceptor in a TiO_2–Re Catalyst System for CO_2 Photoreduction. Journal of the American Chemical Society, 139(3), 1226–1232. https://doi.org/10.1021/jacs.6b11308
[27]. Põldme, N., O'Reilly, L., Fletcher, I., Portoles, J., Sazanovich, I. V., Towrie, M., Long, C., Vos, J. G., Pryce, M. T., & Gibson, E. A. (2019). Photoelectrocatalytic H_2 evolution from integrated photocatalysts adsorbed on NiO. Chemical Science, 10(1), 99–112. https://doi.org/10.1039/c8sc02575d
[28]. Sasada, Y., Langford, S. J., Oyaizu, K., & Nishide, H. (2016). Poly(norbornyl-NDIs) as a potential cathode-active material in rechargeable charge storage devices. RSC Advances, 6(49), 42911–42916. https://doi.org/10.1039/c6ra06103f
[29]. Bian, Z.-Y., Sumi, K., Furue, M., Sato, S., Koike, K., & Ishitani, O. (2009). Synthesis and properties of a novel tripodal bipyridyl ligand tb-carbinol and its Ru(II)–Re(I) trimetallic complexes: investigation of multimetallic artificial systems for photocatalytic CO_2 reduction. Dalton Trans., (6), 983–993. https://doi.org/10.1039/b814340d
[30]. Kanwal, I., Mujahid, A., Rasool, N., Rizwan, K., Malik, A., Ahmad, G., Shah, S. A., Rashid, U., & Nasir, N. M. (2020). Palladium and Copper Catalyzed Sonogashira Cross Coupling an Excellent Methodology for C-C Bond Formation over 17 Years: A Review. Catalysts, 10(4), 443. https://doi.org/10.3390/catal10040443
[31]. Bartusiak, M. Z., McGarry, R. J., Varvarezos, L., Brandon, M. P., & Pryce, M. T. (2023). Incorporation of perylene and naphthalene like ligands into ruthenium complexes: Synthesis, photophysical properties and electrochemistry. Coordination Chemistry Reviews, 495, 215365. https://doi.org/10.1016/j.ccr.2023.215365
[32]. Gunderson, V. L., Krieg, E., Vagnini, M. T., Iron, M. A., Rybtchinski, B., & Wasielewski, M. R. (2011). Photoinduced Singlet Charge Transfer in a Ruthenium(II) Perylene-3,4:9,10-bis(dicarboximide) Complex. The Journal of Physical Chemistry B, 115(23), 7533–7540. https://doi.org/10.1021/jp2016374
[33]. Rashid, A., Mondal, S., Musha Islam, A. S., Mondal, S., & Ghosh, P. (2024). Naphthalene Diimide and Bis-Heteroleptic Ru(II) Complex-Based Hybrid Molecule with 3-in-1 Functionalities. Chemistry – An Asian Journal, 19(23), e202400724. https://doi.org/10.1002/asia.202400724
[34]. Chowdhury, B., Sinha, S., Dutta, R., Mondal, S., Karmakar, S., & Ghosh, P. (2020). Discriminative Behavior of a Donor–Acceptor–Donor Triad Toward Cyanide and Fluoride: Insights into the Mechanism of Naphthalene Diimide Reduction by Cyanide and Fluoride. Inorganic Chemistry, 59(18), 13371–13382. https://doi.org/10.1021/acs.inorgchem.0c01738
[35]. Pereira, L. M., de Oliveira, D. F., Tiburcio, M. A., Ribeiro, G. H., Moraes, C. A., Neto, F. O., Camargo, A. J., De Boni, L., Nascimento, O. R., Homem, M. G., & Carlos, R. M. (2025). Exploring the Reversible Equilibrium State Between ^{3}CS and ^{3}CSS in a Ru(phen)–Naphthalene Diimide Dyad. Inorganic Chemistry, 64(17), 8544–8553 https://doi.org/10.1021/acs.inorgchem.4c05443
[36]. Ghosh, A., Mandoli, A., Kumar, D. K., Yadav, N. S., Ghosh, T., Jha, B., Thomas, J. A., & Das, A. (2009). DNA binding and cleavage properties of a newly synthesised Ru(II)-polypyridyl complex. Dalton Transactions, (42), 9312–9321. https://doi.org/10.1039/b906756f
[37]. Filevich, O., Zayat, L., Baraldo, L. M., & Etchenique, R. (2014). Long Wavelength Phototriggering: Ruthenium-Based Caged Compounds. Structure and Bonding, 165, 47–68. https://doi.org/10.1007/430_2014_169
[38]. Cheng, F., Yu, S., Ren, M., He, C., & Yin, H. (2016). Di- and trinuclear Ru(II) complexes of 1,10-phenanthroline and 2,2′-bipyridine derivatives; synthesis, photophysical and electrochemical properties. Transition Metal Chemistry, 41(3), 305–314. https://doi.org/10.1007/s11243-016-0022-y

[39]. Erten, S., Posokhov, Y., Alp, A., & Icli, S. (2005). The study of the solubility of naphthalene diimides with various bulky flanking substituents in different solvents by UV-vis spectroscopy. Dyes and pigments, 64(2), 171–178. https://doi.org/10.1016/j.dyepig.2004.04.011
[40]. Welsh, T. A., Matsarskaia, O., Schweins, R., & Draper, E. R. (2021). Electronic and assembly properties of a water-soluble blue naphthalene diimide. New Journal of Chemistry, 45(31), 14005–14013. https://doi.org/10.1039/d1nj02557k
[41]. Yiseen, G. A. (2014). Synthesis and Characterization of New Monomer and New Polymer of Naphthalene Diimide: Electrochemical and Optical Studies. International Journal of Electrochemical Science, 9(5), 2575–2588. https://doi.org/10.1016/s1452-3981(23)07949-x
[42]. Wałęsa-Chorab, M. (2024). Towards red-NIR emission of platinum(II) complexes. Journal of Photochemistry and Photobiology C: Photochemistry Reviews, 59, 100664. https://doi.org/10.1016/j.jphotochemrev.2024.100664
[43]. Zubair, T., Hasan, M. M., Ramos, R. S., & Pankow, R. M. (2024). Conjugated polymers with near-infrared (NIR) optical absorption: structural design considerations and applications in organic electronics. Journal of Materials Chemistry C, 12(23), 8188–8216. https://doi.org/10.1039/d4tc01391c
[44]. Pschirer, N. G., Kohl, C., Nolde, F., Qu, J., & Müllen, K. (2006). Pentarylene- and Hexarylenebis(dicarboximide)s: Near-Infrared-Absorbing Polyaromatic Dyes. Angewandte Chemie, 118(9), 1429–1432. https://doi.org/10.1002/ange.200502998
[45]. Auty, A. J., Scattergood, P. A., Keane, T., Cheng, T., Wu, G., Carson, H., Shipp, J., Sadler, A., Roseveare, T., Sazanovich, I. V., Meijer, A. J., Chekulaev, D., Elliot, P. I., Towrie, M., & Weinstein, J. A. (2023). A stronger acceptor decreases the rates of charge transfer: ultrafast dynamics and on/off switching of charge separation in organometallic donor–bridge–acceptor systems. Chemical Science, 14(41), 11417–11428. https://doi.org/10.1039/d2sc06409j
[46]. Pearce, N., Davies, E. S., Horvath, R., Pfeiffer, C. R., Sun, X.-Z., Lewis, W., McMaster, J., George, M. W., & Champness, N. R. (2018). Thionated naphthalene diimides: tuneable chromophores for applications in photoactive dyads. Physical Chemistry Chemical Physics, 20(2), 752–764. https://doi.org/10.1039/c7cp06952a
[47]. Kumari, N., Naqvi, S., & Kumar, R. (2017). Naphthalene diimide self-assembled ribbons with high electrical conductivity and mobility without doping. Journal of Materials Science, 53(6), 4046–4055. https://doi.org/10.1007/s10853-017-1829-4
[48]. Sazanovich, I. V., Alamiry, M. A., Best, J., Bennett, R. D., Bouganov, O. V., Davies, E. S., Grivin, V. P., Meijer, A. J., Plyusnin, V. F., Ronayne, K. L., Shelton, A. H., Tikhomirov, S. A., Towrie, M., & Weinstein, J. A. (2008). Excited State Dynamics of a Pt^{II} Diimine Complex Bearing a Naphthalene-Diimide Electron Acceptor. Inorganic Chemistry, 47(22), 10432–10445. https://doi.org/10.1021/ic801022h
[49]. Liu, J., Feng, R., Zhou, L., Gai, F., & Zhang, W. (2022). Photoenhancement of the C≡N Stretching Vibration Intensity of Aromatic Nitriles. The Journal of Physical Chemistry Letters, 13(41), 9745–9751. https://doi.org/10.1021/acs.jpclett.2c02418
[50]. Martinez, J. F., La Porte, N. T., & Wasielewski, M. R. (2018). Electron Transfer from Photoexcited Naphthalene Diimide Radical Anion to Electrocatalytically Active $Re(bpy)(CO)_3Cl$ in a Molecular Triad. The Journal of Physical Chemistry C, 122(5), 2608–2617. https://doi.org/10.1021/acs.jpcc.7b11999
[51]. La Porte, N. T., Martinez, J. F., Hedström, S., Rudshteyn, B., Phelan, B. T., Mauck, C. M., Young, R. M., Batista, V. S., & Wasielewski, M. R. (2017). Photoinduced electron transfer from rylenediimide radical anions and dianions to $Re(bpy)(CO)_3$ using red and near-infrared light. Chemical Science, 8(5), 3821–3831. https://doi.org/10.1039/c6sc05103k

[52]. Bhosale, S. V., Jani, C. H., & Langford, S. J. (2008). Chemistry of naphthalene diimides. Chem. Soc. Rev., 37(2), 331–342. https://doi.org/10.1039/b615857a
[53]. Gosztola, D., Niemczyk, M. P., Svec, W., Lukas, A. S., & Wasielewski, M. R. (2000). Excited Doublet States of Electrochemically Generated Aromatic Imide and Diimide Radical Anions. The Journal of Physical Chemistry A, 104(28), 6545–6551. https://doi.org/10.1021/jp000706f
[54]. Skaisgirski, M., Guo, X., & Wenger, O. S. (2017). Electron Accumulation on Naphthalene Diimide Photosensitized by $[Ru(2,2'\text{-bipyridine})_3]^{2+}$. Inorganic Chemistry, 56(5), 2432–2439. https://doi.org/10.1021/acs.inorgchem.6b02446
[55]. Kumar, S., Shukla, J., Mandal, K., Kumar, Y., Prakash, R., Ram, P., & Mukhopadhyay, P. (2019). Doubly zwitterionic, di-reduced, highly electron-rich, air-stable naphthalenediimides: redox-switchable islands of aromatic–antiaromatic states. Chemical Science, 10(26), 6482–6493. https://doi.org/10.1039/c9sc00962k
[56]. Ji, Z., & Wu, Y. (2013). Photoinduced Electron Transfer Dynamics of Cyclometalated Ruthenium (II)–Naphthalenediimide Dyad at NiO Photocathode. The Journal of Physical Chemistry C, 117(36), 18315–18324. https://doi.org/10.1021/jp405659m
[57]. Ye, C., Cheng, H., Wrede, S., Diring, S., Tian, H., Odobel, F., & Hammarström, L. (2023). Charge Recombination Deceleration by Lateral Transfer of Electrons in Dye-Sensitized NiO Photocathode. Journal of the American Chemical Society, 145(20), 11067–11073. https://doi.org/10.1021/jacs.3c00269
[58]. Corani, A., Li, M.-H., Shen, P.-S., Chen, P., Guo, T.-F., El Nahhas, A., Zheng, K., Yartsev, A., Sundström, V., & Ponseca, C. S. (2016). Ultrafast Dynamics of Hole Injection and Recombination in Organometal Halide Perovskite using Nickel Oxide as p-Type Contact Electrode. The Journal of Physical Chemistry Letters, 7(7), 1096–1101. https://doi.org/10.1021/acs.jpclett.6b00238
[59]. Qin, L., Zhao, C., Yao, L.-Y., Dou, H., Zhang, M., Xie, J., Weng, T.-C., Lv, H., & Yang, G.-Y. (2022). Efficient Photogeneration of Hydrogen Boosted by Long-Lived Dye-Modified Ir(III) Photosensitizers and Polyoxometalate Catalyst. CCS Chemistry, 4(1), 259–271. https://doi.org/10.31635/ccschem.021.202000741
[60]. Johansson, O., Borgström, M., Lomoth, R., Palmblad, M., Bergquist, J., Hammarström, L., Sun, L., & Åkermark, B. (2003). Electron Donor−Acceptor Dyads Based on Ruthenium(II) Bipyridine and Terpyridine Complexes Bound to Naphthalenediimide. Inorganic Chemistry, 42(9), 2908–2918. https://doi.org/10.1021/ic020420k
[61]. Cui, X., Zhao, J., Lou, Z., Li, S., Wu, H., & Han, K. (2014b). Switching of the Triplet Excited State of Rhodamine/Naphthaleneimide Dyads: An Experimental and Theoretical Study. The Journal of Organic Chemistry, 80(1), 568–581. https://doi.org/10.1021/jo502554y
[62]. Pannwitz, A., & Wenger, O. S. (2016). Proton coupled electron transfer from the excited state of a ruthenium(II) pyridylimidazole complex. Physical Chemistry Chemical Physics, 18(16), 11374–11382. https://doi.org/10.1039/c6cp00437g
[63]. Sahara, G., & Ishitani, O. (2015). Efficient Photocatalysts for CO_2 Reduction. Inorganic Chemistry, 54(11), 5096–5104. https://doi.org/10.1021/ic502675a
[64]. Cerpentier, F. J., Karlsson, J., Lalrempuia, R., Brandon, M. P., Sazanovich, I. V., Greetham, G. M., Gibson, E. A., & Pryce, M. T. (2021). Ruthenium Assemblies for CO_2 Reduction and H_2 Generation: Time Resolved Infrared Spectroscopy, Spectroelectrochemistry and a Photocatalysis Study in Solution and on NiO. Frontiers in Chemistry, 9. https://doi.org/10.3389/fchem.2021.795877
[65]. Camargo, L. G., Palazzo, B. G., Taylor, G., Norris, Z. A., Patel, Y. K., Hettinger, J. D., & Yu, L. (2015). Carbide-Derived Carbon by Electrochemical Etching of Vanadium

Carbides. Journal of The Electrochemical Society, 162(10). https://doi.org/10.1149/2.0031512jes
[66]. Nelson, J.J., Amick, T.J., & Elliott, C.M. (2008). Mass Transport of Polypyridyl Cobalt Complexes in Dye-Sensitized Solar Cells with Mesoporous TiO_2 Photoanodes. The Journal of Physical Chemistry C, 112(46), 18255–18263. https://doi.org/10.1021/jp806479k
[67]. Gibson, E.A., Smeigh, A.L., Le Pleux, L., Hammarström, L., Odobel, F., Boschloo, G., & Hagfeldt, A. (2013). Cobalt Polypyridyl-Based Electrolytes for p–Type Dye-Sensitized Solar Cells. The Journal of Physical Chemistry C, 115(19), 9772–9779. https://doi.org/10.1021/jp110473n
[68]. Snellenburg, J. J., Laptenok, S. P., Seger, R., Mullen, K. M., & Stokkum, I. H. (2012). Glotaran: A Java-Based Graphical User Interface for the R Package TIMP. Journal of Statistical Software, 49(3), 1–22. https://doi.org/10.18637/jss.v049.i03
[69]. Greetham, G. M., Burgos, P., Cao, Q., Clark, I. P., Codd, P. S., Farrow, R. C., George, M. W., Kogimtzis, M., Matousek, P., Parker, A. W., Pollard, M. R., Robinson, D. A., Xin, Z.-J., & Towrie, M. (2010). Ultra: A Unique Instrument for Time-Resolved Spectroscopy. Applied Spectroscopy, 64(12), 1311–1319. https://doi.org/10.1366/000370210793561673
[70]. Leading photoreactor manufacturer. HepatoChem. (n.d.). https://hepatochem.com/?gad_source=1&gad_campaignid=20187654459&gbraid=0AAAADzmD52Oj7WXlMHqgHs-1JqmN4zwQ&gclid=CjwKCAjwwNbEBhBpEiwAFYLtGLIjECwDdq_DvmHpviyvX-MUeUCfqosZyl1G7RIz34yGDDax9w7TExoCZ98QAvD_BwE

CHAPTER 6

Synthesis, Photophysical and Electrochemical Studies of a Porphyrin-Naphthalene Diimide using Picosecond-Nanosecond Transient Absorption Spectroscopy and Assessment for Hydrogen Evolution.

Martyna Bartusiak[1], Michael Brandon[1], Owen Woodford[2], Elizabeth A. Gibson[2], Mary T. Pryce[1]

[1]School of Chemical Sciences, Dublin City University, Ireland

[2]Energy Materials Laboratory, Department of Chemistry, School of Natural and Environmental Science, Newcastle University, Newcastle upon Tyne, United Kingdom

6.1 Abstract

In this chapter the synthetic procedures, characterisation, and photophysical and electrochemical studies are reported for two porphyrin-naphthalene diimide compounds (**TPP-NDI** and **Zn-TPP-NDI**). UV-vis spectroscopy confirmed when the naphthalene diimide (**NDI**) unit is covalently attached to the tetraphenyl porphyrin (**TPP**) the absorption spectrum is a composition of the individual units (**NDI** and **TPP**). However, quenching was observed in the emission studies. When time-correlated single photon counting (TCSPC) measurements were carried out on the free base **TPP-NDI** system in tetrahydrofuran (THF), dimethylformamide (DMF), and ethyl acetate (EtOAc) biexponential fluorescence decays were obtained, with a shorter component of ~ 2 ns and, a longer component in the range 9 – 13 ns. The shorter lifetime contributes ~ 95% to the fluorescence decay profile. The zinc metalated porphyrin **Zn-TPP-NDI** however exhibits a mono-exponential decay (τ = ~ 2 ns, λ_{exc} = 375 or 510 nm). Picosecond and nanosecond transient absorption studies (ps-ns TAS) were carried out to further probe the excited state dynamics and to enhance our understanding of electron transfer kinetics in these compounds. To study the behaviour of the triplet excited state of **TPP-NDI** and **Zn-TPP-NDI**, nanosecond transient absorption spectra were recorded in tetrahydrofuran following excitation at 355 nm. In **TPP-NDI**, the excited state absorption features in the range 440 to 700 nm range, are attributed to the triplet excited state of the porphyrin unit. In contrast, **Zn-TPP-NDI** exhibited a broader, and red-shifted excited state absorption features in the range 400 – 600 nm, which were accompanied by ground-state bleaches at 550 nm and 590 nm. Picosecond transient absorption spectroscopy was performed in solution and

following chemisorption of the compounds on a nickel oxide (NiO) surface. The transient absorption spectra obtained following excitation of **TPP-NDI** and **Zn-TPP-NDI** at 400 nm resembled those recorded in tetrahydrofuran solution. However, charge recombination occurred more rapidly on the surface than in solution. Electrochemical studies provided insights into the reduced and oxidised states of the **TPP-NDI** and **Zn-TPP-NDI**. Consequently, the obtained redox electron potentials were used to estimate the thermodynamic driving force for photocatalytic hydrogen evolution by employing the Rehm-Weller equation. Finally, these compounds were assessed for their ability to generate hydrogen using a range of photocatalytic conditions.

Contribution:

I was responsible for the synthesis of all compounds and writing all sections in this chapter. I conducted the absorption and emission studies, electrochemistry, nanosecond TAS measurements, assisted in picosecond TAS, which were caried out at Newcastle University in collaboration with Professor Elizabeth Gibson and Dr. Owen Woodford. In addition, I performed photocatalytic experiments and processed all the data using Glotaran.

6.2 Introduction

Porphyrin tetrapyrrole macrocycles (TPPs) are excellent photosensitising moieties because they absorb light in the visible region of the UV-vis spectrum and have high molar extinction coefficients at the wavelength corresponding to the Soret band at approximately 420 nm ($\varepsilon = 3 – 7 \times 10^5$ $cm^{-1} \cdot M^{-1}$) [1 – 4]. Porphyrins have suitable redox potentials that enable electron transfer as well as these reduction and oxidation potentials provide feasible thermodynamic driving force for photocatalytic applications for example the water-splitting process [3]. Additionally, long-lived triplet excited states are characteristic of porphyrins, which promote charge transfer reactions and hole-electron pair separation in photocatalytic assemblies [3, 4]. These properties make them promising photosensitisers for a wide range of applications, for example they have been employed in photodynamic therapy [5, 6], solar energy conversion [7, 8], organic semiconductors [9] and artificial photosynthesis [3, 10 – 12]. It is also important to note that these are natural pigments, and they are commonly present in organisms and can be found for example in haemoglobin, cytochromes and chlorophylls [13]. Porphyrins have typically square planar geometry and contain 22 π electrons, 18 of which are delocalised. Additionally, they can be modified through the substitution of various functional groups and the incorporation of ligands at four different positions within the porphyrin framework. Through these structural changes their properties can be modified for specific applications [3, 13].

Naphthalene diimides (NDIs) have received increasing attention in recent years as they are widely known for their electron-accepting capabilities, light and chemical stability, and relatively straightforward synthetic pathways (as described in previous chapters). Due to their planar structure, anion-π interactions and unique electron transfer properties, naphthalene diimides are employed in various applications including sensors for cell imaging [14, 15], electronic devices [16] and DNA intercalation [17 – 19].

The potential of designing donor-acceptor systems, which incorporate both naphthalene diimide (electron acceptor) and a porphyrin unit (electron donor), offers new and promising possibilities for the development of novel materials with desirable photophysical and electrochemical properties, which can be employed in photocatalytic processes, both in solution and on surfaces. The literature presents only a few examples of porphyrin-naphthalene diimide compounds studied from the perspective of electron transfer, which indicates that there is still significant research to be done in this area. The

studies reported in the literature on electron transfer of such assemblies were typically examined on the picosecond and femtosecond timescales and the results published suggest that they could be promising candidates for use in solar cells and photocatalysis. For example, Robotham et al. [20] reported photo-induced electron transfer in a mono-substituted zinc(II) tetraphenylporphyrin-amino naphthalene diimide dyad (ZnTPP-ANDI) (Figure 6.1A). Ultrafast transient absorption studies carried out following excitation at 415 nm, led to electron transfer from the excited S_2 state of the porphyrin, towards the NDI moiety. However, this was followed by charge recombination which led to the formation of the S_1 excited state. The transient spectral profile showcases bands in the range of 400 – 600 nm, attributed to the ZnTPP radical cation. Additionally, the absorption band at 490 nm was assigned to the NDI radical anion. Usually, charge recombination must be avoided in the photocatalytic systems, and the authors suggested that incorporation of the additional electron acceptor could enhance charge separation and consequently prevent charge recombination [20].

Another study focusing on ultrafast excited-state processes in TPP-NDI systems was carried out by Villamaina et al. [21]. The authors synthesised metalated and non-metalated porphyrin-naphthalene diimide (NDI) triads, in which two porphyrin moieties were substituted at the NDI unit (Figure 6.1B). The electron transfer properties of these porphyrin assemblies were examined using ultrafast fluorescence and transient absorption measurements. Following excitation at 544 nm, which corresponded to the ground state absorption of the porphyrin's Q band, charge separation occurred rapidly from the excited porphyrin towards the NDI moiety. The lifetime of the charge separated state for the metalated system (Zn-P triad) was 1 ps and approximately 25 ps for the free-base porphyrin-NDI (FbP triad). In addition, charge recombination occurred within 8 ps for both systems [21]. Banerji et al. [22] also studied the ultrafast excited-states of a number of porphyrin-NDIs, in which the NDI and TPP moieties were connected through an aromatic diaza bridge (Figure 6.1C). The authors reported rapid charge separation (within 1 – 3 ps) following excitation at 395 nm in dichloromethane, and this was followed by charge recombination (within 10 – 20 ps). Once again, charge recombination is viewed as bottleneck for the efficient photocatalytic assemblies. Consequently, similar to the study by Robotham [20], Banerji et al. [22] emphasised the importance of employing secondary donors or acceptors to prevent the process of charge recombination occurring. If charge recombination takes place, then it is impossible to promote an electron via the bridging ligands towards the catalyst in artificial photosynthetic systems.

Wallin et al. [23] reported Zn(II) porphyrins covalently attached to a naphthalene imide (NI) and naphthalene diimide (NDI) (Figure 6.1 (D – E)). In this study the authors reported electron transfer from the S_1 excited state of the porphyrin to NDI, with no evidence for electron transfer from the S_2 state to NDI. However, when the NI moiety was employed as an electron acceptor, where electron transfer occurred rapidly from the S_2 excited state (450 fs in ethanol) [23]. The aforementioned published examples of porphyrin-naphthalene diimide systems primarily investigate ultrafast processes to probe the excited state properties. However, nanosecond transient absorption studies are less commonly carried out for these types of compounds but offer new possibilities to examine longer-lived excited states and the formation of charge-separated species.

In this research study, two novel porphyrin-naphthalene diimide dyads, **TPP-NDI** and **Zn-TPP-NDI** were synthesised and studied. Synthetic pathways were developed and detailed photophysical and electrochemical studies were performed. This allowed us to understand their redox behaviour, light stability, and efficiency in promoting an electron transfer from the porphyrin towards the NDI upon light irradiation. Furthermore, ultrafast laser spectroscopy was carried out both in solution and on a nickel oxide surface in order to examine the electron transfer processes occurring on the picosecond timescale. This provided important insights into the excited-state dynamic processes in **TPP-NDI** and **Zn-TPP-NDI**, for example charge separation and recombination. Electrochemical studies were employed to obtain the redox potentials, which were used to estimate the thermodynamic driving forces for the water-splitting processes in photocatalysis. Finally, photocatalytic studies were conducted in solution. This research contributes to a greater understanding of porphyrin-NDI complexes and provides a foundation for their potential applications. In the previous chapters, ruthenium-NDI complexes were investigated with different functional groups substituted both on the ruthenium moiety and NDI. In this chapter, the focus is to explore the effect of incorporation of a different photosensitising moiety, namely a porphyrin, and its impact on the photophysical and electrochemical properties.

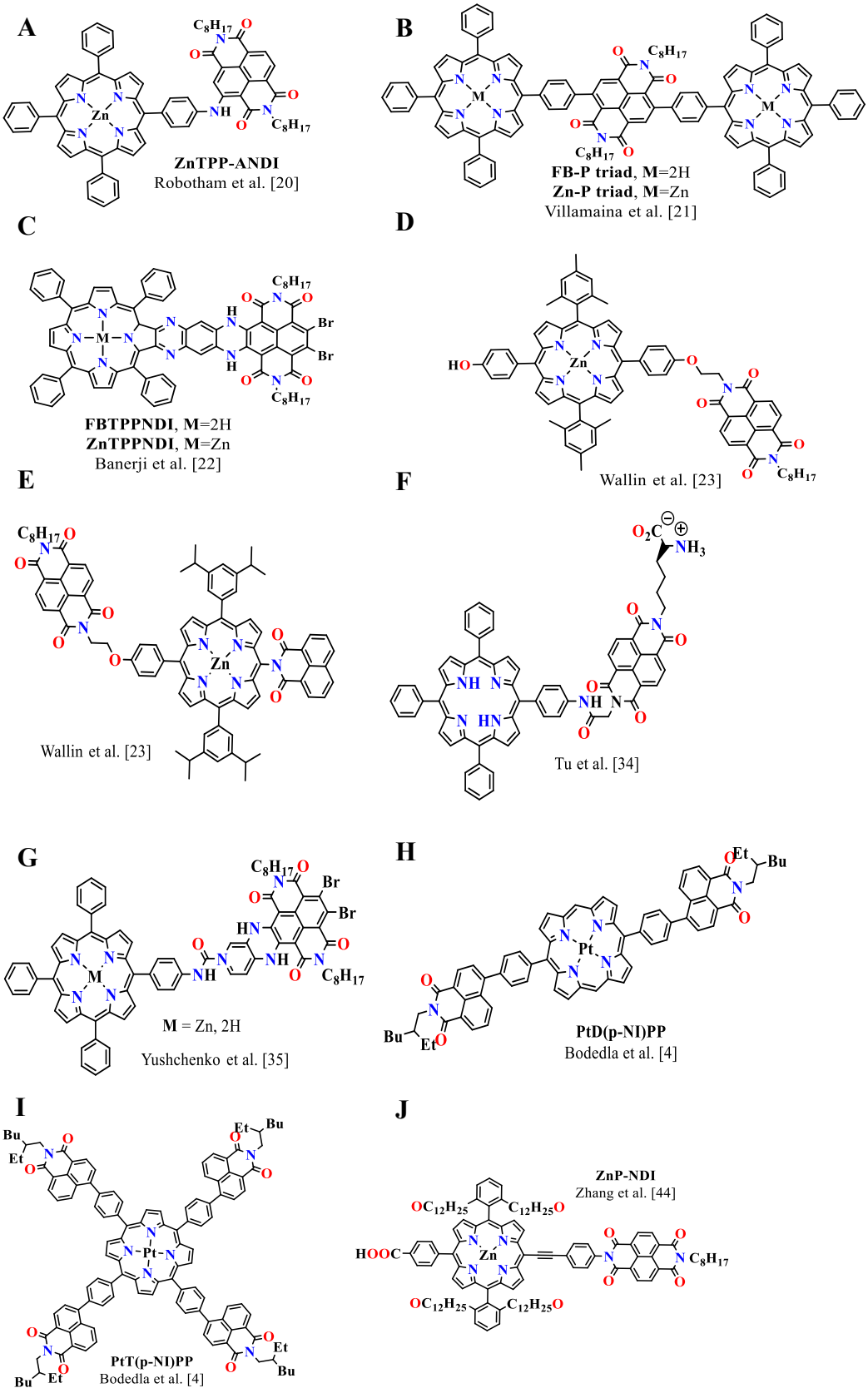


Figure 6.1 Porphyrin-naphthalene diimide assemblies reported in the literature [4, 20 – 23, 34 – 35, 44].

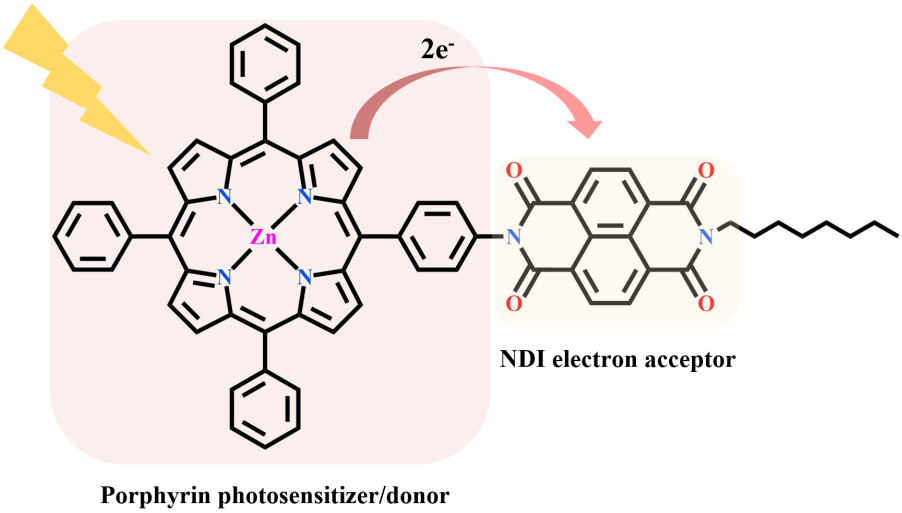


Figure 6.2 Porphyrin-naphthalene diimide assembly, consisting of a porphyrin electron donor and NDI electron-accepting moiety, the focus of this chapter.

6.3 Results and discussion

6.3.1 Synthesis

The synthetic pathways for the **TPP-NDI** and **Zn-TPP-NDI** dyads are presented in Figure 6.3. The first step was the synthesis of the NDI ligand, which consisted of a condensation reaction of 1,4,5,8-naphthalenetetracarboxylic dianhydride (**NDA**) with octylamine to yield octyl-1,4,5,8-napthalenetetracarboxylic monoanhydride (**NDI-octyl)** [24]. The 5-(4-aminophenyl)-10,15,20-(triphenyl)porphyrin (**TPP-NH_2**) was obtained commercially from PorphyChem®. (Note: it is important to highlight that chloroform should be avoided in the synthesis and in the analysis for amino porphyrins, because it can lead to conversion into chlorin). The following step involved a condensation reaction of **TPP-NH_2** with **NDI-octyl**, and this was carried out in dry degassed DMF for 3 days under a nitrogen atmosphere. Afterwards, the reaction mixture was cooled to the room temperature, and the product precipitated out of solution as a purple solid upon the addition of diethyl ether and subsequently it was centrifuged and washed with diethyl ether, water and methanol. The reaction was monitored using thin layer chromatography, and the complete consumption of **TPP-NH_2** was determined using ^{1}H-NMR by the disappearance of amine protons (NH_2) at approximately 5 ppm. In order to remove unreacted naphthalene diimide starting material (**NDI-octyl**), the sample was dissolved in a small quantity (1 ml) of DMF, and diethyl ether was added. The product was precipitated out, centrifuged and filtered. In case, where unreacted **TPP-NH_2** was present, the product **TPP-NDI** was purified by the solvent extraction using acetic acid/water

mixture and dichloromethane (DCM). The use of acetic acid was required in order to protonate **TPP-NH$_2$**, making it soluble in water. The metalation reaction of **TPP-NDI** was carried out in methanol in the presence of an excess of zinc acetate, followed by an overnight reflux in ethyl acetate. The solvent was evaporated under reduced pressure, and the final product was dried using a vacuum. The progress of metalation process was continuously monitored during the reaction, and the formation of the final **Zn-TPP-NDI** product was confirmed by ^{1}H-NMR and UV-vis spectroscopy. The formation of the **Zn-TPP-NDI** was confirmed by ^{1}H-NMR by the disappearance of the singlet at approximately –3 ppm, which was assigned to the two inner pyrrolic protons present in **TPP-NDI**. Additionally, the UV-vis spectrum changed from having four Q-bands in **TPP-NDI** to two Q-bands in **Zn-TPP-NDI**. This indicated the complete metalation of **TPP-NDI** in the reaction. Furthermore, the aromatic protons on the NDI unit appeared as two doublets in the range of 8 – 9 ppm. The mass spectrum obtained using MALDI for **TPP-NDI** and **Zn-TPP-NDI** together with their isotope pattern confirmed successful synthesis of the systems. All synthetic procedures are summarised in a greater detail in Appendix D.

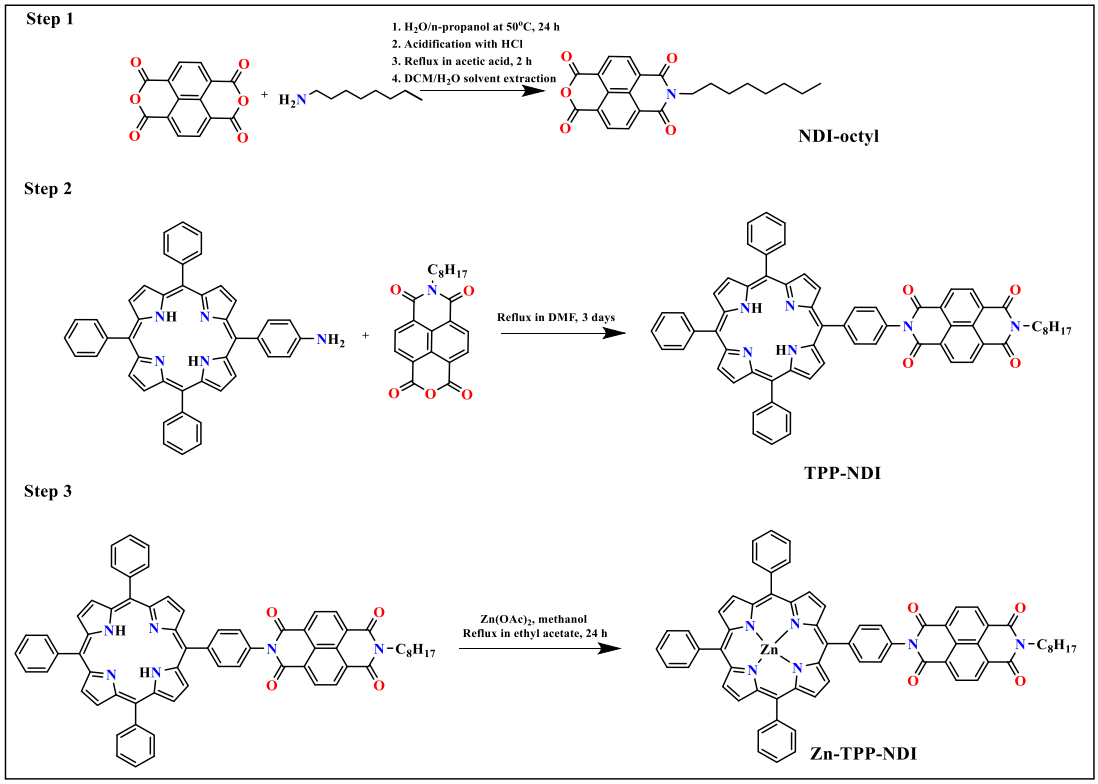


Figure 6.3 Synthetic scheme for the preparation of **TPP-NDI** and **Zn-TPP-NDI**.

6.3.2 UV-vis and emission spectroscopy

The UV-visible and emission spectra for **TPP-NDI** and **Zn-TPP-NDI** were recorded in tetrahydrofuran (THF) and are presented in Figure 6.4. The UV-vis absorption spectra of these compounds consist of distinct and characteristics absorption bands attributed to the porphyrin macrocycle and the NDI moiety. The Soret band occurs at 416 and 424 nm for **TPP-NDI** ($\varepsilon = 5.96 \times 10^5$ $M^{-1}cm^{-1}$) and **Zn-TPP-NDI** ($\varepsilon = 5.74 \times 10^5$ $M^{-1}cm^{-1}$) respectively, with additional weaker Q bands at 555 and 590 nm for **Zn-TPP-NDI**, characteristic of metalloporphyrin, and at 515, 555, 590, and 652 nm for **TPP-NDI** (in Figure 6.4A). The Soret band corresponds to transitions from the ground state (S_0) to the second singlet excited state (S_2), while the Q bands are attributed to transitions from the ground state (S_0) to vibrationally resolved states of the first singlet excited state (S_1) [25]. In both compounds, the absorption bands are observed at 338, 356, 376 nm for NDI based transitions ($\varepsilon = 3.9 - 4.7 \times 10^4$ $M^{-1}cm^{-1}$, calculated at 356 nm) [20 – 23, 26 – 27]. In Figure 6.4A, it is evident that incorporation of the NDI moiety does not change the absorption peaks of the porphyrin system, as there are no significant red or blue shifts in the visible region, when compared to the standard porphyrin reference compound, **TPP-NH_2**. The Soret band of **TPP-NDI** appears slightly broader and blue-shifted, in contrast to **Zn-TPP-NDI**. Similar results were obtained by Wallin et al. [23] for an asymmetric acceptor-Zn(II)porphyrin-acceptor triad, incorporating a naphthalene diimide moiety. The Soret band for the porphyrin-acceptor triad was observed at 420 nm, (transition to the excited S_2 state) and the Q-bands were visible at 540 and 600 nm (transitions to the S_1 state) [23]. The compound, ZnTPP-ANDI reported by Robotham et al. [20] (Figure 6.1A) is characterised with a Soret band at 431 nm and Q-bands at 563 and 601 nm. Consequently, it can be concluded that the condensation reaction of a porphyrin with naphthalene diimide does not change the absorption properties, as the resulting UV-vis spectrum has exactly the same profile typical reference compounds such as **TPP, TPP-NH_2, Zn-TPP** and **NDI**.

The emission spectrum of **TPP-NDI** consists of two bands at 652 and 720 nm, following excitation of the Soret band ($\lambda_{max} = 414$ nm). The emission profile for **TPP-NDI** is similar to the free base porphyrin, **TPP** [28, 29]. In the case of **Zn-TPP-NDI** the emission spectrum is characterised by weak bands at approximately 600 and 650 nm, with the emission profile closely resembling that reported in a study by Ghann et al. [30], in which the authors observed that a zinc porphyrin assembly exhibited fluorescence bands at 599 and 650 nm.

The fluorescence spectra for both **TPP-NDI** and **Zn-TPP-NDI** are strongly quenched compared to the emission spectra observed for the reference porphyrins **Zn-TPP** and **TPP**. In Figure 6.4B, it is evident that the emission is quenched to a greater extent upon metalation with zinc. Moreover, excitation at 350 – 370 nm was employed to directly excite the NDI bands, however no emission was observed. The emission and absorption spectra were also recorded for the **NDI-octyl** ligand (Figure 6.5). Absorption bands were observed in the range of 350 – 400 nm, indicating NDI based π-π* transitions. Upon excitation at 350 nm in THF, a weak band centered at 400 nm was observed. Typically, NDI-based compounds are weakly fluorescent and possess lifetimes of less than 1 ns in THF solution [31, 32]. However, Insuasty et al. [32] reported aggregation-induced emission for NDI complexes, which varied with the length of the chain at the imide positions of the NDI unit. These studies were carried out by adding water to the THF solution of NDI, which subsequently formed nanoaggregates and exhibited emission upon excitation at 365 nm. The emission lifetime of these nanoaggregates was determined to be 22.5 ns [32].

The extent of quenching appears to be more evident in the metalled porphyrin, **Zn-TPP-NDI**. Villamaina et al. [21], reported emission from a zinc metalated porphyrin-NDI compound (Zn-P) in cyclohexane, with a broad band centered at ~ 640 nm. The authors concluded that the emission observed in the Zn-P triad was from the excited Q state (S_1) to the ground state (S_0), and no emission was observed from the S_2 state. In contrast, the free base porphyrin-NDI was emissive in all solvents used with emission bands at 654 and 719 nm. The authors stated that there was little electronic coupling between the chromophores and therefore the absorption spectra consisted of the individual components, namely the porphyrin and the naphthalene diimide, suggesting little if any electronic coupling between the chromophores [21].

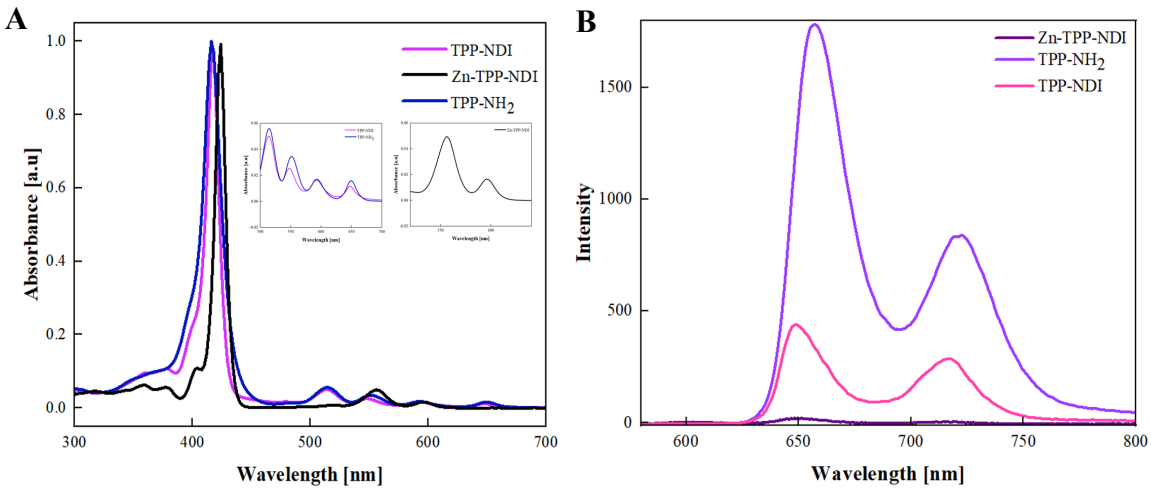


Figure 6.4 (A) Electronic absorption and **(B)** emission spectra of free the base porphyrin **TPP-NDI** and **Zn-TPP-NDI** measured in THF and compared to **TPP-NH₂** following excitation of the Soret band. The inset represents the zoom-in image of the Q-bands region.

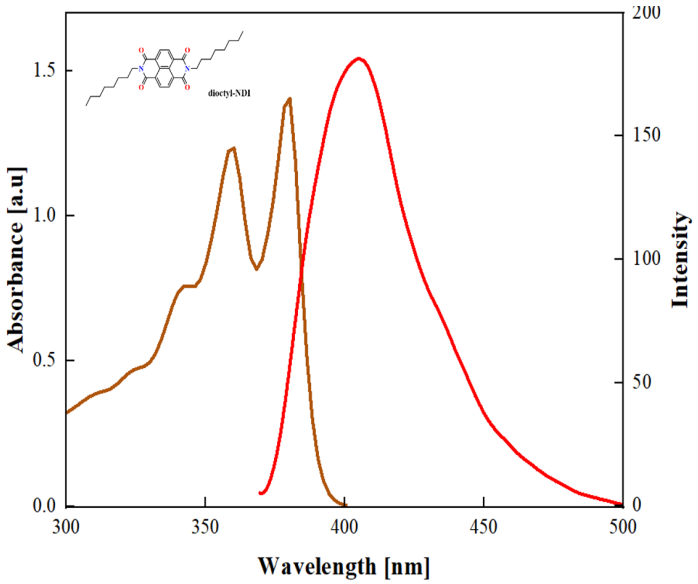


Figure 6.5 Electronic absorption (brown line) and emission (red line) spectra of **NDI-octyl** measured in THF, following excitation of the NDI band (λ_{exc} = 360 nm).

6.3.3 Fluorescence lifetimes using time-correlated single photon counting (TCSPC)

The fluorescence lifetimes were obtained using time-correlated single photon counting (TCSPC). The two compounds (**TPP-NDI** and **Zn-TPP-NDI**) were investigated in a variety of solvents, including deoxygenated tetrahydrofuran, dimethylformamide, and ethyl acetate, to determine if the solvent/ polarity had any impact on the lifetimes (Table 6.1. Similar results were obtained following excitation at both 375 and 510 nm. Furthermore, the choice of solvent had little impact on the lifetimes obtained.

Table 6.1 Fluorescent lifetimes were obtained following excitation (375 or 510 nm) of **TPP-NH$_2$**, **TPP-NDI** and **Zn-TPP-NDI** in a range of solvents. The optical density at the excitation wavelength was ~ 0.2.

Complex	Solvent	λ^a_{em} (nm)	τ^b_1 (ns)	% rel τ_1	τ^b_2 (ns)	% rel τ_2
TPP-NH$_2$	THF	650	–	–	9.4	100
TPP-NDI	THF	651	1.8	96	10.2	3
	DMF	650	2.2	95	13.2	5
	EtOAc	652	2.3	95	9.2	5
Zn-TPP-NDI	THF	651	1.8	100	–	–
	DMF	652	2.1	100	–	–
	EtOAc	652	2.4	100	–	–

[a]**λ_{em} (nm):** emission wavelength (at the maximum emission intensity)

[b]**τ_{fl} (ns):** fluorescence lifetimes

% rel: percentage contribution of the lifetime component to the decay

The fluorescence lifetime (τ_{fl}) of **TPP-NH$_2$** was measured in tetrahydrofuran (THF) solvent. The fluorescence signal was mono-exponential with a lifetime of τ_{fl} = 9.4 ns, attributed to the lowest excited singlet state (S_1) [1]. The lifetimes obtained in this study agree with values reported in the literature for free base porphyrins such as **TPP** [1, 33]. In a review by Taniguchi et al. [1], mono exponential decays with lifetimes ranging from 7 to 13 ns for the metal free unsubstituted porphyrin (tetraphenylporphyrins, H_2TPP),

were reported, while the zinc complex (zinc tetraphenylporphyrins, ZnTPP) exhibited lifetimes from 1.8 – 2.2 ns.

Following excitation (λ_{exc} = 375 or 510 nm) of the **Zn-TPP-NDI** dyad a mono-exponential fluorescence signal was obtained with a lifetime of 2 ± 0.3 ns. This lifetime is consistent with values reported in the literature for the metalated porphyrin [1]. However, in the case of **TPP-NDI** biexponential signals in THF, DMF and ethyl acetate were obtained with $\tau_1 \sim 2$ ns and the percentage contribution (% rel τ_1) of this signal is ~ 95%. Typically, free base porphyrins (TPP), exhibit lifetimes of ~ 10 ns with a 100% contribution, as reported in the review by Taniguchi et al. [1]. For the 3 – 5% component in **TPP-NDI** fluorescence lifetimes in the range 9 – 13 ns were obtained. The second component could be from a trace of unreacted **TPP-NH_2**. However, the ^{1}H-NMR does not indicate any remaining **TPP-NH_2**, therefore it is unclear at this stage why the fluorescent signal is composed of two components. Banerji et al. [22] synthesised porphyrin core-substituted-naphthalene diimide dyads (Figure 6.1C) and reported the lifetimes in toluene for their free base porphyrin NDI and zinc metalated porphyrin NDI, with lifetimes of 2.7 and 0.57 ns, respectively. Tu et al. [34] reported lifetimes for the free-base porphyrin-NDI assembly in THF and also reported biexponential decays with values of 213 ps (% rel τ_1 = 34%) and 92 ps (% rel τ_2 = 66%) respectively upon excitation at 320 nm (excitation of the NDI unit). The lifetime of 213 ps was attributed to fluorescence from the porphyrin-NDI aggregates, and the lifetime of 92 ps assigned to an electron-transfer process. When excited at 593 nm (excitation of the porphyrin unit), lifetimes of 5.86 ns (% rel τ_1 = 70%) and 1.13 ns (% rel τ_2 = 30%), were reported. Since these lifetimes are shorter than the typical singlet lifetime of a porphyrin (approximately 10 ns), the authors concluded that this could be due to electron-transfer from the porphyrin to the NDI moiety or collision-induced excited state decay [34]. Yushchenko et al. [35] synthesised free base and zinc metalated porphyrin-NDI dyads, in which the porphyrin unit was attached to the NDI through a peptide linkage (Figure 6.1G). Following excitation at 395 nm, the authors reported a lifetime of 2.8 ns for a zinc porphyrin-NDI system and attributed this to the electron transfer from the porphyrin to the NDI unit. On the other hand, the fluorescence decay of their free base porphyrin-NDI is characterised with two lifetime components, τ_1 = 2.45 ns (weak signal) and τ_2 = 9.2 ns [35].

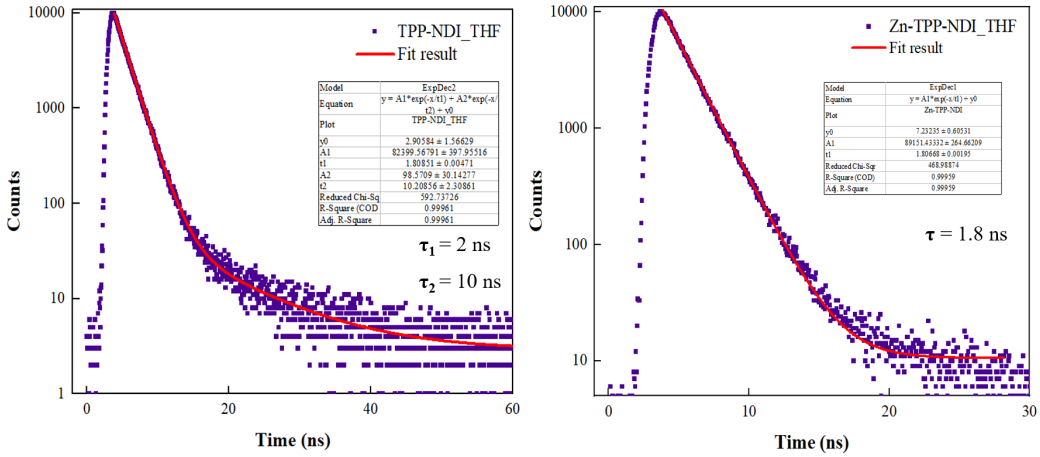


Figure 6.6 Fluorescence signals obtained following excitation of **TPP-NDI** and **Zn-TPP-NDI**, at either λ_{exc} = 375 or 510 nm. The results were obtained in THF.

6.3.4 Nanosecond transient absorption spectroscopy (ns-TAS)

In order to further study the excited-state dynamics of the porphyrin-NDI compounds on longer time bases, ns-TAS measurements were carried out. This technique allowed us to gain insights into the long-lived triplet excited states and helped to understand charge separation processes occurring on the nanosecond timescale. Ns-TAS studies using **TPP-NDI** and **Zn-TPP-NDI** were carried out following excitation at 355 nm in tetrahydrofuran (Figure 6.7). This excitation wavelength was employed as it corresponds to the region where the NDI unit absorbs (and the porphyrin unit to a lesser extent), thus enabling selective excitation of the NDI component. Prior to all measurements, the samples were degassed using three cycles of freeze-thaw-pump.

The spectra of **TPP-NDI** and **Zn-TPP-NDI** presented in Figure 6.7 (A and B) exhibit minor variations in both the shape and position of the absorption bands with respect to each other. UV-vis spectra were recorded before and after the laser flash photolysis measurements and no changes were observed in the absorption spectra. Transient signals were not measured in the range 420 – 430 nm, due to the intensity of the Soret band in this region. Following excitation of **TPP-NDI** at 355 nm, transient bands for the excited state absorption (ESA) are observed in range from 440 to 700 nm, which are assigned to the triplet state (τ_T = 150 µs in THF). **TPP-NDI** is characterised with excited state absorption features at 440, 535, 570, 625 and 670 nm. Negative features in the time transient spectra are observed at 515, 550, 590, 650 nm, indicating bleaching of the Q bands. In contrast, **Zn-TPP-NDI** exhibits a broader, and red-shifted excited state absorption profile within the range of 400 – 600 nm, compared to **TPP-NDI**, accompanied by a bleach at 550 nm and 590 nm, which correspond to the Q bands. The

lifetime of the signal at 425 nm was determined to be 142 μs. Banerji et al. [22] reported similar spectral profiles for transient absorption spectra following excitation of a porphyrin-naphthalene diimide system. The authors reported that the ps-TAS spectra were characterised by an intense bleach between 400 – 430 nm and a broad positive band at approximately 455 nm, which extended to 700 nm, following excitation at 400 nm. Additionally, the authors observed bleaches at around 650 nm, which were attributed to radical anion of the NDI ($HBNDI^{\bullet-}$), indicating electron transfer from the porphyrin to the NDI. Bodedla et al. [4], reported transient absorption studies for both tetrasubstituted (T) and disubstituted (D) Pt(II) porphyrins with naphthalimide (NI) frameworks, namely PtT(p-NI)PP and PtD(p-NI)PP (Figure 6.1 (H – I)). The triplet state lifetimes were 19.5 and 50.6 μs, respectively following excitation between 415 – 430 nm. Additionally, the authors concluded that the disubstituted PtD(p-NI)PP system due to the longer triplet lifetime (50.6 μs) and more feasible thermodynamic driving force than for PtT(p-NI)PP, leads to enhanced electron transfer from the triplet state, and consequently higher photocatalytic hydrogen evolution (750 μmmol g^{-1} h^{-1} vs 300 μmmol g^{-1} h^{-1} for PtT(p-NI)PP) [4]. Shaikh et al. [36] reported a (freebase) metal organic framework (MOF) (referred to as PCN-223) synthesised using meso-tetrakis(4-carboxyphenyl)porphyrin (TCPP). Following excitation at 532 nm, transient absorption studies revealed that TCPP exhibited a lifetime of 260 ± 7 μs at 470 nm, while PCN-223 had a lifetime of 201 ± 27 μs. In another study, Giannoudis et al. [37] carried out nanosecond transient absorption studies on a series of zinc and lead porphyrins used as photosensitisers for hydrogen production. For instance, ZnTPP-$[COOH]_4$ exhibited a lifetime of 278 ± 6 μs, whereas Sn(Cl_2)TPP-$[COOH]_4$ had a lifetime of 182 ± 7 μs. Tabrizi et al. [38] synthesised a porphyrin-Jeffamine polymer and carried out ns-TAS measurement in THF and ethyl acetate following excitation at 355 nm. In ethyl acetate, two lifetimes were observed on the microsecond timescale with τ_1 = 9.95 μs and τ_2 = 49.66 μs, whereas in THF, the corresponding lifetimes were τ_1 = 12.94 μs and τ_2 = 72.26 μs. The authors concluded that two lifetime components are due to the presence of distinct local environments in the porphyrin system, with some environments providing greater shielding in comparison to others [38].

The triplet excited state of **TPP-NDI** and **Zn-TPP-NDI** exhibits lifetimes on the microsecond timescale. For **TPP-NDI**, in THF a lifetime of approximately 150 μs was obtained. In ethyl acetate two-time constants, at 27 and 168 μs were obtained. For the metalated analogue, **Zn-TPP-NDI**, a similar lifetime of 142 μs was obtained in THF.

Unfortunately, **Zn-TPP-NDI** degraded when ethyl acetate was used. The long-lived triplet excited state lifetime results from photoinduced electron transfer from the porphyrin donor to the NDI acceptor, which consequently leads to the formation of a long-lived charge separated state before charge recombination takes place.

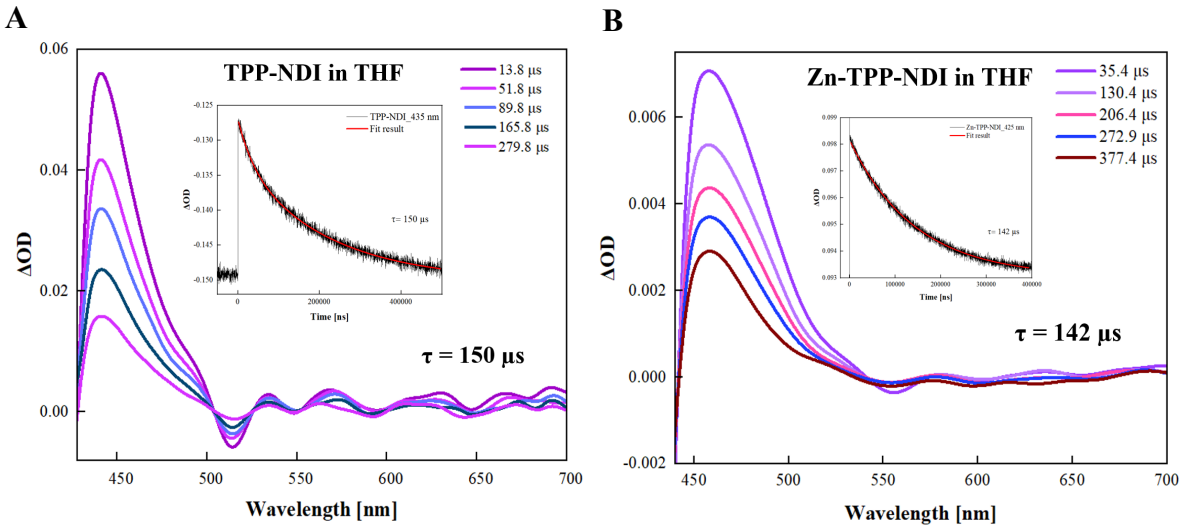


Figure 6.7 Nanosecond transient absorption spectrum of **TPP-NDI (A)** and **Zn-TPP-NDI (B)** in deoxygenated THF upon the excitation at 355 nm at different time delays. Sample was prepared using an absorbance of ~1.0 at the Soret band of porphyrins and the solution was degassed using three freeze-pump-thaw cycles.

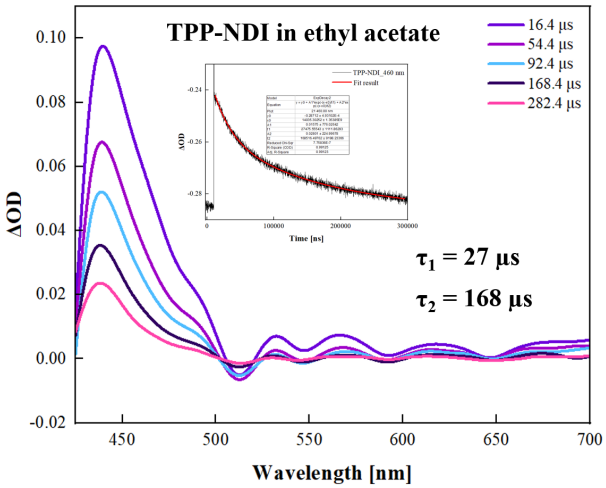


Figure 6.8 Nanosecond transient absorption spectrum of **TPP-NDI** in deoxygenated ethyl acetate upon the excitation at 355 nm at different time delays. Sample was prepared using an absorbance of ~1.0 at the Soret band of porphyrins and the solution was degassed using three freeze-pump-thaw cycles.

6.3.5 Ultrafast transient absorption spectroscopy (ps-TAS)

6.3.5.1 Ultrafast spectroscopic characterisation of TPP-NDI and Zn-TPP-NDI in solution

Picosecond transient absorption spectroscopy was carried out in tetrahydrofuran following excitation at 400 nm. The transient absorption spectra and the corresponding signals for both **TPP-NDI** and **Zn-TPP-NDI** are presented in Figure 6.9 and 6.10. Following excitation, the Q bands deplete at ~ 510, 548, 590, 650 nm together with the formation of new excited state features at 532, 567, 624 and 676 nm. The negative feature at 720 nm is attributed to stimulated emission [39]. Following analysis of the signals, three time constants for **TPP-NDI** were obtained with τ_1 = 2 ps ($S_2 - S_1^*$, indicating internal conversion to a vibrationally hot S_1 state) and τ_2 = 25 ps (vibrational cooling), and a longer-lived component with a lifetime of $\tau_3 > 1000$ ps. Similarly to our findings, Tabrizi et al. [38] reported three lifetimes for their porphyrin-Jeffamine polymer in THF following excitation at 400 nm, τ_1 = 2.3 ps, τ_2 = 16.7 ps and $\tau_3 > 1500$ ps. The first lifetime component was attributed to population of the S_2 state and rapid internal conversion to a vibrationally hot S_1 state. The second lifetime was assigned to vibrational cooling, whereas the third lifetime persisted throughout the experimental window [38].

In the case of the metalated porphyrin, **Zn-TPP-NDI** two bleaches from the Q bands are evident at 550 and 595 nm. The negative feature at 650 nm is stimulated emission. The time constants for **Zn-TPP-NDI** were determined as τ_1 = 2 ps and τ_2 = 46 ps, and a longer-lived component with $\tau_3 > 1000$ ps was observed. The spectral profile of the transient absorption spectrum aligns well with the results reported in the literature [38 – 40].

Furthermore, there is no evidence for electron transfer from the porphyrin and population of the NDI moiety as observed in studies by Banerji et al. [22], where the authors observed bleaches at around 650 nm, assigned to the radical anion of the NDI (following excitation at 400 nm). In general, the NDI exhibits characteristics absorption bands corresponding to the singlet excited state at approximately 480 – 550 nm, also known as the reduced species (radical anions) of the NDI. These species are formed following the excitation of the donor moiety [41]. For example, the NDI-component examined by Ye et al. [41] features a characteristic transient band at around 550 nm in solution, which shifts to 480 nm on the NiO surface, indicating the formation of the NDI radical. For both **TPP-NDI** and **Zn-TPP-NDI**, no evidence for formation of these reduced species (radical

anions) for the NDI moiety was observed and the spectral features are characteristic of a porphyrin based excited state.

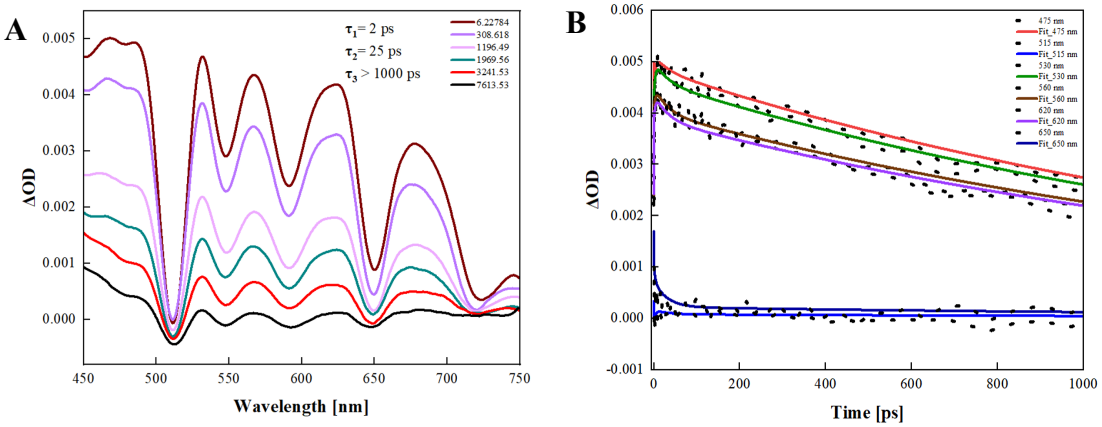


Figure 6.9 (A) Picosecond transient absorption spectrum of **TPP-NDI** in deoxygenated THF following excitation at 400 nm at different time delays. **(B)** Decay kinetic traces for **TPP-NDI** obtained from Glotaran global analysis.

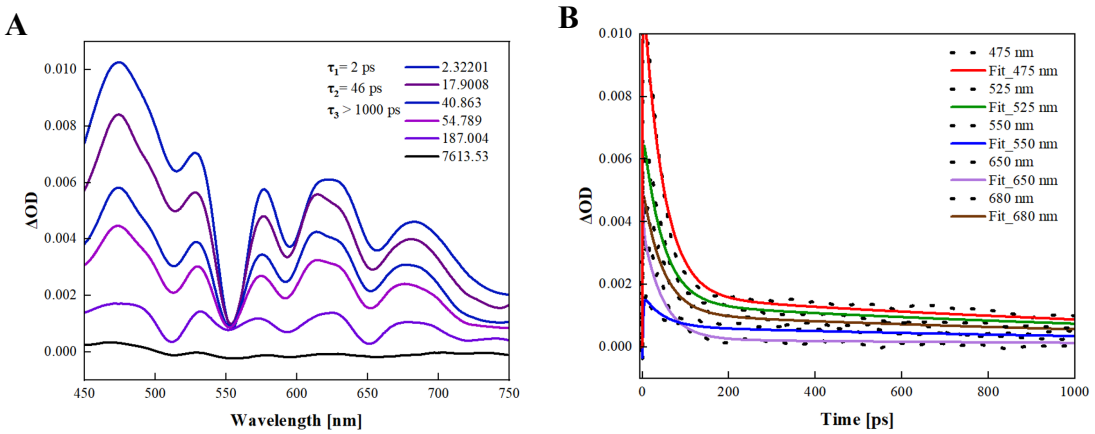


Figure 6.10 (**A**) Picosecond transient absorption spectrum of **Zn-TPP-NDI** in deoxygenated THF following excitation at 400 nm at different time delays. **(B)** Decay kinetic traces for **Zn-TPP-NDI** obtained from Glotaran global analysis.

6.3.5.2 Ultrafast spectroscopic characterisation of TPP-NDI and Zn-TPP-NDI on the NiO surface

Picosecond transient absorption spectroscopy was also performed on a NiO surface to investigate if hole injection (h^+) occurs from the semiconductor to the porphyrin. UV-vis spectra were recorded for both the metalated and non-metalated porphyrins (Figure 6.11). A red shift of approximately 20 nm was observed for the absorption bands when the porphyrins are chemisorbed onto the NiO surface, in contrast to solution. On NiO films, the Soret band appeared at approximately 440 and 435 nm for **Zn-TPP-NDI** and **TPP-NDI**, respectively (Figure 6.11). The Q bands for **Zn-TPP-NDI** were observed at 560 and 602 nm, whereas the Q bands for **TPP-NDI** were at 516, 559, 598 and 650 nm. The spectral profile of **TPP-NDI** and **Zn-TPP-NDI** on a NiO surface resembled those in solution. Farooq et al. [42] have previously reported chemisorption of sulfonic acid functionalised porphyrin onto nickel oxide nanoparticles. Similarly to our findings, the authors also observed a red shift in the Soret band of the porphyrin from 414 to 422 nm upon surface adsorption. Additionally, the authors observed that the Q-band of the free base porphyrin disappeared at 513 nm upon adsorption onto nickel oxide nanoparticles, and they attributed this to stacking of porphyrin molecules on the surface [42].

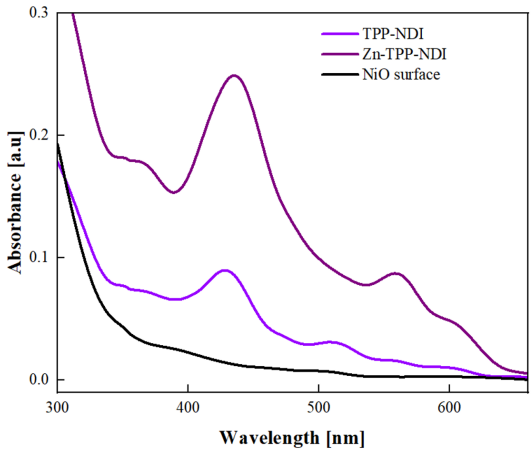


Figure 6.11 UV-vis absorption spectra of **TPP-NDI** and **Zn-TPP-NDI** adsorbed onto NiO surface after 24 hours from a 3 mM THF dye bath.

When comparing the ps-TAS studies in solution and on the NiO for **TPP-NDI** and **Zn-TPP-NDI**, the charge-separated state is formed rapidly within the laser pulse, but on the negative side, it decays faster on the surface compared to that in solution, and similar results were reported in the literature [43]. Electron injection from the NiO semiconductor into **TPP-NDI** and **Zn-TPP-NDI** is proposed to occur, resulting in a hole/positive charge on a NiO (h^+). However, rapid electron-hole recombination occurred, and this is not desirable [43]. All the time constants and their kinetics were determined using Glotaran

global analysis. The lifetimes for **NiO|TPP-NDI**, (Figure 6.12) were $\tau_1 = 2$ ps, $\tau_2 = 30$ ps, $\tau_3 = 235$ ps in addition to a longer-lived component with $\tau_3 > 1000$ ps. Similar behaviour was observed for **NiO|Zn-TPP-NDI** (Figure 6.13), with time constants of $\tau_1 = 2$ ps, $\tau_2 = 24$ ps, $\tau_3 = 239$ ps, together with a long-lived component for which the lifetime(s) could not be determined. The first two lifetime components are attributed to hole injection, and a lifetime of ~200 ps indicates rapid charge-recombination, and this aligns well with the literature results [43]. Benazzi et al. [43] prepared a series of zinc tetraphenylporphyrin photosensitisers with various types of anchoring groups including benzoic acid, phenylphosphonate and coumarin-3-carboxylic acid. They reported similar spectral features were obtained in tetrahydrofuran and on a NiO surface. Additionally, a bleach was reported at 650 nm which was attributed to stimulated emission. Upon excitation of the porphyrin at 550 nm, hole injection into NiO occurred, with time constants ranging from approximately 1 to 40 ps. The authors reported that this was followed by rapid charge recombination within 220 ps and resulted in a 70% recovery of the signal. Similarly to our findings, Benazzi et al. [43] concluded that the excited states on the NiO surface decayed more rapidly than in solution. In order to improve the photovoltaic performance and extend the lifetime of charge separation, the authors employed a pyridyl-functionalised fullerene (C_{60}PPy) and coated it with a layer of phenyl-C61-butyric acid methyl ester (PCBM). It was observed, that in the presence of PCBM, the charge recombination lifetime was longer (extending the experimental window). The rationale was that PCBM intercepts the electrons from the dye/C_{60} conjugate making charge recombination with NiO holes slower [43]. Zhang et al. [44] examined the ZnP-NDI compound (which includes a triple bond in its structure, in contrast to **Zn-TPP-NDI**) (Figure 6.1J) using time-resolved measurement both in solution and on the NiO surface. Femtosecond experiments in solution showed rapid formation of transient absorption bands with a time constant of 11.6 ps. In addition, a slower decay ($\tau = 149$ ps) with a narrow band at 460 nm and a bleach at 440 nm attributed to charge separation, and the formation of ZnP^+-NDI. Moreover, the band at 475 nm corresponded to the radical anion of the NDI. Due to the absorption band of the radical anion of NDI overlapping with the absorption band of ZnP^+ -NDI^-, the authors mentioned that it is difficult to distinguish between them individually. However, based on the short emission lifetimes and rapid decay of transient features, the electron transfer occurred towards the NDI unit. The authors also performed studies on the NiO surface and, similar to the findings of Benazzi et al. [43], transient bands decay together with a ground-state bleach recovery occurred more rapidly on the surface than in the solution. On NiO, the authors reported lifetimes

of $\tau_1 = 0.42$ ps and $\tau_2 = 2.3$ ps, which were attributed to vibrational relaxation and decay of stimulated emission at 620 and 680 nm. Moreover, time constants of $\tau_3 = 16.3$ ps, $\tau_4 = 219$ ps, $\tau_5 > 2$ ns were employed to fit the data [44]. Tu et al. [34] studied a TPP-NDI system, which differed slightly from our systems in the linker between TPP and NDI, as in their study they employed an NH=O-CH_2 linker (Figure 6.1F). The authors conducted transient absorption measurements in THF following excitation at 360 nm (where the NDI absorbs) and 400 nm (absorption of the porphyrin). Upon excitation at 400 nm, transient absorption bands were evident at 440, 450 and 570 nm, with time constants in the range 119 – 128 ps, attributed to the porphyrin radical cation excited state. However, following excitation at 360 nm, absorption bands were observed at 460, and 490 nm, with lifetimes of 128 and 60 ps, respectively. Another band was observed at 550 nm with a lifetime of 54 ps, along with a broad and weak band within 580 – 650 nm range. A triexponential decay fit for the excited state absorption at 620 nm resulted in lifetimes of 5.5, 93 ps and > 2 ns, where $\tau_2 = 93$ ps was attributed to the NDI excited singlet state. The authors suggested that the electron transfer occurs from the excited porphyrin to the NDI upon excitation of the porphyrin moiety. The TAS spectrum following 400 nm excitation is consistent with formation of a porphyrin excited state, and the observed lifetime $\tau \sim$ 122 ps was shorter than those reported from their TCSPS data (5.86 and 1.13 ns, at 593 nm excitation), likely due to charge-recombination from the charge-separated species, H_2TPP^+-NDI^- [34].

In summary, **TPP-NDI** and **Zn-TPP-NDI** are characterised by rapid formation of the charge-separated state, both in solution and on the surface. However, further optimisation of the molecular structure is necessary to extend the lifetime of the charge-separated state and, as a result, to slow down the charge recombination.

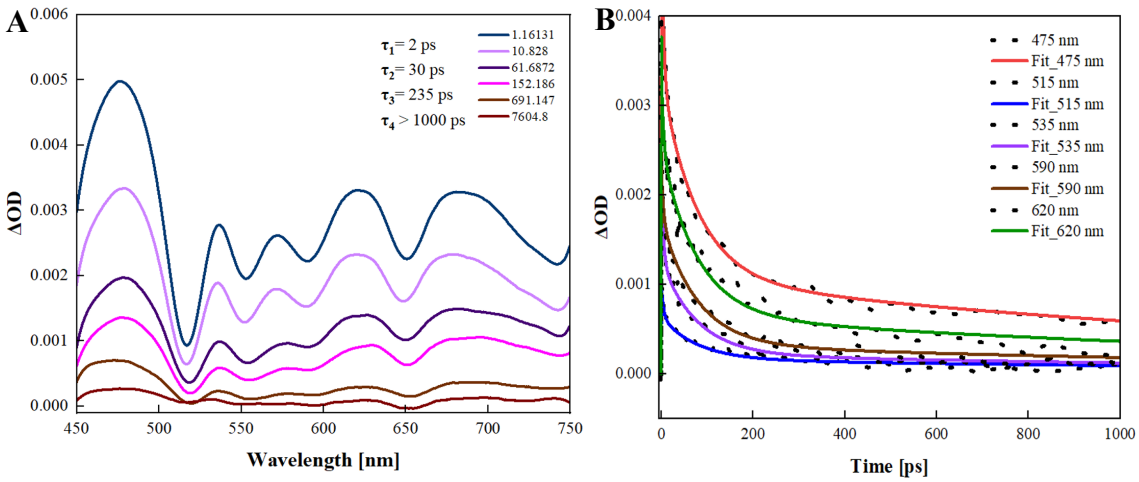


Figure 6.12 (A) Picosecond transient absorption spectrum of **TPP-NDI** on the NiO surface upon the excitation at 400 nm at different time delays. **(B)** Decay kinetic traces for **TPP-NDI** obtained from Glotaran global analysis.

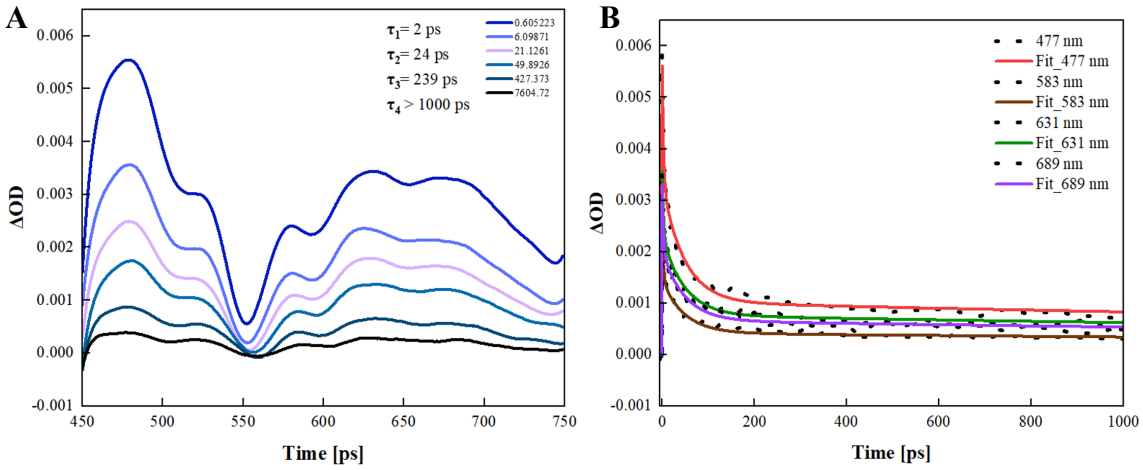


Figure 6.13 (A) Picosecond transient absorption spectrum of **Zn-TPP-NDI** on the NiO surface following excitation at 400 nm at different time delays. **(B)** Decay kinetic traces for **Zn-TPP-NDI**.

6.3.6 Electrochemistry

Standard cyclic voltammetry procedures were employed to investigate the reduced and oxidised states of the **TPP-NDI** and **Zn-TPP-NDI** (Figure 6.14) and to determine the redox potentials. Consequently, these reduction and oxidation potentials enabled us to approximate the thermodynamic driving force for photocatalytic hydrogen evolution employing the Rehm-Weller estimation. Electrochemical studies were carried out in dimethylformamide with 0.1 M tetrabutylammonium hexafluorophosphate functioning as the supporting electrolyte. Summarised in Table 6.2 are the potentials reported versus the ferrocene/ferrocenium redox couple. The CVs of standard references TPP (tetraphenyl porphyrin) and Zn-TPP (zinc tetraphenyl porphyrin) are well known from the literature. Moura et al. [45] reported that for the free base porphyrin there are two reversible reductions at $E_{1/2}$ = –1.41 and –1.86 V and are assigned to the porphyrin's π-system. In addition, the authors reported the oxidation peak at $E_{1/2}$ = 0.76 V, and they assigned this value to the oxidation of the porphyrin ring, resulting in the formation of the π-radical cation [45, 46]. In the CV of zinc metalated porphyrin**,** there are two reduction peaks, however, they are shifted to more negative values in contrast to TPP, and were observed at $E_{1/2}$ = –1.69 and –2.07 V. The oxidation process is evident at lower potential $E_{1/2}$ = 0.51 V [45, 46].

TPP-NH_2 and **NDI** are studied as references for the **TPP-NDI** and **Zn-TPP-NDI** systems. This comparison is important so that the anodic/cathodic shifts can be studied, which can contribute to understanding the direction of electron transfer as well as the ground state interactions within those systems. Cyclic voltammetry was carried out using, **TPP-NH_2**, NDI moiety (R_1-NDI-R_1; where R_1 = C_8H_{17}), and the dyads **TPP-NDI,** and **Zn-TPP-NDI**. **Zn-TPP-NDI** showcased four well separated reversible reduction waves. The first and second anodic peaks at –1.0 and –1.48 V are consistent with two reductions on the NDI moiety [47]. The porphyrin moiety of the **Zn-TPP-NDI** system displays two reversible oxidations and two reversible reductions. The potential values in the positive range at E° = 0.42 V and at E° = 0.62 V for **Zn-TPP-NDI** are assigned to oxidation of the porphyrin, indicating the formation of the porphyrin cation and dication radicals respectively [3, 44 – 46]. The two reversible reduction processes at E° = –1.84 and –2.24 V correspond to the porphyrin anion and dianion species. Comparable results were obtained for **TPP-NDI**. The reduction of NDI is observed at E° = –1.0 and ~ –1.48 V. Moreover, the reduction of the porphyrin moiety is evident at E° = ~ –1.59 V. The additional reduction of the porphyrin moiety is observed at E° = –2.04 V. The potential at

E° = 0.63 V for **TPP-NDI** corresponds to the oxidation of the porphyrin. It can be observed, that upon the metalation of **TPP-NDI**, the reduction potentials are shifted towards more negative values, and the oxidation potential is lower in **Zn-TPP-NDI**. Additionally, the reduction potentials for both of these compounds are consistent with **TPP-NH$_2$** and **NDI** (Figure 6.15) suggesting negligible ground state interactions between the porphyrin light-harvester and the NDI acceptor. Our findings are further supported by results obtained in the literature. Zhang et al. [44] carried out electrochemical measurements in DMF using 0.1 M Bu_4NPF_6 as supporting electrolyte for their ZnP-NDI system. The first reduction was observed –0.59 V and assigned to the NDI moiety, while the reduction at –1.46 V occurs on the porphyrin. The oxidation potential of ZnP-NDI was determined to be 0.75 V [44].

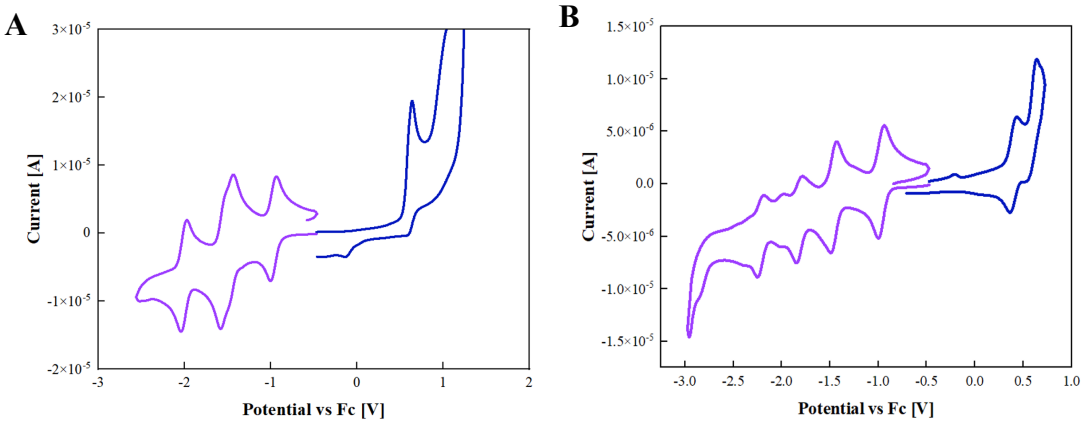


Figure 6.14 A cyclic voltammogram of **TPP-NDI (A)** and **Zn-TPP-NDI (B)** vs ferrocene was recorded under the following experimental conditions: 1 mM of the compound was dissolved in DMF (dimethylformamide) purged with nitrogen, and 0.1 M tetrabutylammonium hexafluorophosphate serving as the supporting electrolyte. The working electrode used was a glassy carbon electrode, while a platinum wire and an $Ag/AgNO_3$ electrode were employed as the counter and reference electrodes, respectively. The scans were performed at a scan rate of 0.1 V/s.

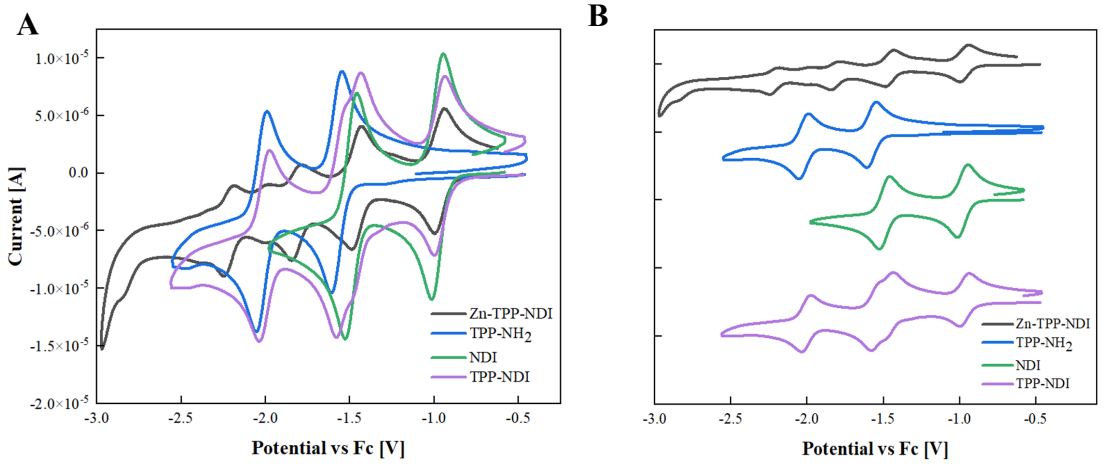


Figure 6.15 (A) The superposition of the CVs of the individual moieties, namely **NDI**, **TPP-NH$_2$** and the dyads **TPP-NDI**, **Zn-TPP-NDI** in order to present a minimal variation in their redox potentials. **(B)** Vertical stacking of CVs offsets for better visualisation and clarity.

6.3.7 Rehm-Weller estimation for the thermodynamic driving force for photocatalytic hydrogen evolution

The electrochemical data is very helpful in determining the thermodynamic driving force and the feasibility of an efficient photocatalytic water-splitting process. It is assumed that, following a reductive quenching mechanism, the electron transfer occurs from the highest occupied molecular orbital (HOMO) level of the electron donor, in this case the porphyrin moiety to the lowest unoccupied molecular orbital (LUMO) of the acceptor, which in this case is the NDI unit [3, 48, 49]. Therefore, the following reactions in Figure 6.16 summarise the electron transfer process occurring within the systems of **TPP-NDI** and **Zn-TPP-NDI**:

$$Acceptor + Donor \rightarrow Acceptor^{\cdot -} + Donor^{\cdot +}$$

$$Acceptor + electron \rightarrow Acceptor^{\cdot -}$$

$$Donor \rightarrow Donor^{\cdot +} + electron$$

Figure 6.16 The equations that summarise the process of photoinduced electron transfer in donor-acceptor assemblies [3, 49].

According to these equations, the potential of the first reduction wave of the acceptor corresponds to the potential of its LUMO level, whereas the first oxidation potential of the donor indicates its HOMO level [3]. The Rehm-Weller approach was used to identify and examine the thermodynamic feasibility and to evaluate the potential of **TPP-NDI** and **Zn-TPP-NDI** for photocatalytic reactions.

$$E^{*}_{ox}\left(\frac{D^{*}}{D^{\cdot +}}\right) = E_{ox}(\frac{D}{D^{\cdot +}}) - E_{0,0} + w$$

Where, $E_{0,0}$ is the energy difference between the lowest vibrational levels of the ground and the excited state, and this is determined from the intersection of normalised absorbance and emission spectra (1240/ λ). W is an electrostatic work term corresponding to charge separation, often disregarded in calculations. All equations and the estimation

of the thermodynamic driving force was based on the literature review carried out by O'Neill et al. [3].

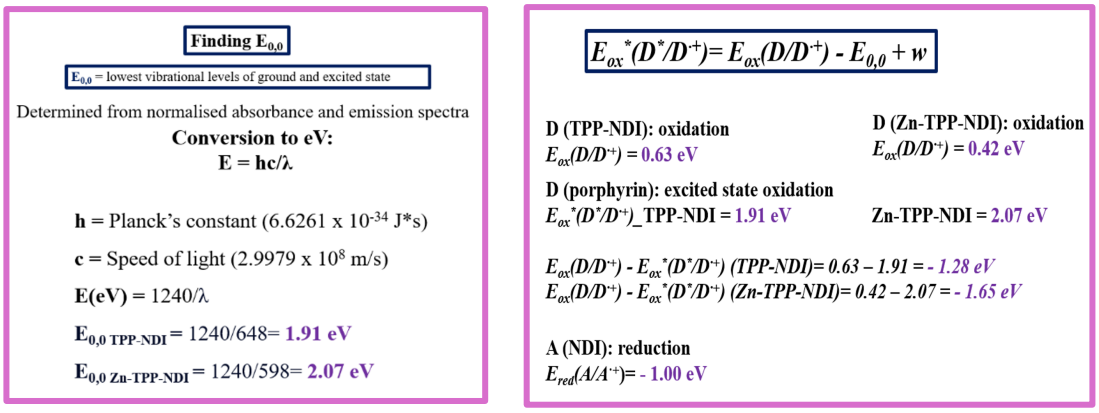


Figure 6.17 The equations that summarise the calculations of the Rehm-Weller estimation [3, 49].

Determining the redox potentials of **TPP-NDI** and **Zn-TPP-NDI** enables us to approximate the thermodynamic driving force of photoinduced electron transfer between the photosensitisers (porphyrin) and the catalyst [3]. The first step involves the estimation of the oxidation potential of the excited state (E_{ox}^{*}) of both porphyrins and this is calculated using the equation E = hc/ λ, where λ represents the wavelength at which the normalised emission and absorption spectra overlap [3, 50]. For **TPP-NDI**, this overlap occurred at 648 nm, whereas for **Zn-TPP-NDI**, it was at 598 nm (Figure 6.18). The oxidation potential of triethylamine (TEA) was reported in the literature as 0.31 V, while that of triethanolamine (TEOA) is 0.19 V [51]. Sacrificial electron donors such as TEA and TEOA must have oxidation potentials lower and more negative (less positive) than the ground-state oxidation potential of the porphyrin donor [3, 51, 52]. Additionally, the porphyrin excited state oxidation potential (E^{*}_{ox} in Figure 6.19 – 6.20) should be more negative than the ground-state reduction potential of the NDI unit [3, 51, 52]. Consequently, this could enable effective transfer of electrons from higher energy levels of sacrificial electron donors to lower energy levels of photoexcited photosensitisers and allow the process to proceed in a thermodynamically favourable manner [52]. For both **TPP-NDI** and **Zn-TPP-NDI**, it was determined that TEA and TEOA should be suitable sacrificial electron donors for the photocatalytic hydrogen production. Furthermore, the thermodynamic feasibility of **TPP-NDI** and **Zn-TPP-NDI** revealed that the oxidation potential of porphyrin (donor excited state E^{*}_{ox}) provided sufficient energy to donate electrons to the NDI acceptor and finally to the catalyst. This occurs because the reaction

follows a downhill thermodynamic pathway, hence it is considered to be thermodynamically favourable [3, 53], as illustrated in Figure 6.19 and Figure 6.20.

Platinum ($Pt(DMSO)_2I_2$) or cobaloxime catalysts are suitable for photocatalysis with these porphyrin systems, as their reduction potentials are more positive than the reduction potential of the NDI moiety [50, 54 – 56]. For efficient electron transfer, the reduction potential of the catalyst should be less negative than the reduction of the NDI in this case [3, 55]. However, the accurate determination of these potentials can be challenging as various factors such as the presence of water as a proton source in photocatalysis could influence the values [57, 58]. The Rehm-Weller approach serves only as an estimation, and it is primarily used to understand electron transfer dynamics and thermodynamic feasibility.

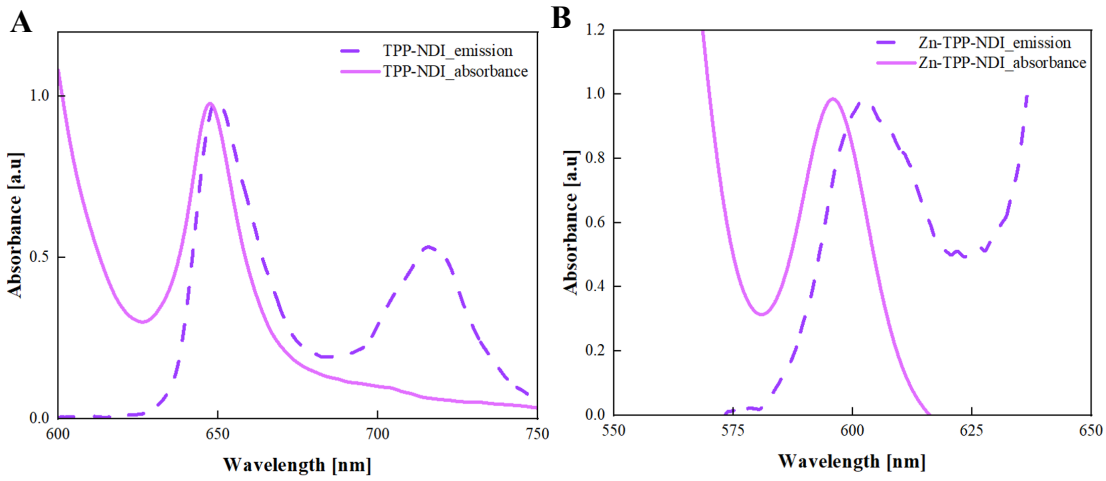


Figure 6.18 Spectral overlap of the normalised emission and absorption spectra for both **(A) TPP-NDI** and **(B) Zn-TPP-NDI** in THF.

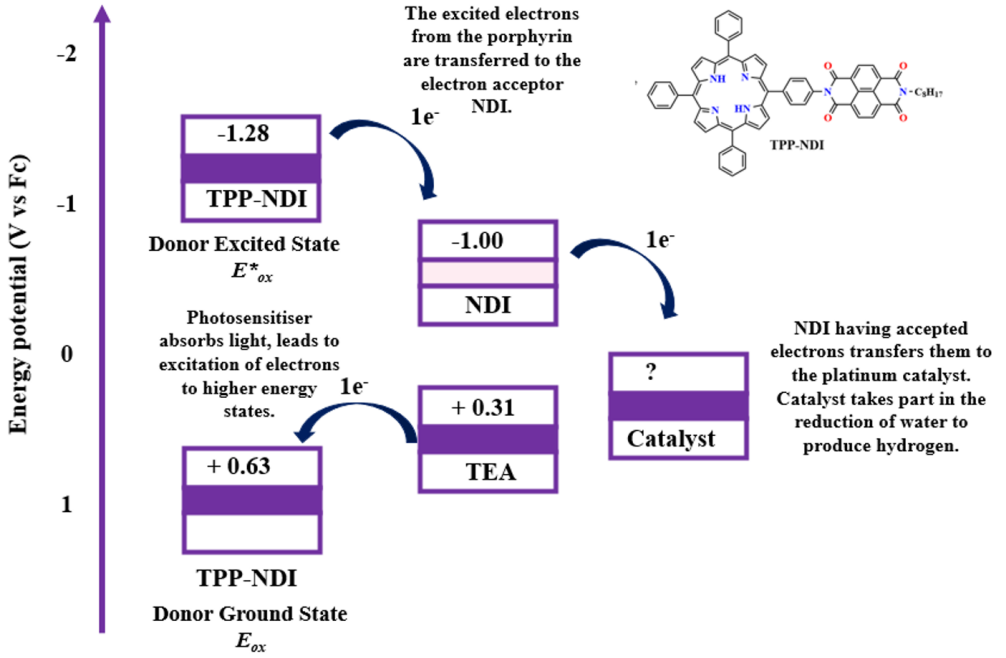


Figure 6.19 The thermodynamic driving force feasibility for electron transfer from the **TPP-NDI** photosensitiser to the NDI acceptor and subsequently to the catalyst.

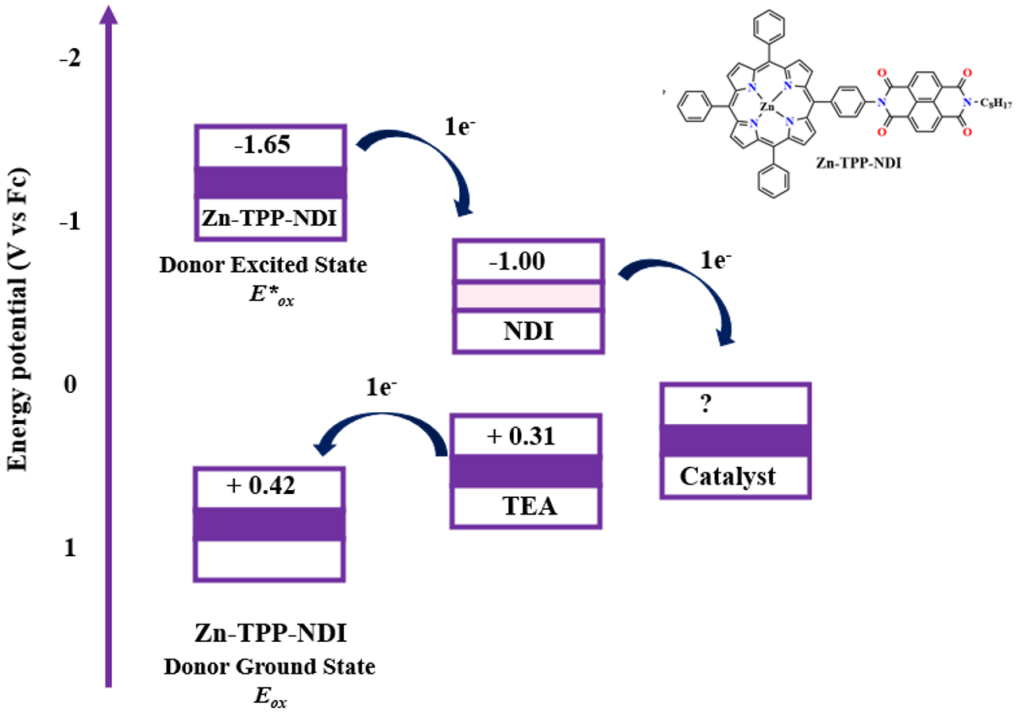


Figure 6.20 The thermodynamic driving force feasibility for electron transfer from the **Zn-TPP-NDI** photosensitiser to the NDI acceptor and subsequently to the catalyst.

6.3.8 Photocatalytic hydrogen evolution

These dyads were assessed as photosensitisers for photocatalytic hydrogen production under various experimental conditions. Unfortunately, no hydrogen evolution was detected in any of the experiments. Some of the conditions examined the choice of different sacrificial electron donors for example ascorbic acid, triethylamine, triethanolamine and the catalysts used were $Pt(DMSO)_2I_2$ and cobaloxime. Additionally, another experiment was carried out following the procedure reported by Bodedla et al. [59] who reported photocatalytic hydrogen evolution using the naphthalimide conjugated porphyrins ZnT(p-NI)PP, ZnT(m-NI)PP and ZnT(o-NI)PP which differ in the substitution of naphthalimide moieties. Their findings indicated that the para substituted complex ZnT(p-NI)PP, exhibited the highest hydrogen evolution efficiency, reaching 973 μmol g^{-1} h^{-1}. In their study, triethanolamine in water solution was used as the electron donor and 3 wt.% of Pt as co-catalyst was loaded by an in situ photoreduction deposition method from an aqueous H_2PtCl_6 solution [59]. The same procedure and conditions were used in our experiments, however no hydrogen generation was observed.

6.4 Conclusion

TPP-NDI and **Zn-TPP-NDI** were studied using UV-vis and emission spectroscopy, and picosecond/nanoseconds-transient absorption spectroscopy. The emission for both **TPP-NDI** and **Zn-TPP-NDI** was strongly quenched. Picosecond-TAS studies were carried out on a NiO surface to examine hole injection from the semiconductor to the porphyrin dyad. Upon chemisorption on the surface, there was a red-shift for the absorption bands, in comparison to the absorption profile of **TPP-NDI** and **Zn-TPP-NDI** in solution. Additionally, following excitation at 400 nm, the spectral profile of **TPP-NDI** and **Zn-TPP-NDI** resembled those reported in solution. However, the charge-separated state decayed more rapidly on the surface than in solution, and hence further optimisation of the molecular structure is necessary to extend the lifetime of this excited state and prevent the rapid charge recombination. In addition, cyclic voltammetry was carried out to determine the redox potentials of these systems, which is helpful in determining the thermodynamic driving force for electron transfer. Using the Rehm-Weller approach photocatalytic water-splitting should be feasible, however no hydrogen was detected in the photocatalytic studies carried out. This indicates that further optimisation of the experimental conditions and procedures is necessary to determine the ideal conditions

for the porphyrin systems in this study. Furthermore, this highlights that the Rehm-Weller equation only serves as an estimation tool to assess the potential feasibility of a system to for hydrogen evolution applications but does not guarantee success based only on electrochemical potentials.

6.5 Experimental

6.5.1 Materials and methods

All chemicals were supplied by Aldrich Chemicals Co. and Fluorochem Ltd. 5-(4-aminophenyl)-10,15,20-(triphenyl)porphyrin was purchased from Porphychem. ^{1}H-NMR of porphyrins was conducted using Bruker 600 MHz spectrometer in deuterated dichloromethane. UV-vis and Emission Spectroscopy spectra were obtained from a Duetta Absorbance and Fluorescence Spectrometer in tetrahydrofuran. Mass Spectrometry (MALDI) results were carried out by researchers at the University of Bath.

6.5.2 Electrochemical measurements

Cyclic voltammetry was carried out using 0.1 mM solutions of complexes in DMF with 1 M tetrabutylammonium hexafluorophosphate acting as supporting electrolyte. A glassy carbon disk (polished with a diamond paste and cleaned in ultrasonic bath) and platinum wire were used as working and counter electrodes, respectively, together with an $Ag/AgNO_3$ reference electrode. All obtained potentials were corrected versus ferrocene. T = 298 K, v = 100 mV s^{-1}.

6.5.3 Picosecond transient absorption measurements

Ps-TAS were recorded at the Newcastle University in the United Kingdom. The optical density of the samples was in the range 0.3 – 0.9 at 400 nm.

6.5.4 Time-correlated single photon counting (TCSPC)

TCSPC studies were conducted using an FLS 1000 Photoluminescence spectrometer from Edinburgh Instruments, using a 375 and 510 nm diode laser and the optical density (OD) of the samples was 0.2 at the excitation wavelength.

6.5.5 Nanosecond transient absorption measurements

Nanosecond TAS were recorded using the LP980 transient absorption spectrometer, Edinburgh Instruments, using excitation at 355 nm. All samples were deaerated over three cycles of freeze-pump-thaw before measurements (OD ~ 1.0 at ~ 420 nm).

6.5.6 Photocatalytic hydrogen evolution

Photocatalytic hydrogen evolution was carried in a 19 ml glass Schlenk tube stopped with an air-tight rubber spectrum. The sample (0.03 mmol) and the $Pt(DMSO)_2I_2$ or cobaloxime catalyst (0.03 mmol) were dissolved in a 65:30:5 mixture of tetrahydrofuran, triethylamine or ascorbic acid or triethanolamine and deionised water. Photocatalysis was also carried out following the method reported in the literature [59] using 0.3 mg of **TPP-NDI** and **Zn-TPP-NDI** in 1 ml THF. To this solution, 5 mg of 1 wt.% Pt deposited on TiO_2 was added and the mixture was sonicated for 30 minutes. The solvent was evaporated and 3 ml of 0.8 M ascorbic acid (the pH of the solution was adjusted to 5 – 6 pH using 0.2 M of sodium hydroxide) was added to the mixture [59]. The solution in each photocatalytic experiment was deoxygenated using three cycles of freeze-pump-thaw and subsequently exposed to light irradiation using Solar Simulator supplied by G2V Optics [60]. Gas Chromatography was used to quantify the amount of hydrogen produced.

6.5.7 Immobilisation studies on a NiO film

Immobilisation studies on NiO films were carried out at the Newcastle University in the United Kingdom. The NiO sol gel was prepared by mixing anhydrous $NiCl_2$ (1 g) and tri-block co-polymer F108 [poly (ethylene glycol)-block-poly (propylene glycol)-block-poly (ethylene glycol)] (1 g) in ethanol (6 ml) and ultrapure water (5 ml). The solution was aged for two weeks. The NiO films were prepared using conductive fluorine doped tin oxide glass and placed in dye baths overnight. Next, the films were dried at 450 ° C and cooled down to room temperature. The films were then placed in the porphyrin dye bath overnight to be successfully adsorbed onto the surface. The above procedure was followed by the method reported in the literature [61] and it was the same as reported in the previous chapters.

6.6 References

[1]. Taniguchi, M., Lindsey, J. S., Bocian, D. F., & Holten, D. (2021). Comprehensive review of photophysical parameters (ε, φ_f, τ_s) of tetraphenylporphyrin (H_2TPP) and zinc tetraphenylporphyrin (ZnTPP) – Critical benchmark molecules in photochemistry and photosynthesis. Journal of Photochemistry and Photobiology C: Photochemistry Reviews, 46, 100401. https://doi.org/10.1016/j.jphotochemrev.2020.100401

[2]. Liu, Q., Ntim, T., Wu, Z., Houson, H. A., Lapi, S. E., & Lindsey, J. S. (2024). Molecular design for sub-micromolar enzyme-instructed self-assembly (EISA). New Journal of Chemistry, 48(25), 11233–11242. https://doi.org/10.1039/d4nj01798f

[3]. O'Neill, J. S., Kearney, L., Brandon, M. P., & Pryce, M. T. (2022). Design components of porphyrin-based photocatalytic hydrogen evolution systems: A Review. Coordination Chemistry Reviews, 467, 214599. https://doi.org/10.1016/j.ccr.2022.214599

[4]. Bodedla, G. B., Dong, Y., Tang, G., Zhao, J., Zhang, F., Zhu, X., & Wong, W.-Y. (2022). Long-lived excited states of platinum(II)-porphyrins for highly efficient photocatalytic hydrogen evolution. Journal of Materials Chemistry A, 10(25), 13402–13409. https://doi.org/10.1039/d2ta02543d

[5]. Kou, J., Dou, D., & Yang, L. (2017). Porphyrin photosensitizers in photodynamic therapy and its applications. Oncotarget, 8(46), 81591–81603. https://doi.org/10.18632/oncotarget.20189

[6]. Ethirajan, M., Chen, Y., Joshi, P., & Pandey, R. K. (2011b). The role of porphyrin chemistry in tumor imaging and photodynamic therapy. Chem. Soc. Rev., 40(1), 340–362. https://doi.org/10.1039/b915149b

[7]. Higashino, T., & Imahori, H. (2014). Porphyrins as excellent dyes for dye-sensitized solar cells: recent developments and insights. Dalton Transactions, 44(2), 448–463. https://doi.org/10.1039/c4dt02756f

[8]. Birel, Ö., Nadeem, S., & Duman, H. (2017). Porphyrin-Based Dye-Sensitized Solar Cells (DSSCS): a Review. Journal of Fluorescence, 27(3), 1075–1085. https://doi.org/10.1007/s10895-017-2041-2

[9]. La, D. D., Jadha, R. W., Gosavi, N. M., Rene, E. R., Nguyen, T. A., Xuan-Thanh, B., Nguyen, D. D., Chung, W. J., Chang, S. W., Nguyen, X. H., Tran, L. D., & Bhosale, S. V. (2021). Nature-inspired organic semiconductor via solvophobic self-assembly of porphyrin derivative as an effective photocatalyst for degradation of rhodamine B dye. Journal of Water Process Engineering, 40, 101876. https://doi.org/10.1016/j.jwpe.2020.101876

[10]. Kobuke, Y., & Ogawa, K. (2003). Porphyrin Supramolecules for Artificial Photosynthesis and Molecular Photonic/Electronic Materials. ChemInform, 34(28). https://doi.org/10.1002/chin.200328253

[11]. Kim, J. H., Lee, S. H., Lee, J. S., Lee, M., & Park, C. B. (2011). Zn-containing porphyrin as a biomimetic light-harvesting molecule for biocatalyzed artificial photosynthesis. Chemical Communications, 47(37), 10227–10229. https://doi.org/10.1039/c1cc12222c

[12]. Mirgane, H. A., More, K. S., Veeranagaiah, N. S., & Bhosale, S. V. (2024). Porphyrin-based covalently bonded nanoarchitectonics of organic donor-acceptor system for artificial photosynthesis: A Review. Dyes and Pigments, 225, 112113. https://doi.org/10.1016/j.dyepig.2024.112113

[13]. Tahoun, M., Gee, C. T., McCoy, V. E., Sander, P. M., & Müller, C. E. (2021). Chemistry of porphyrins in fossil plants and animals. RSC Advances, 11(13), 7552–7563. https://doi.org/10.1039/d0ra10688g

[14]. Doria, F., Folini, M., Grande, V., Cimino-Reale, G., Zaffaroni, N., & Freccero, M. (2015). Naphthalene diimides as red fluorescent pH sensors for functional cell imaging.

Organic & Biomolecular Chemistry, 13(2), 570–576. https://doi.org/10.1039/c4ob02054e
[15]. Singha, N., Gupta, P., Pramanik, B., Ahmed, S., Dasgupta, A., Ukil, A., & Das, D. (2017). Hydrogelation of a Naphthalene Diimide Appended Peptide Amphiphile and its Application in Cell Imaging and Intracellular pH sensing. Biomacromolecules, 18(11), 3630–3641. https://doi.org/10.1021/acs.biomac.7b01048
[16]. Jameel, M. A., Yang, T. C.-J., Wilson, G. J., Evans, R. A., Gupta, A., & Langford, S. J. (2021). Naphthalene diimide-based electron transport materials for perovskite solar cells. Journal of Materials Chemistry A, 9(48), 27170–27192. https://doi.org/10.1039/d1ta08424k
[17]. Al Kobaisi, M., Bhosale, S. V., Latham, K., Raynor, A. M., & Bhosale, S. V. (2016). Functional Naphthalene Diimides: Synthesis, Properties, and Applications. Chemical Reviews, 116(19), 11685–11796. https://doi.org/10.1021/acs.chemrev.6b00160
[18]. Gianolio, D. A. (2000). Tethered naphthalene diimide-based intercalators for DNA triplex stabilization. Nucleic Acids Research, 28(10), 2128–2134. https://doi.org/10.1093/nar/28.10.2128
[19]. Pirota, V., Platella, C., Musumeci, D., Benassi, A., Amato, J., Pagano, B., Colombo, G., Freccero, M., Doria, F., & Montesarchio, D. (2021a). On the binding of naphthalene diimides to a human telomeric G-quadruplex multimer model. International Journal of Biological Macromolecules, 166, 1320–1334. https://doi.org/10.1016/j.ijbiomac.2020.11.013
[20]. Robotham, B., Lastman, K. A., Langford, S. J., & Ghiggino, K. P. (2013a). Ultrafast electron transfer in a porphyrin-amino naphthalene diimide dyad. Journal of Photochemistry and Photobiology A: Chemistry, 251, 167–174. https://doi.org/10.1016/j.jphotochem.2012.11.002
[21]. Villamaina, D., Bhosale, S. V., Langford, S. J., & Vauthey, E. (2013). Excited-state dynamics of porphyrin–naphthalene diimide–porphyrin triads. Phys. Chem. Chem. Phys., 15(4), 1177–1187. https://doi.org/10.1039/c2cp43595k
[22]. Banerji, N., Bhosale, S. V., Petkova, I., Langford, S. J., & Vauthey, E. (2011). Ultrafast excited-state dynamics of strongly coupled porphyrin/core-substituted-naphthalenediimide dyads. Phys. Chem. Chem. Phys., 13(3), 1019–1029. https://doi.org/10.1039/c0cp01544j
[23]. Wallin, S., Monnereau, C., Blart, E., Gankou, J.-R., Odobel, F., & Hammarström, L. (2010b). State-Selective Electron Transfer in an Unsymmetric Acceptor−Zn(II)Porphyrin−Acceptor Triad: Toward a Controlled Directionality of Electron Transfer from the Porphyrin S_2 and S_1 States as a Basis for a Molecular Switch. The Journal of Physical Chemistry A, 114(4), 1709–1721. https://doi.org/10.1021/jp907824d
[24]. Ghule, N. V., La, D. D., Bhosale, R. S., Al Kobaisi, M., Raynor, A. M., Bhosale, S. V., & Bhosale, S. V. (2016). Effect of Amide Hydrogen Bonding Interaction on Supramolecular Self-Assembly of Naphthalene Diimide Amphiphiles with Aggregation Induced Emission. ChemistryOpen, 5(2), 157–163. https://doi.org/10.1002/open.201500201
[25]. Zhang, A., Kwan, L., & Stillman, M. J. (2017). The spectroscopic impact of interactions with the four Gouterman orbitals from peripheral decoration of porphyrins with simple electron withdrawing and donating groups. Organic & Biomolecular Chemistry, 15(43), 9081–9094. https://doi.org/10.1039/c7ob01960b
[26]. Doria, F., Oppi, A., Manoli, F., Botti, S., Kandoth, N., Grande, V., Manet, I., & Freccero, M. (2015). A naphthalene diimide dyad for fluorescence switch-on detection of G-quadruplexes. Chemical Communications, 51(44), 9105–9108. https://doi.org/10.1039/c5cc01536g

[27]. Rogers, J. E., Weiss, S. J., & Kelly, L. A. (2000). Photoprocesses of Naphthalene Imide and Diimide Derivatives in Aqueous Solutions of DNA. Journal of the American Chemical Society, 122(3), 427–436. https://doi.org/10.1021/ja992332d
[28] Ishihara, S., Labuta, J., Van Rossom, W., Ishikawa, D., Minami, K., Hill, J. P., & Ariga, K. (2014). Porphyrin-based sensor nanoarchitectonics in diverse physical detection modes. Physical Chemistry Chemical Physics, 16(21), 9713–9746. https://doi.org/10.1039/c3cp55431g
[29]. Ke Xin, T., O. Lintang, H., Tamuri, A. R., Endud, S., & Bakar, M. B. (2014). Synthesis and Emission Properties of Meso-Substituted Porphyrins. Jurnal Teknologi, 71(1). https://doi.org/10.11113/jt.v71.3610
[30]. Ghann, W., Chavez-Gil, T., Goede, C. I., Kang, H., Khan, S., Sobhi, H., Nesbitt, F., & Uddin, J. (2017). Photophysical, Electrochemical and Photovoltaic Properties of Porphyrin-Based Dye Sensitized Solar Cell. Advances in Materials Physics and Chemistry, 07(05), 148–172. https://doi.org/10.4236/ampc.2017.75013
[31]. Basak, S., Nandi, N., Paul, S., & Banerjee, A. (2018). Luminescent Naphthalene Diimide-Based Peptide in Aqueous Medium and in Solid State: Rewritable Fluorescent Color Code. ACS Omega, 3(2), 2174–2182. https://doi.org/10.1021/acsomega.7b01813
[32]. Insuasty, A., Carrara, S., Xuechen, J., McNeill, C. R., Hogan, C., & Langford, S. J. (2024). Aggregation-Induced Emission of Naphthalene Diimides: Effect of Chain Length on Liquid and Solid-Phase Emissive Properties. Chemistry – An Asian Journal, 19(9), e202400152. https://doi.org/10.1002/asia.202400152
[33]. Sun, X., Li, D., Chen, G., & Zhang, J. (2006). A series of new porphyrin dyads: The synthesis and photophysical properties. Dyes and Pigments, 71(2), 118–122. https://doi.org/10.1016/j.dyepig.2005.06.008
[34]. Tu, S., Kim, S. H., Joseph, J., Modarelli, D. A., & Parquette, J. R. (2013). Proton-Coupled Self-Assembly of a Porphyrin-Naphthalene Diimide Dyad. ChemPhysChem, 14(8), 1609–1617. https://doi.org/10.1002/cphc.201300023
[35]. Yushchenko, O., Hangarge, R. V., Mosquera-Vazquez, S., Boshale, S. V., & Vauthey, E. (2014). Electron, Hole, Singlet, and Triplet Energy Transfer in Photoexcited Porphyrin-Naphthalenediimide Dyads. The Journal of Physical Chemistry B, 119(24), 7308–7320. https://doi.org/10.1021/jp5108685
[36]. Shaikh, S. M., Chakraborty, A., Alatis, J., Cai, M., Danilov, E., & Morris, A. J. (2019). Light Harvesting and Energy Transfer in a Porphyrin-Based Metal Organic Framework. Faraday Discussions, 216, 174–190. https://doi.org/10.1039/c8fd00194d
[37]. Giannoudis, E., Benazzi, E., Karlsson, J., Copley, G., Panagiotakis, S., Landrou, G., Angaridis, P., Nikolaou, V., Matthaiaki, C., Charalambidis, G., Gibson, E. A., & Coutsolelos, A. G. (2020). Photosensitizers for H_2 Evolution Based on Charged or Neutral Zn and Sn Porphyrins. Inorganic Chemistry, 59(3), 1611–1621. https://doi.org/10.1021/acs.inorgchem.9b01838
[38]. Tabrizi, L., McGarry, R., Turzanska, K., Varvarezos, L., Fallon, M., Brannigan, R., Costello, J. T., Fitzgerald-Hughes, D., & Pryce, M. T. (2024). Porphyrin-Polymer as a Photosensitizer Prodrug for Antimicrobial Photodynamic Therapy and Biomolecule Binding Ability. Biomacromolecules, 25(12), 7736–7749. https://doi.org/10.1021/acs.biomac.4c01011
[39]. Hanna, L., Movsesian, E., Orozco, M., Bernot Jr., A. R., Asadinamin, M., Shenje, L., Ullrich, S., Zhao, Y., Marshall, N., Weeks, J. A., Thomas, M. B., Teprovich Jr., J. A., & Ward, P. A. (2022). Spectroscopic investigation of the electronic and excited state properties of para-substituted tetraphenyl porphyrins and their electrochemically generated ions. Spectrochimica Acta Part A: Molecular and Biomolecular Spectroscopy, 278, 121300. https://doi.org/10.1016/j.saa.2022.121300
[40]. Barbosa Neto, N. M., Correa, D. S., De Boni, L., Parra, G. G., Misoguti, L., Mendonça, C. R., Borissevitch, I. E., Zílio, S. C., & Gonçalves, P. J. (2013). Excited states

absorption spectra of porphyrins – Solvent effects. Chemical Physics Letters, 587, 118–123. https://doi.org/10.1016/j.cplett.2013.09.066
[41]. Ye, C., Cheng, H., Wrede, S., Diring, S., Tian, H., Odobel, F., & Hammarström, L. (2023a). Charge Recombination Deceleration by Lateral Transfer of Electrons in Dye-Sensitized NiO Photocathode. Journal of the American Chemical Society, 145(20), 11067–11073. https://doi.org/10.1021/jacs.3c00269
[42]. Farooq, M., & Mujtaba Shah, S. (2021b). Fabrication and Characterization of NiO Nanoparticle–Porphyrin-Based Organic–Inorganic Nanohybrid Assembly: A Sustainable Redox Mediator in Dye-Sensitized Solar Cell Construction. Journal of Electronic Materials, 50(8), 4827–4833. https://doi.org/10.1007/s11664-021-09008-1
[43]. Benazzi, E., Summers, G. H., Black, F. A., Sazanovich, I. V., Clark, I. P., & Gibson, E. A. (2019). Assembly, charge-transfer and solar cell performance with porphyrin-C_{60} on NiO for p-type dye-sensitized solar cells. Philosophical Transactions of the Royal Society A: Mathematical, Physical and Engineering Sciences, 377(2152), 20180338. https://doi.org/10.1098/rsta.2018.0338
[44]. Zhang, L., Favereau, L., Farre, Y., Maufroy, A., Pellegrin, Y., Blart, E., Hissler, M., Jacquemin, D., Odobel, F., & Hammarström, L. (2016). Molecular-structure control of electron transfer dynamics of push–pull porphyrins as sensitizers for NiO based dye sensitized solar cells. RSC Advances, 6(81), 77184–77194. https://doi.org/10.1039/c6ra15195g
[45]. Moura, N. M., Serra, V. V., Bastos, A., Biazotto, J. C., Castro, K. A., Faustino, M. A., Lodeiro, C., da Silva, R. S., & Neves, M. da. (2022). New Bis-Cyclometalated Iridium(III) Complexes with β-substituted Porphyrin-Arylbipyridine as the Ancillary Ligand: Electrochemical and Photophysical Insights. International Journal of Molecular Sciences, 23(14), 7606. https://doi.org/10.3390/ijms23147606
[46]. Wilson, G. S., & Neri, B. P. (1973). Cyclic Voltammetry of Porphyrins and Metalloporphyrins*. Annals of the New York Academy of Sciences, 206(1), 568–578. https://doi.org/10.1111/j.1749-6632.1973.tb43237.x
[47]. Wiberg, C., Busch, M., Evenäs, L., & Ahlberg, E. (2021). The electrochemical response of core-functionalized naphthalene diimides (NDI) – a combined computational and experimental investigation. Electrochimica Acta, 367, 137480. https://doi.org/10.1016/j.electacta.2020.137480
[48]. Zegkinoglou, I., Ragoussi, M.-E., Pemmaraju, C. D., Johnson, P. S., Pickup, D. F., Ortega, J. E., Prendergast, D., de la Torre, G., & Himpsel, F. J. (2013). Spectroscopy of Donor−π–Acceptor Porphyrins for Dye-Sensitized Solar Cells. The Journal of Physical Chemistry C, 117(26), 13357–13364. https://doi.org/10.1021/jp402590u
[49]. Romero, N. A., & Nicewicz, D. A. (2016). Organic Photoredox Catalysis. Chemical Reviews, 116(17), 10075–10166. https://doi.org/10.1021/acs.chemrev.6b00057
[50]. Li, L., Bodedla, G. B., Liu, Z., & Zhu, X. (2020). Naphthalimide-porphyrin hybridized graphitic carbon nitride for enhanced photocatalytic hydrogen production. Applied Surface Science, 499, 143755. https://doi.org/10.1016/j.apsusc.2019.143755
[51]. Giereth, R., Obermeier, M., Forschner, L., Karnahl, M., Schwalbe, M., & Tschierlei, S. (2021). Exploring the Full Potential of Photocatalytic Carbon Dioxide Reduction using a Dinuclear Re_2Cl_2 Complex Assisted by Various Photosensitizers. ChemPhotoChem, 5(7), 644–653. https://doi.org/10.1002/cptc.202100034
[52]. Lowe, G. A. (2023). Enabling artificial photosynthesis systems with molecular recycling: A review of photo- and electrochemical methods for regenerating organic sacrificial electron donors. Beilstein Journal of Organic Chemistry, 19, 1198–1215. https://doi.org/10.3762/bjoc.19.88
[53]. Bie, C., Wang, L., & Yu, J. (2022). Challenges for photocatalytic overall water splitting. Chem, 8(6), 1567–1574. https://doi.org/10.1016/j.chempr.2022.04.013

[54]. Mintrop, L., Windisch, J., Gotzmann, C., Alberto, R., Probst, B., & Kurz, P. (2015). Sn^{IV} Metalloporphyrin/Co^{III} Complex: An All-Abundant-Element System for the Photocatalytic Production of H_2 in Aqueous Solution. The Journal of Physical Chemistry B, 119(43), 13698–13706. https://doi.org/10.1021/acs.jpcb.5b03106
[55]. Beyene, B. B., & Hung, C.-H. (2018). Photocatalytic hydrogen evolution from neutral aqueous solution by a water-soluble cobalt(II) porphyrin. Sustainable Energy & Fuels, 2(9), 2036–2043. https://doi.org/10.1039/c8se00253c
[56]. Sideri, I. K., Charalambidis, G., Coutsolelos, A. G., Arenal, R., & Tagmatarchis, N. (2022). Pyridine vs. Imidazole Axial Ligation on Cobaloxime Grafted Graphene: Hydrogen Evolution Reaction Insights. Nanomaterials, 12(17), 3077. https://doi.org/10.3390/nano12173077
[57]. Stratakes, B. M., Dempsey, J. L., & Miller, A. J. (2021). Determining the Overpotential of Electrochemical Fuel Synthesis Mediated by Molecular Catalysts: Recommended Practices, Standard Reduction Potentials, and Challenges. ChemElectroChem, 8(22), 4161–4180. https://doi.org/10.1002/celc.202100576
[58]. Rosspeintner, A., Kattnig, D. R., Angulo, G., Landgraf, S., & Grampp, G. (2008). The Rehm–Weller Experiment in View of Distant Electron Transfer. Chemistry – A European Journal, 14(20), 6213–6221. https://doi.org/10.1002/chem.200701841
[59]. Bodedla, G. B., Li, L., Che, Y., Jiang, Y., Huang, J., Zhao, J., & Zhu, X. (2018). Enhancing photocatalytic hydrogen evolution by intramolecular energy transfer in naphthalimide conjugated porphyrins. Chemical Communications, 54(82), 11614–11617. https://doi.org/10.1039/c8cc06919k
[60]. LED solar simulator manufacturer: Sunbrick Solar Simulator. G2V Optics Inc. (2025, June 17). https://g2voptics.com/
[61]. Cerpentier, F. J., Karlsson, J., Lalrempuia, R., Brandon, M. P., Sazanovich, I. V., Greetham, G. M., Gibson, E. A., & Pryce, M. T. (2021). Ruthenium Assemblies for CO_2 Reduction and H_2 Generation: Time Resolved Infrared Spectroscopy, Spectroelectrochemistry and a Photocatalysis Study in Solution and on NiO. Frontiers in Chemistry, 9. https://doi.org/10.3389/fchem.2021.795877

CHAPTER 7
CONCLUSIONS AND FUTURE WORK

Chapter 1 highlighted the concerns regarding global warming and continuous climate changes over the past decades. Significant greenhouse gas emissions have contributed greatly to changes in weather patterns but have also caused negative impacts on the environment. This chapter summarised photocatalytic methods, whose purpose is to introduce more renewable and green energy sources, and to slow down the process of global warming and support the development of sustainable fuel components. Hydrogen is considered as promising fuel, and therefore this work focused on photocatalytic hydrogen evolution processes carried out in laboratory settings. For this purpose, a wide variety of complexes has been designed and synthesised, as reported in the literature. This chapter presented their molecular structures as well as briefly explained their applications. Photophysical and electrochemical techniques were also described in this chapter to introduce the analytical techniques used in this dissertation and to provide insights into how these analyses were conducted in the subsequent chapters.

Chapter 2 presented a literature review on a range of Ru(II)-NDI and Ru(II)-PDI compounds. Their synthetic methods, along with their photophysical and electrochemical properties were summarised. Insights into their charge separation as well as electron transfer pathways were also discussed. Additionally, promising applications were highlighted and this review showed that there is still a great amount of research needed in this area. Consequently, in this thesis, the focus was primarily placed on Ru-NDI systems for photocatalytic hydrogen evolution and carbon dioxide reduction.

Chapter 3 presented a novel ruthenium (II)-naphthalene diimide **RuNDI^{2+}** photosensitiser for photocatalytic hydrogen evolution. UV-vis/IR and TRIR-spectroelectrochemistry were used to examine the photoactive intermediates formed during photocatalysis. Ns-TAS studies were employed to probe the excited state properties both in solution and under photocatalytic conditions. The hydrogen evolution efficiency resulted in a TON value of 64 and the recyclability of the complex was

investigated. Future work could include TRIR studies carried out under photocatalytic conditions. In this chapter, TRIR was conducted on electrochemically reduced species of the NDI-based systems. However, this work could be expanded to investigate the photophysical properties of these reduced species when they are chemically reduced rather than electrochemically, and examination of their triplet lifetime under photocatalytic conditions could be further examined by employing a range of different sacrificial electron donors. This would provide a greater understanding of the active species being formed during photocatalysis. Moreover, low temperature studies for UV-vis/IR-spectroelectrochemistry could be also carried out to enhance our understanding of the photophysical properties of the reduced/photoactive intermediates.

Chapter 4 presented a novel ruthenium (II)-naphthalene diimide **Ru(dceb)-NDI^{2+}** for photocatalytic hydrogen production. It was observed that incorporation of ester moieties had a significant impact on the photophysical and electrochemical properties. The hydrogen evolution efficiency resulted in a TON value of 100, which showed a greater efficiency compared to the complex without the ester groups discussed in Chapter 3. TRIR studies revealed a wavelength-dependent behaviour. Ns- and ps-TAS studies were carried out to examine the complex in solution, under photocatalytic conditions and on a NiO film. The **Ru(dceb)-NDI^{2+}** complex was successfully adsorbed on a NiO surface and photoinduced electron transfer from the NiO surface to the **Ru(dceb)-NDI^{2+}** complex occurred. Therefore, future work could include the study of this complex for photoelectrochemical hydrogen evolution. These studies could be conducted on a NiO surface in the presence of a suitable catalyst and under optimal conditions. Additionally, other peripheral ligands and substituents for example carboxylic acid groups could be incorporated into the Ru-NDI system, and their impact on photophysical and electrochemical behaviour could be analysed.

Chapter 5 involved photophysical and electrochemical studies on Ru-NDI complexes, in which different substituents were incorporated into their molecular structures. Ns- and ps-TAS studied were carried out in order to investigate their photophysical behaviour in solution, under photocatalytic conditions and on a NiO surface. TRIR studies presented a significant increase in absorption associated with the C=O stretching vibrations of the NDI moiety, and a smaller enhancement in triple bond features upon photoexcitation. Ru-NDI complexes examined in this study showed poor photocatalytic activity for hydrogen evolution, however they could be further explored for photoelectrochemical hydrogen

evolution upon surface immobilisation, as well as for photocatalytic conversion of carbon dioxide to carbon monoxide or formic acid. Additionally, from the perspective of TRIR studies, nitrile functional groups could be introduced (C≡N) to track electron density upon photoexcitation. Moreover, NDI complexes could be synthesised with a focus of transitioning to earth-abundant metal systems for example iron, nickel and cobalt.

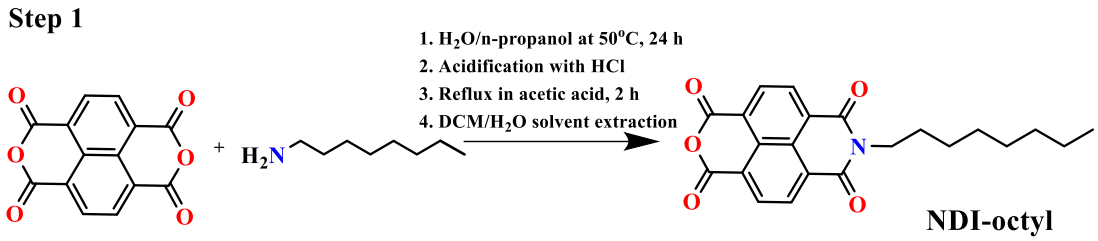
Chapter 6 presented **TPP-NDI** and **Zn-TPP-NDI** compounds and these were examined using UV-vis and emission spectroscopy, fluorescence lifetime measurements using TCSPC and ps/ns-TAS spectroscopy. Cyclic voltammetry was performed to obtain the redox potentials of these systems, which were then used to estimate the thermodynamic driving force for electron transfer. Thermodynamic driving force was feasible for these systems, however no hydrogen evolution was observed in the photocatalytic experiments. Future work could include optimisation of the conditions for photocatalysis for example employing different sacrificial electron donors, varying the pH of the photocatalytic solutions, modifying the concentrations of the photosensitiser and the catalyst, and also explore different catalysts. Another possible study could include the development of an intramolecular system, in which catalyst is covalently attached to the porphyrin. Moreover, ester or acid groups could be introduced at the meso position of the porphyrin, hence this would allow to carry out studies on semiconductor surfaces.

Appendix A

CHAPTER 3
Ruthenium (II)-Naphthalene Diimide Photosensitiser in Catalytic Hydrogen Production Probed by Time-Resolved Infrared Spectroelectrochemistry- Supplementary information

Synthesis Section

N-octyl-1,4,5,8-napthalene-tetra-carboxylic monoanhydride.



The preparation of NDI-octyl ligand was carried out following the procedure in the literature [1]. 1,4,5,8-naphthalenetetracarboxylic dianhydride (1g, 3.73 mmol) and octyl amine (2 mL, 1.56 g, 12 mmol, excess) were dissolved in a 20 ml solvent mixture of water and isopropanol (1:1). The solution was subsequently degassed using nitrogen for approximately 30 minutes and it was heated to 50°C. After 24 hours, the reaction mixture was cooled down to room temperature and 1 M HCl was added in order to lower the pH. Then the reaction mixture was filtered and refluxed in acetic acid (excess) for 1h to give yellow clear solution, which was then cooled down to the room temperature. The obtained precipitate was washed by solvent extraction using DCM and water. The organic layer was collected, and the solvent was removed using vacuum. To remove the remaining DCM, ethanol was added to precipitate out the product. That was filtered off and washed with ethanol, hexane, and small amount of diethyl ether. ^{1}H-NMR (600 MHz, $CdCl_3$ d_6): δ (ppm) 0.85 (t, 3H), 1.2–1.4 (m, 10H), 1.79 (t, 2H), 4.21 (t, 2H), 8.75 (s, 4H).

The reference compound employed in cyclic voltammetry and transient absorption spectroscopy experiments, R_1-NDI-R_1 ($R_1 = C_8H_{17}$) was synthesised in a similar manner to NDI-octyl precursor, using 1.119 mmol (0.299 g) of 1,4,5,8-naphthalenetetracarboxylic dianhydride and 3.356 mmol of octyl amine (0.556 ml). ^{1}H-NMR (600 MHz, $CdCl_3$ d_6): δ (ppm) 0.80 (t, 6H), 1.2–1.4 (m, 20H), 1.66 (t, 4H), 4.12 (t, 4H), 8.68 (s, 4H).

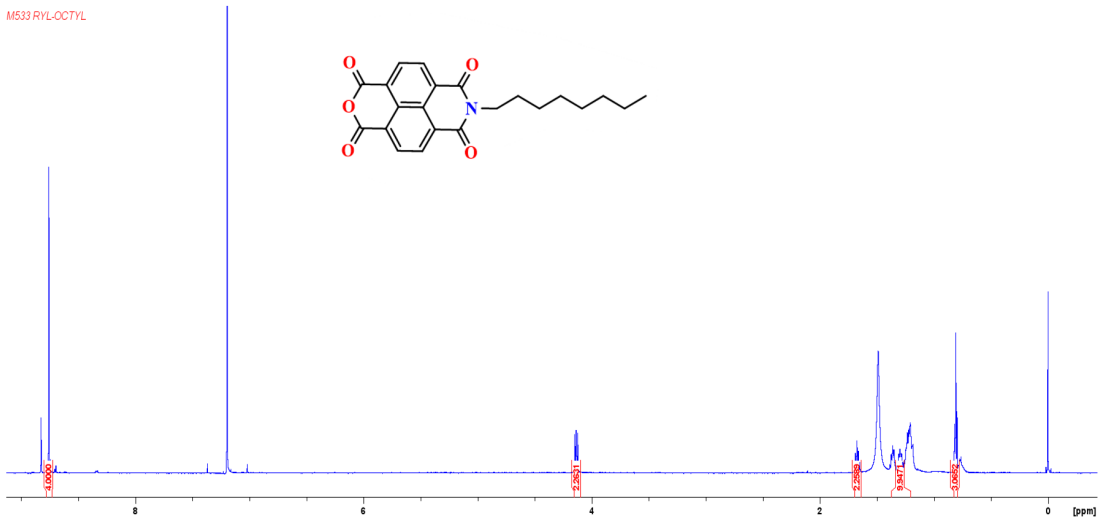


Figure SA3.1 ^{1}H-NMR of NDI-octyl in $CdCl_3$-d_6.

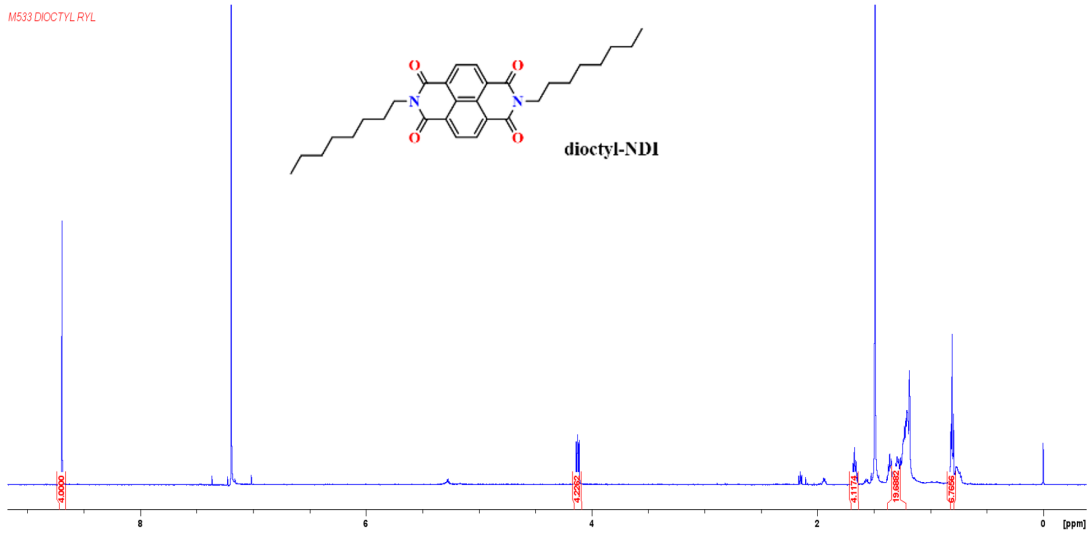
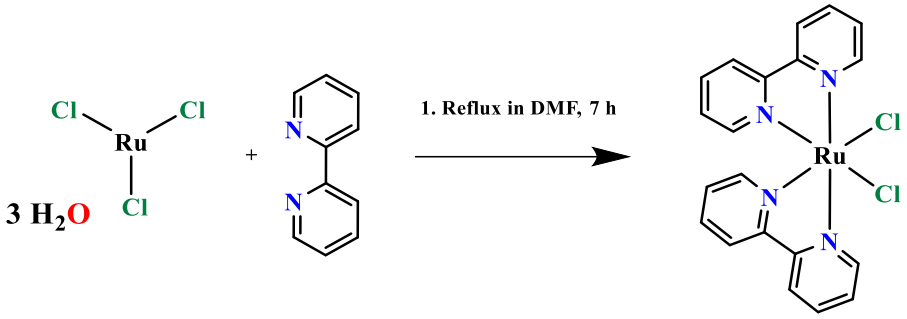


Figure SA3.2 ^{1}H-NMR of dioctyl-NDI in $CdCl_3$-d_6.

[Ru(bpy)$_2$Cl$_2$]

Step 2



[Ru(bpy)$_2$Cl$_2$] was synthesised as follows. $RuCl_3.3H_2O$ (1 g, 8.8 mmol), bipyridine (1.2 g, 7.7 mmol), and LiCl (1.3 g) were heated at reflux in dimethylformamide (4 ml) for 6 hours [2]. After the reaction mixture was cooled to room temperature, 200 ml of acetone was added, and the solution was placed in the freezer overnight. Next, the solution was filtered and washed multiple times with water and diethyl ether. ^{1}H-NMR (DMSOd_6): 7.09 (m, 2H), 7.50 (d, 2H), 7.67 (m, 2H), 7.76 (m, 2H), 8.05 (m, 2H), 8.48 (d, 2H), 8.63 (d, 2H), 9.97 (d, 2H)

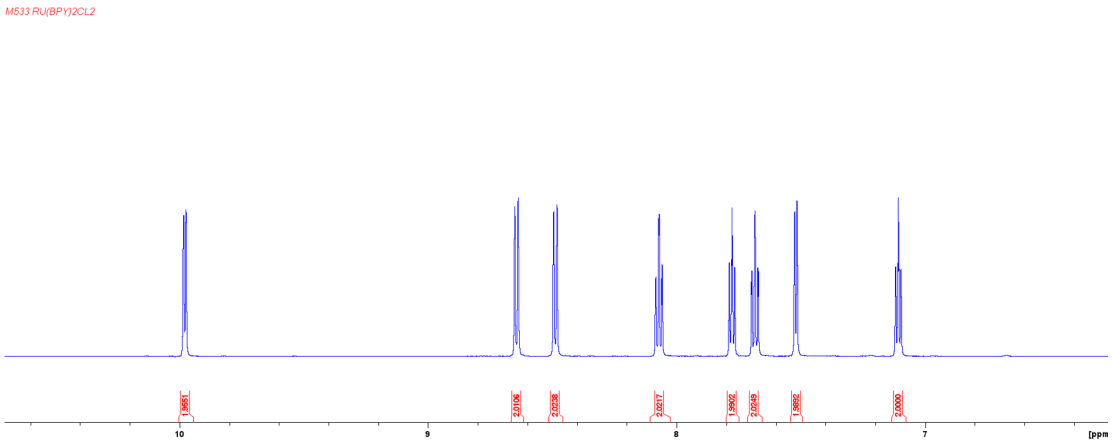
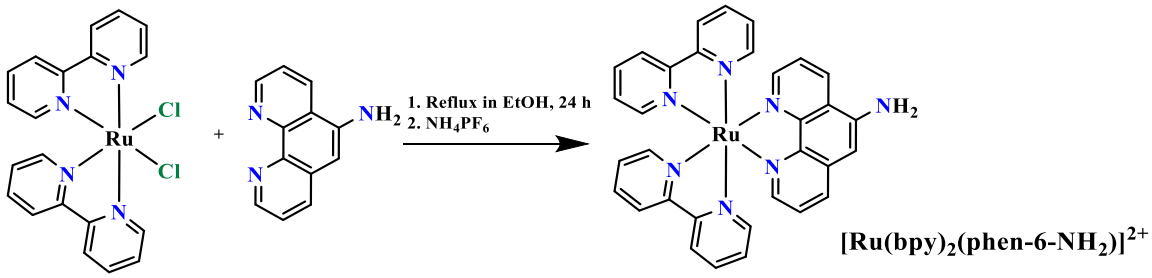


Figure SA3.3 ^{1}H-NMR of [Ru(bpy)$_2$Cl$_2$] in DMSO-d_6.

$[Ru(bpy)_2(phen\text{-}6\text{-}NH_2)]^{2+}$

Step 3



310 mg (0.64 mmol) of [Ru(2,2'-bipyridine)$_2$Cl$_2$] was refluxed with 125 mg (0.64 mmol) of 1,10-phenathrolin-5-amine in 30 ml of ethanol at 78°C overnight. Ethanol was removed under reduced pressure, 200 ml of water was added, and 0.4 g (2.45 mmol) of NH_4PF_6 was added. The product precipitated out of solution as a red solid, and it was washed with diethyl ether. ^{1}H-NMR (600 MHz, DMSOd_6): δ (ppm) 6.92 (s, 2H, br), 7.06 (s, 1H), 7.34–7.40 (m, 2H), 7.52–7.57 (m, 5H), 7.60 (m, 1H), 7.78–7.80 (m, 3H), 8.04 (m, 1H), 8.07–8.11 (m, 2H), 8.15–8.20 (m, 2H), 8.28–8.31 (m, 1H), 8.79–8.86 (m, 4H), 8.88–8.91 (m, 1H)

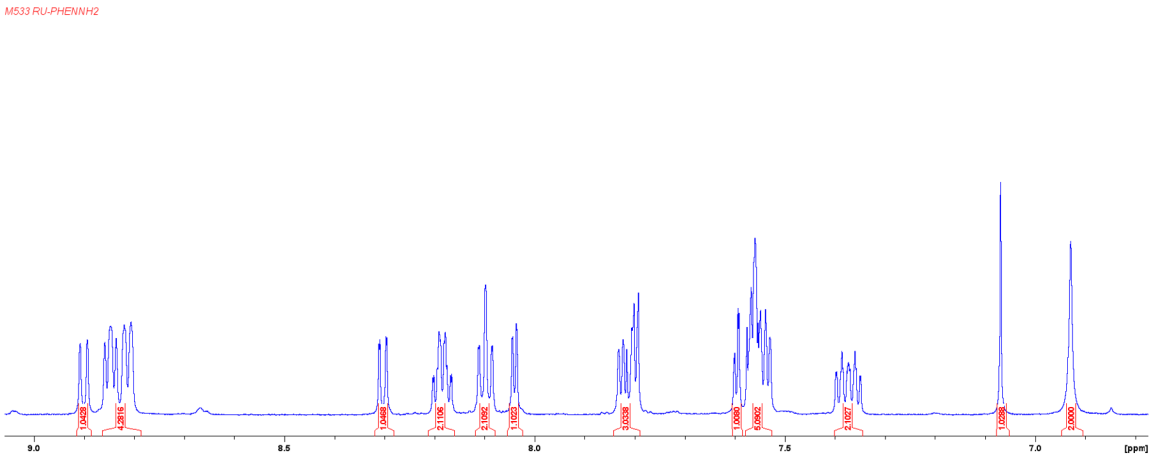
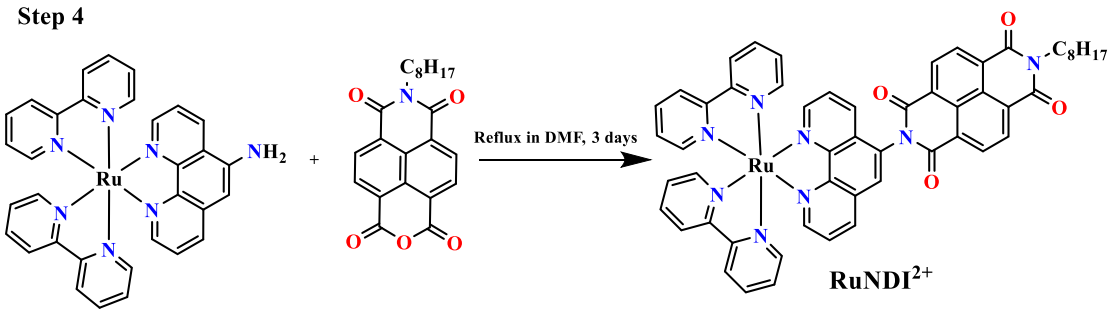


Figure SA3.4 ^{1}H-NMR of $[Ru(bpy)_2(phen\text{-}6\text{-}NH_2)]^{2+}$ in DMSO-d_6.

RuNDI^{2+}



$[Ru(bpy)_2(phen\text{-}6\text{-}NH_2)]^{2+}$ (0.27 mmol, 169 mg) and n-octyl-1,4,5,8-napthalene-tetra-carboxylic monoanhydride (NDI-octyl, 0.27 mmol, 105 mg) were stirred in dry degassed DMF at 140°C for 3 days with the protection of nitrogen. The solvent was reduced, and the crude product was dissolved in a small volume of DMF, and diethyl ether was added. The product precipitated out of solution as an orange solid and it was washed with diethyl ether, water. In order to remove naphthalene diimide starting material (**NDI-octyl**), the sample was dissolved in a small quantity of DMF, and diethyl ether was added. The product was precipitated out and filtered. Column Chromatography was carried out using acetonitrile, water and saturated KNO_3 solution (ratio 10:1:0.1) as a mobile phase. ^{1}H-NMR (600 MHz, $DMSOd_6$): δ (ppm) 0.85 (t, 3H), 1.2–1.4 (m, 10H), 1.69 (t, 2H), 4.09 (t, 2H), 7.44 (m, 1H), 7.48 (m, 1H), 7.59 (m, 2H), 7.65–7.68 (m, 2H), 7.80–7.82 (m, 1H), 7.85 (m, 2H), 7.93–7.95 (m, 1H), 8.12–8.17 (m, 2H), 8.18–8.25 (m, 4H), 8.64 (s, 1H), 8.66–8.79 (m, 4H), 8.83–8.91 (m, 5H), 8.99 (m, 1H) ESI mass spectroscopy: $C_{54}H_{44}F_{12}N_8O_4P_2Ru$ $[M]^{2+}$ calculated at m/z = 485.1259 and found at 485.1248.

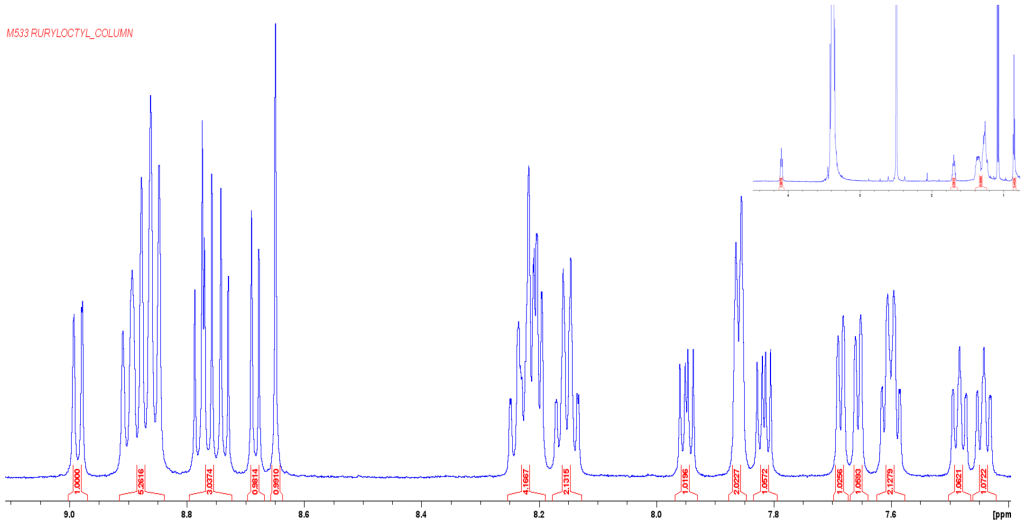


Figure SA3.5 ^{1}H-NMR of **RuNDI^{2+}** in DMSO-d_6.

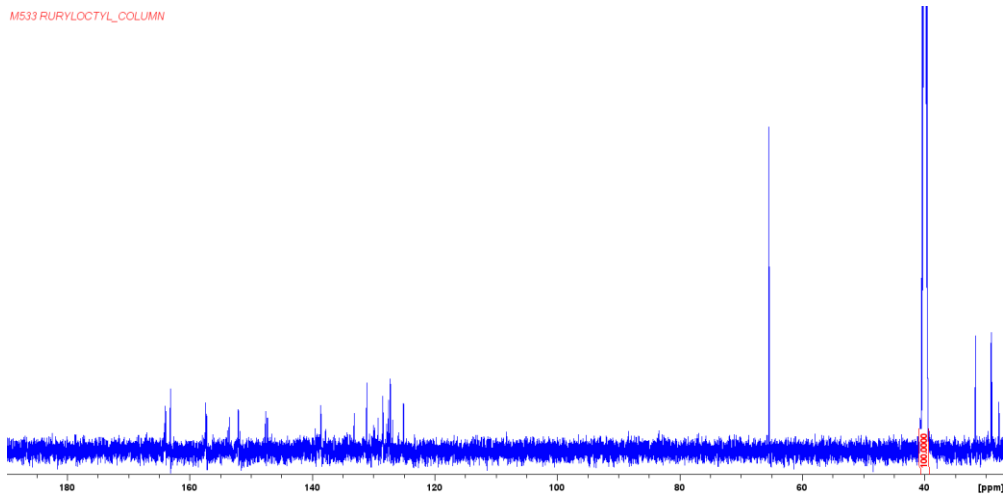


Figure SA3.6 ^{13}C-NMR of **RuNDI^{2+}** in DMSO-d$_6$.

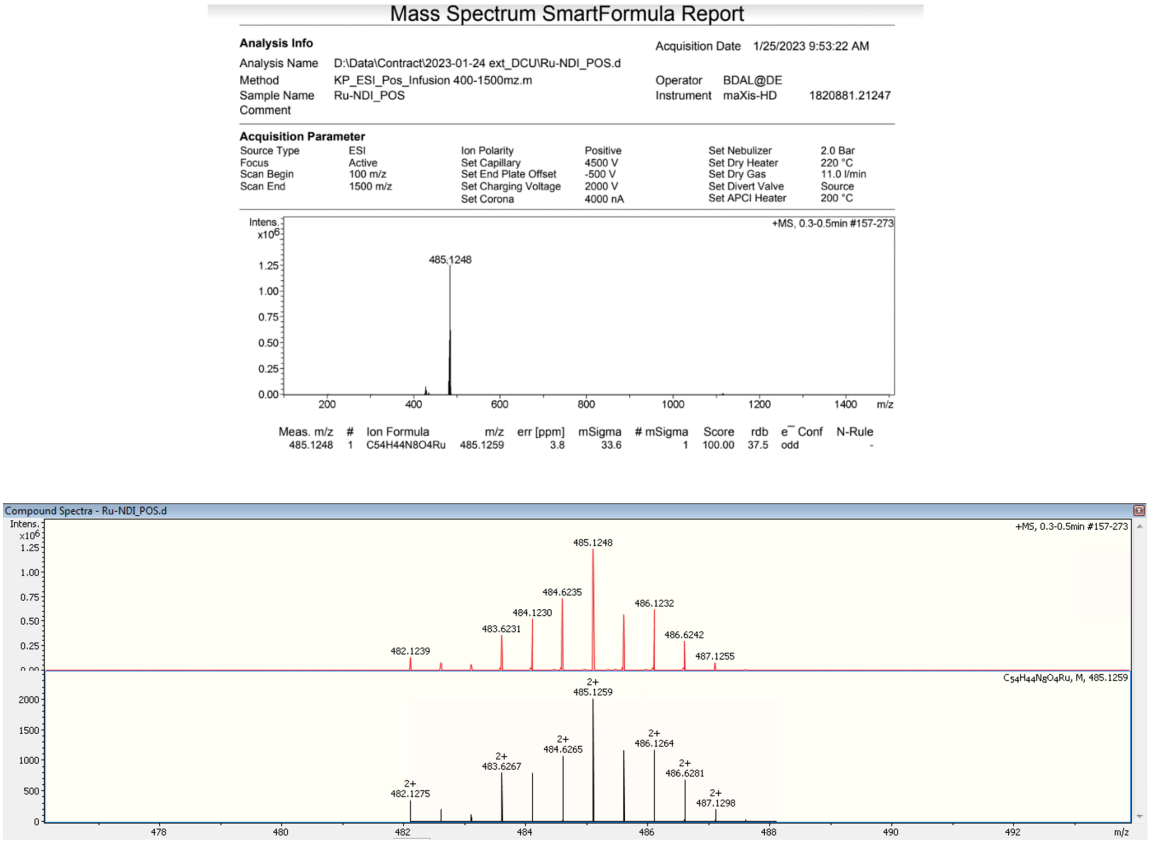
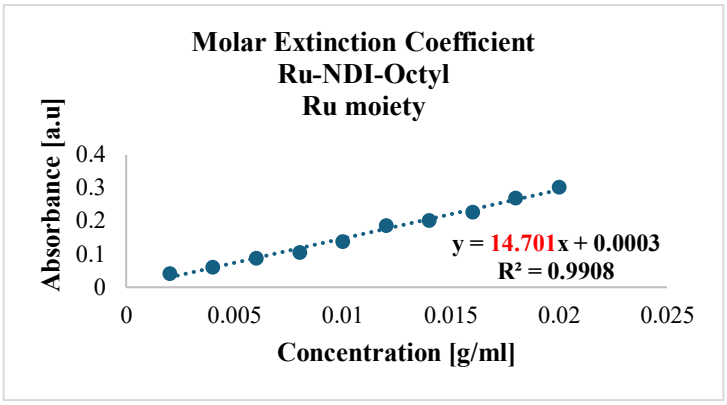


Figure SA3.7 High-resolution ESI-mass spectrum of **RuNDI^{2+}** in acetonitrile, calculated m/z = 485.1259, found in positive mode 485.1248.



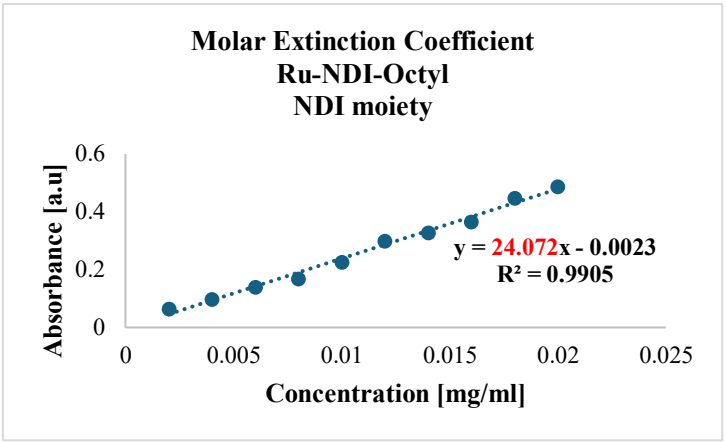


Figure SA3.8 Calculation of molar extinction coefficients.

Theoretical Calculations



Figure SA3.9 Two different structures of **RuNDI**$^{2+}$.

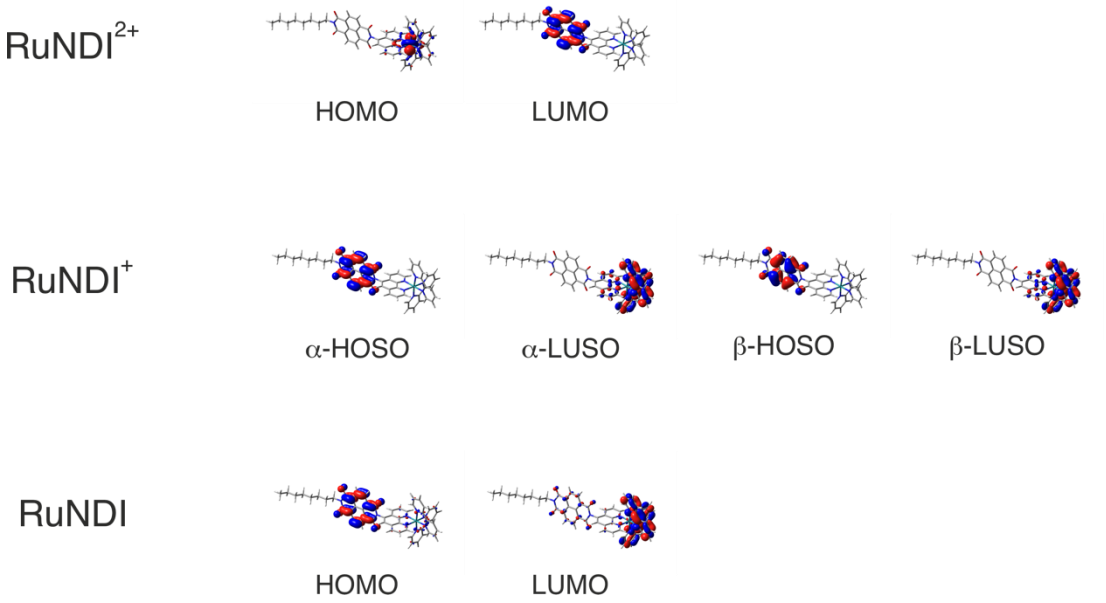


Figure SA3.10 Frontiers orbitals of **RuNDI**$^{2+/+/0}$.

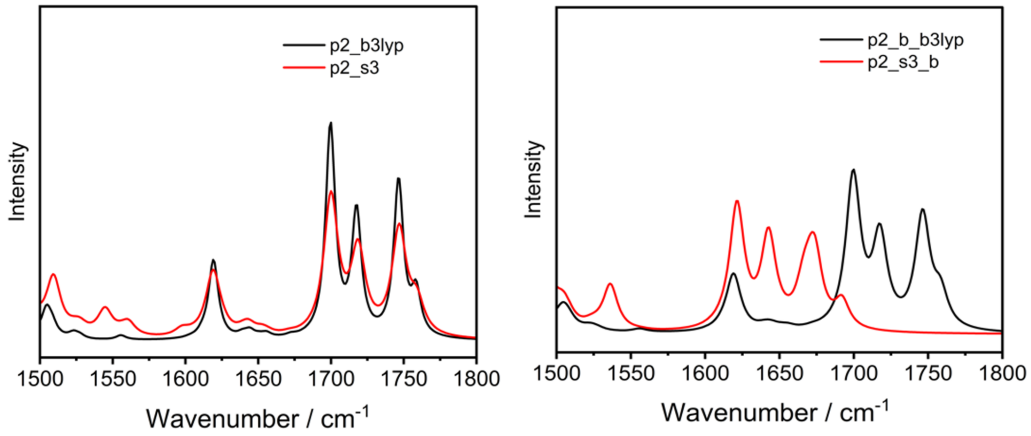


Figure SA3.11 IR spectra of **RuNDI**$^{2+}$ in the ground (black) and triplet state (red). The left spectrum is for ***a*** structure and the right is for ***b*** structure from Figure SA3.9.

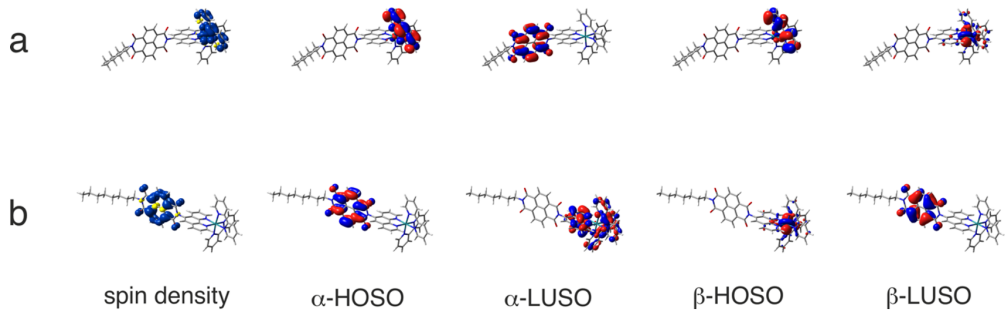


Figure SA3.12 Frontiers orbitals and spin density for ^{3}**RuNDI**$^{2+}$.

Table SA3.1 Energy differences of **RuNDI**$^{2+}$ between structure ***a*** and ***b*** in the ground and triplet excited states.

	state	local.	ΔE [kcal/mol]
RuNDI_p2_s3	a	bpy	4.88
	b	NDI	0.00
RuNDI_p2	a		0.66
	b		0.00

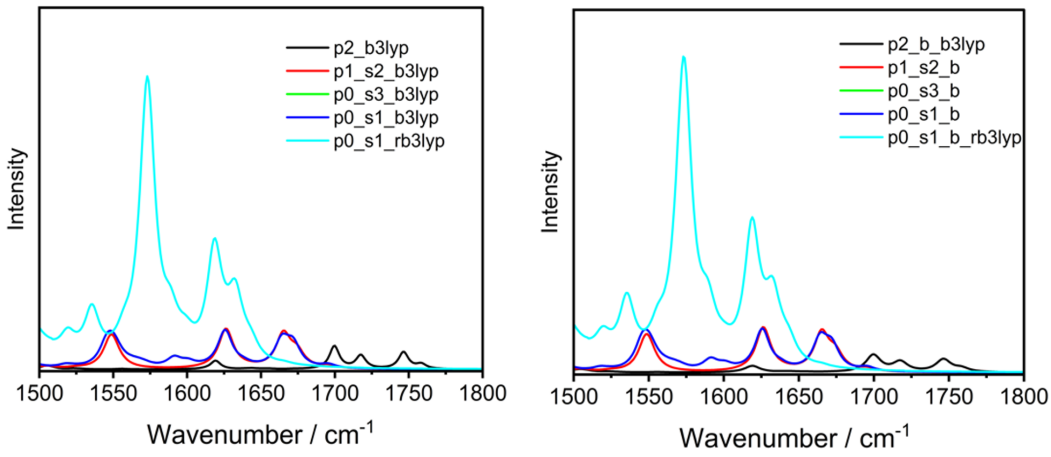


Figure SA3.13 IR spectra of **RuNDI**^{x} (x = 2+, +, 0). The left spectrum is for ***a*** structure, and the right is for ***b*** structure, as shown in Figure SA3.9.

Table SA3.2 Energy differences of **RuNDI**$^{+/0}$ in all possible reduced states.

structure	state	red. local.	ΔE [kcal/mol]	comments
b	RuNDI_p0_s1	bpy	5.16	spin + on NDI, spin – on bpy
	RuNDI_p0_s1	NDI	8.53	all paired electron
	RuNDI_p0_s3	bpy	0.00	spin + on NDI, spin + on bpy
	RuNDI_p1_s2	NDI		
a	RuNDI_p0_s1	bpy	0.65	spin + on NDI, spin – on bpy
	RuNDI_p0_s1	NDI	8.38	all paired electron
	RuNDI_p0_s3	bpy	0.00	spin + on NDI, spin + on bpy
	RuNDI_p1_s2	NDI		

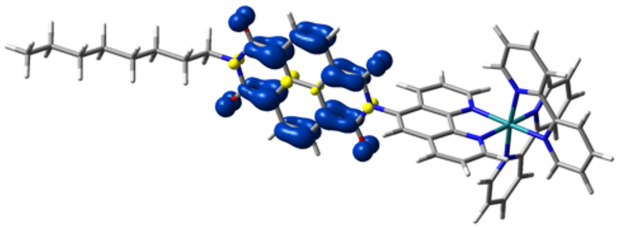


Figure SA3.14 Spin densities in **RuNDI**$^{+}$ showing localisation of the first reduction NDI ligand.



Figure SA3.15 Spin densities in **RuNDI** showing localisation of the second reduction on bpy; triplet (p0_s3, left), singlet (p0_s1, right).

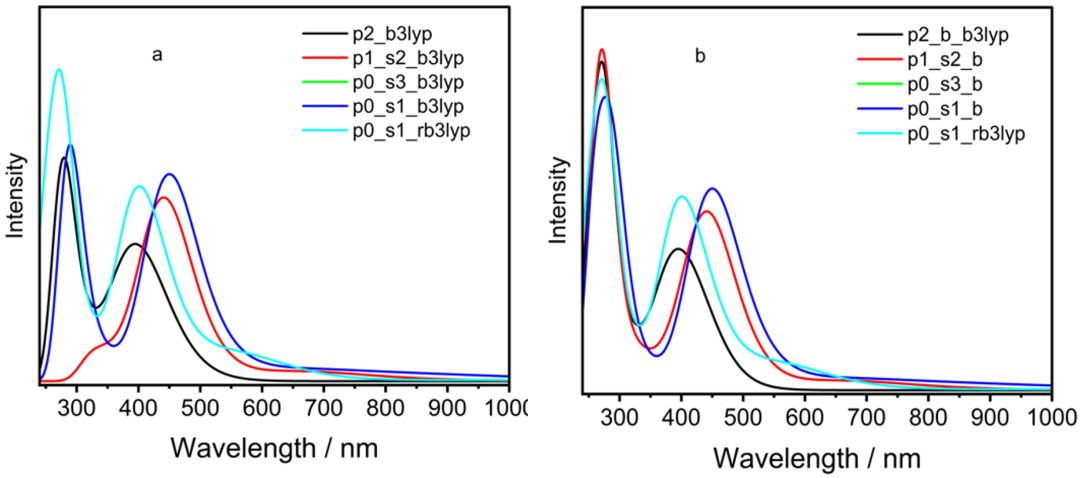


Figure SA3.16 Calculated electronic spectra for **RuNDI**$^{2+/+/0}$. The left spectrum is for ***a*** structure and the right is for ***b*** structure, as shown in Figure SA3.9.

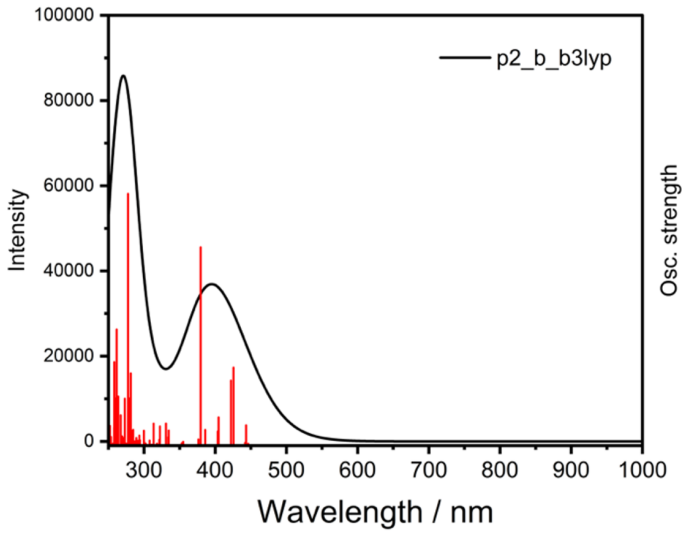


Figure SA3.17 TDDFT-calculated UV-vis absorption spectrum of **RuNDI**$^{2+}$.

Table SA3.3 Major electronic excitations in **RuNDI^{2+}** determined by TDDFT calculations.

Wavelength (nm)	Osc. str (*f*)	Major contributions (%)
501	0.0000	HOMO → LUMO (71)
483	0.0010	HOMO → LUMO+1 (60) HOMO → LUMO+2 (32)
476	0.0010	HOMO → LUMO+1 (37) HOMO → LUMO+2 (54) HOMO → LUMO+3 (20)
443	0.0473	HOMO–1 → LUMO+1 (62) HOMO → LUMO+4 (20)
426	0.1817	HOMO–2 → LUMO+2 (22) HOMO–2 → LUMO+3 (42) HOMO–1 → LUMO+1 (28) HOMO–1 → LUMO+2 (28) HOMO → LUMO+4 (21)
422	0.1513	HOMO–2 → LUMO+1 (23) HOMO–2 → LUMO+2 (44) HOMO–2 → LUMO+3 (24) HOMO–1 → LUMO+3 (34)
405	0.0657	HOMO–2 → LUMO+2 (20) HOMO–2 → LUMO+4 (64)
403	0.0328	HOMO–1 → LUMO+2 (28) HOMO–1 → LUMO+4 (58)
386	0.0368	HOMO–2 → LUMO+3 (39) HOMO–1 → LUMO+2 (34) HOMO–1 → LUMO+3 (23)
379	0.461	HOMO–3 → LUMO (69)
331	0.0514	HOMO–12 → LUMO (39) HOMO–9 → LUMO (51)
314	0.0516	HOMO–1 → LUMO+7 (48) HOMO → LUMO+17 (21)
281	0.1681	HOMO–6 → LUMO+2 (22) HOMO–6 → LUMO+3 (48) HOMO–6 → LUMO+4 (23) HOMO–1 → LUMO+10 (20)
280	0.1093	HOMO–6 → LUMO+3 (20) HOMO–1 → LUMO+10 (48)
279	0.1097	HOMO–6 → LUMO+4 (59)
278	0.5855	HOMO–7 → LUMO+3 (24) HOMO–7 → LUMO+4 (38) HOMO–6 → LUMO+2 (23)
273	0.1091	HOMO–10 → LUMO+1 (48) HOMO–10 → LUMO+2 (41)
267	0.0708	HOMO–10 → LUMO+4 (42) HOMO–8 → LUMO+1 (30)
264	0.1141	HOMO–11 → LUMO+1 (25) HOMO–10 → LUMO+4 (29) HOMO–8 → LUMO+1 (23) HOMO–8 → LUMO+2 (38)
261	0.2699	HOMO–10 → LUMO+2 (21) HOMO–8 → LUMO+3 (50) HOMO–8 → LUMO+4 (20)
260	0.1094	HOMO–8 → LUMO+3 (37) HOMO–8 → LUMO+4 (50)
258	0.1941	HOMO–11 → LUMO+1 (26) HOMO–11 → LUMO+3 (26) HOMO–11 → LUMO+4 (30) HOMO–8 → LUMO+4 (26) HOMO → LUMO+12 (23)

Wavelength (nm)	Osc. str (*f*)	Major contributions (%)
241	0.0875	HOMO–7 → LUMO+5 (45) HOMO–4 → LUMO+5 (22) HOMO → LUMO+14 (40)
233.6	0.0580	HOMO–25 → LUMO (38) HOMO–9 → LUMO+6 (29) HOMO–5 → LUMO+6 (30) HOMO–3 → LUMO+12 (31)
233.3	0.2824	HOMO–3 → LUMO+11 (59)
233.1	0.1965	HOMO–4 → LUMO+7 (26) HOMO–4 → LUMO+8 (23) HOMO–1 → LUMO+14 (40) HOMO → LUMO+16 (22)
223	0.0521	HOMO–23 → LUMO+1 (24) HOMO–20 → LUMO+3 (25) HOMO–18 → LUMO+3 (20)
222	0.0701	HOMO–27 → LUMO (23) HOMO–27 → LUMO+2 (20) HOMO–24 → LUMO+2 (28) HOMO–18 → LUMO+2 (20) HOMO–10 → LUMO+7 (23)
221	0.1354	HOMO–20 → LUMO+1 (23) HOMO–4 → LUMO+10 (25)
214	0.0576	HOMO–35 → LUMO (21) HOMO–33 → LUMO (33) HOMO–23 → LUMO+4 (27)
210	0.0776	HOMO–28 → LUMO+2 (21) HOMO–25 → LUMO+4 (30) HOMO–10 → LUMO+10 (27)
207	0.0905	HOMO–29 → LUMO+1 (20) HOMO–8 → LUMO+10 (21) HOMO → LUMO+21 (22) HOMO → LUMO+23 (28)
205	0.1328	HOMO–31 → LUMO+3 (24) HOMO–29 → LUMO+1 (22) HOMO–14 → LUMO+6 (29) HOMO → LUMO+24 (20)
204	0.0743	HOMO–14 → LUMO+6 (41) HOMO–9 → LUMO+11 (24) HOMO–6 → LUMO+11 (24)
203	0.1609	HOMO–9 → LUMO+12 (51) HOMO–5 → LUMO+12 (26)
201	0.0913	HOMO–18 →LUMO+6 (24) HOMO–13 →LUMO+5 (22) HOMO–13 →LUMO+6 (47)
200	0.1041	HOMO–30 → LUMO+1 (26) HOMO–4 → LUMO+13 (21) HOMO–1 → LUMO+24 (31)

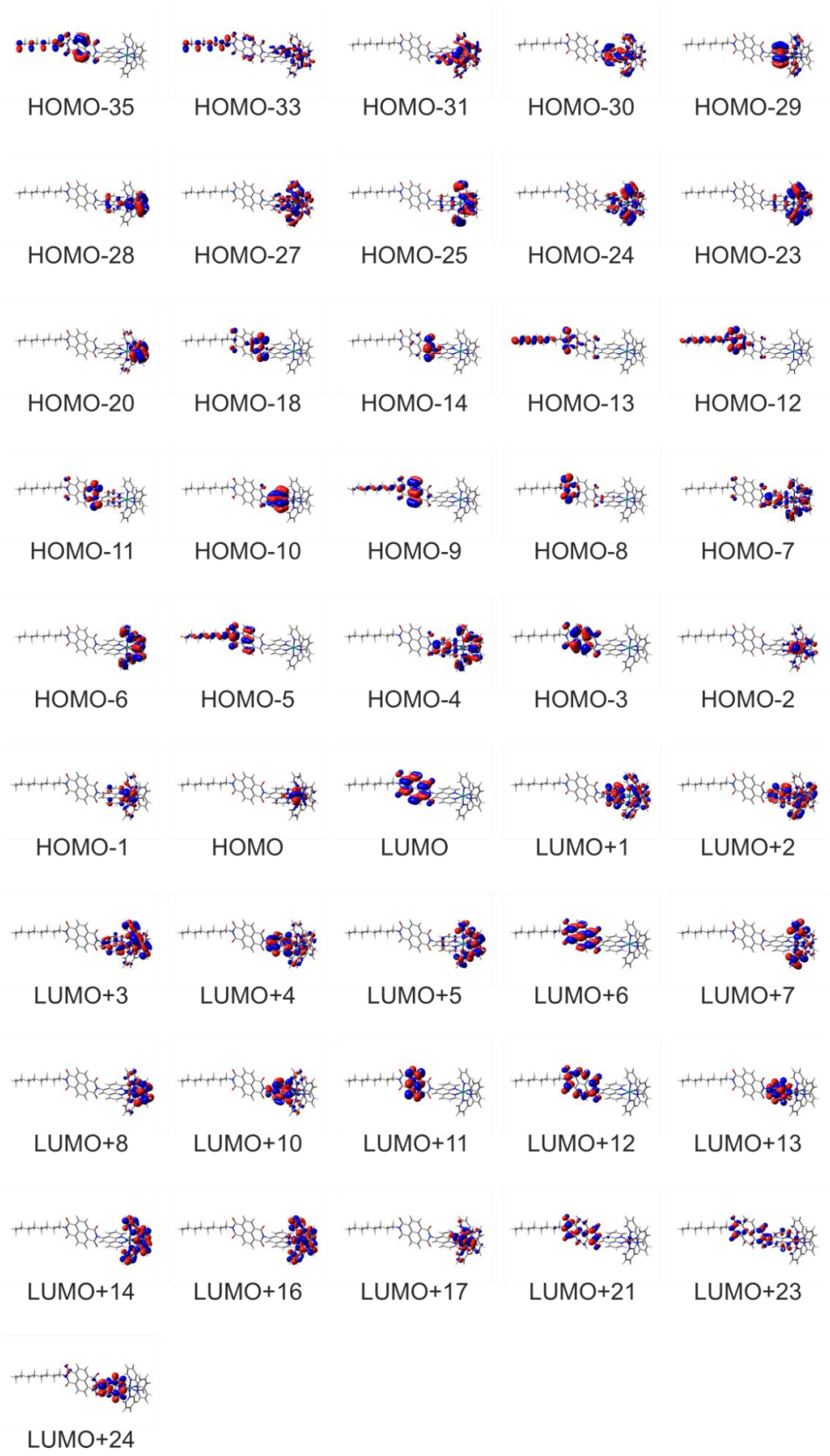


Figure SA3.18 Molecular orbitals involved in electronic transitions of **RuNDI**$^{2+}$ (listed in Table SA3.3).

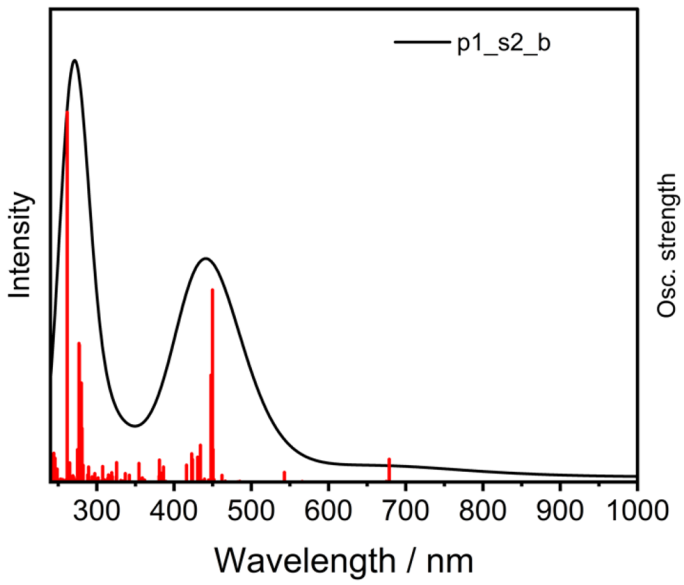


Figure SA3.19 TDDFT-calculated UV-vis absorption spectrum of **RuNDI**$^{+}$.

Table SA3.4 Major electronic excitations in **RuNDI**$^{+}$ determined by TDDFT calculations.

Wavelength (nm)	Osc. str (*f*)	Major contributions (%)
679	0.0480	α–HOSO → α–LUSO+8 (59) α–HOSO → α–LUSO+9 (77)
543	0.0203	α–HOSO → α–LUSO+11 (42) β–HOSO → β–LUSO+3 (82) β–HOSO → β–LUSO+4 (29)
451	0.0690	α–HOSO–4 → α–LUSO (30) α–HOSO–4 → α–LUSO+2 (20) α–HOSO–3 → α–LUSO (27) α–HOSO–3 → α–LUSO+1 (51) β–HOSO–3 → β–LUSO (30) β–HOSO–2 → β–LUSO (28) β–HOSO–2 → β–LUSO+1 (48)
450	0.406	α–HOSO–3 → α–LUSO (36) α–HOSO–3 → α–LUSO+1 (25) α–HOSO → α–LUSO+10 (33) α–HOSO → α–LUSO+11 (45) β–HOSO–2 → β–LUSO (39) β–HOSO–2 → β–LUSO+1 (28) β–HOSO → β–LUSO+3 (31)
448	0.2261	α–HOSO–3 → α–LUSO (43) α–HOSO → α–LUSO+10 (34) α–HOSO → α–LUSO+11 (42) β–HOSO–2 → β–LUSO (44) β–HOSO → β–LUSO+2 (27) β–HOSO → β–LUSO+3 (26)
434.1	0.0777	α–HOSO–4 → α–LUSO (52) α–HOSO–3 → α–LUSO+1 (23) β–HOSO–3 → β–LUSO (61) β–HOSO–3 → β–LUSO+2 (39) β–HOSO–2 → β–LUSO+1 (26)
430.5	0.0525	α–HOSO → α–LUSO+10 (68) α–HOSO → α–LUSO+11 (40) α–HOSO → α–LUSO+12 (26) β–HOSO → β–LUSO+4 (42)

Wavelength (nm)	Osc. str (*f*)	Major contributions (%)
422.9	0.0596	α–HOSO–4 → α–LUSO+1 (40) α–HOSO–3 → α–LUSO+2 (47) α–HOSO–1 → α–LUSO+3 (21) β–HOSO–3 → β–LUSO+1 (40) β–HOSO–2 → β–LUSO+2 (48) β–HOSO–1 → β–LUSO+4 (22)
281	0.1134	α–HOSO–12 → α–LUSO+2 (39) α–HOSO–11 → α–LUSO+1 (30) β–HOSO–15 → β–LUSO (20) β–HOSO–14 → β–LUSO+2 (45) β–HOSO–12 → β–LUSO+1 (23) β–HOSO–11 → β–LUSO (22) β–HOSO–10 → β–LUSO+1 (27)
280	0.2092	α–HOSO–12 → α–LUSO+1 (40) α–HOSO–12 → α–LUSO+2 (22) α–HOSO–11 → α–LUSO+2 (32) β–HOSO–14 → β–LUSO+1 (38) β–HOSO–14 → β–LUSO+2 (29) β–HOSO–12 → β–LUSO+2 (31) β–HOSO–10 → β–LUSO+1 (29)
277.4	0.2892	α–HOSO–12 → α–LUSO+2 (30) α–HOSO–11 → α–LUSO+1 (27) β–HOSO–14 → β–LUSO+2 (34) β–HOSO–12 → β–LUSO+1 (25) β–HOSO → β–LUSO+15 (23)
276.9	0.293	α–HOSO–11 → α–LUSO+1 (22) α–HOSO–2 → α–LUSO+8 (20) α–HOSO–2 → α–LUSO+9 (22) α–HOSO–2 → α–LUSO+15 (27) β–HOSO–14 → β–LUSO+2 (20) β–HOSO–12 → β–LUSO+1 (22) β–HOSO → β–LUSO+15 (47)
275.0	0.0686	α–HOSO–8 → α–LUSO+15 (37) α–HOSO–6 → α–LUSO+15 (38) β–HOSO–11 → β–LUSO+10 (22) β–HOSO–6 → β–LUSO+15 (30) β–HOSO–4 → β–LUSO+15 (50)
262	0.7819	α–HOSO–15 → α–LUSO+2 (51) α–HOSO–10 → α–LUSO+3 (28) β–HOSO–15 → β–LUSO+2 (48) β–HOSO–9 → β–LUSO+4 (27)
245.9	0.0503	α–HOSO–12 → α–LUSO+4 (48) α–HOSO–3 → α–LUSO+10 (41) β–HOSO–14 → β–LUSO+5 (49) β–HOSO–2 → β–LUSO+11 (43)
244.3	0.0608	α–HOSO–7 → α–LUSO+8 (31) α–HOSO–5 → α–LUSO+8 (21) β–HOSO–9 → β–LUSO+5 (25) β–HOSO–7 → β–LUSO+9 (35) β–HOSO–5 → β–LUSO+9 (43) β–HOSO–1 → β–LUSO+12 (26)
240.6	0.0540	α–HOSO–4 → α–LUSO+10 (62) β–HOSO–3 → β–LUSO+11 (63)
237.2	0.1939	α–HOSO–2 → α–LUSO+15 (59) α–HOSO–1 → α–LUSO+15 (29) β–HOSO–16 → β–LUSO+3 (31) β–HOSO → β–LUSO+15 (37)

Wavelength (nm)	Osc. str (*f*)	Major contributions (%)
229.9	0.0855	α–HOSO–9 → α–LUSO+6 (20) α–HOSO–9 → α–LUSO+8 (21) α–HOSO–9 → α–LUSO+9 (27) α–HOSO–8 → α–LUSO+8 (24) α–HOSO–8 → α–LUSO+9 (24) β–HOSO–8 → β–LUSO+10 (47) β–HOSO–6 → β–LUSO+10 (46) β–HOSO–5 → β–LUSO+18 (28)
224.5	0.0705	α–HOSO–32 → α–LUSO (28) α–HOSO–26 → α–LUSO (27) α–HOSO–24 → α–LUSO (21) α–HOSO–10 → α–LUSO+8 (20) β–HOSO–31 → β–LUSO (26) β–HOSO–28 → β–LUSO (20) β–HOSO–25 → β–LUSO (29) β–HOSO–23 → β–LUSO (22) β–HOSO–19 → β–LUSO+3 (23)
222.9	0.1214	α–HOSO–10 → α–LUSO+8 (51) β–HOSO–10 → β–LUSO+9 (21) β–HOSO–9 → β–LUSO+9 (41)
221.0	0.0811	β–HOSO–13 → β–LUSO+8 (20) β–HOSO–13 → β–LUSO+10 (20) β–HOSO–10 → β–LUSO+9 (32) β–HOSO–8 → β–LUSO+9 (40)

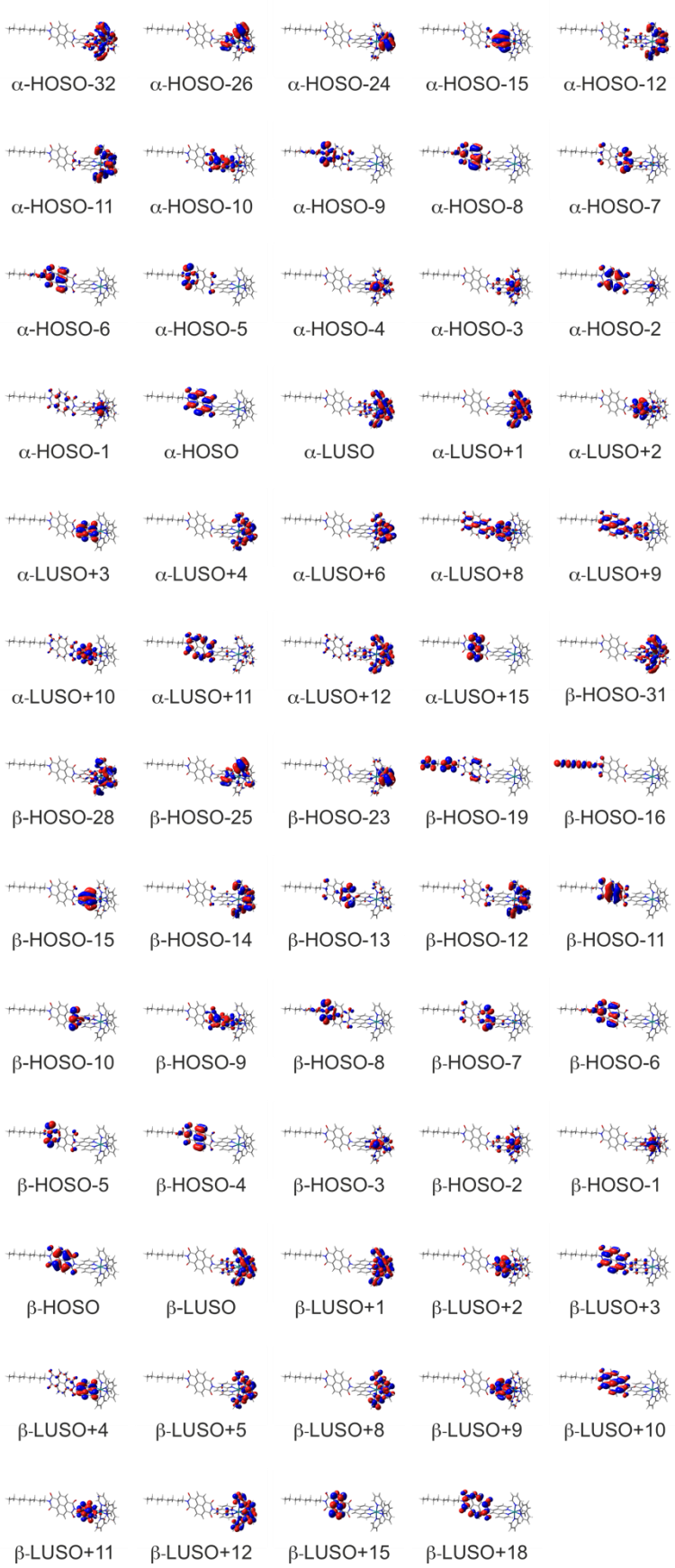


Figure SA3.20 Molecular spin orbitals involved in electronic transitions of **RuNDI**$^{+}$ (listed in Table SA3.4).

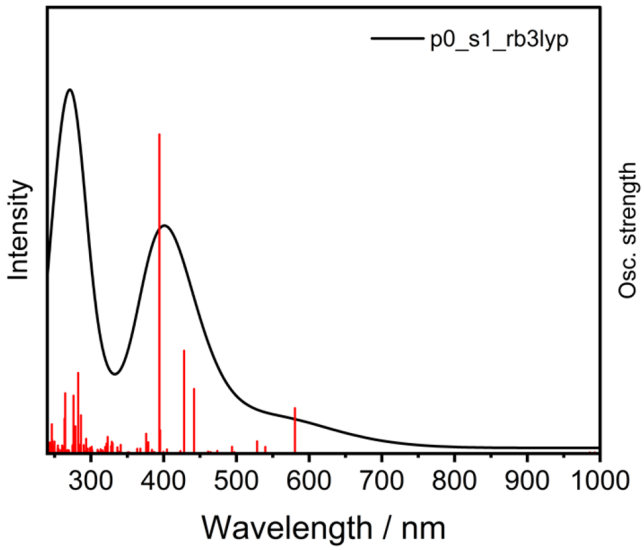


Figure SA3.21 TDDFT-calculated UV-vis absorption spectrum of **RuNDI**.

Table SA3.5 Major electronic excitations in **RuNDI** determined by TDDFT calculations.

Wavelength (nm)	Osc. str (*f*)	Major contributions (%)
8884.2	0.0337	HOMO → LUMO (106) HOMO ← LUMO (79)
580	0.1019	HOMO → LUMO+9 (70)
529	0.0273	HOMO → LUMO+10 (58) HOMO → LUMO+12 (40)
442	0.1449	HOMO–6 → LUMO (60) HOMO–4 → LUMO+1 (34)
428	0.2306	HOMO–6 → LUMO+1 (53) HOMO–4 → LUMO (24) HOMO–4 → LUMO+2 (37)
395	0.0523	HOMO → LUMO+19 (66)
394	0.7151	HOMO → LUMO+16 (47) HOMO → LUMO+17 (41) HOMO → LUMO+19 (22)
286.3	0.0856	HOMO–16 → LUMO+1 (33) HOMO–15 → LUMO+1 (52) HOMO–14 → LUMO+1 (27)
282	0.1806	HOMO–16 → LUMO+1 (56) HOMO–14 → LUMO+1 (20)
281	0.5388	HOMO–16 → LUMO (27) HOMO–15 → LUMO+1 (25) HOMO–14 → LUMO+1 (39)
278.6	0.0610	HOMO–15 → LUMO+2 (27) HOMO–14 → LUMO+2 (62)
276	0.1299	HOMO–16 → LUMO+2 (45) HOMO–15 → LUMO+2 (44)
265	0.1352	HOMO–14 → LUMO+3 (58)
263.8	0.0782	HOMO–15 → LUMO+3 (50) HOMO–10 → LUMO+4 (24) HOMO–2 → LUMO+8 (24)
263	0.6096	HOMO–16 → LUMO+2 (35) HOMO–15 → LUMO+2 (26) HOMO–14 → LUMO+3 (32) HOMO–13 → LUMO+3 (24)
246.3	0.0655	HOMO–3 → LUMO+10 (28) HOMO–3 → LUMO+12 (44)
243	0.2740	HOMO–1 → LUMO+18 (62)
237.3	0.1117	HOMO–17 → LUMO+3 (38) HOMO–9 → LUMO+8 (24) HOMO–1 → LUMO+16 (23)
233.5	0.0786	HOMO–9 → LUMO+9 (31) HOMO–8 → LUMO+9 (39)
228.3	0.0776	HOMO–12 → LUMO+8 (20) HOMO–11 → LUMO+8 (43) HOMO–11 → LUMO+9 (27) HOMO–9 → LUMO+8 (26)
224.0	0.1617	HOMO–13 → LUMO+8 (23) HOMO–12 → LUMO+8 (48) HOMO–11 → LUMO+8 (26) HOMO–10 → LUMO+8 (23)

Wavelength (nm)	Osc. str (*f*)	Major contributions (%)
223.4	0.0670	HOMO–26 → LUMO (23) HOMO–24 → LUMO (28) HOMO–23 → LUMO (45)
220.8	0.2570	HOMO–23 → LUMO+1 (23) HOMO–13 → LUMO+8 (32) HOMO–12 → LUMO+8 (20) HOMO–10 → LUMO+9 (20)
218.7	0.0783	HOMO–26 → LUMO+1 (25) HOMO–18 → LUMO+3 (25) HOMO–10 → LUMO+9 (26)
217.2	0.0987	HOMO–13 → LUMO+8 (21) HOMO–10 → LUMO+9 (45) HOMO–5 → LUMO+12 (22)
214.9	0.0648	HOMO–35 → LUMO (31) HOMO–12 → LUMO+9 (24)
214.6	0.1173	HOMO–35 → LUMO (20) HOMO–12 → LUMO+9 (34) HOMO–8 → LUMO+10 (20)
207.4	0.0940	HOMO–15 → LUMO+8 (20) HOMO–10 → LUMO+10 (27) HOMO–10 → LUMO+12 (22) HOMO–9 → LUMO+10 (22) HOMO–8 → LUMO+12 (22)
207.2	0.0953	HOMO–34 → LUMO (22) HOMO–23 → LUMO+3 (20) HOMO–15 → LUMO+8 (24)
206.2	0.2551	HOMO–8 → LUMO+18 (29) HOMO–5 → LUMO+18 (47)
201.1	0.0885	HOMO–34 → LUMO+2 (32) HOMO–28 → LUMO+3 (34) HOMO–3 → LUMO+18 (22)
201.1	0.2050	HOMO–34 → LUMO+2 (30) HOMO–9 → LUMO+18 (22) HOMO–8 → LUMO+18 (25)
201.0	0.0523	HOMO–4 → LUMO+16 (40) HOMO–4 → LUMO+17 (30) HOMO–3 → LUMO+18 (21)
200.8	0.0739	HOMO–37 → LUMO+1 (25) HOMO–19 → LUMO+4 (50)
199.9	0.1044	HOMO–10 → LUMO+11 (24) HOMO–9 → LUMO+16 (21) HOMO–8 → LUMO+16 (28) HOMO–4 → LUMO+16 (22)
199.9	0.0560	HOMO–10 → LUMO+11 (39)

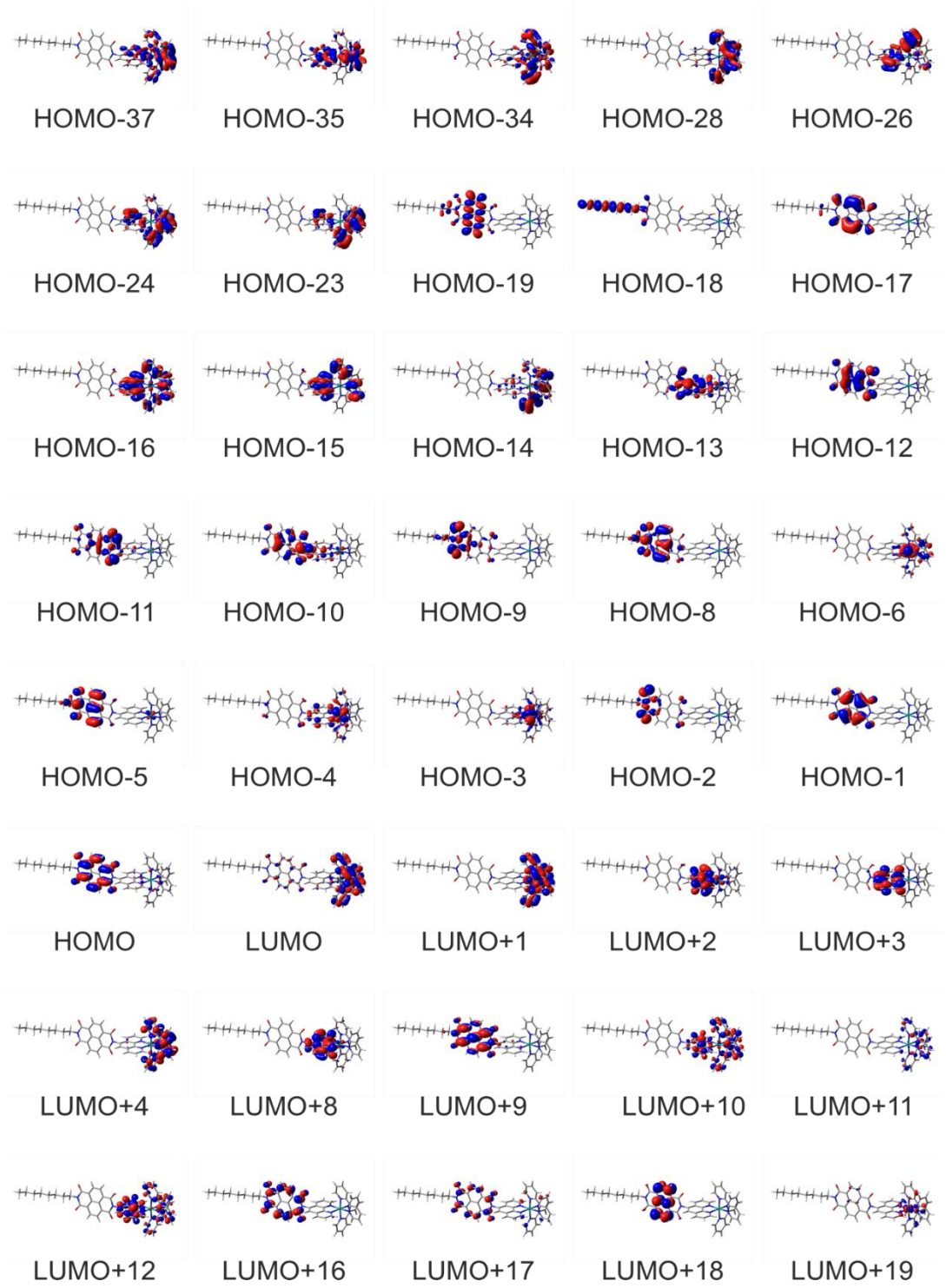


Figure SA3.22 Molecular orbitals involved in electronic transitions of **RuNDI** (listed in Table SA3.5).

Electrochemistry

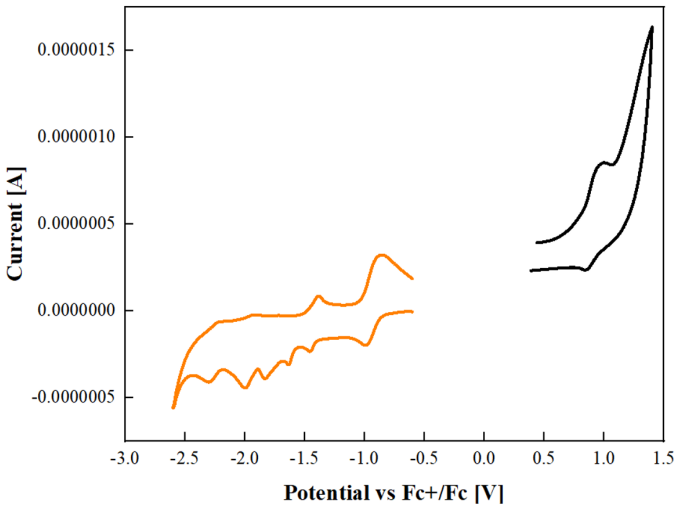


Figure SA3.23 A cyclic voltammogram of **RuNDI**$^{2+}$ in THF/TBAH showing the reductions step to the corresponding monocationic, neutral, anionic, dianionic, and trianionic species and also $Ru^{2+/3+}$ oxidation. Experimental conditions: glassy carbon working electrode, T = 298 K, v = 100 mV/s.

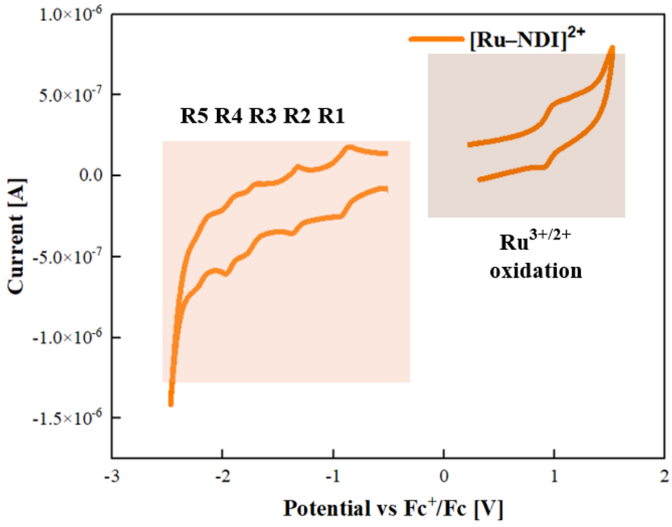


Figure SA3.24 A cyclic voltammogram of **RuNDI**$^{2+}$ in acetonitrile/TBAH showing similar pattern as in DMF. Experimental conditions: Pt microdisc working electrode, T = 298 K, v = 100 mV/s.

UV-vis spectroelectrochemistry

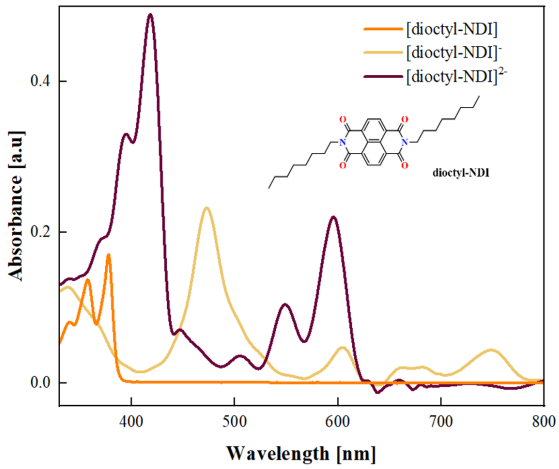


Figure SA3.25 The UV-vis absorption spectra of the reference NDI compound (R_1-NDI-R_1 = dioctyl-NDI), parent species [dioctyl-NDI] (orange), one electron-reduced [dioctyl-NDI)]$^{-}$ (yellow), and two-electron-reduced [dioctyl-NDI)]$^{2-}$ (brown) in ACN/TBAH. Experimental conditions: Pt minigrid working electrode, OTTLE cell, T = 298 K.

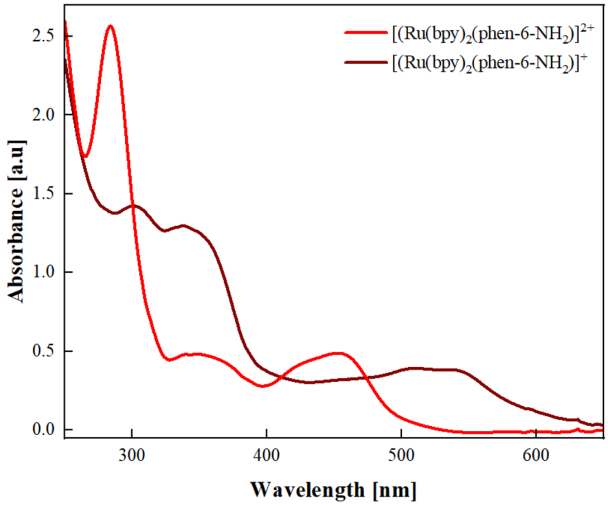


Figure SA3.26 The UV-vis absorption spectra of [(Ru(bpy)$_2$(phen-6-NH$_2$)]$^{2+}$ (red), and electron-reduced [(Ru(bpy)$_2$(phen-6-NH$_2$)]$^{+}$ (brown) in ACN/TBAH. Experimental conditions: Pt minigrid working electrode, OTTLE cell, T = 298 K.

Time-resolved infrared spectroscopy

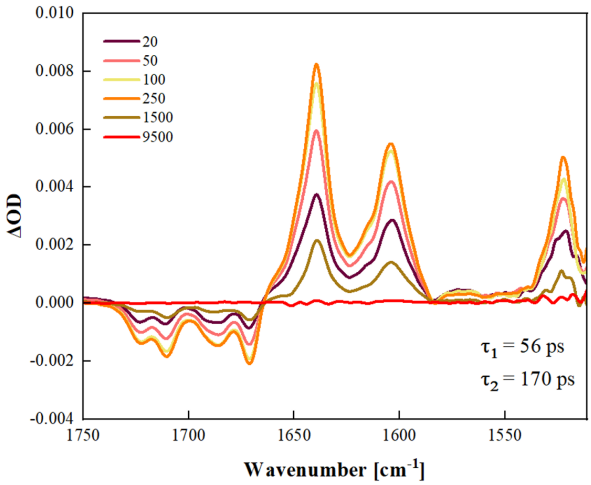


Figure SA3.27 TRIR spectra recorded upon 420-nm photoexcitation of parent **RuNDI**$^{2+}$ in THF.

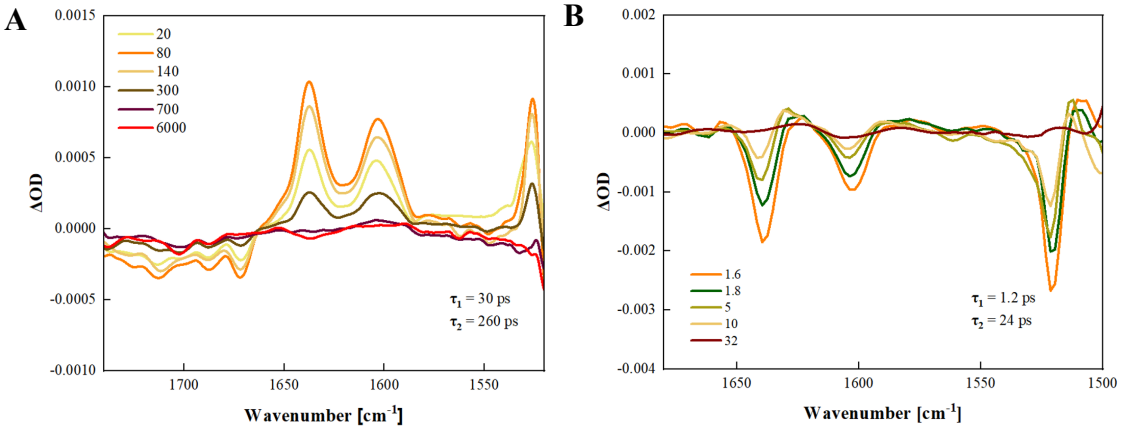


Figure SA3.28 (A) TRIR spectra recorded upon 510-nm photoexcitation of parent **RuNDI**$^{2+}$ and **(B)** one-electron-reduced **RuNDI**$^{+}$ in ACN/TBAH, obtained in situ from **RuNDI**$^{2+}$ using an adapted OTTLE cell.

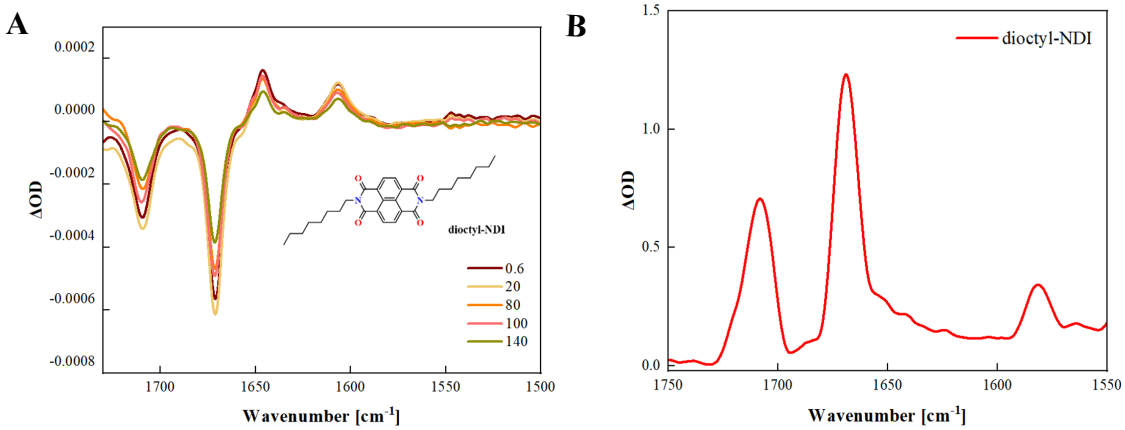


Figure SA3.29 (A) TRIR spectra recorded upon 365-nm photoexcitation of the reference NDI compound (R_1-NDI-R_1 = dioctyl-NDI), parent species [dioctyl-NDI] in THF. **(B)** The FTIR of the NDI compound recorded in THF.

Nanosecond transient absorption studies in solution

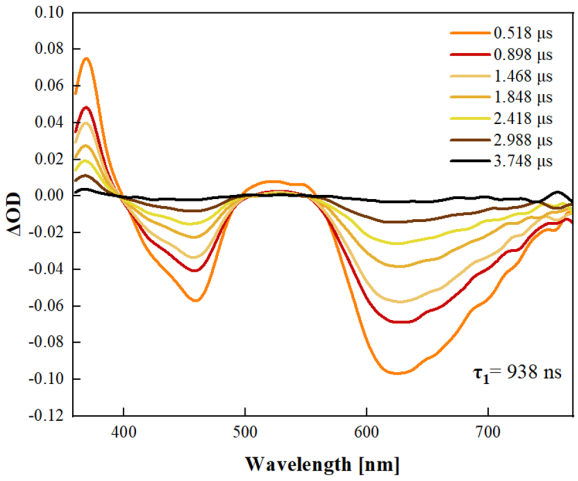


Figure SA3.30 Nanosecond transient absorption spectrum of the ruthenium precursor, $[Ru(bpy)_2(phen\text{-}6\text{-}NH_2)]^{2+}$ under an nitrogen atmosphere in acetonitrile, following excitation at 355 nm at different time delays.

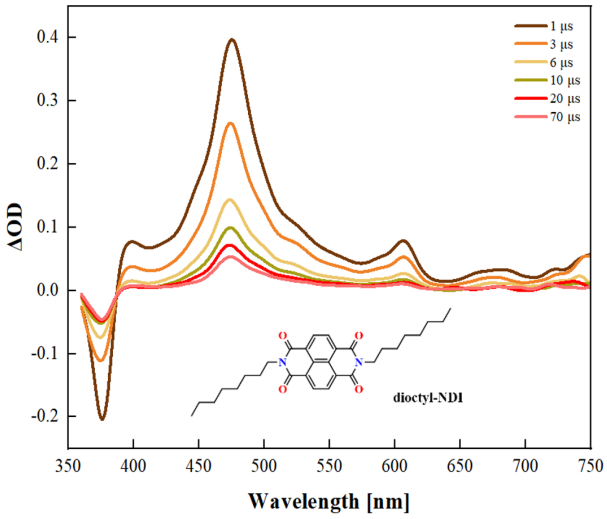


Figure SA3.31 Nanosecond transient absorption spectrum of the reference NDI compound (R_1-NDI-R_1 = dioctyl-NDI), under an nitrogen atmosphere in acetonitrile, following excitation at 355 nm at different time delays.

Nanosecond transient absorption studies under photocatalytic conditions

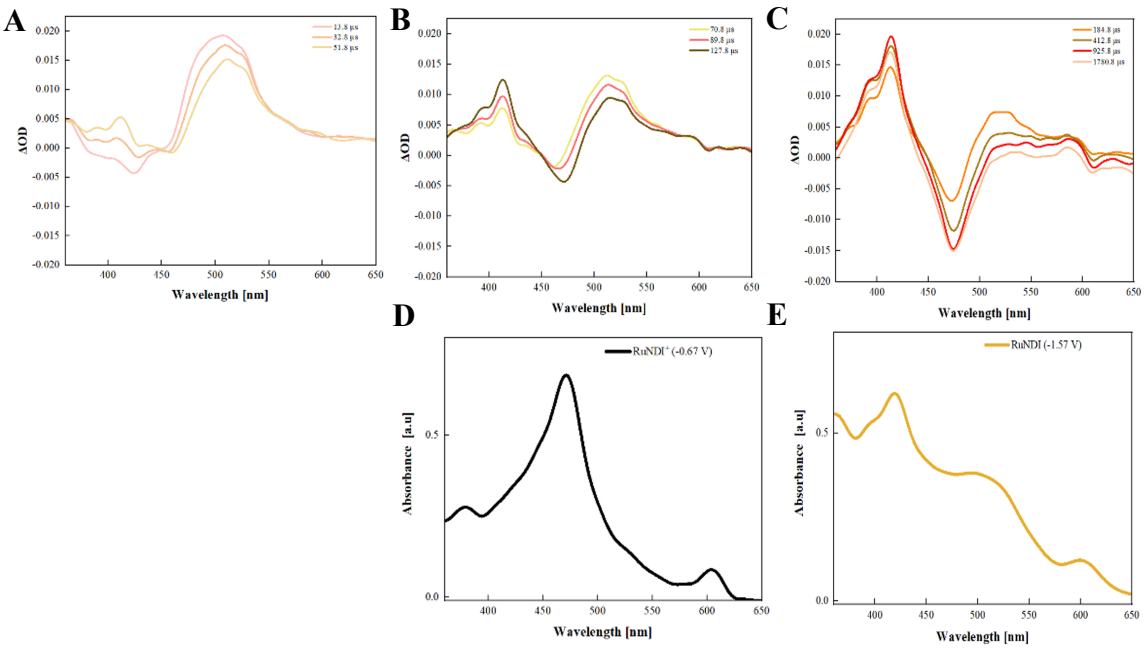


Figure SA3.32 Nanosecond transient absorption spectrum of **Ru-NDI^{2+}** at different time decay constants under an nitrogen atmosphere in acetonitrile/TEA/H_2O/[$Pt(DMSO)_2I_2$] following excitation at 355 nm at different time delays. Samples were degassed using three freeze-pump-thaw cycles. **(A)** indicates reduced species of ruthenium, **(B)** and **(C)** indicate formation of the reduced NDI species supported by UV-vis-SEC experiments **(D** and **E)**.

Photocatalysis

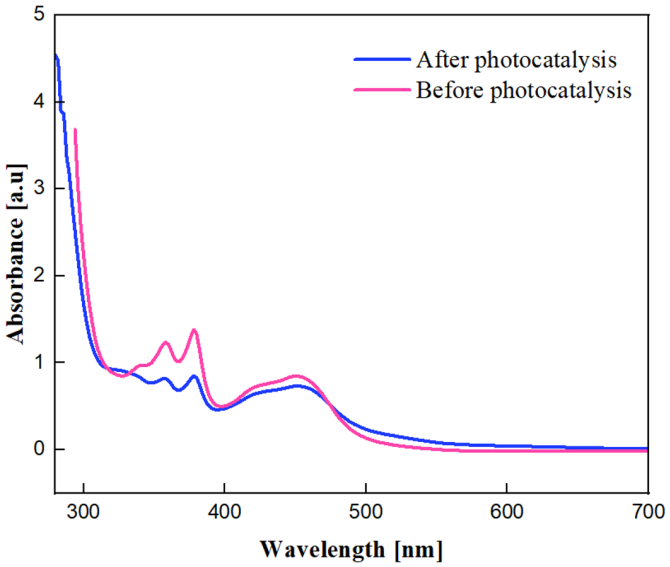


Figure SA3.33 The UV-vis spectrum of **RuNDI^{2+}** in a mixture of acetonitrile, triethylamine and water (65:30:5 ratio) was recorded before (pink) and after (blue) 24 hours of irradiation with a 470 nm light source.

References:

[1]. Ghule, N. V., La, D. D., Bhosale, R. S., Al Kobaisi, M., Raynor, A. M., Bhosale, S. V., & Bhosale, S. V. (2016). Effect of Amide Hydrogen Bonding Interaction on Supramolecular Self-Assembly of Naphthalene Diimide Amphiphiles with Aggregation Induced Emission. ChemistryOpen, 5(2), 157–163. https://doi.org/10.1002/open.201500201

[2]. Cerpentier, F. J., Karlsson, J., Lalrempuia, R., Brandon, M. P., Sazanovich, I. V., Greetham, G. M., Gibson, E. A., & Pryce, M. T. (2021). Ruthenium Assemblies for CO_2 Reduction and H_2 Generation: Time Resolved Infrared Spectroscopy, Spectroelectrochemistry and a Photocatalysis Study in Solution and on NiO. Frontiers in Chemistry, 9. https://doi.org/10.3389/fchem.2021.795877

Appendix B

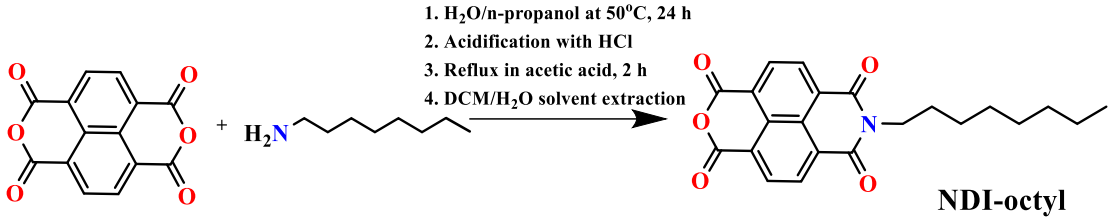
CHAPTER 4

Time-Resolved Infrared Spectroscopy, Spectroelectrochemical, and Transient Absorption Studies of a Ruthenium-Naphthalene Diimide Ester Complex: Insights into Charge Transfer Dynamics and the Excited States Populated in Solution and on a NiO Surface - Supplementary Information

Experimental

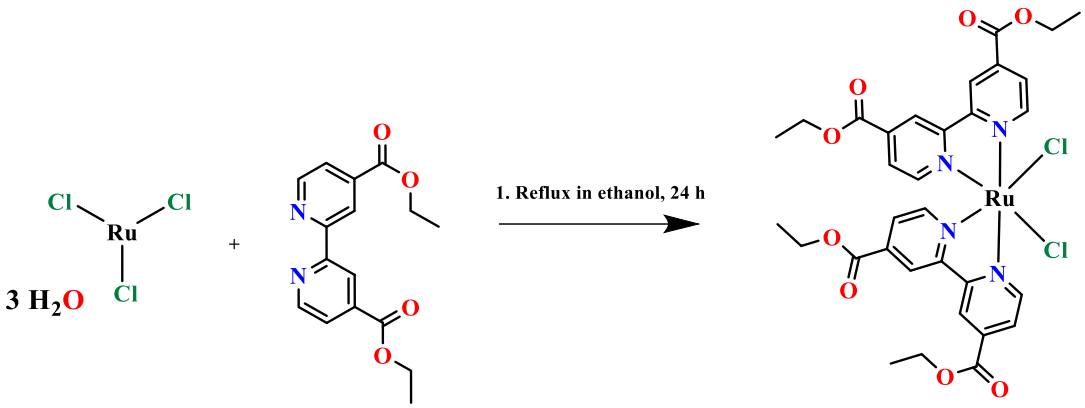
Synthesis

N-octyl-1,4,5,8-napthalene-tetra-carboxylic monoanhydride (NDI-octyl)



The preparation of NDI-octyl ligand was carried out following the procedure in the literature as well as the one described in Chapter 3 [1]. In a 1:1 solvent ratio of water and isopropanol, 1,4,5,8-naphthalenetetracarboxylic dianhydride (NDA) (1g, 3.73 mmol) and octyl amine (2 mL, 1.56 g, 12 mmol, excess) were added. The reaction mixture was heated to 50°C for 24 hours. Then the solution was acidified using 1 M HCl to pH 1 to obtain beige coloured precipitate. The reaction mixture was filtered and refluxed in acetic acid (excess) for 1h to give yellow clear solution, which was subsequently cooled at room temperature. The obtained precipitate was purified using solvent extraction, diluted by DCM (200 – 300 mL) and then H_2O was added. The organic layer was dried using anhydrous Na_2SO_4 and then reduced in volume under vacuum. The product was washed with ethanol, hexane, and small amount of diethyl ether. ^{1}H-NMR (600 MHz, $DMSOd_6$): δ (ppm) 0.85 (t, 3H), 1.2–1.4 (m, 10H), 1.79 (t, 2H), 4.21 (t, 2H), 8.75 (s, 4H)

$Ru(dceb)_2Cl_2$

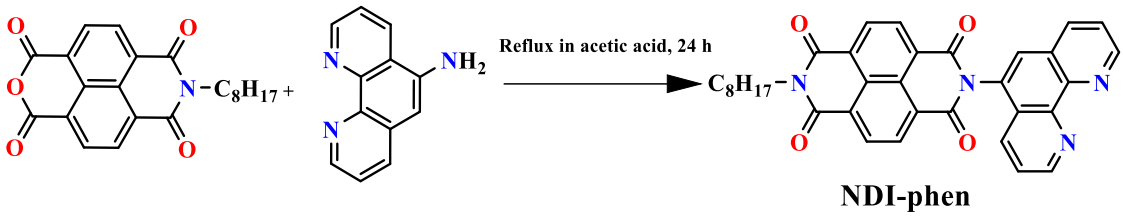


$Ru(dceb)_2Cl_2$

The $Ru(dceb)_2Cl_2$ was synthesised following the method reported in the literature [2]. 0.42 g (2.05 mmol) of $RuCl_3.xH_2O$ was dissolved in 40 mL ethanol. The solution was purged with N_2 for 5 minutes and heated to reflux for 20 minutes. 1.23 g (4.1 mmol) of (4,4′-di(carboxyethyl)bipyridine ligand (dceb) was added over a 30-minute period. The mixture was heated to reflux for 24 hours. The ethanol was removed under reduced pressure, and the remaining solid was suspended in 50 mL of ether. The suspension was stirred for 30 minutes, and the solid was collected by vacuum filtration. The microcrystalline product was washed with diethyl ether (10 mL) and airdried to yield $Ru(dceb)_2Cl_2$ as a brown-black powder (1.20 g, 1.56 mmol, 76%). ^{1}H-NMR (DMSO-d_6, 600 MHz): 1.31 (t, 6H), 1.46 (t, 6H), 4.36 (q, 4H), 4.53 (dd, 4H), 7.50 (dd, 2H), 7.77 (dd, 2H), 8.27 (dd, 2H), 8.96 (s, 2H), 9.14 (s, 2H), 10.12 (d, 2H).

^{1}H-NMR (DMSOd_6): 7.09 (m, 2H), 7.50 (m, 2H), 7.67 (m, 2H), 7.76 (m, 2H), 8.05 (m, 2H), 8.48 (m, 2H), 8.63 (m, 2H).

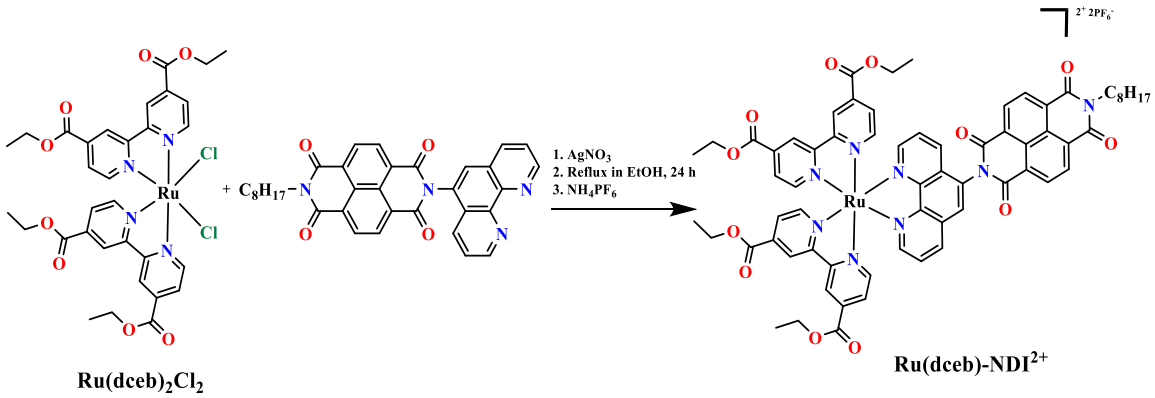
2-octyl-7-(1,10-phenanthrolin-5-yl)benzo[lmn][3,8]phenanthroline-1,3,6,8(2H,7H)-tetraone *(*NDI-phen)



NDI-phen

0.2 g (0.527 mmol) of 7-octyl-1H-isochromeno[6,5,4-def]isoquinoline-1,3,6,8(7H)-tetraone and 0.123 g (0.63 mmol) of 5-amino-1,10-phenanthroline were dissolved in 20 mL of glacial acetic acid [3]. The solution was brought to reflux for 24 hours resulting in a bright orange solution. The mixture was allowed to cool to room temperature and was slowly added to 50 mL of a saturated sodium carbonate solution. The resulting precipitate was collected by vacuum filtration. To remove residual acetic acid and starting materials the solid was suspended in 50 mL ethanol and refluxed for 30 minutes. The suspension was cooled to room temperature, and the product was collected by vacuum filtration, washed with diethyl ether (10 mL) and airdried to yield the NDI-phen ligand as a beige powder (0.180 g, 0.32 mmol, 61%). ^{1}H-NMR ($CDCl_3$, 600 MHz): 0.89 (t, 3H), 1.27–1.37 (m, 6H), 1.40 (q, 2H), 1.47 (q, 2H), 1.78 (q, 4H), 4.25 (t, 2H), 7.61 (dd, 1H), 7.73 (dd, 1H), 7.91 (s, 1H), 8.01 (dd, 1H), 8.31 (dd, 1H), 8.87 (s, 4H), 9.26 (d, 1H), 9.31 (dd, 1H).

Ru(dceb)-NDI^{2+}



The complex was synthesised by modified reactions reported in the literature [4, 5]. 0.33 g (0.44 mmol) of $Ru(dceb)_2Cl_2$ was dissolved in 40 mL of ethanol. The solution was purged with N_2 for 5 minutes. 0.22 g (1.32 mmol, 3 equivalents) of $AgNO_3$ was added and the solution was refluxed in the absence of light for 1 hour. The purple solution was filtered over celite, the filtrated was transferred to a clean round bottom flask and 0.247 g (0.44 mmol) of NDI-phen ligand was added. The solution was refluxed for 24 hours resulting in a dark red/brown solution. The ethanol was removed under reduced pressure, and the residue was dissolved in 20 mL of acetonitrile. 0.40 g (2.2 mmol, 5 equivalents) of ammonium hexafluorophosphate in 5 mL of acetonitrile was added to the solution. The solution was left to stir for 5 minutes, and the acetonitrile was removed under reduced pressure. 50 mL of water was added to the residue, and the suspension was allowed to stir for 10 minutes. The dark red precipitate was collected by vacuum filtration and purified by column chromatography using SiO_2 as the stationary phase and 10:1:0.1 acetonitrile:water:20% aqueous potassium nitrate solution as the mobile phase. The desired product eluded as a red band. Acetonitrile was removed from the collected fractions, 50 mL of water was added, and the product was precipitated using a small amount of aqueous potassium hexafluorophosphate solution. The precipitate was collected by vacuum filtration, washed with 10 mL of water and 10 mL of diethyl ether and airdried to yield **Ru(dceb)-NDI^{2+}** as a dark red microcrystalline material (0.229 g, 0.15 mmol, 34%). ^{1}H-NMR (CD_3CN, 600 MHz): 0.89 (t, 3H), 1.31 (m, 8H), 1.41 (m, 14H), 1.76 (q, 2H), 4.15 (t, 2H), 4.42–4.52 (m, 8H), 7.70 (dd, 1H), 7.76 (dd, 1H), 7.79 (dd, 1H), 7.82 (dd, 1H), 7.84 (d, 1H), 7.86–7.90 (m, 3H), 8.02 (d, 1H), 8.03 (d, 1H), 8.10 (d, 1H), 8.12 (d, 1H), 8.43 (s, 1H), 8.59 (d, 1H), 8.72–8.79 (m, 5H), 9.08 (dd, 2H), 9.10 (dd, 2H). ^{13}C-NMR (CD_3CN, 150 MHz): 13.97, 14.00, 14.03, 22.97, 27.42, 28.23, 29.53, 29.59, 32.15, 41.24, 63.34, 124.35, 124.38, 124.42, 127.11, 127.14, 127.18, 127.21, 127.23, 127.28, 127.49, 128.11, 128.36, 129.77, 129.84, 130.89, 131.06, 131.10, 131.71,

131.74, 133.50, 134.06, 138.77, 140.02, 140.05, 140.07, 147.64 148.01, 153.69, 153.84, 153.97, 154.05, 154.06, 154.29, 158.04, 158.12, 158.43, 158.46, 163.48, 163.96, 163.99, 164.01, 164.11. ESI mass spectrometry: $C_{66}H_{60}N_8O_{12}Ru$ $[M]^{2+}$ calculated at m/z = 629.1691 and found at 629.1682.

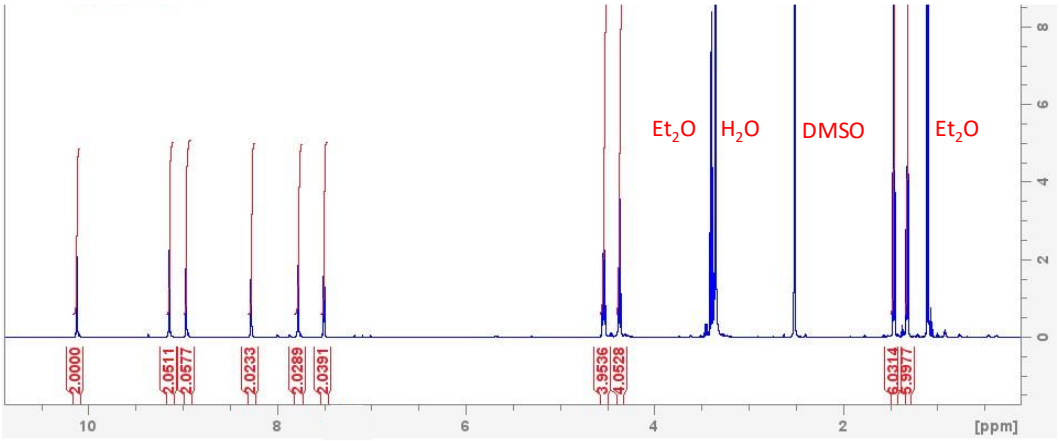


Figure SB4.1 ^{1}H-NMR of **Ru(dceb)$_2$Cl$_2$** in DMSO-d$_6$.

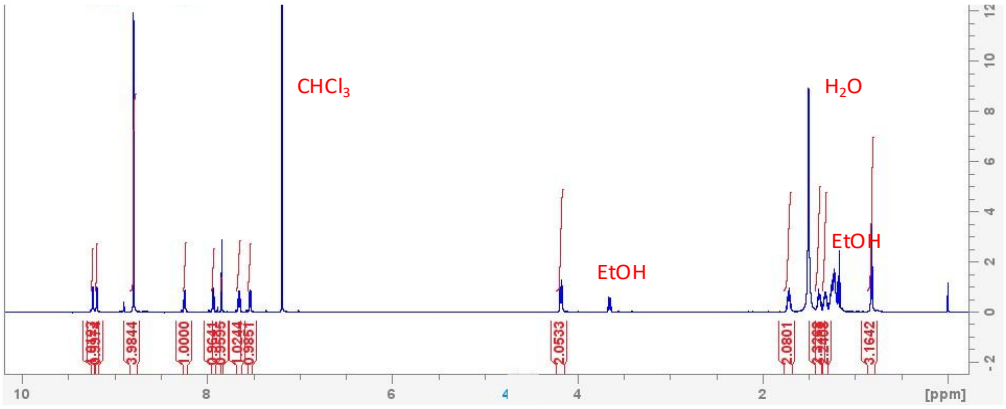


Figure SB4.2 ^{1}H-NMR of the **NDI-phen** ligand in CDCl$_3$-d$_6$.

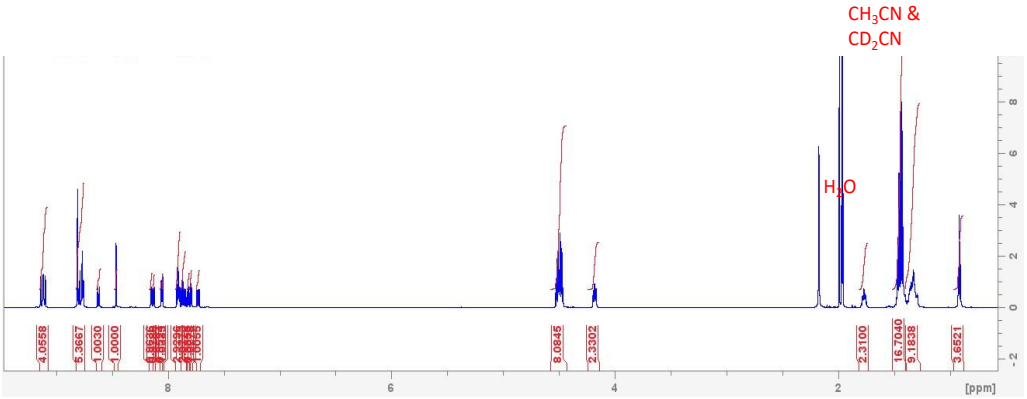


Figure SB4.3 ^{1}H-NMR of **Ru(dceb)-NDI^{2+}** in CD$_3$CN-d$_6$.

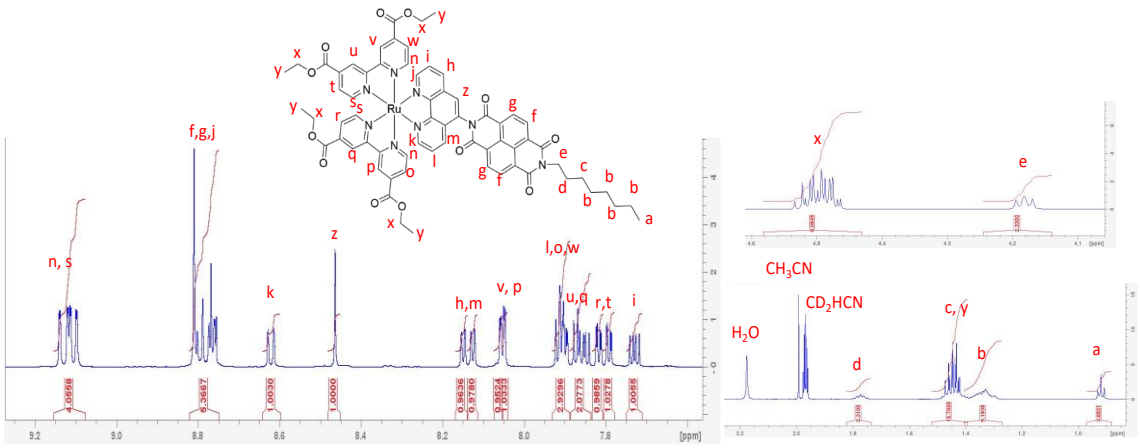


Figure SB4.4 ^{1}H-NMR of **Ru(dceb)-NDI^{2+}** in CD_3CN-d_6 with assignments.

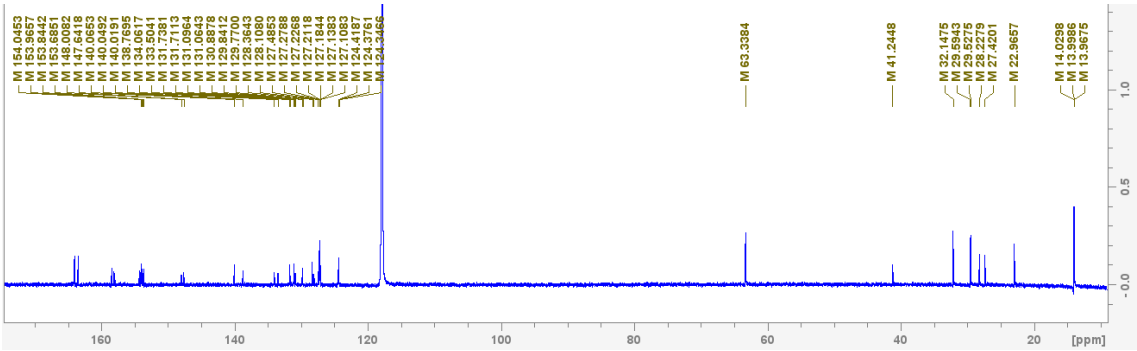


Figure SB4.5 ^{13}C-NMR of **Ru(dceb)-NDI^{2+}** in CD_3CN-d_6.

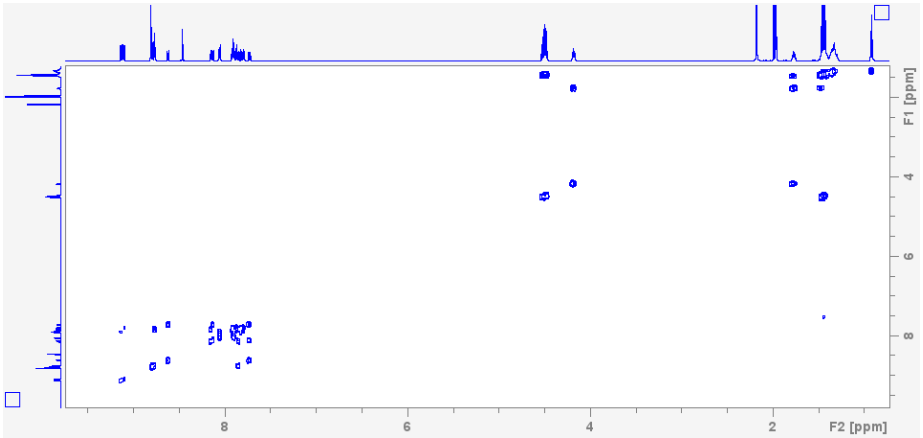


Figure SB4.6 COSY spectrum of **Ru(dceb)-NDI^{2+}**.

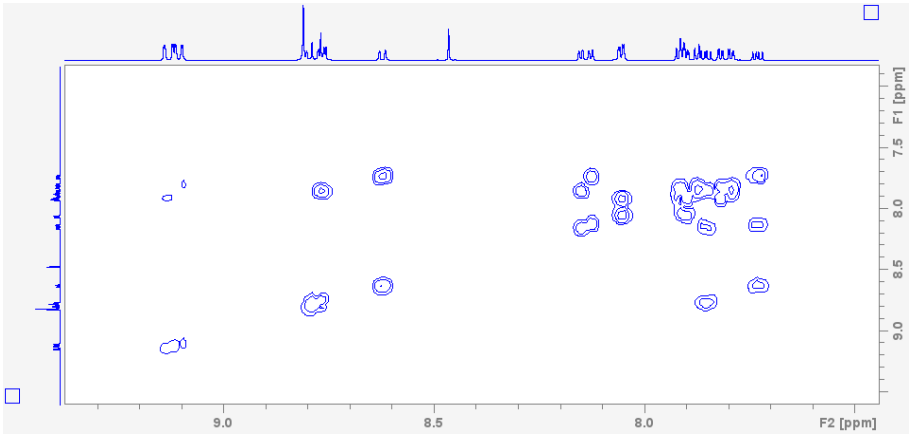


Figure SB4.7 Aromatic region of the COSY spectrum of **Ru(dceb)-NDI^{2+}**.

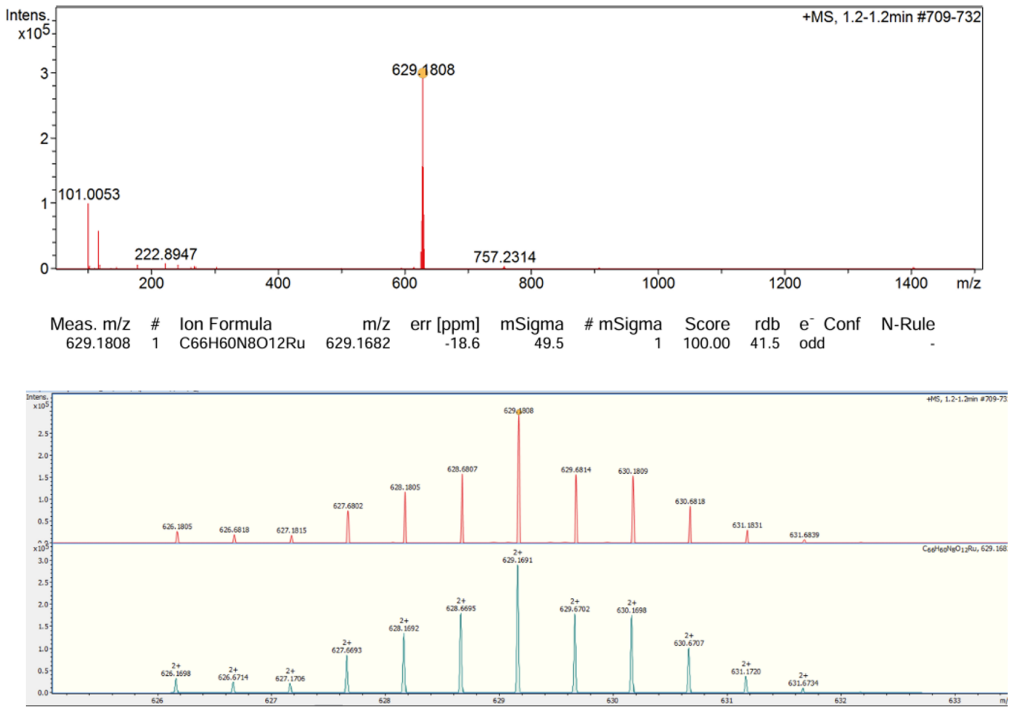


Figure SB4.8 Mass spectrometry results (ESI mode) for **Ru(dceb)-NDI^{2+}**. The measurements were carried out by researchers at the University of Bath.

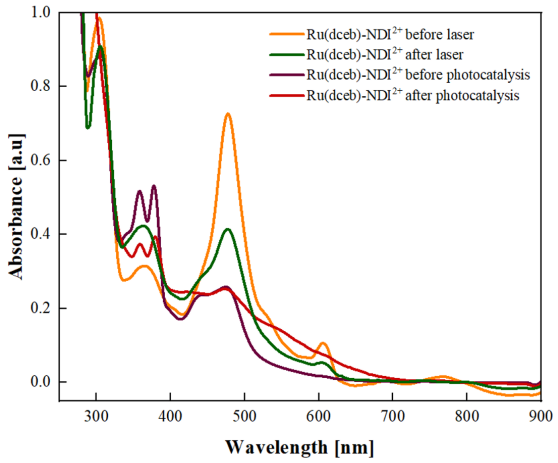


Figure SB4.9 UV-vis absorption spectra of **Ru(dceb)-NDI^{2+}**, before and after photocatalysis (brown and red) and before and after laser studies under photocatalytic conditions (orange and green lines).

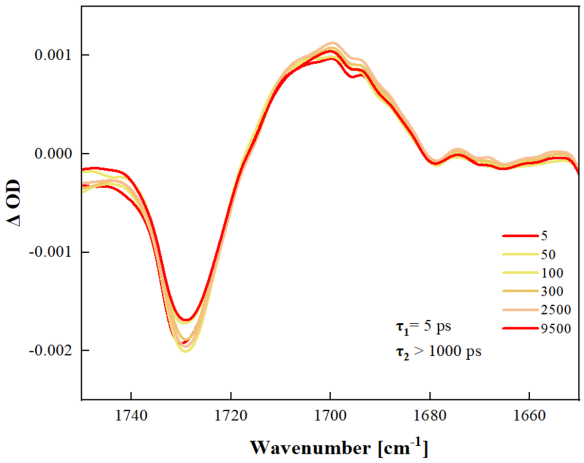


Figure SB4.10 TRIR spectra recorded upon 510-nm photoexcitation of parent **Ru(dceb-NDI^{2+}** in acetonitrile, using Harrick cell.

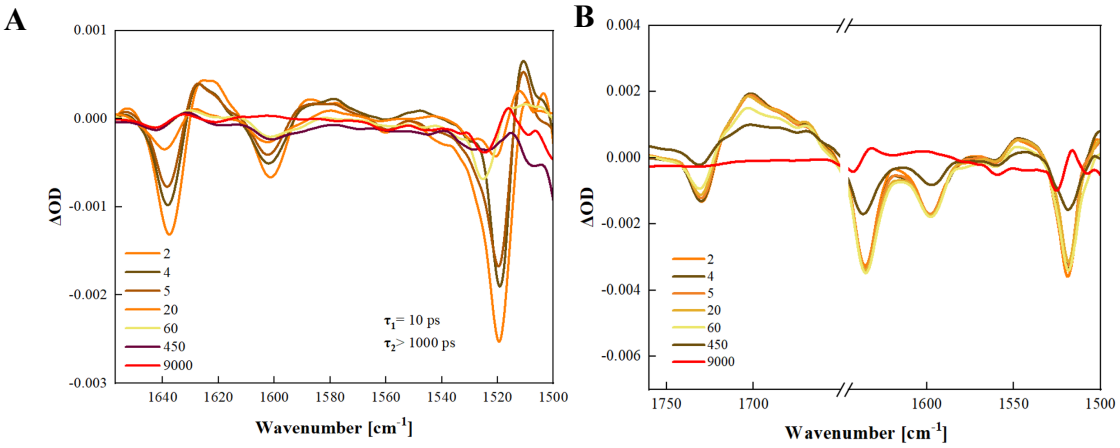


Figure SB4.11 (A) TRIR spectra recorded upon 510-nm photoexcitation of one-electron-reduced **Ru(dceb)-NDI^{+}** in ACN/TBAH in the range of 1500 – 1650 cm^{-1}, **(B)** TRIR spectra recorded upon 510-nm photoexcitation of one-electron-reduced **Ru(dceb)-NDI^{+}** in ACN/TBAH in the range of 1500 – 1760 cm^{-1}, obtained in situ from **Ru(dceb)-NDI^{2+}** using an adapted OTTLE cell.

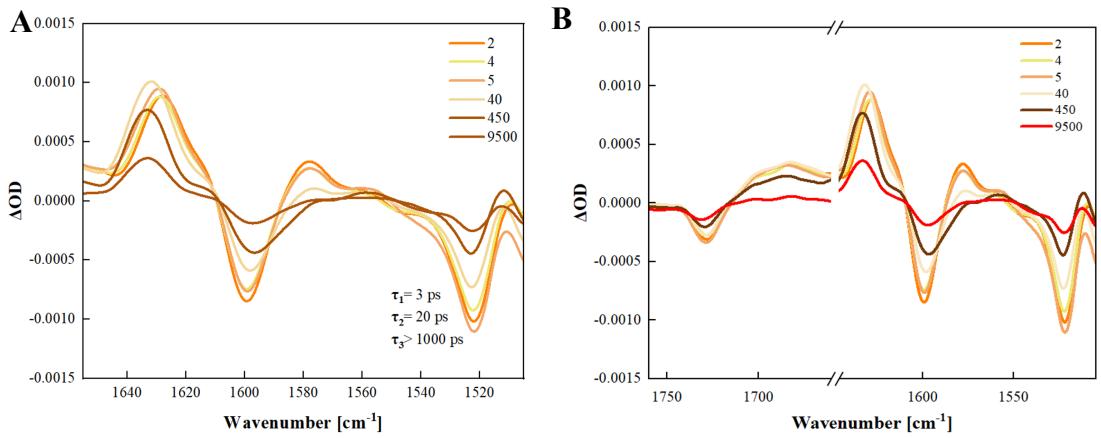


Figure SB4.12 (A) TRIR spectra recorded upon 600-nm photoexcitation of two-electron-reduced **Ru(dceb)-NDI** in ACN/TBAH in the range of 1500 – 1650 cm^{-1}, **(B)** TRIR spectra recorded upon 600-nm photoexcitation of two-electron-reduced **Ru(dceb)-NDI** in ACN/TBAH in the range of 1500 – 1760 cm^{-1}, obtained in situ from **Ru(dceb)-NDI**$^{2+}$ using an adapted OTTLE cell.

References

[1]. Ghule, N. V., La, D. D., Bhosale, R. S., Al Kobaisi, M., Raynor, A. M., Bhosale, S. V., & Bhosale, S. V. (2016). Effect of Amide Hydrogen Bonding Interaction on Supramolecular Self-Assembly of Naphthalene Diimide Amphiphiles with Aggregation Induced Emission. ChemistryOpen, 5(2), 157–163. https://doi.org/10.1002/open.201500201

[2]. Cerpentier, F. J., Karlsson, J., Lalrempuia, R., Brandon, M. P., Sazanovich, I. V., Greetham, G. M., Gibson, E. A., & Pryce, M. T. (2021). Ruthenium Assemblies for CO_2 Reduction and H_2 Generation: Time Resolved Infrared Spectroscopy, Spectroelectrochemistry and a Photocatalysis Study in Solution and on NiO. Frontiers in Chemistry, 9. https://doi.org/10.3389/fchem.2021.795877

[3]. Sur, S., Tiwari, V., Sinha, D., Kamran, M. Z., Dubey, K. D., Suresh Kumar, G., & Tandon, V. (2017). Naphthalenediimide-Linked Bisbenzimidazole Derivatives as Telomeric G-Quadruplex-Stabilizing Ligands with Improved Anticancer Activity. ACS Omega, 2(3), 966–980. https://doi.org/10.1021/acsomega.6b00523

[4]. Ioachim, E., Medlycott, E. A., Hanan, G. S., Loiseau, F., & Campagna, S. (2006). Synthesis and properties of red emitter Ru(II) complexes based on 6,6′-disubstituted-4,4′-bipyrimidine. Inorganica Chimica Acta, 359(3), 766–774. https://doi.org/10.1016/j.ica.2005.03.057

[5]. Bhuiyan, A. A., Dossey, R., Anderson, T. J., Millett, F., & Durham, B. (2008). Synthesis and Characterization of Ruthenium(II) Phenanthroline Complexes Containing Quaternary Amine Substituents. Journal of Coordination Chemistry, 61(13), 2009–2016. https://doi.org/10.1080/00958970701861367

Appendix C

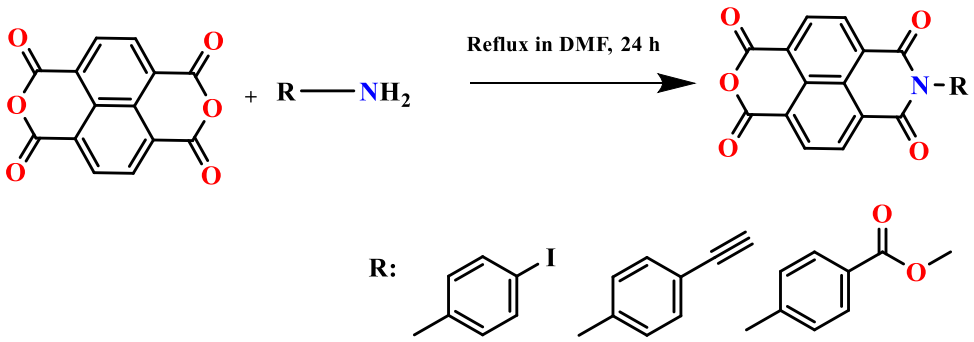
CHAPTER 5

Photophysical Properties and Photocatalytic Performance of Ruthenium (II)-Naphthalene Diimide Photosensitisers/Photocatalysts for H_2 Evolution and CO_2 Reduction: Insights from Time-Resolved Infrared, Ultrafast Transient Absorption, and NiO Surface Studies - Supplementary Information

EXPERIMENTAL

Synthesis

R-1,4,5,8-napthalene-tetra-carboxylic monoanhydride (NDI-R)



All NDI-based ligands (NDI-R) were synthesised using the same procedure. R ligand (1.09 mmol), where R= 4-iodoaniline, methyl 4-aminobenzoate, or 4-ethynylaniline and n-octyl-1,4,5,8-napthalene-tetra-carboxylic monoanhydride (NDA) (2.18 mmol) were refluxed in dry degassed DMF at 155°C for 24 hours with the protection of nitrogen [1]. The solvent was reduced, and the crude product was dissolved in a small volume of DMF (0.5 – 1.0 ml), and diethyl ether was added (~ 20 – 30 ml). The product precipitated out of solution as a beige solid and it was washed with diethyl ether and water. In order to remove naphthalene diimide starting material (NDA), the sample was dissolved in ethanol and refluxed for 3 hours. The product was filtered via hot filtration. All ligands namely NDI-iodine, NDI-ethynyl and NDI-benzoate contained some extent of impurities, hence, their purification was carried out in the next steps of the synthesis.

^{1}H-NMR (600 MHz, $DMSOd_6$): **NDI-iodine** δ (ppm) 7.28 (d, 2H), 7.93 (d, 2H), 8.72 (dd, 4H)

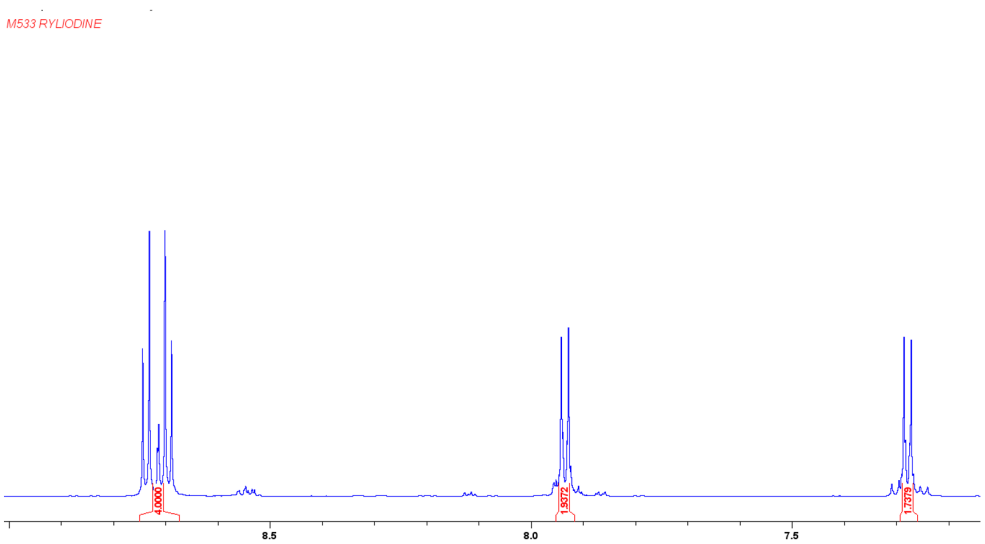


Figure SC5.1 ^{1}H-NMR of **NDI-iodine** in DMSO-d_6.

^{1}H-NMR (600 MHz, DMSOd_6): **NDI-ethynyl** δ (ppm) 4.30 (s, 1H), 7.46 (d, 2H), 7.66 (d, 2H), 8.72 (dd, 4H)

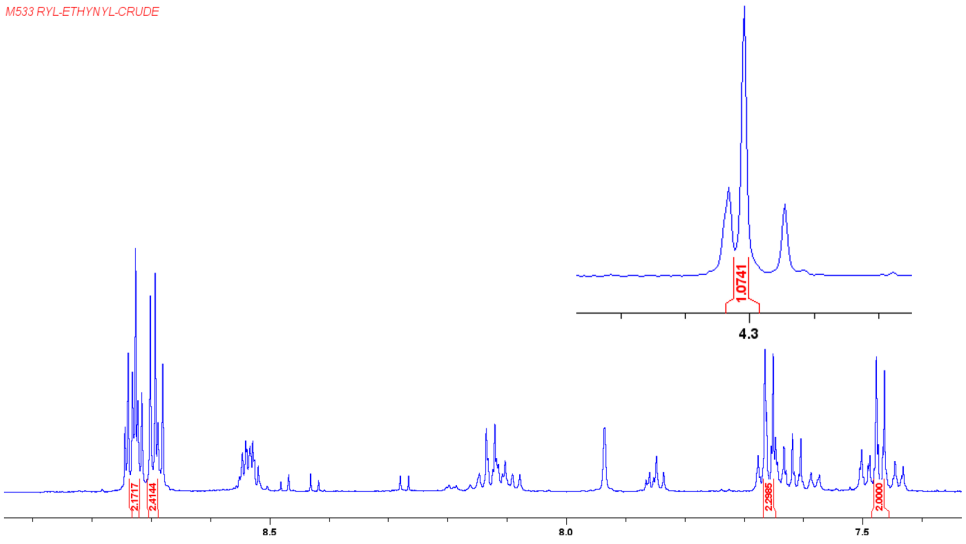


Figure SC5.2 ^{1}H-NMR of **NDI-ethynyl** in DMSO-d_6.

^{1}H-NMR (600 MHz, DMSOd$_6$): **NDI-benzoate** δ (ppm) 3.85 (s, 3H), 7.56 (d, 2H), 8.09 (d, 2H), 8.68 (dd, 4H)

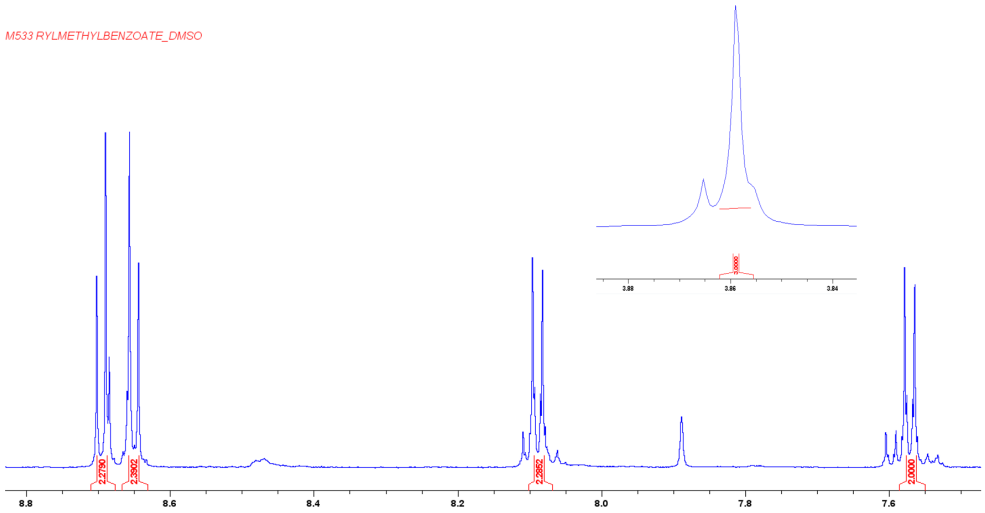
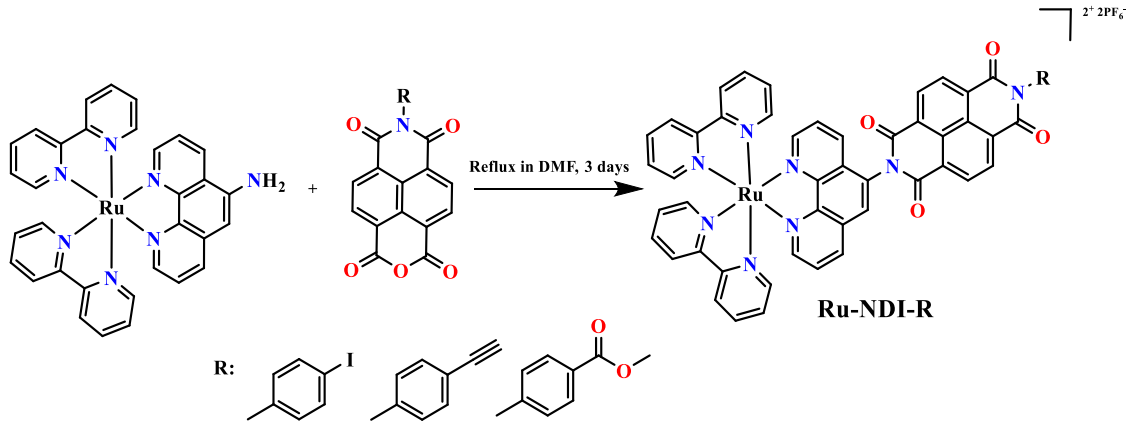


Figure SC5.3 ^{1}H-NMR of **NDI-benzoate** in DMSO-d$_6$.

Ru-NDI-R



Ru(bpy)$_2$(NH$_2$-phen) (0.3 mmol) and R-1,4,5,8-napthalene-tetra-carboxylic monoanhydride (0.3 mmol) were stirred in dry degassed DMF at 155°C for 3 days with the protection of nitrogen [1]. The solvent was reduced, and the crude product was dissolved in a small volume of DMF, and diethyl ether was added. The product precipitated out of solution as an orange solid and it was washed with diethyl ether, water. Column chromatography was carried out using acetonitrile, water and saturated KNO$_3$ solution (ratio 10:1:0.1) as a mobile phase.

^{1}H-NMR **Ru-NDI-iodine** (600 MHz, DMSOd_6): δ (ppm) 7.33 (d, 2H), 7.46 (m, 1H), 7.50 (m, 1H), 7.61 (m, 2H), 7.67 (d, 1H) 7.71 (d, 1H), 7.83–7.88 (m, 3H), 7.96 (m, 3H), 8.17 (m, 2H), 8.21–8.26 (m, 4H), 8.69 (s, 1H), 8.71–8.79 (m, 4H), 8.86–8.92 (m, 5H), 9.01 (dd, 1H) ESI mass spectrometry ($C_{52}H_{31}F_{12}IN_8O_4P_2Ru$) $[M]^{2+}$ calculated at m/z = 530.0273 and found at 530.0274.

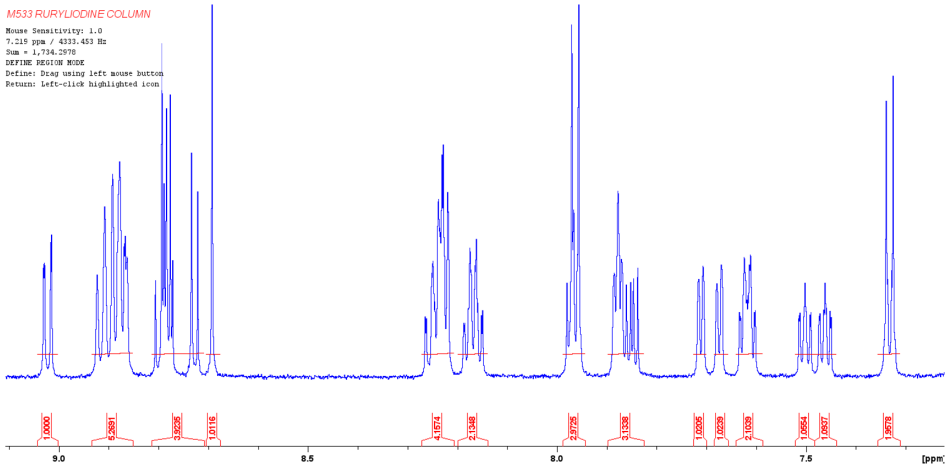


Figure SC5.4 ^{1}H-NMR of **Ru-NDI-iodine** in DMSO-d_6.

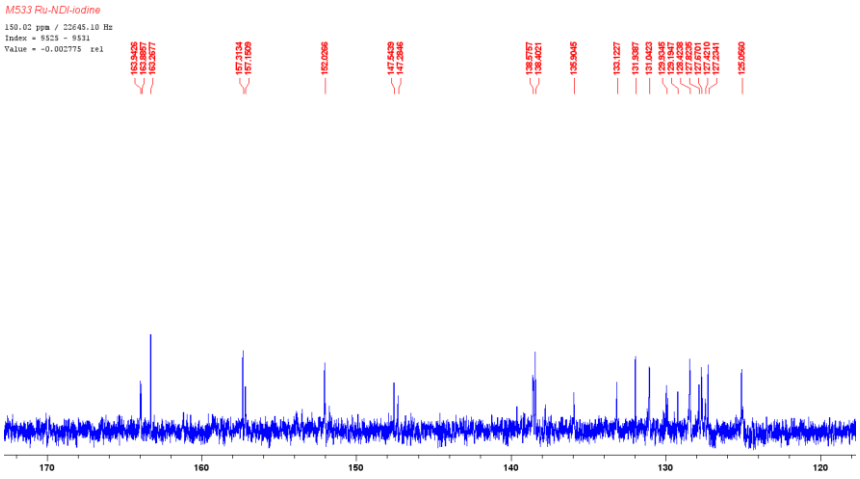


Figure SC5.5 ^{13}C-NMR of **Ru-NDI-iodine** in DMSO-d_6.

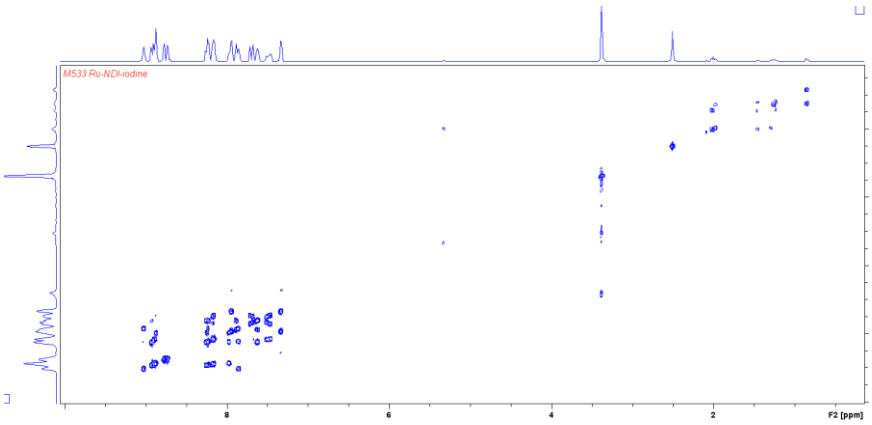


Figure SC5.6 COSY ^{1}H-NMR of **Ru-NDI-iodine** in DMSO-d_6.

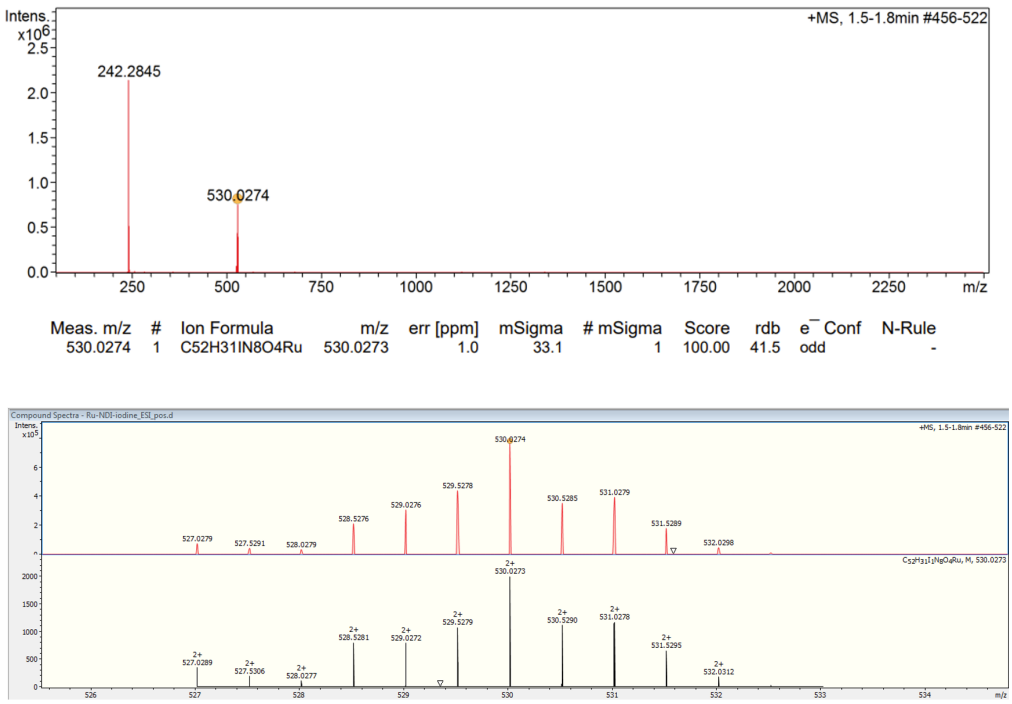


Figure SC5.7 ESI-mass spectrometry results of **Ru-NDI-iodine** in acetonitrile. ($C_{52}H_{31}F_{12}IN_8O_4P_2Ru$) $[M]^{2+}$ calculated at m/z = 530.0273 and found at 530.0274.

^{1}H-NMR **Ru-NDI-benzoate** (600 MHz, DMSOd$_6$): δ (ppm) 3.93 (s, 3H), 7.46 (d, 1H), 7.50 (m, 1H), 7.62 (m, 2H), 7.66–7.72 (m, 4H), 7.83–7.91 (m, 3H) 7.97 (m, 1H), 8.15–8.19 (m, 4H), 8.21–8.26 (m, 4H), 8.70 (s, 1H), 8.72–8.20 (m, 4H), 8.86–8.93 (m, 5H), 9.03 (dd, 1H) ESI mass spectrometry: ($C_{54}H_{34}F_{12}N_8O_6P_2Ru$) $[M]^{2+}$ calculated at m/z = 496.0824 and found at 496.0907.

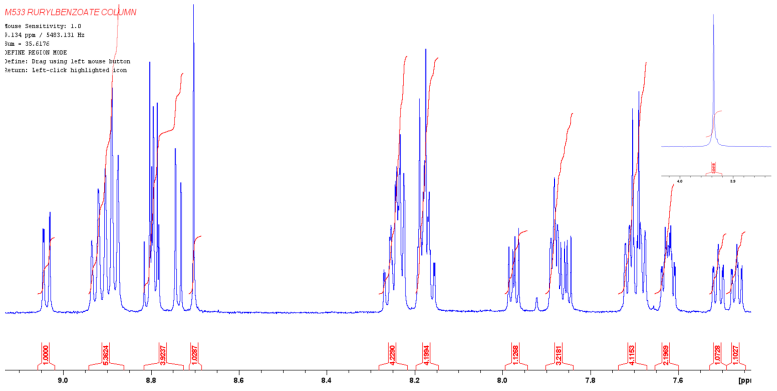


Figure SC5.8 ^{1}H-NMR of **Ru-NDI-benzoate** in DMSO-d$_6$.

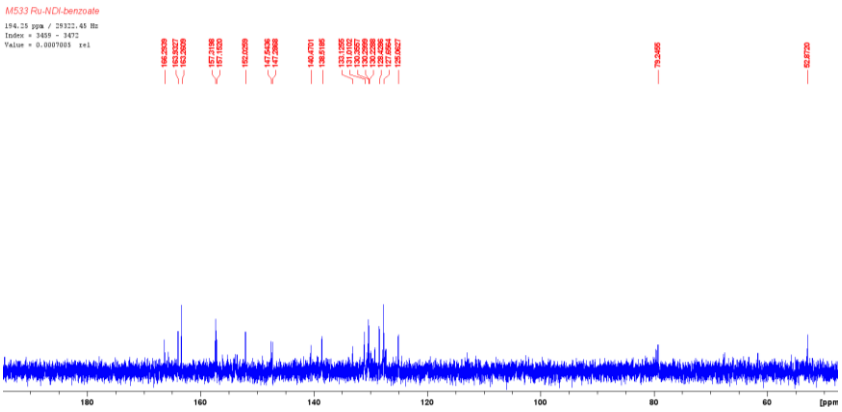


Figure SC5.9 ^{13}C-NMR of **Ru-NDI-benzoate** in DMSO-d$_6$.

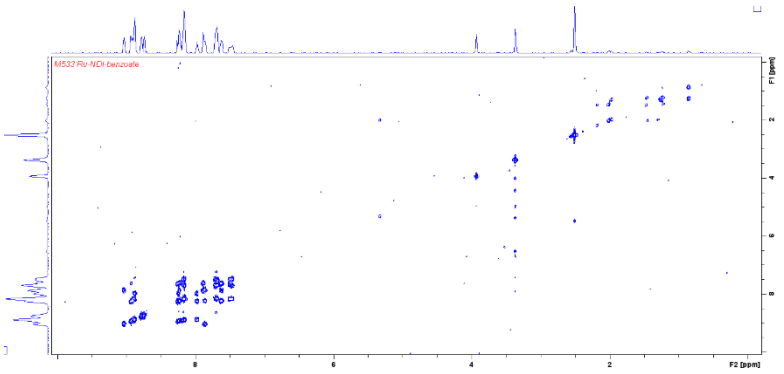


Figure SC5.10 COSY ^{1}H-NMR of **Ru-NDI-benzoate** in DMSO-d$_6$.

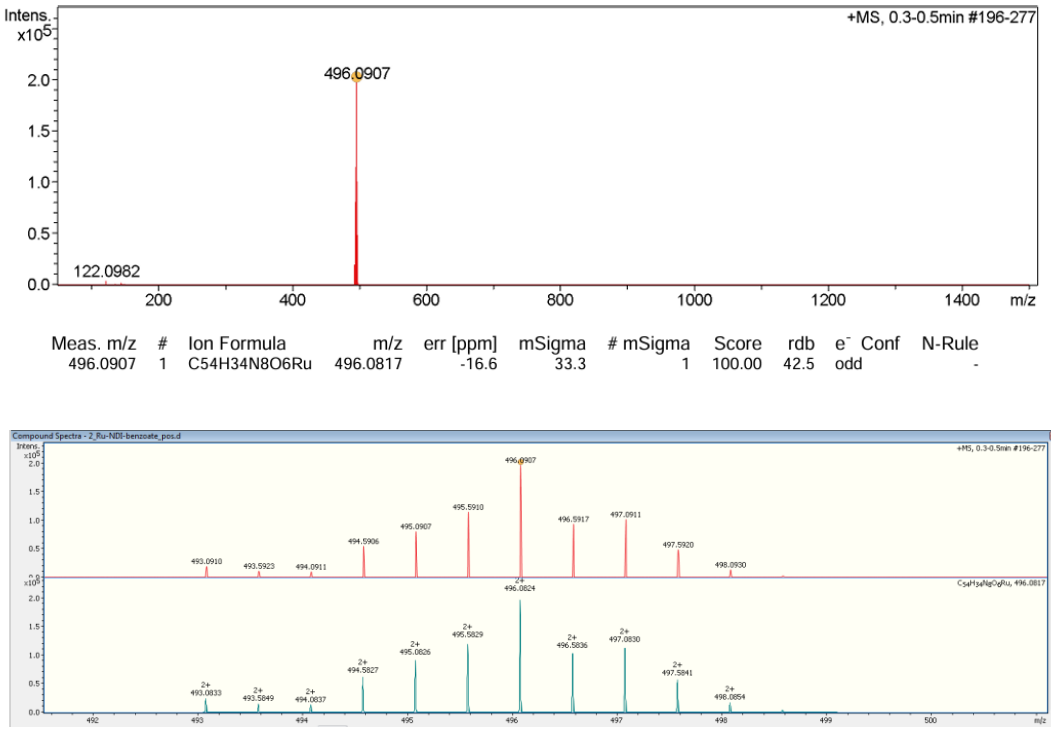


Figure SC5.11 ESI-mass spectrometry results of **Ru-NDI-benzoate** in acetonitrile. ($C_{54}H_{34}F_{12}N_8O_6P_2Ru$) $[M]^{2+}$ calculated at m/z = 496.0824 and found at 496.0907.

^{1}H-NMR **Ru-NDI-ethynyl** (600 MHz, DMSOd_6): δ (ppm) 4.34 (s, 1H), 7.45 (d, 1H), 7.49 (m, 1H), 7.53 (d, 2H), 7.59–7.63 (m, 2H), 7.65–7.71 (m, 4H), 7.82–7.87 (m, 3H), 7.95 (m, 1H), 8.13–8.15 (m, 2H), 8.20–8.25 (m, 4H), 8.68 (s, 1H), 8.70–8.79 (m, 4H), 8.85–8.92 (m, 5H), 9.02 (dd, 1H). ESI mass spectrometry: ($C_{54}H_{32}F_{12}N_8O_4P_2Ru$) $[M]^{2+}$ calculated at m/z = 479.0797 and found at 479.0832.

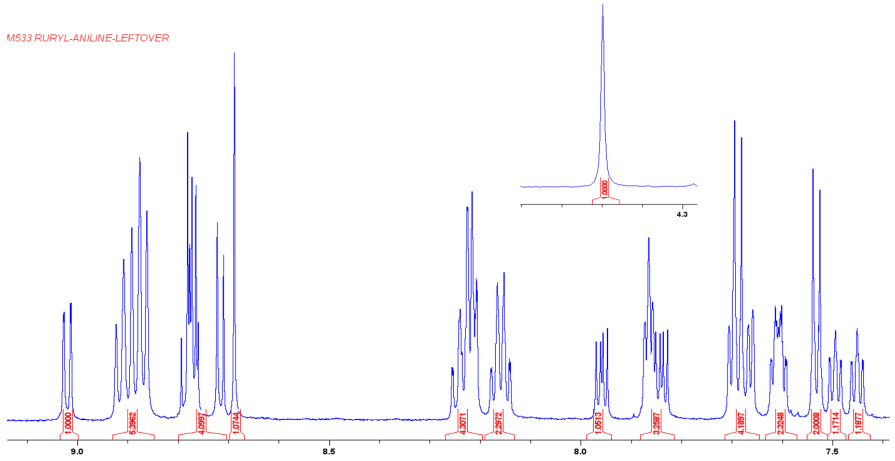


Figure SC5.12 ^{1}H-NMR of **Ru-NDI-ethynyl** in DMSO-d_6.

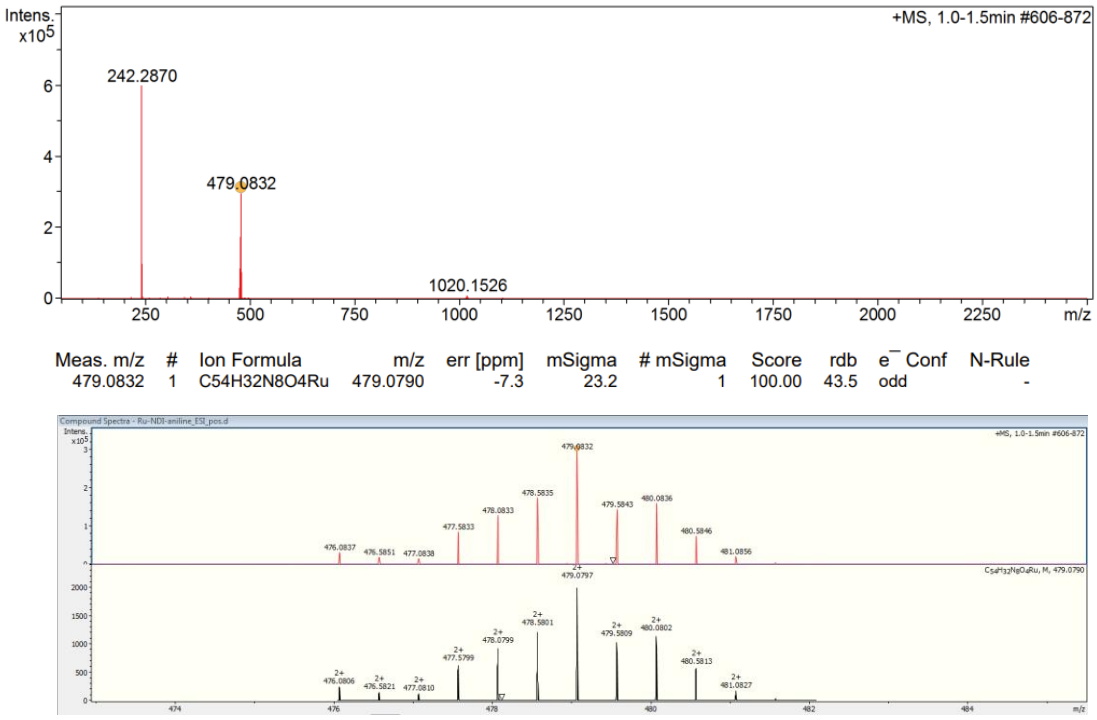
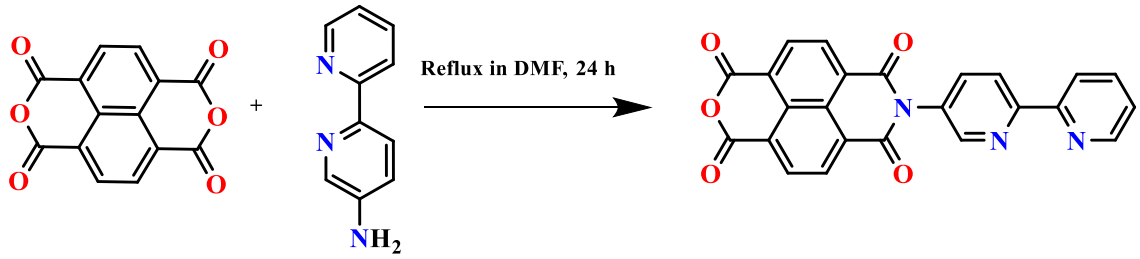


Figure SC5.13 ESI-mass spectrometry results of **Ru-NDI-ethynyl** in acetonitrile. ($C_{54}H_{32}F_{12}N_8O_4P_2Ru$) $[M]^{2+}$ calculated at m/z = 479.0797 and found at 479.0832.

Bipyridine-1,4,5,8-napthalene-tetra-carboxylic monoanhydride (NDI-bpy)



5-Amino-2,2'-bipyridine ligand (1.09 mmol, 187 mg) and 1,4,5,8-napthalene-tetra-carboxylic monoanhydride (NDA) (2.18 mmol, 584 mg) were refluxed in dry degassed DMF at 155°C for 24 hours with the protection of nitrogen [1]. The solvent was reduced, and the crude product was dissolved in a small volume of DMF, and diethyl ether was added. The product precipitated out of solution as a beige solid and it was washed with diethyl ether and water. In order to remove naphthalene diimide starting material (NDA), the sample was dissolved in ethanol and refluxed for 3 hours. The product was filtered

via hot filtration. The ligand contained some extent of impurities hence, its purification was continued in the later stages of synthesis.

^{1}H-NMR **NDI-bpy** (600 MHz, DMSOd_6): δ (ppm) 7.53 (m, 1H), 8.02 (m, 1H), 8.08 (dd, 1H), 8.47 (d, 1H), 8.59 (d, 1H), 8.73–8.78 (m, 6H).

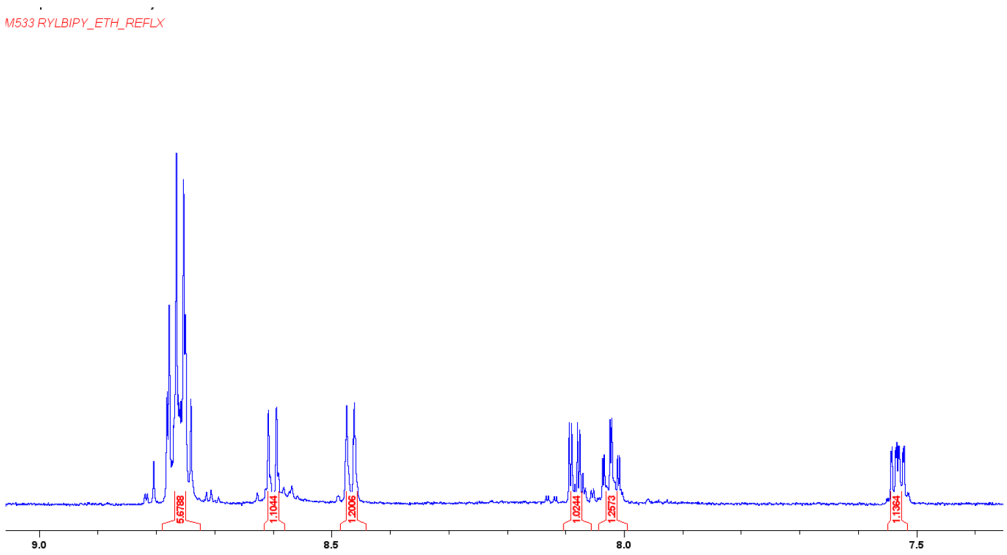
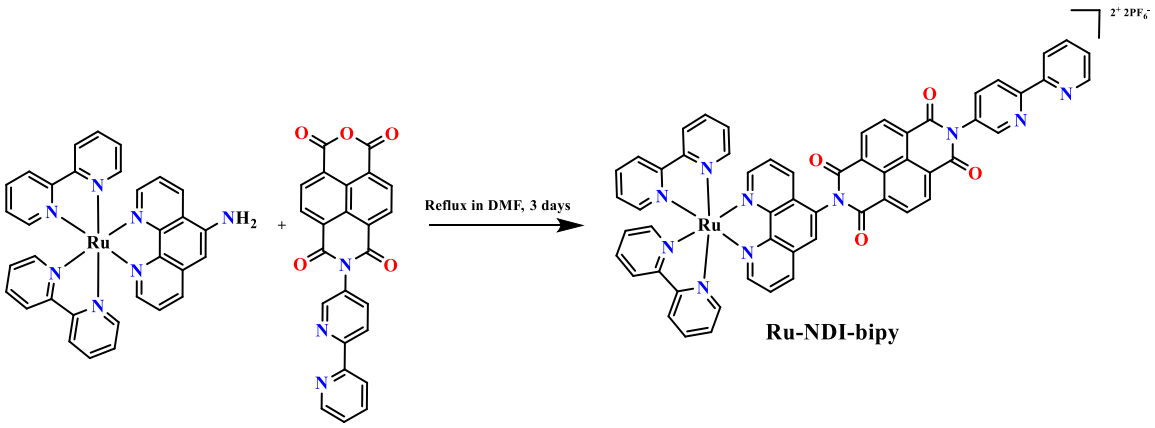


Figure SC5.14 ^{1}H-NMR of **NDI-bpy** in DMSO-d_6.

Ru-NDI-bpy



$Ru(bpy)_2(NH_2\text{-phen})$ (0.2 mmol, 122 mg) and bipyridine-1,4,5,8-napthalene-tetra-carboxylic monoanhydride (0.2 mmol, 85 mg) were stirred in dry degassed DMF at 155°C for 3 days with the protection of nitrogen [1]. The solvent was reduced, and the crude product was dissolved in a small volume of DMF, and diethyl ether was added. The product precipitated out of solution as an orange solid and it was washed with diethyl

ether, water. Column Chromatography was carried out using acetonitrile, water and saturated KNO_3 solution (ratio 10:1:0.1) as a mobile phase.

^{1}H-NMR (600 MHz, $DMSOd_6$): δ (ppm)), 7.46 (m, 1H), 7.51 (m, 1H), 7.54 (m, 1H), 7.62 (m, 2H), 7.67 (d, 1H), 7.71 (d, 1H), 7.84–7.93 (m, 3H), 7.97 (m, 1H), 8.03 (m, 1H), 8.13–8.19 (m, 3H), 8.21–8.27 (m, 4H), 8.47 (d, 1H), 8.63 (d, 1H), 8.70 (s, 1H), 8.73–8.85 (m, 6H), 8.86–8.93 (m, 5H), 9.04 (dd, 1H). ESI mass spectrometry ($C_{56}H_{34}N_{10}O_4Ru$) $[M]^{2+}$ calculated at m/z = 506.0906 and found at 506.0942.

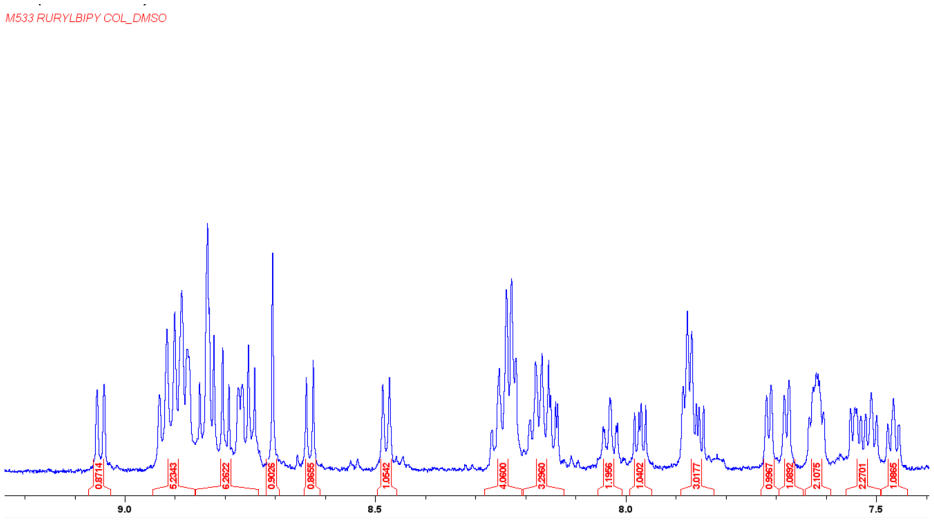


Figure SC5.15 ^{1}H-NMR of **Ru-NDI-bpy** in DMSO-d_6.

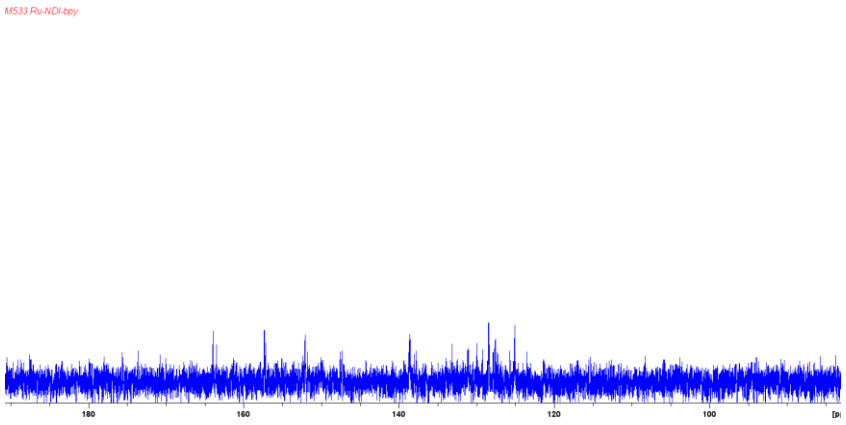


Figure SC5.16 ^{13}C-NMR of **Ru-NDI-bpy** in DMSO-d_6.

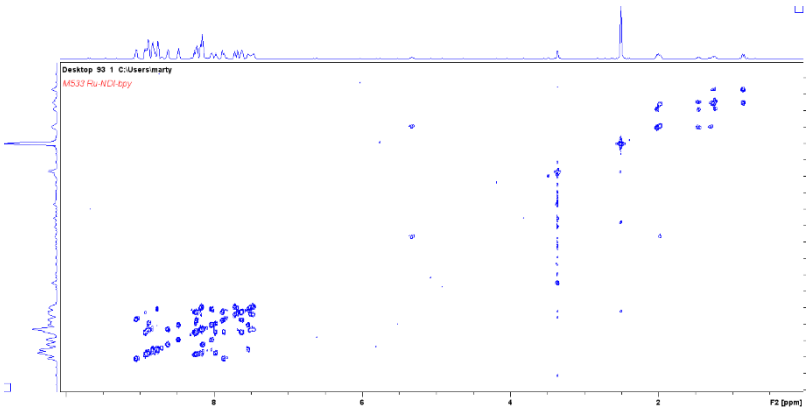
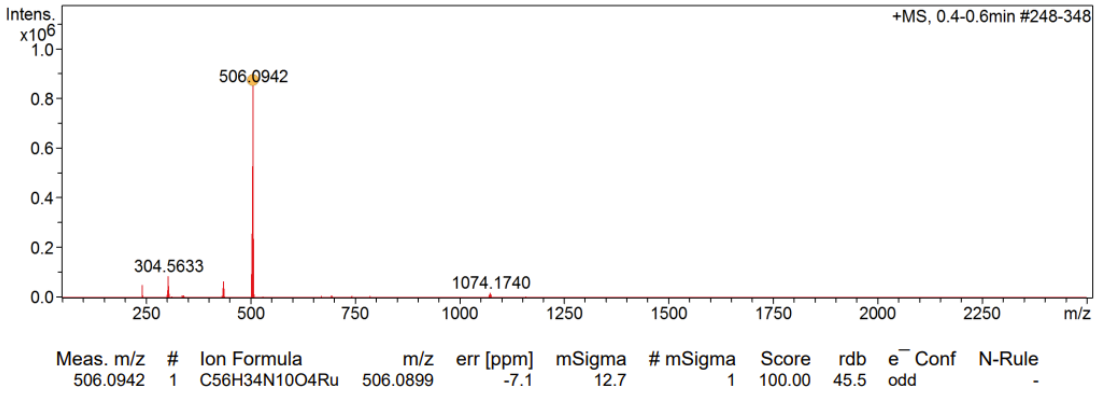


Figure SC5.17 COSY ^{1}H-NMR of **Ru-NDI-bpy** in DMSO-d_6.



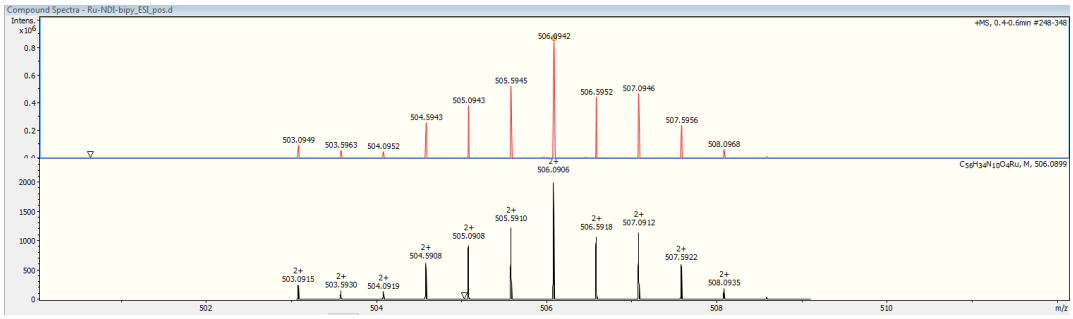
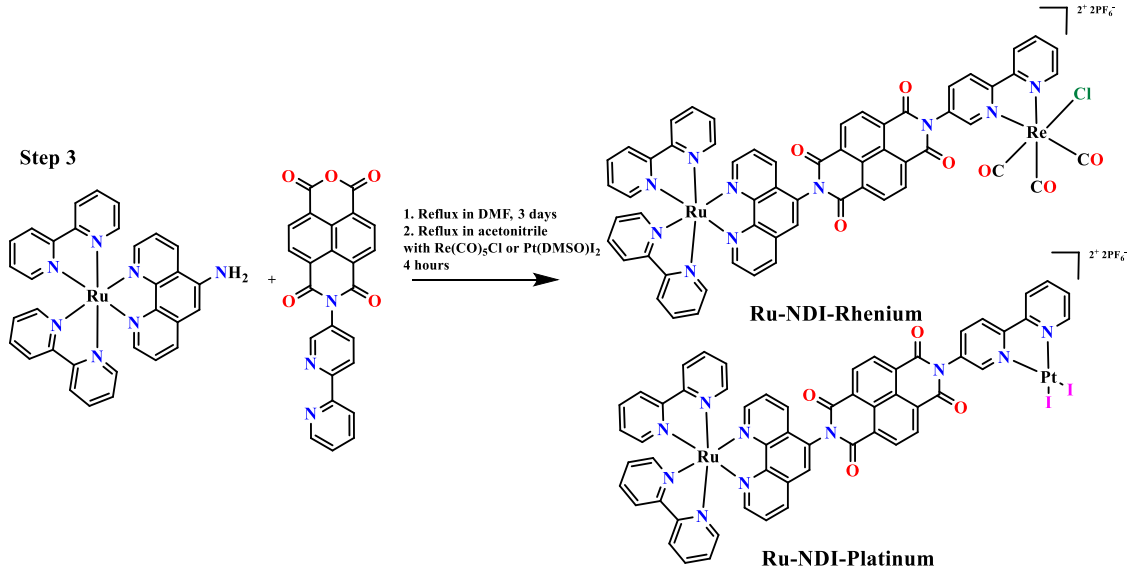


Figure SC5.18 ESI-mass spectrometry results of **Ru-NDI-bpy** in acetonitrile. ($C_{56}H_{34}N_{10}O_4Ru$) $[M]^{2+}$ calculated at m/z = 506.0906 and found at 506.0942.

Ru-NDI-rhenium and Ru-NDI-platinum



0.089 g (0.07 mmol) of **Ru-NDI-bpy** was dissolved in 7 ml of acetonitrile. 0.031 g (0.084 mmol, 1.2 equivalents) of $Re(CO)_5Cl$ was added [2]. The flask was wrapped in tin foil to avoid any contact with light. The reaction was refluxed for 4 hours. The solvent was removed under reduced pressure. Diethyl ether was added to precipitate the product out and to remove any unreacted $Re(CO)_5Cl$. The same procedure was employed to coordinate $Pt(DMSO)_2I_2$ to **Ru-NDI-bpy.**

^{1}H-NMR **Ru-NDI-rhenium** (600 MHz, $DMSOd_6$): δ (ppm)), 7.46 (m, 1H), 7.51 (m, 1H), 7.62 (m, 2H), 7.67 (d, 1H), 7.72 (d, 1H), 7.83–7.89 (m, 4H), 7.97 (m, 1H), 8.15–8.20 (m, 2H), 8.21–8.27 (m, 4H), 8.43 (m, 1H), 8.58 (m, 1H), 8.71 (s, 1H), 8.76 (d, 1H), 8.82 (d, 1H), 8.85–8.94 (m, 8H), 9.04–9.10 (m, 3H), 9.31 (d, 1H). ESI mass spectrometry ($C_{59}H_{34}ClN_{10}O_7ReRu$) $[M]^{2+}$ calculated at m/z = 659.0445 and found at 659.0464.

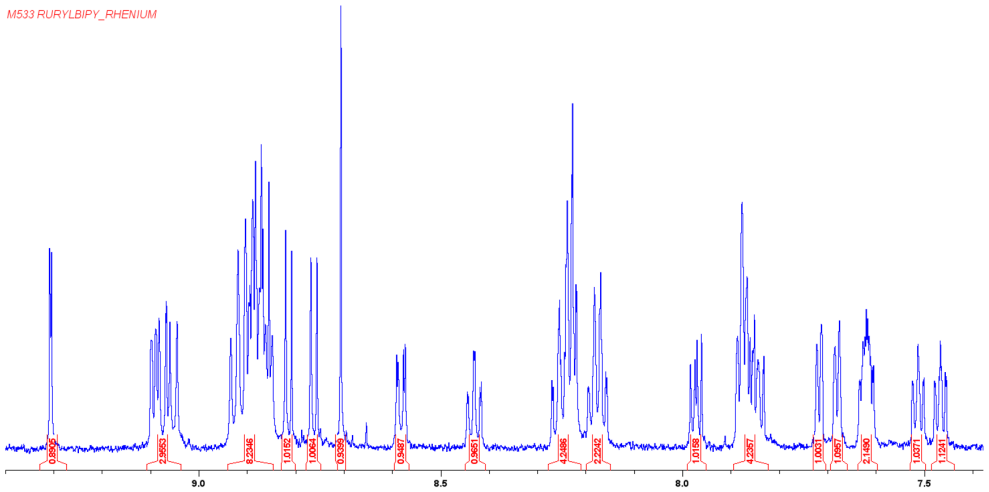
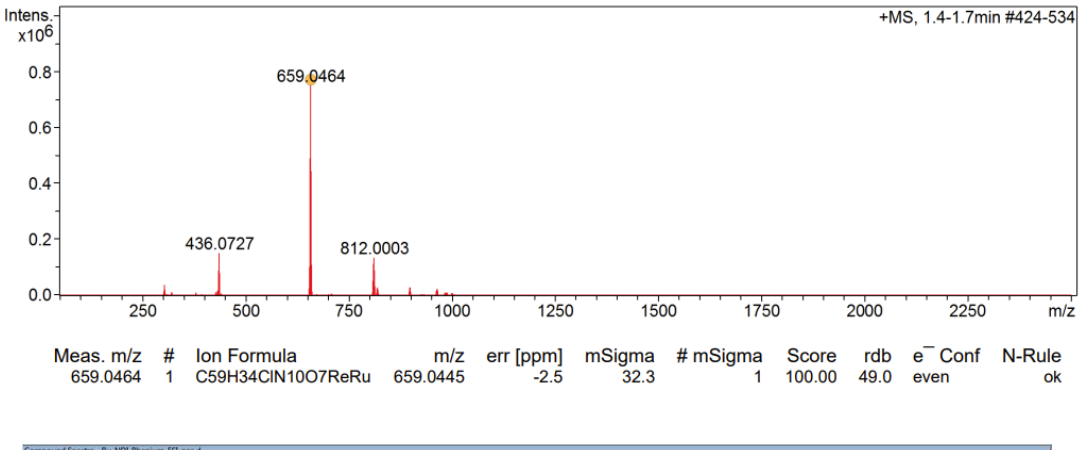


Figure SC5.19 ^{1}H-NMR of **Ru-NDI-rhenium** in DMSO-d_6.



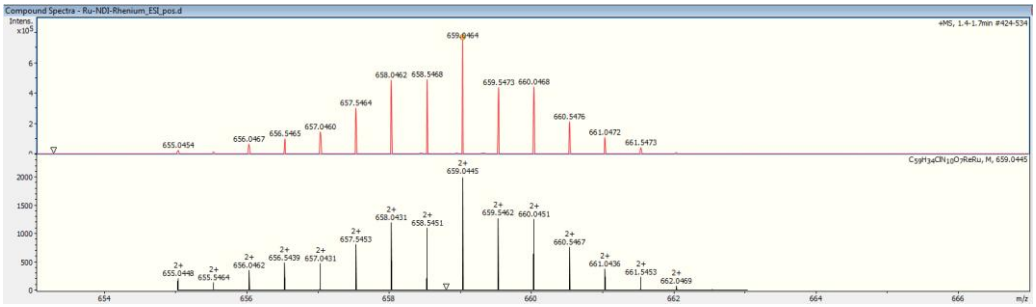


Figure SC5.20 ESI-mass spectrometry results of **Ru-NDI-rhenium** in acetonitrile. ($C_{59}H_{34}ClN_{10}O_7ReRu$) $[M]^{2+}$ calculated at m/z = 659.0445 and found at 659.0464.

^{1}H-NMR **Ru-NDI-platinum** (600 MHz, DMSOd_6): δ (ppm)), 7.46 (m, 1H), 7.51 (m, 1H), 7.62 (m, 2H), 7.67 (d, 1H), 7.72 (d, 1H), 7.83–7.89 (m, 3H), 7.97 (m, 2H), 8.15–8.20 (m, 2H), 8.21–8.27 (m, 4H), 8.71 (m, 2H), 8.76 (d, 2H), 8.82 (d, 2H), 8.85–8.94 (m, 10H), 9.31 (d, 1H). ESI mass spectrometry ($C_{56}H_{34}I_2N_{10}O_4PtRu$) $[M]^{2+}$ calculated at m/z = 730.4777 and found at 730.4774.

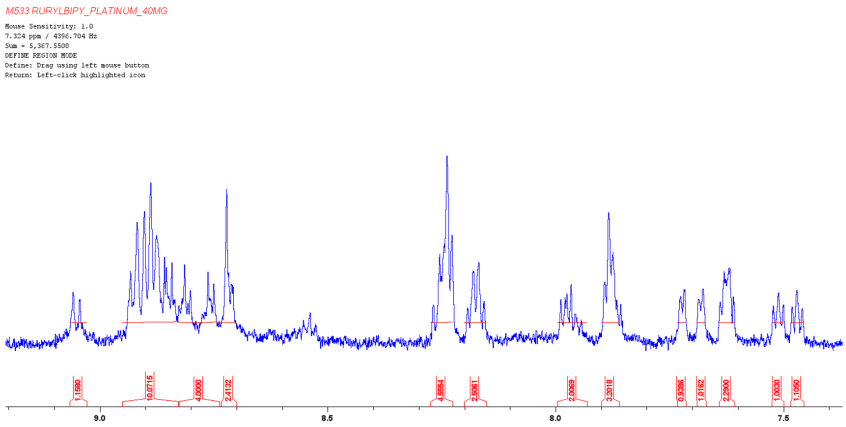
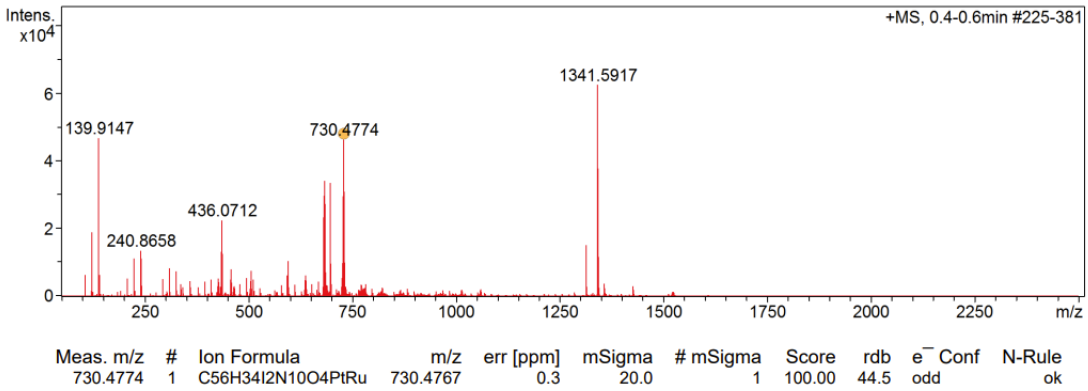


Figure SC5.21 ^{1}H-NMR of **Ru-NDI-platinum** in DMSO-d_6.



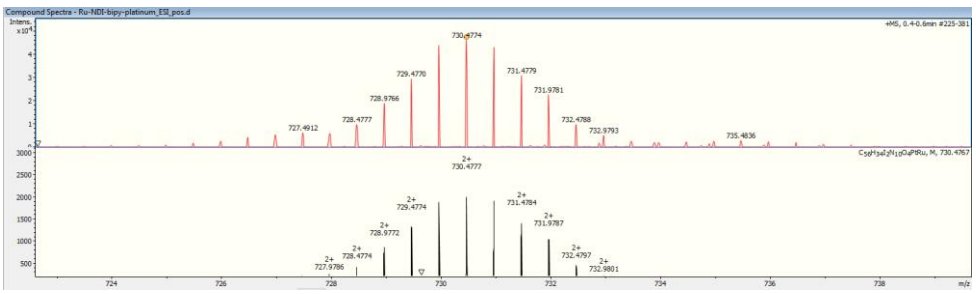
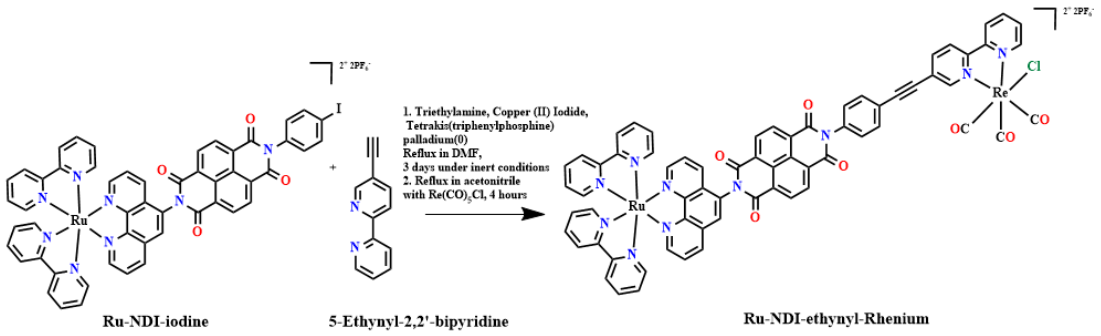


Figure SC5.22 ESI-mass spectrometry results of **Ru-NDI-platinum** in acetonitrile. ($C_{56}H_{34}I_2N_{10}O_4PtRu$) $[M]^{2+}$ calculated at m/z = 730.4777 and found at 730.4774.

Ru-NDI-ethynyl-rhenium



Ru-NDI-ethynyl-rhenium was prepared following the Sonogashira coupling reaction. A total of 0.103 g (0.097 mmol) of **Ru-NDI-iodine** was dissolved in 3 ml of DMF. Next, 0.021 g (0.1164 mmol, 1.2 equivalents) of 5-ethynyl-2,2ʾ-bipyridine, 0.0015 g of copper (II) iodine (8%, 0.00776 mmol), 0.018 g of tetrakis(triphenylphosphine) palladium (0) (0.01552 mmol) were added under inert conditions [3]. To ensure the absence of oxygen, the reaction flask was freeze-thaw-pumped three times, followed by filling with nitrogen. The flask was wrapped in tin foil to avoid any contact with light. The reaction was refluxed for 3 days to yield **Ru-NDI-ethynyl-bpy**. Diethyl ether was added to precipitate the product out. Finally, the product was dissolved in acetonitrile and reacted with of $Re(CO)_5Cl$ [2] to give **Ru-NDI-ethynyl-rhenium**.

^{1}H-NMR **Ru-NDI-ethynyl-bpy** (600 MHz, $DMSOd_6$): δ (ppm)), 7.47 (m, 1H), 7.51 (m, 2H), 7.68 (m, 3H), 7.68 (d, 1H), 7.71 (d, 1H), 7.86 (m, 5H), 7.96–8.01 (m, 3H), 8.15–8.27 (m, 8H), 8.44 (d, 1H), 8.49 (d, 1H), 8.70 (s, 1H), 8.74 (m, 2H), 8.78–8.83 (m, 2H), 8.87–8.94 (m, 6H), 9.04 (d, 1H). ESI mass spectrometry ($C_{64}H_{38}F_{12}N_{10}O_4P_2Ru$) $[M]^{2+}$ calculated at m/z = 556.1064 and found at 556.1071.

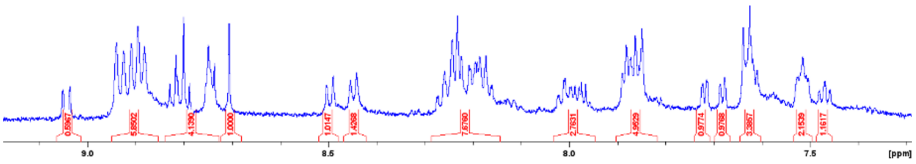
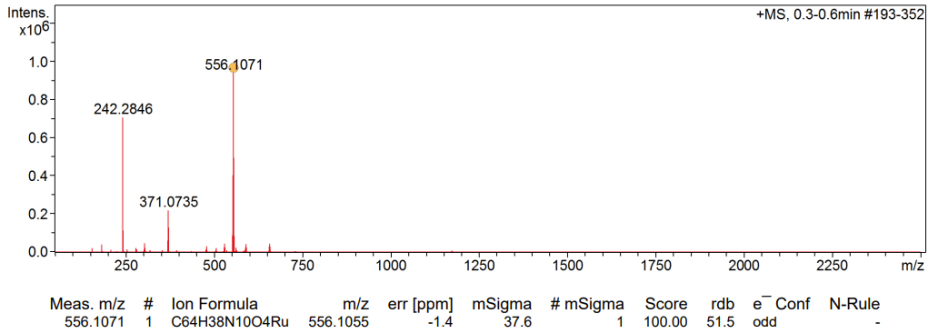


Figure SC5.23 ^{1}H-NMR of **Ru-NDI-ethynyl-bpy** in DMSO-d_6.



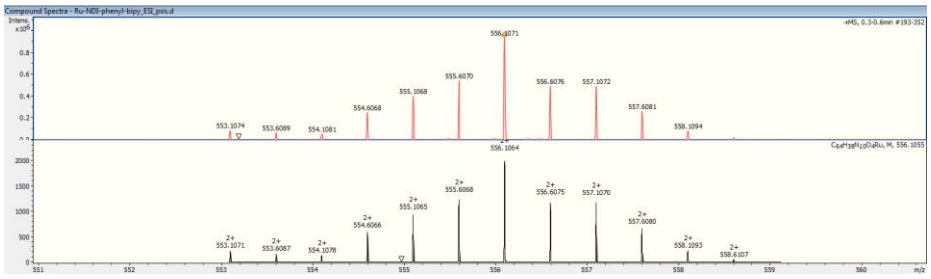


Figure SC5.24 ESI-mass spectrometry results of **Ru-NDI-ethynyl-bpy** in acetonitrile. ($C_{64}H_{38}F_{12}N_{10}O_4P_2Ru$) $[M]^{2+}$ calculated at m/z = 556.1064 and found at 556.1071.

^{1}H-NMR **Ru-NDI-ethynyl-rhenium** (600 MHz, DMSOd_6): δ (ppm)), 7.47 (m, 1H), 7.50 (m, 1H), 7.61 (m, 2H), 7.67 (m, 2H), 7.71 (d, 1H), 7.79 (m, 2H), 7.83–7.89 (m, 4H), 7.93–7.99 (m, 3H), 8.14–8.19 (m, 2H), 8.21–8.27 (m, 4H), 8.36 (m, 1H), 8.57 (m, 1H), 8.69 (s, 1H), 8.74 (d, 1H), 8.78–8.84 (m, 4H), 8.85–8.93 (m, 5H), 9.03 (d, 1H), 9.08 (d, 1H), 9.20 (d, 1H). ESI mass spectrometry ($C_{67}H_{38}ClF_{12}N_{10}O_7P_2ReRu$) $[M]^{2+}$ calculated at m/z = 709.0605 and found at 709.0615.

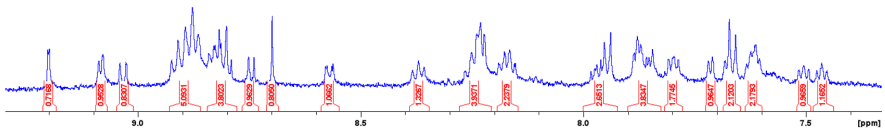


Figure SC5.25 ^{1}H-NMR of **Ru-NDI-ethynyl-rhenium** in DMSO-d_6.

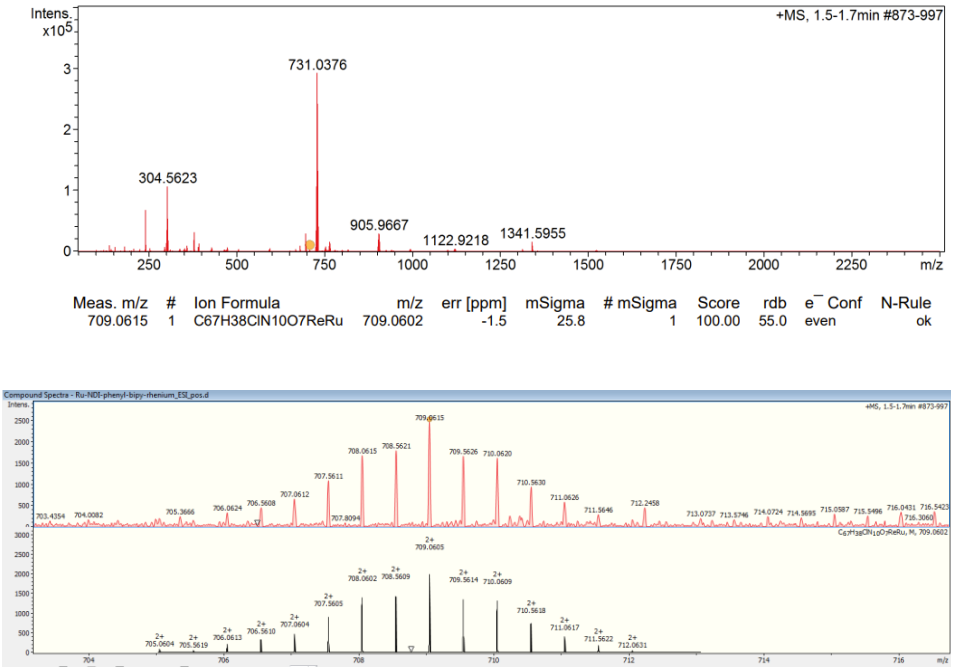


Figure SC5.26 ESI-mass spectrometry results of **Ru-NDI-ethynyl-rhenium** in acetonitrile. ($C_{67}H_{38}ClF_{12}N_{10}O_7P_2ReRu$) $[M]^{2+}$ calculated at m/z = 709.0605 and found at 709.0615.

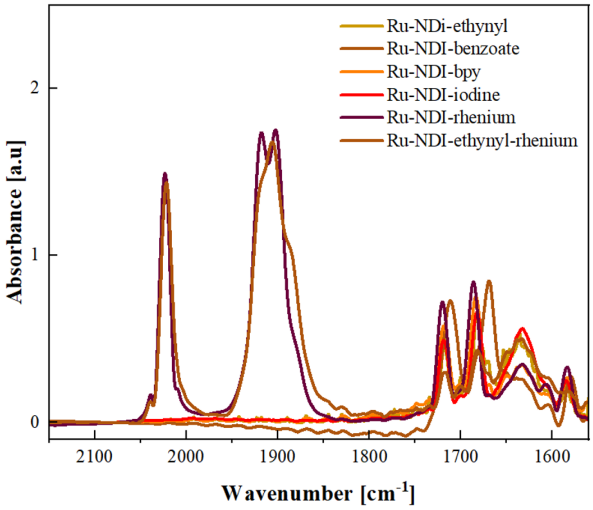


Figure SC5.27 FTIR spectroscopy results of **Ru-NDI** complexes in acetonitrile. The band (*) at ~1630 cm^{-1} indicates residual solvent.

References:

[1]. Sasada, Y., Langford, S. J., Oyaizu, K., & Nishide, H. (2016). Poly(norbornyl-NDIs) as a potential cathode-active material in rechargeable charge storage devices. RSC Advances, 6(49), 42911–42916. https://doi.org/10.1039/c6ra06103f

[2]. Bian, Z.-Y., Sumi, K., Furue, M., Sato, S., Koike, K., & Ishitani, O. (2009). Synthesis and properties of a novel tripodal bipyridyl ligand tb-carbinol and its Ru(II)–Re(I) trimetallic complexes: investigation of multimetallic artificial systems for photocatalytic CO_2 reduction. Dalton Trans., (6), 983–993. https://doi.org/10.1039/b814340d

[3]. Kanwal, I., Mujahid, A., Rasool, N., Rizwan, K., Malik, A., Ahmad, G., Shah, S. A., Rashid, U., & Nasir, N. M. (2020). Palladium and Copper Catalyzed Sonogashira Cross Coupling an Excellent Methodology for C-C Bond Formation over 17 Years: A Review. Catalysts, 10(4), 443. https://doi.org/10.3390/catal10040443

Appendix D

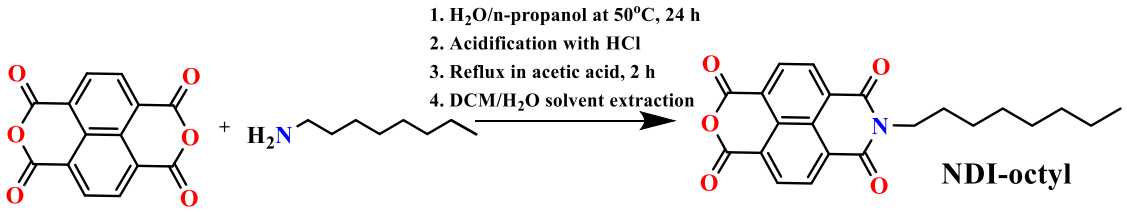
CHAPTER 6

Synthesis, Photophysical and Electrochemical Studies of a Porphyrin-Naphthalene Diimide using Picosecond-Nanosecond Transient Absorption Spectroscopy and Assessment for Hydrogen Evolution - Supplementary Information

Experimental

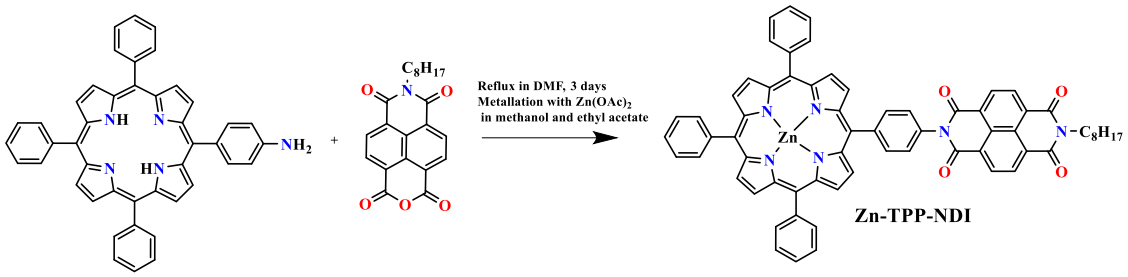
Synthesis

N-octyl-1,4,5,8-napthalene-tetra-carboxylic monoanhydride



The reaction was carried out by following the method in the literature, in a similar manned to the ones reported in the previous chapters [1]. In a 100 mL round bottom flask, water (10 mL) and n-propanol (10 mL) 1:1 were stirred for 10 min at room temperature under N_2 atm, to this 1,4,5,8-naphthalenetetracarboxylic dianhydride (1g, 3.73 mmol) was added along with the octyl amine (2 mL, 1.56 g, 12 mmol, excess). Then the suspension was heated at 50 °C. The reaction mixture was acidified using 1 M HCl to pH 1. Then the reaction mixture was refluxed in acetic acid. The obtained precipitate was diluted by DCM (200 – 300 mL) and then H_2O was added. The solvent was reduced in volume under vacuum and washed with ethanol, hexane, and small amount of ether. ^{1}H-NMR (600 MHz, $DMSOd_6$): δ (ppm) 0.85 (t, 3H), 1.2–1.4 (m, 10H), 1.79 (t, 2H), 4.21 (t, 2H), 8.75 (s, 4H)

TPP-NDI and **Zn-TPP-NDI**



TPP-NH_2 (0.18 mmol, 116 mg) and n-octyl-1,4,5,8-napthalene-tetra-carboxylic monoanhydride (0.18 mmol, 70 mg) were stirred in dry degassed DMF at 140°C for 3 days with the protection of nitrogen. The product was washed with water and methanol. In order to remove naphthalene diimide starting material, the sample was dissolved in a small quantity of DMF, and diethyl ether was added. The product was precipitated out and filtered. In case, where TPP-NH_2 was present, the product was purified by the solvent extraction using acetic acid/water mixture and DCM. The yield obtained was 40%.

^{1}H-NMR (600 MHz, DCMd_6) **TPP-NDI**: δ (ppm) –2.92 ppm (s, 2H), 0.82 (s, 3H), 1.21–1.40 (m, 10H), 1.69 (t, 2H), 4.13 (t, 2H), 7.66–7.76 (m, 12H), 8.16 (m, 6H), 8.36 (d, 2H), 8.70 (d, 2H), 8.73 (d, 2H), 8.79 (m, 3H), 8.85 (d, 2H), 8.94 (d, 2H). MALDI-TOF MS ($C_{66}H_{50}N_6O_4$) Calculated at 991.397 and found at 991.293.

Metalation reaction was carried out following the method reported in the literature, but instead of dichloromethane/chloroform, ethyl acetate was used [2 – 4]. To a boiling solution of **TPP-NDI** (0.62 mmol, 62 mg) in ethyl acetate (8 ml) was added a saturated solution of zinc acetate dihydrate (0.93 mmol, 17 mg), in methanol (0.2 ml). The reaction mixture was heated under reflux at 77°C overnight. Afterwards, it was cooled down to room temperature, the solvent was removed, and the product **Zn-TPP-NDI** was washed with water and methanol. The yield obtained was 80%.

^{1}H-NMR (600 MHz, DCMd_6) **Zn-TPP-NDI**: δ (ppm) 0.82 (s, 3H), 1.21–1.40 (m, 10H), 1.69 (t, 2H), 4.13 (t, 2H), 7.69–7.75 (m, 12H), 8.16 (m, 6H), 8.35 (d, 2H), 8.71 (d, 2H), 8.80 (d, 2H), 8.88 (s, 3H), 8.94 (d, 2H), 9.02 (d, 2H). MALDI-TOF MS ($C_{66}H_{48}N_6O_4Zn$) Calculated at 1052.302, found at 1052.234.

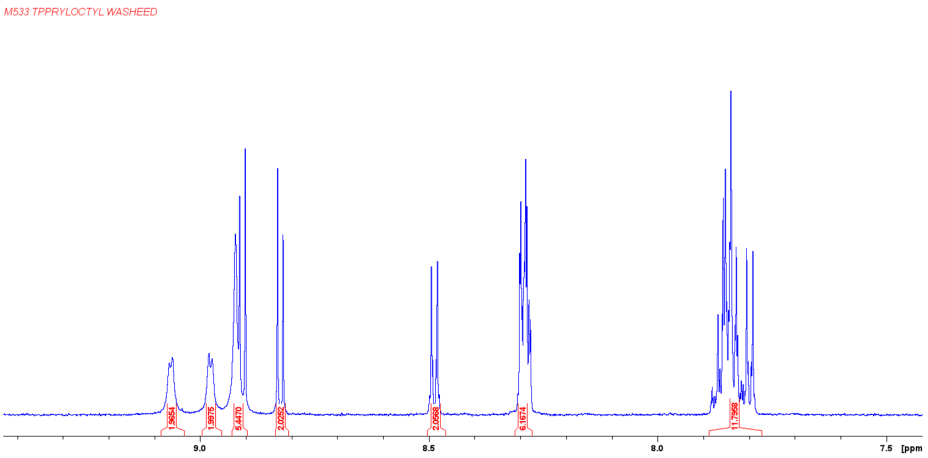


Figure SD6.1 ^{1}H-NMR of **TPP-NDI** in $DCMd_6$ in the aromatic region.

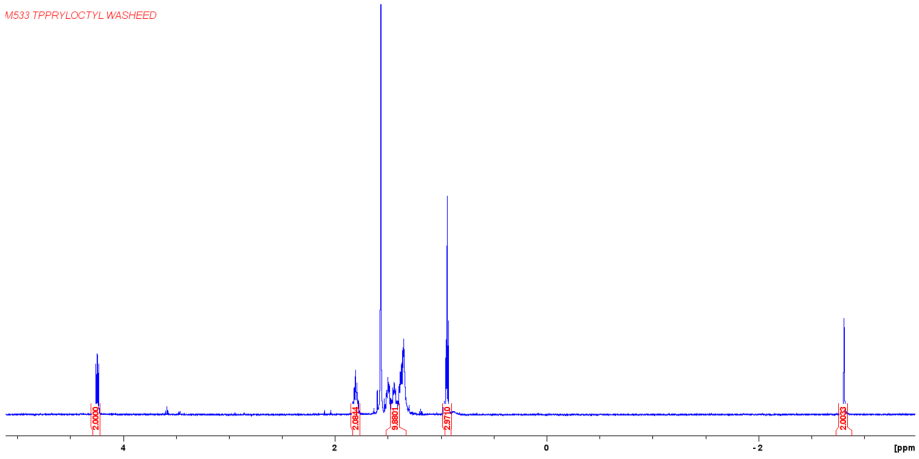


Figure SD6.2 Aliphatic region ^{1}H-NMR in $DCMd_6$ of **TPP-NDI**.

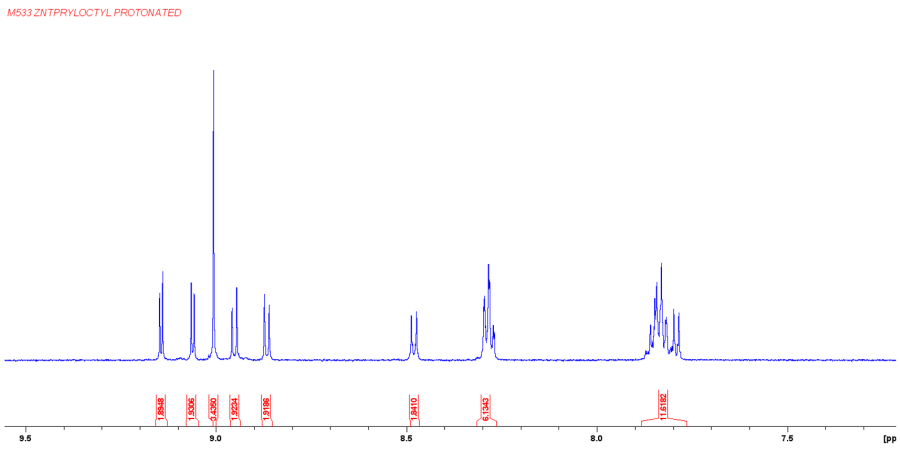


Figure SD6.3 Aromatic region ^{1}H-NMR in $DCMd_6$ of **Zn-TPP-NDI**.

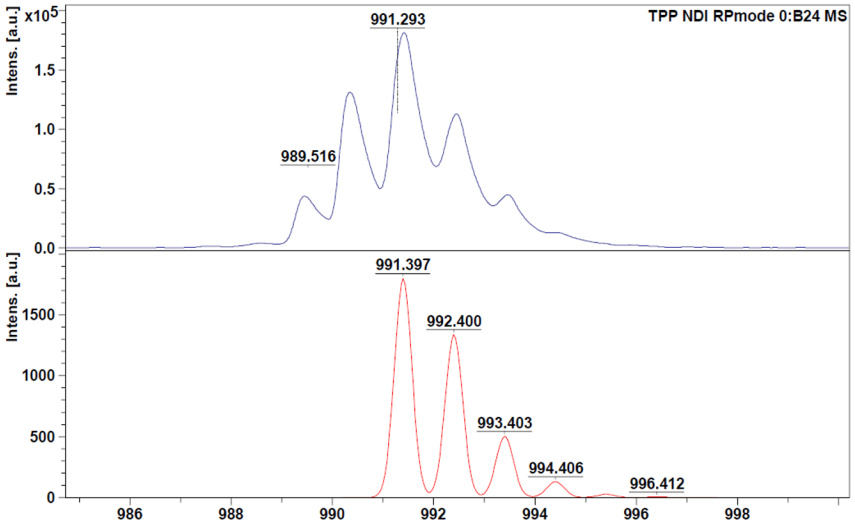


Figure SD6.4 MALDI-TOF MS spectrum of **TPP-NDI** (experimental, black) and simulated isotope pattern (red). The measurements were carried out by researchers at the University of Bath in the UK.

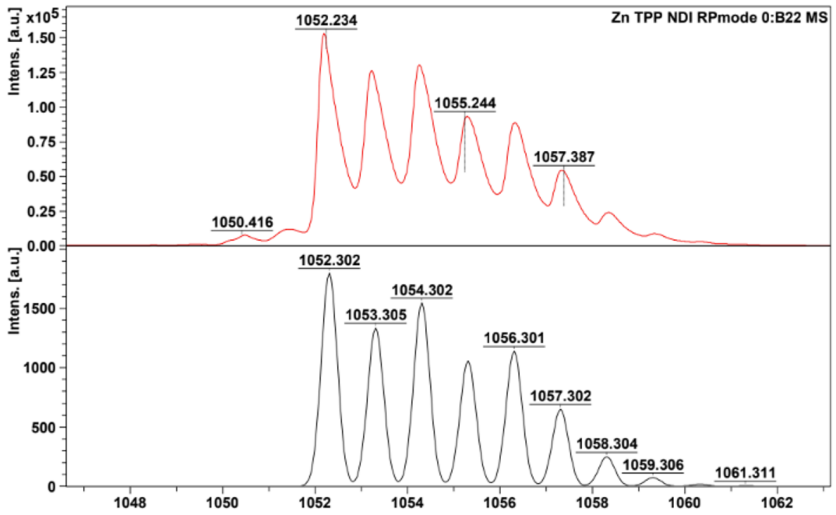
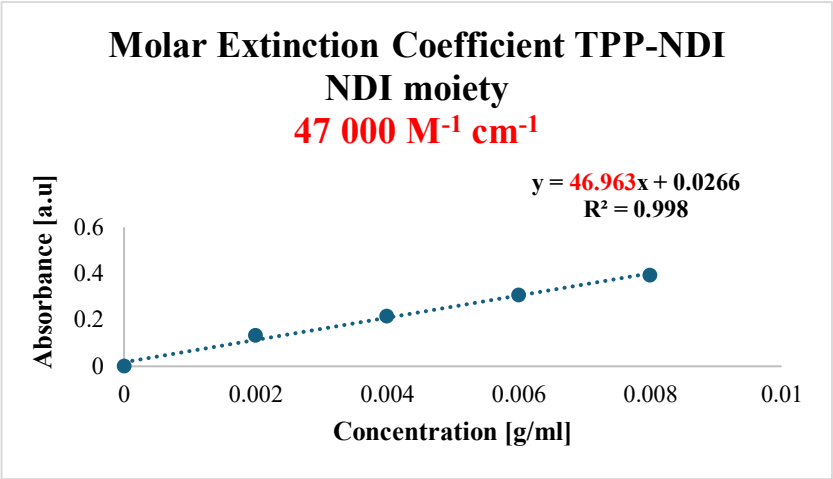


Figure SD6.5 MALDI-TOF MS spectrum of **Zn-TPP-NDI** (experimental, red) and simulated isotope pattern (black). The measurements were carried out by researchers at the University of Bath in the UK.



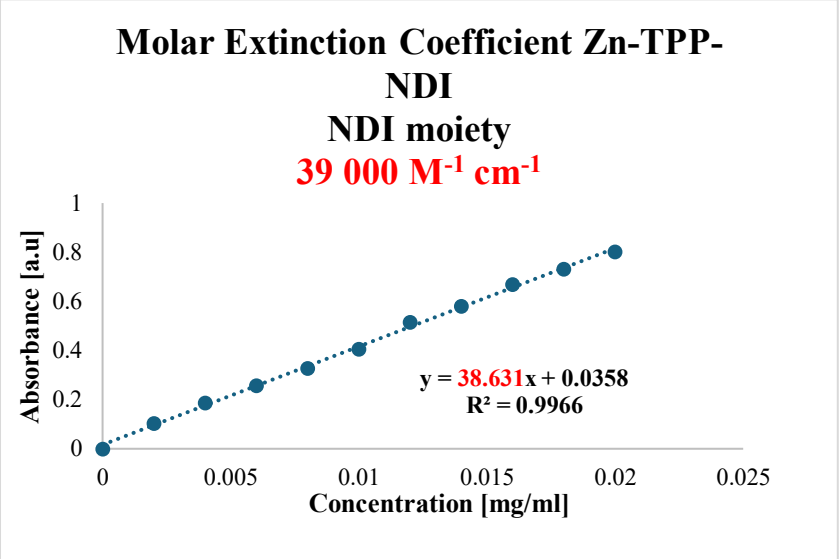
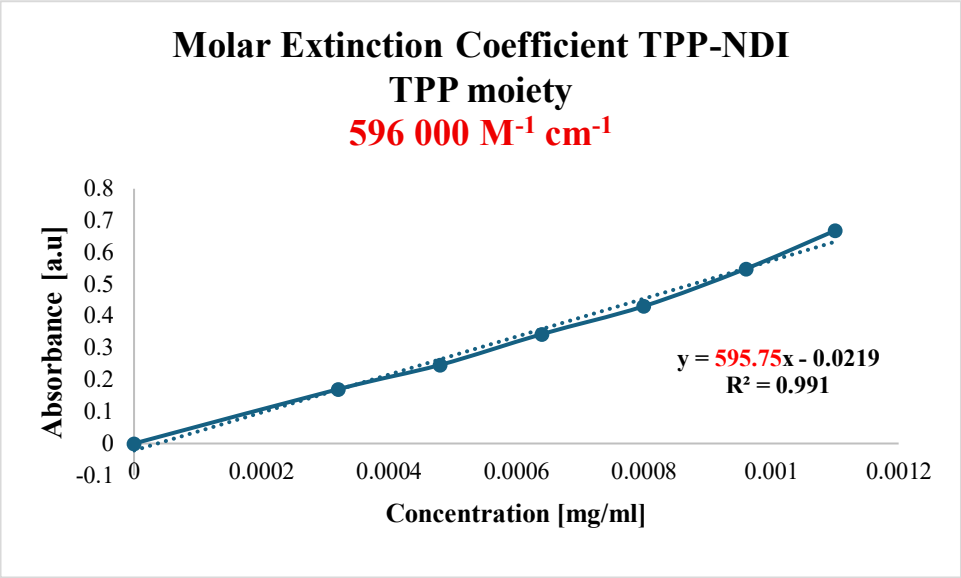


Figure SD6.6 Calculation of molar extinction coefficients for **TPP-NDI** and **Zn-TPP-NDI** attributed to the NDI moiety. The measurements were carried out in THF. The values were obtained at the NDI moiety ($\varepsilon = 3.9 \times 10^4$ $M^{-1}cm^{-1}$, at 356 nm for **Zn-TPP-NDI** and $\varepsilon = 4.7 \times 10^4$ $M^{-1}cm^{-1}$, at 356 nm for **TPP-NDI**).



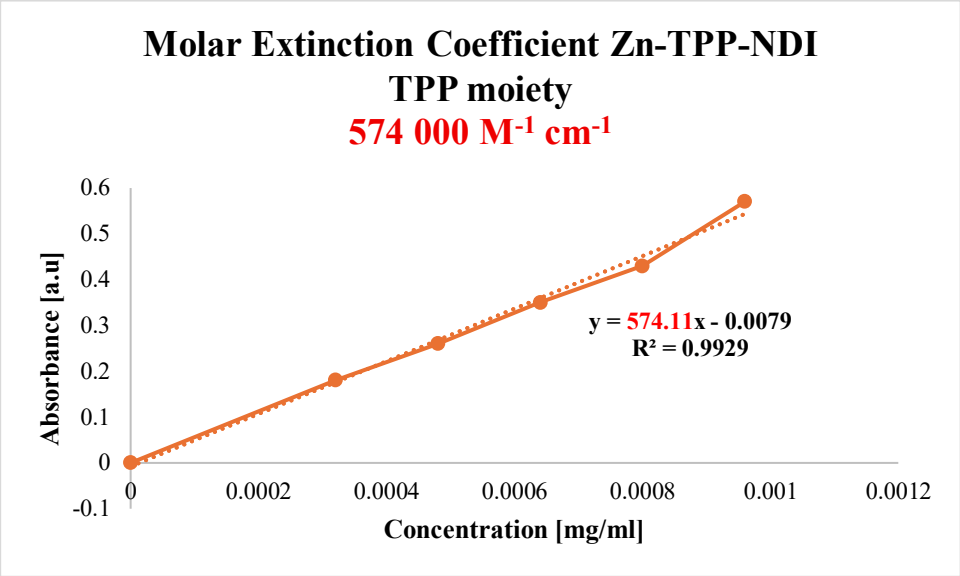


Figure SD6.7 Calculation of molar extinction coefficients for **TPP-NDI** and **Zn-TPP-NDI** attributed to the porphyrin moiety. The measurements were carried out in THF. The values were obtained at 416 and 424 nm for **TPP-NDI** ($\varepsilon = 5.96 \times 10^5$ $M^{-1}cm^{-1}$, at 416 nm) and **Zn-TPP-NDI** ($\varepsilon = 5.74 \times 10^5$ $M^{-1}cm^{-1}$, at 424 nm) respectively.

References:

[1]. Ghule, N. V., La, D. D., Bhosale, R. S., Al Kobaisi, M., Raynor, A. M., Bhosale, S. V., & Bhosale, S. V. (2016). Effect of Amide Hydrogen Bonding Interaction on Supramolecular Self-Assembly of Naphthalene Diimide Amphiphiles with Aggregation Induced Emission. ChemistryOpen, 5(2), 157–163. https://doi.org/10.1002/open.201500201

[2]. Tabrizi, L., McGarry, R., Turzanska, K., Varvarezos, L., Fallon, M., Brannigan, R., Costello, J. T., Fitzgerald-Hughes, D., & Pryce, M. T. (2024). Porphyrin-Polymer as a Photosensitizer Prodrug for Antimicrobial Photodynamic Therapy and Biomolecule Binding Ability. Biomacromolecules, 25(12), 7736–7749. https://doi.org/10.1021/acs.biomac.4c01011

[3]. Giannoudis, E., Benazzi, E., Karlsson, J., Copley, G., Panagiotakis, S., Landrou, G., Angaridis, P., Nikolaou, V., Matthaiaki, C., Charalambidis, G., Gibson, E. A., &

Coutsolelos, A. G. (2020). Photosensitizers for H_2 Evolution Based on Charged or Neutral Zn and Sn Porphyrins. Inorganic Chemistry, 59(3), 1611–1621. https://doi.org/10.1021/acs.inorgchem.9b01838

[4]. Kalyanasundaram, K., & Neumann-Spallart, M. (1982). Photophysical and Redox Properties of Water-Soluble Porphyrins in Aqueous Media. The Journal of Physical Chemistry, 86(26), 5163–5169. https://doi.org/10.1021/j100223a022